Title
Influence of Subsurface Spatial Variability on Ground Deformations in Earthquakes

Author
Bassal, Patrick C.

Publication Date
2022

Peer reviewed|Thesis/dissertation

Influence of Subsurface Spatial Variability on Ground Deformations in Earthquakes

By

PATRICK CHERINE BASSAL
DISSERTATION

Submitted in partial satisfaction of the requirements for the degree of

DOCTOR OF PHILOSOPHY

in

Civil and Environmental Engineering

in the

OFFICE OF GRADUATE STUDIES

of the

UNIVERSITY OF CALIFORNIA

DAVIS

Approved:

Ross W. Boulanger, Chair

Jason T. DeJong

Katerina Ziotopoulou

Committee in Charge

2022

“All models are wrong, but some are useful.”

– George E. P. Box

Abstract

Interlayered soil deposits with alternating and discontinuous beds of sands, silts, and clays underlie and interact with infrastructure worldwide. However, common simplified methods have been shown to typically over-predict earthquake ground deformations at interlayered sites, due to limitations in site characterization tools and methods, triggering and strain correlations, and analysis approaches. The most common of these simplified methods are one-dimensional liquefaction vulnerability indices (LVIs) that integrate strains and factors of safety against liquefaction triggering using empirical correlations with geotechnical site investigation data [e.g., cone penetration tests (CPTs) and borings]. Recent improvements of computational models for evaluating seismic soil responses have shown great value in resolving over-prediction biases.

This dissertation first provides a framework for site-specific CPT-based fines content (FC) correlations, which has posed significant uncertainty for both LVIs and nonlinear dynamic analysis (NDA) evaluations of liquefaction effects in interlayered deposits. Next, a system-level workflow that integrates detailed subsurface modeling with two-dimensional (2D) NDAs is utilized to evaluate the spatial extent and magnitude of ground deformation at three well-documented post-earthquake case history sites. These sites produced sediment ejecta, lateral spreading, and an extensional graben, within unique geologic environments in New Zealand, Taiwan, and California, respectively. Alternate geostatistical approaches for modeling subsurface spatial variability conditioned on available CPT data and geological details were considered, including deterministic, transition probability-based indicator simulation, kriging, and sequential Gaussian simulation (SGS) methods. The NDAs were performed with the Fast Lagrangian Analysis of Continua (FLAC) finite-difference program, with site-specific calibrations of the PM4Sand and PM4Silt constitutive models. The factors and neglected mechanisms that most contributed to prediction biases at each of these sites are explored, and improvements as well as limitations of the NDA workflow relative to LVIs and other simplified methods are discussed. This dissertation concludes with a holistic

discussion of insights gained from a larger set of post-earthquake NDA case studies, and future research needs for evaluating interlayered deposits in practice.

Acknowledgements

The research presented in this dissertation was made possible from the financial support of the National Science Foundation (award CMMI-1635398) and the California Department of Water Resources (contract 4600009751). Additional support was provided by the EERI/FEMA NEHRP Graduate Fellowship, ConeTec Graduate Student Award, Fugro West Fellowship, Richard and Kate Faulkner Fellowship, Elizabeth P. Wood Fellowship, and UC Davis Graduate Student Association. These organizations and donors are gratefully acknowledged for their generous support. Any opinions, findings, conclusions, or recommendations expressed in this dissertation are those of the authors and do not necessarily represent the views of these organizations.

I am grateful to have had many inspirational mentors and colleagues throughout my career who have motivated and supported my aspirations as I transitioned from an exciting career in industry to pursue my passions for research and teaching. Despite obstacles posed by the COVID-19 pandemic, I have fortunately been able to continue my work and strengthen my relationships among my family, friends, and UC Davis research community. This dissertation is ultimately attributed to the support of many of these relationships in my life.

I am sincerely grateful for the unwavering encouragement and guidance of my research advisor, Professor Ross W. Boulanger. He selflessly prioritized supporting my own professional growth and goals over our present research undertakings. Our research conversations have been academically enlightening; they went beyond soil mechanics theories and facts, and have helped me re-align my perspectives towards unbiased engineering judgement. He has been my ultimate role model as a passionate researcher, equitable educator, dependable collaborator, and motivational mentor, all while prioritizing family above all else.

Professor Jason T. DeJong has been my go-to for straightforward, honest advice in some of my important life decisions. I aspire to his steadfast characteristics of integrity and perseverance, and I am grateful for his unique and practical insights for this research. I am grateful to Professor Katerina Ziotopoulou, who has been an inspirational teacher and researcher, and has taught me to not lose sight of

my own unique path. I am grateful to Professor Alejandro Martinez who has supported me as both a friend and mentor.

I am grateful for my UC Davis friends and colleagues, especially fellow “Geo-Movers” Renmin Pretell, Francisco Humire, and Sumeet Sinha, as well as Ahmad Hassan, Mandeep Singh, and Matt Burrall. I am also grateful for the enjoyable collaborations among my research cohort peers, Tyler Oathes and Nick Paull. There are too many other friends to mention here that have made my time at UC Davis memorable.

I am grateful to my past coworkers and mentors who supported my growth as a geotechnical engineer, especially Jim French, Kevin Burlingham, and Alex Wright at Amec Foster Wheeler, and Monty Du, Ismail Karatas, Lijun Shi, Daniela Zellers, and Sissy Nikolaou at WSP. Again, there are too many other names I should mention here. I am also grateful for several impactful conversations I had with my good friends Erin Zeqja and Rouz Vakili, as I was considering my career move back to academia.

My passion for geotechnical research all started at UC Davis when I was an undergraduate research assistant for the “city block” soil-structure-interaction centrifuge study in 2011. I was fortunate to work with several inspiring mentors at the time, particularly Nick Trombetta, Josh Zupan, and Chandu Bolisetti, as well as Professors Gregg Fiegel, Bruce Kutter, Ben Mason, Jon Bray, and Tara Hutchinson. These collaborations, coupled with Professors Robb Moss’ and Gregg Fiegel’s intriguing courses at Cal Poly, prompted my initial interests in geotechnical earthquake engineering. I am truly thankful for these experiences and the opportunity to circle back to UC Davis several years later for a PhD.

Most importantly, I am indebted to the unconditional love and support of my family. To Mama, who devoted her life to raising me and my siblings to be the best versions of ourselves, and who instilled us with the highest values for faith, love, and education. To Baba, who taught us to stay proud of who we are without filters, and to keep a sense of humor. To my siblings, Freddy and Angela, it’s been great hanging out with you both often during my PhD.

Finally, to my wife Laura, you have essentially been my unlisted co-author with your love and support through all this work. It’s been a challenge, but also amazing working side-by-side towards our PhDs together. This dissertation would not have been possible without our much needed breaks together:

game nights of Pandemic, Dominion, and Ticket to Ride; television binges of the MCU, Casa de Papel, Parks and Rec, Ted Lasso, Stranger Things, etc.; guitar/piano duets; and spontaneous travel adventures. Above all, thank you for bringing us Arabella, the greatest gift for both of our lives. Arabella, the joy of watching you grow these past few months have pulled me away from my desk much more than I would have imagined. If you read this by the time you are old enough, you don't have to get a PhD in engineering like your parents, but it's not a bad option.

Table of Contents

1. Introduction

1.1. Overview

Case histories have historically been the catalyst and primary data source for understanding and evaluating earthquake ground deformations affected by the liquefaction of sand-like soils and cyclic softening of clay-like soils. In 1964, the Good Friday earthquake in Alaska and the Niigata earthquake in Japan first intrigued geotechnical engineers towards studying the destructive slope failures, bridge collapses, and building foundation displacements caused by transient and permanent ground deformations. Compilations of damage and soil investigations from worldwide post-earthquake datasets have contributed to simplified methods based on standard penetration test (SPT) and cone penetration test (CPT) correlations for the triggering potential of liquefaction and cyclic softening, that are still commonly used today (e.g., Seed et al. 1984, Youd et al. 2001, Boulanger and Idriss 2015). The depth-weighted integration of predicted factors of safety against liquefaction triggering and strains along individual borings or CPT soundings have been correlated with post-earthquake observations of ground deformations and surface manifestations for the development of Liquefaction Vulnerability Indices (LVIs) (e.g., Iwaski et al. 1978, Zhang et al. 2002, van Ballegooy et al. 2014). With more recent improvements of numerical tools for modeling seismic soil responses consistent with advanced laboratory tests, post-earthquake case studies continue to provide opportunities to evaluate site-specific failure mechanisms at a system-level, as well as validate and refine the use of such tools for engineering design.

Evaluations of post-earthquake ground deformations at case history sites in the 1999 Koceali earthquake, the 1999 Chi-Chi earthquake, and the 2010-11 Canterbury Earthquake Sequence (CES) have particularly exposed the tendencies of simplified liquefaction triggering and LVI methodologies to over-predict liquefaction effects at sites with interlayered soil deposits (e.g., Chu et al. 2006, Youd et al. 2009, Maurer et al. 2014, Beyzaei et al. 2019). Interlayering is taken broadly herein to account for sedimentary stratigraphies with discontinuous and alternating beds of distinct lithologies (e.g., sands, silts, and clays) at various scales (i.e., bed thicknesses from < 10 cm to > 1 m). While such interlayered deposits are common,

especially in fluvial and alluvial environments, the simplified formulations were traditionally developed for deposits with thick, uniform, and laterally extensive critical soil beds. Thus, several factors may contribute to the over-estimation bias of liquefaction effects within interlayered deposits, including limitations in site characterization tools and methods, triggering and strain correlations, and analysis approaches and neglected mechanisms (Boulanger et al. 2016). Table 1.1 describes specific limiting factors for each of these categories.

The use of advanced nonlinear dynamic analyses (NDAs) have shown great value in resolving the bias for over-predicting ground deformations at interlayered soil deposits (e.g., Cubrinovski et al. 2019, Boulanger et al. 2019). NDAs are computational models that account for coupled soil-fluid processes, site-specific ground motions, constitutive liquefaction and cyclic softening behaviors, and other systemic soil deposit interactions within a continuum-based framework. When applied in two- or three-dimensions (2D or 3D), they can additionally incorporate site geometry features and subsurface spatial variability to predict spatial distributions of complex ground deformation patterns. Thus, while still prone to limitations in the site characterization and engineering correlations, NDAs have the potential to explicitly model most of the neglected mechanisms listed as part of the third category of limiting factors in Table 1.1. However, the use of NDAs for evaluating seismic ground deformations in practice is typically reserved for high-budget engineering projects. A National Academy of Engineering committee (NASEM 2016) suggests that such mechanics-based computational models must be validated against well-documented field case histories prior to their acceptance for routine liquefaction assessments.

This dissertation presents a compilation of manuscripts addressing the subsurface characterization and numerical evaluations of three well-documented post-earthquake case history sites with interlayered soil deposits, and offers practical tools and workflows for the evaluation of similar sites. The motivation of this work is to evaluate, refine, and advocate state-of-art methodologies for the nonlinear dynamic analysis of sites with generally heterogeneous soils subjected to earthquakes. The work herein considers the influence of several of the limiting factors outlined in Table 1.1, with a primary focus on the influence of spatial variability. A framework is first provided for site-specific CPT-based fines content (FC) correlations,

which has posed large uncertainties for both simplified and NDA evaluations of liquefaction effects in interlayered deposits. An NDA evaluation of the Palinurus Road site next provides an illustrative example for the influence of both diffusion processes and dynamic responses on the spatial location of sediment ejecta manifestations. The subsequent NDA evaluations of Wufeng Site C and Wynne Avenue showcase alternative geologically-informed geostatistical methods [i.e., transition probability, and sequential Gaussian simulations (SGS)] for incorporating details and uncertainties of subsurface spatial variability, for predicting the spatial distribution of ground deformations. The modeling approaches considered in these case studies clarify the failure mechanisms that occurred at each case history site to greater detail than what could be inferred from LVIs and other simplified methods. Practical lessons for implementing NDAs and subsurface modeling techniques for interlayered sites are summarized, based on collective findings from the current case studies and previous studies.

1.2. Organization of Dissertation

This dissertation is organized into five main content chapters that each present a research manuscript that has been published or has been submitted for publication. Appendices are also provided with supplementary materials for the main content chapters, including additional figures and tables, as well as an example workflow of NDA and geostatistical methods used for this work.

- Chapter 2 presents a percentile matching framework for site specific CPT-based FC correlations. The framework reduces model and measurement errors inherent to common regression-based FC correlations. An example application of this method is provided, and its performance is evaluated for 13 sites with interlayered soil deposits affected by the 2010-11 CES. Appendix A includes supplementary figures detailing the framework performance for these 13 sites, relative to other correlation methods. A workflow for using this framework for both deterministic and probabilistic liquefaction evaluations is presented as a Jupyter Notebook in Python in Appendix D.
- Chapter 3 presents a 2D NDA evaluation of the Palinurus Road case history in the 2010-11 CES, where liquefaction-induced sediment ejecta was preferentially located along one side of a 160 m x

90 m grass field, located in a geologically complex estuarine environment. The subsurface stratigraphy was modeled deterministically to elucidate the influence of discontinuous silt and silty sand lenses on the dynamic response and post-earthquake pore water diffusion processes. The analyses explore the spatial distribution and relative magnitude of surface manifestations and reconsolidation, relative to subsurface liquefaction occurrences. Sensitivity analyses of various modeling choices were also assessed.

- Chapter 4 presents a 2D NDA evaluation of the Wufeng Site C case history in the 1999 Chi-Chi earthquake, where lateral spreading displacements of 45-205 cm were observed adjacent to a meandering stream channel. The fluvial floodplain and channel-fill sand subsurface deposits were modeled with 3D transition probability geostatistics to simulate the detailed lithological heterogeneity. The analyses explore the influence of geological features (e.g., soft clay lens near channel, connectivity of liquefied soils) on spatial patterns of ground displacements towards the channel face. Sensitivity analyses of various modeling choices were also assessed. Supplementary figures for this chapter are included in Appendix B.
- Chapter 5 supports the main content of Chapter 4 for the Wufeng Site C case history. It presents an investigation of alternative PM4Sand constitutive model calibrations for the post-liquefaction shear deformation rate. It presents a unique case where calibrations for significantly different post-liquefaction shear deformation rates had an insignificant influence on the overall system response and modeled ground deformations.
- Chapter 6 presents a 2D NDA evaluation of the Wynne Avenue case history in the 1994 Northridge earthquake, where a 12-m wide extensional graben with vertical offsets of 10-20 cm was observed along a shallow 1 to 2% sloping residential roadway. The distal alluvial fan subsurface deposit was modeled both deterministically, with uniform stratigraphic units, and geostatistically, with a conditional SGS framework for critical units. The analyses explore the advantages and limitations incurred with increased refinements of subsurface modeling choices. Sensitivity analyses of various

other modeling choices were also assessed. Supplementary figures for this chapter are included in Appendix C.

- Chapter 7 presents lessons learned from both the individual case studies and a collection of case studies at interlayered sites for the practical implementation of NDA and subsurface modeling techniques. Future research needs for better understanding the influence of spatial variability at interlayered sites and improving predictions of earthquake ground deformations at such sites, via both simplified and advanced methods, are discussed.
- Appendices A, B, and C present supplementary materials for chapters 2, 4, and 6, respectively.
- Appendix D presents an example workflow that was used for executing a set of stochastic NDAs with SGS simulations for the Wynne Avenue case study (Chapter 6). These workflows are included as instructional aids for practicing engineers and students who are interested in running similar analyses. CPT processing tools for the determination of representative material properties, conditioning data, and spatial correlations are presented through a series of annotated Jupyter Notebooks in Python. Input files for developing SGS simulations in the open-source geostatistics program SGeMs (Remy et al. 2009) are presented. The FISH language files used for executing a batch of 2D NDAs in the command-driven mode of FLAC 8.1 (Itasca 2019) are also presented.

Tables

Table 1.1. Factors affecting the prediction of liquefaction effects in interbedded soil deposits (after Boulanger et al. 2016).

Factor	Role
Limitations in site characterization tools and procedures	
Interface transitions	Penetration resistance (e.g., q_t) in sand is reduced near interfaces with clays or silts. I_c values increase in the sandy soils and decrease in the clays/silts near the interface.
Thin layer effects	Penetration resistance (e.g., q_t) reduced throughout sand layers less than about 1 m thick (with clays/silts on either side of the layer).
Graded bedding	In-situ tests measurements may not differentiate between material transitions that occur across distinct interfaces (e.g., erosional contacts) and material transitions that are gradual (e.g., beds with normal or reverse grading, or bed series in fining-upward or coarsening-upward patterns). Transition and thin layer effects in interbedded soils with graded bedding are not well understood.
Continuity of lenses	Large horizontal spacing of explorations may not enable the lateral continuity of weak or liquefiable layers to be evaluated or quantified.
Saturation	Presumption of 100% saturation below the groundwater table may underestimate cyclic strengths for partially saturated zones.
Limitations in correlations for liquefaction triggering or consequences	
Triggering correlations	Triggering correlations are not well constrained for intermediate soils with certain FC and PI combinations; CRR likely underestimated if treated as sand-like, and overestimated if treated as clay-like. Effects of age, stress & strain history, K_o, and cementation not explicitly accounted for.
Strain correlations	Correlations for estimating shear and volumetric strains have been developed primarily from data for sands or clays; the applicability of these correlations for intermediate soils is uncertain.
Limitations from analysis approaches and neglected mechanisms	
Spatial variability	The assumption that liquefiable layers are laterally continuous can contribute to over-estimation of potential liquefaction effects. Composite strength from nonliquefied and liquefied zones may limit deformations.
Thick crust layers	Thick crust layers can reduce surface manifestations of liquefaction at depth in areas without lateral spreading.
Dynamic response	Liquefaction of loose layers in one depth interval may reduce seismic demand on soils in other depth intervals.
Geometry & scale	The 2D or 3D scale of a deformation mechanism affects the dynamic response and role of spatial variability.
Diffusion	Seepage driven by excess pore pressures may increase or decrease ground deformations depending on stratigraphy, permeability contrasts, geometry, seismic loading, and other factors.

2. Site-Specific CPT-based Fines Content Correlations using Percentile Matching

Author's Note

The full content of this chapter has been published in the conference proceedings for *Geo-Congress 2022*. The author assisted in developing the percentile matching framework, performed and interpreted the analyses, and drafted the manuscript. Appendix A includes supplementary figures detailing the framework performance relative to other correlation methods for 13 sites with interlayered soil deposits affected by the 2010-11 CES.

Publication

Bassal, P. C., Boulanger, R. W., and DeJong, J. T. (2022). "Site-Specific CPT-based Fines Content Correlations using Percentile Matching." In Proc., Geo-Congress 2022. Reston, VA: ASCE. https://doi.org/10.1061/9780784484043.053.

Abstract

Correlations relating laboratory measured fines content (FC) from borehole samples with soil behavior type index (I_C) measurements from cone penetration tests (CPTs) have large uncertainties. Improved estimates of FC can be important for evaluating liquefaction resistance for use in simplified liquefaction vulnerability index (LVI) calculations or nonlinear dynamic analyses (NDAs). Application of regression-based correlations can be especially problematic in thinly interlayered soil deposits, where spatial variability of soil behavior is greater and measurements may be unreliable. This study introduces a user-informed approach to developing site-specific CPT-based correlations for FC estimation using accompanying borehole data, including visual classifications and laboratory test results. It uses a percentile matching framework to honor the cumulative distributions of FC and I_C. This approach has the potential to reduce biases related to spatial variability between adjacent CPT-boring pairs, insufficient or non-representative sampling, and model applicability. The approach is evaluated using data from several sites in Christchurch, New Zealand, and shown to generally improve LVI predictions for liquefaction manifestation during the 2010 Darfield and 2011 Christchurch earthquakes.

2.1. Introduction

Evaluation of liquefaction at sites with interlayered soil deposits depends on numerous factors related to site characterization tools and methods, correlations for liquefaction evaluation, and analysis approaches (Boulanger et al. 2016). Uncertainty and variability associated with these factors contribute to the false predictions observed in case study evaluations using liquefaction vulnerability indices (LVIs) or other semi-empirical approaches at both a regional scale (e.g., van Ballegooy et al. 2014, Maurer et al. 2019) and a site-specific scale (e.g., Chu et al. 2006, Boulanger et al. 2018, Beyzaei et al. 2019). While better accounting for realistic mechanisms, even site-specific nonlinear dynamic analyses (NDAs) heavily rely on site characterization assumptions and simplifications as well as liquefaction resistance correlations, which may pose sufficient uncertainty to alter the evaluated consequences (e.g., Cubrinovski et al. 2018, Boulanger et al. 2019, Bassal and Boulanger 2021).

One influencing factor is the apparent dependence of liquefaction resistance on the presence of non-plastic or low-plasticity fines (e.g., Suzuki et al. 1997, Robertson and Wride 1998, Idriss and Boulanger 2008). The effect of fines is typically modeled by an estimate of the fines content (FC; i.e., percent of dry soil mass passing a 75 μm sieve), which is obtained from laboratory sieve or laser diffraction tests. Alternatively, cone penetration test (CPT) data have been used to infer soil characteristics, including FC, from CPT measurements or indices like the soil behavior type index (I_C) (e.g., Robertson and Wride 1998; RW98). FC-I_C correlations based on global datasets have large uncertainties, which can be potentially reduced using site-specific calibrations to FC data from boring samples (e.g., Boulanger and Idriss 2014; BI14).

The efficacy of FC-I_C correlations and their implications for liquefaction triggering assessments have been evaluated in several recent studies. McLaughlin (2017) found that the site-specific BI14 correlation typically reduced LVI over-predictions for 31 sites in Christchurch, New Zealand. Beyzaei et al. (2019) evaluated detailed boring logs and mini-CPTs (i.e., 5 cm^2 area) for thinly interbedded deposits in Christchurch, and discussed the influence of bulk sampling on FC measurements and CPT spatial averaging on I_C readings. They suggest that liquefaction assessments at these deposits should emphasize variations of

soil hydraulic conductivity and plasticity, rather than FC. Maurer et al. (2019) evaluated the liquefaction potential index (LPI) for thousands of case studies from three earthquakes in Christchurch to compare general FC-I_C correlations (i.e., RW98 and BI14 without site-specific calibration) to a regional trend fitted to local data. Based on receiver operator characteristic (ROC) analyses comparing liquefaction predictions to observations, they concluded that using the regional FC-I_C trend did not sufficiently reduce false LPI predictions to justify its use over general correlations for typical projects.

The current study proposes a user-informed approach based on a percentile matching framework for developing site-specific FC-I_C correlations for use in liquefaction evaluations. The approach provides flexibility for the user to use judgment in combining quantitative and qualitative data to overcome potential biases caused by data limitations. Uncertainties and limitations affecting development and application of FC-I_C correlations are first briefly reviewed. The percentile matching framework is detailed and an example application at a Christchurch site is presented. Finally, the method is tested for its influence on liquefaction vulnerability predictions at several other Christchurch sites during the 2010 Darfield and 2011 Christchurch earthquakes.

2.2. Uncertainties in Regression-Based Correlations

Current regression-based FC-I_C correlations are based on case study datasets that exhibit a high degree of scatter. For instance, Maurer et al. (2019) compiled data from the New Zealand Geotechnical Database (NZGD) for 2620 FC samples from adjacent (i.e., < 5 m apart) CPT-boring pairs across Christchurch. Fig. 2.1 shows the mean and one standard deviation bounds of I_C that they measured within a 0.3 m interval vertically centered with each associated boring sample. A least squares regression was performed on this data by Maurer et al. (2019) to obtain the regional correlation shown. Also, shown are the RW98 and BI14 general correlations. The differences in these relationships are reflective of the different datasets they represent.

Boulanger and Idriss (2014) introduced an FC fitting parameter (C_{FC}) that could be adjusted to site-specific data for individual geologic strata. The recommended method for calibrating C_{FC} is by regressing site-specific I_C against FC, while holding a constant linear slope per the formula:

$$I_C = (FC + 137)/80 - C_{FC} \quad \text{(Eq. 1)}$$

The C_{FC} fitting parameter uniformly shifts the I_C values above or below a regression line fitted to global data considered by BI14, so that C_{FC}=0 is the mean general correlation and C_{FC}= ±0.29 represents one standard deviation bounds. Also, C_{FC}=0.13 provides a close approximation of the Maurer et al. (2019) regional correlation (Fig. 2.1).

While allowing for a site-specific calibration, the BI14 methodology is still prone to several uncertainties that affect all regression-based FC-I_C correlations, specifically at heterogeneous or interlayered soil deposits. These uncertainties can be grouped into categories used by Phoon and Kulhawy (1999) for general geotechnical parameterization: (1) inherent soil variability, (2) measurement errors, and (3) transformation uncertainty.

2.2.1.Inherent Variability

Natural soil variability is problematic for developing an FC-I_C dataset from CPT-boring pairs within a heterogeneous soil deposit. Even at close distances (e.g., < 5m), lateral differences in lithology caused by within-bed variability (e.g., gradation, soil behavior) or between-bed variability (e.g., discontinuous or inclined bed transitions) may influence the mapping of FC values from boring samples to the I_C measurements of nearby CPT soundings. Seemingly minor elevation misalignments may produce mismatches when there is frequent interlayering from depositional successions.

2.2.2.Measurement Error

Measurement errors are typically related to bulk averaging, sampling bias, and equipment and operator errors. Bulk averaging can refer to both the CPT's spatial smoothing of soil resistances over a

volume of soil surrounding the cone tip or the laboratory FC testing of a bulk sample obtained from a boring. In both cases, thin soil interlayers or interface transitions are not properly characterized, such that the measurements represent averages over some volume rather than values for particular points. Sampling bias may occur when limited data is available for obtaining a site-specific correlation, and the number and distribution of collected samples is insufficient to represent the mean FC of a stratum. Other measurement errors may occur due to CPT inconsistencies (e.g., variable push rate, probe size, cone condition, operator handling) and imprecise laboratory readings of FC.

2.2.3. Transformation Uncertainty

The transformation uncertainty refers to the inherent uncertainty in transforming I_C measurements to FC. The I_C metric possesses shortcomings as a sole predictor of FC and is influenced by other attributes not considered by current correlation models (e.g., plasticity, gradation, density, cementation, stress history, organic content, consolidation stress, saturation, layer sequencing, cone tip and sleeve details and wear). The best form for the FC-I_C correlation for a specific site or region may not be well constrained by data and may not be identified by certain regression approaches. Finally, the spatial extent and geologic conditions for which a regional or site-specific model may apply is often not well-understood.

2.3. Percentile Matching Approach

A user-informed approach to developing site-specific FC-I_C correlations is introduced based on a "percentile matching" framework that fixes FC estimates at selected representative percentiles to I_C measurements at the same percentiles for individual geologic strata. The FC estimates can be obtained from both laboratory measurements and visual classifications recorded on borehole logs, thus maximizing the use of available site data. The developed trend is intended to honor the empirical cumulative distribution of FC and I_C within individual geologic strata with relatively consistent soil characteristics. This approach has the potential to reduce uncertainty related to variability between nearby CPT-boring pairs, selective and insufficient sampling, and model applicability. The required calculations are easily performed in a

spreadsheet or coding software, but the calibration inputs are best supported by non-quantitative data and engineering judgement so that full automation may not be possible or desirable.

The method requires the availability of at least one closely spaced (i.e., about 3 m or less) CPT-boring pair and sufficient FC data to develop an understanding of some of the intricacies of the geologic stratum of interest (e.g., interlayering, gradational changes, transition locations). First, I_C values ($I_{C,meas}$) over the full thickness of the stratum should be calculated from the CPT tip and sleeve measurements. A cumulative distribution function (CDF) of all I_C values less than a cut-off value ($I_{C,cut\text{-}off}$) for liquefaction susceptibility (e.g., $I_{C,cut\text{-}off}$ =2.6 per RW98) should then be obtained by simply rank ordering each susceptible I_C value and assigning a percentile value (over the total number of values) to each. Similarly, only FC data from samples susceptible to liquefaction (e.g., little to no plasticity) should be considered. Next, three successively increasing percentile values (P_1, P_2, and P_3) and associated FC values (FC_1, FC_2, and FC_3) are selected to approximate the expected distribution of FC over the full thickness of liquefiable soils in the stratum. The I_C CDF should then be used to obtain the associated I_C values (I_{C1}, I_{C2}, and I_{C3}) for the same three percentiles (P_1, P_2, and P_3). Finally, the functional form for estimating FC (in percent) for the stratum of interest from $I_{C,meas}$ is calculated as:

$$FC = (FC_2 - FC_1)/(I_{C2} - I_{C1}) \times (I_{C,meas} - I_{C2}) + FC_2 \quad \text{for } I_{C,meas} \leq I_{C2}$$

$$FC = (FC_3 - FC_2)/(I_{C3} - I_{C2}) \times (I_{C,meas} - I_{C2}) + FC_2 \quad \text{for } I_{C,meas} > I_{C2} \qquad \text{(Eq. 2)}$$

Computed FC are capped to $0 \leq FC \leq 100\%$. The resulting correlation results in a pair of positively sloped piecewise lines for the susceptible region, which are anchored at the three modeled FC and I_C points and allowed to change in slope at either side of the middle point (FC_2-I_{C2}).

The initial determination of the three percentiles and associated FC values requires judgment, but can be well-guided by considering all available data. For example, if the susceptible soils can be grouped into two or three characteristically distinct soil layer groups, a mean expected FC can be assigned to each group at percentiles that honor their accumulated thicknesses. Descriptions of thin or interbedded layers

and their prevalence (i.e., frequency and thickness) from boring log notes, as well as interfaces delineated from CPT readings, can be used to assist in segregating soil groups. If the laboratory FC values are from samples that are not representative of the stratum (e.g., targeting silty lenses within an otherwise clean sand deposit), then visual classifications on the borehole logs can be used to develop a more representative CDF for FC. If sufficient representative FC samples are available, the parameters can be chosen to match the actual percentiles (i.e., CDF) of FC measurements.

2.4. Example Application: Shirley Intermediate School

An application of the percentile matching methodology and a comparison to other state-of-practice approaches is presented for a site at Shirley Intermediate School in Christchurch. At this site, no liquefaction surface ejecta was observed after the September 2010 M7.1 Darfield (*Sep2010*) earthquake, and moderate amounts of liquefaction ejecta were observed after the February 2011 M6.2 Christchurch (*Feb2011*) earthquake (Tonkin & Taylor 2015), with approximate peak ground accelerations (PGAs) of 0.19 and 0.38 g, respectively (Bradley and Hughes 2012a). The ground water table is assumed from nearby boring logs to be located 2.0 m below the ground surface during the investigation and seismic events.

Data obtained from the NZGD for a seismic CPT (SCPT 57366) and adjacent sonic borehole (BH 57258), both conducted in August 2015, are shown in Fig. 2.2. The NZGD indicates coinciding coordinate locations for the CPT and boring, so they are assumed to be spaced less than 3 m apart. The leftmost graph indicates the cone tip resistance normalized by atmospheric pressure (q_{tN}) with depth, categorized for I_C above and below an assumed $I_{C,cut\text{-}off}$ =2.6. The next graph shows I_C with depth, with shaded regions bounding a 0.3 m thick interval for each boring sample. The two graphs at the right of Fig. 2.2 indicate the FC with depth from the boring, and a simplified version of the boring log with FC, plasticity index (PI), and descriptions of soil type and gradation characteristics. The 6 m thick portion of the Christchurch formation from 3.2 to 9.2 m is the most critical stratum for liquefaction evaluations.

Three FC-I_C correlation models were evaluated for the critical stratum, referred to as: (1) BI14 regional, (2) BI14 site-specific, and (3) percentile match. The BI14 regional trend uses Equation 1 with

C_{FC}=0.13 to match the Christchurch-specific correlation by Maurer et al. (2019). The BI14 site-specific trend uses a site-specific C_{FC}=0.28 determined by linearly regressing the FCs of available soil samples with the median I_C value from each 0.3 m interval considered (Fig. 2.2). The percentile match trend uses the approach previously described to assign FC values of 7, 24, and 41% to percentiles of 37, 75, and 88%, respectively. These values were determined from a close examination of the CPT and boring log descriptions. About 75% (i.e., 4.5 m) of the total liquefiable stratum thickness is composed of sand with trace silt, and the remaining 25% (i.e., 1.5 m) is either logged as siltier (e.g., sand with some silt, silty sand) or represented as such by q_{tN} fluctuations. The FC=29% sample taken at a depth of 3.8 m appears to represent a bulk average of nearby material, inclusive of a 50 mm sandy silt interlayer. Bulk averaging may have also influenced the FC sample at a depth of 4.6 m, near a sandy silt to sand transition interface. Thus, the sand portion of the stratum can be represented by a median FC_1=7% (informed by the sample at 5.8 m) at P_1=37% (halfway from 0 to 75%), and the siltier portion can be represented by a median FC_3=41% (informed by the sample at 6.7 m) at P_3=88% (halfway from 75 to 100%). Also, FC_2=24% was judged to represent material at the interface between both portions with P_2=75%.

The FC-I_C correlation models and FC data for the critical stratum are presented in Fig. 2.3. The top left graph represents the FC-I_C trends plotted in linear scale, the bottom left graph depicts the CDFs of FC based on the CPT data for each model and from the FC samples, and the right graph shows the FC estimates with depth for each model. The site-specific BI14 model over-predicts the FC throughout the stratum (which is predominantly sand with only trace silt) because two of the four FC measurements were biased by the presence of thin silt seams or silt interfaces. This case illustrates how automated calibration processes can lead to biases (high or low) if the representativeness of the lab data relative to the visual logs is not checked. The regional BI14 model predicts FC throughout the stratum that are more consistent with the visual classifications on the borehole log, while under-predicting the FC that would be expected in the silt lenses. The percentile match has shallower FC-I_C slopes than the BI14 models, which causes more rapid changes in FC with changes in I_C and thus predicts higher FC at the various silt lenses.

The liquefaction vulnerability estimated at the site during the *Sep2010* and *Feb2011* events for the different FC-I_C correlation models is shown in Fig. 2.4. The middle two graphs depict two depth-accumulated LVIs: the Liquefaction Potential Index (LPI; Iwasaki et al. 1978) and Liquefaction Severity Number (LSN; van Ballegooy et al. 2014). The right graph shows the magnitude and stress normalized cyclic resistance ratio (CRR) relative to the normalized cyclic stress ratio (CSR) from both events. All calculations were performed with the stress-based liquefaction triggering framework of Boulanger and Idriss (2014). A maximum depth of 10 m is shown, since liquefaction is negligible below the critical stratum. All models assume the BI14 regional correlation above the critical stratum. Liquefaction triggering and corresponding increases in LPI and LSN are expected at depths where the CSR exceeds CRR. Binary LPI and LSN thresholds of 8 and 16 are respectively assumed to separate between "none to marginal" and "moderate to severe" predictions of liquefaction effects (McLaughlin 2017). For the *Sep2010* event, all models correctly predict none to marginal liquefaction (i.e., LPI=0-2, LSN=4-8). For the *Feb2011* event, moderate to severe liquefaction is correctly predicted by the BI14 regional and percentile match models (i.e., LPI=10-13, LSN=19-21), but is significantly under-predicted by the BI14 site-specific model (i.e., LPI=5-6, LSN=11-12). The BI14 site-specific model was biased by the limited, non-representative FC lab test data toward over-predicting FC elsewhere in the profile. The BI14 regional model predicted slightly greater LVIs than the percentile match model, with the greatest differences occurring at depths near 9.0, 7.3, and 6.6 m where percentile matching estimated a higher FC in the silty sands and silts.

2.5. Evaluation at Selected Christchurch Sites

The LPI and LSN for twelve additional interlayered Christchurch sites were evaluated for the *Sep2010* and *Feb2011* events, based on similar assumptions considered in the preceding example. The sites were selected from a larger database of level-ground free-field case histories examined by Cubrinovski et al. (2019), and were ensured to have sufficient FC samples for a meaningful site-specific analysis (i.e., four or more samples for each critical stratum). The FC-I_C percentile matching approach was individually tuned to the site investigation data (NZGD) for each site. Fig. 2.5 compares LPI (left figure) and LSN (right

figure) predictions obtained from the BI14 regional model and percentile matching approach for all 26 cases considered (i.e., 13 sites in 2 events). Each case is denoted by whether liquefaction was or was not observed at the site. The LSN and LPI prediction thresholds are indicated by dashed lines, and the similarity in predictions between FC-I_C models is indicated by the 1:1 sloped line. It can be observed that (1) all of the "liquefaction" cases correctly predicted by the BI14 regional model plot relatively close to the 1:1 line, indicating similar predictions by percentile matching; (2) the majority of "no liquefaction" cases over-predicted by the BI14 regional model plot below the 1:1 lines for both LVIs, indicating that percentile matching generally improved predictions of these cases; and (3) only 2 to 4 of the cases over-predicted by the BI14 regional model are corrected to plot below the LVI thresholds (i.e., none to marginal liquefaction) after percentile matching. As expected, percentile matching only corrected prediction categories for cases that were already near the LVI prediction thresholds (e.g., LPI ≈ 5-13, LSN ≈ 12-22) with the BI14 regional model.

Alternative procedures for estimating FC would not be expected to significantly improve the LVI-based predictions of liquefaction manifestation categories for cases further from the thresholds, especially considering the greater influence of other significant limitations in the site characterization data (e.g., thin-layers, transition zones, saturation), engineering correlations (e.g., triggering, shear and volumetric strains), and analysis methods (e.g., neglected consideration of dynamic response, pore water diffusion effects) (e.g., Boulanger et al. 2016, Cubrinovski et al. 2018). It is similarly not surprising that the ROC analyses of the larger regional dataset using alternative FC estimation procedures did not show improved aggregate predictions (e.g., Maurer et al. 2019) given the secondary role of FC estimates relative to all other sources of uncertainties and bias in LVI methodologies.

Improved approaches for developing site-specific FC-I_C relationships can have greater effects on the results of NDA studies where many of the limitations of LVI analysis methods are avoided. Several NDA case studies at interlayered sites have shown that minor changes to the FC-dependent clean sand corrected tip resistance (q_{c1Ncs}), within a range that is consistent with the differences in the FC-I_C correlation

models evaluated herein, could have a minor to moderate influence on the ground motion response and liquefaction effects (e.g., Boulanger et al. 2019, Bassal and Boulanger 2021).

2.6. Conclusion

A user-informed, percentile matching approach for developing site-specific FC-I_C relationships was described. The percentile matching framework considers the distributions of FC and I_C within individual strata and has the potential to reduce model errors due to spatial soil variability between CPT-boring pairs. The approach provides flexibility for users to exercise judgment in combining quantitative and qualitative borehole data, including visual descriptions of gradations, soil types, thin interbeds, and layer transitions, thereby providing an opportunity to reduce measurement errors (e.g., bulk averaging, sampling bias).

Development of site-specific FC-I_C relationships depends on the sufficiency and quality of site characterization data and the user's judgments in combining qualitative and quantitative data. The potential benefits of developing site-specific FC-I_C relationships for a liquefaction assessment can be first evaluated using general correlations in sensitivity studies (e.g., BI14 with C_{FC} = -0.29, 0, 0.29) before undertaking the additional engineering effort. Application of the percentile matching approach to several liquefaction case studies has produced minor to moderate improvements in LVI and NDA predictions, consistent with expectations that improved FC estimates are just one of several factors affecting liquefaction evaluations.

2.7. Acknowledgements

The authors appreciate the financial support of the National Science Foundation (award CMMI-1635398) and California Department of Water Resources (contract 4600009751) for different aspects of the work presented herein. Any opinions, findings, conclusions, or recommendations expressed herein are those of the authors and do not necessarily represent the views of these organizations. The authors benefited from discussions with Max Rudolph on the proposed method.

Figures

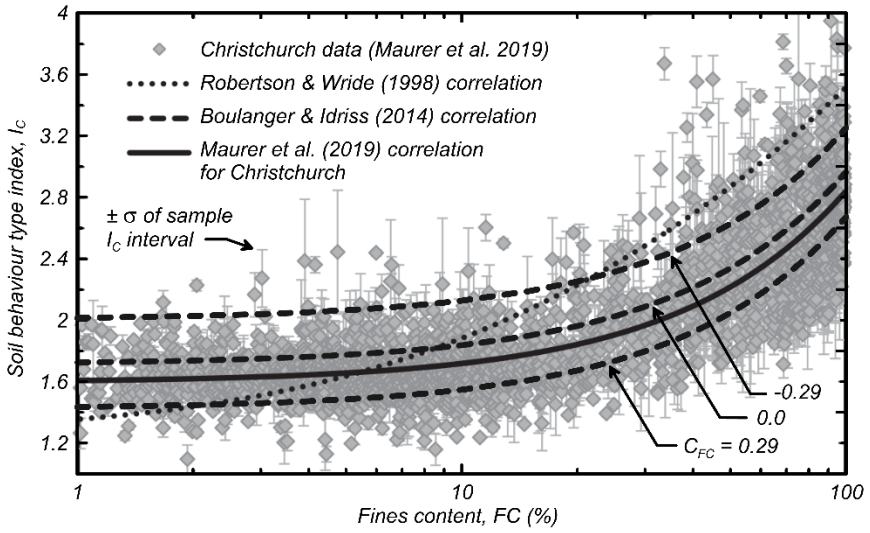

Figure 2.1. FC-I_C correlations and Christchurch data (modified from Maurer et al. 2019).

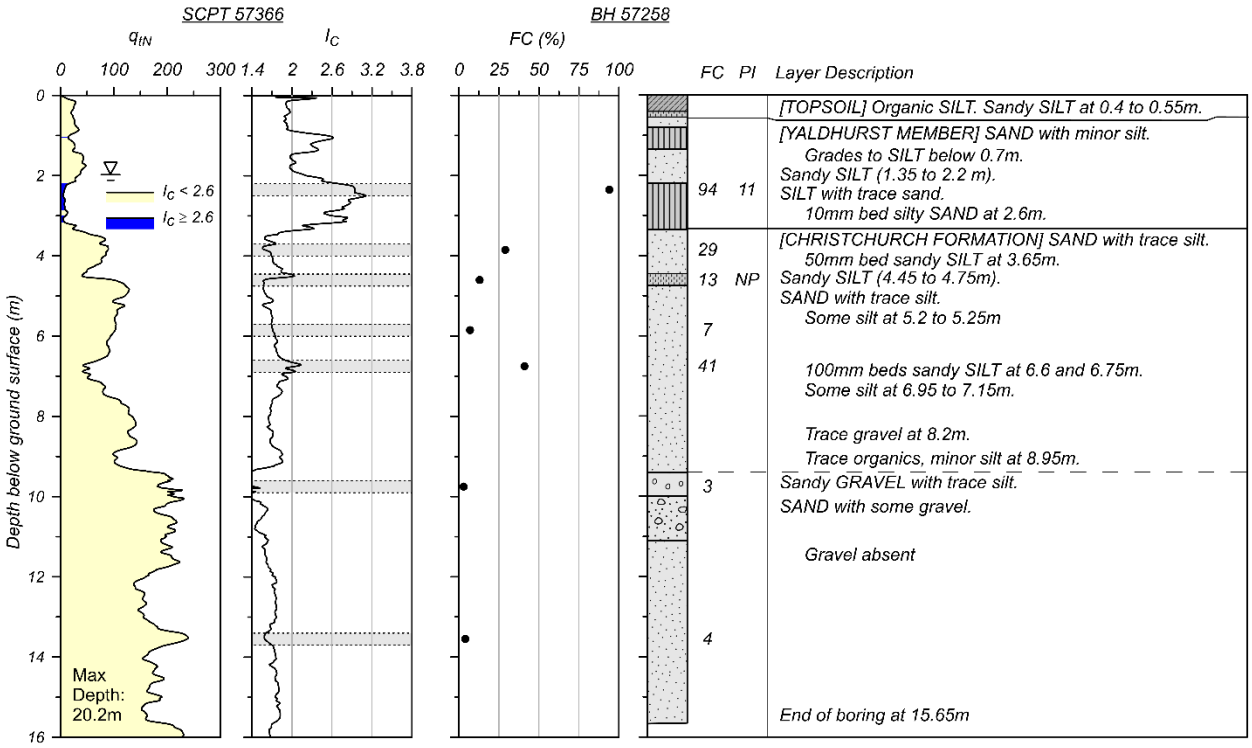

Figure 2.2. Adjacent CPT and boring data from Shirley Intermediate School.

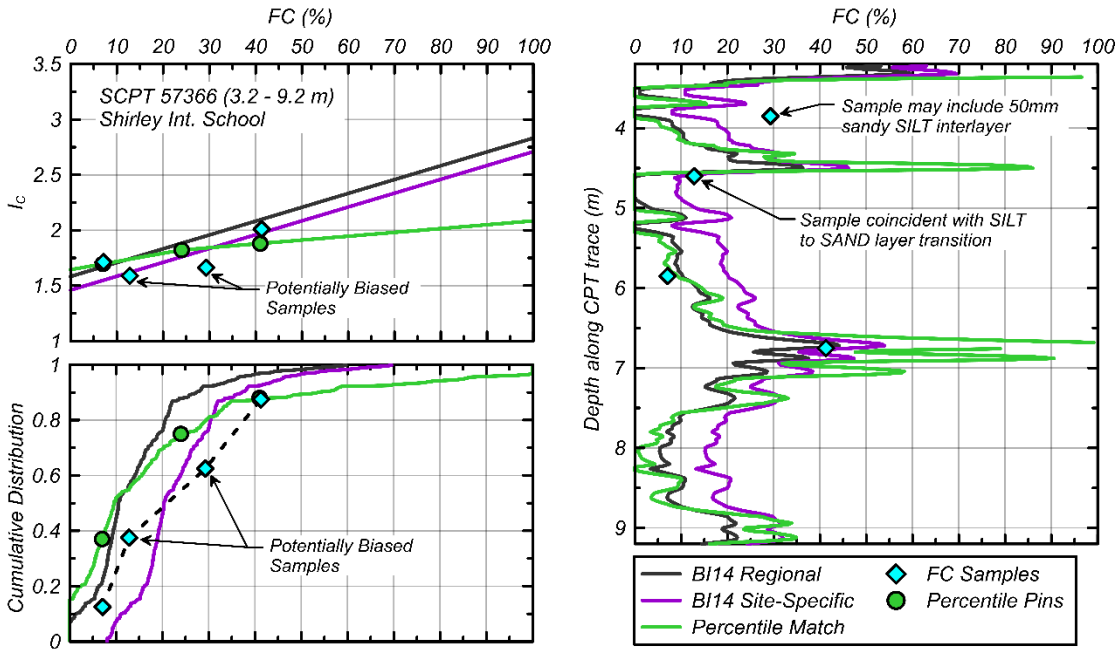

Figure 2.3. Comparison of FC-I_C models for critical stratum at Shirley Intermediate School.

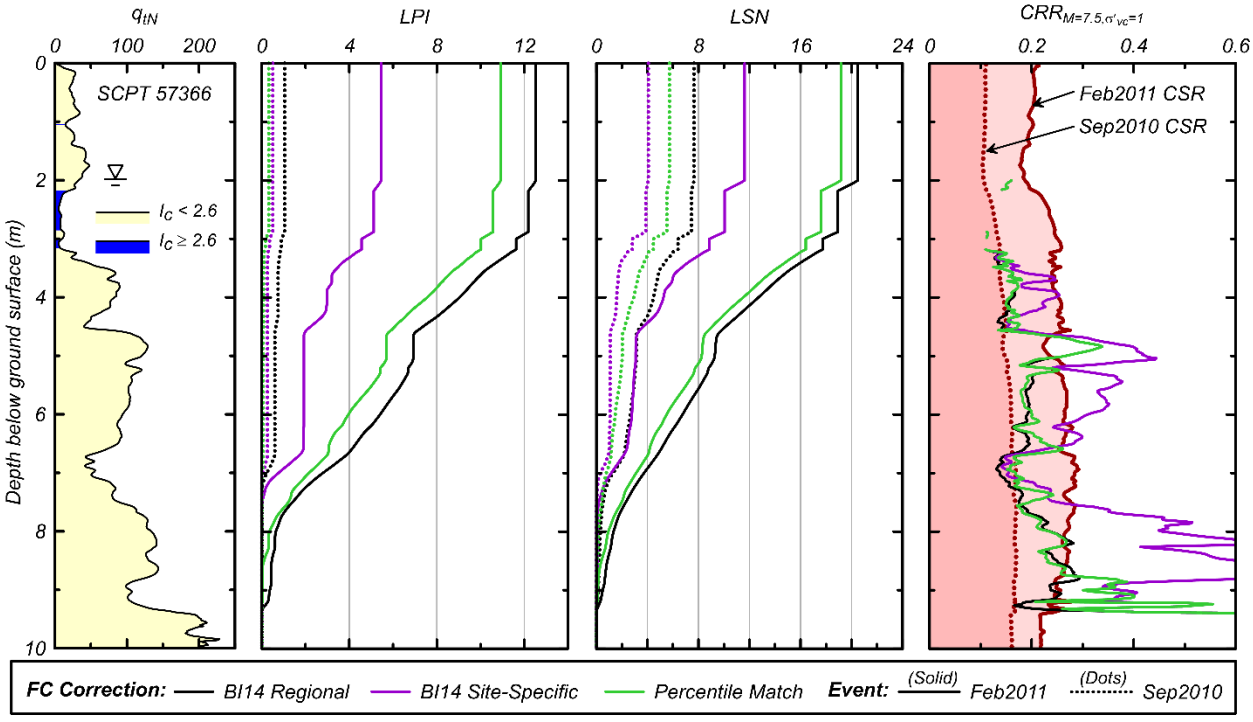

Figure 2.4. LVI results for different FC-I_C models at Shirley Intermediate School.

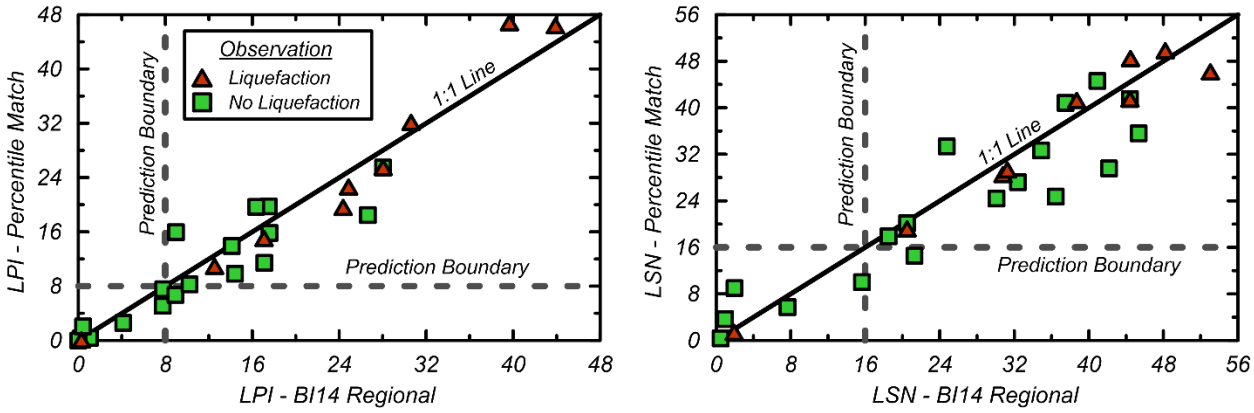

Figure 2.5. Comparisons of LPI and LSN predictions from the BI14 regional and percentile match FC-I_C models for thirteen Christchurch sites in the *Sep2010* and *Feb2011* events.

3. System Response of an Interlayered Deposit with Spatially Preferential Liquefaction Manifestations

Author's Note

The full content of this chapter has been published in the *Journal of Geotechnical and Geoenvironmental Engineering*. The author performed and interpreted the analyses, and drafted the manuscript.

Publication

Bassal, P. C., and Boulanger, R. W. (2021). "System Response of an Interlayered Deposit with Spatially Preferential Liquefaction Manifestations." Journal of Geotechnical and Geoenvironmental Engineering, 147 (12): 05021013. doi:10.1061/(ASCE)GT.1943-5606.0002684.

Abstract

The Canterbury Earthquake Sequence produced a spatial pattern of liquefaction-induced surface ejecta at an open field along Palinurus Road in Christchurch, New Zealand, that would not be expected based on simplified liquefaction evaluation procedures. Half the site discharged sand boils and the other half did not. Two-dimensional fully-coupled nonlinear dynamic analyses (NDAs) are performed to examine why simplified one-dimensional liquefaction vulnerability indices (LVIs) over-estimated liquefaction manifestations at this site for the 2010 Darfield and 2011 Christchurch earthquakes and did not distinguish between areas with and without surface ejecta. The NDAs use the PM4Sand and PM4Silt constitutive models for sand-like and clay-like portions of the subsurface, respectively, within the FLAC finite difference program. Material parameters are obtained from in-situ geophysical and cone penetration test (CPT) data. A sensitivity study is performed to assess the influence of: (1) representative soil property selections and the use of a CPT inverse filtering procedure to correct for thin-layer and transition zone effects, (2) ground motions developed by two distinct methods (i.e., recordings and physics-based simulations), and (3) model assumptions affecting diffusion during reconsolidation. Ground deformations and flow patterns during and after ground shaking are examined. The results provide insights on how

stratigraphic details and other factors can affect the system response and dictate the degree and extent of liquefaction surface manifestations.

3.1. Introduction

Numerous case history studies (e.g., Chu et al. 2006, Maurer et al. 2014, van Ballegooy et al. 2014, Beyzaei et al. 2018b, Cubrinovski et al. 2019, Boulanger et al. 2019) have shown that simplified liquefaction analysis methods can systematically over-estimate the degree and extent of liquefaction surface manifestations, such as sand boils or ground deformations, in specific geologic settings or site conditions. The simplified liquefaction analysis methods examined include a number of one-dimensional (1D) liquefaction vulnerability indices (LVIs) that generally involve depth-weighted integration of predicted strains or factors of safety against liquefaction triggering (as obtained from a stress-based liquefaction triggering analysis) using data from individual borings or cone penetration test (CPT) soundings. Several of these past studies have shown 1D LVIs tend to over-estimate liquefaction effects for deposits where the sedimentary stratigraphy includes interbedded or alternating beds of sands, silts, and clays.

Several factors may contribute to a tendency for over-estimating liquefaction effects in deposits with interbedded or alternating beds of sands, silts, and clays (Boulanger et al. 2016). These include limitations in: (1) site characterization tools and methods, (2) liquefaction triggering or deformation correlations, and (3) analysis approaches and neglected mechanisms. The first set of limitations includes challenges in characterizing thin layers, transition zones, graded bedding, lateral discontinuities, and partial saturation near the water table. The second set includes the uncertainties and biases associated with correlations for cyclic resistance ratio (CRR), and shear and volumetric strains, which are not well-constrained for intermediate soils (e.g., low-plasticity silty sands, clayey sands, or sandy silts) and do not typically account for the effects of age, stress-strain history, cementation, and anisotropy. The third set includes difficulties in addressing spatial variability, pore pressure diffusion, deformation geometries, and the dynamic response. The over-estimation bias of 1D LVIs for these types of deposits is likely due to a combination of the above limitations, depending on the available data, and intricacies of the stratigraphy

and soil characteristics for each deposit. By better accounting for several of these limitations, nonlinear dynamic analyses (NDAs) can provide an improved basis, relative to LVIs, for interpreting case histories, as demonstrated by Cubrinovski et al. (2019), Hutabarat and Bray (2019), and Boulanger et al. (2019). NDAs can account for site-specific ground motions and realistic cyclic stress-strain responses; all of which are neglected by LVIs. When performed with a two or three-dimensional (2D or 3D) model, NDAs can additionally account for spatially variable subsurface profiles, pore pressure diffusion, and ground deformation patterns.

This paper describes a 2D NDA study of a site located along Palinurus Road in Christchurch, New Zealand, where: (1) the soil profile includes laterally continuous and discontinuous layers of sands and clayey silts, (2) surficial manifestations of liquefaction (i.e., sand boils) exhibited a preferential spatial pattern, and (3) 1D LVIs were shown by Yost et al. (2019) to over-estimate liquefaction manifestations during the 2010 Darfield and 2011 Christchurch earthquakes. Preliminary NDA results for this case study were presented by Bassal et al. (2020), which showed that accurate modeling of the dynamic response and pore pressure diffusion patterns (mechanisms neglected by 1D LVIs) was necessary to explain the post-earthquake observations. This current work refines the previous study with more detailed examination of how the spatial and temporal responses during and after the 2010 Darfield and 2011 Christchurch earthquakes are influenced by the input ground motions and the NDA model assumptions that affect excess pore water pressure diffusion. The site performance, subsurface conditions, and results of updated 1D LVI analyses are described first. The NDA procedures, constitutive model calibrations, and input ground motions are then described. The NDAs are performed using FLAC (Itasca 2019) with the user defined constitutive models PM4Sand and PM4Silt. Detailed NDA results are presented for a baseline set of parameters, followed by results of parametric studies examining sensitivity to representative property selections and different modeling assumptions. The NDA results are used to evaluate how the dynamic response, ground distortion, and pore pressure diffusion patterns are influenced by details of the subsurface stratigraphy and how such patterns may relate to different liquefaction manifestations across this site during these earthquakes. Insights on system response mechanisms provided by the NDA results are shown to be

generally robust despite the uncertainties and limitations in the analysis results and field observations. Implications of these results for informing the interpretation of liquefaction case histories and using NDAs and LVIs in practice are discussed.

3.2. Palinurus Road Site

The 2010-2011 Canterbury Earthquake Sequence (CES) produced a series of strong earthquakes that affected the Canterbury region of New Zealand between September 2010 and December 2011. The CES resulted in well-documented and widespread liquefaction damage throughout the city and adjoining suburbs of Christchurch. Fault projections (Beavan et al. 2012) of the four most destructive events of the CES are shown in Fig. 3.1. These events are the 4 September 2010 M_w 7.1 Darfield earthquake, the 22 February 2011 M_w 6.2 Christchurch earthquake, the 13 June 2011 M_w 5.3 and M_w 6.0 earthquakes, and the 23 December 2011 M_w 5.8 and M_w 5.9 earthquakes (these events are hereafter labeled as *Sep2010, Feb2011, Jun2011, and Dec2011*). Also mapped is the Riccarton High School Strong Motion Station (RHSC SMS), and the location of the Palinurus Road site (-43.5512°, 172.6885°).

The Palinurus Road site is an approximately 90 m by 160 m rectangular and level grass field in the Woolston suburb of Christchurch. The site exhibited little to no evidence of liquefaction during the *Sep2010* and *Dec2011* events, but produced several moderate sand boils during the *Feb2011* and *June2011* events. As depicted in the aerial photograph of Fig. 3.2, the sand boil ejecta extents were primarily limited to the northeast portion of the site (*NE;* above the dashed line of Fig. 3.2) during the *Feb2011* event. A similar spatial extent of liquefaction was observed following the *June2011* event. Practically no sand boils emanated on the southwest portion (*SW;* below the dashed line of Fig. 3.2) during any of the events.

Estimates of the moment magnitude (M_W), rupture distance (R_{rup}), peak ground acceleration (PGA), and observed performance of the Palinurus Road site in the aforementioned four CES events is summarized in Table 3.1. The PGA was determined based on contours from Bradley & Hughes (2012a, 2012b) for all events except *Feb2011*, for which an interpreted 20% reduction was applied to minimize the influence of high frequency dilation "spikes" recorded at nearby SMS sites that also liquefied (Wotherspoon et al. 2015;

Upadhyaya et al. 2019). Although some uncertainty in the actual ground motions at this site is expected, the contour maps and interpreted reduction for the PGA provide reasonable estimates for the LVI analyses that will be presented herein. The observed land damage was assessed based on satellite images depicting the aerial spread of liquefaction ejecta following each event (CGD 2012), and classified based on simplified categories presented by Tonkin & Taylor (2015) ["none to minor" indicates no signs of ejecta, "minor to moderate" indicates < 25% of site covered with ejecta, and "moderate to severe" indicates > 25% of site covered with ejecta]. These land damage classifications are further confirmed by on-the-ground road and property inspections near the site following the *Feb2011 and June2011* events (CGD 2013). The aerial LiDAR surveys performed after the *Feb2011* event do not provide reliable estimates of liquefaction-induced settlements because the vertical accuracy of ±0.15 m in the pre-earthquake surveys (CGD 2014a) encompasses the expected range of settlement. Some ejecta observed following the *June2011* and *Dec2011* events is likely "leftover" from previous events, and thus the reported land damage category is based on an interpretation of "new" or additional ejecta following each event.

The geologic structure of the Christchurch area is highly complex due to its tectonic environment, exposure to pre-Holocene glaciation cycles, and location near the mouth of Pegasus Bay (Begg et al. 2015). Quaternary sedimentary units within the Canterbury basin typically extend to depths of at least 200 m below sea level, and are composed of alternating bands of glacial deposits (i.e., primarily gravels with varying amounts of finer sediments; Riccarton Gravel is the most recent of these deposits), and interglacial deposits (i.e., primarily variable layers of sands, silts, and clays). The current interglacial (i.e., Holocene) sediments are in part comprised of the Christchurch formation (i.e., primarily sands and silts), created by early marine transgressions and ongoing embayment infilling of shallow marine, estuarine, and swamp deposits. The Springston formation (i.e., fluvial silts, sands, and gravels) constitutes the remainder of the Holocene sediments placed by alluvial deposition. The Palinurus Road site is situated about 400 m to the northeast of the meandering Heathcote River, 1100 m to the west of the Heathcote-Avon estuary, and is bounded by a small (~ 4 m wide) stream at its northeast edge. As such, the site is located at an intricate junction of fluvial,

estuarine, and swamp deposits, which likely explains the observed stratigraphic heterogeneity and presents difficulty in ascertaining the Holocene soils as Christchurch or Springston formation.

The Palinurus Road site plan shown in Fig. 3.2 depicts the aerial locations of available site investigation data obtained from the New Zealand Geotechnical Database (NZGD). The site plan includes eight CPTs (5462 to 5469) pushed to refusal and two sonic boreholes (BHs 6000 and 6001) that were conducted in April 2012 as part of a geotechnical investigation considering potential sites for a proposed sewer pump station. Between 2015 and 2016, three additional CPTs (62759, 62760, and 62761), a seismic CPT (SCPT 57360), an additional sonic borehole (BH 57235), and a direct-push crosshole test (DPCH) were completed as part of a regional liquefaction study. The three additional CPTs were pushed to a maximum depth of 16 m, and are the only available information at the *NE* side of the site.

The subsurface profile presented in Fig. 3.3 shows the nearest BH and CPT data along the cross-section line depicted in Fig. 3.2. The cone tip resistances normalized by atmospheric pressure (q_{tN}) are presented as measured and after correction for thin-layers and transition zones using the inverse filtering procedure of Boulanger and DeJong (2018) with baseline input parameters. The diagram of BH 57235 in Fig. 3.3 displays the unified soil classification system (USCS) index, plasticity index (PI), and fines content (FC; percent by soil mass passing a 0.075 mm sieve) with depth.

The subsurface at Palinurus Road is interpreted to have four primary Holocene soil strata (i.e., A, B, C, D) above Riccarton Gravel as shown in Fig. 3.3. Several of these strata have been divided into subgroups based on variations in engineering properties. The ~3 m thick surface stratum A, is primarily composed of reworked surficial material, with non-plastic silts atop loose silty sands. This is underlain by stratum B, which typically extends to a depth of ~17 m, and is composed of loose to medium dense clean sands with occasional thin (< 10 cm) and very thin (< 1 cm) silt and organic interbeds. At the *SW*, stratum B is interrupted by stratum C at depths of ~6 to 9 m. The upper portion of stratum C (i.e., C1 in subsequent analyses) is composed of soft to firm silt of moderate plasticity, with an estimated overconsolidation ratio (OCR) of 2 to 4, and occasional thin silty sand interbeds. This overlies very loose to loose silty sand with thinly interbedded clayey silt (i.e., C2). Stratum C was not observed in the three CPTs at the *NE* half of the

site. Stratum D underlies B, and is composed of a ~1-m thick layer (i.e., D1) of soft clayey silt of moderate plasticity, with an interpreted OCR of 1 to 1.3, often overlying loose to medium dense silty sand lenses with occasional silt interbeds to a depth of ~20.5 m (i.e., D2). D2 silty sands were encountered in six of the nine CPTs that were pushed to refusal. Stratum D may belong to the Avonside Member of the Christchurch formation; a distinct unit, prevalent throughout eastern Christchurch (Begg et al. 2015). Finally, stratum E represents the upper few meters of the Riccarton Gravel formation, comprised of very dense silty and sandy gravel.

The groundwater table depth is estimated at 1.2 m below the ground surface during the earthquakes, based on nearby piezometer readings (CGD 2014b). The compression wave velocity (V_P) was observed to be about 1,500 m/s just below a depth of 1.2 m, which suggests the soil is fully saturated (Yost et al. 2019). Partial saturation is therefore not expected to affect the cyclic resistance of soils below the water table. The drillers of BH 6000 and 6001 reported inflowing artesian pressures at depths of 24 m, with a head of ~1 m above the ground surface. These conditions indicate the existence of high excess pore pressures (Δu) within the Riccarton Gravel, likely obstructed from dissipating upwards by the relatively continuous and low permeability stratum D1.

3.3. Liquefaction Vulnerability Index Analysis

One-dimensional LVI analyses by Yost et al. (2019), performed with the stress-based liquefaction triggering procedure of Boulanger and Idriss (2014), for this site generally indicated an over-estimation of liquefaction manifestations for the 1D LVI metrics considered and for both the *Sep2010* and *Feb2011* earthquakes. These LVI analyses were repeated using the same assumptions made by Yost et al. (2019), with the following exceptions: (1) integration was extended to a depth of 16 m rather than being limited to 10 m, (2) a reduced PGA (as given in Table 3.1) was considered for the *Feb2011* event, (3) inverse filtering of the CPT data for transition and thin layer effects was evaluated, and (4) site-specific calibration for the fines content correction factor (C_{FC}) per Boulanger and Idriss (2014) of 0.21 for measured and 0.27 for inverse filtered CPT data determined based on correlating laser diffraction readings of the fines content

(i.e., percent particles by mass less than 0.075 mm) in samples from BH 57235 with readings from adjacent SCPT 57360. For brevity, results are presented for only the Liquefaction Severity Number (LSN; van Ballegooy et al. 2014) and the 1-D vertical reconsolidation settlement ($S_{v\text{-}1D}$; Zhang et al. 2002) indices, together with the cumulative liquefied thickness (CLT). The liquefaction potential index (LPI; Iwasaki et al. 1978) and Ishihara-inspired index (LPI_{ISH}; Maurer et al. 2015) were also determined to result in generally similar predictions.

The results of the LVI analysis are summarized in Table 3.2 listing the range and mean values obtained for the CPTs in the *SW* and *NE* areas. A predicted damage category of expected liquefaction manifestations is also indicated based on LSN thresholds proposed by McLaughlin (2017), where LSN < 16 correlates to "none to marginal," 16 ≤ LSN < 26 correlates to "moderate," and LSN ≥ 26 correlates to "severe." The overall conclusions for the *Sep2010* and *Feb2011* earthquakes are essentially the same as those by Yost et al. (2019). The LVI values obtained for the *NE* CPTs (i.e., near sand boils) are similar to those for the *SW* CPTs (i.e., away from sand boils) for each earthquake, and thus the LVIs provide no delineation between the areas that did and did not have surface ejecta. For example, the mean LSN for the *SW* versus *NE* areas for the *Feb2011* earthquake were 36 versus 39 when using the measured CPT data and essentially equal at 26 when using inverse filtered CPT data. Overall, the LSN and $S_{v\text{-}1D}$ in Table 3.2 are generally consistent in showing: (1) an over-prediction of liquefaction manifestations for these earthquakes, (2) a slight reduction in the degree of over-prediction when using inverse filtered CPT data, and (3) a lack of differentiation between the areas that did and did not have surface ejecta.

3.4. Nonlinear Dynamic Analysis Methodology

3.4.1. Numerical Model

Two-dimensional NDAs of the *SW*-*NE* trending cross section (Fig. 3.3) were performed using the finite-difference program FLAC 8.1 (Itasca 2019) and the user-defined constitutive models PM4Sand (Version 3.1; Ziotopoulou and Boulanger 2016, Boulanger and Ziotopoulou 2017) and PM4Silt (Version 1; Boulanger and Ziotopoulou 2018, 2019). The idealized profile is depicted on the 100-m-long central

portion of the plane-strain mesh shown in Fig. 3.4. Stratum B is divided into B1 and B2 to account for slight property differences with depth. Strata C and D are modeled as having a fine-grained layer (i.e., C1 and D1) overlying a sand layer (i.e., C2 and D2) to reflect the typical apportioning of these interbedded layers. The full model mesh is 200 m long by 25 m tall, and is made up of 10,000 elements, each 1.0 m long by 0.5 m tall. Sensitivity analyses showed that the dynamic response of the 100-m long central portion of the mesh is insensitive to the lateral boundary conditions for this mesh length, although the mesh length does influence pore pressure dissipation after the end of shaking as discussed later. Stress conditions were initialized prior to dynamic loading with elastic moduli that produce a coefficient of earth pressure at-rest (K_o) of 0.5 for all soil strata. The water table was initialized with a static phreatic surface at 1.2 m below the ground surface.

The dry density, porosity, vertical hydraulic conductivity (k_V), horizontal to vertical hydraulic conductivity ratios (k_H/k_V), and soil models used in the dynamic analyses are listed in Table 3.3. The primary set of analysis models assumed isotropic permeability for all strata (i.e., $k_H/k_V = 1$), whereas other analysis models used the listed k_H/k_V ratios to evaluate the effects of anisotropic permeability. Stratum E was modeled as an elastic material with a Poisson's ratio of 0.33; the elastic shear modulus was set to 70% of the small strain shear modulus corresponding to a shear wave velocity of 400 m/s, estimated for this strata based on surface wave (MASW) measurements at nearby sites (Wotherspoon et al. 2015). Rayleigh damping of 0.5% at a frequency of 1 Hz was used in the analyses.

Boundary conditions were selected to approximate free-field conditions during earthquake excitation. A compliant (quiet) base was used, with the outcrop input motion applied as a horizontal stress-time history. The left and right boundaries of the model (50 m away from the boundaries shown in Fig. 3.4) were attached together; other analyses using "free field" side boundary conditions (absorbing boundaries) confirmed that the system responses in the 100 m long central portion were generally insensitive to the choice of boundary condition. The pore pressure boundary conditions were freed (i.e., impermeable) at the sides of the model and fixed (i.e., allowed to flow outside the model) at the base and top of the model. Thus,

the dissipation of excess pore pressures (Δu) generated during shaking is accompanied by net seepage flows into the soils above the static phreatic surface or downward through the model base.

Groundwater flow was modeled both during and following earthquake excitation. Seepage rates during dynamic shaking were relatively small, such that the FLAC solution process was controlled by dynamic time step requirements (i.e., including ground water flow did not significantly slow the solution process). For simulating post-shaking pore pressure diffusion, an alternative solution process is required for efficiency because of the long time frames involved. For the present analyses, the post-shaking reconsolidation process was sped up by scaling all k_V (with k_H/k_V held constant) by a factor of 100 at the end of strong shaking, which effectively scales the post-shaking time by a factor of 1/100. In addition, the k_V of the surficial stratum A was further increased by a factor of 10 to 1.0E-04 m/s (e.g., equivalent to k_V of stratum B) to approximately account for the effects of cracking and the formation of sand boil pipes which cannot be explicitly simulated using FLAC. The influence of this permeability reduction is evaluated as part of the sensitivity studies later described. The PostShake option of the PM4Sand and PM4Silt constitutive models was activated at the end of strong shaking to more reasonably simulate volumetric reconsolidation strains after shaking. Analysis results are compared for the time when at least 80% of Δu has dissipated in all vertical soil columns above D1 and within the central 60 m of the model mesh, which was sufficient time for the majority of surface settlements to have developed (the influence of mesh dimensions and consolidation time are later discussed).

3.4.2. Calibration of Constitutive Models

The PM4Sand and PM4Silt constitutive models were calibrated for four sets of representative values for the normalized clean sand corrected tip resistance (q_{c1Ncs}) for the sand strata and the undrained shear strength ratio (s_u/σ'_{vc}) for the fine-grained soil strata, respectively. The representative value sets were determined as: (1) 33rd percentile from measured CPT data (*33Meas*), (2) 50th percentile from measured CPT data (*50Meas*), (3) 33rd percentile from inverse filtered CPT data (*33IF*), and (4) 50th percentile from inverse filtered CPT data (*50IF*). Inverse filtering was performed per Boulanger & DeJong (2018) with

baseline filter parameters. For each stratum, 33rd and 50th percentile values for q_{c1Ncs} or s_u/σ'_{vc} were obtained based on all CPTs at the site. The 33rd to 50th percentile range is expected to encompass reasonably unbiased estimates of expected responses based on the findings of Montgomery and Boulanger (2016) for NDAs involving an evaluation of post-liquefaction reconsolidation settlements.

Fig. 3.5 depicts cumulative distribution functions (CDFs) of q_{c1Ncs} for all sand strata (i.e., A, B1, B2, C2, D2). The q_{c1Ncs} values were calculated using the relationships of Boulanger and Idriss (2014) with a site-specific C_{FC} from all CPT readings with $I_c \leq 2.6$. The faded lines depict the CDFs for data from individual CPTs, while the bold line represents the CDF for the data from all CPTs combined. For stratum B, the CDFs for all CPT data in the upper B1 and lower B2 substrata show relatively small differences between these two substrata. Inverse filtering of the CPT data results in slightly greater q_{c1Ncs} values and increased CDF variability among individual CPTs for each stratum. As most evident in strata C2 and D2, the difference in q_{c1Ncs} between the measured and inverse filtered data tends to increase at larger q_{c1Ncs} values. The stratum B CDFs display the least variation among individual CPTs, as expected since (1) it is a thicker stratum (i.e., more sample points are expected to better constrain the shape of the distribution), and (2) it is consistently represented in all CPTs with only occasional interbeds.

Fig. 3.6 depicts CDFs of the undrained shear strength ratio (s_u/σ'_{vc}) for the fine-grained soil strata (i.e., C1, D1). In the absence of vane shear testing or site-specific laboratory data, the undrained shear strength ratio (s_u/σ'_{vc}) was calculated based on an assumed cone bearing factor (N_{kt}) of 15 for all soil with $I_c > 2.6$. Only selective depth intervals of fine-grained soils were targeted within the C and D strata, to further minimize the influence of thin interbeds and transition zones. The individual and combined CPT CDFs depict s_u/σ'_{vc} typically decreasing due to inverse filtering. As with the sand strata, the individual CPTs show greater variability with inverse filtering.

The calibrated PM4Sand parameters for the four sets of representative properties are presented in Table 3.4. The unitless shear modulus coefficient (G_o) was determined based on the V_s and effective stresses at the middle of each stratum, as approximated from the DPCH and SCPT data. The apparent relative

densities (D_R) were derived from the applicable representative q_{c1Ncs} for each stratum using the relationship in Boulanger and Idriss (2014). The contraction rate parameter (h_{po}) was chosen based on an iterative adjustment to obtain a peak shear strain of 3% with a target normalized cyclic resistance ratio ($CRR_{M7.5,1atm}$) in 15 uniform stress cycles of simulated undrained direct simple shear (DSS) loading. The $CRR_{M7.5,1atm}$ target value was obtained based on the q_{c1Ncs} relationship by Boulanger and Idriss (2014). Default values were used for all secondary PM4Sand parameters.

The calibrated PM4Silt parameters are presented in Table 3.5. The G_o was determined based on the V_s and effective stresses at the middle of each stratum, as approximated from the DPCH and SCPT data. The undrained strength ratio at critical state under earthquake loading ($s_{u,cs,eq}/\sigma'_{vc}$) for each stratum is based on a 25% increase for strain rate effects and the assumption of relatively modest post-peak strain softening for the range of strains that develop in these simulations. The h_{po} parameter was chosen based on an iterative adjustment to obtain a reasonable slope of cyclic resistance against the number of uniform loading cycles to cause a 3% peak shear strain under simulated DSS loading; e.g., cyclic stresses of 0.7 times $s_{u,eq}$ reached the failure criterion in about 15-20 cycles. The simulated undrained cyclic loading response with a default shear modulus parameter (h_o) resulted in shear modulus reduction and equivalent damping behavior similar to the empirical relationships of Darendeli (2001) for strata C1 and D1. Default values were used for all other secondary PM4Silt parameters.

The differences in the calibrated constitutive responses are illustrated in Fig. 3.7 showing the cyclic stress ratio versus number of uniform cycles to 3% peak γ (N) for the B2 sand (Fig. 3.7a) and D1 clayey silt (Fig. 3.7b) for the *33Meas*, *50Meas*, *33IF*, and *50IF* property sets. These results illustrate that using the inverse filtered CPT data generally produced greater strengths for the sands and lower strengths for the clays and silts. These property sets cover a range of conceivable model parameterizations for the different interlayered soils encountered at the site, thereby indirectly encompassing model parameter variations that could have been derived by varying other components of the liquefaction analysis procedures (e.g., overburden stress corrections; liquefaction triggering correlations; fines content corrections).

3.4.3. Development of Ground Motions

Input motions for each of the *Sep2010* and *Feb2011* events were developed by two approaches: (1) deconvolution of a nearby recording over a "stiff" profile with scaling for site-to-source path effects, per the approach used by Ntritsos et al. (2018), (2) physics-based ground motion simulations by Razafindrakoto et al. (2016). Two horizontal components, labeled H1 for north-south and H2 for east-west trending motions, were considered separately for each ground motion set of each event. Fig. 3.8 depicts acceleration time-histories and associated response spectra for the eight horizontal input motions considered.

The first approach used to develop input ground motions involved a modification of the outcropping motions recorded ~10 km away at the RHSC SMS (GeoNet n.d.). This station, located in an area that did not experience liquefaction during the CES, was chosen to avoid strong nonlinear soil site effects that could invalidate deconvolution procedures. The recordings at that station were first deconvolved to the Riccarton Gravel stratum using the 1D equivalent-linear site response program Strata (Kottke et al. 2018), following the guidance and recommended procedure detailed in Markham et al. (2016). To account for site-to-source path effects, the resulting motions were scaled with a least-squares fit to the mean empirical ground motion model (GMM) by Bradley (2013) between spectral periods of 0.5 to 1.0 seconds. This range of periods spans the initial fundamental period of the modeled soil profile (above Riccarton Gravel) under initial conditions ($T_{n,i}$), to $2T_{n,i}$, to account for period lengthening that may occur during the earthquake. The GMM and associated standard deviation bands were developed for each event, assuming a shear wave velocity over 30 m (Vs_{30}) of 400 m/s (representing the profile at depths greater than those being explicitly modeled), and fault parameter estimates from Beavan et al. (2012). The modified RHSC input motions are hereafter labeled as RHSC*. The applied scaling factors were 1.0, 1.25, 1.8, and 2.6 for the *Sep2010* H1 and H2, and *Feb2011* H1 and H2 RHSC* motions, respectively.

The second approach involved obtaining ground motions from 3D physics-based simulations, which can account for some of the complexity of the Canterbury basin and source-to-site path effects. Ground motion simulations (hereafter labeled as GMSs) have been shown to typically predict ground motions with comparable bias and uncertainty as empirical GMMs for Christchurch sites during the CES,

provided local site effects are properly considered (de la Torre et al. 2020). For the present study, GMSs by Razafindrakoto et al. (2016), which are based on the methodology of Graves and Pitarka (2010), were obtained from the *SeisFinder* database (QuakeCore n.d.), at a location within 200 m from Palinurus Road for the *Sep2010* and *Feb2011* events. These GMSs use a finite difference scheme to propagate low frequency (< 1 Hz) waves through a 3D viscoelastic model with a grid spacing of 100 m and a minimum shear wave velocity (V_S) of 500 m/s. High frequency (> 1 Hz) waves are modeled using a semi-empirical approach with a stochastic source radiation pattern and simplified 1D wave propagation. The motions obtained from *Seisfinder* include a pre-applied V_{S30}-based site amplification function by Campbell and Bozorgnia (2014), with truncation at short and long periods as recommended by Graves and Pitarka (2010), to account for local site conditions. To allow for proper input of the GMSs within Riccarton Gravel, the amplification function was removed in the frequency domain for each simulation, using an iterative procedure recommended by C. de la Torre (personal communications). The resulting GMSs did not require further deconvolution due to the model V_S cap at 500 m/s, which is an adequate assumption for an elastic halfspace boundary within Riccarton Gravel. A vertical GMS motion was also obtained for the *Feb2011* event and was included as part of a sensitivity analysis as later discussed.

Differences in the intensity, frequency content, and duration of the input ground motions are depicted in Fig. 3.8. For the *Feb2011* event, the GMS motions have a shorter duration and different frequency content than the RHSC* motions. In particular, the GMS motions begin with a long period (1 to 2 s) pulse, preeminent in the fault normal (i.e., H1) direction, which may be expected due to near-fault directivity effects. Recordings at nearby PRPC (~2.8 km N of Palinurus Road) and CCCC (~3.5 km NW) SMSs each exhibit similar short durations and at least one long period pulse, albeit with a slightly greater distance from the fault and location atop different profiles that liquefied (Wotherspoon et al. 2015). The RHSC* motions may have unrepresentative longer durations due to the far-field distance of the recording station, which may have been influenced by surface waves and path-dependent dispersion. The GMS motions may therefore provide more realistic interpretations of the actual motions at Palinurus Road for the *Feb2011* event. For the *Sep2010* event, although the duration between the motions from each approach is

similar (i.e., as expected, since both approaches consider similar path effects relative to the source location), the GMS motions have consistently higher spectral accelerations than the GMM at all periods between 0.4 and 3 s. Simulations for the *Sep2010* event generally over-estimate both recordings and the GMM (Razafindrakoto et al. 2016), which may in part be due to complications in modeling the multi-fault rupture of this event (de la Torre et al. 2020). Thus, the RHSC* motions may better represent the motions experienced at Palinurus Road during the *Sep2010* event. Nonetheless, it is of interest to examine how the dissimilarities of the two sets of motions, both derived through reasonable approaches, affect the computed response at Palinurus Road for each event.

3.5. Dynamic Simulation Results

Results are presented for NDAs examining the effects of using the *33Meas*, *50Meas*, *33IF*, and *50IF* property sets and the four different input motions for the *Feb2011* and *Sep2010* events, followed by sensitivity analyses that include the effects of parameters that influence pore pressure diffusion. Dynamic responses for the *Feb2011* event are described in greater detail for three cases to illustrate some key features of the responses when there are significant liquefaction effects. Dynamic responses for the *Sep2010* event are described in less detail because many of the analysis cases did not exhibit significant liquefaction effects, consistent with observations at the site following this event.

3.5.1. Dynamic Response during February 2011 Event with 33rd Percentile Measured Properties

The dynamic response of the model with *33Meas* properties subjected to the GMS-H1 input motion for the *Feb2011* event is depicted in Fig. 3.9 showing time histories of the cyclic stress ratio (CSR), engineering shear strain (γ), and excess pore pressure ratio (r_u) at six depths on both the southwest (*SW*, x=19.5 m) and northeast (*NE*, x=89.5 m) sides of the site. Also shown is the calculated CSR within stratum E, at x=50 m, which was modeled as linear elastic. The CSR is computed as the ratio of the cyclic horizontal shear stress to initial vertical consolidation stress (σ'_{vc}). The r_u is computed as one minus the ratio of the current to initial vertical effective stress (i.e., $1 - \sigma'_v/\sigma'_{vc}$), which is preferred over using $\Delta u/\sigma'_{vc}$ for system level analyses wherein the total vertical stress may fluctuate; the two definitions are equivalent if the total

vertical stress does not change during loading. For presentation purposes, liquefaction of an element is considered to have been triggered wherever r_u becomes greater than or equal to 95%.

Several observations can be made from the CSR, γ, and r_u plots of Fig. 3.9. A significant aspect of the GMS-H1 motion is that it contains a large full-cycle velocity pulse, which causes CSR to reach a peak at 5.2 s. This pulse causes large shear strains within the soft D1 clayey silt stratum, reaching a maximum γ of 19% (note the depicted element responses in D1 at a depth of 17.25 m on the *SW* and *NE* sides reach a slightly lower peak γ of 10% due to their position one row above the D1 row that reaches γ of 19%). During the last half-cycle of the pulse (e.g., 6.3 s), liquefaction is triggered throughout much of the C2 and B2 sands. Following the pulse, several smaller cycles of loading (CSR < 0.2) continue causing significant cyclic variations in shear strain and contribute to slight increases of r_u with time, as observed in the *NE*-7.75 m plots between 7 to 12 s. The r_u steadily increases from 6.5 s until the end of shaking for the shallow *NE*-3.25 and *NE*-6.25 m plots, which is attributed to pore pressure migration from deeper layers that liquefied earlier (a sensitivity analysis confirmed that 20-30% less soil liquefies without flow during shaking). Fig. 3.9 also shows the dissipation of r_u for 100 minutes after shaking. Pore pressures within the *SW* sand layers underlying the low-permeability C1 silt stratum, are the slowest to dissipate due to their elongated dissipation path around the silt layer.

Contours of the maximum r_u and γ during shaking are shown in Fig. 3.10. The responses are relatively uniform across the model for depths below 7.5 m, including the extent of liquefaction triggering (i.e., high r_u) across the B2 sand and the peak strain strains across the underlying D1 clayey silt. Along the top 6 m of the profile, there is significantly more liquefaction in the B1 sand at the *NE* as opposed to the *SW* despite these two areas experiencing almost equal CSR time histories (Fig. 3.9). The more extensive triggering of liquefaction in the B1 sand at the *NE* is attributed to upward seepage (i.e., pore pressure diffusion) from the underlying B2 sand which liquefied earlier. Pore pressure diffusion and seepage from the B2 sand at the *SW* is impeded in the vertical direction by the lower permeability C1 silt, such that upward flow into the overlying B1 sand during strong shaking is greatly reduced in this area. Pore pressure

diffusion from the B2 sand at the *SW* is instead controlled by horizontal seepage toward the *NE* until it passes beyond the end of the C1 silt, which takes more time and thus occurs primarily after the end of strong shaking.

The temporal trend of excess pore pressure diffusion and ground water flow following strong shaking indicates that the majority of the outflow occurred on the *NE* side, just beyond the right edge (x=53 m) of the low-permeability C1 stratum. Isochrones of the total outflow volume per area (Q_{VOL}/A) at the phreatic surface are plotted versus the x-position along the model in Fig. 3.11. The Q_{VOL}/A as defined herein provides a unit length measure of the cumulative pore water volume that drains vertically towards the phreatic surface, normalized by the horizontal area perpendicular to flow. It is calculated along the row of mesh elements just below the phreatic surface and is used to provide a general understanding of the spatial distribution of the total flow quantity at the ground surface. In reality, this value is likely affected by several details in the crust that might affect the exact flow path and formation of ejecta at the surface, and so it is only treated as a relative indicator among the models considered in this report. Associated isochrones of the vertical settlement (Δy) relative to stratum D1 during reconsolidation are also shown in Fig. 3.11; settlements relative to the middle of stratum D1 are used for this comparison because the ground water flow during pore pressure diffusion is upward toward the phreatic surface for soils above D1 and downward toward the model base for stratum D2 that underlies D1. At 100 s after shaking, Q_{VOL}/A is approximately equal to Δy along the full width of the model. This synchronicity is expected because the outflows at this time are associated with volumetric strains in the near surface soils (i.e., closest to the drainage boundary), without much influence from flow processes at greater depths. The Δy and Q_{VOL}/A at this time are greater at the *NE* than at the *SW* because there is more extensive shallow liquefaction at the *NE*, which results in greater upward hydraulic gradients and outflow rates. As time progresses, the Δy and Q_{VOL}/A isochrones gradually diverge with $Q_{VOL}/A \geq$ Δy to the *NE* and $Q_{VOL}/A <$ Δy to the *SW*. The Q_{VOL}/A is greatest just north of the end of the C1 stratum (x between ~50 to 70 m), with the peak "final" Q_{VOL}/A of 20 cm being more than three times the "final" Δy of 6 cm. The Q_{VOL}/A does remain approximately equal to Δy further to the

NE (e.g., x > 100 m) where pore pressure diffusion is not significantly influenced by lateral flows. Conversely, the Q_{VOL}/A remains small above the C1 stratum on the *SW* side (x < 40 m), with the final Q_{VOL}/A of 1 cm being a small fraction of the final Δy of 3-4 cm.

The results in Fig. 3.11 correspond to a common final time of 6.6 hours, which is when 80% of Δu has dissipated in all soil columns above D1 and within the central 60 m of the model. The post-earthquake Δy time histories in Fig. 3.12 depict how the displacements at times beyond 80% reconsolidation (i.e., beyond the dashed line at 6.6 hours) level out towards a constant value for soil columns located at the *SW* (x = 19.5 m) and *NE* sides (x = 89.5 m). Allowing reconsolidation to progress from 80% to about 95% (i.e., 6.6 to 14 hours) in all columns causes about 10 to 20% more settlement at only the *SW* side, increases the outflow at only the center of the site by 10 to 20% (i.e., the peak outflow is slightly more pronounced), and more than doubles the computational times to approximately one week. The peak outflows are more strongly dependent on the horizontal length of the model because that controls the consolidating soil volume. The field stratigraphy is not known outside the area of site explorations, such that the reconsolidation analyses primarily serve to illustrate relative values and patterns in surface outflows.

The results in Fig. 3.11 illustrate that reconsolidation of the soils beneath the lower permeability C1 silt stratum on the *SW* side is accommodated by ground water flowing laterally toward the *NE* side, where it can more easily escape to the ground surface. Ground water fluxes of less than 1 cm on the *SW* side appear consistent with the absence of sand boils in this area, and ground water fluxes of up to 20 cm on the *NE* side appear consistent with observations of sand boils in that area. The delayed development of outflow is also consistent with the documented time span of sand boil formations; the spouting of ejecta often begins after shaking and continues for tens of minutes (Housner 1958, Ambraseys and Sarma 1969). The computed settlements of 3-4 cm to the *SW* and 6 cm to the *NE* are reasonably consistent with the absence of visible ground cracking, given that settlements of less than ~10 cm would be difficult to detect visually in a grass field unless they varied sharply over short distances.

3.5.2. Dynamic Response during February 2011 Event – Effect of Properties

The effect of the alternative representative property sets (Tables 4 and 5) on dynamic response was evaluated using the GMS-H1 input motion for the *Feb2011* event. As depicted in Figs. 3.7(a and b), the *33Meas*, *50Meas*, *33IF*, and *50IF* property sets represent variable cyclic responses for which clay-like soils may be weaker or stronger than sand-like soils for a given set. For instance, the cyclic strengths for the D1 clayey silt is greater than for the B2 sand when using the *33Meas* property set for all cycles greater than N=3, but smaller when using the *33IF* property set for all cycles.

The dynamic response for *33IF* properties is depicted by the time history, contour, and isochrone plots in Figs. 3.13, 3.14, and 3.15, respectively. Referring to the time histories of CSR, γ, and r_u in Fig. 3.13, the initial large pulse in the input motion causes yielding and large shear strains (i.e., > 10%) in the D1 clayey silt, which limits the magnitude of the cyclic stresses transmitted to the overlying strata. The CSR in D1 at *NE*-17.25 m and *SE*-17.25 m tend to cap at ~0.25, consistent with the cyclic strength shown in Fig. 3.7b. The transmitted stresses produce CSR in the overlying strata that are insufficient to trigger liquefaction or significant shear strains except within the C2 loose sand at *SE*-7.75 m. The CSR time series in Fig. 3.13 are significantly weaker than those obtained for the *33Meas* property set (Fig. 3.9), with the reductions in CSR attributed primarily to the D1 stratum being significantly weaker for the *33IF* property set (Fig. 3.7b). Comparing the contours of r_u and maximum γ for the *33IF* properties (Fig. 3.14) and *33Meas* properties (Fig. 3.10) similarly illustrates how the weaker D1 strength limited large shear strains to the D1 stratum and limited liquefaction triggering to the C2 stratum on the *SE* side.

The isochrones of Q_{VOL}/A and Δy following strong shaking for the *33IF* case (Fig. 3.15) show the effects of lateral ground water flow during pore pressure diffusion are similar to those for the *33Meas* case (Fig. 3.11), notwithstanding the less extensive triggering of liquefaction. In this case, the *SW* experiences a larger Δy than the *NE* (i.e., 1 cm versus 0.2 cm) because liquefaction triggering was largely limited to the C2 stratum on the *SW* side. Diffusion of excess pore pressures from the C2 stratum is again dominated by lateral seepage toward the *NE*, leading to the seepage outflow at the phreatic surface (Q_{VOL}/A) being greatest

just past the northern edge of the C1 silt stratum. The maximum final Q_{VOL}/A of 5.4 cm is far greater than the Δy of 0.2 cm at this location or the Δy of 1 cm toward the *SW*. These Δy are consistent with the absence of visible surface settlements or ground cracking, whereas the maximum seepage outflow seems sufficient to have produced visible sand or water ejecta in this local area.

Results of the NDAs using the four representative property sets with the GMS-HI input motion for the *Feb2011* event are summarized in the first four rows of Table 3.6, which lists several metrics of the dynamic response (i.e., maximum γ in D1, CLT at the *SW* and *NE*) and post-earthquake response (i.e., Δy at the *NE* and *SW*, maximum Q_{VOL}/A, reconsolidation time). The response metrics using the *50Meas* properties are similar to those obtained using *33Meas* properties (e.g., Figs. 3.9-3.11), with both cases predicting the CLT to be more than 6 m on both the *SW* and *NE* sides, surface settlements of about 3.5 cm to the *SW* and 6 cm to the *NE*, and peak surface outflows of 20-21 cm just north of the C1 stratum. The response metrics using the *50IF* properties are similar to those obtained using *33IF* properties (e.g., Figs. 3.13-3.15), with both cases predicting the CLT to be about 1 m to the *SW* and 0 m to the *NE*, surface settlements of about 1 cm to the *SW* and 0.2 cm to the *NE*, and peak surface outflows of 5 cm just north of the C1 stratum. The limited extent of liquefaction triggering for the *50IF* case is attributed to it having the greatest cyclic strengths for the B1 and B2 sand strata (Table 3.4 and Fig. 3.7a), whereas the limited extent of liquefaction triggering for the *33IF* case was attributed to it having the weakest cyclic strengths for the D1 stratum (Fig. 3.7b).

3.5.3. Dynamic Response during February 2011 Event – Effect of Input Motion

The effect of alternative input motions for the *Feb2011* event was evaluated first using the RHSC*-H1 motion with the *33Meas*, *50Meas*, *33IF*, and *50IF* property sets. The metrics of the dynamic response for these four cases are summarized in rows 5 through 8 of Table 3.6. The relative effect of changing property sets were similar to those obtained using the GMS-H1 motion (rows 1 through 4 of Table 3.6). The responses for the two motions however do affect certain features of the response that are described for the *33Meas* property set below.

The dynamic response for the RHSC*-H1 motion with the *33Meas* property set is depicted by the time history and contour plots shown in Figs. 3.16 and 3.17, respectively. The RHSC*-H1 motion contains several large cycles, though none are as large as the initial pulse of the GMS-H1 motion (Fig. 3.8). Consequently, the maximum γ in the D1 clayey silt is less than 2% for this motion compared to 19% with the GMS-H1 motion (Table 3.6). Excess pore pressures in the sand strata generally increase with each cycle of loading leading to liquefaction being triggered in C2 (7.75 m depth) at 6.2 sec, in D2 (18.25 m depth) and the middle portion of B2 (7.75m depth) at ~9 sec, and in B1 (3.25 m depth) and more widely in B2 (5.25 m and 13.25 m depths) at ~12 sec. The effects of liquefaction triggering at different depths and times are evident in the waveform characteristics of the acceleration and CSR time series. The more extensive liquefaction in B2 at the *NE* as compared to the *SW* was likely caused by the early liquefaction triggering in C2, which altered the dynamic response and limited the peak CSR that could be experienced on that side thereafter.

Contours of the maximum r_u and γ during shaking in Fig. 3.17 show that the B1 and B2 strata have greater volumes of liquefied soil at the *NE* side as opposed to the *SW* side. The greatest γ (5 to 9%) developed in the C2 and D2 silty sands, although significant strains also developed along the bottom of stratum A (~3%) and throughout stratum B2 on the *NE* side (~ 2 to 5%). The overall pattern of strains are consistent with the cyclic behavior and relative densities of each stratum. The isochrones of Q_{VOL}/A and Δy following strong shaking for the RHSC*-H1 motion shown in Fig. 3.18 are similar to those for the GMS-H1 motion (Fig. 3.11), except for the Δy being slightly greater to the *NE* (10 cm versus 6 cm). The peak final Q_{VOL}/A is 20-21 cm just north of the edge of the C1 stratum for both motions, which suggests that the C1 stratum would be expected to have similar effects on the likely distribution of surface ejecta despite the differences in the input motions and dynamic site response.

The effects of other variations in input motions were evaluated with the *33Meas* properties, with the results summarized in the last four rows of Table 3.6. For the *33Meas* properties, the GMS-H1, GMS-H2, RHSC*-H1, and RHSC*-H2 motions produced generally similar values for the CLT (4.5-7.5 m to *SW*,

7-17 m to *NE*), surface settlements (2.7-3.7 cm to *SW*, 4.3-9.7 cm to *NE*), and maximum Q_{VOL}/A (15-21 cm). Responses using the GMS-H1 motion with reversed polarity and the GMS-H1 motion with the vertical component included were both within 10% of the response for the GMS-H1 motion alone.

The GMS and RHSC* alternative input ground motion sets produce differences in the dynamic response but ultimately similar liquefaction effects, which may partially be explained by differences in the ground motion's intensity near the site period and duration (number of effective cycles). These effects have similarly been observed to have a compensating influence on simplified liquefaction triggering when comparing near-fault motions in the strike normal direction (i.e., with larger cyclic stresses but fewer equivalent cycles), with the strike parallel direction (e.g., Green et al. 2008). GMS-H1 in this case is characteristic of a motion with directivity effects and RHSC*-H1 may be likened to a motion without directivity effects. For this site, similar liquefaction effects may also be attributed to a complex interplay between different soil layers and the timing of high intensity cycles, whereby early yielding in some layers have influenced the transmitted CSR to other layers (as also observed by Cubrinovski et al. 2019).

3.5.4. Lateral Variations in Surface Motions and Horizontal Ground Strains

The variation in ground surface motions from the *SW* to *NE* are illustrated by the acceleration time series and response spectra for the *33Meas* properties with the GMS-H1 and RHSC*-H1 motions in Fig. 3.19. The accelerations at the ground surface for locations to the *SW* and *NE* for the GMS-H1 motion have only slight differences over the full duration of shaking, with both showing significant damping of motions after liquefaction is triggered during the first strong pulse of motion. The response spectra for the surface motions are higher than the base spectrum at low periods up to 0.04 s, are primarily lower between 0.04 to 1.5 s, and are very slightly higher at periods above 1.5 s. Both surface spectra are fairly consistent with one another, except the *SW* motion is slightly lower at all periods below 0.1 s. The accelerations at the ground surface for points to the *SW* and *NE* for the RHSC*-H1 motion also have only slight differences over the full duration of shaking, with the effects of liquefaction triggering evident after about 7 s. The surface time histories for this motion display prominent high frequency "dilation spikes" after the onset of liquefaction.

These spikes are attributed to "liquefaction shockwaves" (Kutter and Wilson 1999) associated with the constructive wave interference that can develop if the waves passing through a liquefied soil are strong enough to produce incremental dilation and stiffening (e.g., the transient stiffening phase during cyclic mobility). The response spectra for the surface motions are higher than the base spectrum at low periods up to ~0.07 s, are then lower up to 0.7 s, and are higher at periods above 1.0 s. The *NE* surface spectrum is at least 30% higher than the *SW* at low periods up to 0.3 s, but they are roughly equal at larger periods. The peak surface acceleration for both input motions is slightly smaller on the *SW* side, which may be attributed to the influence of the relatively weaker/looser C1 and C2 strata on this side.

Variations in horizontal ground strains across the site are illustrated by the contours of maximum horizontal extensional and compressive strains (ε_x) in Fig. 3.20 for the *33Meas* model subjected to the GMS-H1 (Fig. 3.20a) and RHSC*-H1 (Fig. 3.20b) motions. The slight differences in the ground motions on the *SW* and *NE* sides of the site, due to the slightly different profiles and differences in liquefaction responses, produce horizontal strains in the near surface soils near the central portion of the site (i.e., around the northern edge of the C1 stratum). These maximum horizontal strains are greater for the RHSC*-H1 motion than for the GMS-H1 motion, which is consistent with greater differences in surface accelerations between the *SW* and *NE* sides (Fig. 3.19). Additional deformations in the near surface soils can be expected to arise from lateral variability in soil properties (e.g., Montgomery and Boulanger 2016), which is not accounted for in these analyses. The maximum horizontal strains in this area during shaking exceed 0.2% for the RHSC*-H1 motion and for several other of the analysis cases listed in Table 3.6. The cycling of horizontal extensional and compressive strains in this area may be sufficient to promote surface cracking and facilitate sand boil formation, particularly in combination with the local concentration of seepage outflows.

3.5.5. Sensitivity of Diffusion Behavior to Other Model Variations

Four different model assumptions that influence pore pressure diffusion were examined using the *33Meas* model with the GMS-H1 motion: (1) reduced lateral extent of stratum C, (2) anisotropic

permeabilities, (3) decreased crust permeability, and (4) increased crust permeability at locations assigned cracks due to excessive tensional strains. All five models had similar extents of liquefaction triggering and ground surface settlements, with the only significant differences being in the pore pressure dissipation responses. The final distributions of Q_{VOL}/A and Δy are shown in Fig. 3.21, at the time when at least 80% of Δu has dissipated in all vertical soil columns above D1 and within the central 60 m of the model. The first model variation was reducing the length of stratum C. The 200 m long baseline model drains all Δu beneath a 103 m long stratum C to the *NE*. This assumption implies Δu has no other direction to flow (e.g., no water outlets through low permeability stratum C1; no flow to the *SW* or in the third dimension). To check the sensitivity of this assumption, the model extents were reduced to 160 m and C1 was reduced to 83 m, preserving the center portion of the model with minimal boundary disturbance. This ~20% reduction in the length of C1 resulted in only a ~10% reduction of peak outflow, while preserving the same shape as the baseline Q_{VOL}/A. The second model variation was including anisotropic k_H/k_V values listed in Table 3.3. This change caused a ~20% reduction in the peak outflow and slightly broadened the Q_{VOL}/A distribution. This result is expected due to a higher k_H causing flow lines to spread further laterally beyond the edge of the C1 stratum before turning toward the surface. The third model variation was decreasing k_V of stratum A by a factor of 10 relative to the base case (i.e., k_V remains constant at $1/10^{th}$ that of the underlying B2). This reduced the peak outflow by ~40%, broadened the Q_{VOL}/A distribution, and reduced *NE* reconsolidation by 1.9 cm. The broader Q_{VOL}/A distribution is attributed to the buildup of Δu below stratum A, which allowed Δu to spread laterally beneath A as it dissipated into A. The settlement at the *NE* side was reduced because the average degree of consolidation at the *NE* side is about 10% less than the base case, even for the same reconsolidation criteria (Fig. 3.12); these differences in settlement and peak outflows are smaller if the results are compared at closer to 100% consolidation throughout the full profile. The fourth model variation imposed a tenfold increase of k_V for any zone in stratum A with extensional strains greater than 0.05% (this arbitrary threshold value was selected for qualitative insight). This resulted in an irregular Q_{VOL}/A distribution (because the increase in k_V was irregular, as may be expected with the

development of irregular crack patterns) and an almost 40% increase in the peak Q_{VOL}/A value. In all cases, the peak Q_{VOL}/A is located near x=55-60 m, just north of the lateral edge of the C1 stratum.

3.5.6. Dynamic Response during September 2010 Event – All Cases

Results of the NDAs using the four property sets with the RHSC*-H1 motion and the *33Meas* property set with the four alternative input motions for the *Sep2010* event are summarized in Table 3.7. No liquefaction occurred using the *33Meas*, *50Meas*, *33IF*, or *50IF* properties with the RHSC*-H1 motion, and liquefaction was limited to a 0.5-m thick zone on the *SW* side using the *33Meas* properties with the RHSC*-H2 motion. The Δy was less than 1 cm and the maximum Q_{VOL}/A was less than 3 cm for these cases, in congruence with the absence of visible liquefaction manifestations during this event. The responses using the *33Meas* properties with the GMS-H1 and GMS-H2 motions predicted significant CLTs (1.5-7.5 m to *SW*, 4.5-14 m to *NE*), surface settlements (1.6-3.5 cm to *SW*, 2.4-7.3 cm to *NE*), and maximum Q_{VOL}/A (10-22 cm). The input response spectra of the GMS motions produced from the complex multi-fault rupture of this *Sep2010* event have been generally observed to overestimate both the actual recordings and the GMM (Razafindrakoto et al. 2016, de la Torre et al. 2020), and are therefore believed less suited for evaluating dynamic response at this site.

3.6. Discussion

The 2D NDA results provide insights and reasonable bounds on the observed patterns of liquefaction manifestation at Palinurus Road for the *Feb2011* and *Sep2010* earthquakes. The parametric studies were generally consistent in indicating that significant liquefaction effects would be expected in the *Feb2011* event and not expected in the *Sep2010* event, although less consistent results were obtained for some combinations of soil properties and input motions. However, all results were consistent in indicating that surface ejecta would be expected to preferentially develop to the *NE* side, even if liquefaction triggering occurred at depth on both the *SW* and *NE* sides. In contrast, the 1D LVI results provide no differentiation to support why surface ejecta was observed to the *NE* side but not to the *SW* side of the site, and generally over-predict the severity of liquefaction manifestations given current empirical thresholds. The advantages

of the NDAs relative to the 1D LVIs for this case study are primarily the explicit modeling of dynamic response and 2D pore pressure diffusion and ground distortion patterns. Cubrinovski et al. (2019) demonstrated the importance of accurately accounting for the dynamic system response using 1D NDAs for representative idealized soil profiles, and concluded that the cross-interaction of dynamic effects can be critical for an accurate evaluation of liquefaction effects at sites with various sedimentary structures. The present analyses further enforce those observations. Different facets of an input motion (e.g., near-fault directivity effects, frequency content) may also govern the system response, and these may not be captured by an LVI's consideration of PGA and a magnitude scaling factor alone. Accounting for 2D diffusion and ground distortions was essential to modeling and understanding the spatial distribution of surface expressions of liquefaction. The presence of laterally discontinuous lower-permeability layers can influence the patterns of pore pressure diffusion and consequently alter the distribution of surface manifestations (e.g., sand boils) relative to the actual locations of liquefaction triggering in the subsurface. Case studies performed with 1D LVIs may instead misinterpret liquefaction effects by directly correlating analyses at a single soil column with manifestations directly above it.

The NDA analyses presented in this study show that the system level response was sensitive to modest variations in the properties assigned to the different strata for the input motions considered. Property variations due to different uniform percentile choices (i.e., 33^{rd} and 50^{th}) and alternate CPT processing methods (i.e., measured and inverse filtered) result in significantly different responses due to the relative interaction between layers and the time-dependent distribution of stresses throughout the system. These property sets cover a reasonable range of conceivable model parameterizations, thereby indirectly encompassing cases that could have been derived from other uncertainties in the site characterization and liquefaction analysis procedures (e.g., undrained strength corrections for clays; overburden stress corrections; liquefaction triggering correlations; fines content corrections).

Predicting the occurrence of surface ejecta from NDA results is currently subjective, given the complex mechanics of ejecta pathway formation and soil erosion are not well understood nor accounted for in these types of continuum models. Accordingly, the computed $Q_{VOL/A}$ should be interpreted as illustrating

the relative magnitudes and patterns among analyses with similar assumptions, and should not be taken as an accurate predictor of outflows. Hutabarat and Bray (2021) proposed an index for evaluating surface ejecta potential from results of 1D NDAs. The 2D analysis results presented herein suggest that the formation of ejecta pathways can be promoted in areas of differential ground strains, which may be associated with lateral variations in the stratigraphy, soil properties, and extent of liquefaction triggering, along with the influence of stratigraphic variations on pore pressure diffusion patterns.

The potential influence that cyclic softening in strata of soft clays or silts can have on a site's dynamic response was illustrated by NDA cases where the continuous D1 clayey silt stratum was either assigned the lowest scenario strength or was subjected to the stronger initial velocity pulse from the GMS-H1 input motion for the *Feb2011* event. For these cases, cyclic softening in the D1 stratum limited the cyclic stress ratios that developed in the other strata, which greatly reduced the extent of liquefaction triggering. These results reinforce findings by others (e.g., Ghosh et al. 2005) that illustrate the need for adequate characterization of all strata to effectively model highly nonlinear dynamic responses.

NDAs simulate more realistic behavior than LVIs, but nonetheless still have limitations. For instance, they are generally unable to directly simulate some of the physical mechanisms involved with pore pressure dissipation, including void redistribution and the generation of a water film beneath less permeable layers (e.g., Fiegel & Kutter 1994, Boulanger & Truman 1996), changes in permeability during liquefaction, cracking of crust soils due to ground distortions, sedimentation effects during post-liquefaction reconsolidation, and erosion and ground loss during sand boil formation. Such processes may contribute to loosening of sands immediately beneath less permeable layers, such as noted for liquefaction case history sites at Brawley Park in the 1979 Imperial Valley earthquake (Youd 1984) and at the Wildlife Array in the 1987 Superstition Hills earthquake (Holzer et al. 1988), and consistent with the C2 silty sand stratum being looser than the other sand strata at Palinurus Road. Changes in density throughout a sand profile following any one liquefaction event are not expected to be large, but rather to accumulate through several earthquake events, as illustrated by centrifuge model tests with multiple shaking events by Darby et al. (2019). Local pressure gradients from natural permeability contrasts of crust soils may contribute to the precise position

and behavior (e.g., jetting, welling up) of sand boils (Housner 1958). Also, the modeled stratigraphy is a simplification dependent on available site data, and may not adequately capture the spatial variability of soil parameters and layer extents. As with LVIs, NDAs are subject to uncertainty from the input parameters, and good practice requires sensitivity analyses to represent a range of expected behavior. The PM4Sand and PM4Silt constitutive models were chosen for their ability to model the cyclic stress-strain behavior of sand-like and clay-like soils. Reasonably similar insights should be expected using other constitutive models with similar capabilities and calibrations (e.g., Montgomery and Abbaszadeh 2017). In spite of these limitations, the NDA results for Palinurus Road reasonably bound the observed liquefaction manifestations and sand boil patterns during these two earthquakes.

3.7. Conclusion

This paper examined the seismic response of the Palinurus Road site for the *Sep2010* and *Feb2011* earthquakes through a series of 2D NDAs with variations in soil properties, input ground motions, and modeling assumptions. The range of NDA results for each event were generally consistent with, or enveloped, the observed surface manifestations of liquefaction for both events, including the absence of visible liquefaction manifestations for the *Sep2010* event and the development of extensive surface ejecta toward the *NE* side of the site for the *Feb2011* event. Primary observations from these NDAs and companion LVI analyses are summarized as follows.

- The laterally discontinuous lower-permeability C1 stratum on the *SW* side of the site (Figs. 3.3 and 3.5) caused pore pressure diffusion from any underlying liquefied zones to be controlled by horizontal seepage toward the *NE* where it can more easily escape to the ground surface. This caused ground water fluxes at the ground surface to be greatly increased (e.g., $Q_{VOL}/A > 20$ cm) in the area north of the end of the C1 stratum and greatly reduced (e.g., < 1 cm) in the *SW* area above the C1 stratum for the *Feb2011* event. These differences in ground water fluxes are consistent with the observed distribution of surface ejecta, and indicate that the absence of surface ejecta on the *SW* side should not suggest that liquefaction was not triggered at depth in these areas.

- Reasonable variations in the soil parameters altered the timing and location of the onset and progression of liquefaction and/or cyclic softening, ultimately influencing the dynamic response. For example, the use of inverse filtered CPT data (to correct for thin layer and transition zone effects) affected responses by reducing estimated strengths for clay-like layers and increasing estimated strengths for sand-like layers. This typically promoted early yielding of the continuous D1 clayey silt stratum, which limited the extent of liquefaction triggering throughout the soil profile.
- The input ground motions developed by two different approaches had significant effects on the dynamic responses and extent of liquefaction triggering. This was primarily due to variations in the frequency content, duration, and consideration of near fault effects (e.g., velocity pulse). However, this did not affect the observation that lower-permeability stratum C1 had a critical effect on pore pressure diffusion patterns and post-earthquake distributions of surface ejecta.
- Lateral variations in the profile from *SW* to *NE* were sufficient to cause dissimilar dynamic responses, leading to a zone of greater horizontal extensional/compressive strains and distortion during shaking, which would increase the potential for ground cracking and ultimately sand boil formation in that area.
- 1D LVIs were limited in their ability to predict or explain the observed field responses at this site. Instead, explicit consideration of the dynamic response and 2D pore water diffusion patterns was important for differentiating between the performance of the *SW* and *NE* sides of the site in terms of the observed post-earthquake sand boil patterns.

This case history illustrates the advantages of NDA methods, relative to simplified 1D LVI methods, wherein the explicit modeling of dynamic response and pore pressure diffusion were essential for approximating the observed responses. These results reinforce findings from other case history studies, including several from the CES (e.g., Cubrinovski et al. 2019), but are also unique in illustrating how surface patterns of ejecta may be shifted relative to the subsurface distribution of liquefied soils by the influence of laterally discontinuous lower-permeability interlayers on the pore pressure diffusion patterns.

3.8. Data Availability

Some or all data, models, or code used during the study were provided by third parties. Direct request for geotechnical data and ground motions may be made to the providers indicated in the acknowledgements and requests for software can be made to the providers indicated in the references.

3.9. Acknowledgements

The authors appreciate the financial support of the National Science Foundation (award CMMI-1635398) and California Department of Water Resources (contract 4600009751) for different aspects of the work presented herein. Any opinions, findings, conclusions, or recommendations expressed herein are those of the authors and do not necessarily represent the views of these organizations. The site characterization data was sourced from the New Zealand Geotechnical Database. Procurement and preparation of the physics-based ground motion simulations benefited greatly from discussions with Chris de la Torre. Examination of this case history benefited from discussions with Brady Cox, Kaleigh Yost, Sjoerd van Ballegooy, Jonathan Bray, Misko Cubrinovski, Ken Stokoe, and Liam Wotherspoon. The analyses benefited from discussions with Jason DeJong, James Dismuke, Nick Paull, Renmin Pretell, and Katerina Ziotopoulou. The authors are grateful for the above support and interactions.

Tables

Table 3.1. Summary of significant CES events at Palinurus Road.

Event	M_w	R_{rup} (km)	Site PGA (g)[a]	Land damage observation category[b]	
				SW Side	*NE Side*
4 September 2010	7.1	20	0.24	None to minor	None to minor
22 February 2011	6.2	1	0.54	None to minor	Minor to moderate
13 June 2011 (2 events, 80 min. apart)	5.3 & 6.0	1.5	0.29 & 0.42	None to minor	Minor to moderate[c]
23 December 2011 (2 events, 80 min. apart)	5.8 & 5.9	5.5	0.22 & 0.28	None to minor	None to minor[c]

[a] PGA from Bradley & Hughes (2012a, 2012b) contours for all events except *22 February 2011*, for which a 20% reduction was applied to remove the influence of nearby recorded dilation spikes.
[b] Based on categories presented by Tonkin & Taylor (2015).
[c] The noted category represents the authors' interpretation of only the ejecta produced by events of that day.

Table 3.2. LVI results summary at Palinurus Road during the *Feb2011* and *Sep2010* events.

Event	CPT Processing	Value	*SW Side (9 CPTs)*			*NE side (3 CPTs)*		
			LSN	$S_{V\text{-}1D}$ (cm)	CLT (m)	LSN	$S_{V\text{-}1D}$ (cm)	CLT (m)
Sep2010	Measured	Range	15 - 25	7 - 12	2.7 – 6.1	16- 24	8 - 10	4.7 – 5.2
		Mean	20	9	4.6	19	9	5.0
		Category[a]	Moderate			Moderate		
	Inverse Filtered	Range	11 - 18	5 - 8	2.3 – 3.7	10 - 16	4 - 6	2.3 – 3.4
		Mean	14	7	2.9	13	6	3.0
		Category[a]	None to Marginal			None to Marginal		
Feb2011	Measured	Range	34 - 47	16 - 24	9.3 – 13.9	34 - 40	17 - 19	10.1 – 10.9
		Mean	39	18	10.4	36	18	10.3
		Category[a]	Severe			Severe		
	Inverse Filtered	Range	20 - 35	10 - 17	5.5 – 9.4	24 – 31	11 – 14	6.5 – 7.9
		Mean	26	13	7.0	26	12	7.2
		Category[a]	Severe			Severe		

[a] Predicted damage category based on LSN thresholds presented by McLaughlin (2017).

Table 3.3. Soil properties and constitutive models assumed for NDA models.

Stratum	Dry Density (kN/m^3)	Porosity	k_V (m/s)[a]	Anisotropic Model k_H/k_V[b]	Soil Model
A	14.7	0.44	1E-05[c]	2	PM4Sand
B1/B2	14.7	0.44	1E-04	2	PM4Sand
C1	14.7	0.44	1E-09	5	PM4Silt
C2	14.7	0.44	1E-05	5	PM4Sand
D1	14.7	0.44	1E-09	5	PM4Silt
D2	14.7	0.44	1E-06	5	PM4Sand
E	17.9	0.46	1E-02	1	Elastic

[a] k_V, estimated from I_c per Robertson (2010).
[b] k_H/k_V for the anisotropic model. Other models assume isotropic permeability for all strata.
[c] At stratum A, k_V of 1E-05 m/s is assumed during shaking for all models. After shaking, k_V is increased to 1E-04 m/s.

Table 3.4. Dynamic soil properties assumed for PM4Sand strata.

PM4Sand Strata	V_S (m/s)	G_o (-)	*33Meas*			*50Meas*			*33IF*			*50IF*		
			D_R	q_{c1Ncs}	h_{po}	D_R	q_{c1Ncs}	h_{po}	D_R	q_{c1Ncs}	h_{po}	D_R	q_{c1Ncs}	h_{po}
A	115	651	0.53	96	0.32	0.58	106	0.28	0.60	111	0.28	0.65	125	0.30
B1	175	983	0.62	118	0.21	0.66	129	0.23	0.67	132	0.26	0.72	146	0.43
B2	200	839	0.63	119	0.25	0.65	126	0.26	0.71	142	0.42	0.73	149	0.61
C2	165	666	0.54	98	0.30	0.57	105	0.29	0.58	107	0.28	0.62	118	0.28
D2	200	656	0.61	114	0.27	0.64	123	0.29	0.63	120	0.29	0.69	138	0.40

Table 3.5. Dynamic soil properties assumed for PM4Silt strata.

PM4Silt Strata	V_S (m/s)	G_o (-)	*33Meas*		*50Meas*		*33IF*		*50IF*	
			$s_{u,eq,cs}/\sigma'_{vc}$	h_{po}	$s_{u,eq,cs}/\sigma'_{vc}$	h_{po}	$s_{u,eq,cs}/\sigma'_{vc}$	h_{po}	$s_{u,eq,cs}/\sigma'_{vc}$	h_{po}
C1	165	865	0.74	120	0.95	200	0.54	60	0.80	170
D1	175	498	0.37	40	0.44	60	0.24	10	0.36	30

Table 3.6. NDA results for *Feb2011* event.

GM source	Comp.	Soil param.	D1 max γ (%)	CLT (m)[a]		Δy (cm)[b]		Max Q_{VOL}/A (cm)	Post-EQ reconsol. time (min)[c]
				SW	*NE*	*SW*	*NE*		
GMS	*H1*	*33Meas*	19.1	7.5	9.5	3.5	6.3	20.2	397
GMS	*H1*	*50Meas*	12.4	8.5	6	3.4	5.6	21.2	415
GMS	*H1*	*33IF*	64.6	1	0	1.0	0.2	5.2	253
GMS	*H1*	*50IF*	23.3	1	0	1.0	0.2	5.1	233
*RHSC**	*H1*	*33Meas*	1.8	6	17	3.7	9.7	21.3	388
*RHSC**	*H1*	*50Meas*	2.2	5	10.5	2.8	4.5	14.3	323
*RHSC**	*H1*	*33IF*	14.6	1.5	0	1.4	0.4	7.7	283
*RHSC**	*H1*	*50IF*	7.4	2	1.5	1.3	1.1	7.0	230
*RHSC**	*H2*	*33Meas*	0.5	4.5	8.5	2.9	4.3	15.1	345
GMS	*H2*	*33Meas*	1.4	5	7	2.7	4.5	15.6	337
GMS	*H1-Rev*	*33Meas*	18.6	8	9	3.5	6.0	20.3	393
GMS	*H1 & V*	*33Meas*	19.8	7.5	8	3.4	5.5	18.5	308

Note: All measurements at the *SW* and *NE* sides are respectively taken at columns along x = 19.5 and 89.5 m.
[a] CLT accumulates 0.5 m thick elements exhibiting a maximum $r_u \geq 95\%$ during shaking.
[b] Post-earthquake reconsolidation monitored until ≥ 80% consolidation as defined in Fig. 3.12.

Table 3.7. NDA results for *Sep2010* event.

GM source	Comp.	Soil param.	D1 max γ (%)	CLT (m)[a]		Δy (cm)[b]		Max Q_{VOL}/A (cm)	Post-EQ reconsol. time (min)[c]
				SW	*NE*	*SW*	*NE*		
*RHSC**	*H1*	*33Meas*	0.2	0	0	0.1	0.1	0.8	63
*RHSC**	*H1*	*50Meas*	0.2	0	0	0.1	0.1	0.7	65
*RHSC**	*H1*	*33IF*	0.2	0	0	0.1	0.1	0.7	68
*RHSC**	*H1*	*50IF*	0.2	0	0	0.1	0.1	0.6	68
*RHSC**	*H2*	*33Meas*	0.2	0.5	0	0.6	0.2	2.7	135
GMS	*H1*	*33Meas*	0.9	7	14	3.5	7.3	21.9	475
GMS	*H2*	*33Meas*	0.3	1.5	4.5	1.6	2.4	10.4	328

Note: All measurements at the *SW* and *NE* sides are respectively taken at columns along x = 19.5 and 89.5 m.
[a] CLT accumulates 0.5 m thick elements exhibiting a maximum $r_u \geq 95\%$ during shaking.
[b] Post-earthquake reconsolidation monitored until ≥ 80% consolidation as defined in Fig. 3.12.

Figures

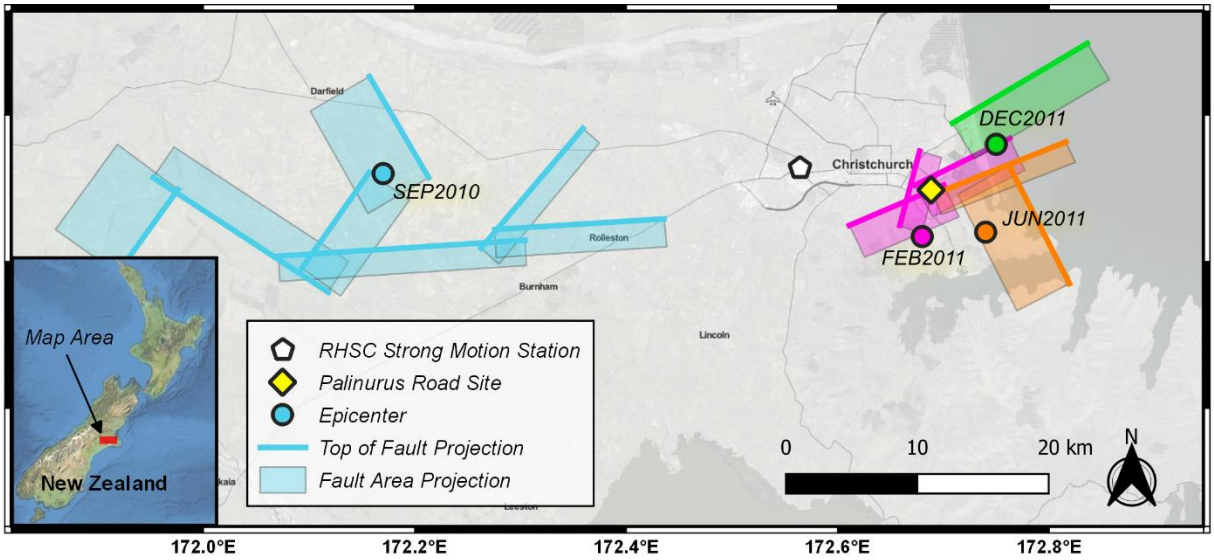

Figure 3.1. Fault map depicting significant CES events affecting the Palinurus Road site [base imagery from Stamen Design (2020); made with QGIS].

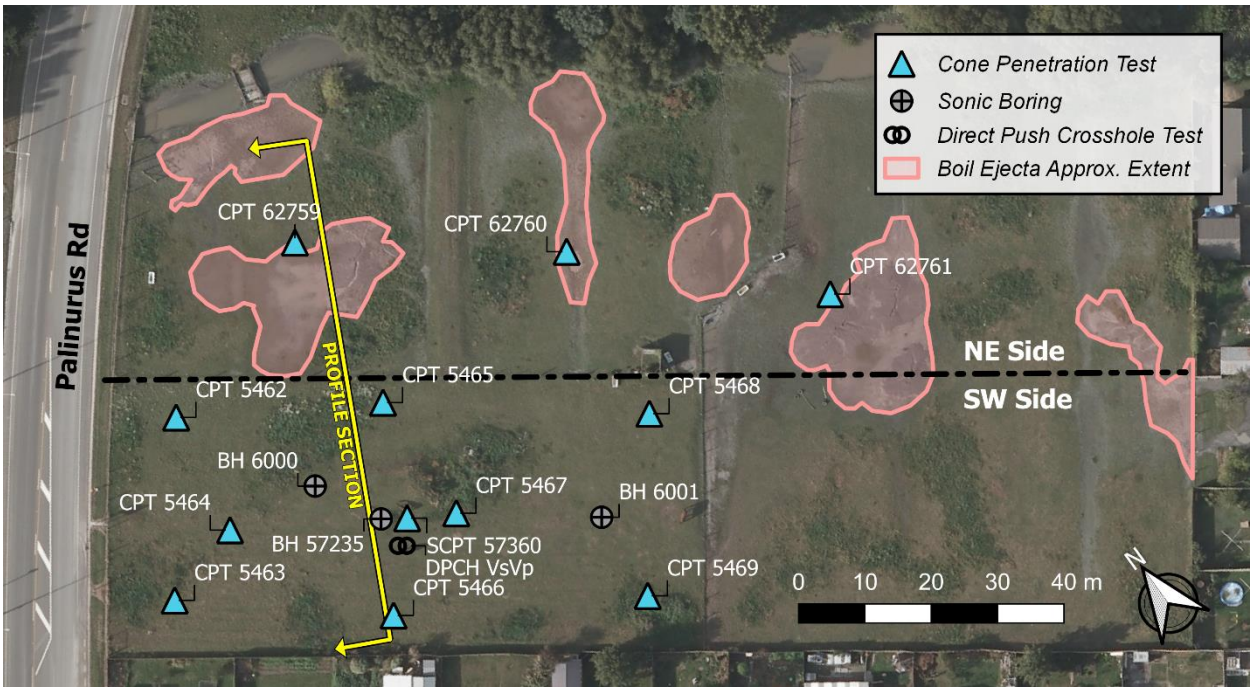

Figure 3.2. Palinurus Road site plan with background image taken after the Christchurch earthquake on 24 February 2011 [base imagery from New Zealand Mapping Ltd. (2014); made with QGIS].

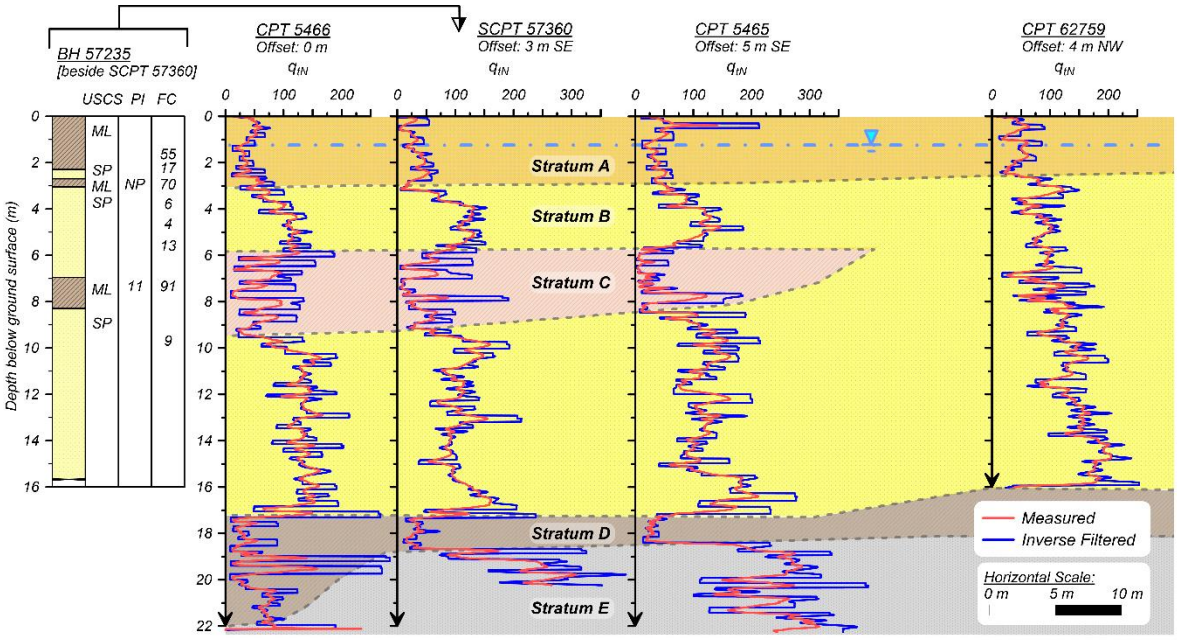

Figure 3.3. Palinurus Road interpreted *SW-NE* subsurface profile section with measured and inverse filtered CPT data.

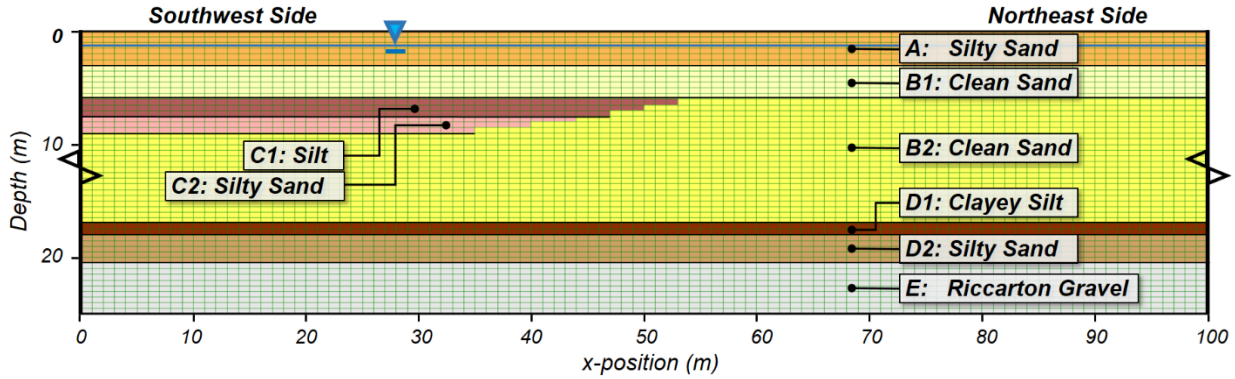

Figure 3.4. Central 100-m long segment of the FLAC mesh used for Palinurus Road NDAs.

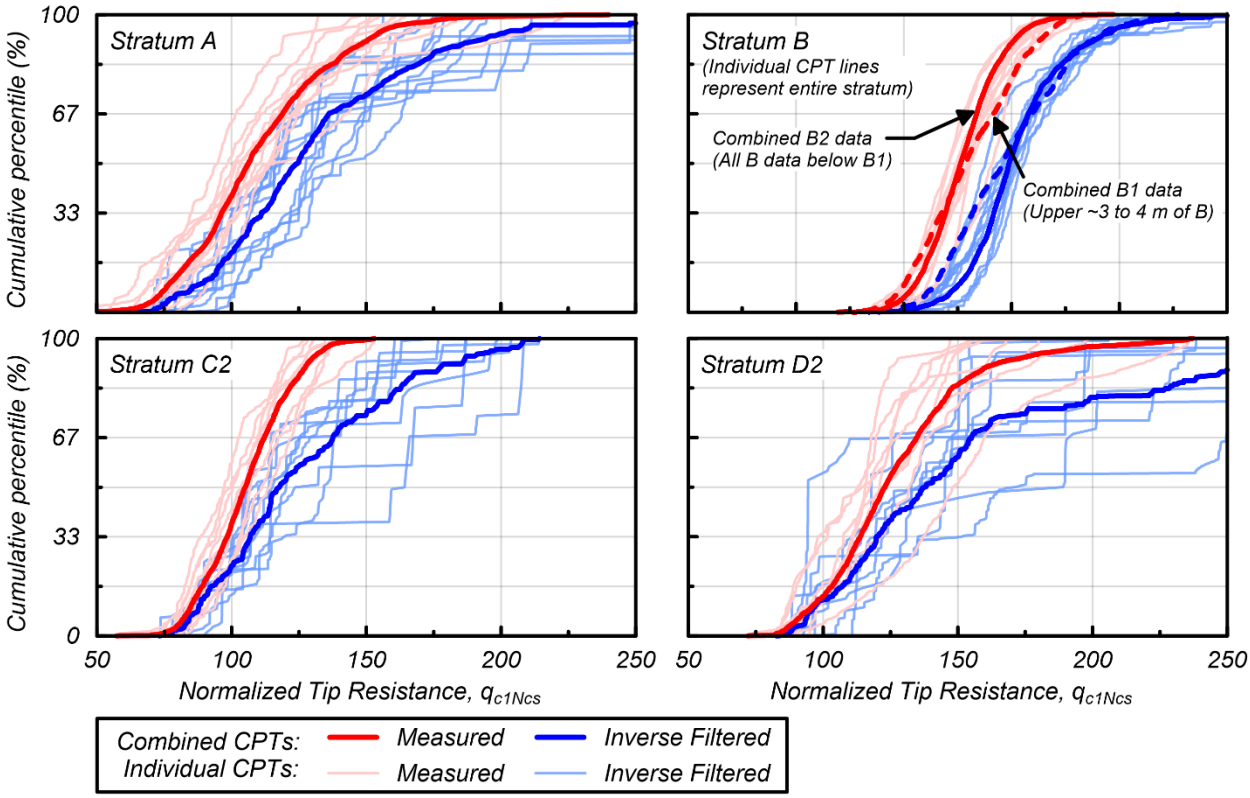

Figure 3.5. Cumulative distributions of the measured and inverse filtered normalized clean sand corrected tip resistance (q_{c1Ncs}) from all CPTs at the site, for all NDA strata modeled as PM4Sand.

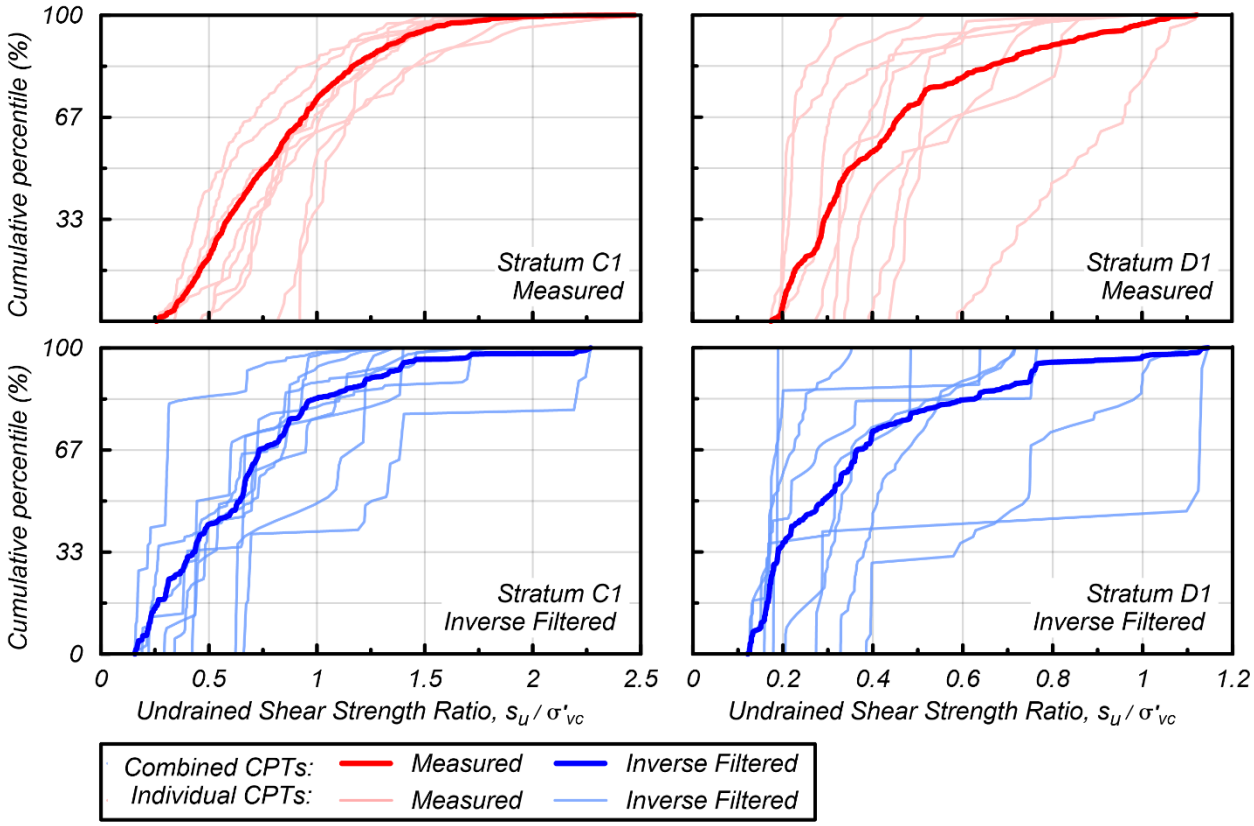

Figure 3.6. Cumulative distributions of the measured and inverse filtered the undrained shear strength ratio (s_u/σ'_{vc}) from all CPTs at the site, for all NDA strata modeled as PM4Silt.

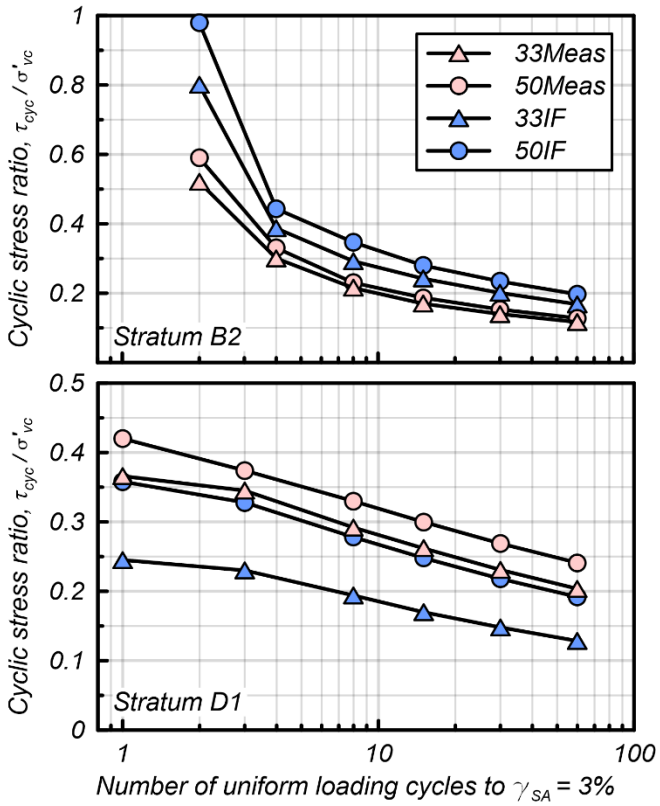

Figure 3.7. Minimum CSR to reach 3% single-amplitude shear strain in a given number (N) of stress cycles for four parametric cases: (a) using PM4Sand for stratum B2, and (b) using PM4Silt for stratum D1.

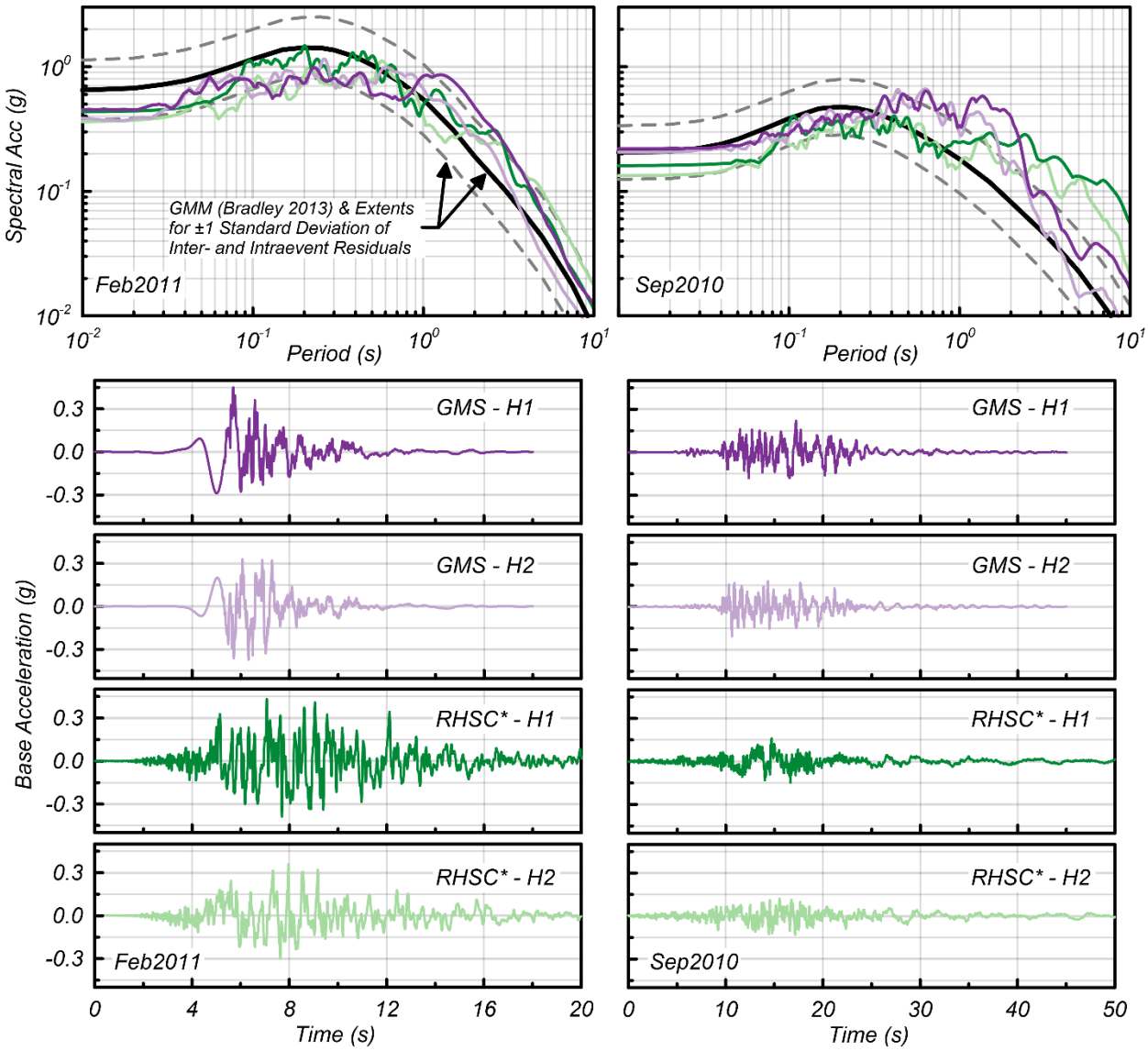

Figure 3.8. Acceleration response spectra and time histories of input ground motions considered for NDAs.

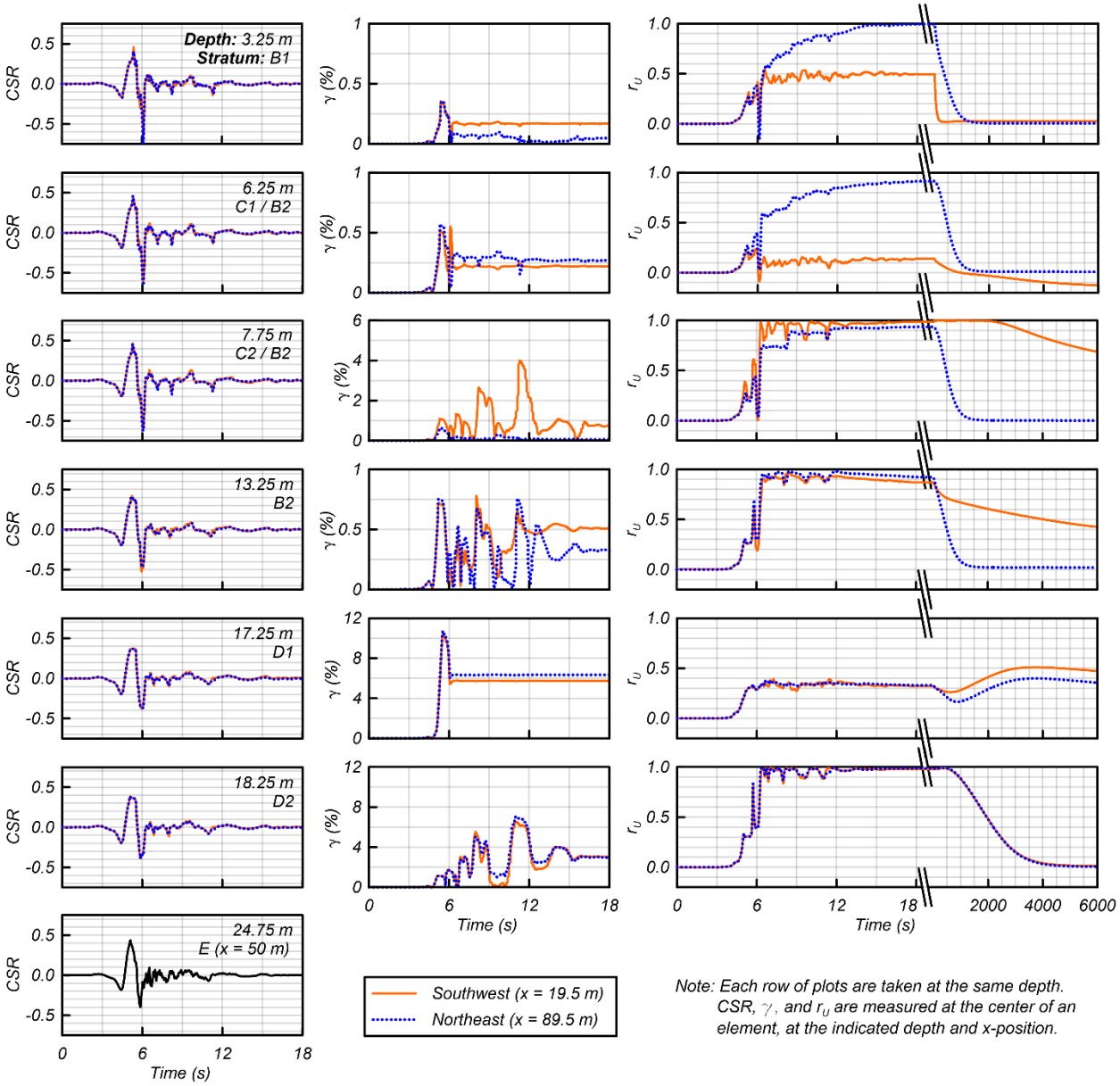

Figure 3.9. Time histories from the *33Meas* model with the *Feb2011* GMS-H1 motion.

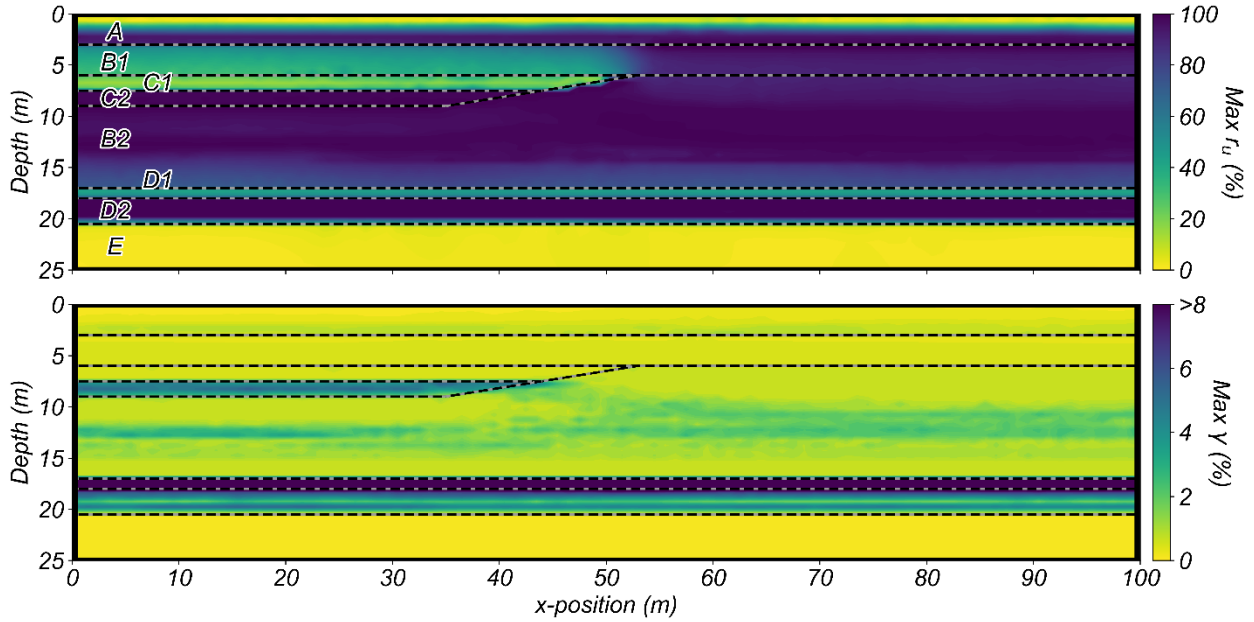

Figure 3.10. Contour plots for the *33Meas* model with the *Feb2011* GMS-H1 motion: (a) maximum excess pore pressure ratio, and (b) maximum shear strain.

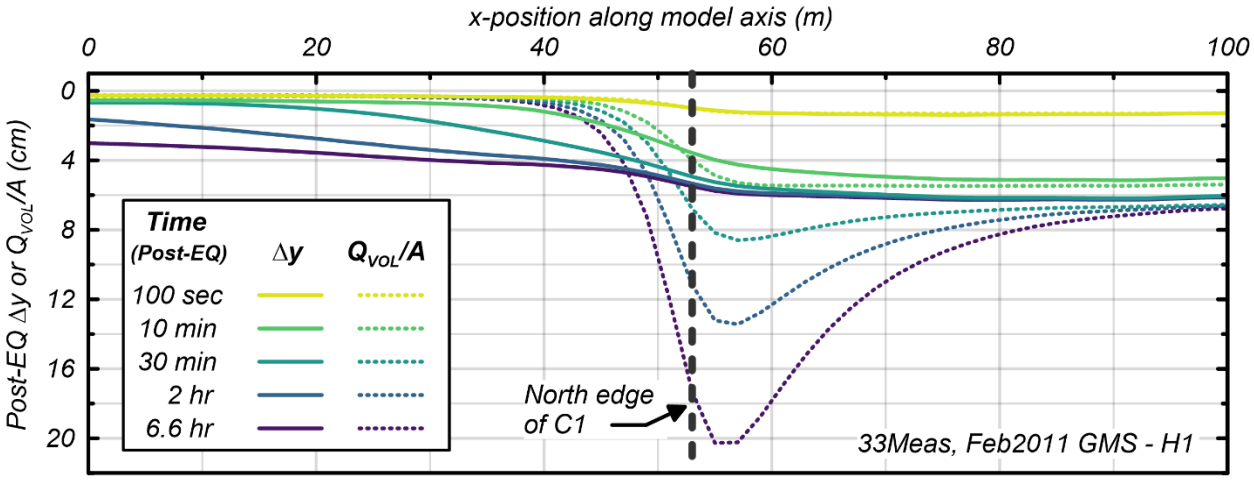

Figure 3.11. Isochrones of the total outflow volume per unit area (Q_{VOL}/A) and vertical displacement relative to stratum D1 (Δy) as measured at the phreatic surface for the *33Meas* model with the *Feb2011* GMS-H1 motion.

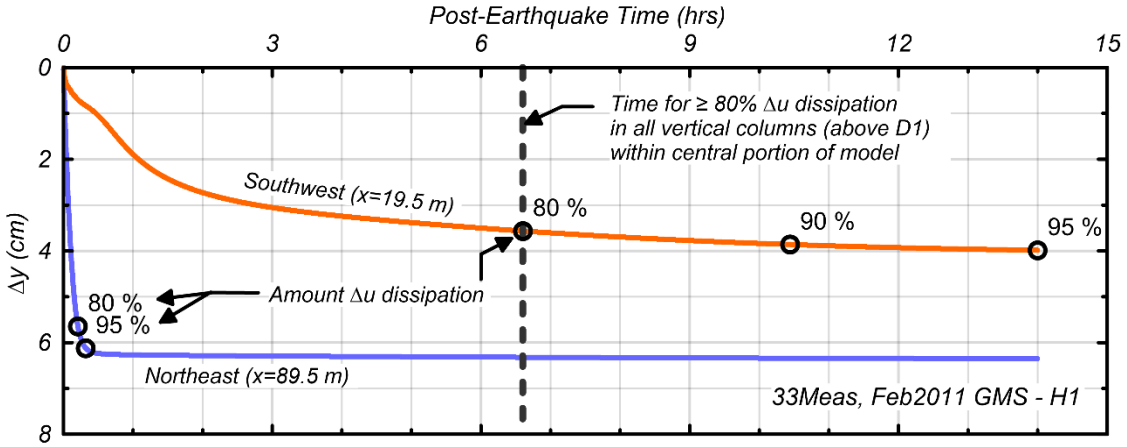

Figure 3.12. Time histories of post-earthquake ground surface vertical displacement relative to stratum D1 (Δy) for the 33Meas model with the Feb 2011 GMS-H1 motion.

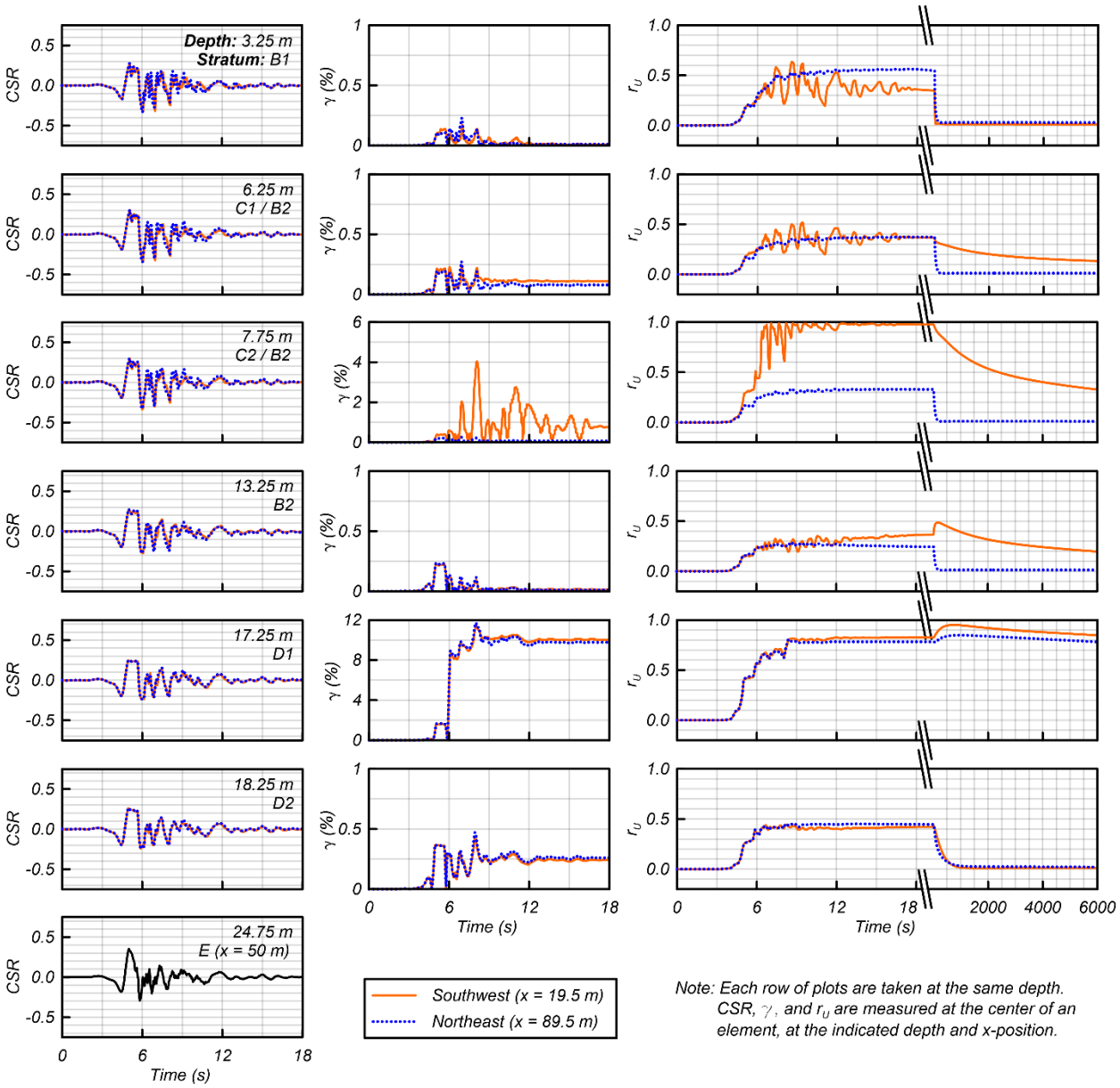

Figure 3.13. Time histories from the *33IF* model with the *Feb2011* GMS-H1 motion.

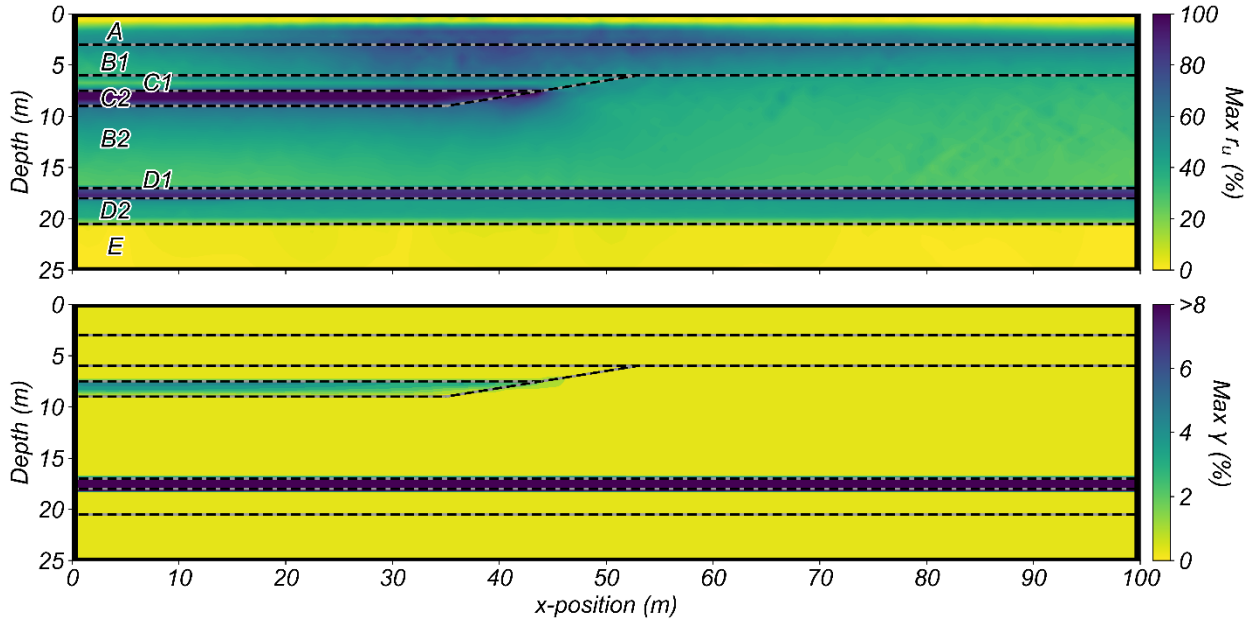

Figure 3.14. Contour plots for the *33IF* model with the *Feb2011* GMS-H1 motion*:* (a) maximum excess pore pressure ratio, and (b) maximum shear strain.

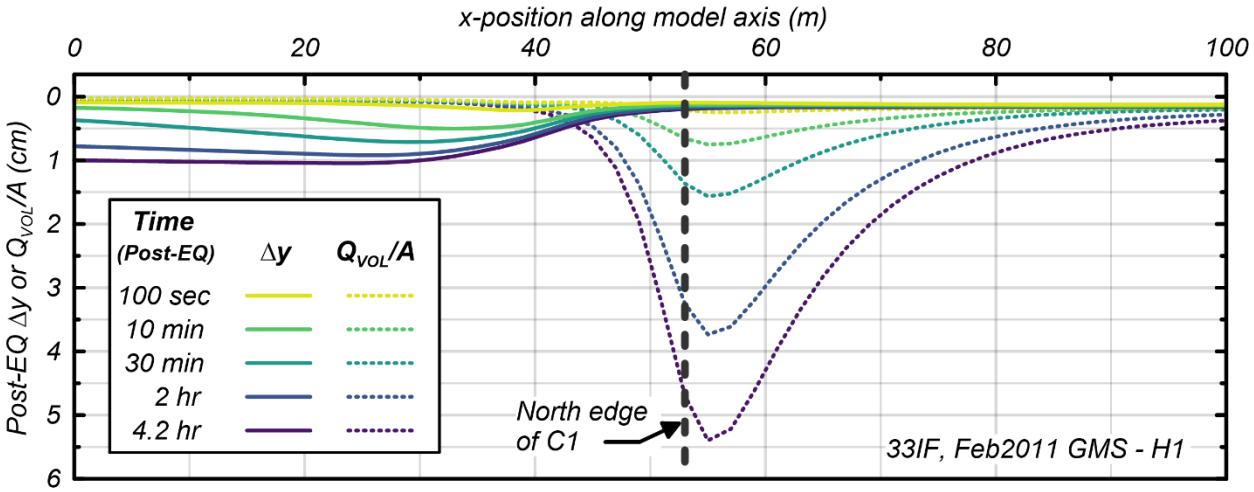

Figure 3.15. Isochrones of the total outflow volume per unit area (Q_{VOL}/A) and vertical displacement relative to stratum D1 (Δy) as measured at the phreatic surface for the *33IF* model with the *Feb2011* GMS-H1 motion.

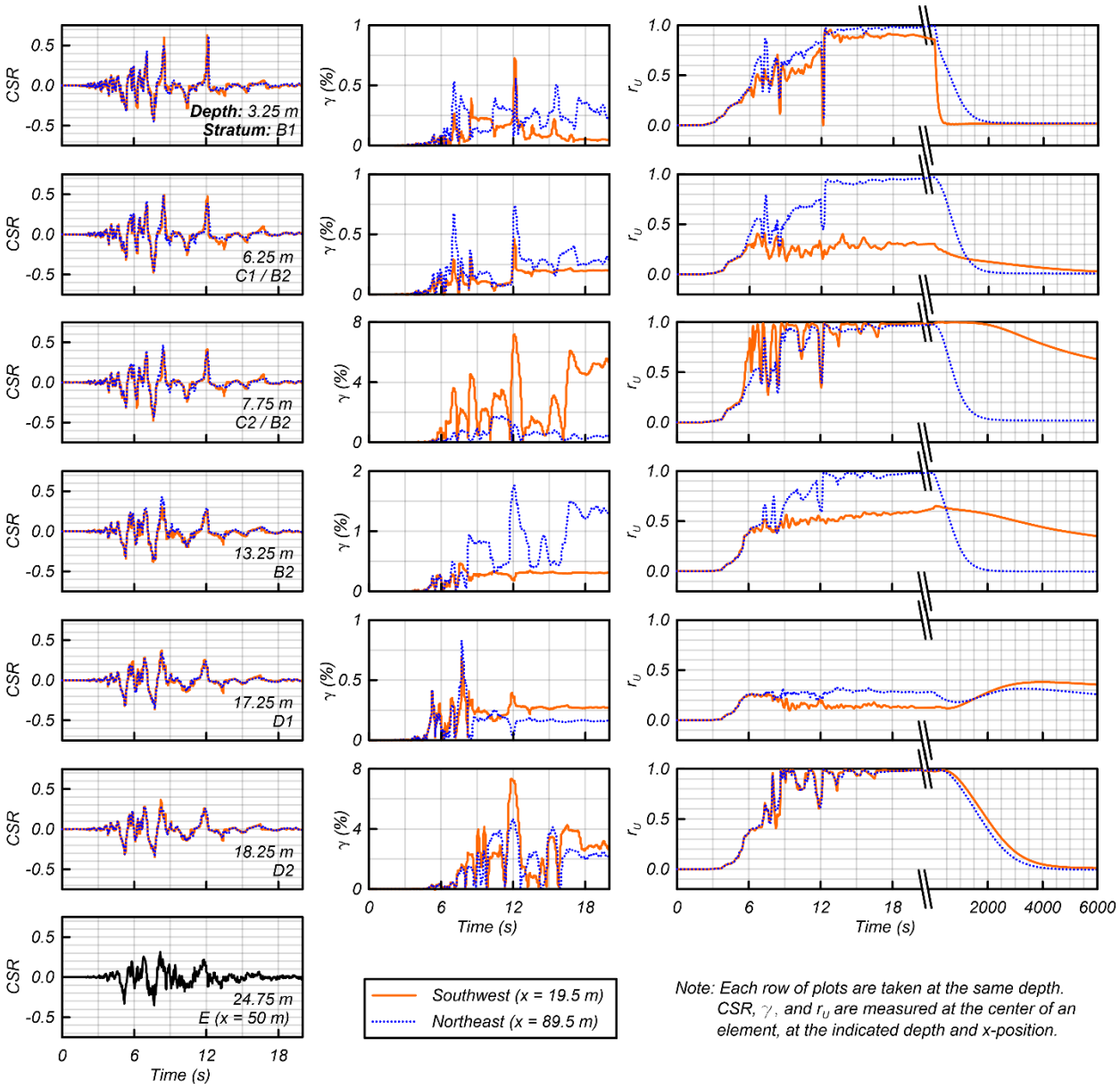

Figure 3.16. Time histories from the *33Meas* model with the *Feb2011* RHSC*-H1 motion.

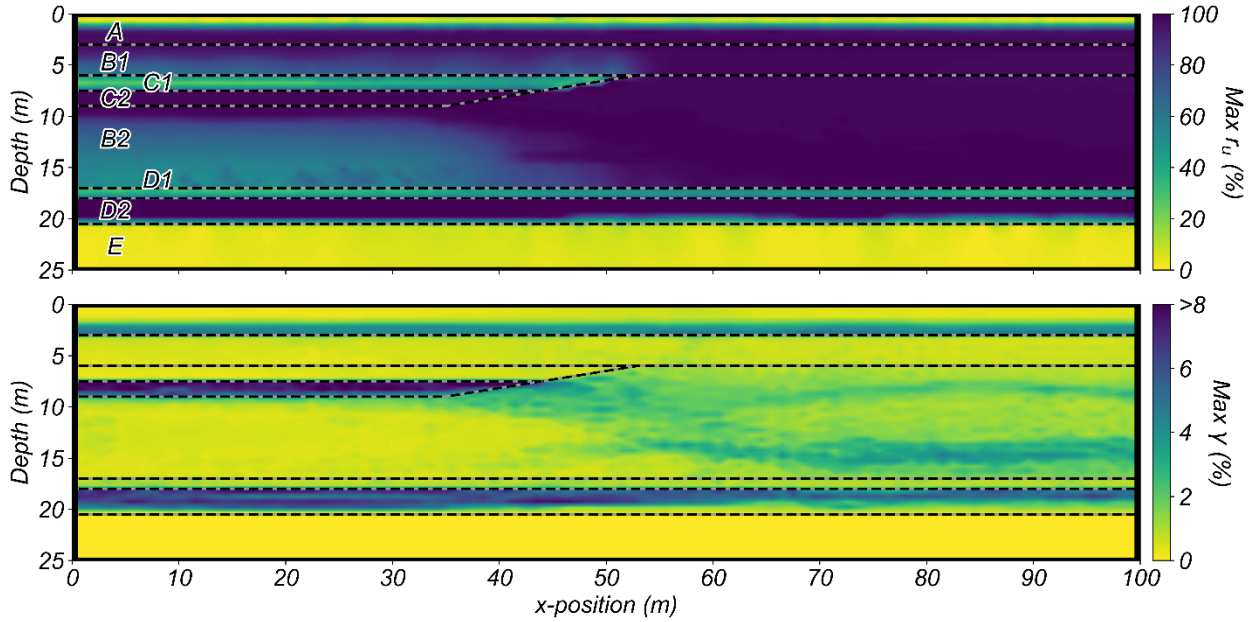

Figure. 3.17. Contour plots for the *33Meas* model with the *Feb2011* RHSC*-H1 motion: (a) maximum excess pore pressure ratio, and (b) maximum shear strain.

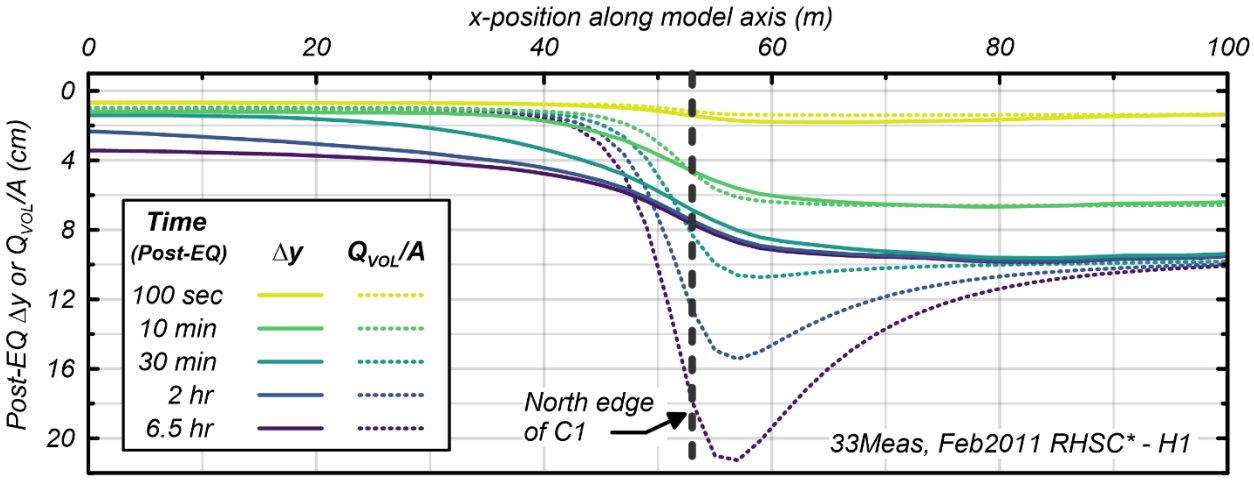

Figure 3.18. Isochrones of the total outflow volume per unit area (Q_{VOL}/A) and vertical displacement relative to stratum D1 (Δy) as measured at the phreatic surface for the *33Meas* model with the *Feb2011* RHSC*-H1 motion.

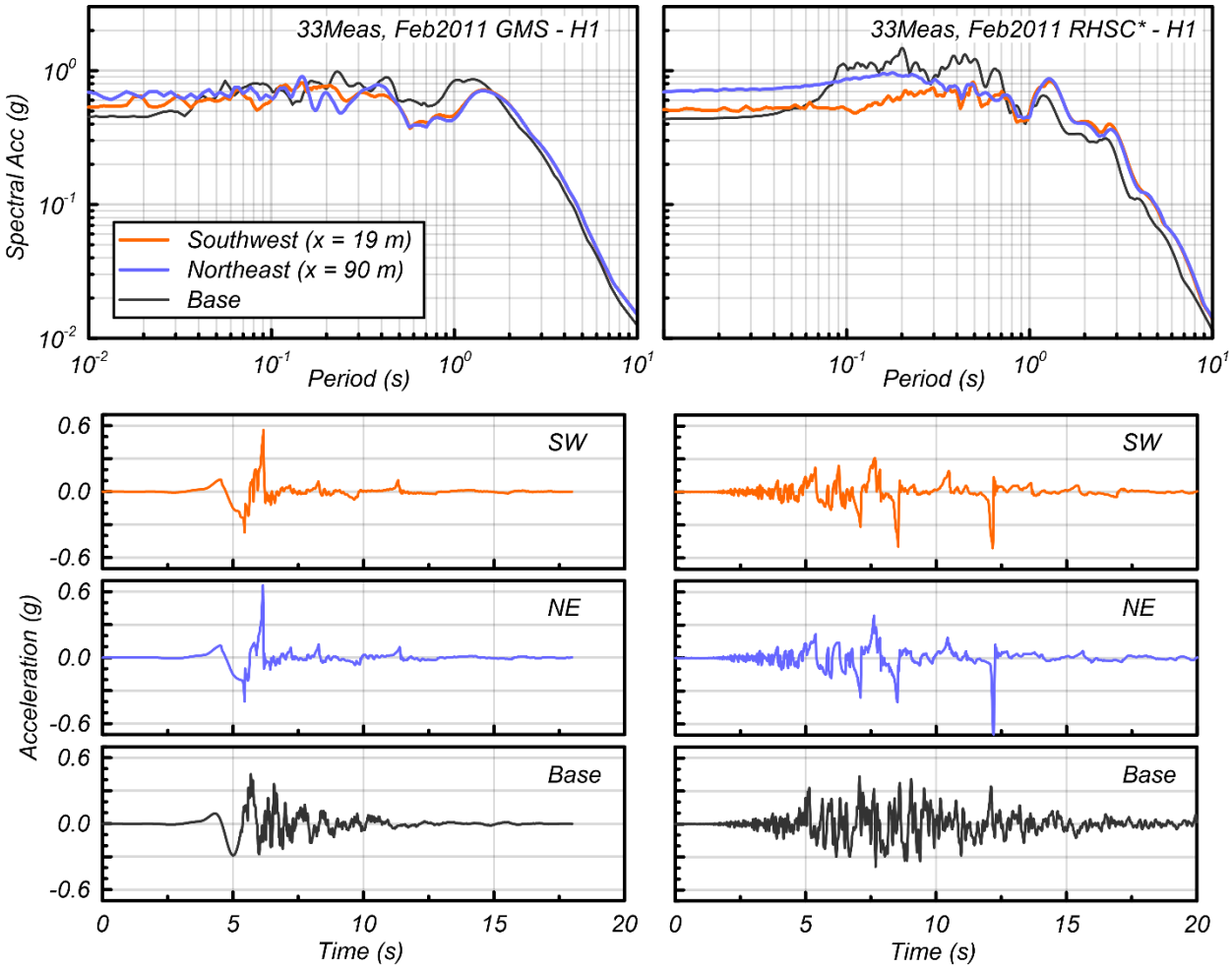

Figure 3.19. Comparison of acceleration response spectra and time histories of base input and surface ground motions from the *33Meas* model with the GMS-H1 and RHSC*-H1 motions for the *Feb2011* event.

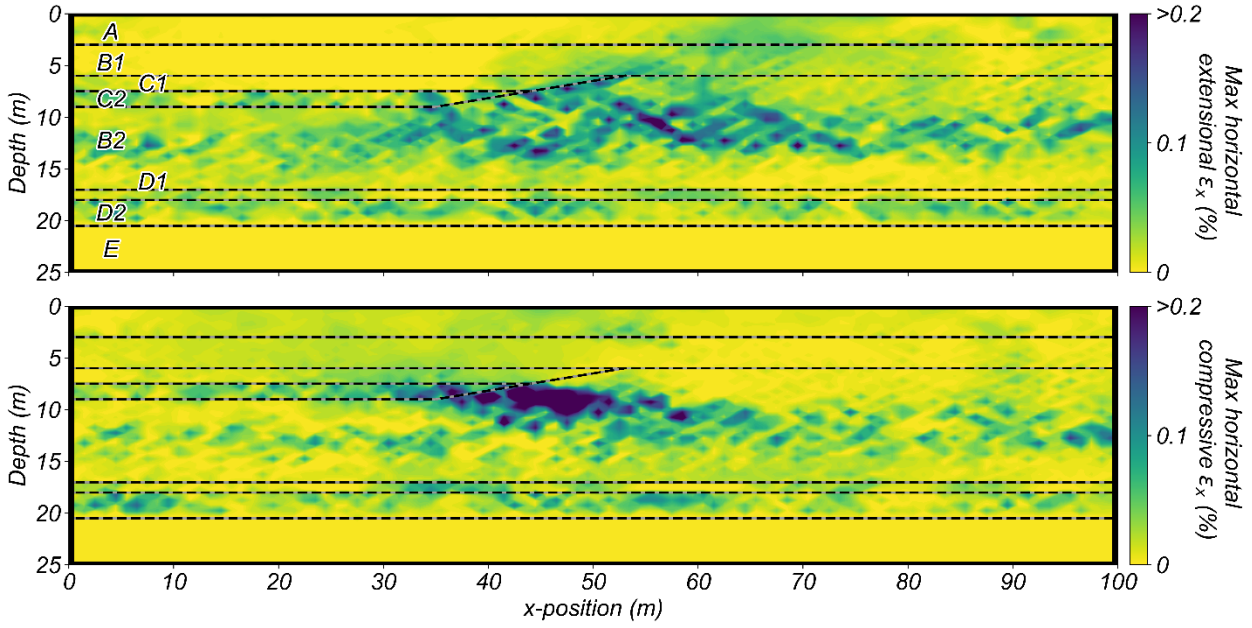

a)

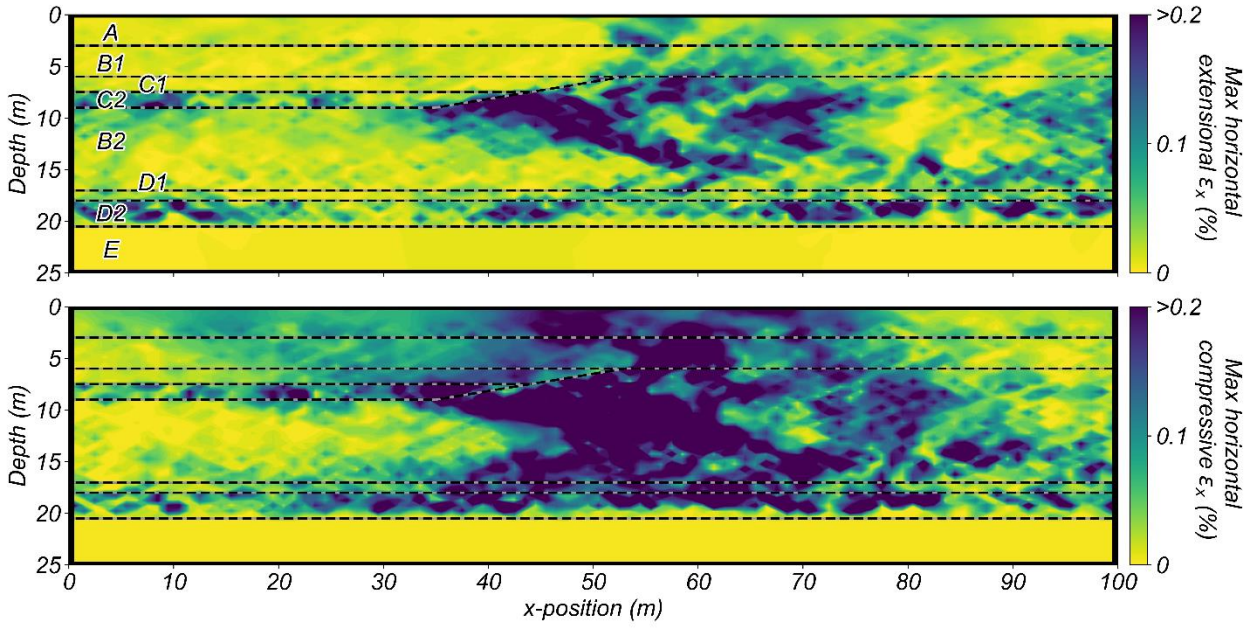

b)

Figure 3.20. Contour plots of maximum horizontal extensional and compressive strains for the (a) *33Meas, Feb2011* GMS-H1 (baseline), and (b) *33Meas, Feb2011* RHSC*-H1 NDA models.

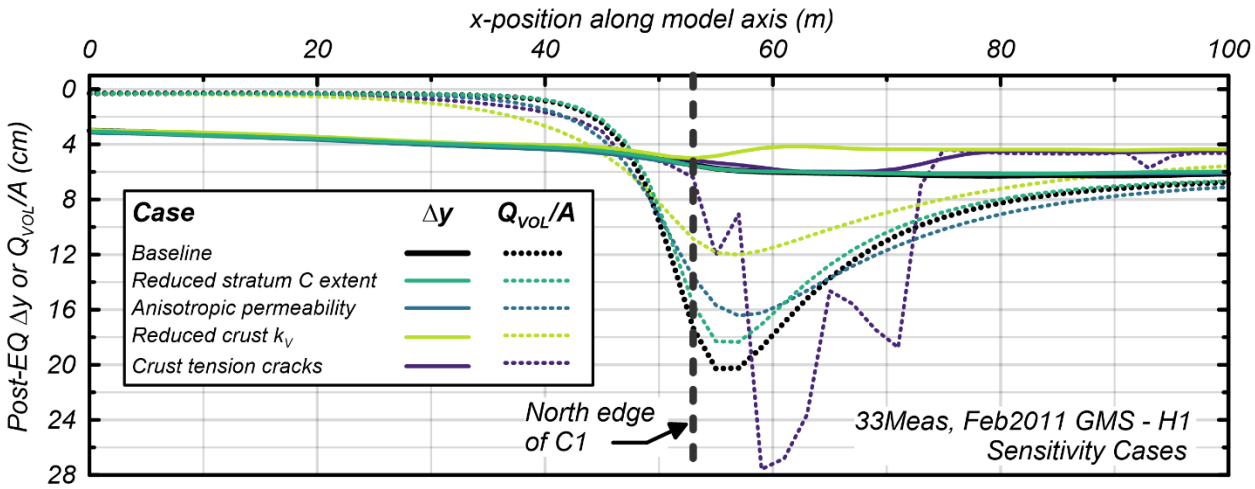

Figure 3.21. Total outflow volume per unit area (Q_{VOL}/A) and vertical displacement relative to stratum D1 (Δy) as measured at the phreatic surface, for different NDA model assumptions related to pore pressure

4. System Response of an Interlayered Deposit with Spatially Distributed Ground Deformations in the Chi-Chi Earthquake

Author's Note

The full content of this chapter has been published in the *Journal of Geotechnical and Geoenvironmental Engineering*. The author performed and interpreted the analyses, and drafted the manuscript. Appendix B includes supplementary figures with the transition probability correlation matrices and example simulation results.

Publication

Bassal, P. C., Boulanger, R. W., & DeJong, J. T. (2022b). "System Response of an Interlayered Deposit with Spatially Distributed Ground Deformations in the Chi-Chi Earthquake." Journal of Geotechnical and Geoenvironmental Engineering. ASCE, 148(10). https://doi.org/10.1061/(ASCE)GT.1943-5606.0002869

Abstract

Lateral spreading of an interlayered deposit adjacent to a meandering stream channel in Wufeng, Taiwan during the 1999 Chi-Chi Earthquake is evaluated using two-dimensional (2D) nonlinear dynamic analyses (NDAs) with geostatistical modeling of the subsurface to assess their ability to approximate the observed magnitude and spatial extent of ground deformations, as well as identify the key factors and mechanisms that most contributed to the overall system response. In-situ data from borings and cone penetration tests (CPTs) depict thinly stratified overbank deposits of low plasticity silty sands, silts, and clays, interlayered with laterally discontinuous channel-deposited sands. The three-dimensional (3D) subsurface is simulated using transition probability-based indicator geostatistics, conditioned on available CPT data and geological inferences. The NDAs are performed using the PM4Sand and PM4Silt constitutive models, within the FLAC finite difference program. Sensitivity analyses are performed to understand the influence of uncertainties in the stratigraphy, channel conditions, soil properties, input ground motions, constitutive model calibration protocols, and numerical boundary conditions, as well as the performance of alternate channel transects. Most analysis cases generally matched the maximum displacements observed near the channel, but over-estimated the extent of displacements away from the channel. The most favorable

results were largely influenced by non-stationary stratigraphic trends and cyclic softening of fine-grained soils, in addition to liquefaction of coarse-grained soils. This case history demonstrates the capabilities and limitations of current subsurface and NDA modeling procedures for predicting ground deformation patterns.

4.1. Introduction

Nonlinear dynamic analyses (NDAs) of case history sites with interlayered soil deposits have been shown to reasonably predict observed ground deformations (i.e. lateral spreading) due to earthquake-induced liquefaction and cyclic softening (e.g., Cubrinovski et al. 2019, Boulanger et al. 2019, Tasiopoulou et al. 2020, Pretell et al. 2021, Bassal and Boulanger 2021). NDAs can account for site-specific ground motions, cyclic stress-strain behavior, and groundwater diffusion, all within a physics-based framework that can capture dynamic fully coupled soil-fluid responses. When performed in two- or three-dimensions (2D or 3D), NDAs can incorporate additional details of the subsurface stratigraphy and overall site geometry to better predict complex ground deformation patterns and other spatially distributed effects.

Simplified estimates of lateral spreading due to liquefiable soils are routinely obtained from site investigation data [e.g., standard penetration tests (SPTs) and cone penetration tests (CPTs)] using (1) empirical approaches (e.g., Bartlett and Youd 1995, Youd et al. 2002) based on regressions of post-earthquake observations with soil, site, and ground motion parameters; or (2) semi-empirical approaches (e.g., Zhang et al. 2004, Faris et al. 2006) that pair regression equations with a displacement index often computed by accumulating incremental ground strains along the depth of a boring or CPT sounding. Among several other simplifications, these methods do not typically account for strains in non-liquefiable soils (e.g., cyclic softening and yielding of soft silts and clays), which have also been observed to cause moderate to large lateral ground deformations in past case studies (e.g., Holzer et al. 1999, Holzer and Bennett 2007). NDAs are well suited to overcome these limitations by allowing for a more complete consideration of the complex system response.

Case histories of post-earthquake ground deformations at sites with interlayered and heterogeneous soil deposits have been well explained by system-level NDA analyses, despite complexities and uncertainties in modeling the subsurface (e.g., Cubrinovski et al. 2019, Boulanger et al. 2019). Such interlayered soil deposits consist of a sedimentary stratigraphy with alternating layers of different lithologies (e.g., sands, silts, and clays). These deposits may further be classified as interbedded when they consist of alternating thin layers (i.e., less than 10 cm thick) (Nichols 2009). Boulanger et al. (2016) describe several factors that may contribute to a tendency for over-estimating liquefaction effects in interlayered deposits. These include limitations in site characterization tools and methods (e.g., thin-layers, transition zones, saturation), engineering correlations (e.g., triggering, shear and volumetric strains), and analysis methods (e.g., neglected consideration of dynamic response, spatial variability, and pore water diffusion). The NDA sensitivity studies of case histories can help elucidate the influence of key contributing factors on the overall response for interlayered sites. Such insight is beneficial to understanding (1) where to focus site investigation efforts for geotechnical studies and post-earthquake reconnaissance efforts for future case histories; (2) which sensitivity studies reasonably bound the system response for site-specific design recommendations; and (3) which limitations and uncertainties need further research.

This paper describes a two-dimensional (2D) NDA study of Wufeng Site C, a rice paddy site adjacent to a meandering stream channel in Wufeng, Taiwan where (1) the soil profile is interlayered and composed of overbank deposits with “intermediate” soil beds (e.g., low-plasticity silty sands and silts) and laterally discontinuous channel-deposited sands, (2) up to about two meters of ground displacements toward the channel were measured following the 1999 Chi-Chi Earthquake, and (3) simplified lateral spreading analyses by Chu et al. (2006) over-estimated observed ground displacements. An early NDA analysis performed by Hsu et al. (2008) that assumed uniform horizontal stratification bands from a single boring log and cyclic soil behavior from the Finn model (Finn et al. 1977) suggested the majority of spreading at this site occurred due to liquefaction of a silty sand band at a depth of 11 m. Yang and Kavazanjian (2021) recently compared NDAs with Newmark sliding block methods for a nearby case history site in Wufeng (Site M), among other case histories, to evaluate the overall magnitude of lateral spreading as determined

at a single ground location. Preliminary NDA results were presented by Bassal et al. (2021a) for Wufeng Site C, which suggested the important influence of stratigraphic details (e.g., geostatistical realizations, the presence of a near-channel soft clay) on the predicted response. Additionally, Bassal et al. (2021b) evaluated the influence of alternate post-liquefaction shear strain-accumulation calibrations on the system response for this site.

This current work enhances the previous studies with an in-depth evaluation of the accuracy by which the NDAs, coupled with geostatistical modeling of the subsurface, could recreate both the magnitude and spatial extent of observed ground deformations, and the key factors and mechanisms that most contributed to the overall system response. The post-earthquake observations and subsurface conditions are first described. Three-dimensional (3D) conditional simulations from transition probability-based indicator geostatistics (Carle and Fogg 1996) were used to model geologically representative realizations of the site stratigraphy for the NDAs. The numerical assumptions, constitutive model calibrations, and input ground motions are then described. The NDAs are performed using FLAC 8.1 (Itasca 2019) with the user-defined PM4Sand (Version 3.1; Boulanger and Ziotopoulou 2017) and PM4Silt (Version 1; Boulanger and Ziotopoulou 2018) constitutive models.. Detailed NDA results are presented for a baseline set of parameters, followed by results of parametric studies examining sensitivity to physically reasonable uncertainties in the stratigraphy (i.e., for different profile transects and geostatistical realizations), channel conditions, soil properties, input ground motions, constitutive model calibration protocols, numerical boundary conditions, and other details. The NDA results are compared to simplified analyses by others and used to evaluate how the dynamic response and ground deformations are influenced by details of the subsurface stratigraphy. The precision by which the NDA results can model the magnitude and spatial extent of ground deformations is shown to be highly dependent on uncertainties in both the model assumptions and field observations. Implications of these results for informing the interpretation of lateral spreading case histories and using NDAs and simplified methods in practice are discussed.

4.2. Ground Failure at Wufeng Site C

On September 21, 1999, the M_W 7.6 Chi-Chi earthquake in central Taiwan produced widespread liquefaction throughout several inland urban centers and coastal areas (e.g., Stewart et al. 2001). Ground shaking within Wufeng was recorded by strong motion stations (SMSs) TCU065 and TCU067, with geometric mean peak ground accelerations (PGAs) of 0.67 g and 0.40 g, respectively (PEER 2013). The Wufeng Site C rice paddy site is located southeast of Chung-Cheng road and experienced moderate ground deformations towards the local west bank of the Ger-Niao-Ken Creek channel (e.g., PEER 2002; Chu et al. 2003, 2006). The stitched photo of Wufeng Site C in Fig. 4.1 was taken less than two months after the Chi-Chi earthquake. The photo depicts a south-facing view of severe building settlements along the northeast bank of the stream channel, and an extensive ground crack network visible through the rice field along the nearly level southwest bank. Additional post-earthquake photos depict the west bank of the channel (i.e., along the rice paddy) was lined with mortar and stones (Chu et al. 2006) with a varying horizontal to vertical side slope ratio of between about 2:1 and 1:1. A visible change of surficial material at the surface may suggest some amount of compacted backfill extending 1 to 2 m behind the lining. The channel has a base width of about 6 m and a depth of about 3 to 3.2 m.

The ground crack locations and lateral spreading displacements at Wufeng Site C were obtained by Chu et al. (2006) based on ground crack-width measurements and aerial photographs. Fig. 2 presents a plan view of the site depicting surface traces of the cracks and displacement vectors (i.e., obtained by superimposing the crack widths from a proposed starting point along a perpendicular transect to the channel). The tail of the vector arrows indicate the locations where crack measurements were obtained. Two essentially distinct lateral spread features occurred with maximum measured displacements of 205 cm oriented east, and 48 cm oriented northeast towards the stream channel. The cracks from the east-oriented displacements extend from between 5 to 25 m from the channel edge from north to south. As traced along section A-A′ the cracks commence about 20 m from the channel edge, and range from 45 to 205 cm. While ground crack measurements provide a reasonable indication of general ground movement adjacent to a channel, several limitations and uncertainties can affect their potential for precisely quantifying the

experienced displacements. Cracks in loose soils may not always be visible and are prone to water-action, caving, and other post-event modifications (e.g., Robinson et al. 2011). Surface cracks are often a secondary effect of deeper ground movement and may not always form in areas with gradual extensional or compressive ground strains.

Several particular features observed at Wufeng Site C may have influenced the surficial expression of observed ground cracks relative to overall displacements. The outer extent of the east-oriented lateral spread feature is bounded by an approximately 37 m long and 45 cm wide crack that is aligned parallel with the orientation of rice crops, an irrigation line, and Chung-Cheng road (Fig. 4.1), suggesting a potential influence of near-surface conditions on the crack location. The southeast end of the site beyond the rice crops in Fig. 4.1 is depicted to be heavily vegetated with concrete reinforcement along the adjacent channel lining in that area. The crack located near CPT WCC-10 extends to over 50 m from the channel in any direction and appears blocked at both ends by the Chung-Cheng roadway, which suggests the possibility for the roadway earthwork to have mitigated far-field displacements.

4.3. Subsurface Conditions

The Wufeng region is in an alluvial valley bounded to the west by the Western Foothills. Holocene sediments extend about 150 m beneath Wufeng (Chu et al. 2003), and are underlain by the Pleistocene Toukoshan formation comprising sandstones, shales, and mudstones (Chang 1971). Wufeng is traversed by the braided Tsao-Hu River at the north, the braided Dry Creek River at the west, and several small meandering streams, including Ger-Niao-Ken Creek.

Thirteen CPT soundings and two borings were conducted at Wufeng Site C within three years following the Chi-Chi earthquake (Chu et al 2004). The locations of the site CPTs (WCC-1 to -11, WCC-13, and RESI-C7) and borings (WCS-1 and -2) are indicated in Fig. 4.2. Index laboratory testing was performed for several boring samples to determine the water content, fines content (FC; percent of dry soil mass passing a 75 μm sieve), and plasticity index (PI). All data are publicly accessible from PEER (2002).

The subsurface profile in Fig. 4.3 shows the measured data from the CPTs nearest to section A-A′ and a deterministic interpretation of the stratigraphy. The cone tip resistance normalized by atmospheric pressure (q_{tN}) is plotted with depth as directly measured for each CPT. The plot is categorized based on the soil behavior type index (I_C) to approximately identify layers of silt mixtures and clays ($I_C > 2.6$), sand mixtures ($2.05 \leq I_C \leq 2.6$), and sands ($I_C < 2.05$); these soil groups respectively map to soil behavior types (SBTs) 3/4, 5, and 6 per Robertson and Wride (1998). The site stratigraphic architecture is shaped by frequent stream channel avulsions, characteristic of highly tectonic regions with cohesive floodplain sediments (Nichols 2009). Surficial reworked miscellaneous sands, silts, and clays (stratum A) were encountered in the top 1 m of the profile. Floodplain deposits (stratum B) extend to a depth of about 15.5 m and are primarily composed of overbank silty sands interlayered with variable lenses of low plasticity, over-consolidated silts and clays, typically less than 50 cm thick. Lenses of channel-deposited sands with trace to little fines are also present within stratum B, as indicated in the borings and typically coinciding with $I_C < 2.05$ from nearby CPT logs. The floodplain deposits in the upper 4 m of stratum B (i.e., B_{upper}) generally have lower q_{tn} values than deeper material (i.e., B_{lower}). A soft and lightly over-consolidated 1-m-thick clay lens is encountered near the channel at a depth of 4 m at WCC-3. This lens is situated near the base of the inner meander bend (i.e., point bar) of the Ger-Niao-Ken Creek and may underlie a zone of lateral accretion deposition from recent channel migration. The orientation of stratification from lateral accretion may dip at angles of up to about 15°, roughly parallel to the inner bank of a natural channel (Nichols 2009). The available data is insufficient to demarcate and constrain the extents of these point bar features. Over-consolidated stiff clays with occasional silty sand seams (stratum C) underlies stratum B to the maximum depth explored.

The groundwater level during drilling was estimated from the CPTs and borings to be 1 to 1.5 m below the ground surface during the site investigation. These levels are likely consistent with conditions during the earthquake (Chu et al. 2006). A lower water level within the channel of less than one meter above the channel base is assumed from post-earthquake photos.

4.4. Geostatistical Subsurface Model

4.4.1. Transition Probability Modeling

The geostatistics software package T-PROGS (Carle 1999) was used to develop 3D conditional categorical realizations of the interlayered stratum B (other strata are considered dominated by single category soil types). Stratum B was modeled with three soil categories: B3 clays and silts, B5 silty sands, and B6 sands. These categories were divided according to the I_C ranges listed in Fig. 4.3 and labeled as B3, B5, and B6; the number indicates the most pertinent SBT per Robertson and Wride (1998). The transition probability-based approach of T-PROGS is advantageous for geotechnical subsurface simulations of interlayered deposits since it accounts for geologically-derived attributes of distinct soil categories, including their (1) proportions, (2) mean thicknesses and lengths, and (3) juxtaposition tendencies (i.e., relative ordering) (Carle and Fogg 1996). These attributes are considered for three spatial dimensions in the development of Markov chain models, which approximate the transition probability between soil categories at a specific location, given a previously defined soil category at a specified lag distance away. Realizations that honor these models and the available site data are then produced with a co-kriging based sequential indicator simulation approach (Deutsch and Journel 1992) and refined with a simulated quenching optimization algorithm.

Details regarding the transition probability analyses were described by Bassal et al. (2021a) and are summarized herein. The stratum B geostatistical realizations were developed for the rectangular area bounded by the dashed line in Fig. 4.2. The measured data from all CPTs within this area for all depths of stratum B (~1 to 15.5 m) were considered for estimating the Markov chain transition probability models and associated soil proportions, mean thicknesses and lengths, and relative ordering for three spatial dimensions. Due to a general consistency between the measured transition probabilities above and below 5 m (i.e., B_{upper} and B_{lower}), one set of Markov chain models were used for the entirety of stratum B. For soils B3, B5, and B6, proportions were estimated as 42, 50, and 8%, and mean thicknesses were estimated as 40, 40, and 100 cm, respectively. The relative ordering of soil units was approximated to allow a fining upwards tendency between categories (e.g., B6 is more often overlain by B5 than B3). The spatial dependence

between the three soil categories for the upwards vertical direction is depicted by the transiograms presented in Fig. B.1 in Appendix B. Despite the relative sparsity of measured data to estimate horizontal transition probabilities, geological inference supported by the channel dimensions and CPT data was used to estimate baseline mean lengths of 20 m for B3 and B5, and 16 m for B6, in the x-orientation (i.e., east-west; aligned with section A-A′), and 20 m for all soil types in the y-orientation (i.e., south-north, perpendicular to A-A′).

As expected in floodplain deposits and observed from the site CPTs, finer materials tend to exist furthest from coarser channel-deposited lenses. The CPTs WCC-11 and -13 indicate a higher proportion of B3 clays (i.e., 60-85%) than all site CPTs within 50 m of the channel (i.e., 35-45%). The observed lateral non-stationarity of mean values was approximately accounted for by conditioning the simulations on the measured CPT data. The full stratum B thickness at the western 3 m end of the site was further conditioned as uniform B3 material to approximate expected behavior beyond the model extents and minimize boundary strains during the dynamic analyses.

A generated 3D realization of stratum B is depicted in Fig. 4.4, hereafter referred to as realization R1. The “xyz” Cartesian coordinate system is referenced to a datum located at the surficial origin point indicated in Fig. 4.2. The mesh element size is x=1.5, y=2.5, and z=0.4 m, within an overall grid size of x=75, y=45, and z=14.4 m. Note that the layers for each soil type are at least 40 cm thick to allow representation by at least two 20 cm thick mesh elements for the NDA analyses. Although this mesh resolution cannot explicitly model soil layers thinner than 40 cm, it captures typical layer thicknesses interpreted from the CPTs and represents the overall soil interlayering at an effective scale. The realizations capture most of the important stratigraphic features depicted in Fig. 4.3 expected to influence the seismic analyses, including the largest B6 channel sand units, and frequent interlayering between the B3 and B5 overbank deposits.

Two-dimensional transects were extracted from the 3D realizations of stratum B for the NDA sensitivity studies later described. Five 2D slices of R1 were taken perpendicular to the channel at 10 m

intervals, as indicated by transects T1-T5 mapped in Fig. 4.2. Transect T2 is representative of the stratigraphy along section A-A′. Four other realizations of stratum B (i.e., R2-R5) were obtained using the same parameters as R1. These realizations were manually selected from a much larger suite of realizations to capture a range of different but plausible near channel soil conditions. Five additional realizations (i.e., R6-R10) were similarly obtained with the exception of assuming halved mean lengths for the B3 and B5 overbank deposits (i.e., 10 m rather than 20 m in the x and y orientations). The five 2D transects T1-T5 of R1, and R2-R10 at transect T2 are depicted in Figs. B.2-B.4 in Appendix B.

4.4.2. Representative Properties

Representative properties were reasonably estimated for baseline NDA analyses from available site data for all distinct materials. The variability of data across the site was considered for determining the normalized clean sand corrected tip resistance (q_{c1Ncs}) for sand-like soils B5 and B6, the peak undrained shear strength ratio ($s_{u,peak}/\sigma'_{vc}$) for B3 clays and silts, and the peak undrained shear strength ($s_{u,peak}$) for stratum C. Baseline NDA properties were ultimately chosen based on CPT data after inverse filtering using the procedure of Boulanger and DeJong (2018) with baseline filter parameters. Inverse filtering is expected to approximately remove thin-layer and transition zone effects from the CPT measurements, and provide more accurate parameter estimates based on q_{tN}. The measured CPT data was used to develop the stratum B subsurface models since the minimum layer thickness in the numerical models was 40 cm and the inverse filtering method primarily provides refinements in layering at smaller layer thicknesses.

Cumulative distribution functions (CDFs) of q_{c1Ncs} values for soils B5 and B6 in the upper and lower portions of stratum B (i.e., denoted $B5_{upper}$, $B6_{upper}$, $B5_{lower}$, and $B6_{lower}$) from all CPTs at the site are depicted in Fig. 4.5. The Boulanger and Idriss (2014) methodology was used to calculate q_{c1Ncs}, with a site-specific fines content correction factor (C_{FC}) of –0.37 for the measured data and –0.24 for the inverse filtered data. These factors were calibrated by regressing sampled fines contents from borings WCS-1 and -2 to median I_C readings from adjacent CPTs over the sampled depth interval. The faint lines in Fig. 4.5 depict the CDFs for data from individual CPTs, while the bold lines represent the CDFs for combined data from

all CPTs. The general consistency between CDFs for the individual CPTs suggests no significant non-stationary trends (i.e., lateral trends between CPTs) in q_{c1Ncs} for the soil groups considered. Inverse filtering of the CPT data results in typically greater q_{c1Ncs} values and increased variability (i.e., shallower CDF slope) among individual CPTs for each soil group. For the baseline NDAs, median (50^{th} percentile) estimates of q_{c1Ncs} were selected from the combined data for inverse filtered CPTs; this is within the recommended 30^{th} to 70^{th} percentile range of Montgomery and Boulanger (2016) for uniform NDAs to provide an unbiased estimate of lateral spreading displacements. The selected representative q_{c1Ncs} values are 76, 89, 116, and 137 for $B5_{upper}$, $B6_{upper}$, $B5_{lower}$, and $B6_{lower}$, respectively.

Representative $s_{u,peak}/\sigma'_{vc}$ values for the B3 clays and silts were determined after considering the variability of the estimated inverse filtered data with depth for all CPTs at the site as depicted in Fig. 4.6. The $s_{u,peak}/\sigma'_{vc}$ for direct simple shear (DSS) loading was calculated with a cone bearing factor (N_{kt}) of 18 (e.g., Mayne and Peuchen 2018). Only layers thicker than 20 cm with $I_C > 2.6$ were considered, and data near transition interfaces were subjectively eliminated to avoid the influence of thin layer transitions even after inverse filtering. The $s_{u,peak}/\sigma'_{vc}$ was estimated for the baseline NDAs in the near-channel region of section A-A′ as 0.38 (i.e., $B3_{channel}$; considering data from WCC-3, assigned to depths above 5 m and laterally within 6 m from the edge of the channel) and away from this region as 0.76 (i.e., B3; considering all other CPTs, assigned to all other distances and depths). These estimates are consistent with the expectation that B3 is normally-to-lightly overconsolidated within the shallow near-channel point bar deposits (i.e., near WCC-3) and moderately overconsolidated in typically older deposits outside the meander bends of the channel (i.e., near RESI-C7 and all other CPTs). Assuming the CPT sleeve friction (f_s) as indicative of the remolded shear strength of the soil (Lunne et al. 1997), the sensitivity is estimated as 1.5 for $B3_{channel}$ soils and 1.0 for typical B3 soils. For stiff clay stratum C, an $s_{u,peak}$ of 150 kPa is assumed from similar calibration factors.

Other soil parameters were estimated based on correlations with CPT data. The mortar and stone channel lining, believed to be loosely bound, is modeled as a Mohr-Coulomb material with a cohesion of 20 kPa and friction angle of 10°. The compacted zone beside the channel is assumed to have a q_{c1Ncs} of 126;

consistent with a relative density (D_R) of 65%. The stratum A surficial reworked material may have been lightly compacted, if at all, and is assumed to have a q_{c1Ncs} of 76, identical to B5. The saturated unit weight (UW_{sat}) is estimated as 20 kN/m^3 for stratum A and 21 kN/m^3 for all other strata. Vertical hydraulic conductivities ranged from 1E-08 m/s for the B3 clays and silts to 1E-05 m/s for the B6 sands, as estimated per Robertson (2010) from I_C averages for each soil group. The horizontal to vertical permeability ratio was assigned as 2 for the B6 sands, and 10 for all other soil and material groups. The normalized shear wave velocity (V_{s1}) was estimated from q_{c1Ncs} and FC estimates for the sand-like soils per Andrus et al. (2004) as 165, 177, 180, and 195 m/s for $B5_{upper}$, $B6_{upper}$, $B5_{lower}$, and $B6_{lower}$, respectively. The mortar and stone lining, compacted zone, and stratum A were similarly assigned V_{s1} values of 125, 188, and 165 m/s, respectively. The V_{s1} for all B3 soils was estimated as 193 m/s per Carlton and Pestana (2012). The V_{s1} in stratum C up to a depth of 30 m was estimated from a seismic CPT and down-hole suspension log performed near TCU065 as 236 m/s (PEER 2002). This nearby data was also used to model an elastic halfspace below 30 m with a V_{s1} of 325 m/s, Poisson ratio of 0.33, and equivalent-linear shear modulus of 300 MPa.

4.5. Nonlinear Dynamic Analysis Methodology

4.5.1. Numerical Model

The Wufeng Site C section A-A′ profile was modeled for 2D NDAs using the finite difference program FLAC 8.1 and the user-defined PM4Sand and PM4Silt constitutive models. The left half of the full plain-strain mesh (with stratum B realization R1) is depicted in Fig. 4.7; the right half of the mesh is an exact mirror image, symmetric about the channel centerline, to reduce detrimental effects of a mesh boundary at mid-channel. The mesh extends to 66 m away from the left edge of the channel to the approximate edge of Chung-Cheng road. The mesh approximates the channel geometry with side slopes of 1.8H: 1V, a base width of 6 m, and a depth of 3.2 m. A 0.25% downgrade slope towards the channel is modeled based on surface elevations surveyed at CPT locations. The mortar and stone channel lining and adjacent compacted soil zone are each approximated with a width of 1 to 2 m. The full model mesh is 150 m long by ~32 m tall, and is comprised of 16,896 elements. Elements are typically 75 cm long by 20 cm

tall above 16 m depth (except they are 50 cm tall in stratum A and skewed near the channel), and are 150 cm long by 100 cm tall below this depth. Stress conditions were initialized prior to dynamic loading by choosing elastic moduli that would produce a coefficient of earth pressure at rest (K_o) of 0.5 for all soil groups. The water table was initialized by setting a static phreatic surface of 1 m outside the channel and 0.6 m above the channel base, and allowing flow to equilibrate between these areas. The moist total density above the phreatic surface was set as 85% of the saturated total density. The water tensile stress limit was initialized at 5 kPa to allow for saturation (capillary rise) up to about 0.5 m above the phreatic surface. This tensile limit was increased to 100 kPa during earthquake excitation to allow for transient negative pore pressures. Groundwater flow was modeled over the duration of ground shaking. The large-strain mode of FLAC was used; sensitivity studies exclusively using large or small strain modes did not significantly affect the predicted ground deformations. The dynamic analyses considered a compliant (quiet) model base, with the outcrop input motion applied as a horizontal stress-time history. Rayleigh damping of 0.5% centered at a frequency of 1 Hz was applied during shaking.

Two alternate side boundary conditions were considered to evaluate the ground deformation mechanisms at this study site: (1) attached boundaries and (2) absorbing boundaries. The first condition attaches the left and right boundaries of the model (symmetric right side is not shown in Fig. 4.7) so that all stresses and strains behave in congruence across the boundary during the analyses. The symmetry of the model essentially allows for any extensive deformation mechanisms to seamlessly propagate through the sides of one boundary to the opposing boundary on the other side. The other condition uses radiating or “free-field" side boundaries and considers all columns within 3 m of the boundaries as elastic, to adequately confine all interior zones after they liquefy or soften. A 30% reduction was applied to the small-strain shear moduli of the elastic columns (i.e., obtained from the V_S of each soil group and a Poisson’s ratio of 0.33) to accommodate cyclic degradation. For all cases, the pore pressure boundary conditions were freed (i.e., impermeable) at the sides and bottom of the model and fixed (i.e., allowed to flow outside the model) at the top of the model.

4.5.2. Calibration of Constitutive Models

Considerations for calibrating the PM4Sand and PM4Silt constitutive models used for all soils at the site are detailed in Bassal et al. (2021a, 2021b), and a summary of values used for the current baseline NDA analyses are presented herein. Other parametric variations considered for the sensitivity NDA analyses are discussed with the results for those variations. The shear modulus coefficient (G_o) was derived from V_{s1} and UW_{sat} for all soils, and default parameters were used unless stated otherwise. The PM4Sand parameters were initially calibrated for representative values of q_{c1Ncs} for all sand-like soils (i.e., stratum A, compacted zone, B5, B6), with relevant parameters shown in Table 4.1. The apparent relative density (D_R) was obtained from the q_{c1Ncs} relationship by Boulanger and Idriss (2014). The contraction rate parameter (h_{po}) was calibrated under single-element undrained DSS simulations until 3% single-amplitude shear strain (γ) was obtained with 15 uniform stress cycles (N) equivalent to the cyclic resistance ratio [$CRR_{M7.5}$; obtained from the relationship of Boulanger and Idriss (2014) for a 50% probability of liquefaction (P_L) and adjusted for the vertical effective stress (σ'_{vc}) near the center of the material zone]. To account for the post-liquefaction shear strain accumulation rate, secondary parameter C_ε was adjusted in the calibrations to match the empirical median post-liquefaction compliance rate ($\Delta\gamma_{post\text{-}liq\ per\ cycle}/\tau_{cyc}$) proposed by Tasiopoulou et al. (2020). Details regarding the influence of alternate considerations of the shear strain-accumulation rate at Wufeng Site C were evaluated by Bassal et al. (2021b).

The PM4Silt parameters were initially calibrated for representative values of $s_{u,peak}/\sigma'_{vc}$ for the B3 and $B3_{channel}$ soils, and $s_{u,peak}$ for stratum C, with all adjusted parameters shown in Table 4.2. The representative residual undrained shear strengths ($s_{u,cs,eq}/\sigma'_{vc}$ and $s_{u,cs,eq}$; i.e., after consideration of a sensitivity of 1.5 for $B3_{channel}$ and 1.0 elsewhere) were increased by 25% to account for the rate of earthquake loading. Undrained DSS simulations were used to calibrate shear modulus parameter (h_o) to approximate the shear modulus reduction and equivalent damping behavior of the empirical relationship of Darendeli (2001). The h_{po} was calibrated to produce a reasonable slope of cyclic stress ratio (CSR) against N to reach a single-amplitude shear strain (γ_{SA}) of 3%. The void ratio (e_o) was estimated from index tests. The $B3_{channel}$

soft clays were assigned a bounding surface parameter ($n^{b,wet}$) of 0.01 and an artificially-high value for the critical state friction angle (ϕ'_{cv}) of 45° to obtain the target $s_{u,peak}/\sigma'_{vc}$ and sensitivity values.

A comparison between the calibrated cyclic strength versus N to γ_{SA} = 3% for all soil groups within the stratum B floodplain deposit are depicted in Figs. 4.8a and 4.8b. While the characteristics of the earthquake ground motion and time- and depth- dependent wave propagation ultimately influence the equivalent N-value and CSR within the soil profile, these responses approximately represent the relative cyclic strengths between soil groups during cyclic loading. The B3 and $B3_{channel}$ soil groups modeled with PM4Silt (Fig. 4.8a) typically have a shallower CSR-N slope than the B5 and B6 soil groups modeled with PM4Sand (Fig. 4.8b) for N < 15, indicating a more subtle influence of strength loss due to cyclic mobility in the clays and silts. The B3 silts and clays are largely more resistant to yielding than all other soil groups for N > 2, whereas the $B3_{channel}$ soft clays have the lowest strengths for N < 2.

4.5.3. Input Ground Motions

Processed ground motions for the 1999 Chi-Chi earthquake event were obtained from the TSMIP (Taiwan Strong Motion Instrumentation Program) station TCU067 (PEER 2013). TCU067 recorded a PGA of 0.50 g along the east trending (270°) component, and is located about 5 km northeast of Wufeng Site C and 350 m northwest of the Chelungpu surface fault rupture. It is situated over stiff material with a shear wave velocity in the upper 30 m (V_{s30}) of 440 m/s (Kuo et al. 2012), making it ideal for direct input at the NDA model base without further deconvolution. TCU067 is believed to provide more reliable data for modeling Wufeng Site C than the nearby TCU065 (i.e., located 0.5 km northeast of the site), which would instead require non-standard modifications for deconvolution through nonlinear soils (Chu 2006, Bassal et al. 2021a).

Since both the study site and TCU067 are about the same distance and direction away from the fault rupture (i.e., within 350 m northeast of the fault), it is assumed that the orientation of each TCU067 ground motion component is representative of the same orientations felt at the site. Thus, the east-oriented (270°) component, or TCU067-E, is believed to best model the motion perpendicular to the river channel

along section A-A′, and is used as a baseline input for the 2D NDAs. However, other orientations, with and without the vertical motion, are used to evaluate the sensitivity of ground deformations to the input motions. The acceleration time histories and response spectra for four ground motion orientations obtained from TCU067 are depicted in Fig. 4.9. These represent recordings oriented in the north (0°), northeast (315°), east (270°; baseline input), and southeast (225°) directions (i.e., TCU067-N, -NE, -E, and -SE). The time histories (Fig. 4.9a) were cropped to an effective duration of 40 s and baseline corrected. The TCU067-SE motion coincides with an approximately fault-normal direction and accordingly has the highest intensity PGA pulse of 0.55 g. Differences in the intensity and frequency content between the four orientations are apparent in the 5% damped acceleration response spectra (Fig. 4.9b). The spectra are compared to median and ±1 standard deviation predictions from four equally-weighted Next Generation Attenuation (NGA) West2 ground motion models (GMMs) by Abrahamson et al. (2014), Boore et al. (2014), Campbell and Bozorgnia (2014), and Chiou and Youngs (2014). Input parameters for the GMMs were estimated from fault attributes described by Lin et al. (2002) and shear wave velocity data compiled by Kwok et al. (2018), as applicable to the study site. The TCU067-N and -NE spectra tend to lie below the standard deviation bounds at periods below 0.5 s, but all spectra reasonably lie within these bounds at larger periods that are more consequential to the dynamic response.

4.6. Dynamic Simulation Results

Results are presented for NDAs to examine the effects from a broad range of reasonable assumptions and realizations of the site stratigraphy, channel conditions, soil properties, input ground motions, constitutive model calibration protocols, numerical boundary conditions, and other details. The influence of these uncertainties on the dynamic response and the resulting ground deformation magnitude and distribution away from the channel face are observed in relation to a baseline case. The baseline case represents one of several cases that use reasonable assumptions for inclusion in a sensitivity analysis for routine design efforts. However, it is not meant to represent the “best” or recommended set of assumptions for routine design. The baseline case is representative of profile section A-A′ (i.e., near transect T2) using

stratigraphic realization R1, ground motion TCU067-E, and attached side boundaries, with other previously defined numerical assumptions, site geometry, and material properties (i.e., Tables 1 and 2).

The dynamic response of the baseline NDA is depicted by maximum engineering shear strain and horizontal displacement contours in Figs. 4.10a and 4.10b. The maximum shear strains (γ; defined as the engineering strain for the principal stress orientation) reached >100% within the $B3_{channel}$ soft clays during the first 12 s of shaking, and >50% within the $B5_{upper}$ and $B6_{upper}$ sand lenses following liquefaction triggering at 10 to 25 s. The early yielding of the $B3_{channel}$ clays promoted shearing paths that aligned with and extended through the shallow liquefied sand lenses up to the model boundary, where there was a gradual increase in the proportion of B3 clays and silts. Liquefaction and cyclic softening in the upper 5 m reduced subsequent seismic demands in the deeper layers. However, strains of up to 30% occurred after additional shaking in several liquefied $B5_{lower}$ lenses at depths from 9 to 15.5 m. The modeled ground displacements were consistent with these shear strains, with maximum displacements of 180 cm at the toe and 140 cm at the top of the channel slope. The largest displacements were concentrated within a rotational slump feature within 10 m from the top of the channel and extending to 5 m below the ground surface. Ground surface displacements gradually decrease from about 100 cm just outside of the slump feature to about 40 cm at the model boundary (i.e., 66 m from the channel). The baseline NDA reasonably captured the magnitude of documented field displacements near the channel. However, it was unable to recreate the documented spatial distribution of displacements, which indicate a greater rate of ground movement near the channel and no visible movement beyond the region of cracks within 25 m from the channel.

4.6.1. Effect of Boundary Conditions

The baseline NDAs were initially evaluated with alternative attached and absorbing numerical side boundary conditions to determine their influence on the resulting ground displacements for the baseline mesh and the same mesh extended an additional 30 m on either side (i.e., to 96 m from the top of the channel). The most influential shear strain concentrations (or paths) within 40 m of the top of the channel were similar for all cases, but differed closer to the model boundaries. The attached boundary condition

produced primarily horizontal shear strain paths that often propagated to the model boundaries. The absorbing boundary condition significantly influenced the shear strain patterns within 15 m of the boundaries, with shearing zones curving upward toward the ground surface near the edges of the elastic boundary columns. The ground displacements with the baseline mesh and attached boundary conditions were similar to those with the extended mesh cases for both boundary conditions, and were thus used for all other sensitivity analyses.

4.6.2. Effect of Input Motions

Lateral ground displacements with distance from the channel from the NDAs are compared for the four input ground motion orientations (Fig. 4.9) and their reversed orientations in Fig. 4.11. As noted previously, the mirrored right-half of the mesh is analogous to considering a reversed ground motion polarity at the left-half (e.g., TCU067-W rather than TCU067-E), and so only one model run was necessary to produce both sets of results. Field observation boundary lines were approximated to envelope the east-trending field displacement measurements near section A-A′ (i.e., between transects T2-T4), and quickly diminish to zero displacement at about 20 m from the channel edge, consistent with the lack of documented visible displacements beyond this distance. Fig 11a depicts the absolute ground displacement results as directly obtained from the NDA model, whereas Fig. 4.11b depicts the same results relative to the model side boundary 66 m from the channel. The absolute displacements (i.e., Fig 11a) depict a significant amount of free-field ground lurch (i.e., ± 40 cm) that varies depending on the input motion orientation. While such ground lurch may be possible away from the channel and are an expected result from any seismic NDA model with long horizontal lenses of yielding material, the actual free-field movements may be affected by nearby structural features (e.g., Chung-Cheng Road), horizontal shaking in a 2D plane, and the continuity of soil layers beyond the boundary, among other factors. Instead, the lateral ground movements relative to the model side boundary (i.e., Fig 11b) allow for more direct comparisons of displacements over the central portion of the mesh which corresponds to the area of observed field cracks. Sensitivity analyses discussed

hereafter will be primarily evaluated for their ability to predict the maximum magnitude of ground displacements relative to the model boundary.

The responses from motions TCU067-SE and -N in Fig. 4.11b bound most of the measured displacements and the range produced by the different input motions. Site and path effects may contribute to differences between the input and actual motions at the site, but these uncertainties are not considered herein. The NDAs with TCU067-E (baseline), -W, -SE, and NW closely match the field measurements adjacent to the channel with maximum lateral ground displacements of 98 to 132 cm (Fig. 4.11b). However, the NDAs indicate a significant contribution to the ground displacements occurred well outside the zone of measured displacements. This suggests that the NDAs under-predict the incremental lateral displacements (ΔLD) near the channel and are unable to resolve the observed location of ground cracks. Specifically, for the mid-field region of the site (i.e., considered herein as 30 to 10 m from channel edge), $\Delta LD_{30\text{-}10m}$ = 60-80 cm was measured, but $\Delta LD_{30\text{-}10m}$ < 15 cm was modeled for all ground motion orientations. The near-channel region (i.e., considered herein as within 10 m of the channel edge, overlying the rotational slump feature indicated by the baseline NDA results), showed slightly better congruence between the measurements of $\Delta LD_{10\text{-}0m}$ = 40-130 cm and the modeled predictions of $\Delta LD_{10\text{-}0m}$ = 30-60 cm. The NDAs that included the vertical motion as an input produced displacements that were all within ±10% of those obtained without the vertical motion.

4.6.3. Effect of Varying Stratigraphic Realizations and Channel Transects

The stratum B stratigraphic realizations R1-R5 at cross-channel transect T2 (i.e., near profile section A-A′, as mapped in Fig. 4.2), and transects T1-T5 from realization R1, were evaluated with 2D NDAs and compared to understand how stratigraphic variations and differences across the site affected the predicted lateral ground displacements towards the channel. All analyses were identical to the baseline NDA, except for changes to the stratum B stratigraphy. The stratum B realizations R2-R5 (Fig. B.3) were generated with the same transition probability metrics and simulation process as the baseline model (i.e., R1). The differences between the modeled ground displacements for R1-R5 at T2 are depicted in Fig. 4.12a,

along with the field displacement range. The modeled maximum displacements vary from 57 to 130 cm at the channel. All displacements remain relatively constant in the mid-field region with $\Delta LD_{30\text{-}10m}$ = 0-10 cm, but are significantly variable in the near-channel region where R1-R3 produced $\Delta LD_{10\text{-}0m}$ = 40-80 cm and R4-R5 produced $\Delta LD_{10\text{-}0m}$ = 0-20 cm. These differences can be explained by the greater amount of clay-like B3 soils just to the left of and below the channel (e.g., within the region parameterized as $B3_{channel}$) for R1-R3, which contribute to a greater local rotational slump as that material yields. The geostatistical realizations depict various possible layering sequences near the channel that are relatively unconstrained due to the sparsity of conditioning CPT data in that area.

Transects T1-T5 were taken at 10 m intervals perpendicular to the channel to determine whether the observed variations in ground deformations from north to south along the site could have been predicted. The NDA for each transect is assumed to be identical to the baseline NDA, except for changes to the stratum B stratigraphy based on the associated 2D slices from the 3D stochastic realization R1 (Fig. 4.4; the interlayering within each slice is depicted in Fig. B.2). The resulting lateral ground displacements towards the channel for transects T1-T5 are depicted in Fig. 4.12b. The depicted field measurement bounds are only indicative of conditions at T2-T4 (i.e., east-trending displacements extended up to 10 m beyond the channel at T1, and were not observed at T5). The maximum modeled channel displacements were 70-100 cm for T1-T4 and 47 cm for T5. The modeled ground movement at T4 and T5 primarily occurred in the far-field region of the site, beyond 30 m from the channel and was associated with liquefaction within thick and connected sequences of $B5_{upper}$ material. The geostatistical simulations as corroborated by the field data did not indicate significant quantities of $B3_{channel}$ material to initiate local slumping at T4 and T5. As with the realization variations, all modeled displacements remained relatively constant in the mid-field region ($\Delta LD_{30\text{-}10m}$ = 0-10 cm). However, the modeled incremental near-channel displacements were quite consistent with the trend of field measurements with $\Delta LD_{10\text{-}0m}$ = 48, 52, 22, ~0, and ~0 cm for T1-T5, respectively.

Overall, the modeled variations between multiple realizations at T2 (Fig. 4.12a) and multiple transects from R1 (Fig. 4.12b) appear to cover a similar range of responses. Most models were able to capture reasonable maximum and incremental displacements within 10 m of the channel. The 3D geostatistical model accounted for non-stationary changes that reduced near-channel incremental displacements at the south end of the site. However, none of the NDAs were able to capture the widest cracks observed within 10 to 30 m from the channel at T2-T4, and instead suggested the influence of a failure mechanism that extended to larger distances from the channel (i.e., to the limits of the mesh).

4.6.4. Effect of Shorter Mean Lengths for Soil Categories

The lateral ground displacement results from alternate stratum B realizations R6-R10 (Fig. B.4) are depicted in Fig. 4.13, along with the displacements from using R1-R5 and the field measurement bounds plotted in the background for comparison. Realizations R6-R10 were obtained with the same geostatistical model parameters and simulation methods as R1-R5, but with 50% mean lateral lengths for the interlayered B3 and B5 overbank deposits of 10 m. The reduced mean lengths create more frequent material fluctuations laterally, however, the connectivity and proportion of the more prevalent B5 sandy silts remains more or less consistent with the R1-R5 realizations. As such, the maximum channel displacements between both sets of realizations remain generally consistent with one another in the mid-field region, where shear strains within the liquefied B5 soils dominate the response. The incremental displacements from R6-R10 near the channel are noticeably greater than those for R1-R5, reaching a maximum of 100-190 cm ($\Delta_{LD10\text{-}0m}$ = 45-110 cm). These increases are due to the larger quantity of $B3_{channel}$ soft clays within the unconstrained region of the realizations beneath and near the channel. This occurrence may be an artifact of conditioning the geostatistical realizations on WCC-4, which has a higher than typical proportion of B5 sands and is more likely to transition to B3 clays beneath the channel (i.e., 10 to 20 m away from WCC-4) for smaller mean lengths. This greater amount of B3 clays may nonetheless be a reasonable occurrence and realizations R6-R10 provide insights for this possibility.

4.6.5. Effect of Material Properties

The influence on lateral ground displacements from several reasonable material parametric choices and calibration protocols were considered relative to the baseline NDA. The baseline NDA was re-evaluated with four alternative considerations of the undrained shear strength and extent of the $B3_{channel}$ soft clay: (1) not present (i.e., $s_{u,eq,cs}/\sigma'_{vc}$ = 0.95, equivalent to B3 soils throughout the site); (2) no sensitivity with $s_{u,eq,cs}/\sigma'_{vc}$ = 0.48 (with re-calibrated PM4Silt parameters h_{po}=2, $n^{b,wet}$=default, and ϕ_{cv}'=default); (3) no sensitivity with $s_{u,eq,cs}/\sigma'_{vc}$ = 0.32 (with re-calibrated PM4Silt parameters h_o=1.1, h_{po}=2, $n^{b,wet}$ =1, and ϕ_{cv}'=default); and (4) increased extent to 11 m from the edge of the channel. The baseline NDA originally considered $B3_{channel}$ with $s_{u,eq,cs}/\sigma'_{vc}$ = 0.32, a sensitivity of 1.5, and a lateral extent of 6 m. The large differences between these alternatives reflect the large uncertainty in defining the characteristics and extent of the near-channel soft clay, which are primarily dependent on information provided by one CPT (i.e., WCC-3). The resulting displacements from these various considerations relative to the baseline NDA and the measurement bounds are presented in Fig. 4.14. All cases depict generally equivalent displacements at distances beyond 10 m from the channel, except for the case with the increased $B3_{channel}$ extent, which accordingly extended the rotational slump mechanism further from the channel. The case that did not re-define the near-channel B3 soils as $B3_{channel}$ soft clays retains relatively constant displacements near the channel ($\Delta LD_{10\text{-}0m}$ < 10 cm), and did not produce a near-channel slump failure. The case that retained the peak baseline monotonic strength without strain softening due to clay sensitivity (i.e., $s_{u,eq,cs}/\sigma'_{vc}$ = $s_{u,eq,peak}/\sigma'_{vc}$ = 0.48) significantly reduced the baseline incremental displacements near the channel from $\Delta LD_{10\text{-}0m}$ = 52 cm, to 22 cm. The case with a lower strength but no sensitivity (i.e., $s_{u,eq,cs}/\sigma'_{vc}$ = $s_{u,eq,peak}/\sigma'_{vc}$ = 0.32) produced displacements similar to the baseline case.

The baseline NDA was re-evaluated with five alternative assumptions influencing the sand-like stratum B soils (i.e., B5 and B6): (1) the q_{c1Ncs} re-defined by 33rd percentile estimates [i.e., near the lower bound suggested by Montgomery and Boulanger (2016) for uniform NDAs] from measured rather than inverse filtered CPT data (i.e., this case is labeled as 33Meas); (2) a global mean fines content correlation

(C_{FC} = 0) per Boulanger & Idriss (2014); (3) the CRR based on P_L = 16% as typically recommended for deterministic analyses per Boulanger & Idriss (2014); (4) a 50% increase in CRR for the intermediate $B5_{upper}$ and $B5_{lower}$ soils to approximately account for a small amount of fines plasticity (PI=0-6) as might be suggested from laboratory tests by Price et al. (2015); (5) the default PM4Sand calibration for the post-liquefaction cyclic shear strain-accumulation rate [the calibration and results of this scenario are detailed by Bassal et al. (2021b)]. The resulting ground displacements towards the channel face for all alternative considerations of the B5 and B6 sand-like soils are depicted in Fig 15. The distribution of displacements across the profile generally follow the same trend, and the maximum displacements at the channel range from 86 to 120 cm, or within ±20% of the baseline NDA. Since these considerations cause laterally consistent variations of properties that affect the extensive liquefaction response of the sand-like soils, the incremental near-channel displacements were not significantly affected (i.e., $\Delta LD_{10\text{-}0m}$ = 30-60 cm for all cases).

4.6.6. Effect of Other Sensitivity Studies

Several other model choices reflecting common analysis uncertainties were found to have varying degrees of influence on the NDA model response. Analyses considering ±30% of q_{c1Ncs} for the B6 channel-deposited sands and ±30% of $s_{u,eq,cs}/\sigma'_{vc}$ for the typical B3 soils were nearly inconsequential to the interpreted ground displacements since the majority of seismic shear strains were concentrated within the $B3_{channel}$ soft clays and B5 silty sands. Other analyses considered increasing the cohesion of the mortar and stone lining by up to 100 kPa and the width of the compacted zone by up to 4 m to account for uncertainties related to the integrity of the original channel construction. These changes only affected the near-channel region and reduced displacements within 10 m of the channel by up to 20%. Shifting the groundwater table ±1 m (with milder ± 0.4 m fluctuations within the channel) had a slightly greater influence in the far-field region, where displacements remained within ±20 cm of the baseline model.

4.7. Simplified Analyses by Others

Lateral spreading at Wufeng Site C was previously estimated by Chu et al. (2006) using simplified empirical and semi-empirical analyses. Their analyses with the Youd et al. (2002) empirical regression model overestimated displacements along section A-A′ as ranging from 300 to 1200 cm. Their subsequent approximations with the Zhang et al. (2004) approach, only considering strains within laterally continuous liquefaction susceptible soils, also significantly overestimated displacements as 120 to 140 cm in the areas measured to displace 45 to 60 cm. Their subsequent analyses that constrained the Zhang et al. (2004) approach to a maximum depth of 6 m (i.e., twice the channel depth; H=3 m) reduced their estimates in this area to 60 to 75 cm, which improved agreement with the observations of 45 to 60 cm. None of their analyses were able to emulate the spatial trend of observed displacements (i.e., cracks at 20 m from the channel) nor suggest a meaningful difference in displacements between section A-A′ and the south end of the site (i.e., near transect T5; no measured displacements). Independent simplified calculations performed by the authors confirmed these results using assumptions consistent with the NDA models herein (i.e., with inverse filtered CPT data, and updated liquefaction triggering and strain correlations), but were unable to improve upon their estimates.

Chu et al. (2006) obtained reasonable lateral spreading estimates at section A-A′ after applying several simplifying assumptions. Their choice to limit the calculation extent to the upper 6 m (i.e., 2H) of the profile was solely based on the channel height, without consideration of the overall soil conditions at the site. The majority of NDA results coincidentally depicted the greatest concentration of shear strains in the upper 4 m of the interlayered stratum B, within weak layers that yielded earlier and consequently reduced seismic demands on underlying soils in the lower 10.5 m of stratum B. However, had portions of the deeper soils been consistent with or weaker than soils above 6 m, the strains could have been more widely distributed throughout the profile depth, potentially causing the 2H assumption to instead under-estimate lateral displacements. The additional subjective simplifications by Chu et al. (2006) to remove clay-rich and non-continuous soil layers from their analyses may be reasonable, but similar adjustments (e.g., strength increases, stratigraphic realizations) covered by the NDA sensitivity analyses presented

herein did not substantially improve predictions of ground deformation patterns. The NDAs showed that yielding within softer clays near the channel likely had a strong effect on deformation patterns, although cyclic softening in any of the clays was not accounted for in the simplified analyses. The NDAs thus provide an opportunity for understanding the dynamic interplay between the complex stratigraphy and the channel geometry that may not be readily apparent from a simplified analysis.

4.8. Discussion

The 2D NDA sensitivity results elucidated several key factors influencing the dynamic system behavior and ground deformations at Wufeng Site C. Although most of the evaluated NDAs reasonably predicted the maximum displacements near the channel, they could not easily reproduce the spatial trend of displacements with distance from the channel nor constrain the location of ground cracks given the available site data. The sensitivity studies that better matched the observed deformations for different portions of the site are summarized to gauge important considerations and limitations for NDA studies of earthquake-induced ground deformations at sites with interlayered soil deposits.

Most of the NDAs suggested the occurrence of a gradual or block-type failure mechanism extending beyond 30 m from the channel. The only exception to this occurrence resulted from the use of alternate input motions (based on alternate recorded motion orientations) with lower intensities that did not agree with the site orientation relative to the fault. None of the stratigraphic variations limited the zones of large shear strains in liquefied B5 and B6 soils from extending the full length of the modeled site. It is possible that additional site data and more explicit modeling of intricate stratigraphic details (e.g., thinner beds, lateral within-bed parametric variations, or cross-transect variations) could have helped to limit the extent of lenses with large shear strains. Alternatively, it is possible that these far-field displacements actually occurred, but were not adequately recorded in the field (e.g., due to the imperceptibility of gradual strains, influence of surficial features, limited extent of data collection) as previously discussed.

The majority of sensitivity cases were unable to indicate the observed cracks in the mid-field region of the NDA models (i.e., 30 to 10 m from the channel edge). The NDA models cannot explicitly model

crack formation. However, a sharp increase in permanent displacements associated with concentrations of high tensional strains may approximate the location and help identify potential for cracking. The cases that depicted the greatest incremental lateral displacements in this region considered an elongated extent of the $B3_{channel}$ soft clays that accordingly pushed the near-channel rotational slump feature further from the channel. Additional CPT data in this area of the site may have helped support or preclude this possibility.

The majority of sensitivity cases reasonably predicted the magnitude of the displacements in the near-channel region (i.e., 10 m from the channel edge). In particular, all cases that considered $B3_{channel}$ material with weaker properties were able to produce large incremental displacements near the channel. The sensitivity cases that either reduced the strength or volume of the $B3_{channel}$ material, or considered a more robust channel system (e.g., wider compacted zone, increased lining cohesion), typically under-estimated the magnitude of near-channel deformations. It is noteworthy that the NDA with stratum B realization R6 produced the greatest displacements near the channel (Fig. 4.13). Realization R6 depicted a sloped interface between the $B3_{channel}$ soft clays and the B5 silty sands (Fig. B.4) that further facilitated a rotational failure with near-channel displacements that were most consistent with observations. There are geologically plausible reasons (e.g., lateral accretion surfaces or other formational processes) for such sloped interfaces to exist at the study site and their occurrence cannot be ruled out based on the available data.

Across the north to south transects (i.e., T1-T5), the modeled displacements were able to capture near-channel trends, but were unable to distinguish displacements further from the channel. The plain-strain assumption of 2D NDAs is unable to account for the influence of stratigraphic changes and interlayering between transects, and instead assumes infinite connectivity in the channel-axis direction. A consideration of reduced connectivity between transects may have also reduced the lateral extent of shear strain localizations across the liquefied sand lenses. Soil parameter variations perpendicular to failure mechanisms have similarly been observed through 3D numerical studies to influence the magnitudes and extents of static failures of other geo-systems, including embankments and shallow footings (e.g., Griffiths and Marquez 2007, Li et al. 2021). Additionally, the influence of the bend in the channel to the north and the proximity

to the reinforced segment of the channel to the south may have contributed to multi-dimensional straining not captured by the 2D NDAs.

4.9. Conclusion

This paper examined the seismic response of Wufeng Site C in the 1999 Chi-Chi earthquake through a series of 2D NDAs with geostatistical modeling of the subsurface to evaluate their ability to approximate the observed magnitude and distribution of ground deformations, as well as identify the key factors and mechanisms that most contributed to the overall system response. Post-earthquake east-trending lateral displacements, as observed by others from ground cracks (Chu et al. 2006), ranged from about 45 to 205 cm within 25 m of a meandering stream channel. This pattern of displacements is attributed to a complex fluvial subsurface stratigraphy comprised of stratified overbank deposits of low plasticity silty sands, silts, and clays, interlayered with laterally discontinuous channel-deposited sands.

Geologic details interpreted from the available site investigation data and a general understanding of fluvial processes was fundamental to interpreting key attributes of the site stratigraphy that ultimately governed the evaluated deformations. The use of transition probability-based geostatistics allowed for an understanding of the variability in probable profiles as conditioned on the available site data and geologic reasoning, which translated to alternate deformation patterns when applied to 2D NDAs. However, the most impactful stratigraphic influences were due to non-stationary model choices (e.g., the extent of near-channel soft clay, the transition from weaker to stronger soils below 5 m, and the increase in finer soils away from the channel), rather than variability between alternate realizations. The near-channel soft clay lens, as informed by a single CPT, was critical to predicting the large near-channel deformations. However, insufficient data made it difficult to constrain the behavior and extent of this layer, which translates to large uncertainty in the predicted deformations.

The 2D NDAs considered several uncertainties in the stratigraphy, channel conditions, soil properties, input ground motions, constitutive model calibration protocols, numerical boundary conditions, and other details. The NDAs suggested the failure mechanism consisted of a rotational slump initiated by

yielding along the near-channel soft clays, and general lateral spreading along inter-connected liquefied soils within the overbank silty sands and channel-deposited sands. Overall, the analyses depicted a large variation in displacements that generally matched the maximum displacements observed from post-earthquake measurements near the channel for most cases, but overestimated the extent of displacements away from the channel for all cases. The limited extent of observed displacements likely depended on details that were difficult to interpret from the available site data and evaluate with a continuum-based 2D numerical model (e.g., the connectivity of soil lenses, location and orientation of layer interfaces, surface cracking). Additionally, the 3D geostatistical mesh was successful in suggesting a difference in near-channel materials across the site, but was not sufficient to overcome challenges in interpreting 3D effects from 2D plane-strain analyses.

This case history is a demonstrative example of the capabilities and limitations of current analysis tools and methods to recreate observed conditions in the field. The simplified lateral spreading analyses by others typically over-predicted observed deformations and were unable to consider dynamic interactions within the stratigraphy and effects from the near-channel soft clays. The use of 2D NDAs with the consideration of stratigraphic variations can be invaluable for evaluating key system-level mechanisms and guiding engineering decisions, provided limitations in predicted details are recognized.

4.10. Data Availability

Some of the data, models, or code used during the study were provided by third parties. The site characterization data was sourced from the Taiwan Ground Failure Database hosted by the Pacific Earthquake Engineering Research Center (PEER 2002). Ground motions were obtained from the PEER NGA-West2 Ground Motion Database (PEER 2013). Direct requests for software can be made to the providers indicated in the references. Some of the codes that support the findings of this study are available from the corresponding author upon reasonable request.

4.11. Acknowledgements

The authors appreciate the financial support of the National Science Foundation (award CMMI-1635398) and California Department of Water Resources (contract 4600009751) for different aspects of the work presented herein. Any opinions, findings, conclusions, or recommendations expressed herein are those of the authors and do not necessarily represent the views of these organizations. The analyses benefited from discussions with Graham Fogg for the transition probability simulations, Katerina Ziotopoulou for the post-liquefaction model calibrations, and Renmin Pretell and Francisco Humire for peer feedback. The data procurement and initial analyses of this case study are attributed to early efforts by Daniel Chu, Jonathan Stewart, Leslie Youd, Bin-Lin Chu, Shannon Lee, Sung-Chi Hsu, and others. The authors are grateful for the above support and interactions.

Tables

Table 4.1. Baseline PM4Sand constitutive model inputs

Material	σ'_{vc} *(kPa)*	D_R	G_o	$CRR_{M7.5}$	h_{po}	C_ε
Compacted zone	35	0.65	907	0.249	0.35	0.64
A & B5$_{upper}$	42	0.44	700	0.148	1.22	33.0
B6$_{upper}$	42	0.50	805	0.166	0.85	5.7
B5$_{lower}$	123	0.62	837	0.195	0.71	1.5
B6$_{lower}$	123	0.69	982	0.265	0.92	0.5

Note: Default values per Boulanger & Ziotopoulou (2017) are used for all unlisted secondary parameters.

Table 4.2. Baseline PM4Silt constitutive model inputs

Material	$s_{u,eq,cs}/\sigma'_{vc}$	$s_{u,eq,cs}$ *(kPa)*	G_o	h_{po}	h_o	e_o	$n^{b,wet}$	ϕ'_{cv}
B3$_{channel}$	0.32	-	1030	8	0.9	0.55	0.01	45
B3	0.95	-	1030	30	0.9	0.55	-	-
C	-	188	1250	10	1.5	0.51	-	-

Note: Default values per Boulanger & Ziotopoulou (2018) are used for all unlisted secondary parameters.

Figures

Figure 4.1. South-facing view of ground displacements at Wufeng Site C within two months after the Chi-Chi earthquake (Photograph by Sung-Chi Hsu).

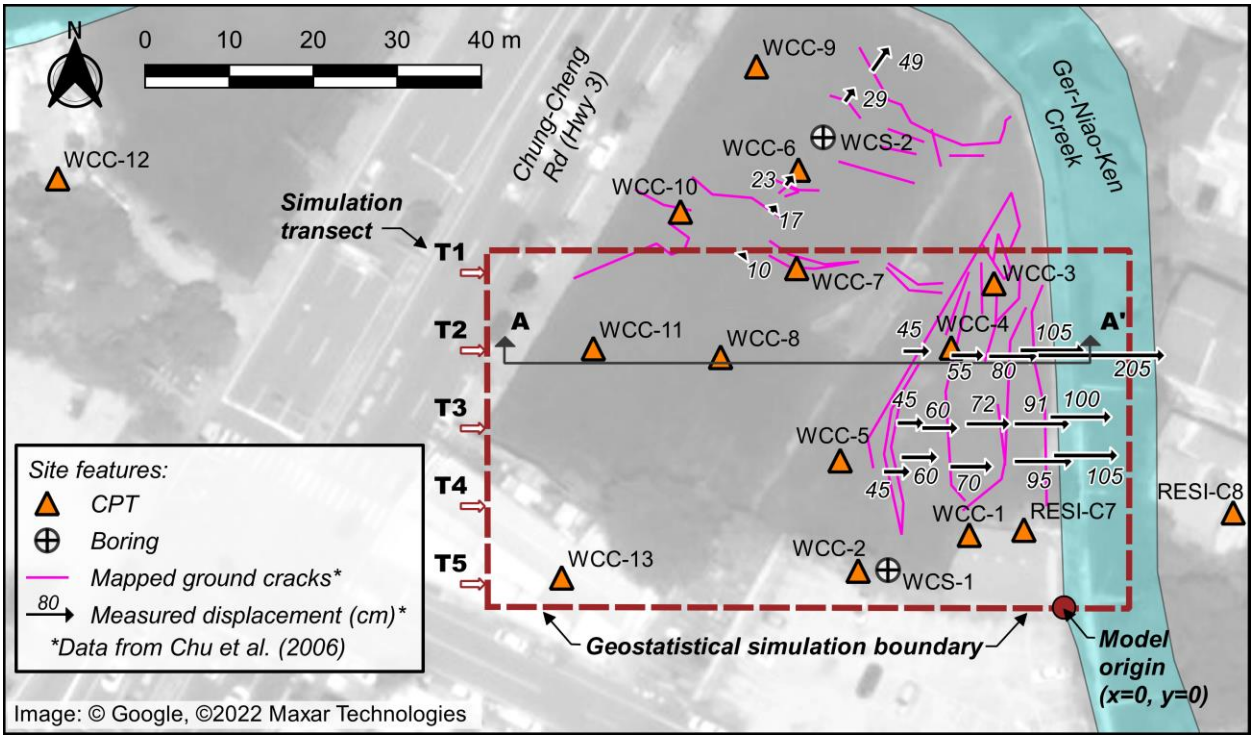

Figure 4.2. Wufeng Site C plan with geotechnical investigations and post-earthquake observations. Crack locations and displacement vector data from Chu et al. (2006). (Image © Google, ©2022 Maxar Technologies).

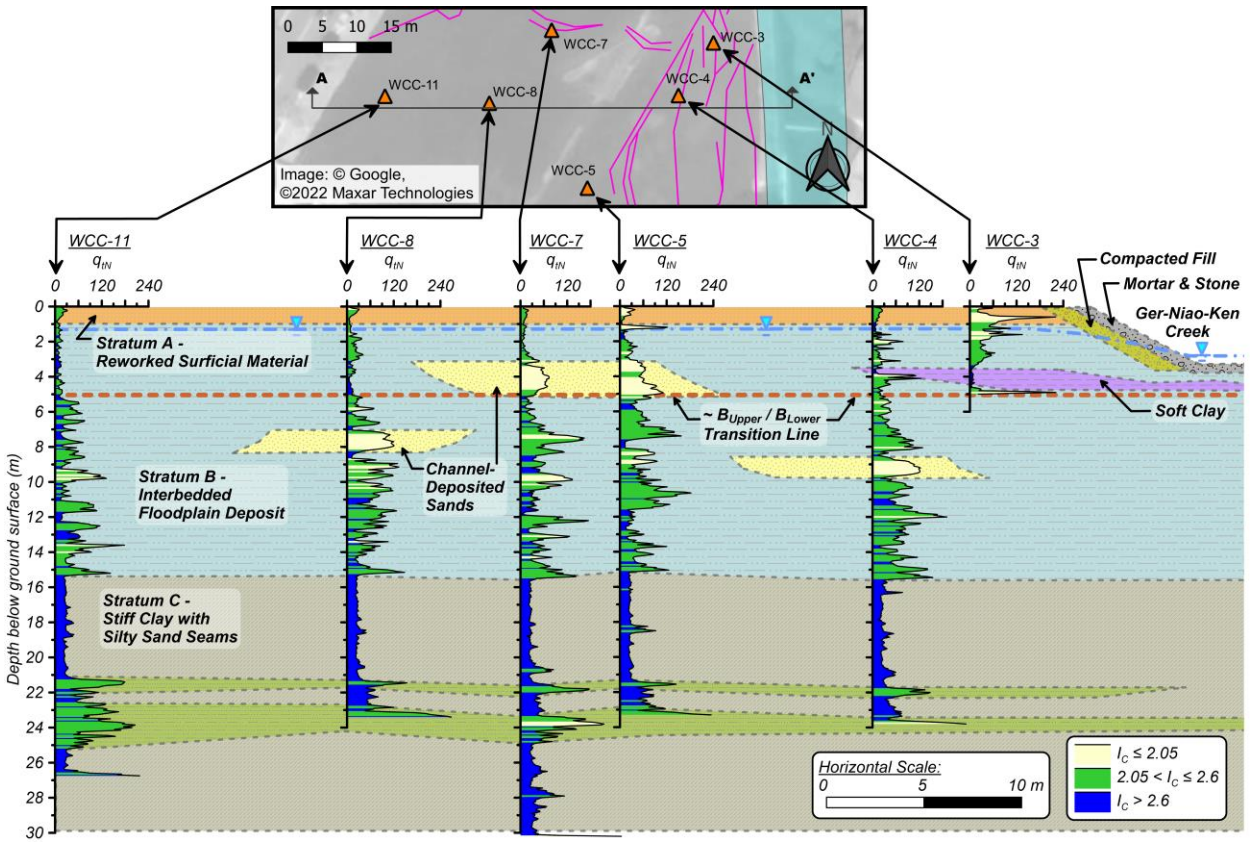

Figure 4.3. Wufeng Site C section A-A′ CPT fence diagram with a geologically interpreted stratigraphy. Crack locations from Chu et al. (2006). (Image © Google, ©2022 Maxar Technologies).

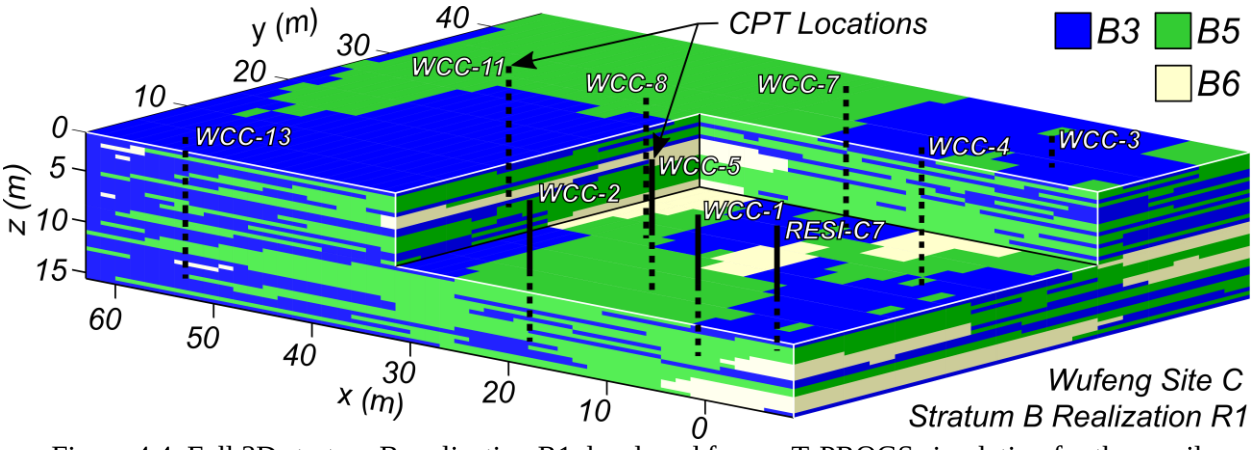

Figure 4.4. Full 3D stratum B realization R1 developed from a T-PROGS simulation for three soil categories.

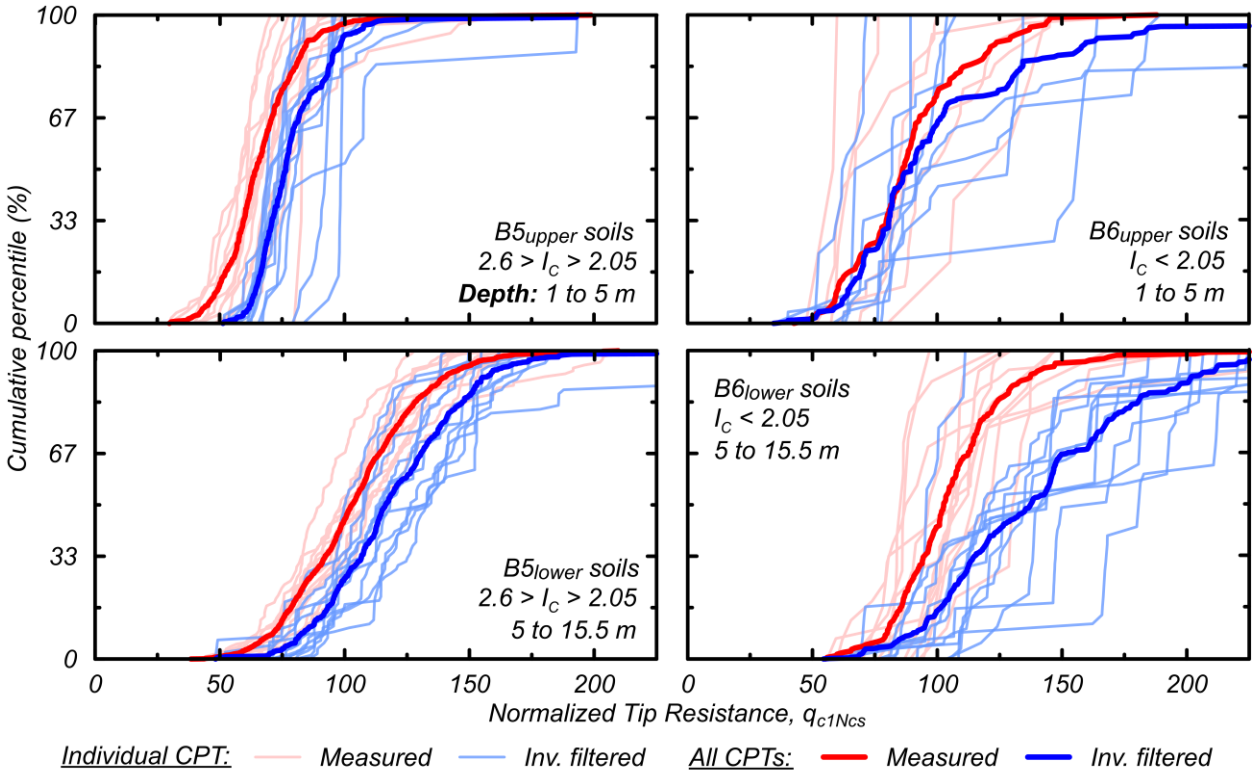

Figure 4.5. Empirical cumulative distributions of normalized tip resistance from measured and inverse filtered CPT data for all B5 and B6 sand-like soils.

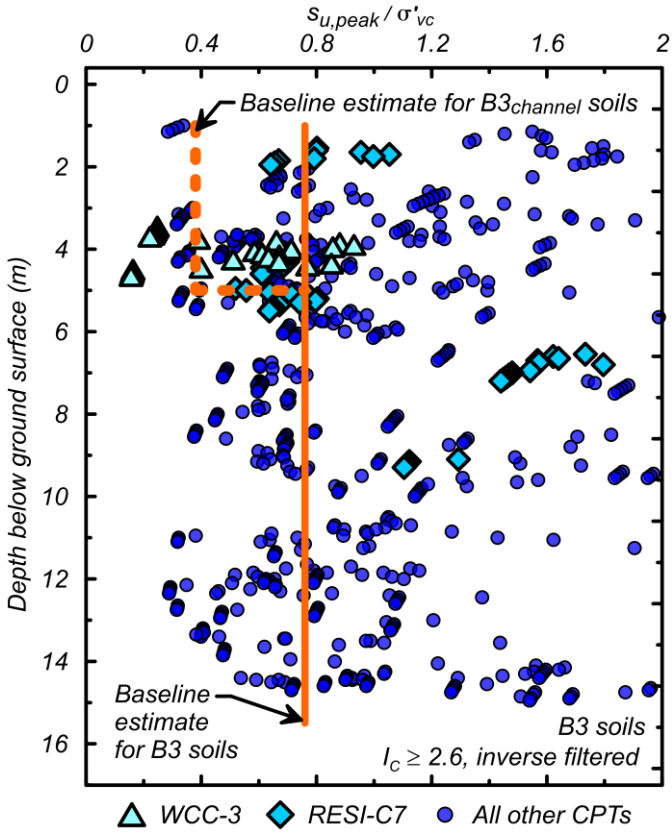

Figure 4.6. Peak undrained shear strength ratios after inverse filtering for all B3 soils thicker than 20 cm from the near-channel CPTs (i.e., WCC-3 and RESI-C7) and all other CPTs. Representative estimates for the B3 and B3channel soils groups used for the baseline NDAs are indicated.

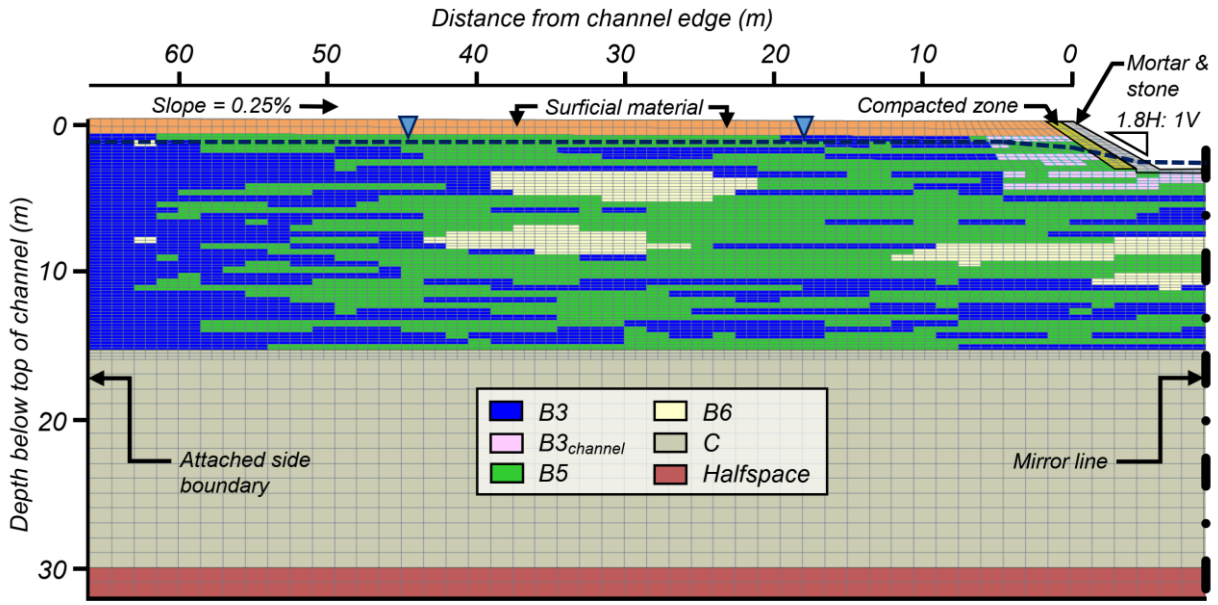

Figure 4.7. Full left-side of the 2D plane-strain baseline NDA mesh as used in FLAC for section A-A′ (transect T2) with stratum B realization R1.

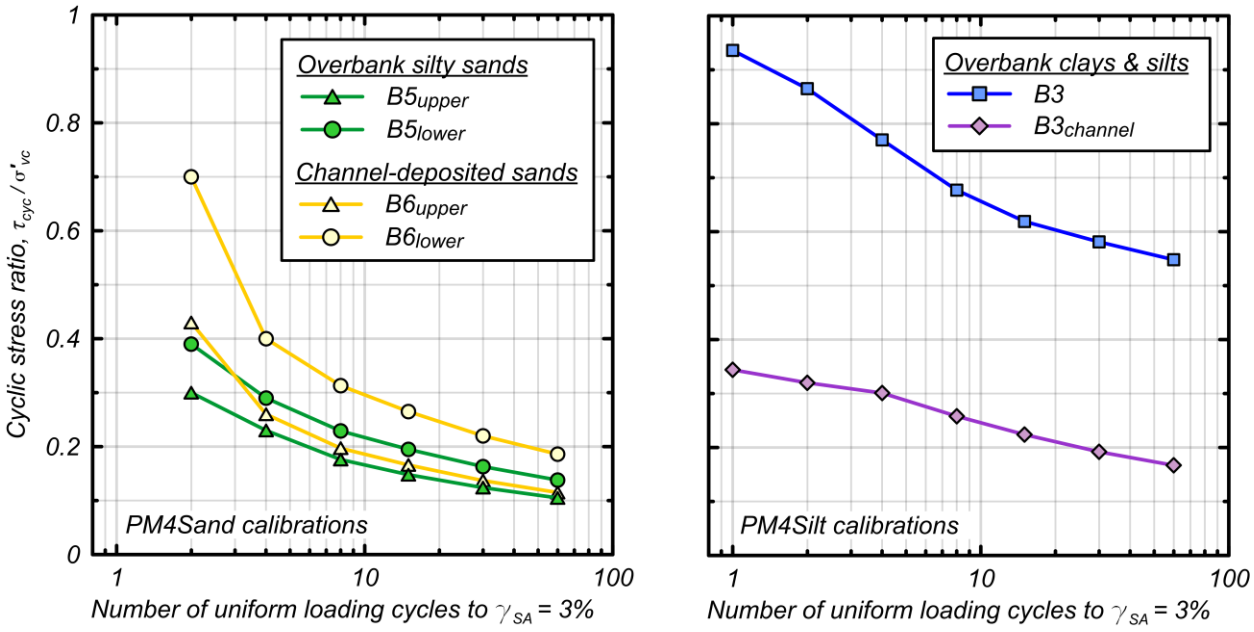

Figure 4.8. Minimum CSR for 3% single amplitude shear strain at a given number (N) of uniform stress cycles as determined from model calibrations of the stratum B soil groups with (a) PM4Sand, and (b) PM4Silt.

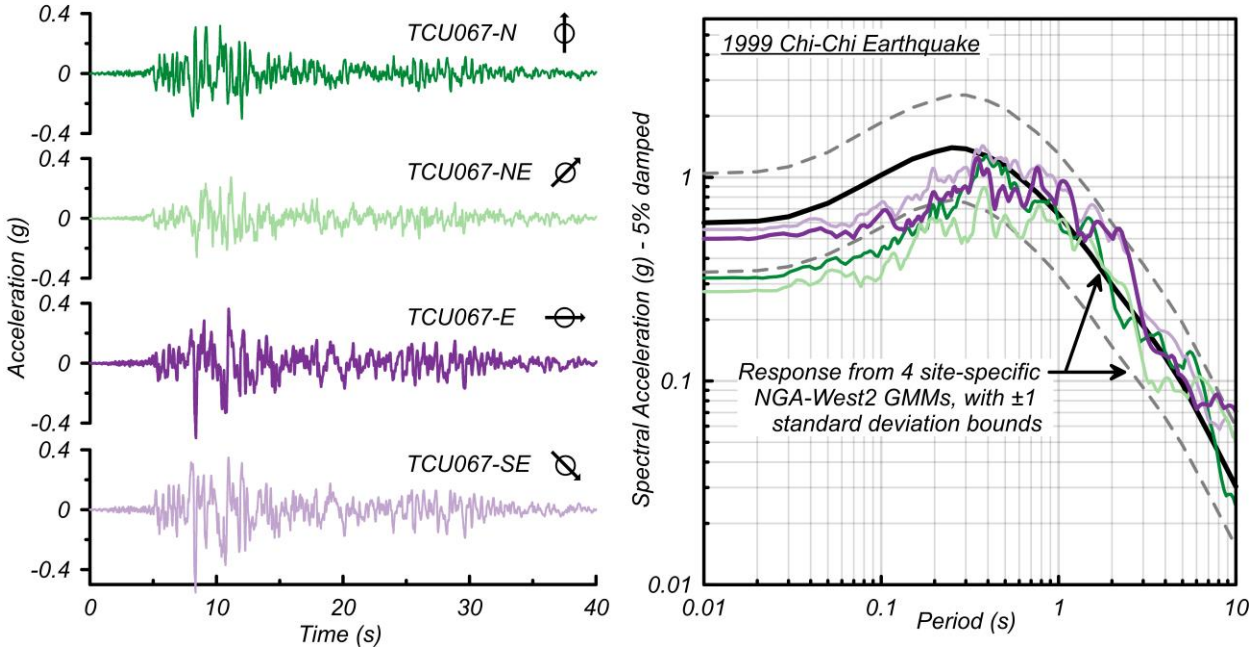

Figure 4.9. Four ground motion orientations from the Chi-Chi earthquake recording at TCU067 represented as (a) acceleration time histories and (b) acceleration response spectra with comparisons to estimates from NGA-West2 ground motion models.

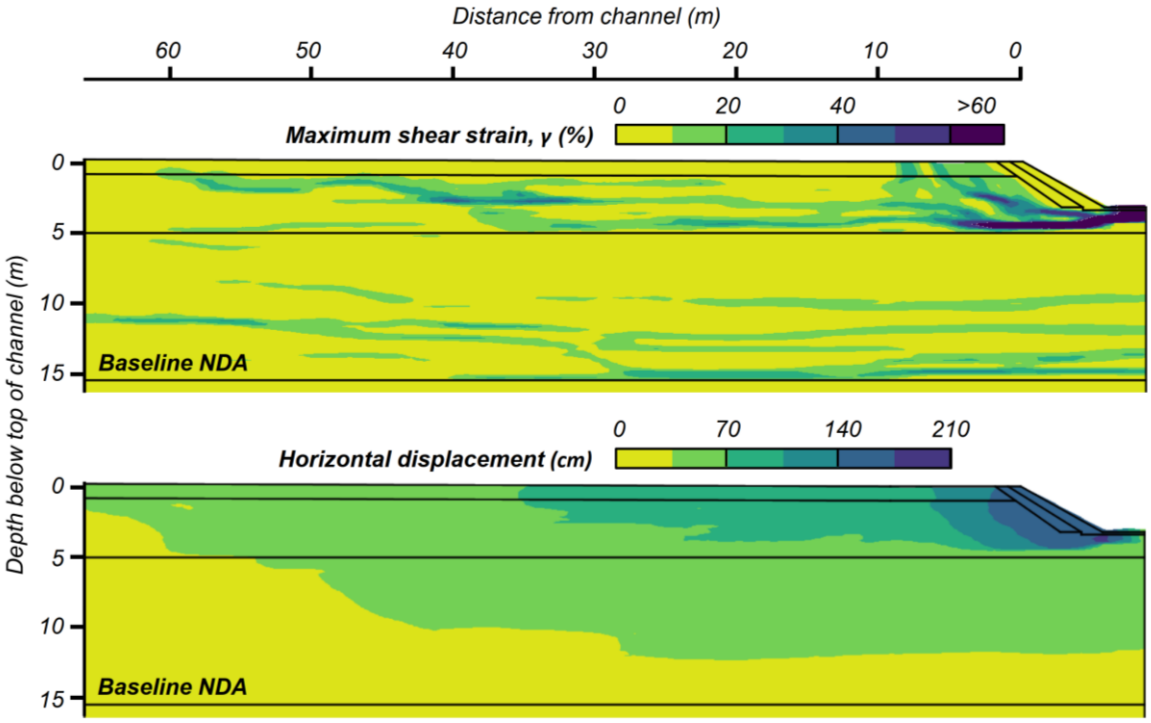

Figure 4.10. Contours of (a) maximum engineering shear strains (in the principle direction), and (b) horizontal displacements for the baseline NDA after shaking.

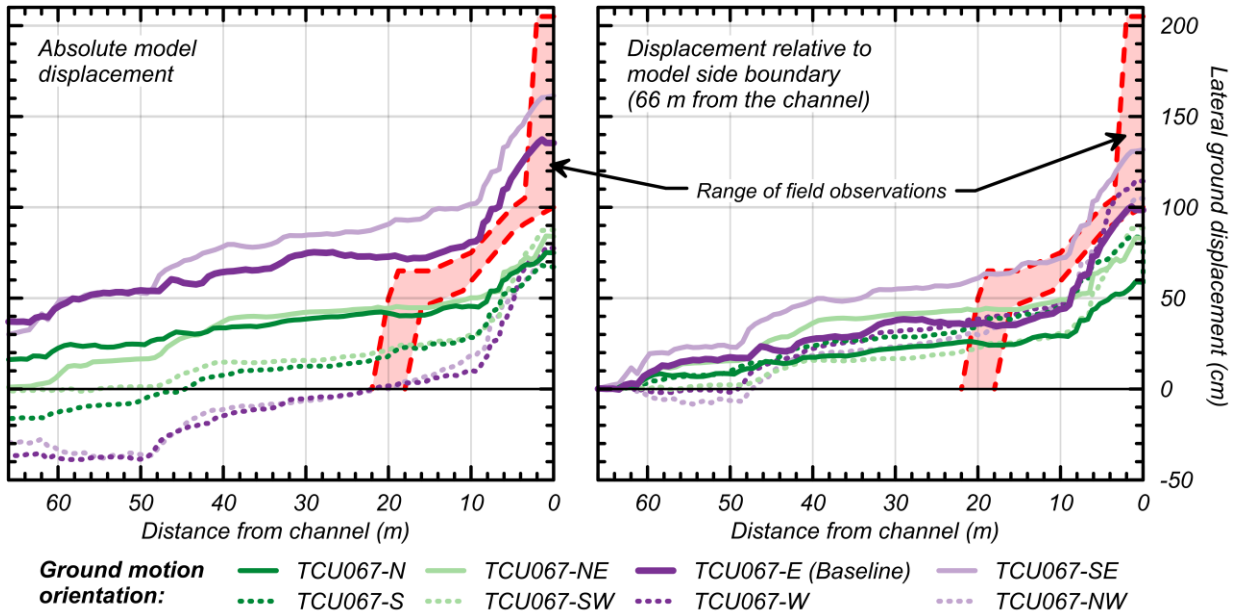

Figure 4.11. Lateral ground displacements from field measurements and baseline NDAs for eight ground motion orientations depicted as (a) absolute model displacements, and (b) displacements relative to model side boundaries located 66 m from the channel.

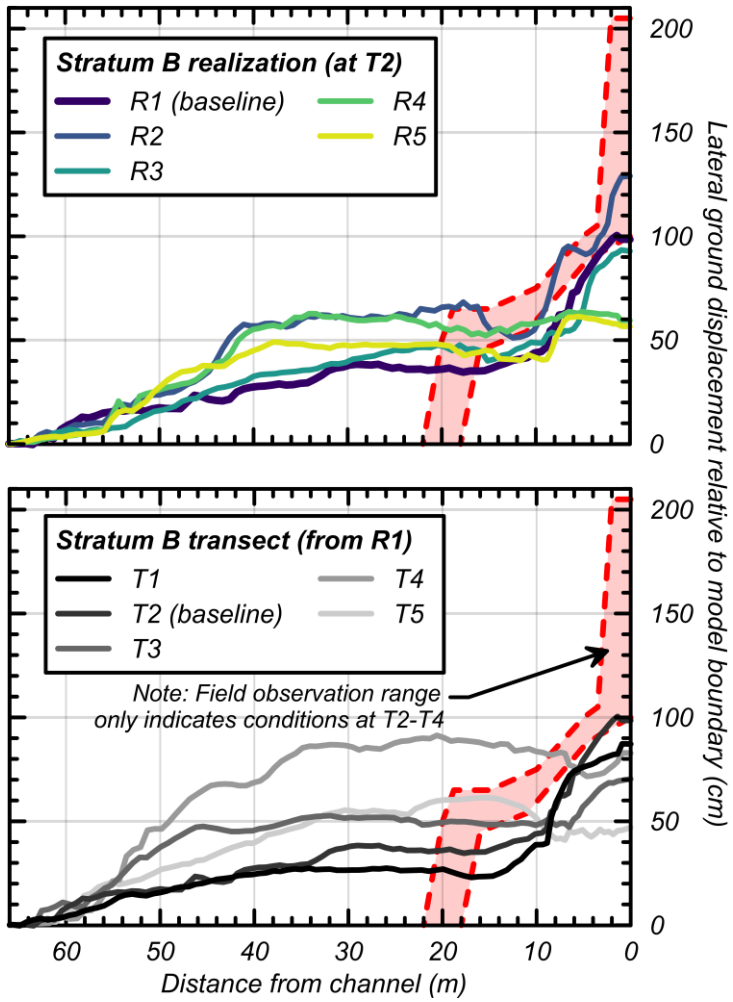

Figure 4.12. Lateral ground displacements from NDAs for (a) stratum B stratigraphic realizations R1-R5 at transect T2, and (b) transects T1-T5 from stratum B realization R1.

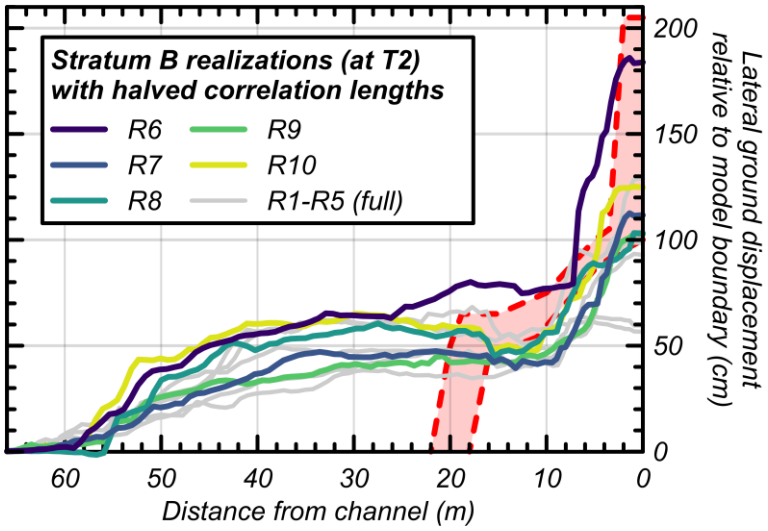

Figure 4.13. Lateral ground displacements from NDAs for stratum B stratigraphic realizations R6-R10 at transect T2 with halved B3 and B5 mean lengths (i.e., 10 m).

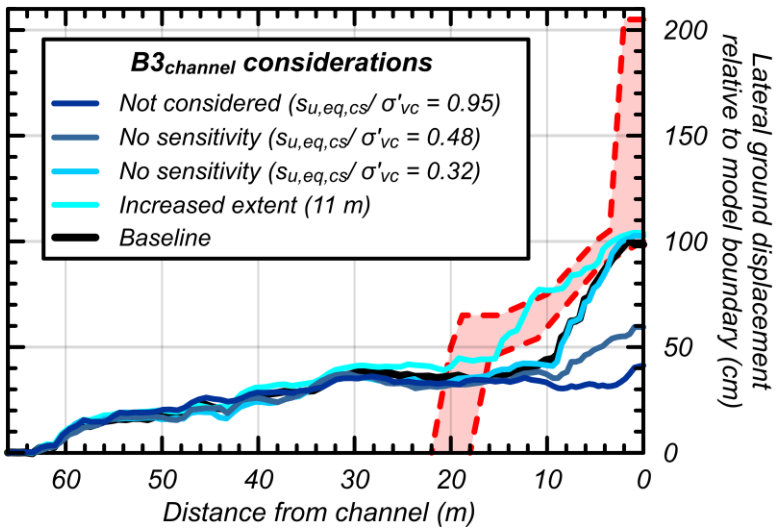

Figure 4.14. Lateral ground displacements from NDAs with alternate parametric and calibration protocol considerations for the B3channel soft clays.

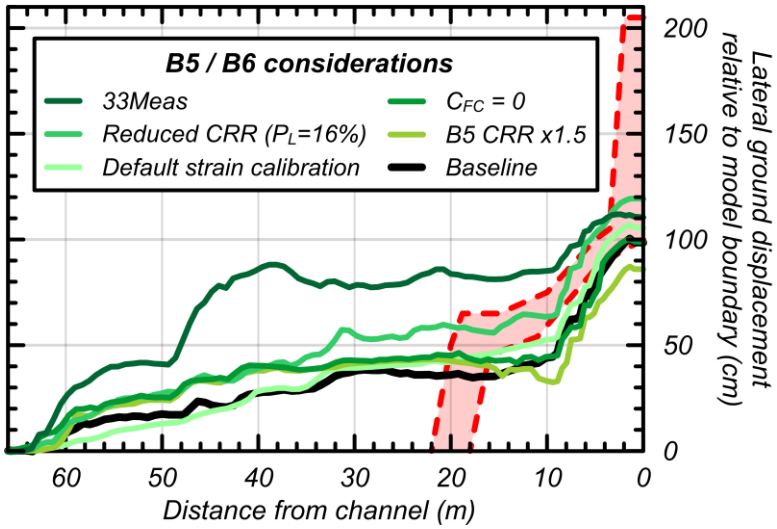

Figure 4.15. Lateral ground displacements from NDAs with alternate parametric and calibration protocol considerations for the B5 and B6 sand-like soils.

5. Calibration of Post-Liquefaction Shear Deformation for a Fluvial Deposit in the Chi-Chi Earthquake

Author's Note

The full content of this chapter has been published in the proceedings of the *17th World Conference on Earthquake Engineering* in Sendai, Japan. This chapter presents a preliminary sensitivity study of alternate post-liquefaction shear deformation PM4Sand calibrations for the Wufeng Site C NDA case study, and complements the material of Chapter 4. The site description and baseline model development is repeated herein, but is retained to reflect the published manuscript. The author performed and interpreted the analyses, and drafted the manuscript.

Publication

Bassal, P. C., Boulanger, R. W., DeJong, J. T., and K. Ziotopoulou (2021b). "Calibration of Post-Liquefaction Shear Deformation for a Fluvial Deposit in the Chi-Chi earthquake." In Proc., 17th World Conference on Earthquake Engineering. Tokyo: International Association for Earthquake Engineering.

Abstract

The performance of a two-dimensional (2D) nonlinear dynamic analysis (NDA) for a case history site of an interlayered soil deposit is evaluated under different constitutive model calibrations to understand the influence of post-liquefaction shear strain accumulation rates on the overall system response. The site is adjacent to a meandering stream channel in Wufeng, Taiwan and exhibited over two meters of liquefaction-induced ground displacements (i.e., lateral spreading) during the 1999 Chi-Chi Earthquake. In-situ data from borings and cone penetration tests (CPTs) at the site depict thinly interlayered floodplain deposits interrupted by laterally discontinuous channel fill sand deposits, typical of a fluvial point bar sequence. A majority of the floodplain deposits can be characterized as "intermediate" (e.g., low-plasticity sandy silts and clays, and silty sands) and may exhibit behavior that is transitional between sand-like and clay-like soils during cyclic loading. The subsurface is simulated using three-dimensional (3D) transition probability-based indicator geostatistics, conditioned on available data and geological inferences, for three

soil categories based on state-of-practice soil behavior type index (I_C) boundary values. The 2D NDAs are performed using the PM4Sand and PM4Silt constitutive models within the FLAC finite difference program along an interpreted subsurface transect perpendicular to the stream channel. Liquefaction at this site is believed to have occurred early during seismic excitation, while a significant amount of the observed ground deformations occurred during the subsequent post-liquefaction period of ground shaking. The PM4Sand model, used for all elements representing sand-like soils, is calibrated for two significantly different post-liquefaction shear strain accumulation regimes and the system level NDA results for both calibrations are compared. The NDAs are evaluated for their ability to predict the spatial trend of ground displacements observed near the channel face. The results provide insights on the mechanistic contributions of post-liquefaction shear deformations and their ultimate influence on lateral spreading predictions for interlayered deposits.

5.1. Introduction

Nonlinear dynamic analyses (NDAs) for case study sites with interlayered soil deposits have been shown to reasonably predict observed ground deformations due to earthquake-induced liquefaction (i.e. lateral spreading) and cyclic softening for reasonable parametric assumptions (e.g., Boulanger et al. 2019, Pretell et al. 2021, Bassal et al. 2021). NDAs can account for site-specific ground motions, cyclic stress-strain responses, and groundwater diffusion, all within a realistic framework that can capture a dynamic fully coupled soil-fluid response. When performed in two- or three-dimensions (2D or 3D), NDAs can incorporate details of the subsurface stratigraphy and overall site geometry to predict complex ground deformation patterns and other spatially distributed effects. As such, NDAs provide a more complete consideration of the complex system response contributing to lateral spreading than simplified empirical and semi-empirical methods (e.g., Youd et al. 2002, Zhang et al. 2004). However, the predictive accuracy of NDAs depends, among other factors, on their ability to realistically model the constitutive responses of the soil elements.

The selection and calibration of constitutive models for saturated sand-like soils undergoing cyclic loading should ideally capture the mechanisms of both (1) liquefaction triggering, and (2) post-liquefaction deformations. In the absence of advanced laboratory tests [e.g., cyclic direct simple shear (DSS), cyclic triaxial tests] obtained from high quality site-specific samples, constitutive models must typically be calibrated based on measurements from in-situ logging tests [e.g., cone penetration tests (CPTs) and borings]. Such in-situ tests are often the best available data for low- and moderate-risk projects, where more costly testing would not be justified (Robertson 2009). Several empirical correlations with in-situ data exist for interpreting cyclic resistance to liquefaction triggering. Tasiopoulou et al. (2020) recently considered a similar framework for interpreting deformations subsequent to triggering. Their study compiled the results of cyclic DSS and hollow cylinder laboratory tests on clean sands and exposed a strong trend relating post-liquefaction shear strain rate normalized by cyclic shear stress per load cycle ($\Delta\gamma_{postliq\ per\ cycle}/\tau_{cyc}$; defined as compliance rate) to the relative density (D_R). Tasiopoulou et al. (2020) demonstrated the application and utility of the proposed framework via two system-level simulations: one of a submerged tunnel surrounded by a liquefiable fill and foundation course wherein the uplift deformations are controlled by the ratcheting of the liquefiable soils, and one of a sheet pile quay wall retaining liquefiable backfill wherein the lateral deformations of the wall are controlled by the progressive accumulation of lateral strains in the backfill. While this framework shows great promise in improving model calibrations for post-liquefaction shear deformations, NDAs on a broad range of well-documented case studies are needed to understand the effects of such calibrations on predicted ground deformations. In addition, it is important to consider that there are scenarios where the system-level response is insensitive to the cyclic mobility regime, for example when the onset of liquefaction alone mobilizes a broader and distinct failure mechanism (e.g., Pretell et al. 2021) or the softening of a liquefied stratum significantly reduces dynamic stresses such that there is no significant cyclic mobility.

The overall effect of constitutive model calibrations on the system-scale response is further complicated for interlayered sites, where the sedimentary stratigraphy consists of alternating layers of different compositions (e.g., sands, silts, and clays). Such sites are affected by several limitations that may

contribute to incorrect predictions of liquefaction and cyclic softening effects. These limitations are related to the site characterization tools and methods, triggering and deformation correlations, and analyzed mechanisms (Boulanger et al. 2016). Any improvements in ascertaining the soil constitutive response at such sites may be overshadowed by other, more critical, limitations.

This paper considers the results of a 2D NDA study for a site adjacent to a meandering stream channel in Wufeng, Taiwan where the soil profile is interlayered and composed of floodplain deposits with "intermediate" soil beds (e.g., low-plasticity silty sands and silts) and laterally discontinuous channel sand deposits. The site performance in the 1999 Chi-Chi Earthquake, in-situ investigation data, subsurface geostatistical interpretations, and assumptions considered for a FLAC finite difference model (Itasca 2019) are first briefly described. An NDA study of this site was first introduced in Bassal et al. (2021); additional details regarding the site data and model building assumptions are considered in that study. Two separate calibrations of post-liquefaction shear strain accumulation rates for all sand-like soils at the site are considered for this current study. The NDA results for both sets of calibrations provide insights on the contributions of post-liquefaction shear deformations and their ultimate influence on lateral spreading predictions for interlayered deposits.

5.2. Wufeng Site C

The Chi-Chi earthquake (M_W 7.6) occurred on September 21, 1999 and produced widespread permanent ground deformations throughout several inland urban centers and coastal areas due to surface faulting, landslides, and liquefaction effects (MCEER 2000). Surface faulting occurred immediately to the east of the urban village of Wufeng, which experienced a peak ground acceleration of at least 0.67 g based on local seismic recording stations (PEER 2013). The urban center of Wufeng is built over an alluvial plain and is traversed by the braided Tsao-Hu River at the north, the braided Dry Creek River at the west, and several small meandering streams, including Ger-Niao-Ken Creek. A rice paddy site located at a juncture between Chung-Cheng road and the Ger-Niao-Ken Creek channel, hereafter designated as "Wufeng Site C," experienced moderate lateral spreading towards the channel. A site plan of Wufeng Site C is depicted

in Fig. 5.1, with indicated ground crack locations and lateral spreading displacements based on field measurements and aerial photographs (Chu et al. 2006). Along section A-A′, measured lateral displacements are directed towards the channel, commence at about 15 m from the channel edge, and range from 0.4 to 2.1 m. Based on photographs, it is assumed that the channel had side slopes of 1.8H: 1V, a base width of 6 m, and a depth of 3.2 m along Section A-A′. A minor downgrading site slope of ~0.25% to the west is assumed from available data. Also, the channel edge was lined with mortar and stones, and is assumed to cover a zone of compacted soil extending 1 to 2 m behind the channel lining.

Fifteen CPT soundings and two borings were performed at Wufeng Site C within the three years following the earthquake, as mapped in Fig. 5.1. Details of the site investigation are discussed in Chu et al. (2004) and all data was obtained from PEER (2002). The subsurface profile in Fig. 5.2 shows the measured data from CPTs near section A-A′. The cone tip resistance normalized by atmospheric pressure (q_{tN}) is plotted with depth for each CPT. The CPTs readings are color-coded based on the soil behavior type index (I_C) to approximately identify layers of silt mixtures and clays ($I_C > 2.6$; blue), sand mixtures ($2.05 \leq I_C \leq 2.6$; green), and sands ($I_C < 2.05$; beige); these groupings respectively map to soil behavior types (SBTs) 3/4, 5, and 6 (Robertson and Wride 1998).

The subsurface layering and features of Fig. 5.2 were interpreted from the site data, based on a general understanding of geologic features commonly present in fluvial settings. Details regarding the stratum delineations are provided in Bassal et al. 2021, with only the most pertinent details described herein. The top 1 m of the profile (stratum A) consists of surficial reworked miscellaneous sands, silts, and clays. Floodplain deposits (stratum B) exist between depths of 1 to ~15.5 m, primarily composed of silty sands interlayered with low plasticity and overconsolidated silts and clays (layers are interpreted as 10 to 50 cm thick). The floodplain deposits are often interrupted by lenses of channel-deposited sands with 0 to 20% fines. The portion of floodplain soils above the 5 m depth are observed to have lower q_{tN} values than deeper material. A soft and lightly overconsolidated clay lens is encountered in WCC-3 at a depth of 4 m, and may indicate a base for recent lateral accretion deposition from the existing channel. An overconsolidated stiff clay unit with occasional silty sand seams (stratum C) underlies stratum B to the maximum depth explored

of 30 m. The groundwater level during drilling was estimated as 1 to 1.5 m below the ground surface away from the channel.

5.3. Nonlinear Dynamic Analyses

5.3.1. Geostatistical Subsurface Model

Conditional 3D simulations of stratum B were developed using the category-based transition probability software package TPROGS (Carle 1999). This geostatistical approach is advantageous for geotechnical subsurface simulations of interlayered deposits since it can be conditioned on available site investigation data and it accounts for geologically-derived attributes of distinct soil categories, including their (1) proportions, (2) mean thicknesses and lengths, and (3) relative ordering. Three categories were defined by the I_C ranges used in Fig. 5.2, and are labeled as B3, B5, and B6; the number indicates the most pertinent SBT (Robertson and Wride 1998). In addition to being conditioned on the CPT measurements, the full stratum B thickness at the western end of the site was further conditioned as uniform B6 material, to approximate the expected behavior beyond the model extents and prevent unrealistic boundary strains during the dynamic analyses. A 2D slice along section A-A′ for one simulation of stratum B is considered for the current analysis as shown in Fig. 5.3.

Representative properties were determined individually for all distinct materials encountered including stratum A, stratum B (i.e., B3, B5, and B6), stratum C, the compacted zone, and the mortar and stone lining. Properties for the soil strata were derived from the CPT data after inverse filtering using the procedure of Boulanger and DeJong (2018) with baseline filter parameters. Inverse filtering is expected to approximately remove thin-layer and transition zone effects, and provide more accurate parameter estimates based on q_{tN}. The normalized clean sand corrected tip resistance (q_{c1Ncs}) for the sand-like soils was calculated per Boulanger and Idriss (2014) using a site-specific fines content correction conditioned on measurements from boring samples. Median (50^{th} percentile) estimates of q_{c1Ncs} were considered from all CPTs at the site for the applicable I_C range. The stratum A surficial reworked material is assumed to have a q_{c1Ncs} of 76. The q_{c1Ncs} is estimated as 76 and 89 above a 5 m depth, and 116 and 137 below a 5 m depth,

for B5 and B6, respectively. The compacted zone beside the channel is assumed to have a q_{c1Ncs} of 126; consistent with a relative density (D_R) of 65%. Two distinct peak undrained shear strength ratios (s_u/σ'_{vc}) are assumed for the B3 interlayers in the near-channel region (i.e., depths above 5 m and laterally within 10 m from the channel base) and the remainder of the profile as 0.38 and 0.76, respectively. Stratum C is assumed to extend to a depth of 30 m and have a constant undrained shear strength (s_u) of 150 kPa. The mortar and stone lining was modeled with Mohr-Coulomb properties and is assumed to have a cohesion of 20 kPa and friction angle of 10 degrees. An elastic halfspace was also assigned to the model base with a shear modulus of 304 MPa and a Poisson ratio of 0.33.

Other soil parameters were estimated based on correlations with CPT data. The saturated unit weight (UW_{sat}) is assumed as 20 kN/m^3 for stratum A and 21 kN/m^3 for all other strata, with a 15% reduction above the phreatic surface. Vertical and horizontal hydraulic conductivities were estimated per Robertson (2010). The normalized shear wave velocity (V_{s1}) was estimated for sand-like soils per Andrus et al. (2004) as 165 and 177 m/s for B5 and B6 in the upper 5m, and 180 and 195 m/s for B5 and B6 below 5 m, respectively. The V_{s1} for all B3 soils was estimated as 193 m/s per Carlton and Pestana (2012). The V_{s1} in stratum C was estimated based on data at a neighboring site as 236 m/s. The V_{s1} in the elastic halfspace is 325 m/s.

The section A-A′ profile (Fig. 5.2) was modeled as a 2D NDA using the finite difference program FLAC 8.1 (Itasca 2019) and the user-defined constitutive models PM4Sand (Version 3.1; Boulanger and Ziotopoulou 2018) and PM4Silt (Version 1; Boulanger and Ziotopoulou 2019). Fig. 5.3 depicts the left-half of the full plane-strain mesh; the right-half of the mesh is an exact mirror image. The full model mesh is 150 m long by ~32 m tall, and is comprised of 16,896 elements. Elements are typically 0.75 m long by 0.2 m tall above a 16 m depth (except they are 0.5 m tall in Stratum A and skewed near the channel), and are 1.5 m long by 1 m tall below this depth. Stress conditions were initialized prior to dynamic loading by choosing elastic moduli that would produce a coefficient of earth pressure at rest (K_o) of 0.5 for all soil strata. The water table was initialized by setting a static phreatic surface at 1.25 m below the ground surface outside the channel and at 0.6 m above the channel base, and allowing flow to equilibrate between these

areas. The moist total density above the phreatic surface was set as 85% of the saturated total density. The water tensile strength limit was initialized at 5 kPa to allow for saturation (capillary rise) up to about 0.5 m above the phreatic surface. This limit was increased to 100 kPa during shaking to allow for transient negative pore pressure development. The boundary conditions for the dynamic analyses include a compliant (quiet) base, where the outcrop input motion is applied as a horizontal stress time history. The left and right boundaries of the full mesh (right side is not shown in Fig. 5.3) are attached together. Although actual soil conditions across the channel may differ, the symmetric model minimizes incongruences in soil behavior between the attached side boundaries. The mirrored right half of the model is expected to behave identically to the left half, but with a reversed ground motion polarity. Additional details regarding the geostatistical subsurface simulations, selection of representative properties, and numerical model assumptions are discussed in Bassal et al. (2021).

5.3.2. Calibration of Constitutive Models

The PM4Sand parameters are presented in Table 1 for all sand-like soils. The shear modulus coefficient (G_o) was determined from V_{s1} and UW_{sat} at the middle of each layer. The apparent D_R was derived from the representative q_{c1Ncs} using Boulanger and Idriss (2014). The contraction rate parameter (h_{po}) was determined from single-element calibrations targeting a single-amplitude shear strain (γ) of 3% at 15 uniform stress cycles (N) of simulated undrained DSS loading, under the initial vertical effective stress (σ'_{vc}) near the center of the layer. Stress cycles equivalent to the cyclic resistance ratio ($CRR_{M7.5}$) were used for calibrating h_{po}; $CRR_{M7.5}$ was obtained based on the q_{c1Ncs} relationship by Boulanger and Idriss (2014) for a 50% probability of liquefaction after overburden corrections at σ'_{vc}. To account for the post-liquefaction shear strain accumulation rate, two separate calibrations were considered for all PM4Sand materials and are herein referred to as (1) default and (2) median. The default calibration included no additional adjustment for post-liquefaction deformations beyond the PM4Sand primary input parameters (i.e., default values were used for secondary parameters). The median calibration involved adjusting the secondary parameter C_ε, until undrained DSS simulations with uniform stress cycles of $CRR_{M7.5}$ matched

the empirical median post-liquefaction compliance rate ($\Delta\gamma_{post\text{-}liq\ per\ cycle}/\tau_{cyc}$) proposed by Tasiopoulou et al. (2020). While calibrating C_ε, it was also necessary to recalibrate h_{po} to maintain $\gamma = 3\%$ at N = 15 cycles. The compliance rates for the default and median calibrations were both evaluated at applied cyclic stress ratios (CSRs; or τ_{cyc}/σ'_{vc}) equivalent to $CRR_{M7.5}$ of 0.1 and 0.4 with the resulting ranges in Table 5.1. Default values were used for all other secondary parameters.

A comparison of the cyclic DSS behavior for the single-element default and median calibrations of the B5 soils (above 5 m) is provided in Fig. 5.4. Both calibrations reach single-amplitude $\gamma = 3\%$ at N = 15 cycles of $CRR_{M7.5} = 0.148$. However, the rate of shear strain accumulation beyond N = 15 cycles is much larger for the median calibration, which reaches $\gamma = 3\%$ at N = 17 cycles as opposed to N = 26 cycles. As seen in Table 1, the compliance rate ranges for the median calibration are larger than for the default calibrations.

PM4Silt parameters used in the NDA analyses are listed in Table 5.2 for all clay-like soils. As for PM4Sand materials, G_o was determined from V_{s1} and UW_{sat}. The representative s_u/σ'_{vc} was increased by a 25% strain rate adjustment to obtain the undrained shear strength ratio at critical state under earthquake loading ($s_{u,cs,eq}/\sigma'_{vc}$). The shear modulus parameter (h_o) was adjusted until the simulated DSS response approximated the shear modulus reduction and equivalent damping behavior of the empirical relationship by Darendeli (2001). The h_{po} parameter was calibrated to produce a reasonable slope of CSR against N to $\gamma = 3\%$. The void ratio (e_o) of the B3 and C soils was estimated from index tests. The near-channel B3 soft clays were assigned a bounding surface parameter ($n^{b,wet}$) of 0.01 and a critical state friction angle (ϕ'_{cv}) of 45 degrees to simulate a modest clay sensitivity of 1.5. Default values were used for all other secondary PM4Silt parameters.

5.3.3. Ground Motion

This study considers a single east-west trending ground motion recording of the Chi-Chi earthquake from TSMIP (Taiwan Strong Motion Instrumentation Program) strong motion station TCU067 (PEER 2013), for direct input at the NDA model base. This motion reached a peak ground acceleration (PGA) of

0.50 g during the event. TCU067 is located 5 km northeast of Wufeng Site C and 350 m from the fault rupture. It is situated over stiff material with a shear wave velocity in the upper 30 m (V_{s30}) of 440 m/s (Kuo et al. 2012).

5.4. Results

The dynamic response obtained with the default calibration for post-liquefaction shear deformations is presented in Fig. 5.5, which shows contours of the maximum (i.e., during shaking) excess pore pressure ratio (r_u; defined as one minus the ratio of the current to initial vertical effective stress) and shear strain (γ; defined as the engineering strain for the principal stress orientation) across the "left-side" NDA model to a depth of 16 m. By comparing the r_u contours with the soil groups (Fig. 5.3), a majority of the B5 silty sand liquefies (i.e., r_u near 100%), except within ~5 m to the side of and below the channel geometry. The soil beneath the channel heaves during ground shaking, with the associated shear stresses limiting the maximum attainable r_u values in this region. Of the four B6 sand lenses in this realization, only the shallowest liquefies, likely due to its calibration to a lower cyclic resistance than the deeper layers. The maximum γ contour plot (Fig. 5.5) shows that the largest shear strains (>300%) coincide with the B3 soft clay below the channel. The path of a rotational slump feature extends from the basal soft clay to the surface at 9 m from the channel. Strains of up to ~30% occur within several laterally continuous B5 and B6 lenses away from the channel, for depths of 1 to 15.5 m.

Contours of maximum r_u and γ obtained with the median calibration for post-liquefaction shear deformations are presented in Fig. 5.6. The r_u contours show slightly fewer zones of liquefaction than the default calibration; particularly at depths of 5 to 7 m in the areas between 8 to 20 m and 28 to 35 m from the channel edge. The maximum γ contours depict a similar rotational slump near the channel as with the default calibration, but typically show much higher maximum strains of up to ~50% along the B5 and B6 lenses away from the channel.

Time histories of three elements, in Fig. 5.7, help explain some similarities and differences between results for the two shear deformation calibrations. The elements are located along a single B5 lens aligned

with the channel depth (3.2 m), and positioned at 4 m (within the slump feature), 8 m (at the outer extent of the slump feature), and 15 m (away from the slump feature) from the channel edge. Time histories are shown for the total shear stress ratio (τ_{hv}/σ'_{vc}), engineering shear strain (γ_{hv}; along a horizontal plane), and r_u during the 40 s ground motion. The τ_{hv}/σ'_{vc} applied at the base of the model is also shown. All three elements begin the motion with similar responses until a peak stress cycle at 8.8 s causes excessive dilation along the entire lens, as evidenced by negative r_u spikes. The element at 15 m cycles back into a contractive state and triggers liquefaction upon completing the stress cycle. However, the r_u for the elements at 4 and 8 m remains low after 8.8 s, likely due to the introduction of a "static" shear bias as evidenced by a baseline shift in τ_{hv}/σ'_{vc}. This shear bias is caused by stress redistribution near the zones sheared by the rotational slump. Soon after liquefaction initiates, the element at 15 m with the median calibration exhibits a more magnified cycling of γ_{hv} than the default calibration, as expected. The γ_{hv} cycling of the elements at 4 and 8 m is less pronounced, due to a rotation of the principal stresses (i.e., maximum shear is instead along an inclined plane). From ~11 s to the end of shaking, the τ_{hv}/σ'_{vc} peaks are typically lower for the median calibration in all three elements. Greater strains in shallower or deeper lenses for the median calibration (Fig. 5.6) are believed to have limited the available τ_{hv}/σ'_{vc} that could be transmitted to this lens, as observed in past studies of system response for layered soils (e.g., Cubrinovski et al. 2019, Bassal and Boulanger 2021). The final 24 seconds of milder shaking have little effect near the channel, but a large effect on the element at 15 m, as both models strain in opposing directions towards a similar final γ_{hv} of ~10%.

The stress-strain and stress path response during shaking of the element at 15 m is depicted in Fig. 5.8 for both calibrations. The labeled times indicate four peaks in τ_{hv}/σ'_{vc} that dominate the response. The post-liquefaction stress-strain response depicts much larger strains with the median rather than default values, for a similar τ_{hv}/σ'_{vc} at 8.8, 10.9, and 11.7 s, in agreement with the single-element calibration (Fig. 5.4). These peaks simultaneously produce a high amount of dilation in the element, with the normalized vertical effective stress (σ'_v/σ'_{vc}) close to or greater than one. However, as previously described, the τ_{hv}/σ'_{vc} peak values are severely reduced for the median calibration after this time. At 13.5 s, the default calibration approaches a peak τ_{hv}/σ'_{vc} of 0.38, which is much higher than the synchronous peak of 0.05 with

the median calibration. This and subsequent large dilation cycles result in the default calibration gradually accumulating deformations to a magnitude similar to that exhibited by the median calibration.

The resulting lateral spreading towards the channel is compared against the field measurements for both calibrations at positive and negative ground motion polarities in Fig. 5.9. Within 20 m of the channel, computed ground deformations are consistent with the field observations. The total range of measured deformations of 45-205 cm is captured with the positive motion (70-140 cm), but slightly underestimated with the negative motion (0-80 cm) for both calibrations. All models also show a gradual reduction of deformations beyond 20 m, which was not recorded and may not have been visible in the field. Overall ground lurching of 30-40 cm extended to the model boundaries 66 m from the channel, and was oriented towards the channel for the positive motion and away from the channel for the negative motion. For each ground motion, the default and median calibrations tend to exhibit practically identical deformations within 40 m of the channel, with some slight differences of up to 20 cm further in the free field. The near-channel response is primarily dominated by the rotational slump that slips along the B3 soft clay, whereas the further regions were more affected by straining in the B5 silty sands. From these observations, it is apparent that the ground motion polarity was able to influence the resulting deformations much more significantly than the shear strain accumulation rate.

5.5. Conclusions

The seismic performance of the interlayered Wufeng Site C during the 1999 Chi-Chi earthquake was evaluated using 2D NDAs with FLAC and the user-defined constitutive models PM4Sand and PM4Silt, for a realization developed from a 3D transition probability geostatistical model. The PM4Sand model for all sand-like soils was calibrated for two different post-liquefaction shear strain accumulation rate assumptions based on: (1) default parameters, and (2) median shear strain accumulation rates proposed by Tasiopoulou et al. (2020) for clean sands without static stress bias. The site experienced up to 2.1 m of lateral spreading displacements adjacent to the meandering stream channel, or about 0.8 m on average within 20 m of the channel.

The geostatistical model allowed for insights on the contributions of interlayering for the shear deformations in the sand-like soils. Comparing the dynamic responses of individual elements within a critical silty sand lens of the NDAs suggested that while greater shear strain accumulation rates caused greater strains soon after liquefaction was triggered, the stresses imposed on this lens were subsequently reduced due to overall greater yielding in other layers. Both models calibrated to different shear deformation rates ultimately resulted in similar post-earthquake strains throughout the profile and lateral spreading patterns at the surface. In contrast, details of the ground motion related to the polarity and distribution of cycles largely affected the magnitude of ground deformations, particularly in the free-field away from the channel. Large deformations within 10 m of the channel were largely independent of the shear deformation calibration and were instead controlled by a rotational shearing surface exacerbated by yielding along a locally weaker clay lens.

These NDA results suggest that in the absence of advanced site-specific laboratory testing, it is meaningful to undertake a sensitivity study to determine how post-liquefaction cyclic mobility affects the computed deformations. For this site, other factors had a stronger effect on the computed deformations. Concurrent studies are evaluating the influence of the subsurface stratigraphy, material properties, input ground motions, and numerical procedures on the deformation patterns for this case history.

5.6. Acknowledgements

The authors appreciate the financial support of the National Science Foundation (award CMMI-1635398) and California Department of Water Resources (contract 4600009751) for different aspects of the work presented herein. Any opinions, findings, conclusions, or recommendations expressed herein are those of the authors and do not necessarily represent the views of these organizations. The authors benefited from discussions with Graham Fogg regarding transition probability geostatistics, as well as the archived data and past studies of this site by Daniel Chu, Jonathan Stewart, Leslie Youd, Bin-Lin Chu, Shannon Lee, Sung-Chi Hsu, and others.

Tables

Table 5.1. PM4Sand constitutive model inputs

Material	*Center*				*Default Calibration*		*Median Calibration*		
	σ'_{vc} *(kPa)*	D_R	G_o	$CRR_{M7.5}$	h_{po}	$\Delta\gamma_{postliq\ per\ cycle}/\tau_{cyc}$	h_{po}	C_ε	$\Delta\gamma_{postliq\ per\ cycle}/\tau_{cyc}$
Compacted Zone	35	0.65	907	0.249	0.15	0.009 - 0.034	0.35	0.64	0.008 - 0.047
A & B5 (above 5m)	42	0.44	700	0.148	0.90	0.070 - 0.086	1.22	33.0	0.170 - 0.430
B6 (above 5m)	42	0.50	805	0.166	0.55	0.038 - 0.060	0.85	5.7	0.110 - 0.200
B5 (below 5m)	123	0.62	837	0.195	0.67	0.026 - 0.038	0.71	1.5	0.037 - 0.077
B6 (below 5m)	123	0.69	982	0.265	0.88	0.013 - 0.022	0.92	0.5	0.024 - 0.028

Table 5.2. PM4Silt constitutive model inputs

Material	$s_{u,eq,cs}/\sigma'_{vc}$	$s_{u,eq,cs}$ *(kPa)*	G_o	h_{po}	h_o	e_o	$n^{b,wet}$	ϕ'_{cv}
B3 (near-channel)	0.32	-	1030	8	0.9	0.55	0.01	45
B3 (typical)	0.95	-	1030	30	0.9	0.55	-	-
C	-	188	1250	10	1.5	0.51	-	-

Figures

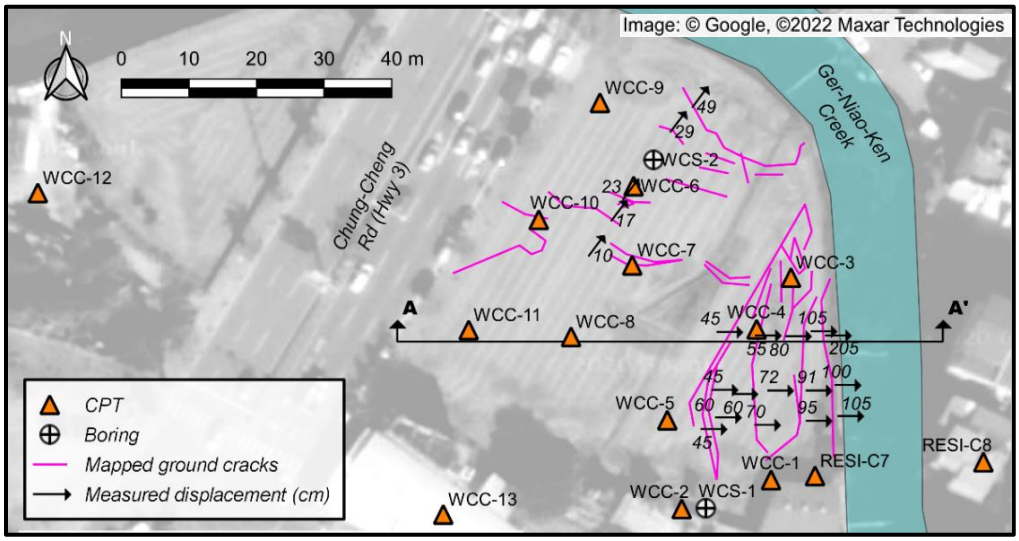

Figure 5.1. Wufeng Site C investigation plan with post-earthquake observations (adapted from Chu et al. 2006 and Bassal et al. 2021). Made in QGIS. (Image © Google, ©2022 Maxar Technologies).

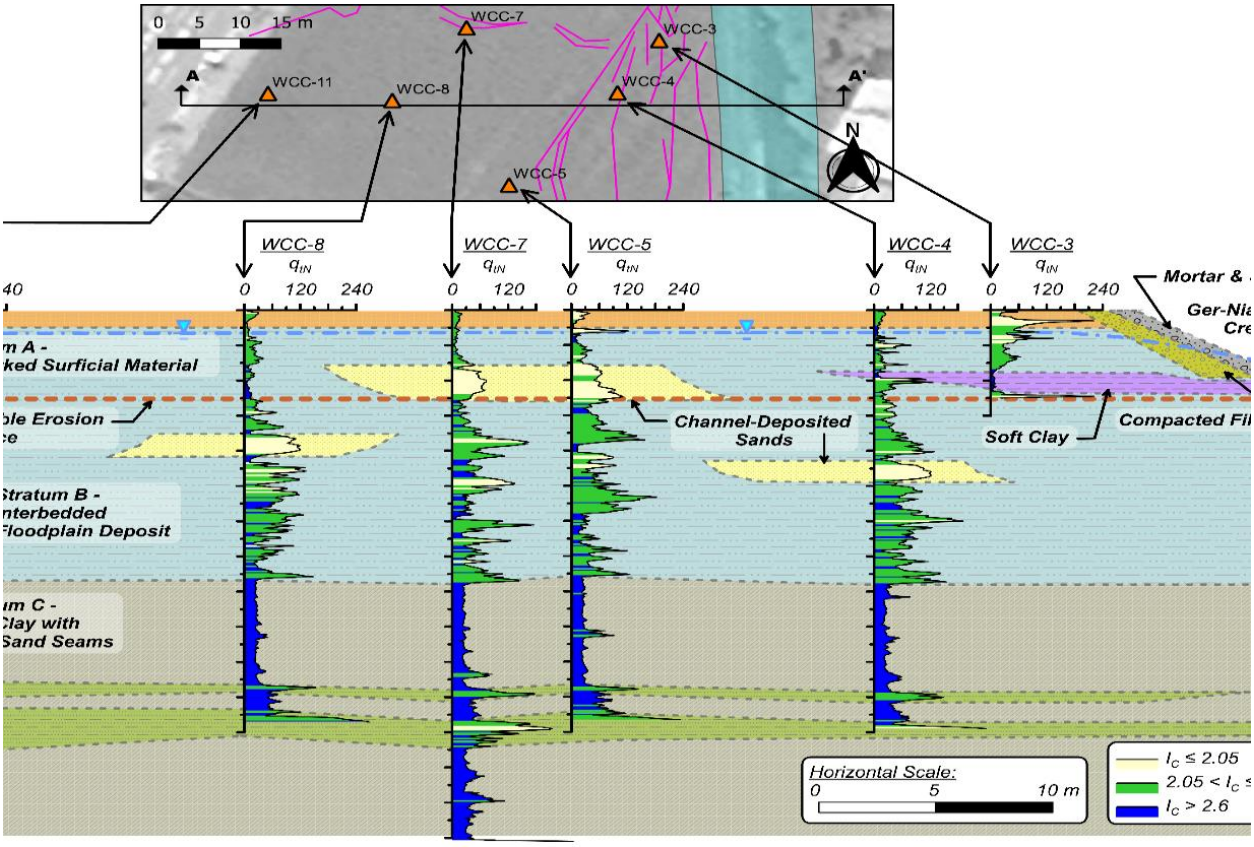

Figure 5.2. Section A-A′ CPT fence diagram with a geologically interpreted stratigraphy.

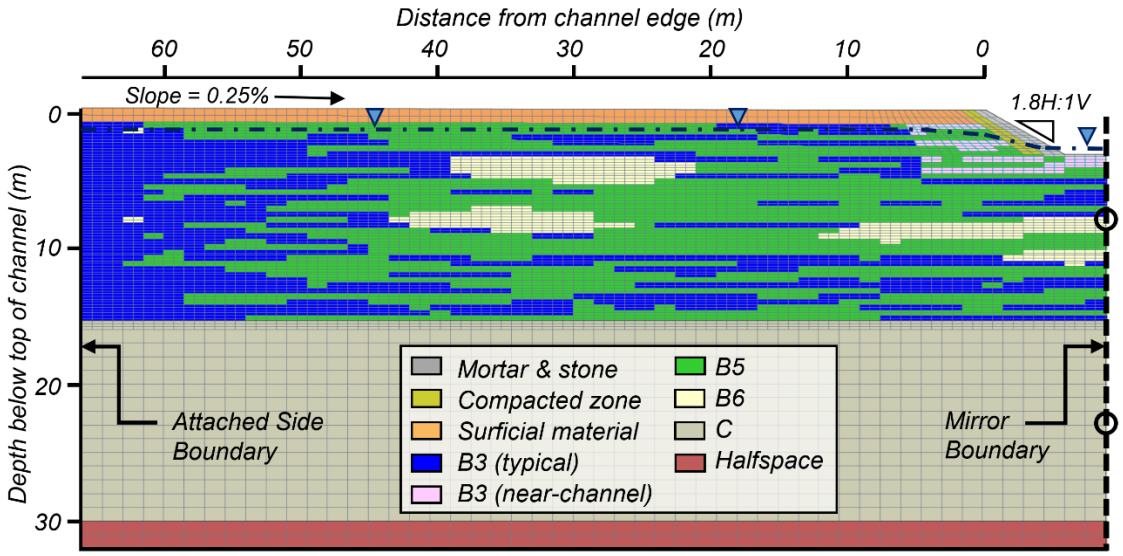

Figure 5.3. NDA "left-side" mesh as used in FLAC with simulated layering for stratum B (adapted from [3]).

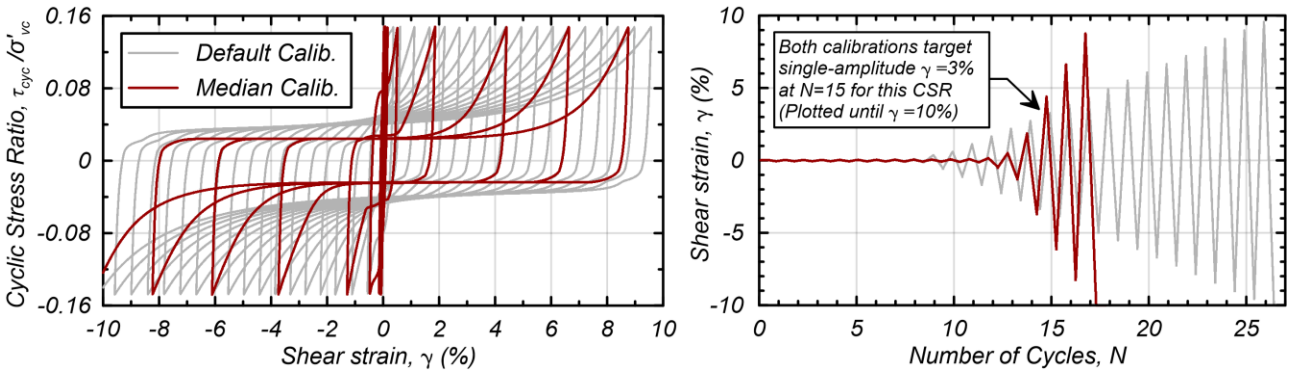

Figure 5.4. Calibration of B5 (above 5m) for default and median post-liquefaction shear strain accumulations.

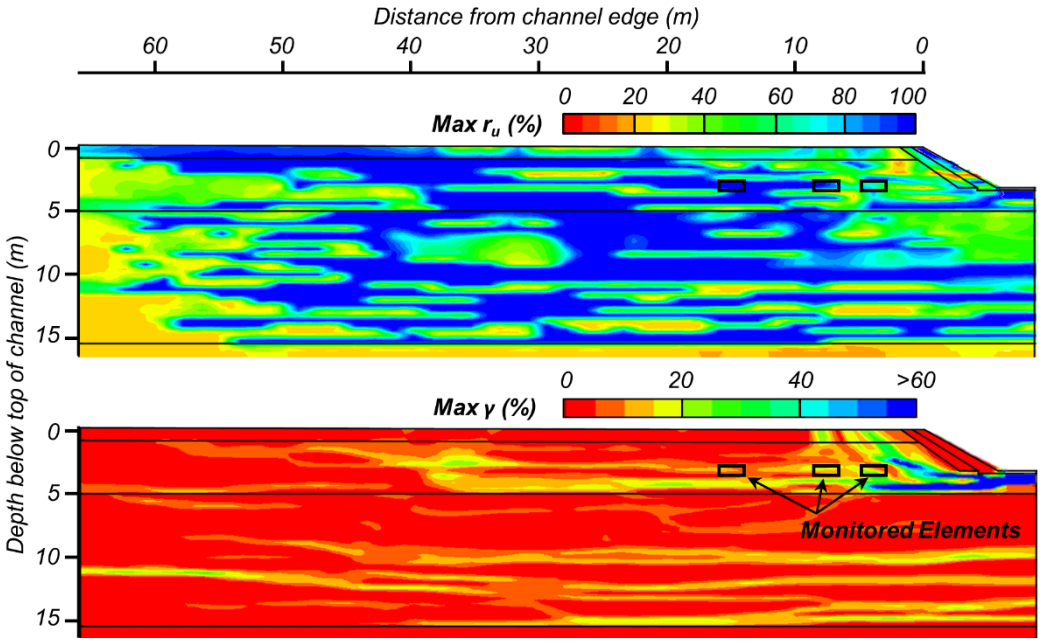

Figure 5.5. Contours of maximum r_u and γ after shaking for NDA with default shear deformation calibration.

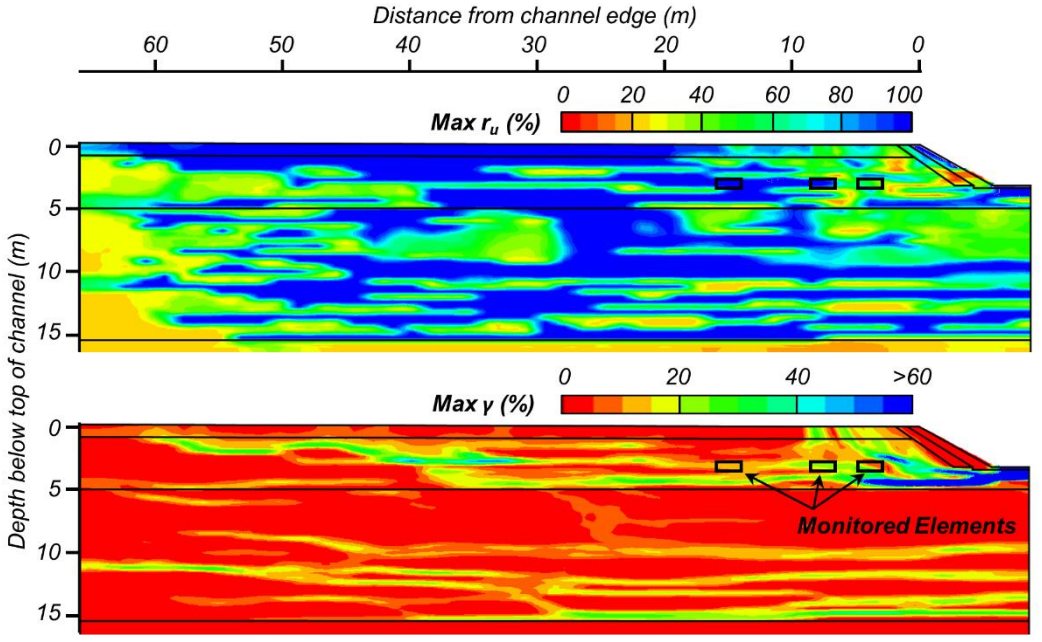

Figure 5.6. Contours of maximum r_u and γ after shaking for NDA with median shear deformation calibration.

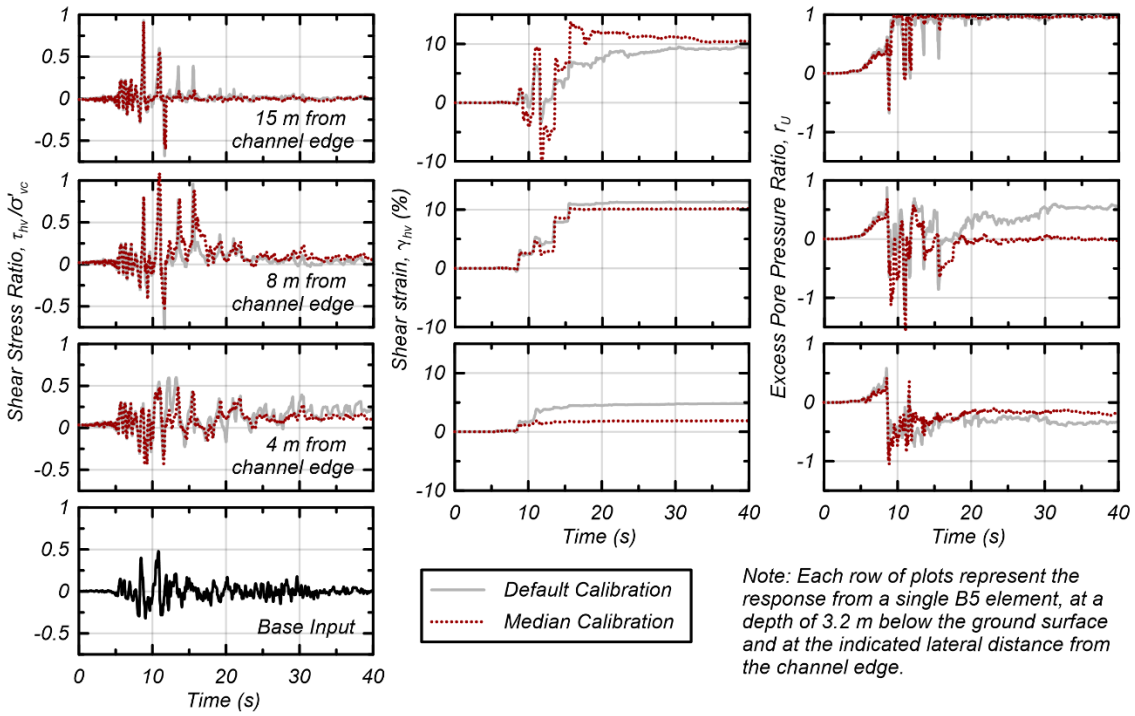

Figure 5.7. Time histories for three B5 elements from two NDAs with different shear deformation calibrations.

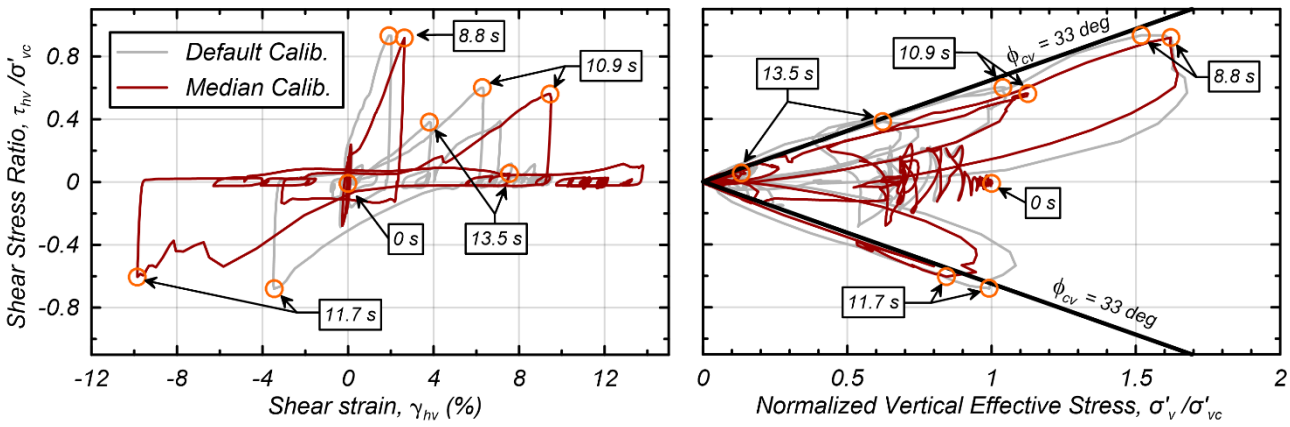

Figure 5.8. Dynamic response for one B5 element (3.2 m below top of channel; 15 m from channel edge) from two NDAs with different shear deformation calibrations.

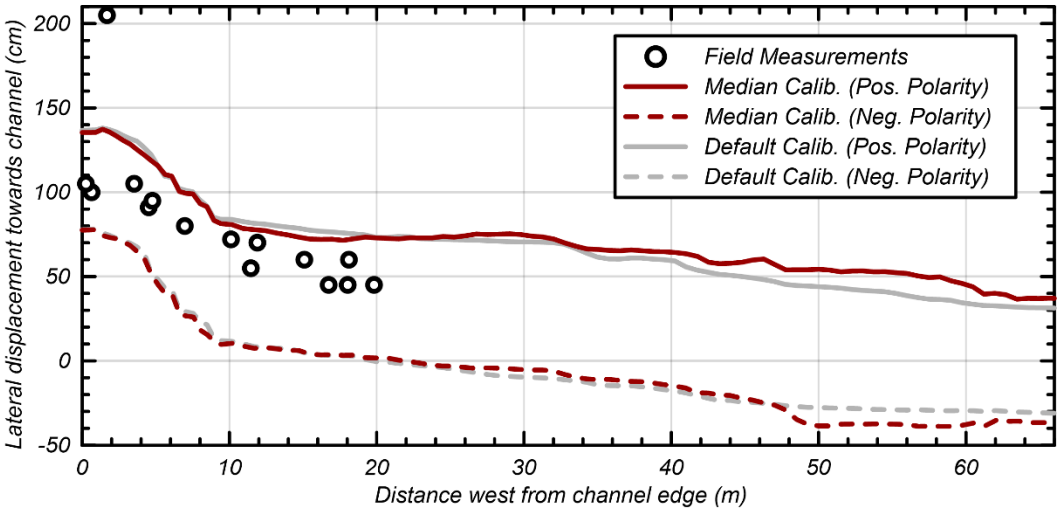

Figure 5.9. Ground deformations from field measurements and NDAs with different calibrations and polarities.

6. System Response of an Interlayered Deposit with a Localized Graben Deformation in the Northridge Earthquake

Author's Note

The full content of this chapter was submitted to the *Soil Dynamics and Earthquake Engineering* journal, as part of a special issue for the *4th International Conference on Performance-Based Design in Earthquake Geotechnical Engineering (PBD-IV)*. The author performed and interpreted the analyses, and drafted the manuscript. Appendix C provides supplementary materials, including look-up tables used for constitutive model calibrations for stochastic soil units, and additional figures for the NDA analysis results. Appendix D provides an example workflow (Bassal 2022) that was used for executing a set of stochastic NDAs with SGS simulations for this case study.

Publication

Bassal, P. C., & Boulanger, R. W. (Submitted). "System Response of an Interlayered Deposit with a Localized Graben Deformation in the Northridge Earthquake." Soil Dynamics and Earthquake Engineering, special issue for the 4th Int. Conf. on Performance-Based Design in Earthquake Geotechnical Engineering.

Abstract

The Wynne Avenue site in the California San Fernando Valley was analyzed using two-dimensional (2D) nonlinear dynamic analyses (NDAs) with geostatistical subsurface modeling to interpret key mechanisms contributing to a 12-m-wide graben deformation with vertical offsets of 10–20 cm in the 1994 Northridge earthquake. In-situ data from borings and cone penetration tests, joined with geological interpretations of the distal alluvial fan deposition, helped delineate interlayered silty sand lenses within a typically fine-grained soil stratigraphy. The NDAs used the PM4Sand and PM4Silt constitutive models with the FLAC finite difference program. NDAs with uniform properties for distinct soil zones closely reproduced the observed graben. However, stochastic NDAs, modeled with sequential Gaussian simulations (SGS) for conditional random field realizations of critical zones, often obscured the expected graben. The NDAs provide new insights on the causal mechanisms of liquefaction-induced ground

oscillations and lurching, that were not easily deduced from common one-dimensional (1D) liquefaction vulnerability indices (LVIs) and Newmark sliding-block analyses. This case study demonstrates the capabilities of system-level NDAs for modeling localized ground deformation patterns, but also highlights cautionary nuances for their implementation with data-driven stochastic subsurface modeling.

6.1. Introduction

The integration of nonlinear dynamic analyses (NDAs) with stochastic field modeling of subsurface soil variability has provided valuable mechanistic insights for the evaluation of earthquake ground motions and deformations (e.g., Popescu et al. 1997, 2005, Asimaki et al. 2003, Montgomery et al. 2017, Montgomery and Boulanger 2016, Paull et al. 2021). NDAs allow for system-level insights of coupled soil-fluid mechanisms (e.g., Cubrinovski et al. 2019), including the seismic responses of soils subjected to liquefaction and cyclic softening. When combined with stochastic subsurface modeling in two- or three-dimensions (2D or 3D), NDAs could potentially predict spatial ground deformation patterns and better quantify performance uncertainties.

Simplified predictions of ground deformations due to earthquake-induced liquefaction and cyclic softening might commonly be obtained from one-dimensional (1D) liquefaction vulnerability indices (LVIs) (e.g., Iwasaki et al. 1978, Zhang et al. 2002, 2004, Maurer et al. 2015) or Newmark sliding-block analyses (e.g., Newmark 1965, Bray and Macedo 2019). However, these methods often misinterpret liquefaction effects at sites with interlayered soil deposits due to limitations in site investigation data, parameter correlations, and neglected mechanisms (Boulanger et al. 2016). Despite the additional engineering effort and proficiency needed, several recent post-earthquake case study evaluations have demonstrated the advantages of NDAs for evaluating the magnitude and spatial distribution of ground deformations at heterogeneous sites (e.g., Luque and Bray 2017, Boulanger et al. 2019, Pretell et al. 2021, Bassal and Boulanger 2021, Bassal et al. 2022b).

Soil heterogeneity can be considered at three different scales for geotechnical evaluations (Uzielli et al. 2006): (1) stratigraphic heterogeneity, or large-scale differences in soil groups (i.e., strata) due to geo-

formational processes, (2) lithological heterogeneity, or the persistence of interlayers or pockets of distinct lithological make-up, and (3) inherent soil variability, or the small-scale variation of soil characteristics within distinct lithological soil masses. The level of detail to consider for a geotechnical subsurface model is not always clear, and depends in part on the local geological setting and the evaluated mechanisms. Furthermore, whereas stratigraphic heterogeneity can be deterministically inferred from available in-situ data, several alternative geostatistical tools and approaches are available to simulate lithological heterogeneity [e.g., sequential indicator (Alabert 1987), transition probability (Carle and Fogg 1996), truncated Gaussian (Matheron et al. 1987), and object modeling (e.g., Pyrcz and Deutsch 2014)] and inherent soil variability [e.g., LU decomposition (Davis 1987), local average subdivision (Fenton and Vanmarcke 1990), sequential Gaussian (e.g., Deutsch and Journel 1997), and Karhunen-Loève expansion (e.g., Phoon et al. 2005)]. While many of these modeling approaches were originally developed for the mining and petroleum industries, demonstrative case studies are expected to extend their utility and accessibility for geotechnical and earthquake engineering applications.

The site examined in this current study is Wynne Avenue, a gently sloped residential roadway in the San Fernando Valley of California where (1) where the subsurface is composed of spatially variable fine-grained soils with discontinuous silty sand lenses within a distal alluvial fan environment, (2) an approximately 150-m-long by 12-m-wide graben deformation feature with vertical offsets of 10 to 20 cm was observed following the 1994 Northridge earthquake, and (3) simplified evaluations by Holzer et al. (1999) suggested the deformation was caused by liquefaction within underlying silty sand lenses despite the lack of observable post-event sediment ejecta. NDAs and Newmark sliding-block evaluations were recently performed for this site by Yang and Kavazanjian (2021) without consideration of variable soil properties nor cyclic softening in the clay-like soils. Their results did not indicate a localized ground deformation, but rather suggested consistent lateral displacements across the site. Preliminary NDA results by Bassal and Boulanger (2022) considered the influence of modeling the subsurface with kriging and the potential contribution of cyclic softening within a shallow saturated sandy clay lens to explain the observed graben deformation.

This paper presents a 2D NDA study of Wynne Avenue, expanding on previous work, with a focus on (1) elucidating the key mechanisms contributing to the moderate localized graben deformation, and (2) evaluating the capabilities and limitations of using an integrated methodology with NDAs and stochastic fields for this site. The post-earthquake observations, subsurface conditions, and hypothesized failure mechanisms by Holzer et al. (1999) are first described. The subsurface modeling workflow and assumptions for capturing both stratigraphic heterogeneity and inherent soil variability are detailed. Data from laboratory testing, as well as in-situ cone penetration tests (CPTs), vane shear tests (VSTs), and borings were processed for developing representative properties. Stochastic realizations of critical strata were obtained from the sequential Gaussian simulation (SGS) approach, with corrections for spatial declustering and non-Gaussian data distributions. The NDAs were subsequently developed using FLAC 8.1 (Itasca 2019) with the PM4Sand (Version 3.1; Boulanger and Ziotopoulou 2017) and PM4Silt (Version 1; Boulanger and Ziotopoulou 2018) constitutive soil models. NDA results are presented for a baseline uniform model (without inherent soil variability) and compared to results for the stochastic models, as well as sensitivity evaluations of alternative parametric assumptions, ground motions, and calibration protocols. Insights on the dynamic response and deformation mechanisms are presented, and contrasted with insights from simplified analyses. The degree by which the stochastic NDAs were capable of spatially locating the graben deformation, and implications and limitations concerning the use of these integrated tools for research and practice are discussed.

6.2. Ground Failure at Wynne Avenue

On January 17, 1994, the M_W 6.7 Northridge earthquake produced widespread damage to buildings, embankments, roads, and lifelines, including the rupture of thousands of water and gas pipelines, throughout the greater Los Angeles area (e.g., Stewart et al. 1996). Permanent ground deformations were most severe near the epicenter, associated with a blind reverse fault that produced recorded horizontal peak ground accelerations (PGAs) as high as 0.94 g and vertical PGAs greater than 0.8 g within the California San Fernando Valley (Chang et al. 1996). Wynne Avenue was one of four sites within and near the valley

that were selected by a United State Geological Survey (USGS) team for detailed geotechnical site investigations and laboratory testing following the earthquake to better understand the mechanisms contributing to the ground failures (Bennett et al. 1998). The site is located about 1 km to the northeast of the earthquake epicenter, on the hanging wall side of the 7-km-deep fault rupture plane (Wald and Heaton 1994).

A photo of permanent ground deformations at the Wynne Avenue site is shown in Fig. 6.1, taken during a site investigation 12 months after the earthquake. Wynne Avenue is a residential roadway that slopes to the south with a 1 to 2% grade, consistent with the regional topography. The deformations were associated with a down-dropped block (i.e., graben) feature that was 12-m-wide along Wynne Avenue, bounded by the cracks visible in the photo and mapped in Fig. 6.2a. The vertical offsets across cracks at the graben boundaries ranged from 10 to 20 cm, and horizontal offsets were similar in magnitude (Holzer et al. 1996, 1999). The graben had an oblique northeast strike across the roadway. The longitudinal extent of the graben was estimated by the field reconnaissance team as 150 m beyond the roadway, but has not been demarcated in published maps (T. L. Holzer personal communications, 2022). No sand boils were observed following the earthquake. The deformation ruptured water lines and sewers (Holzer et al. 1999). Specifically, distribution main leaks in eight 4- to 6-inch cast iron pipelines and a break in one 40-inch trunk line were reported within 300 m of the ground deformations mapped in Fig. 6.2, based on local repair records (C. Davis and J. Hu personal communications, 2022).

6.3. Subsurface Conditions

The Wynne Avenue site is located within the alluvial fan sediments of the gently sloping San Fernando Valley. Gravel, sand, and finer sediments reach a depth of greater than 200 m near the center of the valley (Wentworth and Yerks 1974), of which recent Holecene age sediments make up the upper 8 to 12 m across the valley (Holzer et al. 1996). Fluvial processes originating from ephemeral streams flowing from the surrounding mountains have predominantly deposited coarse-grained sediments along areas of higher relief at the north margins of the valley, and clays along the southern part of the valley.

The subsurface investigation (Bennett et al. 1998, USGS 2021) consisted of a north-south linear array of fourteen CPTs (WYN-1 to -14), five borings (WYN-1, -5, -7, -13, and -14), and three field VSTs (WYN-5, -13, and -14) across the width of the graben deformation, as mapped in Fig. 6.2a. The in-situ tests spanned a total length of about 500 m, extending beyond the northern cul-de-sac of Wynne Avenue to Schoenborn Street.

A general CPT subsurface profile across a 500 m section of the site is depicted in Fig. 6.2b, and a detailed subsurface profile centered on the graben is depicted in Fig. 6.2c. The normalized cone tip resistance (q_{tN} = measured resistance divided by atmospheric pressure) is plotted versus depth for each CPT and categorized by the soil behavior type index (I_C) for silts and clays (>2.6), sand mixtures (2.05-2.6), and sands (<2.05) (Robertson and Wride 1998). The assumed stratigraphic layering was first delineated by Holzer et al. (1999). The top layer of the subsurface, unit A, consists of 1.5 to 3.5 m of road base aggregates, and silty sand to sandy clay fill. This is underlain by unit B, which consists of 3 to 4 m of soft to firm lean clay to sandy lean clay, likely originating from overbank and sheetflood deposits. Unit C next comprises 7 to 10 m of firm to stiff clays of similar origin, with laterally discontinuous, 1- to 3-m-thick, silty sand lenses C1 and C2. Unit D is the deepest layer depicted and consists of very dense Pleistocene silty sands. The ground water table as obtained from borehole observations is between 3.8 to 6.6 m deep, within unit B. The saturated and unsaturated portions of unit B are designated as B_{unsat} and B_{sat} for the current analyses.

The original profile by Holzer et al. (1999) was further refined herein by subdividing the C1 sand lens into (1) zone C1a, thinly interbedded silty sands and sandy silts, with a bulk fines content (FC; percent by soil mass passing a 0.075 mm sieve) > 45% and q_{tN} < 50 on average, and (2) zone C1b, dense silty sands with trace to some gravel, with FC < 30% and q_{tN} > 90 on average. Materials grouped as C1a are observed in CPTs south of the graben (i.e., WYN-8, -7, -6, -9, and -10) and again at the north end of the site (i.e., WYN-14), and those grouped as C1b are observed beneath and to the north of the graben (i.e., WYN-11, -5, -4, -3, -2, and -1). As Holzer et al. (1999) pointed out, an abrupt contrast in these materials is indicated over a distance of 4.5 m between WYN-10 and -11. The episodic alluvial fan sheetflood deposition associated with intermittent stream channel overtopping and avulsion events are likely to produce such

abrupt geologic boundaries (e.g., Nichols 2009) and are a reasonable basis for separating units C1 into these two zones (T. L. Holzer personal communications, 2022). However, the relatively wide 150 m spacing between WYN-1 and -14 makes it difficult to ascertain the location of the contact between C1a and C1b soils at the north end of the site. Similarly, the 90 m spacing between WYN-12 and -8 obscures the southern extent of C1a within unit C.

The upper contact of unit D is typically gently sloped to the south except for a steep 1.1 m offset between WYN-4 and -5 over a 4 m spacing. The cause and effects of this steep declivity are not clear. Similar offsets are not apparent in the overlying soil units, and the declivity is thus inferred by Holzer et al. (1999) to be either a low activity buried fault scarp or erosional feature.

6.4. Hypothesized Failure Mechanisms

Several potential mechanisms for triggering the graben deformation at Wynne Avenue were assessed by Holzer et al. (1996, 1999) based on the site investigation data and simplified analyses. Holzer et al. (1999) ruled out the possibility of secondary faulting caused by large permanent strains from the underlying fault rupture (e.g., Cruikshank et al. 1996), due to the lack of evident offsets in the sand lenses above the aforementioned steep declivity of unit D. They also disregarded dynamic compaction of unsaturated soils due to the generally silty nature of the fill and sand lenses. Additionally, they suggested a low potential for dynamic failure within the lean clays (e.g., units B and C), based on their estimates of cyclic stresses and peak clay strengths.

Holzer et al. (1999) and Holzer and Bennett (2007) ultimately attributed the localized graben deformation to the shift in liquefaction-induced cyclic mobility of unit C1 across the abrupt transition between the silty zone with a higher FC (i.e., C1a) and the zone with a lower FC (i.e. C1b). They hypothesized that larger strains were mobilized within C1b with its lower FC, despite their prediction of a greater thickness of liquefaction triggering within C1a. They suggested that the liquefaction-induced generation of excess pore pressures beneath the graben may have redistributed and reduced the effective stresses within neighboring susceptible areas.

6.5. Subsurface Modeling

6.5.1. Mesh Development

The gridded mesh used for geostatistical analyses and NDA modeling is first described herein, as it was an important prerequisite for the data processing choices made. The 500-m-long 2D mesh is depicted in Fig. 6.3a, along the full extent depicted in the CPT profile (i.e., between northing 3787309 and 3787809 m in Fig. 6.2b). A magnified section near the observed deformation is also shown in Fig. 6.3b, detailing the mesh grid and distinct soil material allocations. A total of 20,000 elements were used, each 1-m-wide in the lateral x-direction, and with variable thicknesses of between 0.25 to 1 m in the vertical y-direction. The mesh accommodates the boundaries of distinct soil zones (i.e., stratigraphic heterogeneity) according to inferences from the available site investigation data. The groundwater table was assigned based on the borehole observations, and the B_{unsat} and B_{sat} materials were assigned to elements with centroids above or below the water table. Unit C1 was zoned such that the southern boundary of C1b was located at x = 273 m based on the closely spaced CPTs in this area, whereas the southern end of C1a and the northern end of C1b were inferred at x = 185 and 460 m. The top of the mesh slopes down towards the south (left side of model), with a varying grade of 1 to 2%. The uniform NDAs consider constant representative parameters within each soil zone labeled in Fig. 6.3, and the stochastic NDAs additionally consider SGS fields for critical B_{sat} and C1 soils. Details regarding NDA boundary conditions, stress and groundwater initialization, and soil model calibrations associated with this mesh are described in Section 6.

6.5.2. Site and Laboratory Data Processing

The site data was used to develop the clean-sand corrected tip resistance normalized for 1 atm overburden stress (q_{c1Ncs}) for sand-like A, C1, C2, and D soils, and the peak undrained shear strength ratio under earthquake loading ($s_{u,peak,eq}/\sigma'_{vc}$) for clay-like B_{unsat}, B_{sat}, and C soils. The CPT measurements were first inverse filtered using the procedure of Boulanger and DeJong (2018) with baseline filter parameters to provide more accurate estimates of q_{tN} by removing thin-layer and transition zone effects. It is believed that the improved parameter estimates from inverse filtering are more representative of soil behavior, even

though the numerical mesh does not explicitly consider layers thinner than 25 cm. The inverse filtered cone tip resistance and sleeve friction readings, originally obtained at 10 cm intervals within each CPT, were next averaged over 30 cm intervals to more closely match the mesh element thicknesses. This allowed for statistical representations of all subsequent spatial and parameter correlations that better matched the modeled element volumes, without need of further volume-variance reductions (e.g., Vanmarcke 1977, Elkateb et al. 2003). A methodology described by Bassal et al. (2022a) was used to develop site-specific FC estimates for sand units C1 and C2 along each CPT, by percentile matching the overall distribution of I_C within these units from CPTs WYN-1, -5, -7, and -14, with the overall distribution of 36 FC measurements from adjacent borings. The q_{c1Ncs} was then estimated per Boulanger and Idriss (2015) for all CPT data with $I_C < 2.6$. The $s_{u,peak,eq}/\sigma'_{vc}$ was estimated from a cone bearing factor (N_{kt}) of 14 and an earthquake loading rate strength increase of 25%. These factors allowed for consistent estimates of $s_{u,peak,eq}/\sigma'_{vc}$ with the peak field VST measurements, for which the field vanes were rotated at a relatively high rate of 90°/min to approximately match the strength of the soil under earthquake loading (Holzer et al. 1999). The residual VST measurements suggested a peak to critical state strength reduction of up to about 20%. Prior to modeling, all $s_{u,peak,eq}/\sigma'_{vc}$ estimates were capped at a minimum of 0.25 to eliminate a small percentage of points that implied dynamic strengths smaller than empirical data for even normally consolidated clays (e.g., Boulanger and Idriss 2007) and may have been affected by CPT measurement errors.

6.5.3. Representative Properties

Site-wide representative values of q_{c1Ncs} and $s_{u,peak,eq}/\sigma'_{vc}$ for modeling all distinct soil zones at the site were next considered. A cell-based declustering algorithm per Pyrcz and Deutsch (2003) as implemented in the GeostatsPy Python package by Pyrcz et al. (2021) was used to spatially weight the CPT soundings associated with each zone. This algorithm allowed all closely clustered CPT soundings near the observed graben to receive less weight than those in sparser areas, including the soundings located at the ends of the cluster (i.e., WYN-6 and -2). Cumulative distribution functions (CDFs) were next developed

for each soil zone with and without decluster-weighting. The CDFs of $s_{u,peak,eq}/\sigma'_{vc}$ for B_{sat} are in Fig. 6.4a and q_{c1Ncs} for unit C1 are in Fig. 6.4b, for individual CPT soundings, all combined CPT data without weighting, and all combined CPT data with decluster-weighting. The B_{sat} CDFs (Fig. 6.4a) span a large range of $s_{u,peak,eq}/\sigma'_{vc}$ from less than 0.25 to greater than 0.9 both within and between individual CPTs, indicative of the significant spatial variability within this unit. The unit C1 CDFs (Fig. 6.4b) show significant segregation between CPT soundings in the C1a and C1b soil zones (Fig. 6.2), but are relatively consistent within each group. Median (50^{th} percentile) decluster-weighted estimates of q_{c1Ncs} and $s_{u,peak,eq}/\sigma'_{vc}$ were selected from the combined CPT data to represent each uniformly modeled soil zone for the NDAs, as consistent with recommendations of Montgomery and Boulanger (2016).

Other representative soil parameters for the fully-coupled NDA modeling of Wynne Avenue were primarily obtained from general correlations with the CPT data and laboratory index tests. The total unit weight (γ_t) was estimated from lab measurements, the vertical hydraulic conductivity (k_v) was estimated per Robertson (2010), and the permeability ratio (k_h/k_v) was estimated as 2 for sand-like and 10 for clay-like soils. To approximate the influence of pore pressure migration within unit C1 for the stochastic models, k_v was assigned as an exponential function of q_{c1Ncs} that varied from $k_v = 10^{-6}$ to 10^{-3} m/s for $q_{c1Ncs} = 100$ to 200, respectively (i.e., k_v was capped at 10^{-6} m/s for $q_{c1Ncs} < 100$, and 10^{-3} m/s for $q_{c1Ncs} > 200$). The small-strain shear wave velocities (V_S) for sand-like soils were estimated from the median q_{c1Ncs} and FC measurements per Andrus et al. (2004). The V_S for zones B_{unsat} and B_{sat} were estimated from water content, unit weight, and liquid and plasticity limit measurements per Carlton and Pestana (2012). The V_S for unit C was estimated per the Mayne and Rix (1995) clay correlation with q_{tN}, and the V_S for unit D was estimated from downhole geophysical tests at the nearby USC3 (i.e., White Oak Church) seismic station (Gibbs et al. 1999). All representative soil parameters discussed herein are presented in Table 1.

6.5.4. Inherent Soil Variability

A detailed sequential Gaussian simulation (SGS) workflow, derived from state-of-practice methods for subsurface geostatistical reservoir modeling (e.g., Pyrcz and Deutsch 2014), was adapted for developing

conditional stochastic realizations of $s_{u,peak,eq}/\sigma'_{vc}$ for zones B_{sat} and q_{c1Ncs} for unit C1. Inherent soil variability was not considered for other soil zones at the site, which were not as significant contributors to the ground deformation. To investigate the abilities of SGS to represent and contend with stratigraphic boundaries, two different stochastic assumptions are considered for unit C1 as (1) separate "zones" of C1a and C1b (i.e., C1-zoned) as depicted in Figs. 6.2 and 6.3, and (2) "grouped" as one unit without detrending (i.e., C1-grouped). The choice of zoning unit C1 is akin to removing a nonstationary mean lateral trend from the C1 dataset, with the added advantage of allowing for unique data distributions and spatial correlations for each zone, as expected for areas with distinct lithologies due to geoformation processes. However, zoning as implemented herein required subjectively locating abrupt geological boundaries and interpreting statistical properties from reduced datasets per zone. The alternative C1-grouped assumption considers a constant parameter distribution and spatial correlation model for unit C1 (i.e., second-order stationarity), as estimated from combined datasets of C1a and C1b. No vertical trends were apparent for B_{sat} and C1, in part because $s_{u,peak,eq}/\sigma'_{vc}$ and q_{c1Ncs} are intrinsically normalized for increasing vertical stresses with depth.

In preparation for SGS modeling, the non-Gaussian CPT data distributions were normal score transformed using the *nscore* algorithm by Deutsch and Journel (1997) as implemented by Pyrcz et al. (2021). Variograms for the normalized B_{sat}, C1a, and C1b datasets were next calculated at non-overlapping lag bins, and estimated as exponential models with a sill of 1, and ranges of 1.6, 0.5, and 1.2 m in the vertical (y) direction, and 80, 30, and 80 m in the lateral dipping direction (i.e., -x direction with 0.5° dip), as depicted in Fig. 6.5. In the vertical direction, the variogram data was easily modeled for B_{sat}, whereas the scatter for C1a and C1b was accommodated by ensuring the model ranges aligned with the frequency of the observed fluctuations and interbedding. The lateral variograms were more difficult to interpret, even though the broad distribution of CPT spacing intervals should have helped reduce spatial correlation bias (e.g., DeGroot and Baecher 2003). The model range in the lateral direction for all soil zones was thus additionally constrained by the expected horizontal-vertical anisotropic ratios typical for braided fluvial environments [e.g., typically ranging from 20:1 to 100:1, per Pyrcz and Deutsch (2014)] and empirical data for the CPT parameters considered (e.g., Phoon and Kulhawy 1999). The alternative assumption of C1-

grouped was similarly estimated by exponential variogram models with relatively higher ranges [as expected for mixed datasets that have not been detrended (e.g., Uzielli et al. 2006)] of 1.2 and 100 m for the vertical and dipping directions.

The variogram models were next used to inform simple kriging and SGS modeling of B_{sat} and C1. The open-source computer package SGeMS (Remy et al. 2009) was used to execute these geostatistical algorithms at the centroids of all associated elements within the numerical mesh. Simple kriging was first performed to develop smoothed 2D interpretations of the subsurface conditioned on the normalized and declustered data and the spatial correlation models. The SGS modeling was then performed to generate several 2D stochastic realizations for each soil zone. The SGS approach steps through each element along a random simulation path and randomly assigns values from Gaussian distributions that honor the kriging estimate and variance at that element; the kriging values are sequentially updated from the data and previously simulated elements. The kriged and simulated models were then back-transformed to the original declustered data distributions via interpolation from data transformation tables produced during the initial *nscore* normalization, and extrapolation at the distribution tails according to a second-order power law (i.e., Deutsch and Journel 1997, Pyrcz et al. 2021).

The variability of the kriged estimates and twenty simulated subsurface realizations (i.e., R1-R20) for B_{sat} and C1-zoned are shown in Fig. 6.6. A 2D depiction of the R1 realization within the full numerical mesh is shown in Fig. 6.6a. The 1D lateral trends and conditioning CPT data for median values along each column of elements are shown in Figs. 6.6b-c. Fig. 6.6b also depicts field and lab VST measurements for comparison. The 1D lateral trends can indicate abrupt inflections at transitions in the row element count (e.g., at x = 130 for kriged B_{sat} soils), however, smoother transitions were observed in the actual 2D models within each soil zone. The scatter between alternate realizations for both datasets is large at locations with sparse data, and small at locations with dense data (i.e., near the graben), as expected. The C1-zoned model enforces discontinuities at the C1a-C1b contacts.

The variability of the kriged estimates and twenty simulated subsurface realizations (i.e., R1-R20) for the alternative assumption with C1-grouped are similarly shown in Fig. 6.7. Under this stationary

assumption, the kriged estimates trend towards a median q_{c1Ncs} = 100 at locations with sparse data. This is especially noticeable at x = 360-500 m (WYN-1 to -14), where a gradual transition in the C1-grouped kriged estimate replaces the discontinuous C1a-C1b contact at x = 460 m for the C1-zoned kriged estimate. Such a gradual transition contrasts with the expected alluvial deposition in this area. However, conditioning to the densely spaced CPT soundings near the observed graben allow the C1-grouped model to naturally capture the abrupt C1a-C1b contact at x = 273 m, while also allowing continuous thin interlayers to gradually extend through this region for some realizations.

6.6. Nonlinear Dynamic Analysis Methodology

6.6.1. Numerical Model

The 2D NDAs for Wynne Avenue were modeled using the finite difference program FLAC 8.1. The 500-m-long numerical mesh (Fig. 6.3) was first initialized for stresses with elastic shear and bulk moduli consistent with V_S and γ_t from Table 6.1, and a coefficient of at-rest earth pressure (K_o) of 0.5. The water table was initialized by setting pore pressures according to the phreatic surface indicated from borehole observations (Fig. 6.2), and a water tensile stress limit of 9.81 kPa to allow negative pore pressures (i.e., approximating the effect of capillary rise) up to 1 m above the phreatic surface. During earthquake shaking, groundwater flow was modeled and the water tensile limit was increased to allow for transient negative pore pressures. The pore pressure boundary conditions were freed (i.e., impermeable) at the sides and bottom of the mesh and fixed (i.e., flow allowed) at the top of the mesh. The input ground motion was applied at the compliant model base as horizontal and vertical stress-time histories. Unit D was set as an elastic material with a small-strain shear modulus reduction ratio of 0.7 during shaking. Rayleigh damping of 0.5% at a frequency of 1 Hz was applied during shaking to limit numerical noise. All models used attached (i.e., periodic) side boundary conditions; sensitivity studies suggested slightly greater boundary effects from absorbing (i.e., free-field) boundaries (e.g., Bassal et al. 2022b). The large-strain mode of FLAC was used for all models.

6.6.2. Calibration of Constitutive Models

The user-defined PM4Sand and PM4Silt constitutive models were calibrated and applied to all soils above unit D during earthquake loading. The calibrations followed similar protocols as previous case studies by the authors (e.g., Bassal and Boulanger 2021, Bassal et al. 2022b). Calibration look-up tables were created for the range of properties required for the stochastic layers. The calibration parameters are listed in Tables 2 and 3 for the baseline model with uniform representative properties (non-stochastic) for the sand-like soils (i.e., A, C1a, C1b, and C2) with PM4Sand and clay-like soils (i.e., B_{unsat}, B_{sat}, C) with PM4Silt. All soils considered a shear modulus coefficient (G_o) computed from V_S and γ_t.

The PM4Sand parameters in Table 6.2 considered an apparent relative density (D_R) as correlated with the representative q_{c1Ncs} per Boulanger and Idriss (2015). The contraction rate parameter (h_{po}) was calibrated such that the cyclic resistance ratio ($CRR_{M7.5}$) per Boulanger and Idriss (2015) for a 50% probability of liquefaction triggering (P_L) at M = 7.5 caused 3% single-amplitude shear strain in 15 uniform cycles of single-element undrained direct simple shear (DSS) loading, confined at vertical effective stresses (σ'_{vc}) representing the mid-point of each soil zone. Secondary parameter C_ε was calibrated such that DSS simulations matched the median rate of post-liquefaction shear strain accumulation as empirically correlated with D_R by Tasiopoulou et al. (2020) for clean sands. The stochastic parametrization of C1a and C1b was obtained from the described q_{c1Ncs} correlations with D_R and G_o, and linear interpolations over generated lookup tables of the h_{po} and C_ε parameters calibrated for 22 q_{c1Ncs} values within a limiting range of 60 to 280 (Table C.1 in Appendix C). An upper limit of $CRR_{M7.5} = 0.8$ for liquefaction triggering was imposed for the calibrations (e.g., Montgomery et al. 2017).

The PM4Silt parameters in Table 6.3 were calibrated for target values of $s_{u,peak,eq}/\sigma'_{vc}$. The undrained shear strength ratio for critical state (i.e., residual) conditions ($s_{u,cs,eq}/\sigma'_{vc}$), an input parameter for PM4Silt, was set equal to $s_{u,peak,eq}/\sigma'_{vc}$ for all $s_{u,peak,eq}/\sigma'_{vc} \geq 0.425$ (i.e., dense of critical state) which produces a sensitivity $S_t = s_{u,peak,eq}/ s_{u,cs,eq} = 1.0$. For loose of critical state conditions, $s_{u,cs,eq}/\sigma'_{vc}$ was set to produce an $S_t = 1.2$ for $s_{u,peak,eq}/\sigma'_{vc} \leq 0.35$ and an S_t that varied linearly between $s_{u,peak,eq}/\sigma'_{vc} = 0.425$ and 0.35. The

bounding surface parameter ($n^{b,wet}$) was adjusted to obtain the target $s_{u,peak,eq}/\sigma'_{vc}$ under single-element simulations of monotonic undrained DSS loading. The shear modulus parameter (h_o) was calibrated using DSS simulations to approximate the empirical shear modulus reduction and damping relationships of Darendeli (2001). The h_{po} was calibrated to approximate reasonable trends of the cyclic stress ratio (CSR) against the number of cycles for a single-amplitude shear strain of 3%. The void ratio (e_o) was estimated from index tests for each soil zone. The stochastic parametrization of B_{sat} was obtained from linear interpolations over generated lookup tables of the $s_{u,cs,eq}/\sigma'_{vc}$, $n^{b,wet}$, and h_{po} parameters calibrated for 14 $s_{u,peak,eq}/\sigma'_{vc}$ values between a range of 0.25 to 1.2 (Table C.2 in Appendix C).

6.6.3. Input Ground Motions

The nearest recorded ground motions for the 1994 Northridge event were obtained from the USC3 ground motion station, located 1.7 km southeast of the Wynne Avenue site. The USC3 station recorded horizontal PGAs of 0.45 and 0.33 g for the south and east oriented components, and a vertical PGA of 0.80 g, as processed by the Pacific Earthquake Engineering Center (Ancheta et al. 2013). The horizontal component motions applied at the base of the NDA models were obtained by first deconvolving the recordings to deep bedrock, and then re-convolving them as outcropping motions at the input depth within unit D. This process was similar to that recommended by Pretell et al. (2019), but did not require use of a seismic source model because the deconvolution was numerically well behaved for this site. The V_S and soil boring descriptions to a depth of 90 m beneath the USC3 site were obtained from Gibbs et al. (1999), and Vs to a depth of 5000 m beneath both the USC3 and Wynne Avenue sites was obtained from a local velocity model (Small et al. 2017). Transfer functions for deconvolution and re-convolution were developed for outcropping motions via equivalent-linear site response using the program Strata (Kottke et al. 2016), with shear modulus and damping behavior of shallow (i.e., < 150 m) clay-like and sand-like soils per Vucetic and Dobry (1991) and EPRI (1993).

Acceleration time histories for the input (outcrop) motions at the base of the Wynne Avenue NDAs are depicted in Fig. 6.8. The baseline NDAs used the vertical and reversed-polarity north-oriented motions,

in congruence with the polarity of the 2D mesh orientation with the x-position increasing from south to north. Acceleration response spectra are also shown for both the input motions and original recordings, depicting some minor differences typically at periods (T) below 1 s. These discrepancies primarily indicate influences from shallow soils at the recording site prior to modification (i.e., de-convolution and re-convolution) for the NDA input depth at Wynne Avenue.

6.7. Dynamic Simulation Results

6.7.1. Baseline Uniform Model

The results of three NDA model groups representing alternate subsurface assumptions are explored: (1) NDA models with uniform representative parameters for each soil zone of the heterogeneous stratigraphic section in Fig. 6.3, (2) stochastic NDA models with SGS fields for critical soil layers B_{sat} and C1-zoned, and (3) stochastic NDA models with SGS fields for critical soil layers B_{sat} and C1-grouped. The uniform NDA models were evaluated for alternative parametric assumptions, ground motions, and calibration protocols. Results for the baseline uniform NDA model with median representative soil properties and calibrated model inputs from Tables 1-3, and modified USC3-North and USC3-Vertical ground motions are first presented.

The resulting dynamic response contours of the maximum shear strain (γ_{max}), final excess pore pressure ratio (r_u), final horizontal displacement (Δx), and final vertical displacement (Δy) for a central section of the baseline uniform NDA (i.e., at x = 205–355 m, encompassing the observed graben at about x = 277–293 m) immediately after shaking are presented in Figs. 6.9a-d. The γ_{max}, representing the maximum engineering shear strain for the principle stress orientation during shaking (Fig. 6.9a), reached > 30% along the base of the zone C1a interbedded silts and sands, and was near 12% within the overlying portion of C1a and at the base of the B_{sat} clays. These strains were primarily associated with liquefaction-induced yielding of C1a, as indicated by $r_u \approx 100\%$ initiated at 5 s into shaking, as well as cyclic softening-induced yielding initiated at 7.5 s in B_{sat}. The r_u contours (Fig. 6.9b) also indicate a thin 1–2 m thick zone of liquefaction in the portion of the C2 sands directly below the observed graben, which initiated at 9 s into shaking, as well

as some flow-induced liquefaction caused by the gradual diffusion of excess pore pressures from C1a extending 7 m into the southern end of C1b.

The γ_{max} contours (Fig. 6.9a) ultimately indicate two complementary slip surfaces breaching the ground surface at the upslope end of the overall slide mass. The base of the slide mass corresponds to a slip surface that extends along the base of C1a, terminating at the northern contact between C1a and C1b near x =280m. At that C1a-C1b contact, the slide mass movement produces complementary upslope- and downslope-dipping slip surfaces that propagate to the ground surface. The overall slide mass displaces up to 36.4 cm downslope as depicted by the Δx contours (Fig. 6.9c). The complementary slip surfaces at the upslope end of the slide mass bound a 10- to 15-m-wide extensional graben feature depicted by downward Δy displacements of up to 13.8 cm (Fig. 6.9d). The modeled graben closely matches the 10–20 cm vertical offsets and 12 m feature width measured in the field, but is shifted 10 m to the south.

The resulting Δx and Δy ground displacements and horizontal strains (ε_x) along the ground surface for the baseline uniform NDA model are plotted in Figs. 6.10a-c. Results are plotted for x = 50–450 m; the ends of the model were slightly influenced by the boundary conditions and are not shown herein. The extensional graben is predicted at x = 266–280 m as indicated by a steep reduction in Δx (Fig. 6.10a), a large localized dip in Δy (Fig. 6.10b), and two bounding extensional peaks of ε_x at 2.0% and 3.1% (Fig. 6.10c). The toe of the downslope sliding mass coincides with the southern boundary of C1a near x = 180–200 m, with a vertical bulge of up to Δy = 7.5 cm and a peak compressive ε_x of 1.7%.

The effects of porewater diffusion and reduced post-earthquake shear strengths for the clay-like soils were monitored in analyses that allowed for full dissipation of excess pore pressures. These effects increased the peak Δy at the graben by no more than 2 cm, as reconsolidation settlements typically occurred over a broad area above liquefied portions of C1a and C2. In general, the strains and displacements did not change significantly with time after shaking as pore pressures dissipated, and thus all subsequent results are compared at the end of shaking.

6.7.2. Effect of Spatial Variability with C1-zoned

The ground deformations predicted by NDAs with kriged fields and twenty stochastic SGS fields for both critical layers B_{sat} and C1-zoned (as represented in Fig. 6.6) are depicted in Figs. 6.10a-c. The soil parameterization and input earthquake motions were identical to the baseline uniform NDA, with the exception of modeling the variability within these two layers. The predicted deformations for the kriged model follow similar trends as the baseline uniform model with a similar peak downslope Δx = 37.7 cm above C1a (Fig. 6.10a). However, the Δx displacements are slightly more gradual near the observed graben, resulting in shallower vertical downward offsets of up to Δy = 9.2 cm (Fig. 6.10b), and lower extensional strains of ε_x = 1.0% and 2.1% at x = 263 and 276 m (Fig. 6.10c). The R1-R20 stochastic realizations match the overall trends in Δx, Δy, and ε_x for the kriged model, but have higher spatial fluctuations (i.e., less smooth) and show minor scatter about the peak values. The peak Δx for R1–R20 range is 34.9–45.0 cm with a median of 37.3 cm (Fig. 6.10a), and the peak Δy range is 7.9–12.6 cm with a median of 9.3 cm (Fig. 6.10b). The 20th percentile of peak Δx from the stochastic realizations is consistent with the baseline uniform model, however, the peak Δy from all stochastic realizations is below the baseline uniform model prediction. Furthermore, the grabens predicted from the kriged and stochastic models slightly under-predict the field measured vertical offsets, over-predict the measured graben width, and are centered >15 m to the south of the observed graben.

The general behavior of the stochastic NDAs (with variability in both B_{sat} and C1-zoned) is exemplified by the response contours for the R1 model depicted in Figs. 6.11a-d. Similar to the baseline uniform model, the γ_{max} exceeded 30% along the base of zone C1a (Fig. 6.11a). However, the continuous pocket of soft clays ($s_{u,peak,eq}$ < 0.30) within the overlying B_{sat} for x = 210–300 m (e.g., Fig. 6.6a) also sustained a shear zone with γ_{max} > 30%, and various continuous thin interlayers within zone C1b (e.g., siltier soils at the top of C1b for x = 300–330 m) promoted liquefaction ($r_u \approx$ 100% in Fig. 6.11b) and yielded with γ_{max} up to 5%. As in the baseline uniform model, a slip surface breaches the surface above the C1a-C1b contact and bounds a large south-trending sliding mass with Δx > 35 cm (Fig. 6.11c). The Δy displacements

(Fig. 6.11d) indicate a graben feature that is wider than the baseline uniform model, facilitated by the wider distribution of straining within weaker pockets and interlayers of B_{sat} and C1b.

The relative influence of modeling kriged and stochastic SGS fields for only B_{sat} and only C1-zoned are shown in the ground deformation plots of Figs. C.1 and C.2 in Appendix C, and the peak values are included in Table 6.4. For the R1–R10 models with variability in only B_{sat}, the peak Δx range is 34.9–41.6 cm, and the peak Δy range is 8.5–12.4 cm. For the R1–R10 models with variability in only C1-zoned, the peak Δx range is 38.3–44.8 cm, and the peak Δy range is 10.6–13.0 cm. The deformation trends in NDA models with variability in B_{sat} only or variability in C1-zoned only are generally similar to those obtained with variability for both layers, although the spatial pattern and magnitude of shear strains show some differences, as expected.

6.7.3. Effect of Spatial Variability with C1-grouped

The ground deformations predicted by NDAs with kriged fields and twenty stochastic SGS fields for both B_{sat} (as represented in Fig. 6.6) and C1-grouped (as represented in Fig. 6.7) are depicted in Figs. 6.12a-c. Recall that the C1-grouped stochastic models assume the entirety of unit C1 (i.e., inclusive of C1a and C1b soils) has a stationary parameter distribution and spatial correlation. Even though the kriged and R1–R20 stochastic realizations retain the sharp interface at the expected C1a-C1b contact near x = 273 m, the results are noticeably different than Fig. 6.10. Just downslope of x = 273 m, the peak Δx for R1–R20 (Fig. 6.12a) slightly exceeds the baseline uniform model, ranging between 31.1–44.6 cm with a median of 40.3 cm. At x = 273–330 m, Δx reduces with minima of 15–35 cm. Upslope of x = 330 m, all realizations tend to regain large and highly variable Δx displacements of 20–55 cm. The Δy displacements (Fig. 6.12b) suggest a spread of minor local settlement features at x = 260–300 m, with peak Δy ranging between 3.3–8.0 cm with a median of 5.3 cm, under-predicting the field measured vertical offsets. The median peak ε_x (Fig. 6.12c) associated with these Δy peaks is 0.9%, well-below the values for the baseline uniform model.

Example dynamic response contours for the R1 model (with variability in both B_{sat} and C1-grouped) are shown in Figs. 6.13a-d. The γ_{max} contours (Fig. 6.13a) are similar to the stochastic models

with C1-zoned (e.g., Fig. 6.11a) for x < 260 m. However, there are continuous strain paths with γ_{max} > 30% within the C1b region, associated with liquefaction (Fig. 6.11b) within extensive weak interlayers (i.e., q_{c1Ncs} < 100 as depicted in Fig. 6.7a). The liquefaction-induced strains in the C1a region are thus provided with a weaker path to laterally connect with and shear through B_{sat} and C1b, rather than propagate to the ground surface. This caused gradual Δx displacements (Fig. 6.11c) and subtle Δy displacements (Fig. 6.11d), that suppressed formation of a graben near the C1a-C1b contact.

The relative influence of modeling kriged and stochastic SGS fields for only C1-grouped (with uniform soil zones modeled elsewhere) is shown in the ground deformation plots of Fig. C.3 in Appendix C, and the peak values are included in Table 6.4. For the R1–R10 models with variability in only C1-grouped, the peak Δx range is 36.1–43.9 cm, and the peak Δy range is 3.4–6.9 cm. These deformation trends are generally similar to those of Fig. 6.12. This is expected due to the larger strains in liquefied interlayers within the C1b region of C1-grouped than in B_{sat} as observed in Fig. 6.13a. The time history responses of three monitored soil interface points are compared between the baseline uniform and the R1 model (with variability in both B_{sat} and C1-grouped) in Fig. C.4 in Appendix C.

6.7.4. Effect of Parametric Variations with Uniform NDA Models

The Δx ground displacements for uniform NDA models with alternative parametric assumptions, ground motions, and calibration protocols relative to the baseline uniform model are shown in Figs. 6.14a-d. Fig.14a depicts alternative ground motion considerations for the Northridge event as obtained from the USC3 recording station. The recorded USC3-North motion results in a slightly greater peak Δx, about 5 cm greater than for the modified USC3-North (i.e., baseline) motion. This suggests that while modification (i.e., de-convolution and re-convolution) of this ground motion was necessary to represent conditions at the site, the overall influence of modification for the site deformations was relatively minor. The modified USC3-South motion (i.e., reverse polarity from USC3-North) increased the peak Δx by 10 cm, and the modified USC3-West motion decreased the peak Δx by 11 cm. Removal of the vertical motion reduced the

peak Δx by less than 2 cm. Regardless of differences in Δx, all ground motions considered herein suggest the formation of a graben with peak $\Delta y \geq 10$ cm.

Fig. 6.14b depicts alternate soil modeling choices and calibration protocols for unit C1. Moving the northern end of zone C1b from x = 460 to 360 m continued to provide sufficient buffer to prevent strains across the model, such that Δx displacements near the graben were unchanged. A trial with the default post-liquefaction shear strain accumulation rate of PM4Sand (i.e., without re-calibrating to the empirical regression of Tasiopoulou et al. 2020), lowered shear deformations for loose-of-critical-state soils. The peak Δx above zone C1a (i.e., south of the graben) was consequently reduced by about 11 cm. The FC correlation of Boulanger and Idriss (2015) with a generic FC correction (C_{FC}) of 0 reduced the q_{c1Ncs} of both C1a and C1b, which increased Δx by up to 7 cm above most of unit C1 at x > 200 m. Finally, calibrating C1a and C1b to a $CRR_{M7.5}$ based on P_L=16%, as recommended by Boulanger and Idriss (2015) for deterministic analyses, increased Δx by up to 5 cm south and 11 cm north of the graben. All of these modeling choices suggest the formation of a graben with peak $\Delta y \geq 8$ cm.

Figs. 6.14c-d depict the impact of alternate representative percentile values [i.e., 16th, 33rd, 50th (baseline), 67th, 84th] of $s_{u,peak,eq}$ for B_{sat} and q_{c1Ncs} for C1a and C1b. For different $s_{u,peak,eq}$ percentiles in B_{sat}, the peak Δx response south of the expected graben reached an upper limit of 39 cm for the 50th percentile or greater. North of the expected graben, Δx was less than 5 cm for all but the 16th percentile $s_{u,peak,eq}$, for which larger shear strains in B_{sat} occurred and prevented graben formation. For different q_{c1Ncs} percentiles in C1a and C1b, the peak Δx response south of the graben reached a lower limit of 33 cm for the 67th percentile or greater, and increased to over 50 cm for lower percentiles. Zone C1b is expected to develop liquefaction for 33rd percentile q_{c1Ncs} or smaller, which also suppressed formation of a graben. While lower representative percentiles were conservative in the sense of increasing overall displacements, they under-predicted the graben deformation, as might be expected for such complex mechanisms affected by system interactions of layered soils (e.g., Cubrinovski et al. 2019, Montgomery and Boulanger 2016).

Other sensitivity studies that assumed no C2 sand lens, a flat unit D upper boundary surface, and a constant permeability within C1a and C1b, had negligible effects on the ground deformations.

6.8. Performance of Simplified Evaluations

6.8.1. Liquefaction Vulnerability Indices

Simplified analyses using 1D liquefaction vulnerability indices (LVIs) and Newmark sliding-block analyses were performed at Wynne Avenue for comparison with the NDA analyses. The LVIs considered herein provided a depth-weighted integration of liquefaction factors of safety [obtained from the stress-based analyses of Boulanger and Idriss (2015) with fines content corrections per Bassal et al. (2022a)] or strains [obtained from correlations by Idriss and Boulanger (2008)] along the inverse filtered CPT soundings. Four LVIs were evaluated: (1) liquefaction potential index (LPI) (Iwasaki 1978), (2) Ishihara-inspired index (LPI_{ISH}) (Maurer et al. 2015), (3) post-liquefaction reconsolidation settlement (S_{v-1D}) (Zhang et al. 2002), and (4) lateral displacement index (LDI) (Zhang et al. 2004). The LDI was additionally adjusted to estimate the lateral displacement (LD), including the influence of the sloping ground with a grade of about 1.75% (or 1°) (Zhang et al. 2004). Site CPTs were binned into two groups representing the lateral variation of liquefaction susceptible soils encountered in zone C1a to the left of the graben (i.e., WYN-6 to -10), and in zone C1b beneath and to the right of the graben (i.e., WYN-1 to -5, and -11). A horizontal PGA of 0.51 g was used (e.g., Holzer et al. 1999).

A summary of the mean, range, and liquefaction manifestation severity categories (McLaughlin 2017) for the 1D LVIs and LD within each CPT group are presented in Table 6.5. The LPIs for three of the CPTs at zone C1a predict "moderate" liquefaction severity (LPI > 8), whereas all CPTs at C1b predict "none to marginal" severity (LPI ≤ 8). However, the index values are generally similar (i.e., just above and below the LPI = 8 prediction threshold), due to the increased contribution of liquefaction severity from unit C2 for several of the CPTs pushed through C1b. The LPI_{ISH} values predict "none to marginal" severity and are well below the LPI_{ISH} = 5 threshold for "moderate" severity, when considering a thick 6 to 8 m non-liquefiable crust across the site. The S_{v-1D} predicts generally consistent reconsolidation settlements across

the site of < 7 cm, which is reasonable given this index does not account for vertical displacements caused by lateral movement or graben formation. The LDs (which are about twice the LDIs) predict significant displacements across the entire site with an average of 137 cm for CPTs at C1a, and 95 cm for CPTs at C1b. While the overall magnitude of the LDs is much higher than observed, the difference of 42 cm between the two adjacent groups of CPTs aligns with the expectation of extensional strains capable of producing the observed graben.

6.8.2. Newmark Sliding-Block Analyses

Newmark sliding-block analyses were performed with time history integration for an assumed rigid sliding-block (Newmark 1965), and with the seismic slope displacement regression model for shallow crustal earthquakes by Bray and Macedo (2019). The sliding mass yield acceleration coefficient (k_y) was determined from a simplified model for lurch block movement, as used by O'Rourke (1998) for evaluating the nearby Malden Street case study that similarly experienced an extensional graben deformation in the Northridge earthquake. The model as used herein considers a block with a constant slope of 1°, sliding over a 100 m extent of liquefied zone C1a (at a depth of 7 m). Active and passive lateral earth pressures under Rankine conditions were assumed at the ends of the block as 0.3 and 3.3, respectively. A uniform liquefied residual shear strength ratio of 0.092 was estimated from Idriss and Boulanger (2008) for a median overburden-corrected cone tip resistance (q_{c1N}) of 40, FC = 45%, and the expectation of void redistribution (due to overlying low permeability unit B). The evaluation indicated a k_y of 0.18 in the downslope (south) direction. The south-trending USC3 surface ground motion recording was used for both sliding-block evaluations.

The rigid sliding-block analyses were performed using the time history integration scheme implemented in the open-source program SLAMMER (Jibson et al. 2013). Upslope movement was considered with an assumed thrust angle of 1°. This resulted in downslope movements of 13.3 cm for the input motion, and 2.4 cm for the inversed motion (i.e., reversed polarity). The Bray and Macedo (2019) regression model, which allowed for consideration of a flexible sliding mass with an estimated pre-shaking

period of 0.20 s, predicted downslope displacements in the 16th to 84th percentile range of 4.5 to 19 cm. The sliding-block models predicted lateral displacements well-below the estimates from the baseline uniform NDA, but still within a reasonable magnitude of the observed offsets at the graben. Both the sliding-block analyses and NDAs depended on detailed site characteristics, such as the extents and behavior of critical strata. However, the sliding-blocks were unable to detect the complex failure mechanism and consequent graben deformation due to their inability of modeling the time-dependency of liquefaction and cyclic softening behavior, dynamic interactions of interlayered deposits, and the distribution of strains throughout the weak liquefied layer (e.g., Makdisi and Kramer 2019), among other limitations.

6.9. Discussion

6.9.1. Insights on Deformation Mechanisms

The system-level NDAs provide insights regarding the graben formation mechanism at Wynne Avenue that are otherwise inconclusive from the LVIs, Newmark sliding-block analyses, and other simplified evaluations (e.g., Holzer et al. 1999). During shaking, cyclic shear strains within liquefiable C1a soils, confined by laterally adjacent non-yielding materials (i.e., unit C clays and C1b dense sands), contributed to transient ground oscillations (e.g., Youd and Keefer 1994, Pease and O'Rourke 1997). The shallow site slope simultaneously allowed permanent ground lurch of the soil block above C1a. Shear and extensional strains were sufficient to breach the ground surface above the abrupt C1a-C1b contact, including formation of the secondary slip surface bounding the graben feature. Permanent ground lurch was also evaluated by O'Rourke (1998) as a cause of the graben at the nearby Malden Street site, except that failure occurred over a soft clay deposit rather than a confined liquefiable deposit. The high lateral extensional and compressive strains predicted in the current analyses concur with the high concentration of nearby pipe repairs following the earthquake.

The predicted failure mechanism is in agreement with the observations of Holzer et al. (1999), specifically regarding the importance of the C1a-C1b contact. However, it appears unlikely that the greater thickness of liquefaction susceptible C1b and C2 soils immediately beneath the observed graben had as

large of an impact as hypothesized by Holzer et al. (1999). The NDAs suggest liquefaction was not widespread and did not cause significant straining in C1b and C2, despite explicit modeling of excess pore pressure diffusion during and after shaking. On the contrary, the localized failure depended on the overall integrity of C1b to resist excessive straining.

6.9.2. Comparisons of Alternate Evaluations

The baseline and parametric variations of the uniform NDA models accurately predicted the observed graben deformation at Wynne Avenue. This was especially the case when representative values between the 33rd to 67th percentiles were used for each soil zone (e.g., Montgomery and Boulanger 2016). Considerations of alternative ground motions, as well as all other reasonable soil modeling and calibration protocols were capable of predicting a graben despite variations in the displacement magnitudes. The basic assumption of stratigraphic heterogeneity within the NDA models was sufficient for this site.

The stochastic NDA models more accurately honored the available data, but the accuracy of the predicted deformation patterns depended on the approach for generating the stochastic realizations. The modeled soil variability within B_{sat} typically had a minor influence on the overall strain pattern interactions. The stochastic NDAs with the C1-zoned assumption, which modeled abrupt transitions at inferred locations within unit C1 similar to the uniform NDAs, slightly under-predicted the observed deformations. The stochastic NDAs with the C1-grouped assumption, which allowed the SGS fields to honor the site data for the entirety of unit C1 under a second-order stationary assumption (e.g., Deutsch and Journel 1997), produced unreasonable predictions. Liquefaction-induced strains within interconnected thin layers of unit C1 typically caused more gradual ground deformations and suppressed graben formation by allowing shear strains to pass laterally across the subsurface rather than breach the surface. The true strain behavior of such variable deposits depends on the spatial variability of the soil characteristics, connectivity of liquefiable interlayers, ground motion characteristics, and other system-level interactions (e.g., Munter et al. 2016). Even with the unusually dense conditioning CPT data at this site, the SGS fields were insufficient to capture

all pertinent details. An understanding of geologic depositional processes specific to this site was necessary to constrain the complex soil variability and associated strain patterns.

An animation sequence comparing the development of shear strain patterns in time during shaking for the baseline uniform NDA, the stochastic NDA for R1 of B_{sat} and C1-zoned, and the stochastic NDA for R1 of B_{sat} and C1-grouped will be provided with the online journal publication for this work, showcasing the distinct responses for each subsurface interpretation.

6.9.3. Challenges for Stochastic NDAs

Fine-scale subsurface variability and details, such as thinly interbedded layers, can alter the composite response of a soil mass to earthquake loading (e.g., Beyzaei et al. 2019) and are challenging to quantify due to limitations in site characterization, stochastic modeling, and NDA modeling methods. The CPTs were unable to directly measure and detect thin layers and interface transitions, especially with the 10 cm measurement interval at Wynne Avenue, and so an inverse filtering approach (Boulanger and DeJong 2018) was used to approximate this behavior. This data was then smoothed for input in a coarser mesh with element thicknesses $\geq$ 25 cm. These simplifications cannot explicitly capture finer scale details. Also, the CPT data near the observed graben for this case study was more abundant than what might be available for typical forward designs of other linear geosystems. This helped locate subsurface features that were important for modeling the graben deformation, but may not have been apparent otherwise. This suggests the importance of a site characterization framework that considers the local geology, hypothesized failure mechanisms, and an iterative site investigation and modeling approach (e.g., DeJong et al. 2020).

Subsurface modeling depends on several choices that include the scale of interest (i.e., stratigraphic heterogeneity, lithological heterogeneity, inherent soil variability), the delineation of discontinuous layer boundaries, the grouping of similar materials, the spatial correlation and simulation methods, and the consideration of nonstationary trends. The inability of explicitly quantifying the uncertainty of these epistemic modeling choices is one of the challenges posed by Phoon et al. (2022) for data-driven site

characterization. The divergent responses obtained in this study for different subsurface modeling choices specifically reflects the necessity of augmenting site data with geological insights.

The 2D NDAs could not explicitly capture some fine-scale processes, including cracks and sand boil formations, transient permeability fluctuations, and post-liquefaction sedimentation. Additionally, the 2D plane-strain assumption can typically overestimate the straining behavior within thin yielding layers, depending on their connectivity and extents in the out-of-plane direction (i.e., the out-of-plane direction assumes no variability). All predicted grabens were centered about 10 to 15 m from the observed graben, which may be attributable to the obliquity of the failure relative to the roadway (Figure 2) and potential three-dimensional (3D) subsurface variations that were not measured or modeled.

6.10. Conclusion

This study examined the seismic response of Wynne Avenue in the 1994 Northridge earthquake using 2D NDAs with geostatistical subsurface modeling to identify the critical mechanisms that prompted a 12-m wide graben deformation with 10-20 cm vertical offsets, and assess the utility of such advanced methods for engineering evaluations of similar, moderate localized ground deformations.

Stratigraphic heterogeneity was delineated from the CPT data, with the additional enforcement of zoning a critical liquefiable unit with discontinuous lithological boundaries, as expected for a distal alluvial fan environment at Wynne Avenue. The NDAs that considered this stratigraphy with uniform representative properties for distinct soil units most closely modeled the observed graben. Furthermore, the graben was detected for several reasonable alternative parametric assumptions, ground motions, and calibration protocols. These uniform NDAs were better at predicting the expected lateral ground displacements near the graben than common 1D LVIs and Newmark sliding-block analyses, and also clarified the complex failure mechanisms associated with ground oscillations and permanent ground lurching.

Inherent soil variability was additionally considered by incorporating kriging and SGS fields within the liquefiable unit and the overlying saturated clays. Stochastic NDAs that retained discontinuous zones within the liquefiable unit slightly under-predicted the observed graben, and stochastic NDAs without

zoning of the liquefiable unit greatly under-predicted the observed graben. This suggests that a geologically-informed representation of stratigraphic (and lithological) heterogeneity was a necessary prerequisite for the stochastic modeling of inherent soil variability. Also, limitations in the site characterization, stochastic modeling, and NDA modeling methods may have obscured any expected improvements from detailed refinements associated with inherent variability. Ultimately, the choices for modeling subsurface stratigraphic (and lithological) details mattered more than modeling inherent variability within stratigraphic units for this case history.

The results of this case study contribute to validation of the NDA modeling procedures employed herein, recognizing that good agreement for any one case history can involve compensating errors and poor agreement can involve an accumulation of errors. The results also illustrate how the combination of uniform and stochastic NDA modeling provided a basis for querying alternative hypotheses or scenarios, which may be particularly valuable for quantifying modeling uncertainty for other sites and applications.

6.11. Data Availability

Some of the data, models, or code used during the study were provided by third parties. The CPT data was obtained from the United States Geological Survey (USGS 2021) and the borings, field VSTs, and laboratory index test data was obtained from Bennett et al. (1998). Ground motions were obtained from the PEER NGA-West2 Ground Motion Database (Ancheta et al. 2013). Direct requests for software can be made to the providers indicated in the references. Many of the codes and general workflows that support the findings of this study have been made publically available by the authors and can be accessed at the DesignSafe Data Depot (Bassal 2022; https://doi.org/10.17603/ds2-nne2-2s11).

6.12. Acknowledgements

The authors appreciate the financial support of the National Science Foundation (award CMMI-1635398) and California Department of Water Resources (contract 4600009751) for different aspects of the work presented herein. Any opinions, findings, conclusions, or recommendations expressed herein are those of the authors and do not necessarily represent the views of these organizations. The authors

appreciate discussions with Thomas L. Holzer regarding the post-earthquake observations, the updated subsurface characterization, and interpretations of this case history. The authors also benefited from discussions with Katerina Ziotopoulou, Jason T. DeJong, and Renmin Pretell. The authors thank Craig Davis and Jianping Hu for sharing post-earthquake pipeline repair data and details. The data procurement and initial analyses of this case study are attributed to early efforts by Thomas L. Holzer, Michael J. Bennett, Daniel J. Ponti, and John C. Tinsley III.

Tables

Table 6.1. Representative soil properties for distinct soil units at Wynne Avenue.

Unit/Zone	γ_t (kN/m^3)	k_v (m/s)	k_h/k_v	q_{c1Ncs}	$s_{u,peak,eq}/\sigma'_{vc}$	V_S (m/s)
A	18	1 x 10^{-6}	2	88	-	120
B_{unsat}	18	1 x 10^{-8}	10	-	0.54	127
B_{sat}	19	1 x 10^{-8}	10	-	0.37	142
C1a	19	1 x 10^{-6}	2	92	-	171
C1b	19	3 x 10^{-5}	2	135	-	185
C2	19	3 x 10^{-7}	2	130	-	197
C	19	1 x 10^{-8}	10	-	0.83	180
D	20	3 x 10^{-7}	2	-	-	320

Table 6.2. PM4Sand constitutive model inputs for baseline uniform NDA soil units.

Unit/Zone	σ'_{vc} (kPa)	D_R	G_o	$CRR_{M7.5}$	h_{po}	C_ε
A	23	0.50	705	0.166	0.60	3.5
C1a	102	0.51	680	0.156	0.94	32
C1b	102	0.68	796	0.261	0.96	0.33
C2	134	0.67	784	0.232	0.84	0.50

Note: Default values per Boulanger & Ziotopoulou (2017) are used for all unlisted secondary parameters.

Table 6.3. PM4Silt constitutive model inputs for baseline uniform NDA soil units.

Unit/Zone	$s_{u,cs,eq}/\sigma'_{vc}$	G_o	h_{po}	h_o	e_o	$n^{b,wet}$
B_{unsat}	0.54	597	120	0.5	0.83	-
B_{sat}	0.33	592	55	0.5	0.77	0.41
C	0.83	646	120	0.9	0.83	-

Note: Default values per Boulanger & Ziotopoulou (2018) are used for all unlisted secondary parameters.

Table 6.4. Summary of results near the observed graben for the stochastic NDAs.

NDA case set	Number of realizations	Median (range) peak $\|\Delta x\|$ (cm)	Median (range) peak $\|\Delta y\|$ (cm)	Median (range) peak extensional ε_x (%)
Baseline uniform	1	36.4	13.8	3.1
Stochastic B_{sat} & C1-zoned	20	37.3 (34.9–45.0)	9.3 (7.9–12.6)	2.0 (1.5–2.7)
Stochastic B_{sat} only	10	37.2 (34.9–41.6)	9.1 (8.5–12.4)	2.0 (1.4–2.5)
Stochastic C1-zoned only	10	42.1 (38.3–44.8)	12.1 (10.6–13.0)	3.0 (2.1–3.6)
Stochastic B_{sat} & C1-grouped	20	40.3 (31.1–44.6)	5.3 (3.3–8.0)	0.9 (0.4–2.0)
Stochastic C1-grouped only	10	40.3 (36.1–43.9)	4.5 (3.4–6.9)	0.7 (0.4–1.4)

Note: Results are for peak absolute values near the observed graben as determined between x = 220 and 320 m. The peak Δx is directed downslope, and the peak Δy is a downward settlement for all cases.

Table 6.5. Summary of 1D LVI and LD results for two groups of CPTs near the graben deformation.

CPT group	Value	LPI	LPI_{ISH}	S_{v-1D} (cm)	LDI (cm)	LD (cm)
At C1a	Range	4.4–9.3	1.4–3.6	3.2–6.7	42–94	81–183
(WYN-6 to 10)	Mean	7.7	2.8	5.1	70	137
	Category[a]	None to Moderate	None to Marginal	-	-	-
At C1b	Range	3.9–6.2	0.2–2.1	3.5–4.3	36–59	70–115
(WYN-1 to -5, -11)	Mean	5.1	1.6	3.8	49	95
	Category[a]	None to Marginal	None to Marginal	-	-	-

[a] Predicted damage category for LVI ranges based on thresholds presented by McLaughlin (2017).

Figures

Figure 6.1. Ground cracks and extensional graben deformation along Wynne Avenue, one year after the Northridge earthquake (photograph taken on January 19, 1995 by T. L. Holzer).

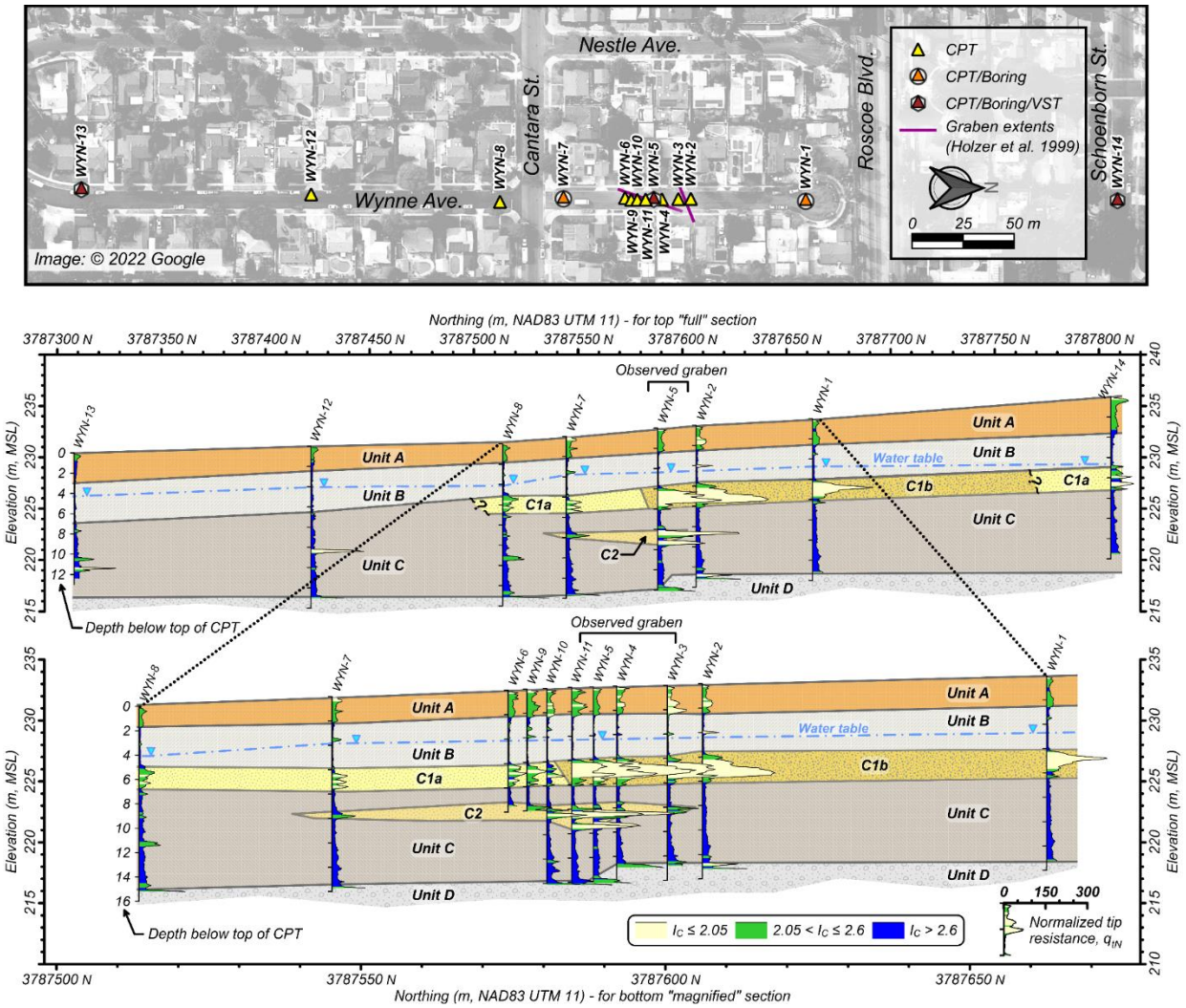

Figure 6.2. (a) Map of Wynne Avenue with site investigation locations and graben extents along roadway as demarcated from ground cracks (Image © 2022 Google); and interpreted subsurface cross section with CPT soundings for (b) the full length of the study site; and (c) a magnified section near the graben. Site investigation locations, graben extents, and general figure organization are adapted from Holzer et al. (1999).

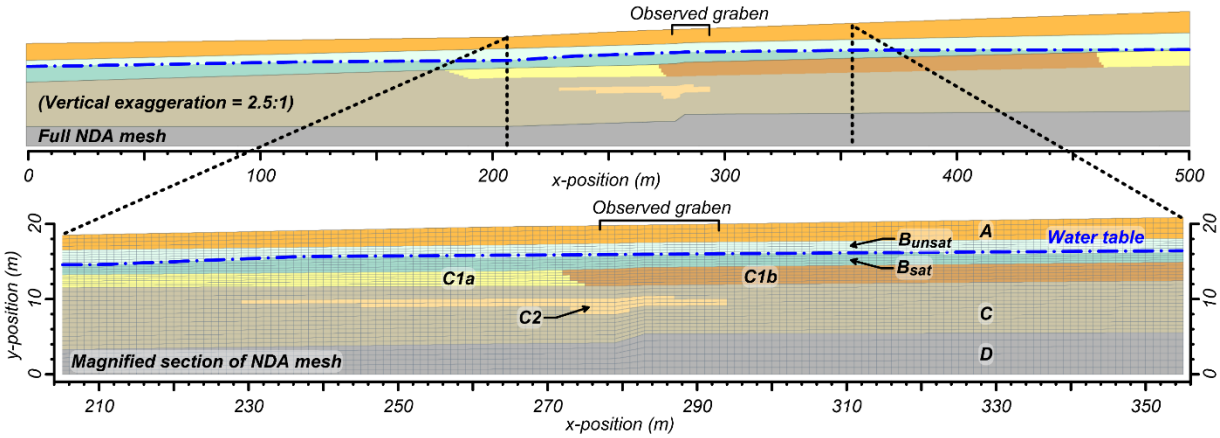

Figure 6.3. Mesh for subsurface and NDA modeling for (a) the full length of the study site; and (b) a magnified section near the graben.

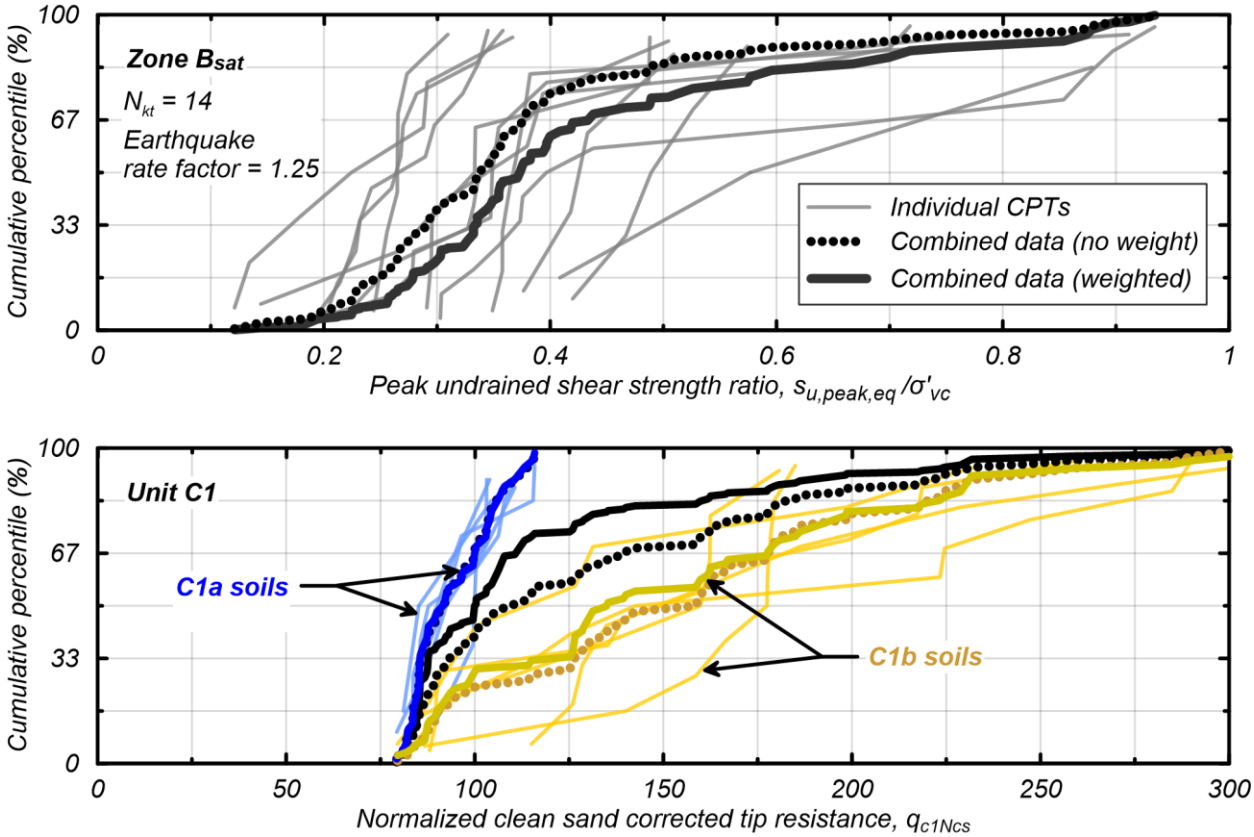

Figure 6.4. Empirical cumulative distributions of (a) the peak undrained shear strength ratio for the B_{sat} soil zone; and (b) the normalized clean sand corrected tip resistance for unit C1 with divisions for the C1a and C1b soil zones. Distributions are shown for data from individual CPTs, combined over all CPTs, and combined over all CPTs with spatial decluster-weighting.

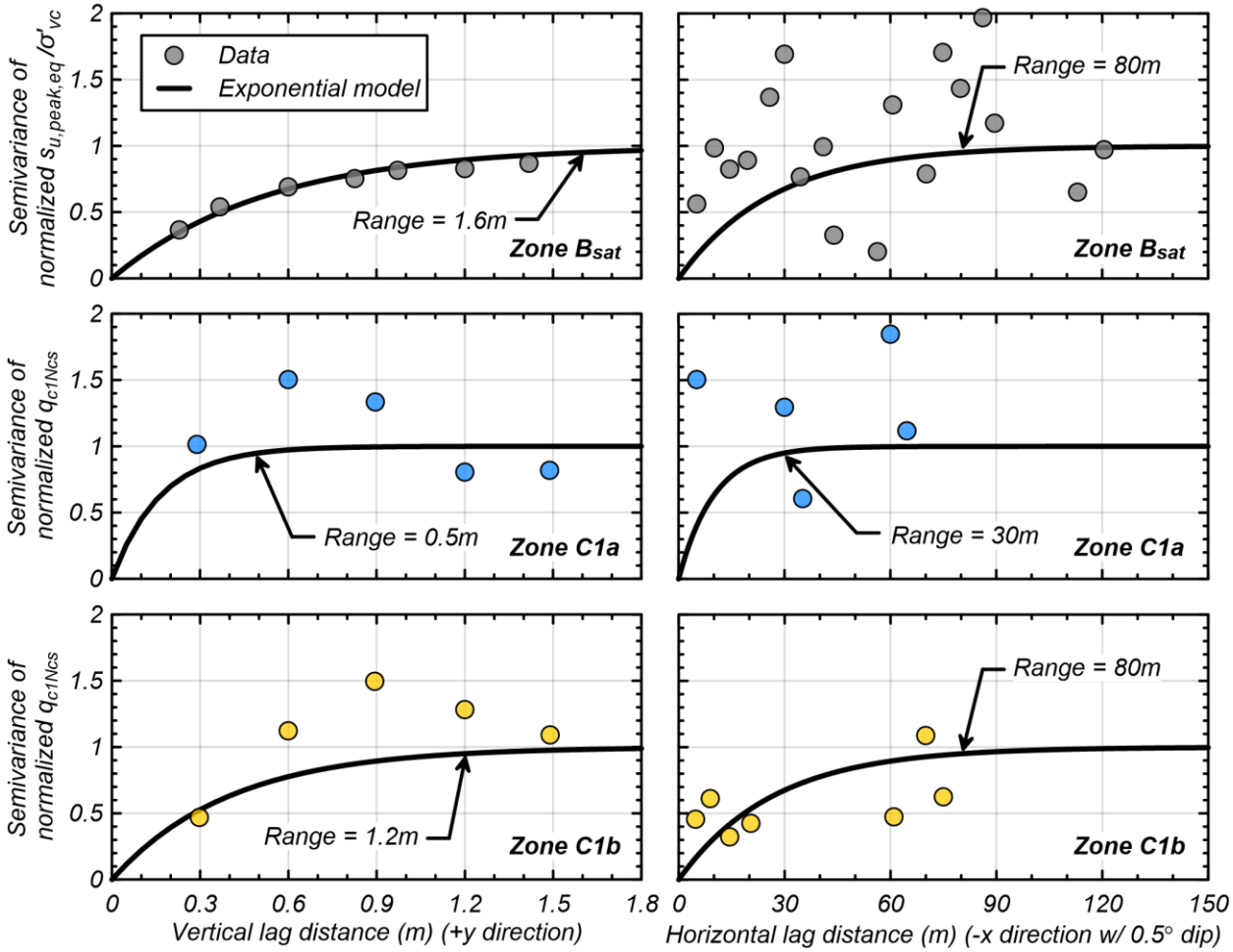

Figure 6.5. Calculated variogram data and approximated exponential variogram models for soil zones B_{sat}, C1a, and C1b in the vertical and lateral directions.

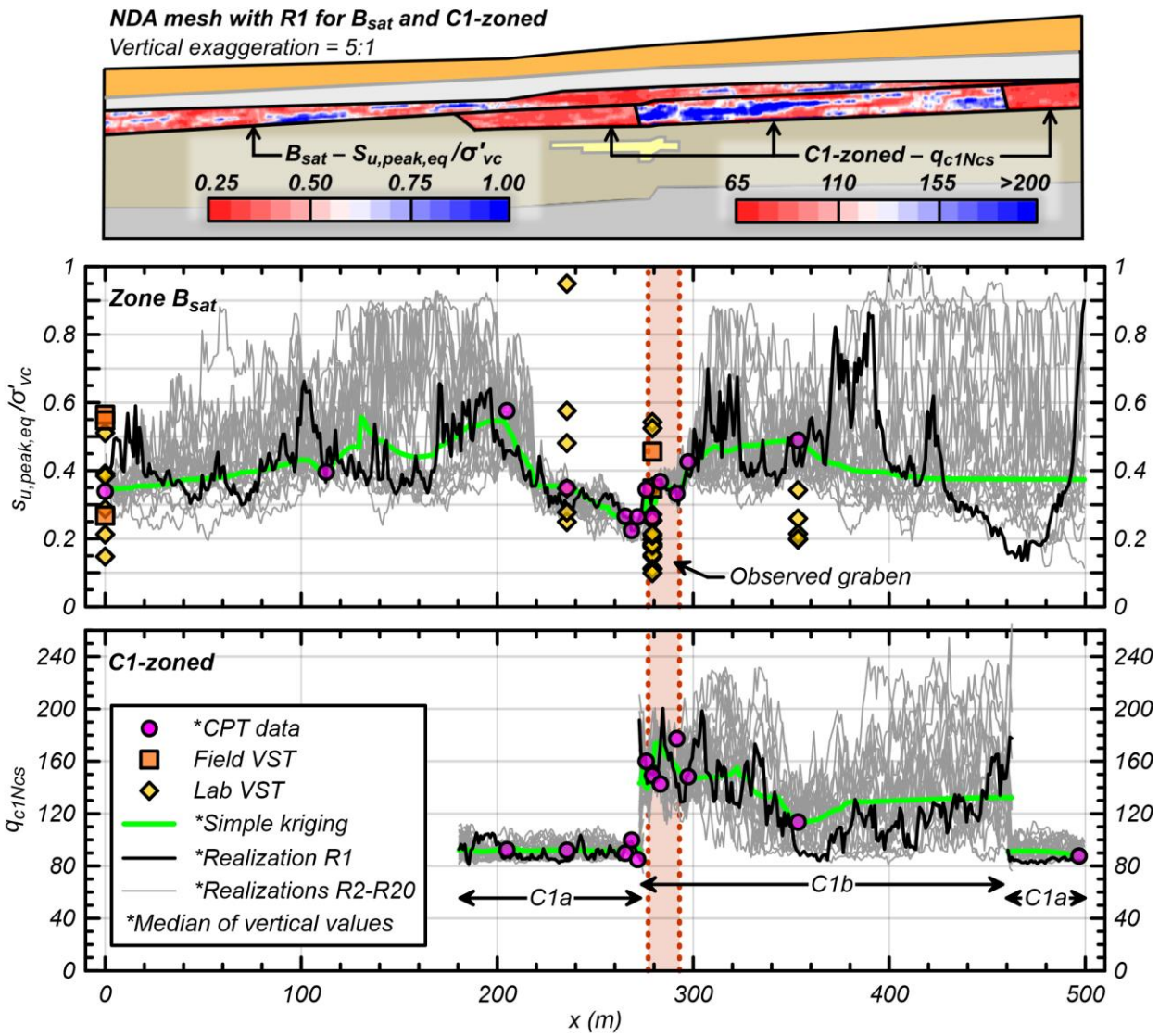

Figure 6.6. (a) Full NDA mesh with stochastic realization R1 for soil zones B_{sat} and C1-zoned; and site data and lateral trends for kriged estimates and twenty simulated subsurface realizations for (b) zone B_{sat}; and (c) unit C1-zoned.

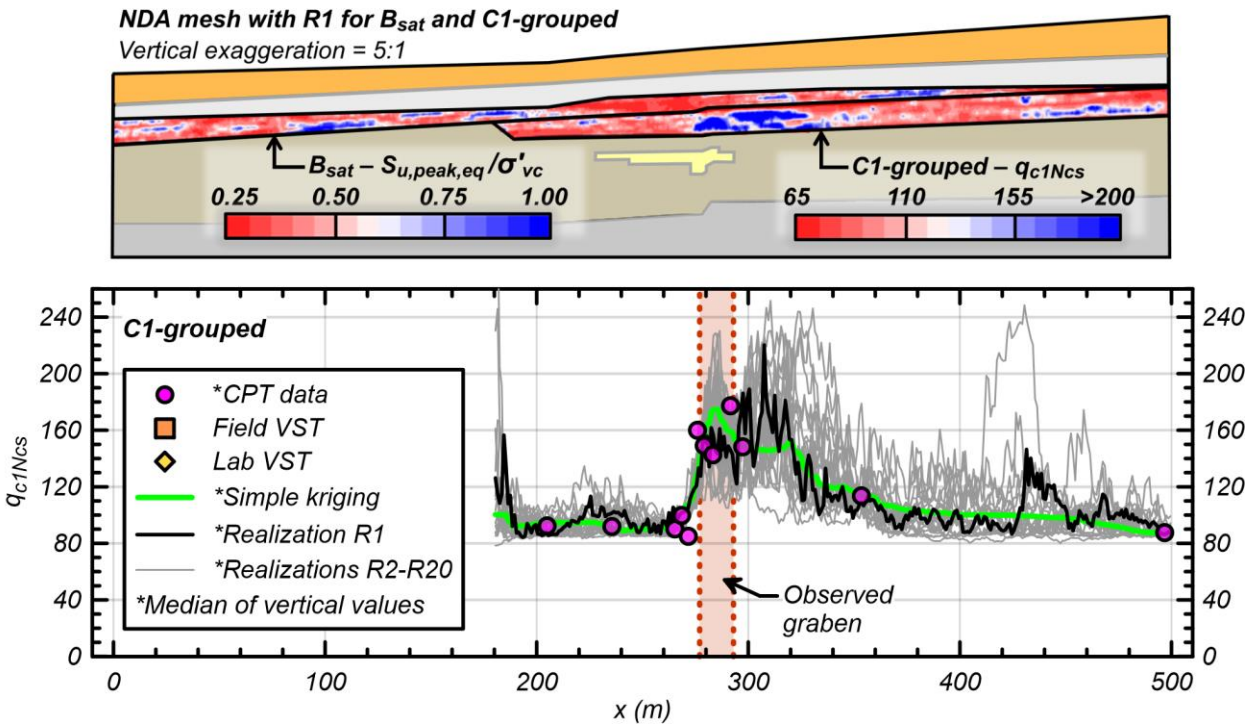

Figure 6.7. (a) Full NDA mesh with stochastic realization R1 for soil zones B_{sat} and C1-grouped; and (b) site data and lateral trends for kriged estimates and twenty simulated subsurface realizations for unit C1-grouped.

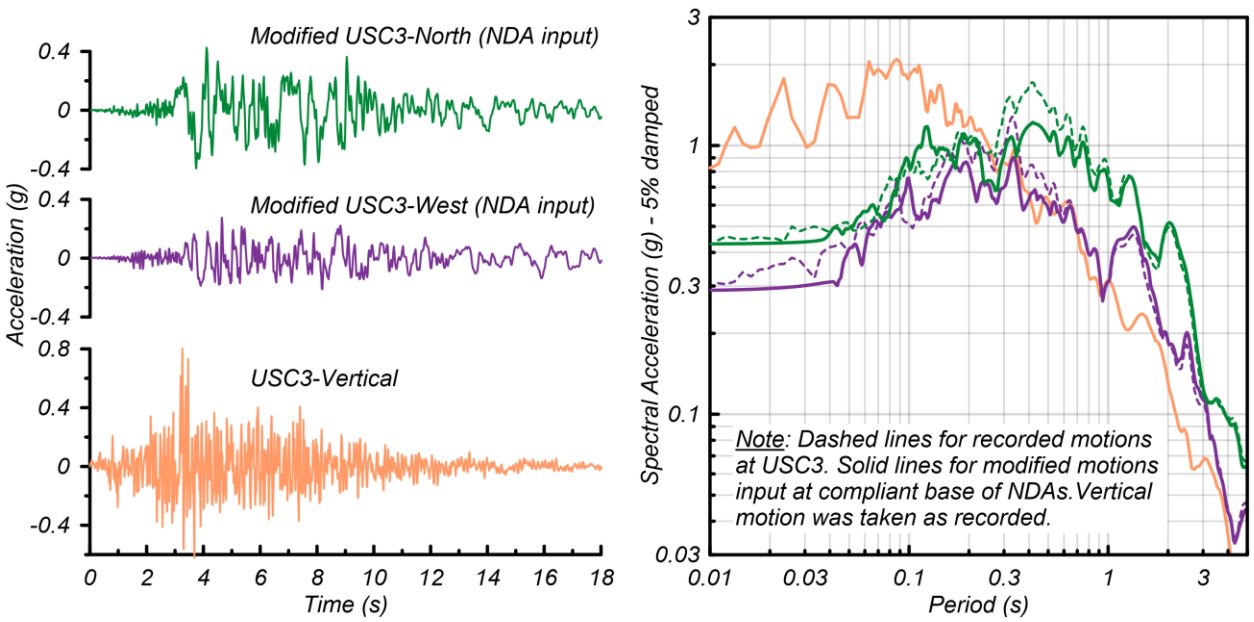

Figure 6.8. Recorded and modified ground motions from USC3 for three component directions represented as (a) acceleration time histories; and (b) acceleration response spectra.

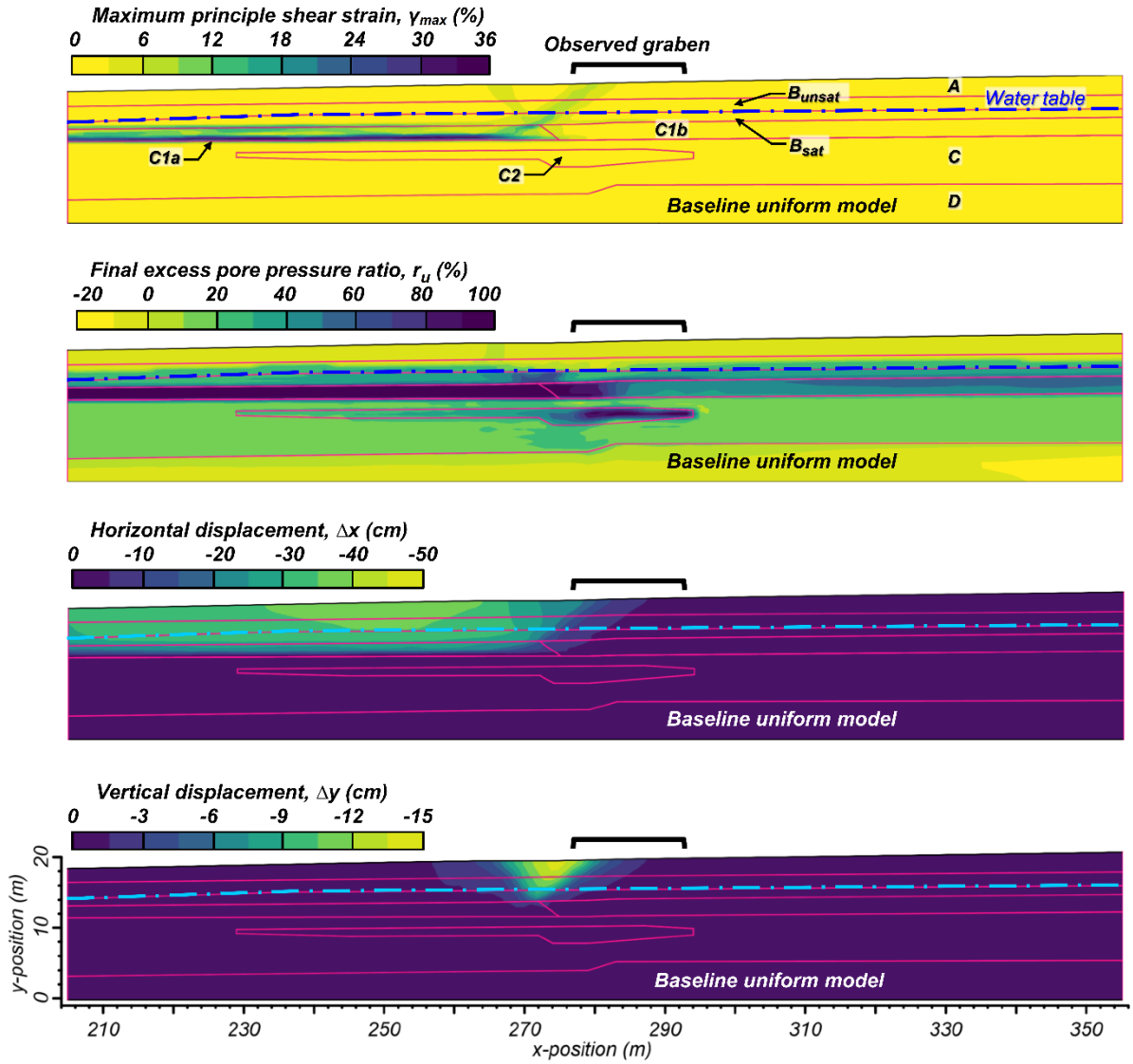

Figure 6.9. Contours for the baseline uniform NDA model of the (a) maximum engineering shear strains (in the principle direction); (b) final excess pore pressure ratio after shaking; (c) horizontal displacements; and (d) vertical displacements.

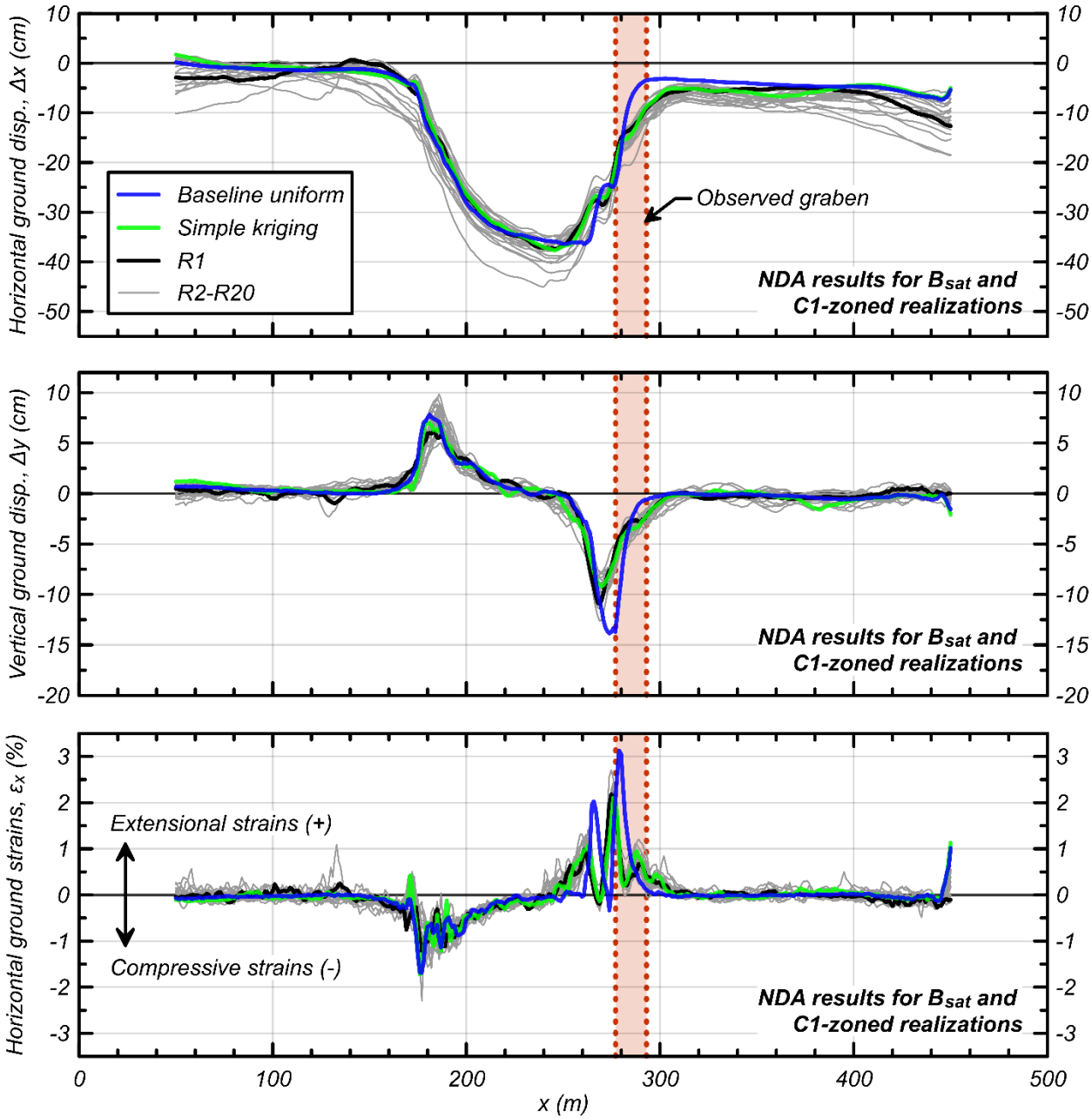

Figure 6.10. Ground deformation results from NDAs for twenty stochastic realizations of B_{sat} and C1-zoned, depicting the (a) horizontal displacements; (b) vertical displacements; and (c) horizontal ground strains. Deformations for NDAs with kriged fields and the baseline uniform model are also shown. All results were obtained at 1 m increments along the model surface for x = 50-450 m.

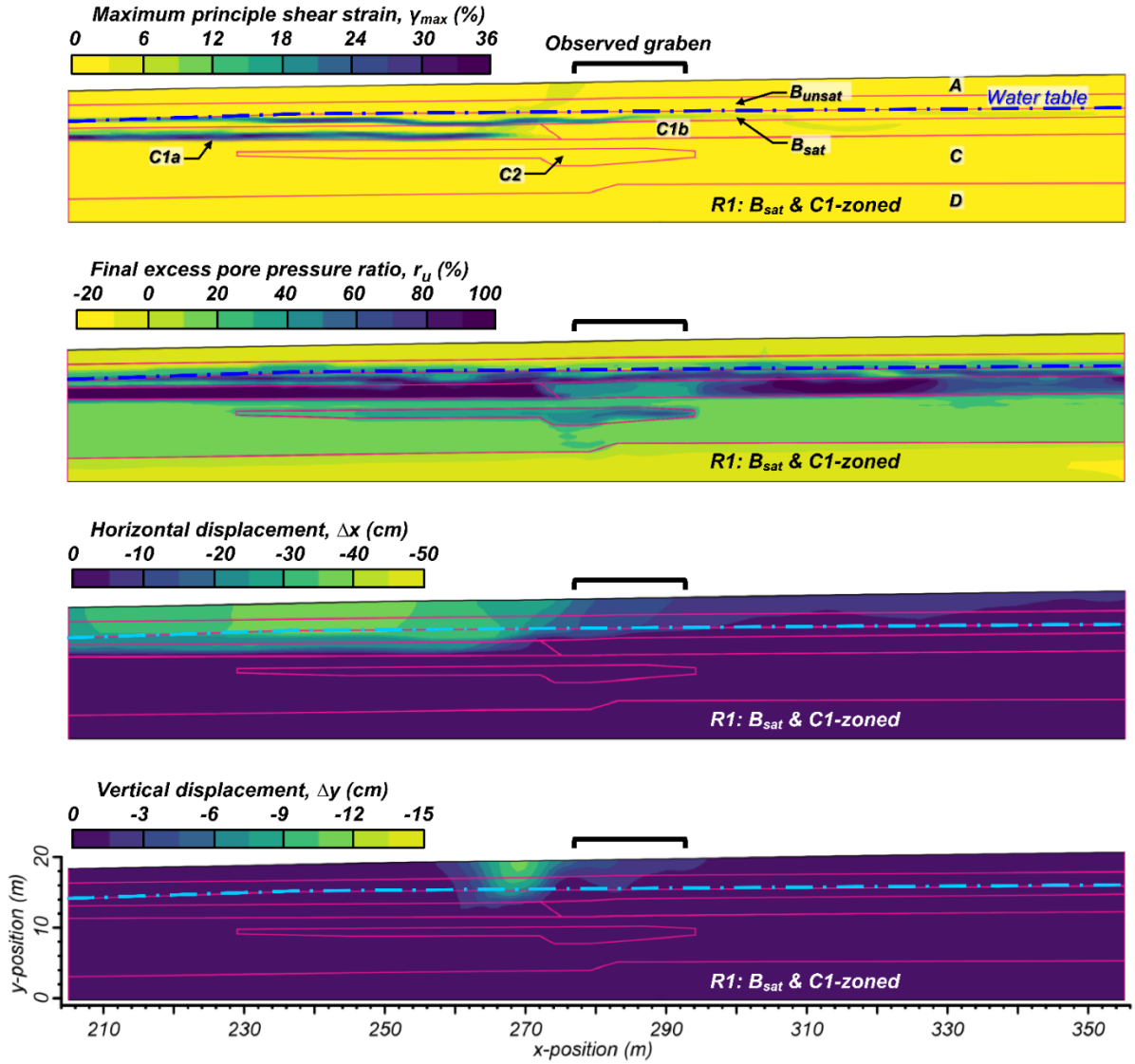

Figure 6.11. Contours for NDAs with stochastic realization R1 for B_{sat} and C1-zoned of the (a) maximum engineering shear strains (in the principle direction); (b) final excess pore pressure ratio after shaking; (c) horizontal displacements; and (d) vertical displacements.

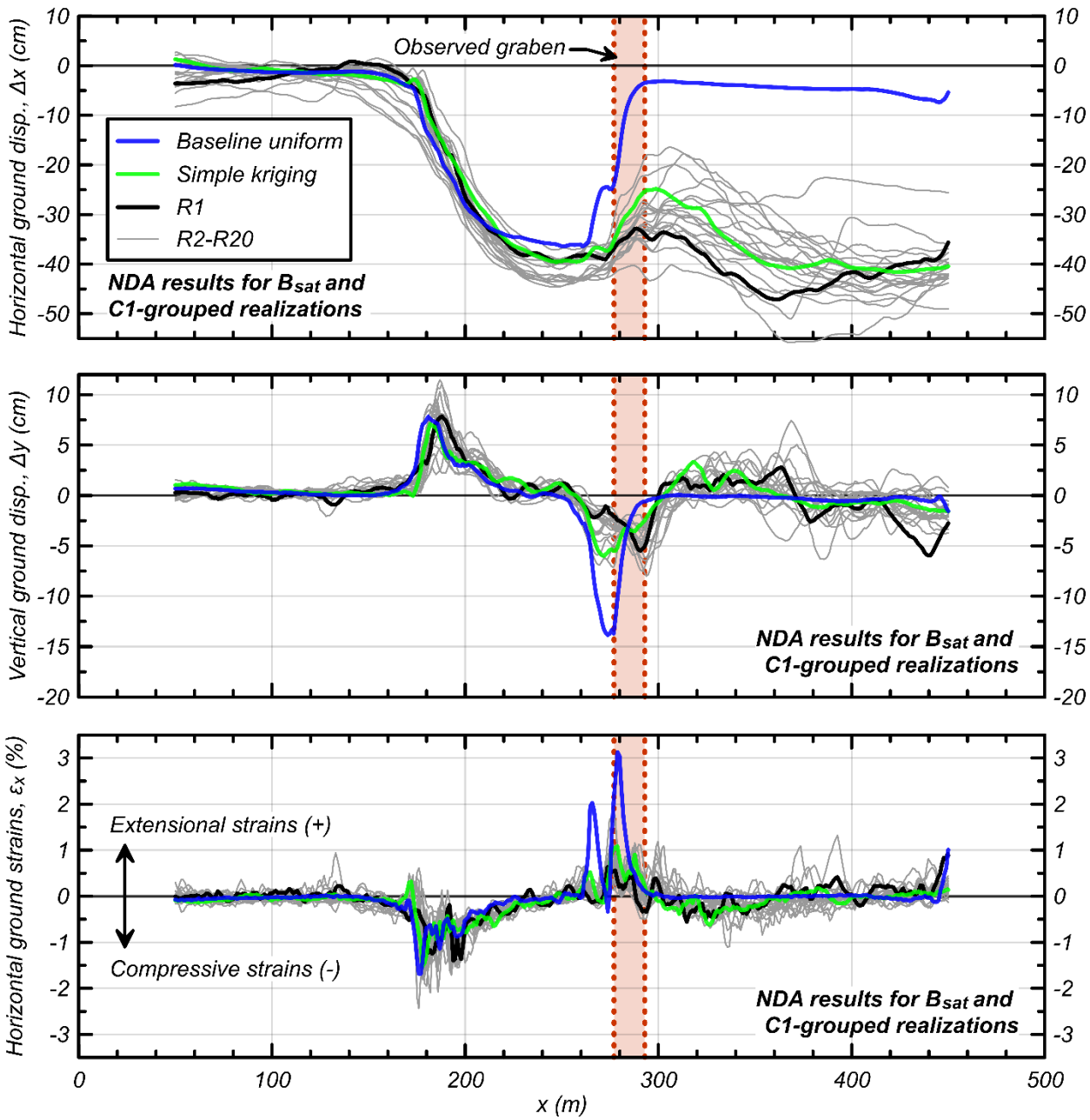

Figure 6.12. Ground deformation results from NDAs for twenty stochastic realizations of B_{sat} and C1-grouped, depicting the (a) horizontal displacements; (b) vertical displacements; and (c) horizontal ground strains. Deformations for NDAs with kriged fields and the baseline uniform model are also shown. All results were obtained at 1 m increments along the model surface for x = 50-450 m.

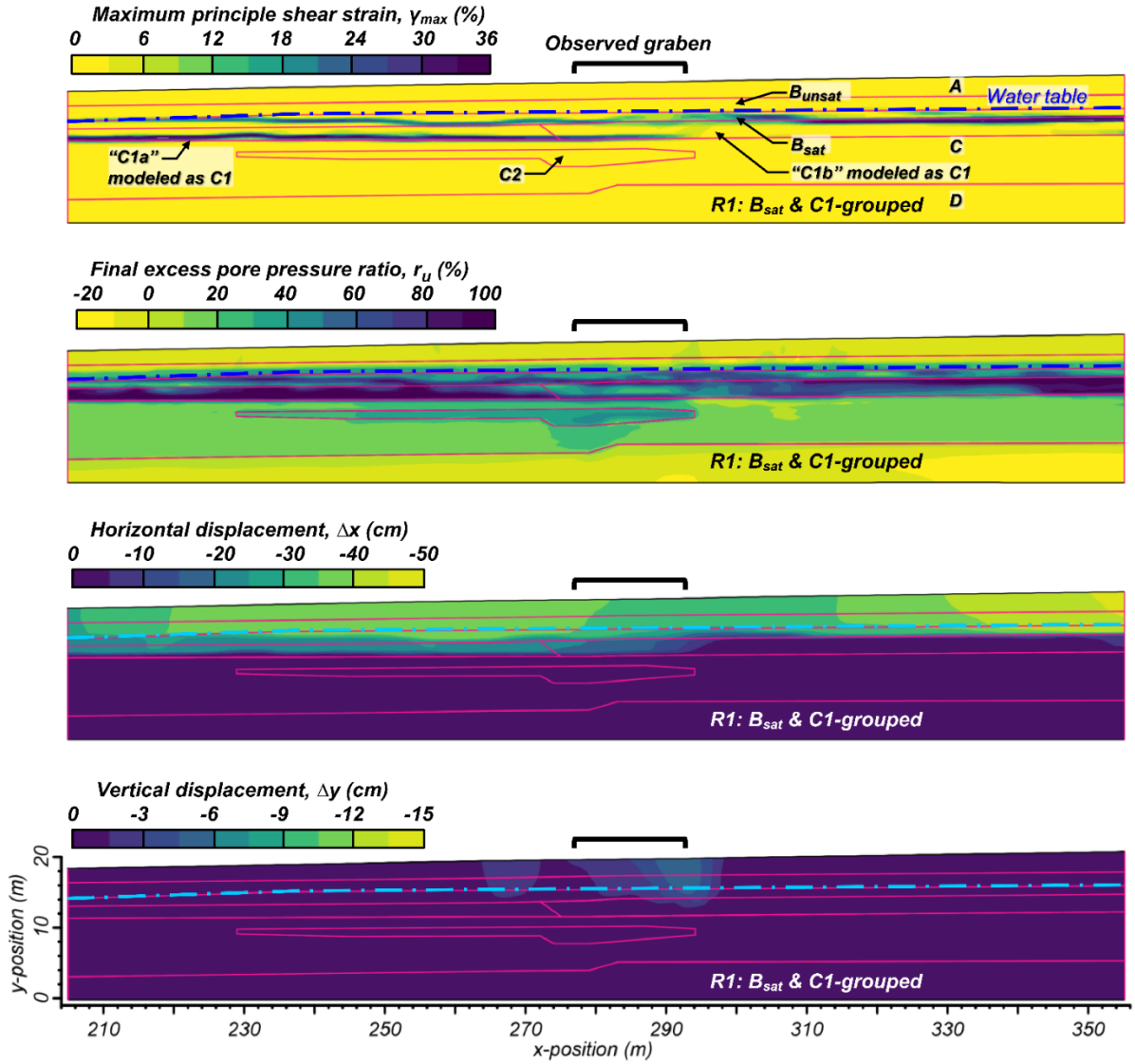

Figure 6.13. Contours for NDAs with stochastic realization R1 for B_{sat} and C1-grouped of the (a) maximum engineering shear strains (in the principle direction); (b) final excess pore pressure ratio after shaking; (c) horizontal displacements; and (d) vertical displacements.

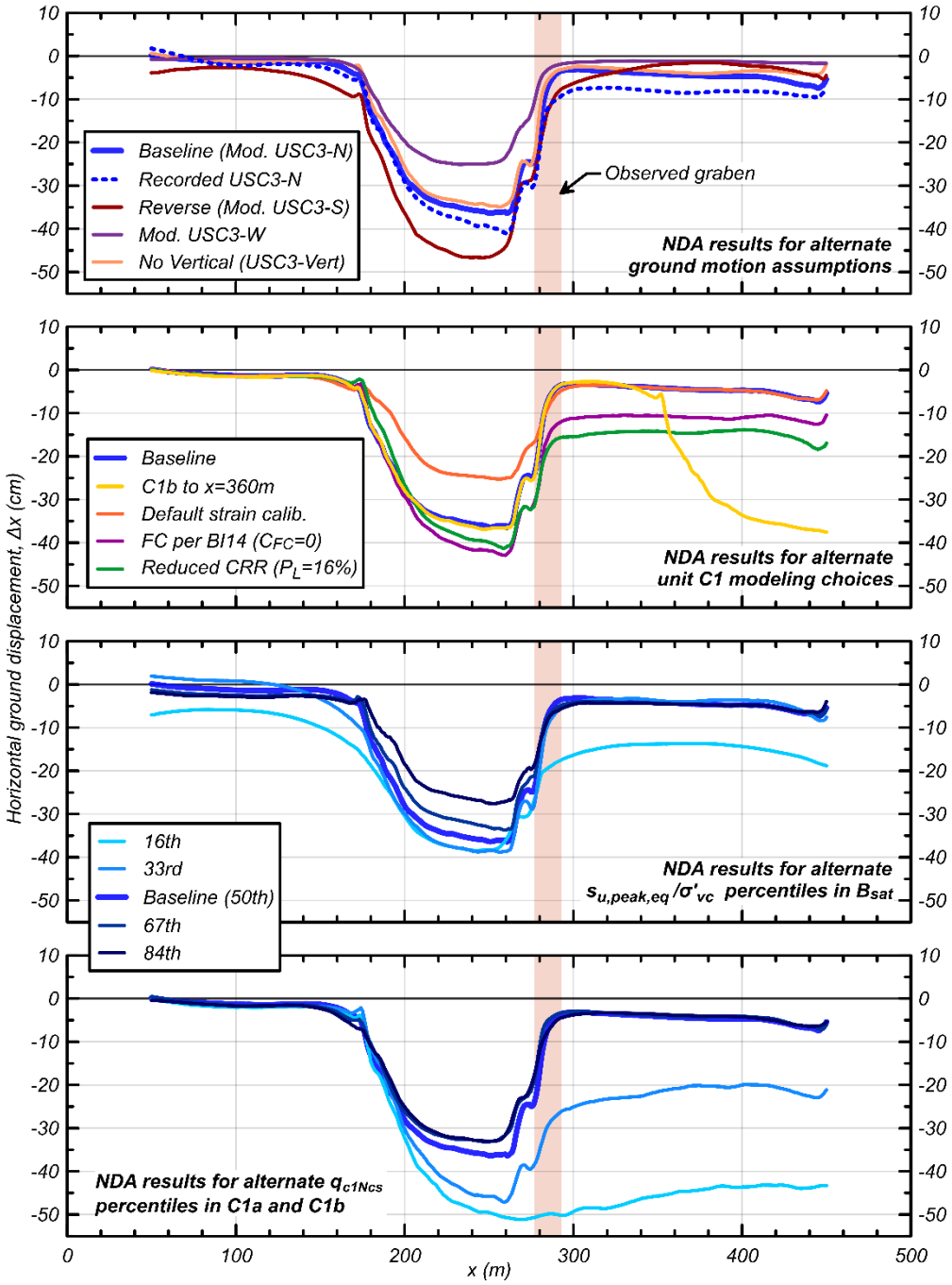

Figure 6.14. Horizontal ground displacements from NDAs for alternative (a) ground motion assumptions; (b) unit C1 modeling choices; (c) $s_{u,peak,eq}/\sigma'_{vc}$ percentiles in B_{sat}; and (d) q_{c1Ncs} percentiles in C1a and C1b. All results were obtained at 1 m increments along the model surface for x = 50-450 m.

7. Conclusions

7.1. Summary

This dissertation covered the subsurface characterization and numerical evaluations of three well-documented post-earthquake case history sites with interlayered soil deposits (i.e., Chapters 3-6), and offered practical tools and workflows for similar evaluations (i.e., Chapter 2 and Appendix D). The 2D NDA case studies evaluated in this dissertation were for sites at which subsurface variability played a key role for estimating the spatial extent and distribution of ground deformations, broadly encompassing liquefaction-induced sediment ejecta and reconsolidation, lateral spreading and slope failure towards a free-face, and an extensional graben. Each case study presented its own unique lessons regarding the causes of failure, and the capabilities of NDAs to predict the observed performance relative to simplified methods. More general lessons can also be gleaned by collectively considering the NDA case studies herein with other past NDA case studies.

7.1.1. Individual Lessons from NDA Case Studies

The 2D NDA case studies at Palinurus Road, Wufeng Site C, and Wynne Avenue provided several insights regarding ground deformation mechanisms and current modeling capabilities.

The Palinurus Road case study (Chapter 3) indicated that a laterally discontinuous low-permeability layer influenced pore pressure diffusion patterns, and thereby shifted the location of observed sediment ejecta relative to subsurface liquefaction triggering. This highlights the importance of holistically evaluating the spatial extent of liquefaction-induced surface manifestations relative to subsurface conditions. A modest variation in resistance parameters (due to alternative representative percentiles for uniform stratigraphic units, and alternative CPT processing protocols) significantly influenced the dynamic response, by altering the timing and location of the onset and progression of liquefaction and cyclic softening. The use of time histories containing a strong velocity pulse, as obtained from ground motion simulations with near-fault directivity effects, also greatly influenced the dynamic response. Ultimately, the 2D NDA models provided a closer match to post-earthquake field observations of ejecta, than could be observed from 1D LVIs.

The Wufeng Site C case study (Chapters 4 and 5) particularly highlighted the influence of subsurface modeling choices for predicting the moderate 45–205 cm of lateral spreading displacements towards a meandering stream channel. An understanding of the fluvial environment at this site assisted the development of non-stationary subsurface simulations, via transition probability geostatistics. The stochastic 2D NDAs successfully captured dynamic layer interactions overlooked by simplified evaluations, including the softening and yielding of clays near the channel, the gradual deformations produced by liquefaction away from the channel, and the overall influence of interbedding on the site response. The magnitude of deformations were generally well predicted by most sensitivity cases, but the spatial extent of spreading was over-predicted due to some indicated modeling limitations. The calibration study in Chapter 5 presents an exemplary case in which the assumption of greater post-liquefaction shear strain accumulation rates had a negligible influence on ground deformations, primarily because large/early strains in liquefied lenses dampened the transmission of cyclic stresses for the remainder of shaking,

The Wynne Avenue case study (Chapter 6) highlighted the influence of stratigraphic details on spatial patterns of ground deformations. The 2D NDAs with uniform properties for distinct stratigraphic units showed that the observed 12-m-wide extensional graben with moderate vertical offsets of 10–20 cm coincided with an abrupt contact between a weaker liquefied unit and a stronger unit with less extensive liquefaction triggering. These 2D NDAs provided closer predictions and modeled the extent and magnitude of the observed graben more objectively than 1D LVIs and Newmark sliding block analyses. The stochastic 2D NDAs with sequential Gaussian simulations for critical units slightly under-predicted the observed deformations when the abrupt stratigraphic contacts were retained, and greatly under-predicted the observed deformations when those contacts were removed. These results indicate that inherent soil variability modeling was of secondary importance to larger-scale stratigraphic details for predicting the extent and magnitude of the failure mechanism.

7.1.2. Collective Lessons from NDA Case Studies

A summary of the 2D NDA case studies of this dissertation, together with three prior 2D NDA case studies of earthquake ground deformations at other interlayered soil sites are presented in Table 7.1. The additional studies of the CTUC and FTG-7 building foundations (i.e., Bray and Luque 2017, Luque and Bray 2017, 2020), Çark Canal (i.e., Munter et al. 2017, Boulanger et al. 2019), and Balboa Boulevard (i.e., Pretell et al. 2021, 2022), were evaluated with alternative subsurface modeling approaches, to accommodate unique geological conditions and evaluated failure mechanisms. These six case studies are not exhaustive, and they build on the work of other seismic NDA studies that have similarly evaluated mechanisms affected by interlayered soils and general subsurface spatial variability (e.g., Popescu et al. 1997, 2005, Montgomery and Boulanger 2016, Paull et al. 2021). However, these six studies collectively present several common lessons for the benefits and applicability of NDAs for predicting earthquake ground deformations.

The NDA studies in Table 7.1 provide the opportunity to develop greater insights of the observed failure mechanisms than simplified methods, as well as discover the parametric choices that mattered most for each site. Current 1D LVIs for instance typically provide an index of potential liquefaction-induced damage that does not account for dynamic layer interactions, pore water diffusion, and other neglected mechanisms (e.g., Table 1.1), which could severely limit the viability of their predictions for interlayered soils. The ability of NDAs to explicitly model these mechanisms greatly improves upon their predictions. The additional consideration of 2D subsurface details for all of these sites further allowed predictions of the spatial extent and distribution of ground deformation mechanisms, which would be exceedingly difficult or impossible to predict from 1D LVIs. For instance, the differential settlement of the CTUC building and the influence of shear-induced settlements for the FTG-7 building would have only been possible to predict considering laterally discontinuous soils within an NDA simulation. Similarly, the spatial patterns of sediment manifestations at Palinurus Road, the spatial extent of lateral spreading at Wufeng Site C, and the spatial location and size of the extensional graben and associated ground displacements at Wynne Avenue were largely mispredicted or altogether missed by LVIs. The LVIs are ultimately still useful for decision-

making and identifying problems, but they possess greater limitations than NDAs for evaluating complicated systems.

The sensitivity of several variable parameters and alternative modeling choices were documented for five of the NDA studies of Table 7.1. Table 7.2 groups these sensitivity analyses into six categories: (1) CPT data processing, (2) soil properties and proportions, (3) subsurface model, (4) constitutive model calibration protocols, (5) numerical assumptions, and (6) ground motions. Note that the CTUC and FTG-7 building studies did not prioritize the documentation of sensitivity analyses and are not considered herein. Some of these case studies have been checked for other sensitivity analyses, but only results that have been documented in the manuscripts referenced in Table 7.1 are considered herein. This checklist does not reflect all possible variations of unique site-specific features (e.g., channel lining at Wufeng Site C), nor does it reflect considerations of compounding uncertainties from updating more than one parameter or model choice at a time. However, this list is intended to be useful as an index for referring back to individual case studies to learn about the influence of various parameters in different situations.

The influence of the sensitivity checks (i.e., Table 7.2) on the variability or dispersion of predictions of performance by the NDAs primarily depended on contributions from uncertainties in the site characterization, loading conditions, and modeling choices. Such uncertainties may be greater for some sites than others (e.g., limited site investigation data relative to the site complexity at Wufeng Site C; nonlinear soil effects for ground motion recordings nearest to Palinurus Road), and these uncertainties may influence predictions at some sites more than others (e.g., the minor influence of alternative subsurface realizations on the negligible lateral displacements of Çark Canal; versus the more major influence of alternative realizations on the moderate lateral displacements of Wufeng Site C). Caution is thus warranted in over-generalizing the influence of any one sensitivity parameter or model choice. Nonetheless, on a case-by-case basis, sensitivity studies provide the invaluable opportunity to identify and focus on the most dominant sources of uncertainty affecting predictions. For the NDA case studies considered herein, alternative ground motions and soil properties often significantly altered the dynamic response and magnitude of deformations to a significant degree. Had these evaluations instead been future designs (i.e.,

without nearby ground motion recordings), the uncertainty in ground motions may have been most dominant. Also, subsurface modeling choices typically had a dominant influence on the overall spatial distribution of ground deformations.

The sensitivity checks considered in Table 7.2 are numerous. The more refined consideration of dynamic soil behavior and spatial processes by NDAs, necessitates more parameter inputs and modeling choices that can posit a wider dispersion of prediction uncertainty than LVIs or other simplified methods. However, a modeler can largely reduce this uncertainty by (1) implementing up-to-date research findings, (2) obtaining purposeful site data, and (3) supporting subsurface inferences with geological insights. For instance, the selection of representative percentiles within ranges recommended by Montgomery and Boulanger (2016), and post-liquefaction shear deformation rates that better matched the experimental data of Tasiopoulou et al. (2020), were typically shown to provide better predictions for several of the case studies herein. Case studies with more abundant site investigation data situated near subsurface anomalies (e.g., stratigraphic contact at Wynne Ave) typically provided more informed subsurface models for NDAs than other sites. The consideration of fluvial, estuarine, and alluvial fan depositional processes helped to delineate stratigraphic boundaries and characterize distinct materials at all the sites (i.e., Table 7.1). NDAs can essentially allow a detailed implementation of more realistic processes and analysis checks that might altogether be ignored by common simplified methods.

These case studies also indicate that there is still a potential of bias in predictions of performance for both 2D NDAs and simplified methods. Limitations might arise from their inability to directly model some granular-scale processes (e.g., crack formations, sedimentation following reconsolidation, fine shear strain localizations) and 3D effects (e.g., out-of-plane ground shaking and soil variability; simplified geometries), as well as their dependence on imperfect site data and engineering correlations. Subsurface modeling in itself has been shown to possess several limitations in capturing geological details and representing a practical level of variability under modeling constraints (e.g., see Chapter 6 discussion for Wynne Avenue).

7.1.3. Note on the Integration of NDAs with Subsurface Modeling

The case studies presented in this dissertation demonstrate that there is no one "best" subsurface modeling approach for all NDAs. As detailed in Chapter 6, soil heterogeneity for subsurface modeling can be grouped into three levels (Uzielli et al. 2006): (1) stratigraphic heterogeneity, (2) lithological heterogeneity, and (3) inherent soil variability. The choice of the level of soil heterogeneity to model in an NDA should depend on several factors including (a) the scale or path of the hypothesized failure mechanism, (b) the depositional environment and stratigraphic architecture, (c) the mesh size and capabilities of the NDA model, (d) the availability of site investigation data, and (e) the desired level of precision for the results.

The NDAs at Palinurus Road, Wufeng Site C, and Wynne Avenue were respectively modeled with each of the three levels of soil heterogeneity. However, case-specific considerations were made prior to applying any subsurface refinements. Palinurus Road only considered stratigraphic heterogeneity, because the intent of that study was to predict the occurrence and general location of sediment manifestations. The influence of the impermeable silt interlayer on pore water diffusion was of primary importance, and thus, smaller scale details were irrelevant to that study. Wufeng Site C considered lithological heterogeneity to specifically model the influence of interlayering within the thick floodplain deposit (i.e., distinct channel fill sands, with thin silty sand and clayey silt beds) on the extensive lateral spreading observed. Smaller-scale details of inherent soil variability were of little importance. Wynne Avenue considered both stratigraphic heterogeneity and inherent spatial variability to model the alluvial fan sheetflood deposits, and their influence on the observed extensional graben. The stratigraphy was complex, but the available data did not depict distinct lithological heterogeneity within each unit. The data indicated parametric variations and a potential influence of small-scale inherent soil variability, which was evaluated, but was ultimately unnecessary for modeling the observed graben. These different situations illustrate some important site-specific considerations prior to choosing a subsurface modeling approach, as well the occasional need to re-evaluate those choices following preliminary analyses.

7.1.4. Tools for Practice

Two practical products of this dissertation are the percentile matching framework for site specific CPT-based FC correlations (Chapter 2), and the example workflow for stochastic NDAs (Appendix D). These tools are intended to assist practicing engineers and students interested in performing similar analyses.

7.2. Future Research Needs

This dissertation work advances our understanding of current capabilities for predicting the magnitude and spatial extent of earthquake ground deformations at interlayered soil deposits, by evaluating well-documented case histories. However, the case studies herein have also presented several gaps in our understanding of mechanisms affecting the system response of interlayered deposits under earthquake loading, the practical use of geostatistical methods for such problems, as well as current evaluation and modeling limitations. Some future research needs that would improve the use of both simplified methods and NDAs for seismic evaluations at interlayered soil deposits are listed below. These encompass various avenues of research, including additional continuum-based NDAs and geostatistical techniques, discrete element modeling (DEM), field and laboratory testing, and physical modeling via centrifuge testing:

- *Applied research for predicting earthquake ground deformations of linear infrastructure* – Real-world example case studies of actual engineering projects (e.g., tunnels, bridge foundations, pipelines) using the stochastic NDA methods presented in this dissertation are needed to substantiate the practicality and benefits of these methods. This is in line with the goals of the National Academies (NASEM 2016) to further validate computational modeling for liquefaction analyses prior to their wider acceptance for engineering practice. Beyond this dissertation, this work can additionally investigate the influence of varying soil conditions on soil-structure interaction and the dynamic coherency of structural alignments. Assessments can be made for probabilistic performance-based evaluations considering the uncertainty of ground motions, subsurface variability, and alternative modeling choices.

- *Additional post-earthquake stochastic NDA case studies at interlayered sites* – This dissertation has covered several well-documented case studies, but there are several others that may add to the lessons learned herein or invoke new lessons. The New Zealand Geotechnical Database (NZGD) and the NGL database (Zimmaro et al. 2019) are excellent sources for considering other case histories for similar evaluations.
- *Bulk cyclic responses of thinly interbedded soils* – Practical NDA analyses for evaluating ground deformations at sites with thinly interbedded deposits are typically constrained by the element size. It is computationally expensive, tedious, and uncommon to perform numerical analyses at a site scale with subsurface element thicknesses less than about 0.5 m. However, thinner interbeds (as low as < 1 cm) are present in certain depositional environments, and tend to significantly bias liquefaction predictions (e.g., Beyzaei et al. 2018b). General recommendations and potential updates to existing constitutive models (e.g., PM4Sand and PM4Silt) are needed to guide engineers in how to best model these soils with practical element sizes, for different depositional environments and various interbedded layer soil types, thicknesses, frequencies, and unconformities. Such work should account for the observed laboratory behavior of undisturbed samples of stratified soils with cyclic direct simple shear or triaxial testing (e.g., Beyzaei et al. 2018a) for validating numerical simulations. Discrete element modeling (DEM) can be used to evaluate granular-scale details affecting the cyclic responses of interbedded soils (e.g., Garcia and Bray 2022). Stochastic NDAs can be used to assess the influence of alternative interbedding configurations. Numerical evaluations of laminated deposits have been considered by Tasiopoulou et al. (2017), however, additional studies are needed to develop universal recommendations for evaluating such sites.
- *Numerical studies of multi-dimensional cyclic shear strain development in interlayered deposits* – The NDAs considered in this dissertation highlighted the dependence of localized ground deformations on the developed patterns of shear strains during shaking (e.g., Wynne Avenue NDAs necessitated abrupt stratigraphic contacts for graben deformations above the confined liquefied layer; NDAs without these contacts sheared laterally through the model). A better understanding of the situations (e.g., geometry,

location, frequency, and properties of weak pockets) that promote daylighting shear strains, can provide great insight for both 2D NDA modeling and simplified evaluations of earthquake-induced lateral spreading and other ground deformations. Studies should also be performed via 3D NDAs to understand the influence out-of-plane spatial variability on shear strain paths, relative to 2D NDAs.

- *Object-based modeling of fluvial processes for earthquake-induced deformations* – Advanced geostatistical techniques using object-based methods (e.g., Pyrcz & Deutsch 2014) conditioned on training images of geological cross sections and estimated temporal depositional processes can be explored for evaluating lateral spreading deformations, as well as the seismic stability of dams and levees above spatially variable foundations in fluvial environments.
- *CPT thin-layer corrections from detailed logs* – The CPT thin-layer corrections from inverse filtering by Boulanger and DeJong (2018) has garnered recent interest from several research groups. This pioneering work suggests the importance of performing site-specific calibrations in several situations, which (similar to previous CPT-based FC correlations) has often been overlooked in favor of automated, one-size-fits-all, methods. The value of performing site-specific inverse filtering corrections using well-characterized detailed boring logs (e.g., Beyzaei et al. 2019) could be explored for multiple case study sites and for controlled centrifuge tests.
- *Centrifuge studies of earthquake deformations within interlayered deposits* – The case studies evaluated herein explored several unique mechanisms. Centrifuge tests could ideally be performed to further validate and confirm the mechanisms in these studies. For example, centrifuge tests using similar methods as the seminal work by Fiegel and Kutter (1994) could explore the precise mechanisms of sediment manifestations around impermeable interlayers (as observed at Palinurus Road), and could provide additional insights regarding the influence of subsurface spatial variability for interpreting sediment manifestations that is not considered in recent 1D NDA methods (e.g., Hutabarat and Bray 2021). Other centrifuge studies could be modeled after a lateral spreading case study like Wynne Avenue, to further explore the influence of abrupt vs. gradational stratigraphic boundaries on shear strain patterns.

- *Practical tools for performing stochastic NDAs* – The stochastic NDA workflow provided in this dissertation (Appendix D) is intended to educate and provide an example workflow for students and practitioners interested in developing better practices for performing NDAs and geostatistical analyses. However, this work has not yet been generalized nor optimized for performance, and relies on some external codes. It is believed that improvements to such tools, and the continued incorporation of the latest research findings, will be invaluable to the geotechnical earthquake engineering profession.

Tables

Table 7.1. Recent 2D NDA studies of earthquake ground deformations at case history sites with interlayered soil deposits.

Case history	*Event*	*Description (observation and model insights)*	*References*
CTUC and FTG-7 buildings	2010-11 Canterbury Earthquake Sequence	Two shallow-founded multistory buildings damaged by moderate liquefaction-induced settlements. Stratigraphic heterogeneity of fluvial deposit modeled deterministically. CTUC models elucidate influence of a buried stream channel on differential settlement. FTG-7 models suggest mechanism of soil-structure-interaction ratcheting.	Bray and Luque (2017); Luque and Bray (2017); (2020)
Çark Canal	1999 Kocaeli earthquake	No ground displacements observed along canal banks, even though simplified liquefaction methods predicted large displacements. Lithological heterogeneity of fluvial deposit modeled geostatistically. Models illustrate importance of CPT thin layer corrections and subsurface variability for improved displacement predictions.	Munter et al. (2017); Boulanger et al. (2019)
Balboa Blvd.	1994 Northridge earthquake	Zones of ground extension and compression associated with horizontal movements of about 50 cm, over a shallow slope. Lithological heterogeneity of distal alluvial fan deposit modeled geostatistically. Models suggest influence of water table shape, as well as cyclic softening in clays and liquefaction of sands, for spatial patterns of ground deformations.	Pretell et al. (2021); (2022)
Palinurus Rd.	2010-11 Canterbury Earthquake Sequence	Sediment ejecta observed at one side of a grass field. Stratigraphic heterogeneity of fluvial and estuarine deposit modeled deterministically. Models elucidate influence of spatially varying dynamic response, and impermeable silt interlayer on spatial patterns of pore water diffusion and ejecta.	Bassal et al. (2020); Bassal and Boulanger (2021)
Wufeng Site C	1999 Chi-Chi earthquake	Moderate lateral spreading displacements of 45–205 cm towards a meandering stream channel. Lithological heterogeneity of fluvial deposit modeled geostatistically. Models particularly highlight influence of geologically subtle features (e.g., soft clay lens near channel, connectivity of liquefied soils) on spatial patterns of ground deformations.	Bassal et al. (2021a); (2021b); (2022b)
Wynne Ave.	1994 Northridge earthquake	Moderate 12-m-wide extensional graben with vertical offsets of 10–20 cm, over a shallow slope. Inherent soil variability of distal alluvial fan deposit modeled geostatistically. Models elucidate influence of abrupt stratigraphic contacts on spatial patterns of ground deformations.	Bassal and Boulanger (2022); (Submitted)

Table 7.2. Checklist of documented sensitivity analyses from 2D NDA studies of earthquake ground deformations for interlayered sites.

Category	*Varied parameter or model choice*	*Çark Canal*	*Balboa Blvd.*	*Palinurus Rd.*	*Wufeng Site C*	*Wynne Ave.*
CPT Data Processing	FC corrections				X	X
	Thin-layer correction (i.e., inverse filtering)	X		X	X	
Soil properties and proportions	Representative properties	X	X	X	X	X
	Ic cutoff (or alt. soil proportions)	X	X			
	Small-strain V_S		X			
	k_H and k_V			X		X
Subsurface model	Stratigraphic unit contacts/extents			X	X	X
	Correlation lengths	X	X		X	
	Alt. realizations	X	X		X	X
	Ground surface topography		X			
	Groundwater table	X	X		X	
Constitutive model calibration protocols	Strain accumulation rate		X		X	X
	Target CRR				X	X
	Target r_u		X			
	Clay sensitivity				X	
Numerical assumptions	Side boundary conditions				X	
	Post-shaking reconsolidation			X	X	X
Ground motions	Orientation or polarity	X	X	X	X	X
	Yes/no vertical motion			X	X	X
	Yes/no pulse		X	X		
	Spatial incoherency		X			
	Alt. sources or scaling	X		X		

References

Abrahamson, N. A., Silva, W. J., and Kamai, R. (2014). "Summary of the ASK14 ground motion relation for active crustal regions." Earthquake Spectra 30, 1025–1055.

Alabert, F. (1987). "Stochastic imaging of spatial distributions using hard and soft information" (Master's thesis). Stanford University, Stanford, CA.

Ambraseys, N. & Sarma, S. (1969). "Liquefaction of soils induced by earthquakes." Bull. Seismol. Soc. Am.V. 59(2), 651-664.

Ancheta, T. D., Darragh, R. B., Stewart, J. P., et al. (2013). "PEER NGA-West2 Database." Pacific Earthquake Engineering Research Center. PEER Report No. 2013/03. University of California, Berkeley, CA.

Andrus R. D., Piratheepan, P., Ellis, B. S., Zhang, J., & Juang, C. H. (2004). "Comparing liquefaction evaluation methods using penetration-VS relationships." Soil Dynamics & Earthquake Engineering, 24, 713-721.

Andrus R. D., Piratheepan, P., Ellis, B. S., Zhang, J., and Juang, C. H. (2004). "Comparing liquefaction evaluation methods using penetration-VS relationships." Soil Dynamics & Earthquake Engineering, 24, 713-721.

Asimaki, D., Pecker, A., Popescu, R., & Prevost, J. H. (2003). "Effects of Spatial Variability of Soil Properties on Surface Ground Motion." Journal of Earthquake Engineering, 7(1), 1–44. DOI: 10.1080/13632460309350472.

Bartlett, S. F., and Youd, T. L. (1995). "Empirical prediction of liquefaction-induced lateral spread." J. Geotech. Eng., 121(4), 316–329.

Bassal, P. (2022). "Stochastic NDA Workflow for Ground Deformations at Wynne Avenue in the Northridge Earthquake", in Stochastic Nonlinear Dynamic Analyses for Earthquake Ground Deformations. DesignSafe-CI. https://doi.org/10.17603/ds2-nne2-2s11

Bassal, P. C., & Boulanger, R. W. (2021). "System Response of an Interlayered Deposit with Spatially Preferential Liquefaction Manifestations." Journal of Geotechnical and Geoenvironmental Engineering. ASCE, 147(12): https://doi.org/10.1061/(ASCE)GT.1943-5606.0002684.

Bassal, P. C., & Boulanger, R. W. (2022). "Dynamic Analyses of Localized Ground Deformation at Wynne Avenue in the Northridge Earthquake." Proc., 12th National Conference on Earthquake Engineering, Salt Lake City, UT.

Bassal, P. C., & Boulanger, R. W. (Submitted). "System Response of an Interlayered Deposit with a Localized Graben Deformation in the Northridge Earthquake." Soil Dynamics and Earthquake Engineering.

Bassal, P. C., Boulanger, R. W., & DeJong, J. T. (2021a). "Dynamic analyses of liquefaction and lateral spreading for an interlayered deposit in the Chi-Chi earthquake." Proc. ASCE Geo-Extreme 2021 Conference, Savannah, GA. https://doi.org/10.1061/9780784483695.042.

Bassal, P. C., Boulanger, R. W., & DeJong, J. T. (2022a). "Site-Specific CPT-based Fines Content Correlations using Percentile Matching." In proc., ASCE Geo-Congress 2022, Charlotte, NC. https://doi.org/10.1061/9780784484043.053.

Bassal, P. C., Boulanger, R. W., & DeJong, J. T. (2022b). "System Response of an Interlayered Deposit with Spatially Distributed Ground Deformations in the Chi-Chi Earthquake." Journal of

Geotechnical and Geoenvironmental Engineering. ASCE, 148(10). https://doi.org/10.1061/(ASCE)GT.1943-5606.0002869.

Bassal, P. C., Boulanger, R. W., Cox, B. R., Yost, K. M., & DeJong, J. T. (2020). "Dynamic analyses of liquefaction at Palinurus Road in the Canterbury Earthquake Sequence." Proc., 40th USSD Annual Meeting and Conference, United States Society on Dams, Denver, CO, 1-17.

Bassal, P. C., Boulanger, R. W., DeJong, J. T., & K. Ziotopoulou (2021b). "Calibration of Post-Liquefaction Shear Deformation for a Fluvial Deposit in the Chi-Chi earthquake." In Proc., 17th World Conference on Earthquake Engineering. Tokyo: International Association for Earthquake Engineering.

Beavan, J., Motagh, M., Fielding, E., Donnelly, N., & Collett, D. (2012). "Fault slip models of the 2010-2011 Canterbury, New Zealand, earthquakes from geodetic data, and observations of post-seismic ground deformation." New Zealand Journal of Geology and Geophysics 55(3).

Begg, J., Jones, K., & Barrell, D. (2015). Geology and geomorphology of urban Christchurch and eastern Canterbury. GNS Science Geological Map 3, Lower Hutt, NZ.

Bennett, M. J., Ponti, D. J., Tinsley III, J. C., Holzer, T. L., & Conaway, C. H. (1998). "Subsurface geotechnical investigations near sites of ground deformations caused by the January 17, 1994, Northridge, California, earthquake." Washington, DC: USGS.

Beyzaei, C. Z., Bray, J. D., Cubrinovski, M., Riemer, M., & Stringer, M. (2018a). "Laboratory-based characterization of shallow silty soils in southwest Christchurch." Soil Dynamics and Earthquake Engineering, 110, 93-109. https://doi.org/10.1016/j.soildyn.2018.01.046.

Beyzaei, C. Z., Bray, J. D., van Ballegooy, S., Cubrinovski, M., Bastin, S. (2018b). "Depositional environment effects on observed liquefaction performance in silt swamps during the Canterbury earthquake sequence." Soil Dynamics and Earthquake Engineering, 107, 303-321. https://doi.org/10.1016/j.soildyn.2018.01.035.

Beyzaei, C. Z., Bray, J. D., Cubrinovski, M., Bastin, S., Stringer, M., Jacka, M., van Ballegooy, S., Riemer, M., & Wentz, R. (2019). "Characterization of silty soil thin layering and groundwater conditions for liquefaction assessment." Can. Geotech. J., 57(2): 263276. https://doi.org/10.1139/cgj-2018-0287

Boore, D. M., Stewart, J. P., Seyhan, E., and Atkinson, G. A. (2014). "NGA-West2 equations for predicting PGA, PGV, and 5% damped PSA for shallow crustal earthquakes." Earthquake Spectra 30, 1057–1085.

Boulanger, R. W., & DeJong, J. T. (2018). "Inverse filtering procedure to correct cone penetration data for thin-layer and transition effects." Proc., Cone Penetration Testing 2018, Hicks, Pisano, & Peuchen, eds., Delft Univ. of Tech., The Netherlands, 25–44.

Boulanger, R. W., & Idriss, I. M. (2007). "Evaluation of cyclic softening in silts and clays." Journal of Geotechnical and Geoenvironmental Engineering, ASCE, 133(6), 641-652.

Boulanger, R. W., & Idriss, I. M. (2014). "CPT and SPT based liquefaction triggering procedures." Report No. UCD/CGM.-14/01.

Boulanger, R. W., & Idriss, I. M. (2015). "CPT-based liquefaction triggering procedure." Journal of Geotechnical and Geoenvironmental Engineering, ASCE, 142(2), 04015065, 10.1061/(ASCE)GT.1943-5606.0001388.

Boulanger, R. W., & Truman, S. P. (1996). "Void redistribution in sand under post-earthquake loading." Canadian Geotechnical Journal, 33, 829-834.

Boulanger, R. W., & Ziotopoulou, K. (2017). “PM4Sand (Version 3.1): A sand plasticity model for earthquake engineering applications.” Report No. UCD/CGM-17/01, Center for Geotech. Modeling, Dept. of Civil and Environ. Eng., Univ. of Cal., Davis, CA, 113 pp.

Boulanger, R. W., & Ziotopoulou, K. (2018). “PM4Silt (Version 1): A silt plasticity model for earthquake engineering applications.” Report No. UCD/CGM-18/01, Center for Geotech. Modeling, Dept. of Civil and Environ. Eng., Univ. of Cal., Davis, CA, 108 pp.

Boulanger, R. W., & Ziotopoulou, K. (2019). "A constitutive model for clays and plastic silts in plane-strain earthquake engineering applications." Soil Dynamics and Earthquake Engineering, 127(2019): 105832, 10.1016/j.soildyn.2019.105832.

Boulanger, R. W., Khosravi, M., Cox, B. R., and DeJong, J. T. (2018). “Liquefaction evaluation for an interbedded soil deposit: St. Teresa’s School, Christchurch, New Zealand.” Proc.,

Boulanger, R. W., Moug, D. M., Munter, S.K., Price, A. B. & DeJong, J. T. (2016). “Evaluating liquefaction in interbedded sand, silt, and clay deposits using the cone penetrometer.” Proc., 5th Int. Conf. on Geotech. & Geophys. Site Char.: Queensland, Australia.

Boulanger, R. W., Munter, S. K., Krage, C. P., & DeJong, J. T. (2019). “Liquefaction evaluation of interbedded soil deposit: Çark Canal in 1999 M7.5 Kocaeli Earthquake.” J. Geotech. Geoenviron. Eng., ASCE, 145(9): 05019007, /10.1061/(ASCE)GT.1943-5606.0002089.

Bradley, B.A. & Hughes, M. (2012a). “Conditional Peak Ground Accelerations in the Canterbury Earthquakes for Conventional Liquefaction Assessment.” Technical Report for the Ministry of Business, Innovation and Employment. 13 April 2012. 22 p.

Bradley, B.A. & Hughes, M. (2012b). “Conditional Peak Ground Accelerations in the Canterbury Earthquakes for Conventional Liquefaction Assessment: Part 2.” Technical Report for the Ministry of Business, Innovation and Employment. 22 December 2012. 19 p.

Bradley, B.A. (2013). “A New Zealand-specific pseudospectral acceleration GMPE for active shallow crustal earthquakes based on foreign models.” Bull. Seismol. Soc. Am. V 103(3). 1801–1822.

Bray, J. D., & Luque, R. (2017). “Seismic performance of a building affected by moderate liquefaction during the Christchurch earthquake.” Soil Dyn. Earthquake Eng., 102 (Nov): 99–111. https://doi.org/10.1016/j.soildyn.2017.08.011.

Bray, J. D., & Macedo, J. (2019). “Procedure for estimating shear-induced seismic slope displacement for shallow crustal earthquakes.” J. Geotech. Geoenviron. Eng. 145 (12): 04019106. https://doi.org/10.1061/(ASCE)GT.1943-5606.0002143.

Campbell, K. W. and Bozorgnia, Y. (2014). “NGA-West2 Ground Motion Model for the Average Horizontal Component of PGA, PGV, and 5% Damped Linear Acceleration Response Spectra.” Earthquake Spectra 30, 1087–1115.

Canterbury Geotechnical Database (CGD) (2013). "Liquefaction and Lateral Spreading Observations", Map Layer CGD0300 - 22 September 2016. Accessed May 15, 2020. https://canterburygeotechnicaldatabase.projectorbit.com/.

Canterbury Geotechnical Database (CGD) (2014a). “Verification of LiDAR acquired before and after the Canterbury Earthquake Sequence.” CGD Technical Specification 03.

Canterbury Geotechnical Database (CGD) (2014b). "Event Specific Groundwater Surface Elevations", Map Layer CGD0800 - 10 June 2014. Accessed May 15, 2020. from https://canterburygeotechnicaldatabase.projectorbit.com/.

Carle, S. F., & Fogg, G. E. (1996). “Transition probability-based indicator geostatistics.” Mathematical Geology 28(4): 453-476.

Carle, S.F. (1999). “TPROGS: Transition Probability Geostatistical Software: Users Guide.” University of California, Davis.

Carlton, B. D., & Pestana, J. M. (2012). "Small strain shear modulus of high and low plasticity clays and silts." 15th World conference on earthquake engineering, Lisbon, Portugal.

Chang, S. S. L. (1971). “Subsurface geologic study of the Taichung basin.” Petroleum geology of Taiwan, 8, 21-45.

Chang, S. W., Bray, J. D., & Seed, R. B. (1996). “Engineering implications of ground motions from the Northridge earthquake.” Bull. Seismol. Soc.Am. 86 (1): 270–288.

Chiou, B. S. J., and Youngs, R. R. (2014). “Update of the Chiou and Youngs NGA model for the average horizontal component of peak ground motion and response spectra.” Earthquake Spectra 30, 1117–1153.

Chu, B. L., Hsu, S. C., and Chang, Y. (2003). “Ground behavior and liquefaction analyses in central Taiwan-Wufeng.” Engineering Geology, 71, 119-139.

Chu, D. B. (2006). “Case studies of soil liquefaction of sands and cyclic softening of clays induced by the 1999 Taiwan Chi-Chi earthquake.” Ph.D. thesis, Dept. of Civil and Environmental Engineering, Univ. of California, Los Angeles.

Chu, D. B., et al. (2004). “Documentation of soil conditions at liquefaction and non-liquefaction sites from 1999 Chi-Chi (Taiwan) earthquake.” Soil Dyn. Earthquake Eng., 24(9-10), 647–657.

Chu, D. B., Stewart, J. P., Youd, T. L. & Chu, B. L. (2006). "Liquefaction-induced lateral spreading in near-fault regions during the 1999 Chi-Chi, Taiwan Earthquake." J. Geotech. & Geoenv. Eng., ASCE, 132(12), 1549-1565.

Cruikshank, K. M., Johnson, A. M., Fleming, R. W., & Jones R. (1996). “Winnetka deformation zone: Surface expression of coactive slip on a blind fault during the Northridge earthquake sequence, California.” Washington, DC: USGS.

Cubrinovski, M., Rhodes, A., Ntritsos, N., & van Ballegooy, S. (2019). “System response of liquefiable deposits.” Soil Dynamics & Earthquake Engineering, 124 (Sep): 212–229. https://doi.org/10.1016/j.soildyn.2018.05.013.

Darby, K. M., Boulanger, R. W., DeJong, J. T., & Bronner, J. D. (2019). “Progressive changes in liquefaction and cone penetration resistance across multiple shaking events in centrifuge tests.” J. of Geotechnical & Geoenvironmental Engineering, ASCE, 140(3): 04018112, 10.1061/(ASCE)GT.1943-5606.0001995.

Darendeli, M. B. (2001). “Development of a new family of normalized modulus reduction and material damping curves.” Ph. D. dissertation, University of Texas at Austin.

Davis, M. (1987). “Production of conditional simulations via the LU decomposition of the covariance matrix.” Mathematical Geology, 19(2): 91–98.

de la Torre, C. A., Bradley, B. A., & Lee, R. L. (2020). “Modeling nonlinear site effects in physics-based ground motion simulations of the 2010–2011 Canterbury earthquake sequence.” Earthquake Spectra 36(2):856-879.

DeGroot, D. J., & Baecher, G. B. (1993). “Estimating autocovariance of in-situ soil properties.” Journal of Geotechnical Engineering, 119 (1): 147-166. DOI: 10.1061/(ASCE)0733-9410(1993)119:1(147)

DeJong, J. T., Krage, C. P., Boulanger, R. W., & DeGroot, D. J. (2020). “Optimization of CPT Soundings to Reduce Uncertainty in Interpretation of Subsurface Stratigraphy.” Proc., 6th Int. Conf. on Geotechnical and Geophysical Site Characterization, ISC6.

Deutsch, C. V. & Journel, A. G. (1997). “GSLIB Geostatistical Software Library and User’s Guide.” Oxford University Press, New York, second edition.

Deutsch, C. V., & Journel, A. G. (1992). “Geostatistical software library and user’s guide.” Oxford University Press, New York, 340 p, first edition.

Electric Power Research Institute (1993). "Guidelines for determining design basis ground motions." Palo Alto, Calif: Electric Power Research Institute, vol. 1-5, EPRI TR-102293.

Elkateb, T., Chalaturnyk, R., & Robertson, P. K. (2003). “An overview of soil heterogeneity: Quantification and implications on geotechnical field problems.” Can. Geotech. J., 40: 1–15. doi: 10.1139/T02-090.

Faris, A. T., Seed, R. B., Kayen, R. E., and Wu, J. (2006). “A Semi-Empirical Model for the Estimation of Maximum Horizontal Displacement Due to Liquefaction-Induced Lateral Spreading.” Proc. 8th U.S. National Conference on Earthquake Engineering, San Francisco, CA.

Fenton, G.A., & Vanmarcke, E. (1990). “Simulation of random fields via local average subdivision.” Journal of Engineering Mechanics, 116(8): 1733–1749.

Fiegel, G. L., & Kutter, B. L. (1994). “Liquefaction mechanism for layered soils.” J. Geotech. Eng. 20(4), 737–755.

Finn, W. D. L., Lee, K. W., and Martin, G. R. (1977). “An Effective Stress Model for Liquefaction.” J. of the Geotech. Eng. Division, ASCE, 103(6): 517-533.

Garcia, F. E., & Bray, J. D. (2022). “Discrete element analysis of earthquake surface fault rupture through layered media.” Soil Dynamics & Earthquake Engineering, 152, 107021. https://doi.org/10.1016/j.soildyn.2021.107021.

GeoNet (n.d.). Geological hazard information for New Zealand: Strong Motion Data Products. Accessed May 1, 2019. ftp://ftp.geonet.org.nz/strong/processed.

Ghosh, B., Klar, A., & Madabhushi, S. P. G. (2005). “Modification of site response in presence of localised soft layer.” J Earthq Eng 9(6):855–876.

Gibbs, J. F., Tinsley, J. C., Boore, D. M., & Joyner, W. B. (1999). “Seismic velocities and geological conditions at twelve sites subjected to strong ground motion in the 1994 Northridge, California, earthquake: A revision of OFR 96-740.” Washington, DC: USGS.

Graves, R., & Pitarka, A. (2010). “Broadband ground-motion simulation using a hybrid approach. Bulletin of the Seismological Society of America.” 100: 2095–2123.

Green, R.A., Lee, J., White, T.M., and Baker, J.W. (2008). "The Significance of Near-Fault Effects on Liquefaction," Proc. 14th World Conf. on Earthquake Engineering, Paper No. S26-019.

Griffiths, D. V., and Marquez, R. M. (2007). “Three-dimensional slope stability analysis by elasto-plastic finite elements.” Geotechnique 57, No. 6, 537–546.

Holzer, T. L., & Bennett M. J. (2007). “Geologic and hydrogeologic controls of boundaries of lateral spreads: Lessons from USGS liquefaction case histories.” In Proc., 1st North American Landslide Conf., edited by V. Schaefer, R. Schuster, and A. Turner, 502–522. Zanesville, OH: Association of Environmental and Engineering Geologists.

Holzer, T. L., Bennett, M. J., Ponti, D. J., & Tinsley III, J. C. (1999). “Liquefaction and Soil Failure during 1994 Northridge Earthquake.” Journal of Geotechnical and Geoenvironmental Engineering, 125(6), 438–452. https://doi.org/10.1061/(ASCE)1090-0241

Holzer, T. L., Bennett, M. J., Tinsley III, J. C., Ponti, D. J., & Sharp, R. V. (1996). “Causes of ground failure in alluvium during the Northridge, California, and earthquake of January 17, 1994.” In Proc.,

6th Japan–US Workshop on Earthquake Resistant Design of Lifeline Facilities and Countermeasures against Soil Liquefaction, edited by M. Hamada and T. O'Rourke, 345–360. Buffalo, NY: National Center for Earthquake Engineering Research.

Holzer, T. L., Youd, T. L., & Bennett, M. J. (1988). "In situ measurement of pore pressure build-up during liquefaction." Proc., 20th Joint Meeting of United States-Japan Panel on Wind and Seismic Effects, Gaithersburg, MD, 1988: 118–130.

Housner, G.W. (1958). "The mechanism of sandblows." Bull. Seismol. Soc. Am. Vol. 48 pp. 155-161.

Hsu, S. C., Chu, B. L., and Lin, C. C. (2008). "Analyses of ground movements caused by lateral spread during an earthquake." Proc. 10th Int. Symp. Landslides and Engineered Slopes, Xian, China.

Hutabarat, D., & Bray, J. D. (2021). "Effective stress analysis of liquefiable sitess to estimate the severity of sediment ejecta." J. Geotech. Geoenviron. Eng., ASCE, 147(5): 04021024, 10.1061/(ASCE)GT.1943-5606.0002503.

Idriss, I. M., & Boulanger, R. W. (2008). "Soil liquefaction during earthquakes." Monograph MNO-12, Earthquake Engineering Research Institute, Oakland, CA, 261 pp.

Ishihara, K., and Yoshimine, M. (1992). "Evaluation of settlements in sand deposits following liquefaction during earthquakes." Soils & Foundations, 32 (1): 173–188.

Itasca (2019). "FLAC, Fast Lagrangian Analysis of Continua, User's Guide, Version 8.1." Itasca Consulting Group, Inc., Minneapolis, MN.

Iwasaki, T., Tatsuoka, F., Tokida K., & Yasuda, S. (1978). "A practical method for assessing soil liquefaction potential based on case studies at various sites in Japan." In Proc., 2nd Int. Conf. on Microzonation. Washington, DC: National Science Foundation.

Jibson, R. W., Rathje, E. M., Jibson, M. W., & Lee, Y. W. (2013). SLAMMER—Seismic LAndslide Movement Modeled using Earthquake Records (ver.1.1, November 2014): U.S. Geological Survey Techniques and Methods, book 12, chap. B1, unpaged.

Kottke, A. R., & Rathje, E. M. (2008). "Technical manual for Strata." Report No.: 2008/10. Pacific Earthquake Engineering Research Center, University of California, Berkeley.

Kuo, C. H., Wen, K. L., Hsieh, H. H., Lin, C. M., Chang, T. M., and Kuo, K. W. (2012). "Site Classification and Vs30 estimation of free-field TSMIP stations using the logging data of EGDT." Engineering Geology, 129-130, 68-75. DOI: 10.1016/j.enggeo.2012.01.013

Kutter, B. L. and Wilson, D. W. (1999). "De-liquefaction shock waves." Proc., 7th US–Japan Workshop on Earthquake Resistant Design of Lifeline Facilities and Countermeasures Against Soil Liquefaction, Tech. Rep. MCEER-99-0019, T. D. O'Rourke, J. P. Bardet, and M. Hamada, eds., State University of New York, Buffalo, N.Y., 295–310.

Kwok, L. A., Stewart, J. P., Kwak, D. Y., and Sun, P. L. (2018). "Taiwan-Specific Model for VS30 Prediction Considering Between-Proxy Correlations." Earthquake Spectra, 34(4): 1973-1993.

Li, Y., Fenton, G. A., Hicks, M. A., & Xu, N. (2021). "Probabilistic Bearing Capacity Prediction of Square Footings on 3D Spatially Varying Cohesive Soils." J. of Geotech. and Geoenvir. Eng., ASCE, 147(6), 04021035. https://doi.org/10.1061/(ASCE)GT.1943-5606.0002538

Lin, C. W., Shih, R. Y., Lin, Y. H., and Chen, W. S. (2002). "Structural characteristics of the Chelungpu fault zone in the Taichung area, Central Taiwan." Western Pacific Earth Sciences, 2(4): 411-426.

Lunne, T., Robertson, P. K., and Powell, J. J. M. (1997). "Cone penetration testing in geotechnical practice." Blackie Academic, EF Spon/Routledge, New York.

Luque, R., & Bray, J. D. (2020). "Dynamic soil-structure interaction analyses of two important structures affected by liquefaction during the Canterbury earthquake sequence." Soil Dyn. Earthquake Eng. 133 (Jun):106026. https://doi.org/10.1016/j.soildyn.2019.106026.

Luque, R., & Bray. J. D. (2017). "Dynamic analyses of two buildings founded on liquefiable soils during the Canterbury earthquake sequence." J. Geotech. Geoenviron. Eng., 143 (9): 04017067. https://doi.org/10.1061/(ASCE)GT.1943-5606.0001736.

Makdisi, A. J., & Kramer, S. L. (2019). "Influence of strain distribution and dynamic response in the prediction of displacements in shallow sloping ground." In Proc., 7th Int. Conf. on Earthquake Geotechnical Engineering (ICEGE), edited by F. Silvestri and N. Moraci, 3740–3747. London: Taylor & Francis.

Markham, C., Bray, J. D., Macedo, J., & Luque, R. (2016). "Evaluating nonlinear effective stress site response analyses using records from the CES." Soil Dynamics & Earthquake Eng. 82, 84–898.

Matheron, G., Beucher, H., de Fouquet, C., Galli, A., Guerillot, D., & Ravenne, C. (1987). "Conditional simulation of the geometry of fluvio-deltaic reservoirs." Proc. Society of Petroleum Engineers of AIME, 123-131.

Maurer, B., Green, R., & Taylor, O. S. (2015). "Moving towards an improved index for assessing liquefaction hazard: Lessons from historical data." Soils Found. 55 (4): 778–787. https://doi.org/10.1016/j.sandf.2015.06.010.

Maurer, B., Green, R., Cubrinovski, M., & Bradley, B. (2014). "Evaluation of the Liquefaction Potential Index for Assessing Liquefaction Hazard in Christchurch, New Zealand." J. of Geotechnical & Geoenvironmental Engineering, ASCE, 140(7): 04014032, A10.1061/(ASCE)GT.1943-5606.0001117.

Maurer, B.W., Green, R.A., van Ballegooy, S., Wotherspoon, L. (2019). "Development of region-specific soil behavior type index correlations for evaluating liquefaction hazard in Christchurch, New Zealand." Soil Dynamics and Earthquake Engineering, 117, 96-105.

Mayne, P. W., & Rix, G. J. (1995). "Correlations between shear wave velocity and cone tip resistance in natural clays." Soils and Foundations, 35: 107-110. DOI:10.3208/SANDF1972.35.2_107

Mayne, P. W., and Peuchen, J. (2018). "Evaluation of CPTU Nkt cone factor for undrained strength of clays." Fourth Int. Symposium on Cone Penetration Testing, Delft.

McLaughlin, K. A. (2017). "Investigation of false-positive liquefaction case history sites in Christchurch, New Zealand." M.Sc. thesis, Dept. of Civil, Architectural, and Environmental Engineering, Univ. of Texas at Austin.

Montgomery, J., & Abbaszadeh, S. (2017). "Comparison of two constitutive models for simulating the effects of liquefaction on embankment dams." Proceedings, 37th Annual USSD Conference, USSD, Denver, CO.

Montgomery, J., & Boulanger, R. W. (2016). "Effects of Spatial Variability on Liquefaction-Induced Settlement and Lateral Spreading." Journal of Geotechnical and Geoenvironmental Engineering, 143(1), 04016086. https://doi.org/10.1061/(ASCE)GT.1943-5606.0001584.

Montgomery, J., Boulanger, R. W., & Ziotopoulou, K. (2017). "Effects of spatial variability on the seismic response of the Wildlife Liquefaction Array." Proc., 3rd International Conf. on Performance Based Design in Earthquake Geotechnical Engineering, Vancouver, BC.

Multidisciplinary Center for Earthquake Engineering Research (MCEER) 2000. "The Chi-Chi, Taiwan Earthquake of September 21, 1999: Reconnaissance Report." Technical Report MCEER-00-0003. University at Buffalo, State University of New York.

Munter, S. K., Boulanger, R. W., Krage, C. P., and DeJong, J. T. (2017). "Evaluation of liquefaction-induced lateral spreading procedures for interbedded deposits: Cark Canal in the 1999 M7.5 Kocaeli earthquake." Geotechnical Frontiers 2017, Seismic Performance and Liquefaction, Geotechnical Special Publication No. 281, T. L. Brandon and R. J. Valentine, eds., 254-266.

Munter, S. K., Krage, C. P., Boulanger, R. W., DeJong, J. T., & Montgomery, J. (2016). "Potential for liquefaction-induced lateral spreading in interbedded deposits considering spatial variability." Proceedings, Geotechnical and Structural Engineering Congress, Phoenix, AZ, Feb. 14-17, ASCE, 1484-1494.

National Academies of Sciences, Engineering, and Medicine (NASEM) (2016). "State of the Art and Practice in the Assessment of Earthquake-Induced Soil Liquefaction and Its Consequences." The National Academies Press, Washington, DC.

New Zealand Geotechnical Database (NZGD) (n.d.). Accessed May 1, 2021. https://www.nzgd.org.nz.

New Zealand Mapping Ltd. (2014). "Christchurch Post-Earthquake 0.1m Urban Aerial Photos (24 February 2011)." LINZ Data Service. Accessed May 1, 2020. https://data.linz.govt.nz/.

Newmark, N. (1965). "Effects of earthquakes on dams and embankments."Géotechnique 15 (2): 139–160. https://doi.org/10.1680/geot.1965.15.2.139.

Nichols, G. (2009). "Sedimentology and stratigraphy." Second edition, Wiley-Blackwell, John Wiley & Sons Ltd., West Sussex, UK.

Nichols, G. (2009). "Sedimentology and stratigraphy." Second edition, Wiley-Blackwell, John Wiley & Sons Ltd., West Sussex, UK.

Ntritsos, N., Cubrinovski, M., and Rhodes, A. (2018). "Evaluation of liquefaction case histories from the 2010-2011 Canterbury Earthquakes using advanced effective stress analysis." Geotechnical Earthquake Engineering and Soil Dynamics V, GSP 292, ASCE, 152-164, https://doi.org/10.1061/9780784481479.016.

O'Rourke, T. D. (1998). "An overview of geotechnical and lifeline earthquake engineering." Proc., Geotechnical Earthquake Engineering and Soil Dynamics – III, ASCE, 75: 1392-1426.

Pacific Earthquake Engineering Research Center (PEER) (2002). "Taiwan Ground Failure Database," retrieved 05/01/2020 from https://apps.peer.berkeley.edu/.

Pacific Earthquake Engineering Research Center (PEER) (2013). "PEER Ground Motion Database: NGA-West2." retrieved 06/01/2020 from https://ngawest2.berkeley.edu/.

Paull, N. A., Boulanger, R. W., DeJong, J. T., & Friesen, S. J. (2021). "Using conditional random fields for a spatially variable liquefiable foundation layer in nonlinear dynamic analyses of embankments." Journal of Geotechnical and Geoenvironmental Engineering, ASCE, 147(11): 04021134, 10.1061/(ASCE)GT.1943-5606.0002610.

Pease, J. W., & O'Rourke, T. D. (1997). "Seismic Response of Liquefaction Sites." Journal of Geotechnical and Geoenvironmental Engineering, 123(1), 37–45. https://doi.org/10.1061/(ASCE)1090-0241(1997)123:1(37)

Phoon, K.-K., Ching, J., & Shuku, T. (2022). "Challenges in data-driven site characterization." Georisk: Assessment and Management of Risk for Engineered Systems and Geohazards, 16(1), 114–126. https://doi.org/10.1080/17499518.2021.1896005.

Phoon, K.-K., Huang, H. W., & Quek, S. T. (2005). "Simulation of strongly non-Gaussian processes using Karhunen–Loève expansion." Probabilistic Engineering Mechanics, 20(2): 188-198. https://doi.org/10.1016/j.probengmech.2005.05.007.

Phoon, K-K, & Kulhawy, F. H. (1999). “Characterization of geotechnical variability.” Can. Geotech. J., 36: 612-624.

Popescu, R., Prevost, J. H. & Deodatis, G. (1997). “Effects of spatial variability on soil liquefaction: some design recommendations.” Géotechnique, 47(5), 1019–1036.

Popescu, R., Prevost, J. H. & Deodatis, G. (2005). “3D effects in seismic liquefaction of stochastically variable soil deposits.” Géotechnique, 55(1), 21–31. DOI: 10.1680/geot.55.1.21.58589.

Pretell, R. A., Ziotopoulou, K., & Davis, C. (2021). “Numerical modeling of ground deformations at Balboa Blvd. in the Northridge 1994 Earthquake.” J. of Geotech. & Geoenvir. Eng., ASCE, 147 (12): 05021013. 10.1061/(ASCE)GT.1943-5606.0002417.

Pretell, R. A., Ziotopoulou, K., & Davis, C. (2022). “Parametric Investigation of Ground Failure at Balboa Boulevard During the 1994 Northridge Earthquake via Nonlinear Deformation Analyses.” Proc., ASCE-UCLA Lifelines 2021-2022 Conference. Los Angeles, CA: UCLA.

Pretell, R., Ziotopoulou, K., & Abrahamson, N. (2019). “Methodology for the development of input motions for nonlinear deformation analyses.” In Proc., 7th Int. Conf. on Earthquake Geotechnical Engineering (ICEGE), edited by F. Silvestri and N. Moraci, 4564–4571. London: Taylor & Francis.

Price, A. B., Boulanger, R. W., DeJong, J. T., Parra Bastidas, A. M., and Moug, D. (2015). “Cyclic strengths and simulated CPT penetration resistances in intermediate soils.” 6th Int. Conf. on Earthquake Geotech. Eng., Nov.1-4, Christchurch, New Zealand.

Pyrcz, M. J., & Deutsch, C. V. (2014). “Geostatistical reservoir modeling.” Oxford University Press.

Pyrcz, M. J., & Deutsch, C.V., (2003). “Declustering and Debiasing.” Geostatistical Association of Australasia, Newsletter 19, October.

Pyrcz, M.J., Jo. H., Kupenko, A., Liu, W., Gigliotti, A.E., Salomaki, T., & Santos, J., (2021). GeostatsPy Python Package, PyPI, Python Package Index, https://pypi.org/project/geostatspy/.

QGIS (2020). QGIS Geographic Information System. Open Source Geospatial Foundation Project. http://qgis.org.

QuakeCore (2016). Seisfinder. Accessed March 1, 2020. https://quakecoresoft.canterbury.ac.nz/seisfinder/.

Razafindrakoto, H. N. T., Bradley, B. A., & Graves, R. W. (2016). “Broadband ground motion simulation of the 2010-2011 Canterbury earthquake sequence.” Proceedings of the 2016 New Zealand Society of earthquake engineering conference, Christchurch, New Zealand, 1–3 April.

Remy, N., Boucher, A., & Wu, J. (2009). “Applied geostatistics with SGeMS : a user's guide.” Cambridge University Press.

Robertson, P. K. (2009). “Interpretation of cone penetration tests - a unified approach.” Can. Geotech. J. 46: 1337-1355. doi: 10.1 l39/T09-065.

Robertson, P. K. (2010). “Estimating in-situ soil permeability from CPT & CPTu.” Proc., 2nd Int. Symp. on Cone Penetration Testing, Huntington Beach, CA.

Robertson, P. K., & Wride, C. E. (1998). “Evaluating cyclic liquefaction potential using the cone penetration test.” Can. Geotech. J., 35(3), 442–459.

Robinson, K., Cubrinovski, M., Kailey, P., and Orense, R. (2011). “Field Measurements of Lateral Spreading following the 2010 Darfield Earthquake.” Proc. Ninth Pacific Conf. on Earthquake Engr., Auckland, New Zealand.

Seed, H. B., Tokimatsu, K., Harder, L. F. Jr., & Chung, R. (1984). “The influence of SPT procedures in soil liquefaction resistance evaluations.” Earthquake Engineering Research Center, University of California, Berkeley, Report No. UCB/EERC-84/15, 50 pp.

Stamen Design (2020). Toner and Terrain: Map Tiles by Stamen Design, under CC BY 3.0. Data by OpenStreetMap, under ODbL. Accessed May 1, 2020. http://maps.stamen.com/.

Stewart, J. P. (2001). “Chapter 4: Soil liquefaction. Chi-Chi, Taiwan Earthquake of September 21, 1999 Reconnaissance Report.” Earthquake Spectra, 17 (Supplement A), 37–60.

Stewart, J. P., Seed, R. B., & Bray, J. D. (1996). “Incidents of ground failure from the 1994 Northridge earthquake.” Bull. Seismol. Soc. Am. 86 (1):300–318.

Suzuki, Y., Koyamada, K., and Tokimatsu, K. (1997). "Prediction of liquefaction resistance based on CPT tip resistance and sleeve friction." Proc., 14th Int. Conf. Soil Mech. and Fdn. Engr., Hamburg, Germany, 1:603–06.

Tasiopoulou, P., Giannakou, A., Chacko, J., & de Wit, S. (2017). “Evaluation of Liquefaction Triggering Resistance and Deformation Accumulation in Laminated Sand and Clay Deposits.” Proc., 3rd International Conf. on Performance Based Design in Earthquake Geotechnical Engineering, Vancouver, BC.

Tasiopoulou, P., Ziotopoulou, K., Humire, F., Giannakou, A., Chacko, J., & Travasarou, T. (2020). “Development and implementation of semiempirical framework for modeling postliquefaction deformation accumulation in sands.” J. Geotech. & Geoenviron. Eng., ASCE, doi.org/10.1061/(ASCE)GT.1943-5606.0002179.

Tonkin & Taylor Ltd. (2015). “Canterbury Earthquake Sequence: Increased Liquefaction Vulnerability Assessment Methodology.” Chapman Tripp acting on behalf of the Earthquake Commission (EQC), Tonkin & Taylor ref. 52010.140.v1.0.

United States Geological Survey (2021). “Table of CPT Data, Los Angeles County.” https://earthquake.usgs.gov/research/cpt/data/losangeles; [accessed 01 August 2021].

Upadhyaya, S., Green, R. A., Rodriguez-Marek, A., Maurer, B. W., Wotherspoon, L., Bradley, B. A., & Cubrinovski, M. (2019). “Influence of corrections to recorded peak ground accelerations due to liquefaction on predicted liquefaction response during the 2010-2011 Canterbury, New Zealand, Earthquake Sequence.” Proc., 13th Australia New Zealand Conference on Geomechanics (13ANZCG).

Uzielli, M., Lacasse, S., Nadim, F., & Phoon, K.-K. (2006). “Soil Variability Analysis for Geotechnical Practice.” In Characterisation and Engineering Properties of Natural Soils (Vol. 3). https://doi.org/10.1201/NOE0415426916.ch3.

van Ballegooy, S., Malan, P., Lacrosse, V., Jacka, M.E., Cubrinovski, M., Bray, J. D., O’Rourke, T.D., Crawford, S.A., & Cowan, H. (2014). “Assessment of liquefaction-induced land damage for residential Christchurch.” Earthquake Spectra, 30(1), 31-55.

van Ballegooy, S., Wentz, F., & Boulanger R. W. (2015). “Evaluation of a CPT-based liquefaction procedure at regional scale.” Soil Dynamics and Earthquake Engineering, 79, 315-334.

Vanmarcke, E. (1977). “Probabilistic modeling of soil profiles.” Journal of the Geotechnical Engineering Division, ASCE, 103(GT11): 1227–1245.

Vucetic, M., & Dobry, R. (1991). “Effect of Soil Plasticity on Cyclic Response.” Journal of Geotechnical Engineering, 117, 89-107. http://dx.doi.org/10.1061/(ASCE)0733-9410(1991)117:1(89).

Wald, D. J., & Heaton, T. H. (1994). “A dislocation model of the 1994 Northridge, California, earthquake determined from strong ground motions.” Washington, DC: USGS.

Wentworth, C. M., and R. F. Yerkes. (1971). “Geologic setting and activity of faults in the San Fernando area, California.” Washington, DC: USGS.

Wotherspoon, L.M., Orense, R.P., Bradley, B.A., Cox, B.R., Wood, C.M. & Green, R.A. (2015). “Geotechnical characterization of Christchurch strong motion stations.” Eq.Comm.Rep. Project No. 12/629; v3.

Yang, Y., & Kavazanjian, E. (2021). “Numerical evaluation of liquefaction-induced lateral spreading with an advanced plasticity model for liquefiable sand.” Soil Dynamics and Earthquake Engineering, 149. https://doi.org/10.1016/j.soildyn.2021.106871.

Yost, K. M., Cox, B. R., Wotherspoon, L., Boulanger, R. W., van Ballegooy, S., & Cubrinovski, M. (2019). “In situ investigation of false-positive liquefaction sites in Christchurch, New Zealand: Palinurus Road Case History.” Geo-Congress 2019: Earthquake Engineering and Soil Dynamics, GSP308, ASCE, 436-451.

Youd, T. L. (1984). "Recurrence of Liquefaction at the Same Site." Eighth World Conference on Earthquake Engineering EERI, San Francisco, 231-238.

Youd, T. L., & Keefer , D. K. (1994). “Liquefaction during the 1977 San Juan Province, Argentina earthquake (M_S=7.4).” Engineering Geology, (37): 211-233.

Youd, T. L., DeDen, D. W., Bray, J. D., Sancio, R., Cetin, K. O., and Gerber, T. M. (2009). "Zero-displacement lateral spreads, 1999 Kocaeli, Turkey, earthquake." J. Geotechnical and Geoenvironmental Eng., ASCE, 135(1), 46-61.

Youd, T. L., Hansen, C. M., & Bartlett, S. F. (2002). “Revised multilinear regression equations for prediction of lateral spread displacement.” J. Geotech. & Geoenviron. Eng., ASCE, 128(12), 1007–1017.

Youd, T. L., Idriss, I. M., Andrus, R. D., Arango, I., Castro, G., Christian, J. T., Dobry, R., Finn, W. D. L., Harder, L. F., Hynes, M. E., Ishihara, K., Koester, J. P., Liao, S. S. C., Marcuson, W. F., Martin, G. R., Mitchell, J. K., Moriwaki, Y., Power, M. S., Robertson, P. K., Seed, R. B., & Stokoe, K. H. (2001). Liquefaction resistance of soils: summary report from the 1996 NCEER and 1998 NCEER/NSF workshops on evaluation of liquefaction resistance of soils, J. Geotechnical and Geoenvironmental Eng., ASCE 127(10), 817–33.

Zhang, G., Robertson, P. K., & Brachman, R. W. I. (2002). “Estimating liquefaction-induced ground settlements from CPT for level ground.” Can. Geotech. J. 39: 1168–1180. DOI: 10.1139/T02-047.

Zhang, G., Robertson, P. K., & Brachman, R. W. I. (2004). “Estimating liquefaction induced lateral displacements using the standard penetration test or cone penetration test.” J. Geotech. & Geoenv. Eng., ASCE, 130(8), 861–871.

Zimmaro P., Brandenberg, S. J., Stewart, J. P., Kwak, D. Y., Franke, K. W., Moss, R. E. S., Cetin, K. O., Can, G., Ilgac, M., Stamatakos, J., Juckett, M., Mukherjee, J., Murphy, Z., Ybarra, S., Weaver, T., Bozorgnia, Y., Kramer, S. L. (2019). “Next-Generation Liquefaction Database.” Next-Generation Liquefaction Consortium. DOI: 10.21222/C2J040.

Ziotopoulou, K., & Boulanger, R. W. (2016). "Plasticity modeling of liquefaction effects under sloping ground and irregular cyclic loading conditions." Soil Dynamics and Earthquake Engineering, 84 (2016), 269-283, 10.1016/j.soildyn.2016.02.013.

Appendix A

Supplementary Material for Chapter 2
(Site-Specific CPT-based Fines Content Correlations using Percentile Matching)

Supplementary Tables and Figures

Table A.1. Summary of percentile matching inputs for evaluation of FC-I_C correlations at 13 Christchurch, New Zealand case studies.

Site Name	CPT ID	Stratum Label[a]	Site-Specific Inputs for Percentile Matching						Liquefaction Observed?[b]	
			P1	*P2*	*P3*	*FC1*	*FC2*	*FC3*	Sep2010	Feb2011
71 Somerfield St	CPT_638	A	40	80	90	30	50	80	N	Y
200 Cashmere Rd	CPT_104673	A	25	50	75	11	51	90	N	N
Barrington Park	CPT_37818	A	25	50	75	35	65	75	N	Y
70 Langdons Rd	SCPT_57338	A	22.5	45	72.5	33	44	52	N	N
15 Cresselly Pl	SCPT_57353	A	24	67	93	4	21	48	N	Y
Palinurus Rd	SCPT_57360	A	25	60	80	20	50	70	N	Y
		B	25	80	90	7	25	50		
St Teresa School	SCPT_57345	A	30	60	80	50	60	89	N	N
North New Brighton School	SCPT_57350	A	20	89	95	3	10	20	N	N
Hillmorton High School	SCPT_57364	A	25	66	91	46	60	82	Y	Y
Shirley Int School	SCPT_57366	B	37	75	88	7	24	41	N	Y
Clarence	CPT_104677	A	10	55	72	41	93	97	N	N
Sabina Playground	SCPT_57346	A	16	32	66	5	8	14	N	Y
Hillsborough Park	SCPT_57365	A	15	50	85	30	50	85	N	N
		B	15	50	85	2	5	11		
		C	15	50	85	50	83	95		

Notes: (a) Stratum label refers to critical stratum depths evaluated with indicated inputs. Depths are indicated on attached figures.
(b) Yes (Y) or no (N) liquefaction observed following the Darfield (Sep2010) and Christchurch (Feb2011) earthquakes as mapped by Cubrinovski et al. (2019)

General note: The following pages present the resulting percentile matching correlations (labeled as "CDF Match") and LPI/LSN results for these sites, relative to the BI14 Regional and BI14 Site-Specific correlations. These results are similar to those presented for Shirley Road in Chapter 2, but with an unaltered format as produced in Python.

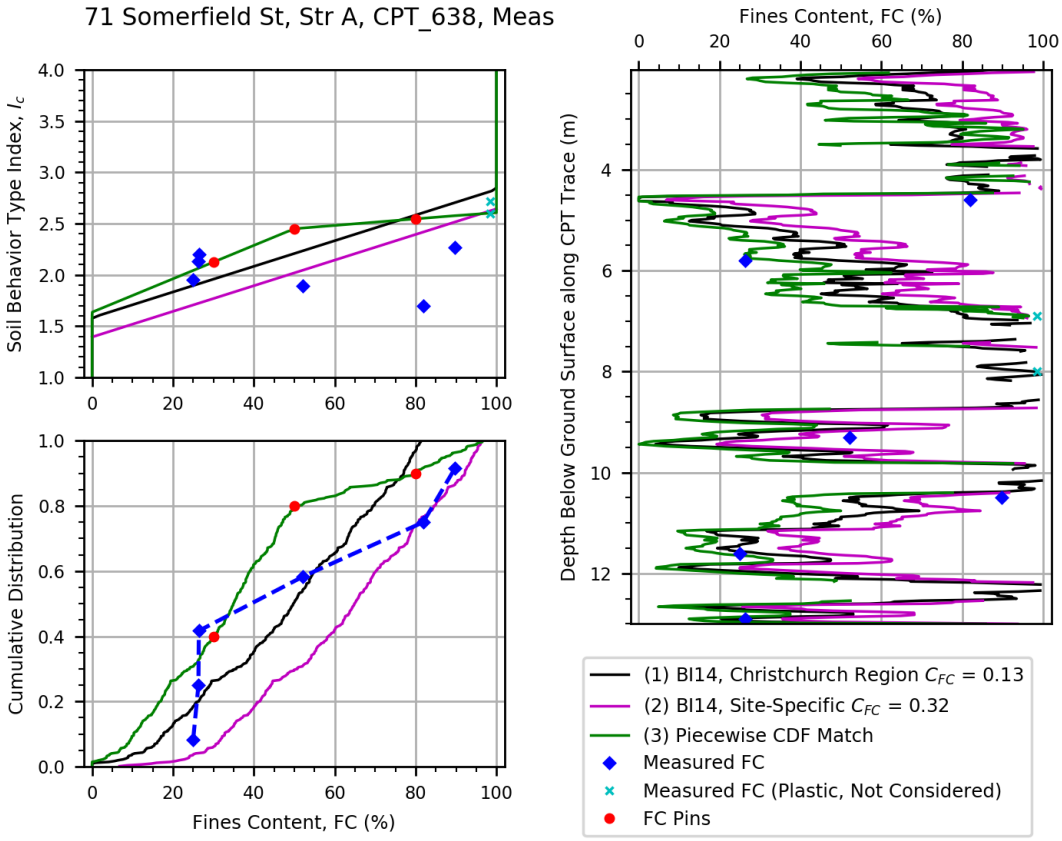
71 Somerfield St, Str A, CPT_638, Meas
Soil Behavior Type Index, I_c
Cumulative Distribution
Fines Content, FC (%)
Fines Content, FC (%)
Depth Below Ground Surface along CPT Trace (m)
(1) BI14, Christchurch Region C_{FC} = 0.13
(2) BI14, Site-Specific C_{FC} = 0.32
(3) Piecewise CDF Match
Measured FC
Measured FC (Plastic, Not Considered)
FC Pins

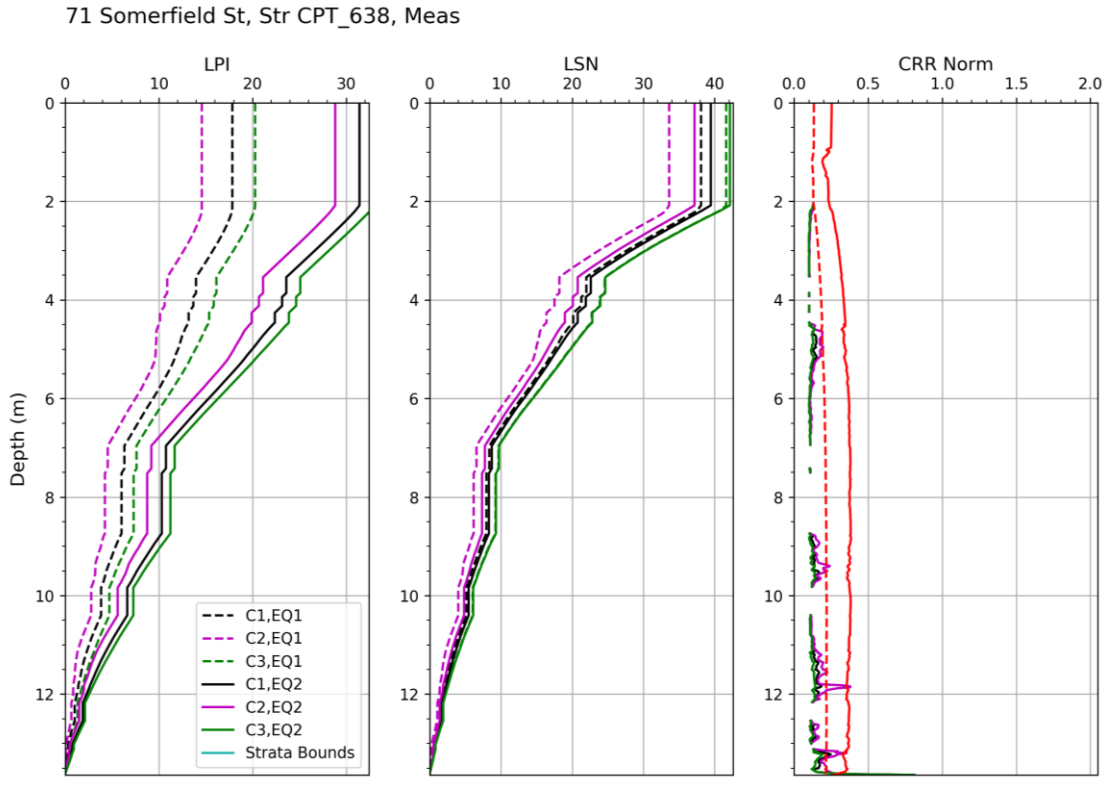
71 Somerfield St, Str CPT_638, Meas
LPI
LSN
CRR Norm
Depth (m)
C1,EQ1
C2,EQ1
C3,EQ1
C1,EQ2
C2,EQ2
C3,EQ2
Strata Bounds

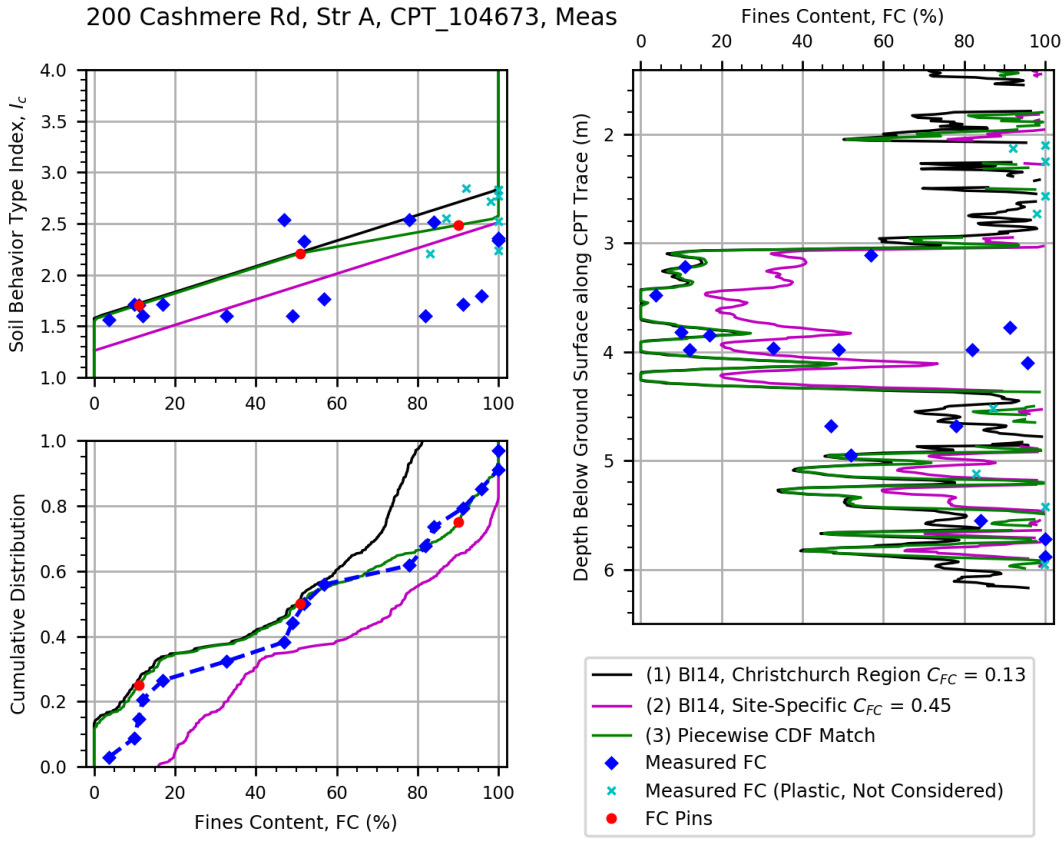
200 Cashmere Rd, Str A, CPT_104673, Meas
Soil Behavior Type Index, I_c
Cumulative Distribution
Fines Content, FC (%)
Fines Content, FC (%)
Depth Below Ground Surface along CPT Trace (m)
(1) BI14, Christchurch Region C_{FC} = 0.13
(2) BI14, Site-Specific C_{FC} = 0.45
(3) Piecewise CDF Match
Measured FC
Measured FC (Plastic, Not Considered)
FC Pins

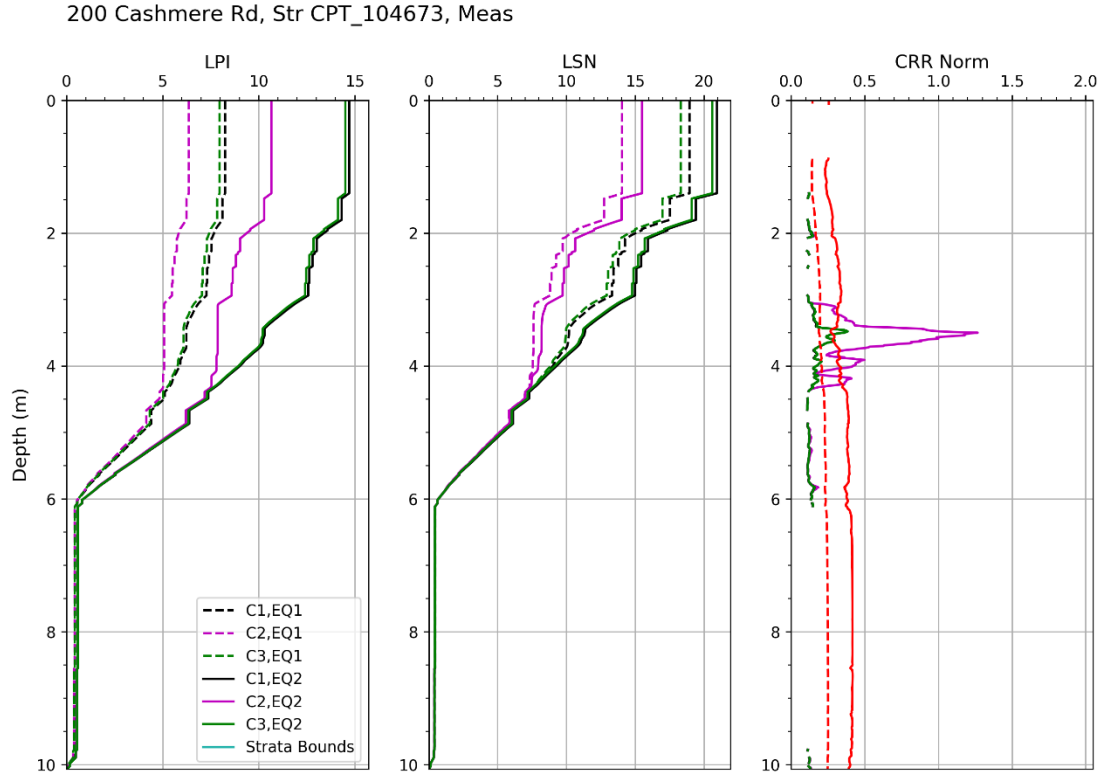
200 Cashmere Rd, Str CPT_104673, Meas
LPI
LSN
CRR Norm
Depth (m)
C1,EQ1
C2,EQ1
C3,EQ1
C1,EQ2
C2,EQ2
C3,EQ2
Strata Bounds

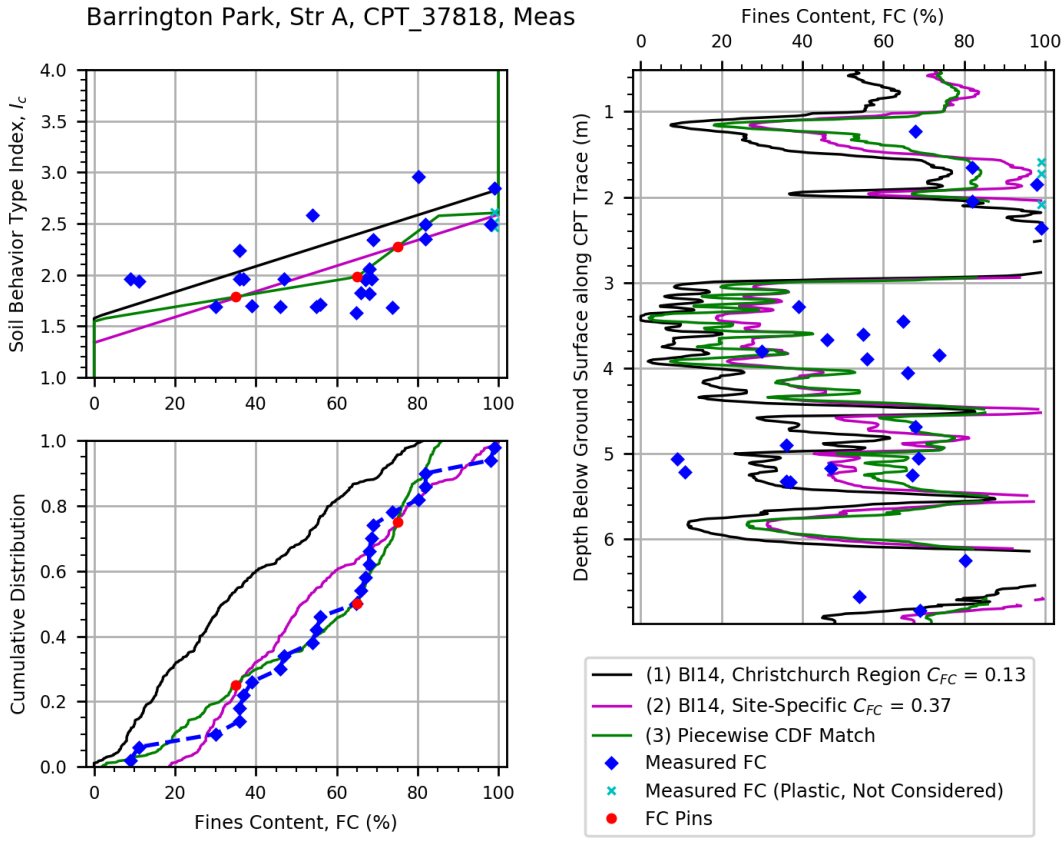
Barrington Park, Str A, CPT_37818, Meas
Soil Behavior Type Index, I_c
Cumulative Distribution
Fines Content, FC (%)
Fines Content, FC (%)
Depth Below Ground Surface along CPT Trace (m)
(1) BI14, Christchurch Region C_{FC} = 0.13
(2) BI14, Site-Specific C_{FC} = 0.37
(3) Piecewise CDF Match
Measured FC
Measured FC (Plastic, Not Considered)
FC Pins

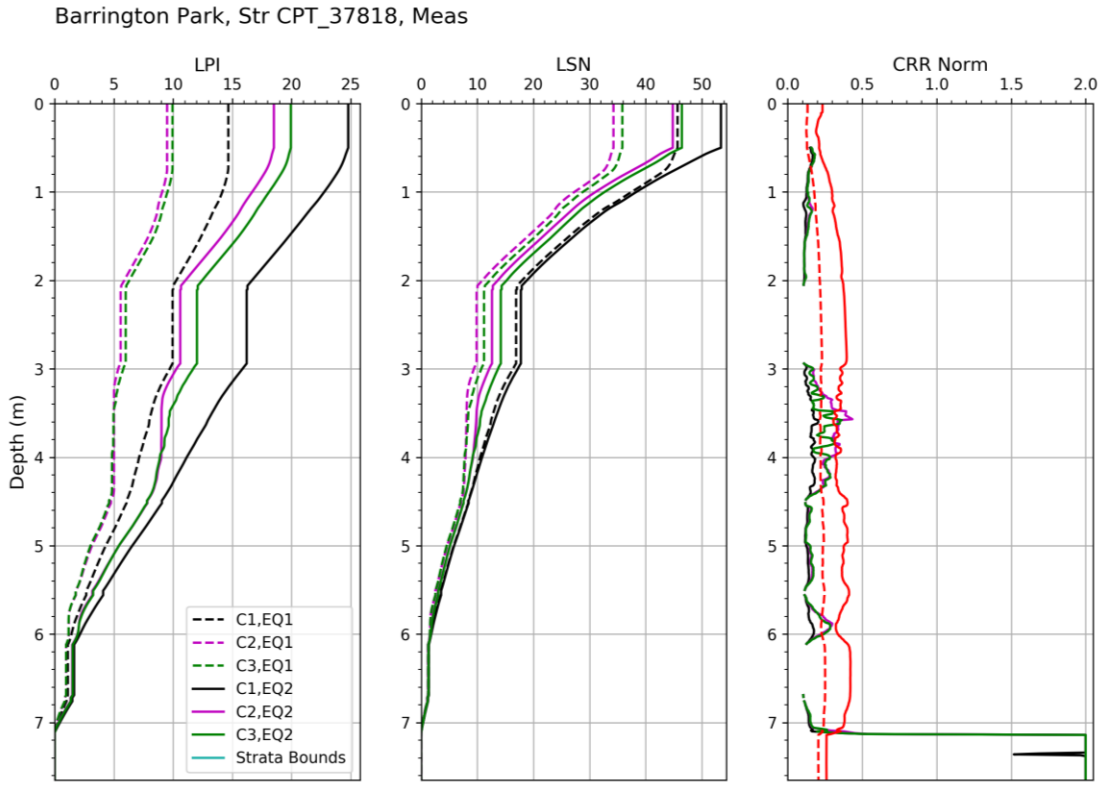
Barrington Park, Str CPT_37818, Meas
LPI
LSN
CRR Norm
Depth (m)
C1,EQ1
C2,EQ1
C3,EQ1
C1,EQ2
C2,EQ2
C3,EQ2
Strata Bounds

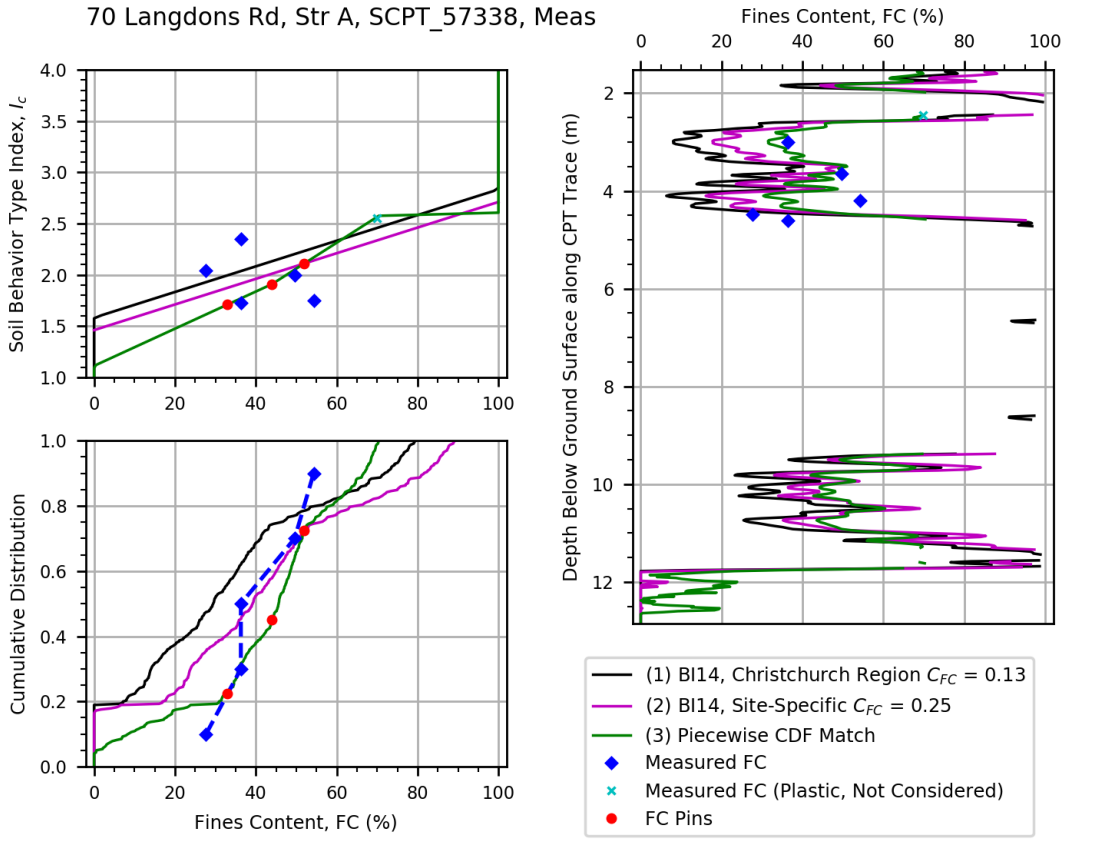
70 Langdons Rd, Str A, SCPT_57338, Meas
Soil Behavior Type Index, I_c
Cumulative Distribution
Fines Content, FC (%)
Fines Content, FC (%)
Depth Below Ground Surface along CPT Trace (m)
(1) BI14, Christchurch Region C_{FC} = 0.13
(2) BI14, Site-Specific C_{FC} = 0.25
(3) Piecewise CDF Match
Measured FC
Measured FC (Plastic, Not Considered)
FC Pins

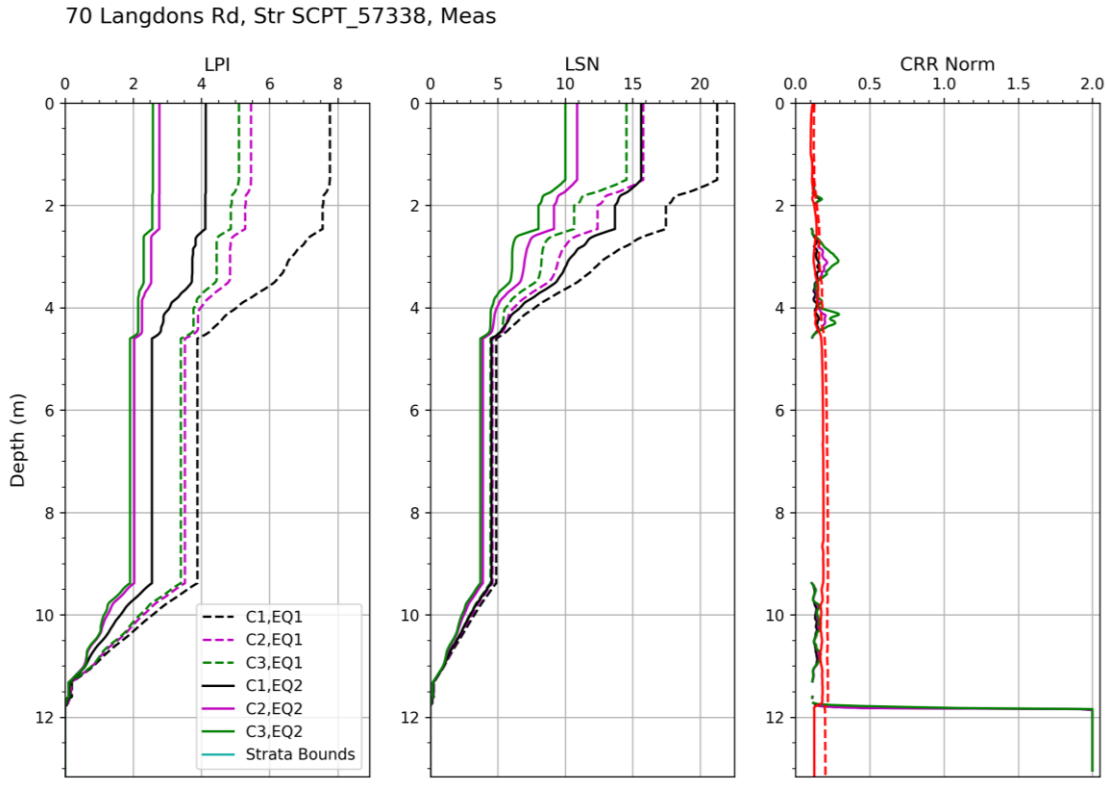
70 Langdons Rd, Str SCPT_57338, Meas
LPI
LSN
CRR Norm
Depth (m)
C1,EQ1
C2,EQ1
C3,EQ1
C1,EQ2
C2,EQ2
C3,EQ2
Strata Bounds

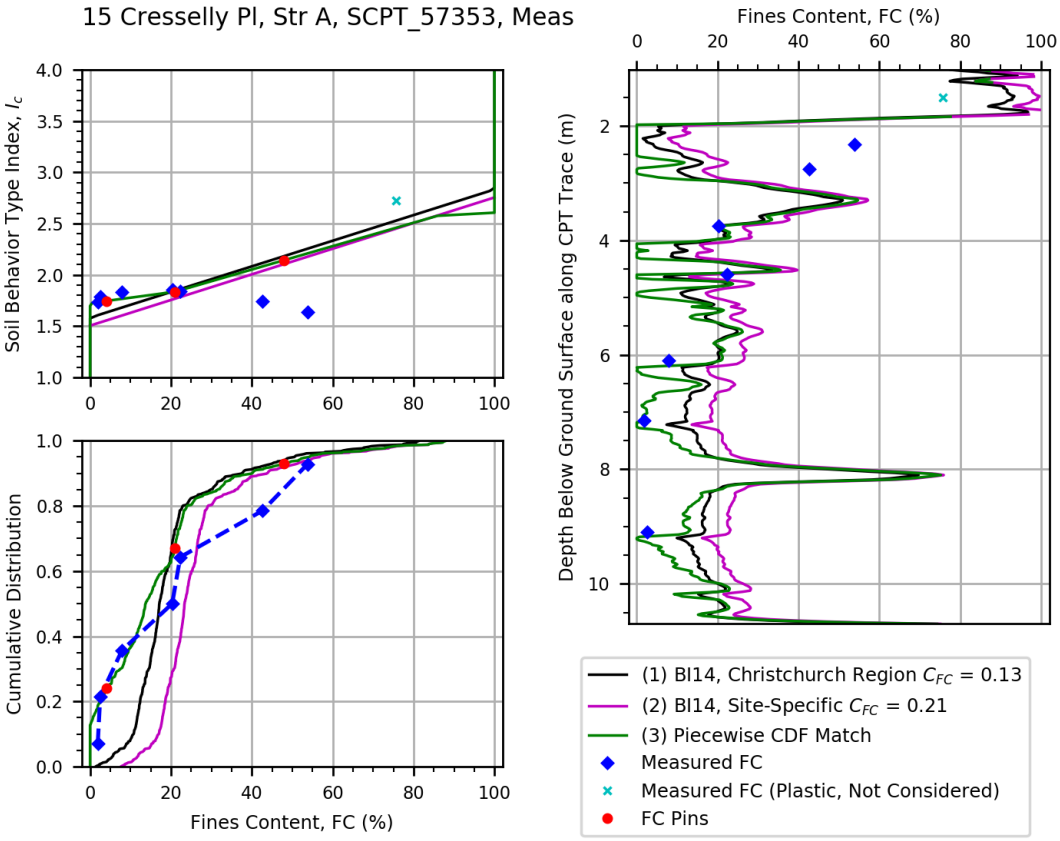
15 Cresselly Pl, Str A, SCPT_57353, Meas
Soil Behavior Type Index, I_c
Cumulative Distribution
Fines Content, FC (%)
Fines Content, FC (%)
Depth Below Ground Surface along CPT Trace (m)
(1) BI14, Christchurch Region C_{FC} = 0.13
(2) BI14, Site-Specific C_{FC} = 0.21
(3) Piecewise CDF Match
Measured FC
Measured FC (Plastic, Not Considered)
FC Pins

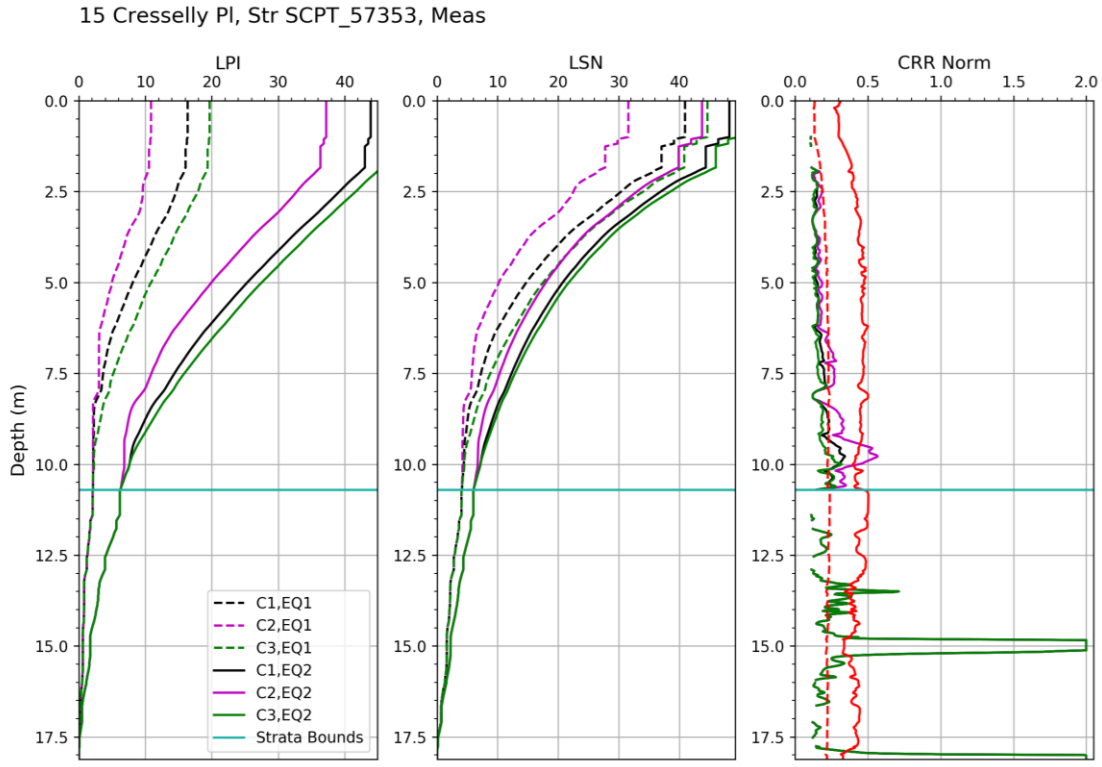
15 Cresselly Pl, Str SCPT_57353, Meas
LPI
LSN
CRR Norm
Depth (m)
C1,EQ1
C2,EQ1
C3,EQ1
C1,EQ2
C2,EQ2
C3,EQ2
Strata Bounds

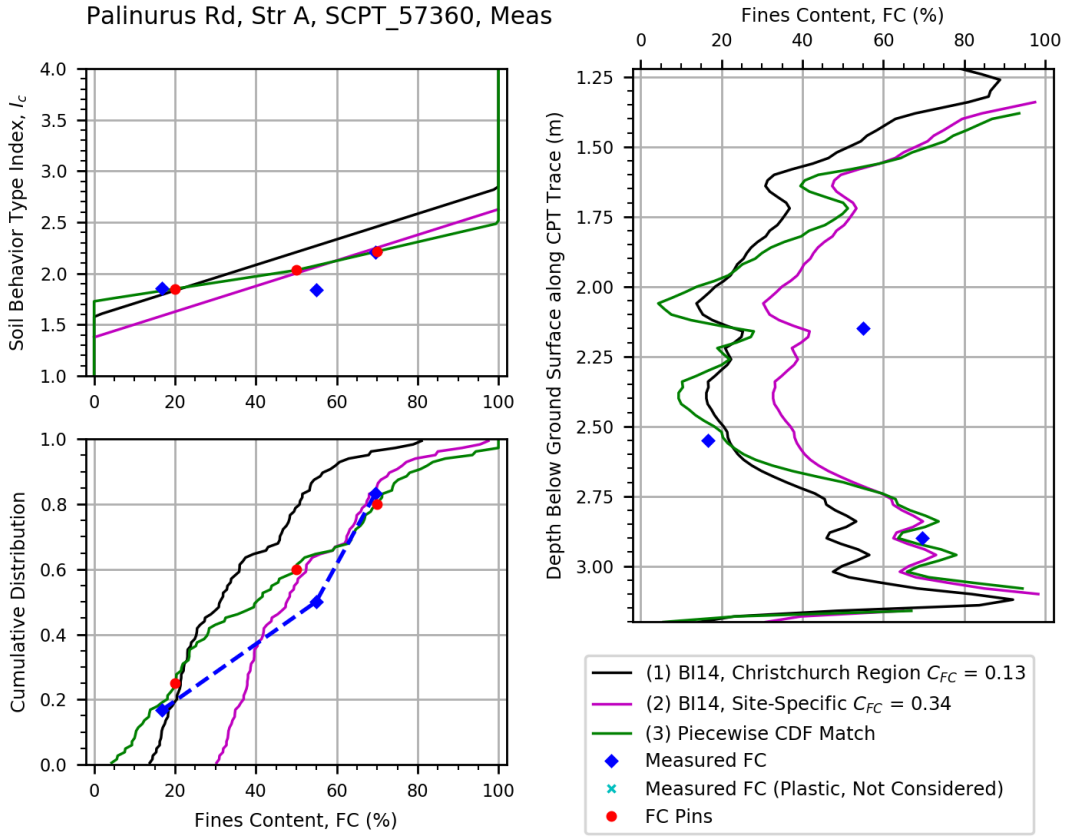
Palinurus Rd, Str A, SCPT_57360, Meas
Soil Behavior Type Index, I_c
Cumulative Distribution
Fines Content, FC (%)
Fines Content, FC (%)
Depth Below Ground Surface along CPT Trace (m)
(1) BI14, Christchurch Region C_{FC} = 0.13
(2) BI14, Site-Specific C_{FC} = 0.34
(3) Piecewise CDF Match
Measured FC
Measured FC (Plastic, Not Considered)
FC Pins

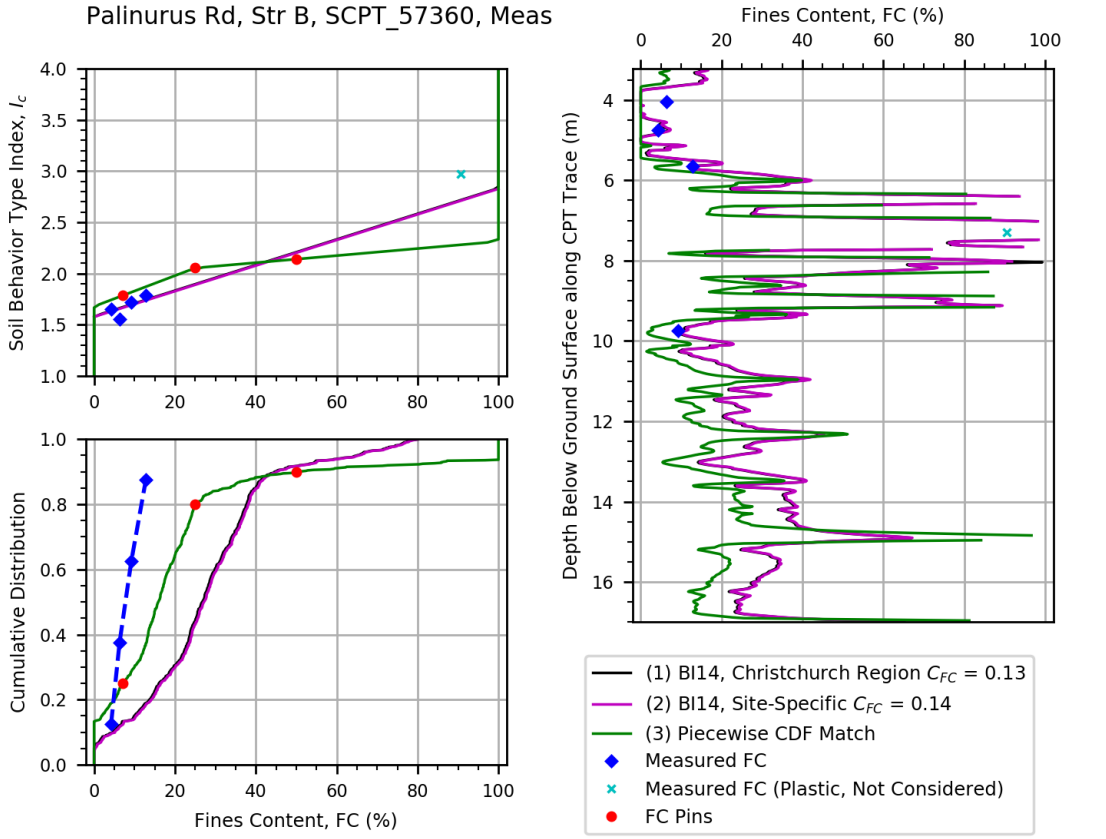
Palinurus Rd, Str B, SCPT_57360, Meas
Soil Behavior Type Index, I_c
Cumulative Distribution
Fines Content, FC (%)
Fines Content, FC (%)
Depth Below Ground Surface along CPT Trace (m)
(1) BI14, Christchurch Region C_{FC} = 0.13
(2) BI14, Site-Specific C_{FC} = 0.14
(3) Piecewise CDF Match
Measured FC
Measured FC (Plastic, Not Considered)
FC Pins

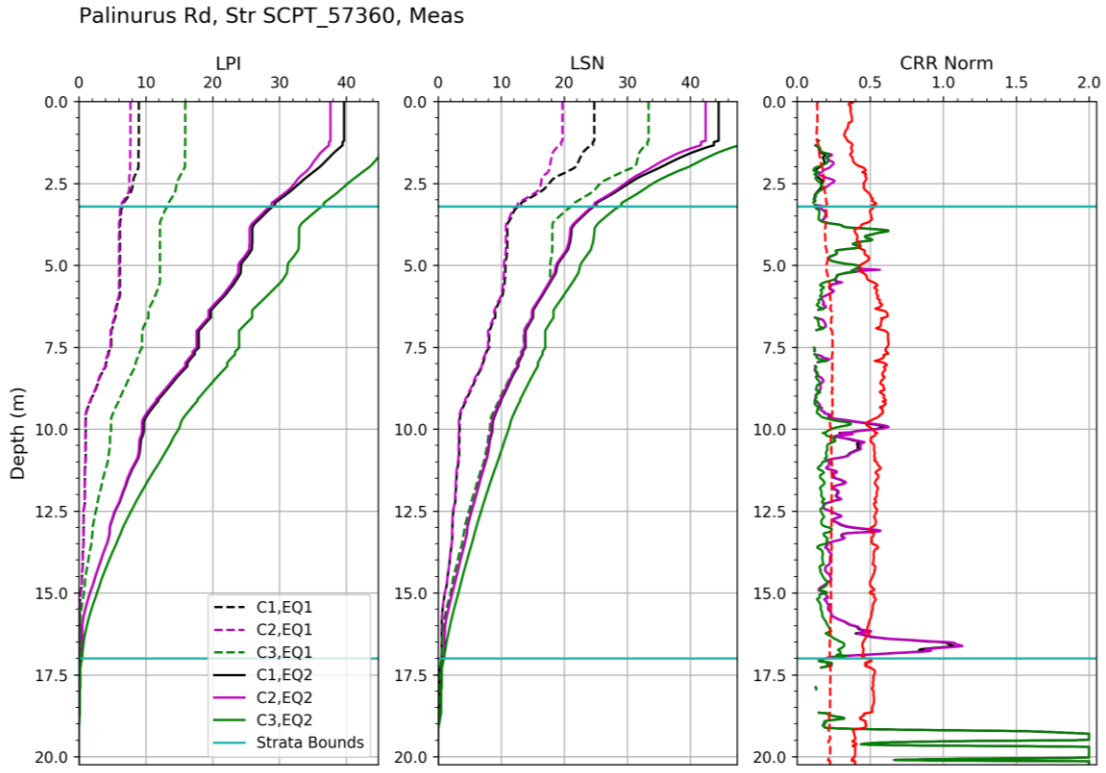
Palinurus Rd, Str SCPT_57360, Meas
LPI
LSN
CRR Norm
Depth (m)
C1,EQ1
C2,EQ1
C3,EQ1
C1,EQ2
C2,EQ2
C3,EQ2
Strata Bounds

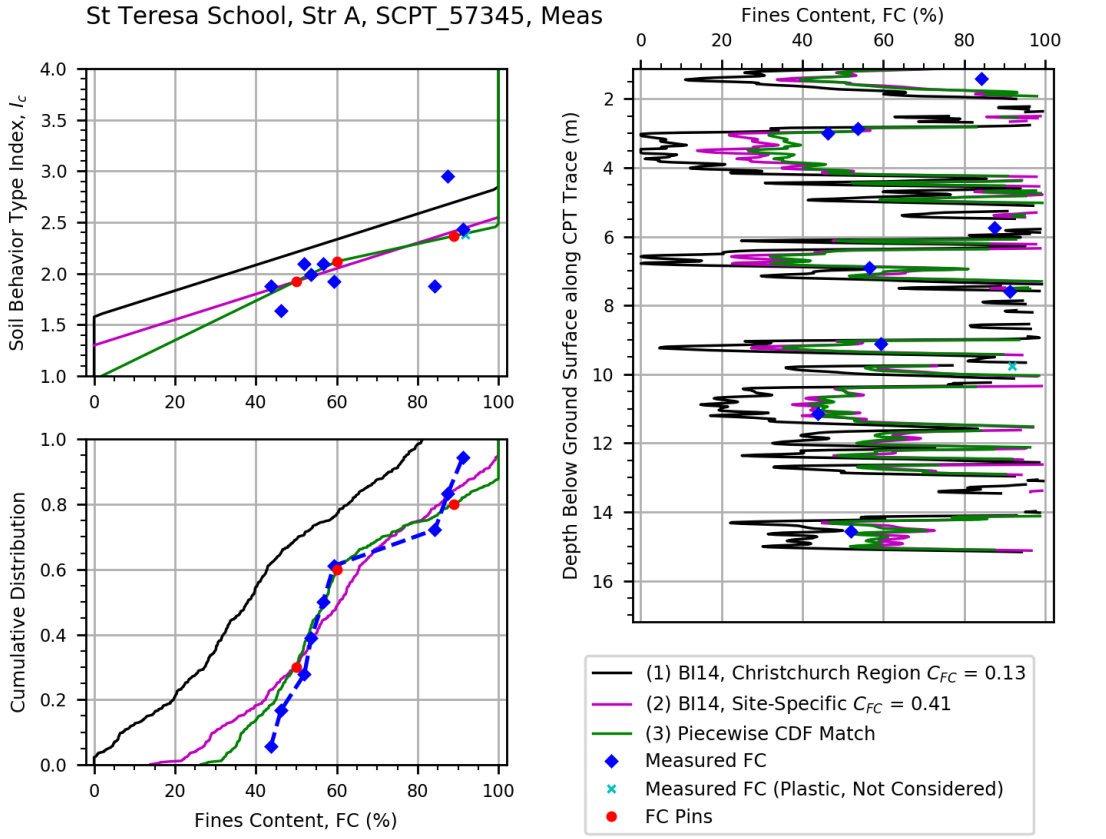
St Teresa School, Str A, SCPT_57345, Meas
Soil Behavior Type Index, I_c
Cumulative Distribution
Fines Content, FC (%)
Fines Content, FC (%)
Depth Below Ground Surface along CPT Trace (m)
(1) BI14, Christchurch Region C_{FC} = 0.13
(2) BI14, Site-Specific C_{FC} = 0.41
(3) Piecewise CDF Match
Measured FC
Measured FC (Plastic, Not Considered)
FC Pins

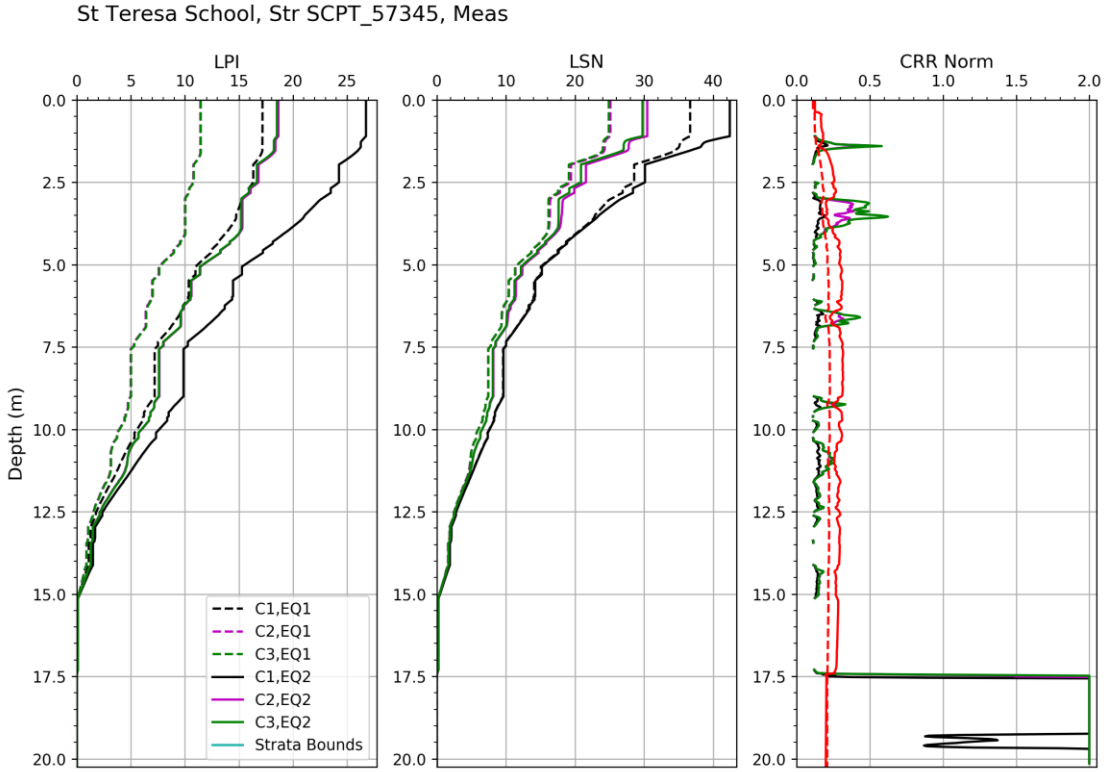
St Teresa School, Str SCPT_57345, Meas
LPI
LSN
CRR Norm
Depth (m)
C1,EQ1
C2,EQ1
C3,EQ1
C1,EQ2
C2,EQ2
C3,EQ2
Strata Bounds

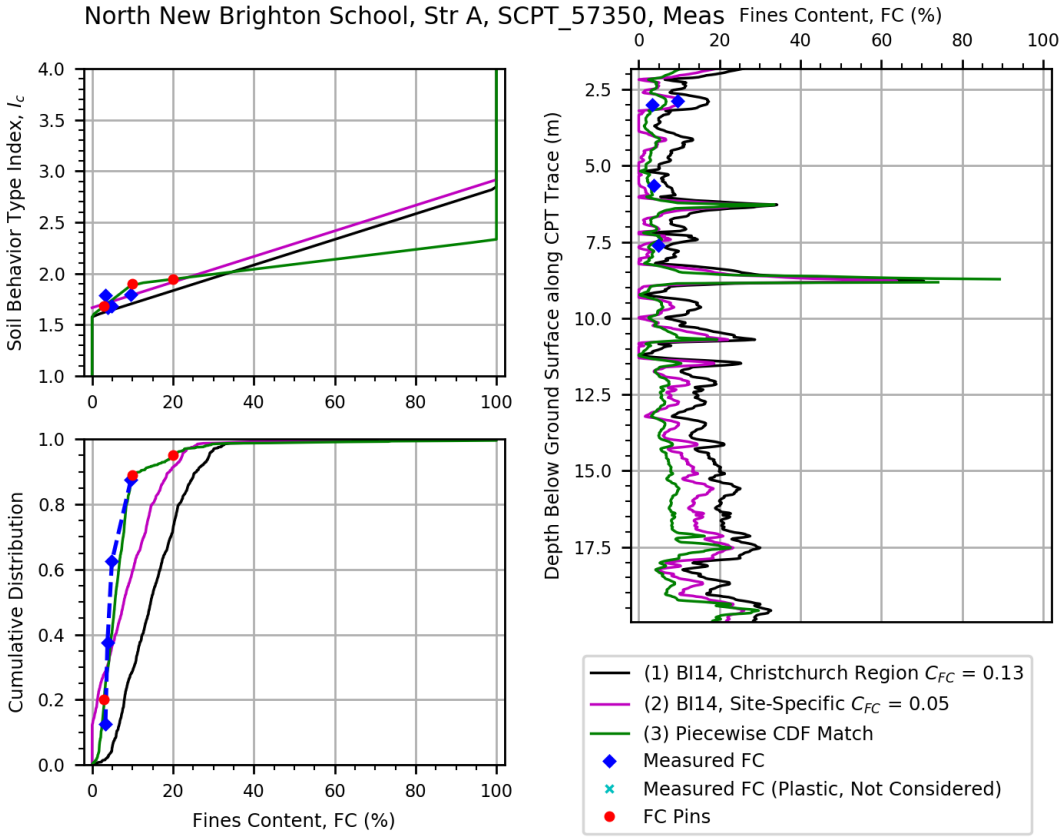
North New Brighton School, Str A, SCPT_57350, Meas
Soil Behavior Type Index, I_c
Cumulative Distribution
Fines Content, FC (%)
Fines Content, FC (%)
Depth Below Ground Surface along CPT Trace (m)
(1) BI14, Christchurch Region C_{FC} = 0.13
(2) BI14, Site-Specific C_{FC} = 0.05
(3) Piecewise CDF Match
Measured FC
Measured FC (Plastic, Not Considered)
FC Pins

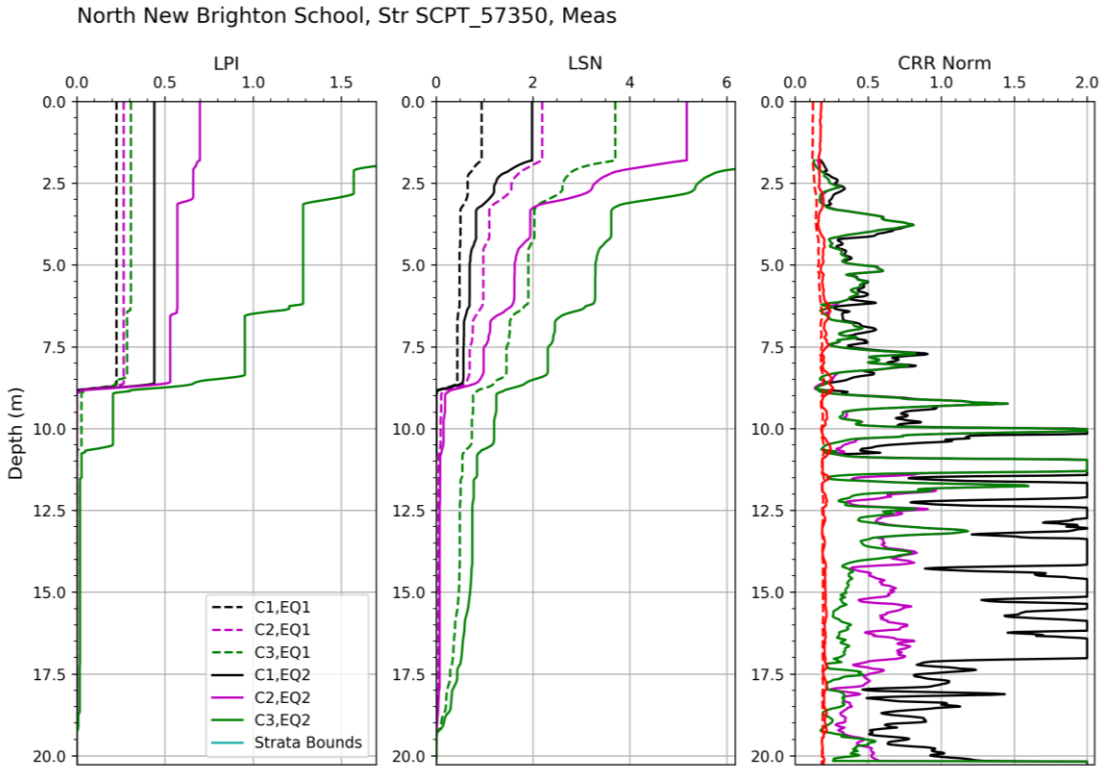
North New Brighton School, Str SCPT_57350, Meas
LPI
LSN
CRR Norm
Depth (m)
C1,EQ1
C2,EQ1
C3,EQ1
C1,EQ2
C2,EQ2
C3,EQ2
Strata Bounds

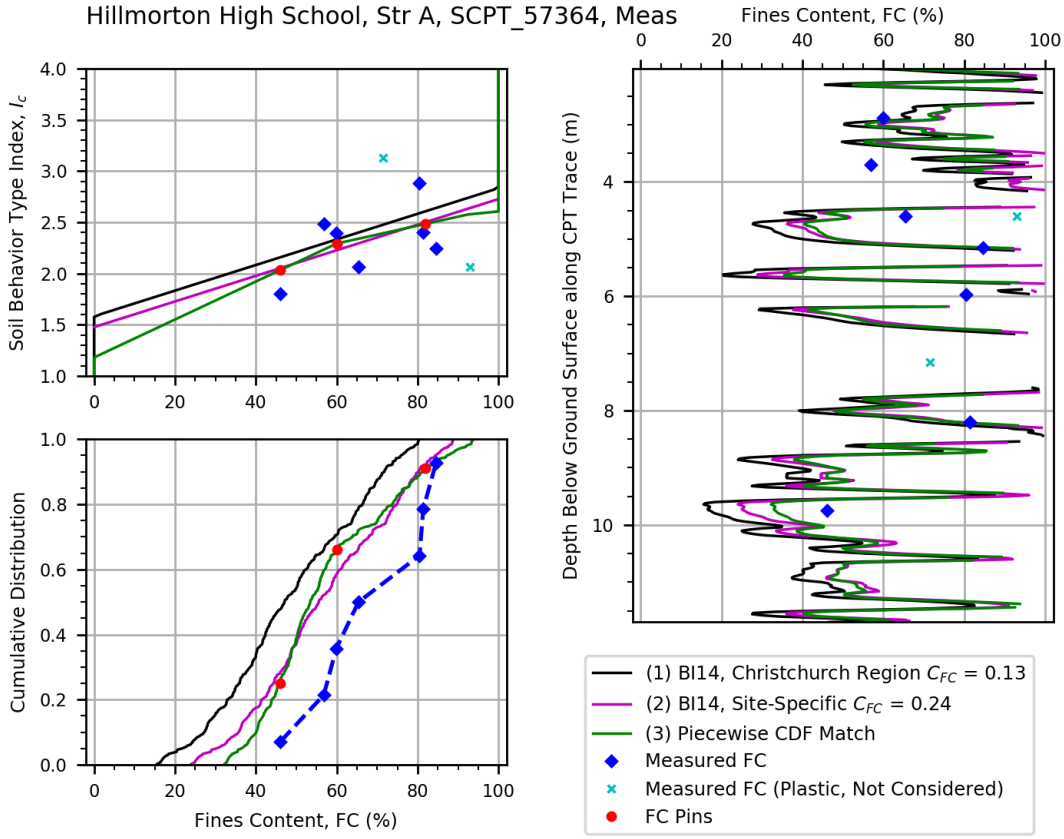
Hillmorton High School, Str A, SCPT_57364, Meas
Soil Behavior Type Index, I_c
Cumulative Distribution
Fines Content, FC (%)
Fines Content, FC (%)
Depth Below Ground Surface along CPT Trace (m)
(1) BI14, Christchurch Region C_{FC} = 0.13
(2) BI14, Site-Specific C_{FC} = 0.24
(3) Piecewise CDF Match
Measured FC
Measured FC (Plastic, Not Considered)
FC Pins

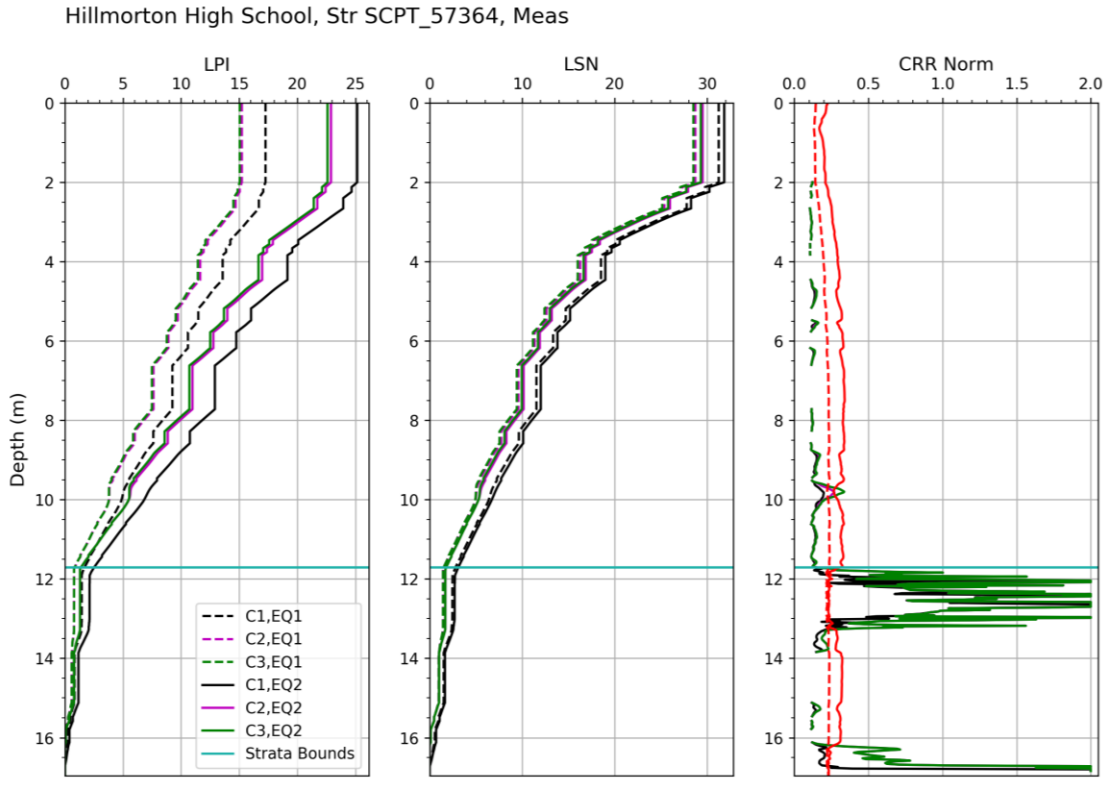
Hillmorton High School, Str SCPT_57364, Meas
LPI
LSN
CRR Norm
Depth (m)
C1,EQ1
C2,EQ1
C3,EQ1
C1,EQ2
C2,EQ2
C3,EQ2
Strata Bounds

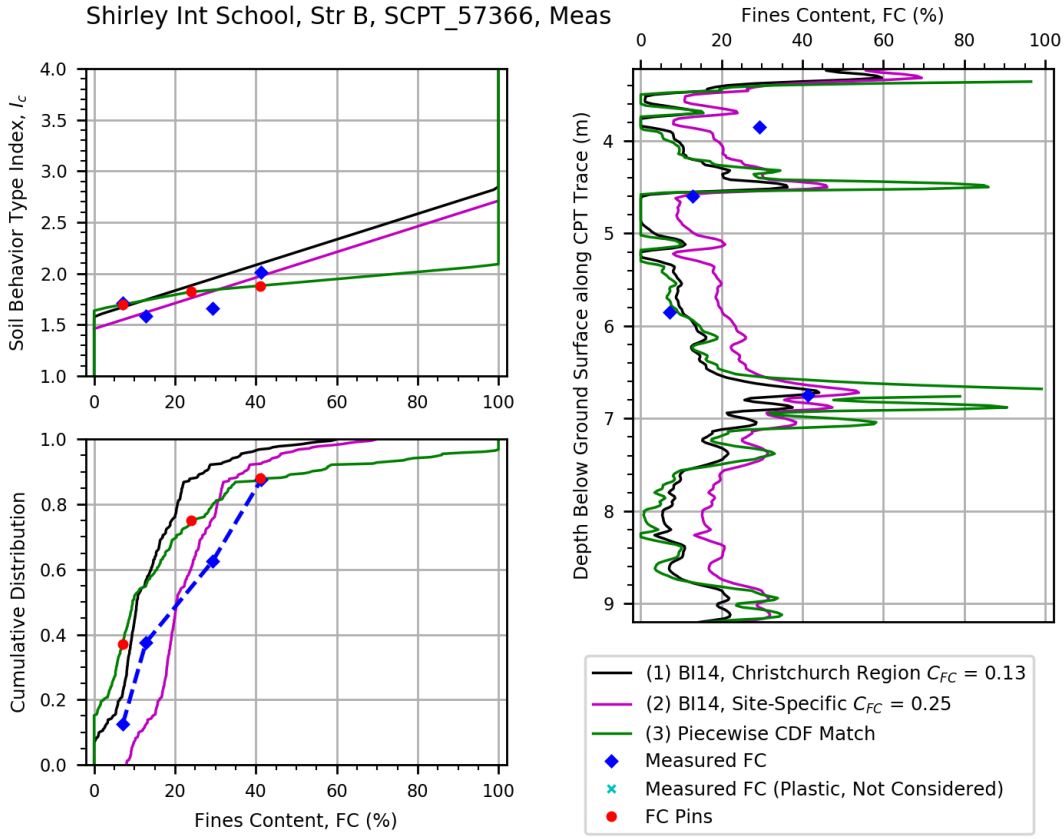
Shirley Int School, Str B, SCPT_57366, Meas
Soil Behavior Type Index, I_c
Cumulative Distribution
Fines Content, FC (%)
Fines Content, FC (%)
Depth Below Ground Surface along CPT Trace (m)
(1) BI14, Christchurch Region C_{FC} = 0.13
(2) BI14, Site-Specific C_{FC} = 0.25
(3) Piecewise CDF Match
Measured FC
Measured FC (Plastic, Not Considered)
FC Pins

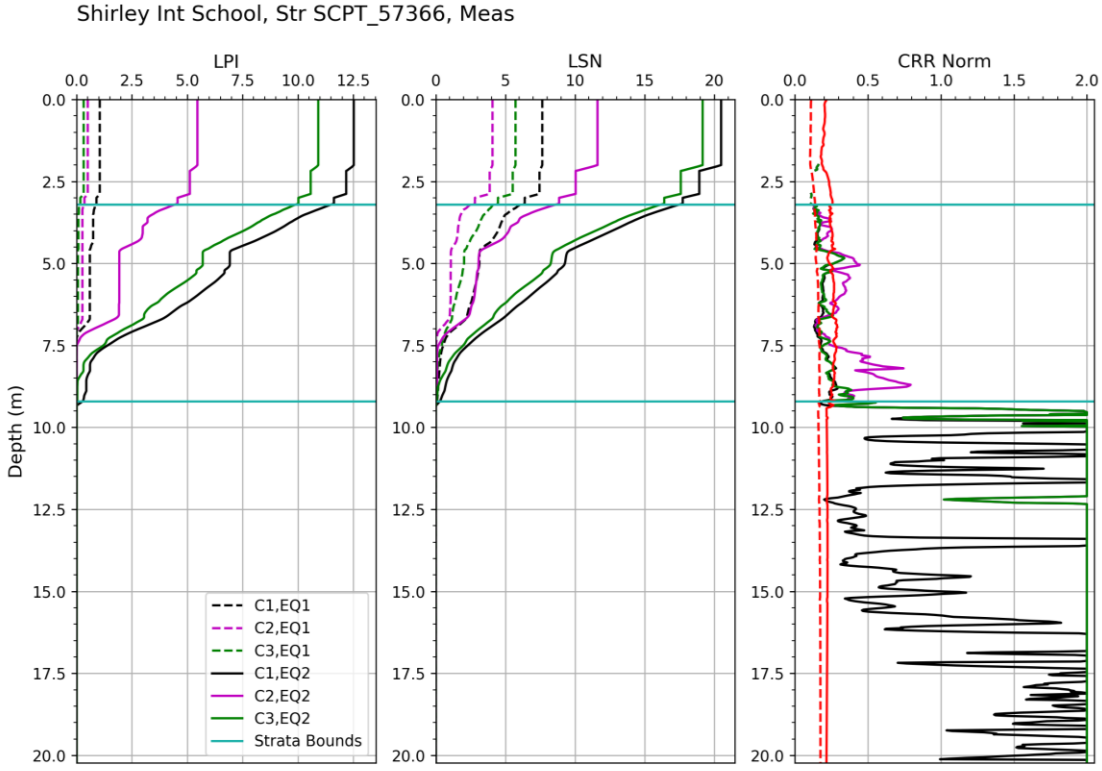
Shirley Int School, Str SCPT_57366, Meas
LPI
LSN
CRR Norm
Depth (m)
C1,EQ1
C2,EQ1
C3,EQ1
C1,EQ2
C2,EQ2
C3,EQ2
Strata Bounds

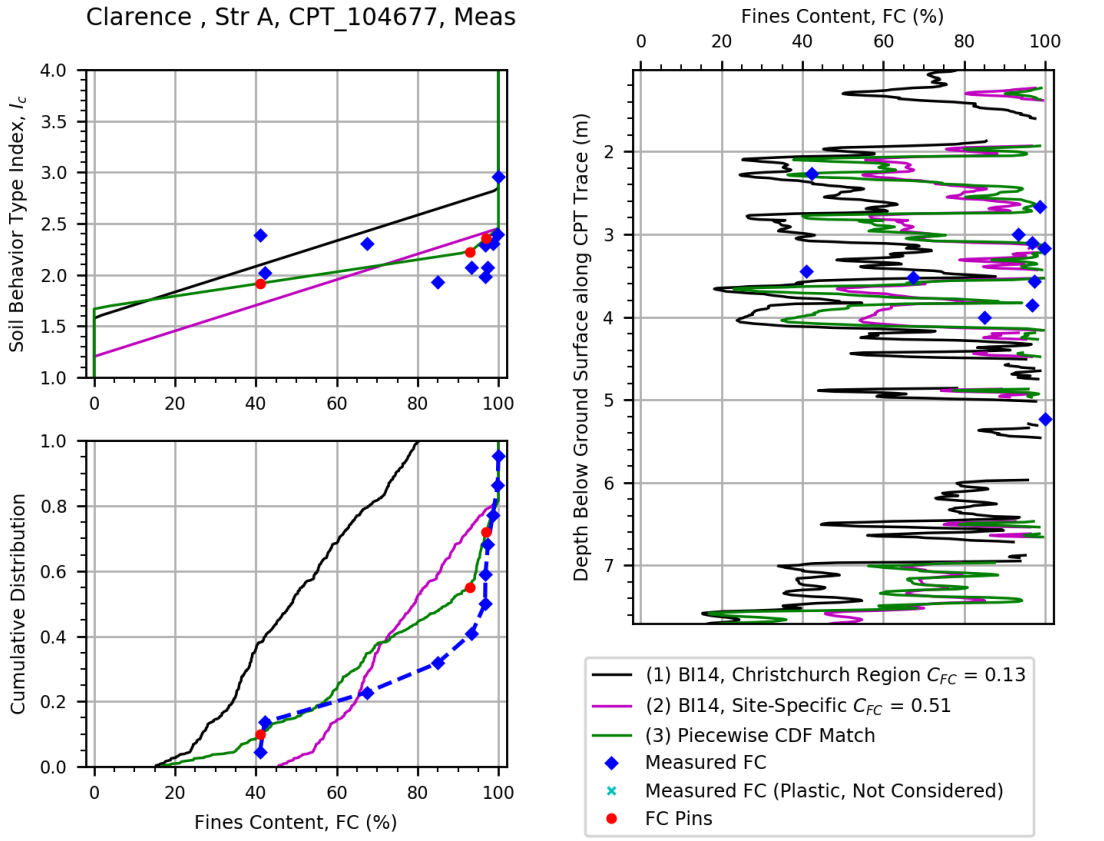
Clarence , Str A, CPT_104677, Meas
Soil Behavior Type Index, I_c
Cumulative Distribution
Fines Content, FC (%)
Fines Content, FC (%)
Depth Below Ground Surface along CPT Trace (m)
(1) BI14, Christchurch Region C_{FC} = 0.13
(2) BI14, Site-Specific C_{FC} = 0.51
(3) Piecewise CDF Match
Measured FC
Measured FC (Plastic, Not Considered)
FC Pins

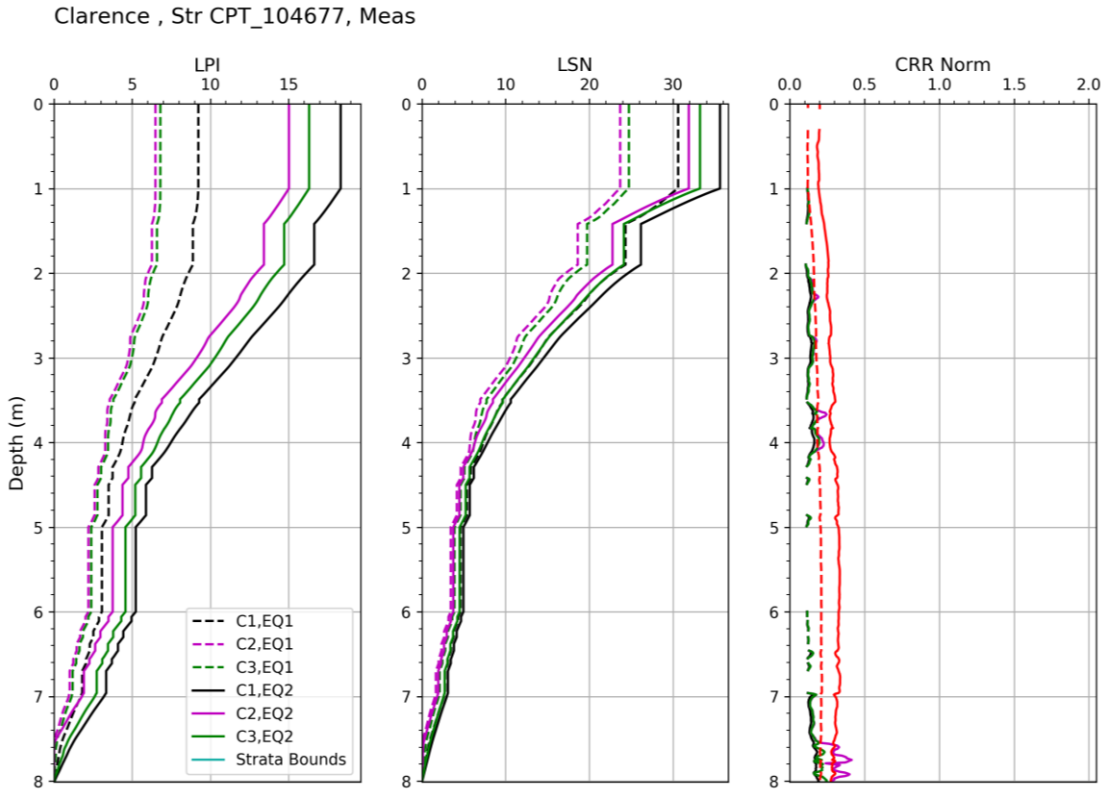
Clarence , Str CPT_104677, Meas
LPI
LSN
CRR Norm
Depth (m)
C1,EQ1
C2,EQ1
C3,EQ1
C1,EQ2
C2,EQ2
C3,EQ2
Strata Bounds

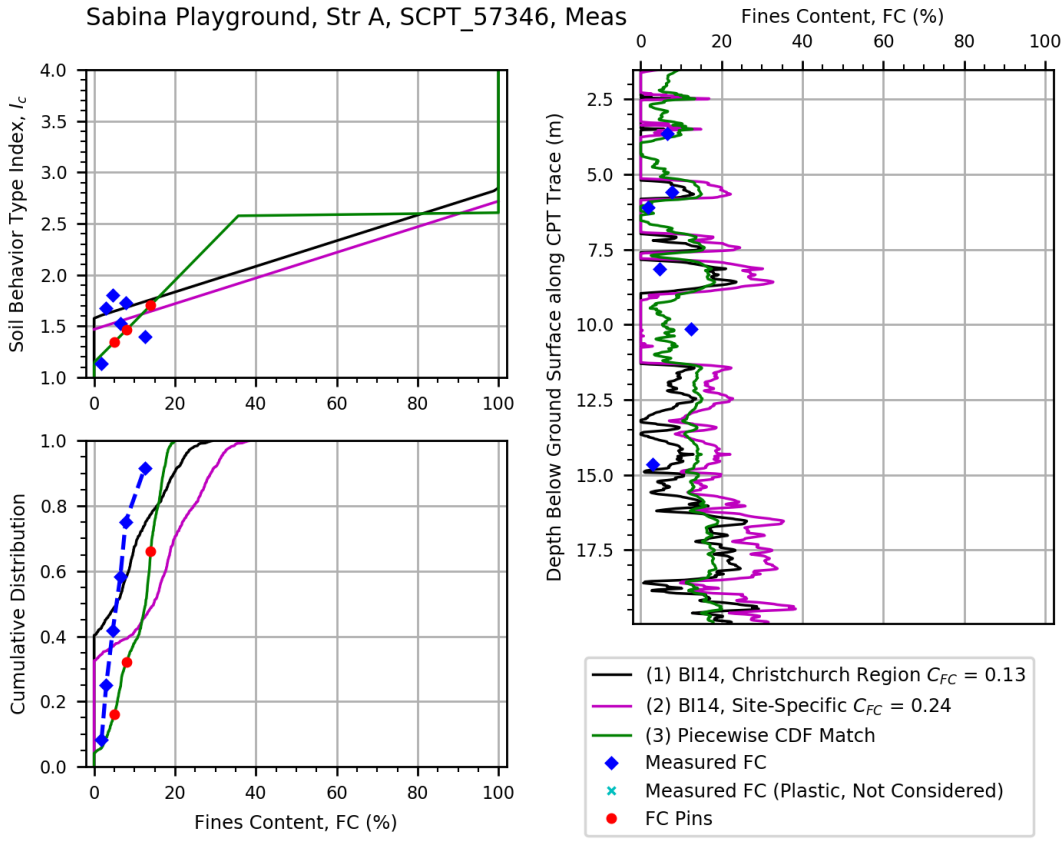
Sabina Playground, Str A, SCPT_57346, Meas
Soil Behavior Type Index, I_c
Cumulative Distribution
Fines Content, FC (%)
Fines Content, FC (%)
Depth Below Ground Surface along CPT Trace (m)
(1) BI14, Christchurch Region C_{FC} = 0.13
(2) BI14, Site-Specific C_{FC} = 0.24
(3) Piecewise CDF Match
Measured FC
Measured FC (Plastic, Not Considered)
FC Pins

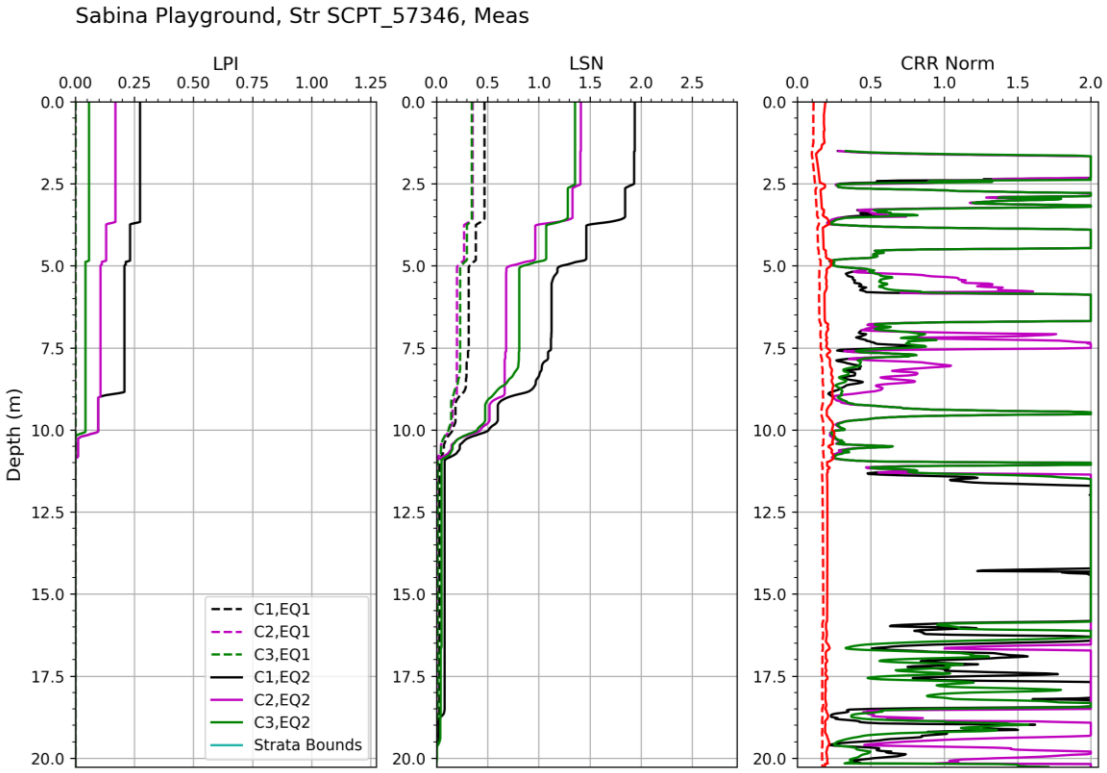
Sabina Playground, Str SCPT_57346, Meas
LPI
LSN
CRR Norm
Depth (m)
C1,EQ1
C2,EQ1
C3,EQ1
C1,EQ2
C2,EQ2
C3,EQ2
Strata Bounds

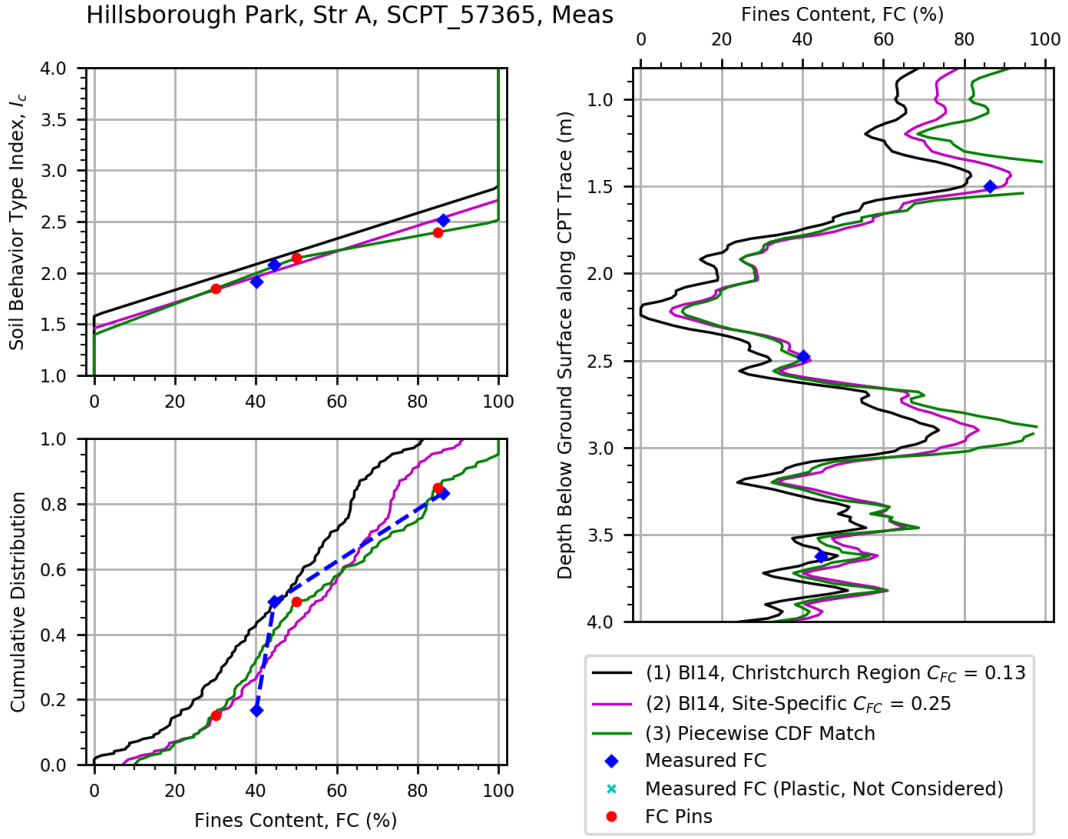
Hillsborough Park, Str A, SCPT_57365, Meas
Soil Behavior Type Index, I_c
Cumulative Distribution
Fines Content, FC (%)
Fines Content, FC (%)
Depth Below Ground Surface along CPT Trace (m)
(1) BI14, Christchurch Region C_{FC} = 0.13
(2) BI14, Site-Specific C_{FC} = 0.25
(3) Piecewise CDF Match
Measured FC
Measured FC (Plastic, Not Considered)
FC Pins

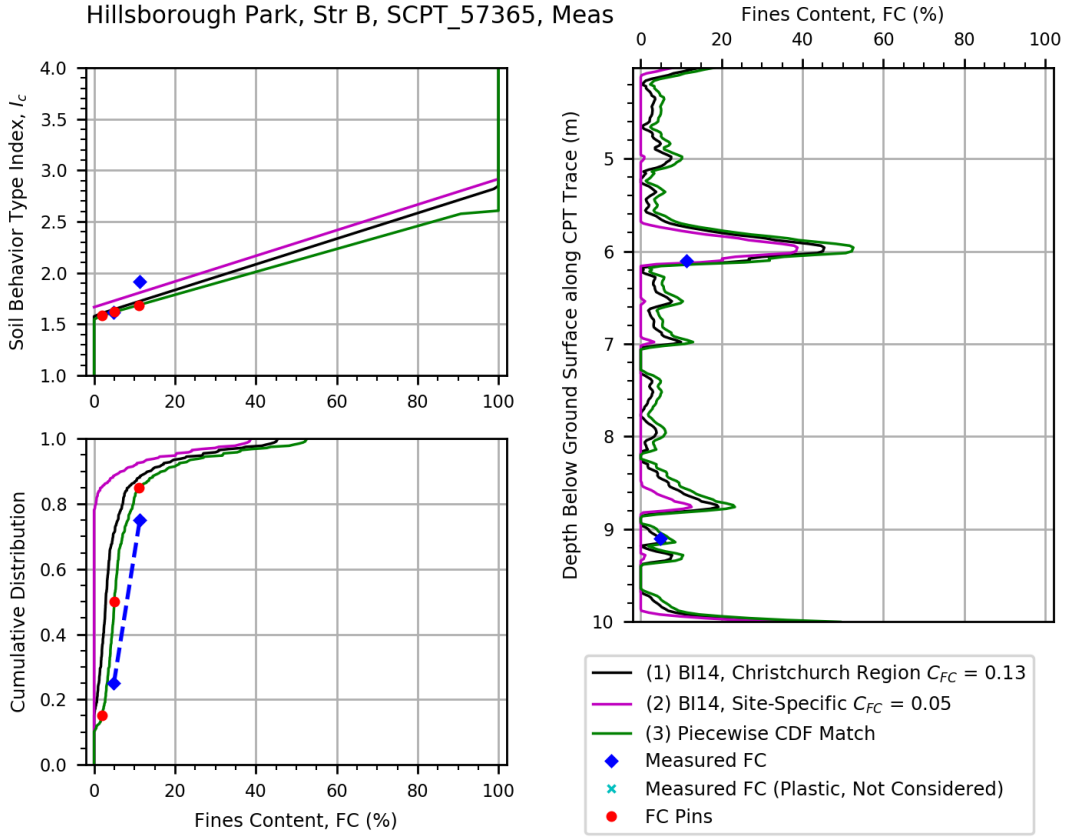
Hillsborough Park, Str B, SCPT_57365, Meas
Soil Behavior Type Index, I_c
Cumulative Distribution
Fines Content, FC (%)
Fines Content, FC (%)
Depth Below Ground Surface along CPT Trace (m)
(1) BI14, Christchurch Region C_{FC} = 0.13
(2) BI14, Site-Specific C_{FC} = 0.05
(3) Piecewise CDF Match
Measured FC
Measured FC (Plastic, Not Considered)
FC Pins

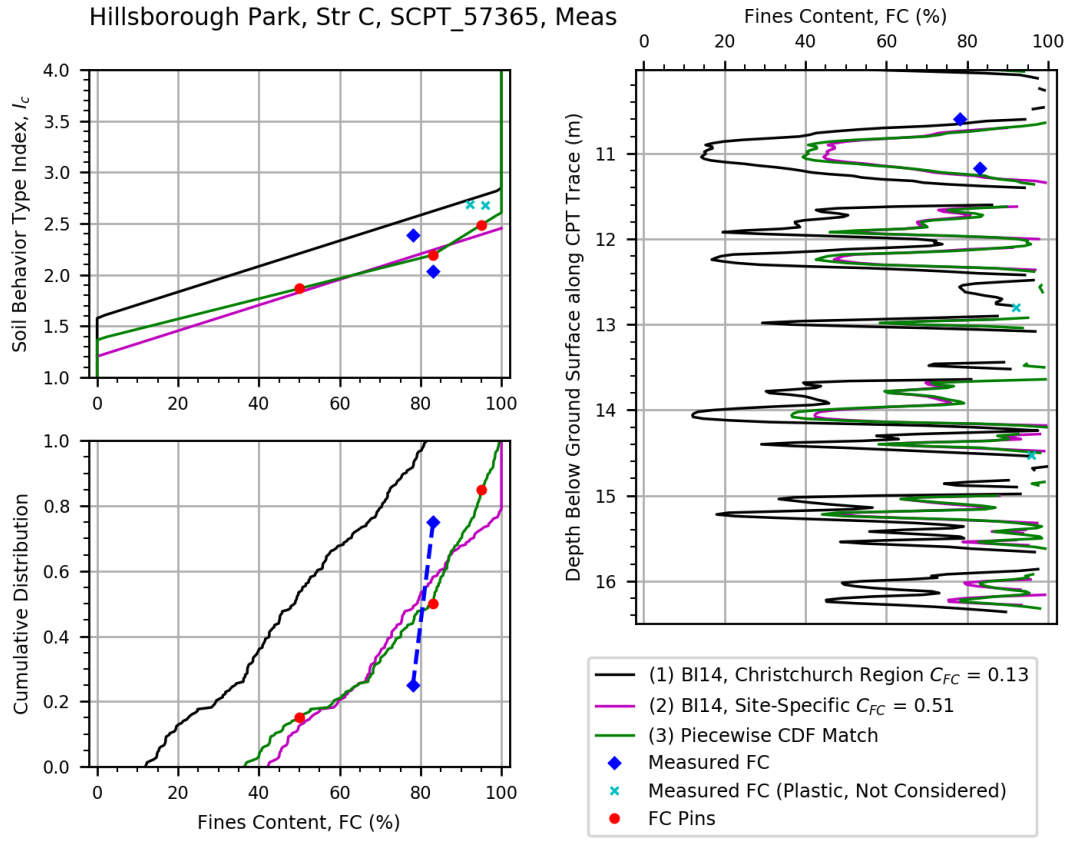
Hillsborough Park, Str C, SCPT_57365, Meas
Soil Behavior Type Index, I_c
Cumulative Distribution
Fines Content, FC (%)
Fines Content, FC (%)
Depth Below Ground Surface along CPT Trace (m)
(1) BI14, Christchurch Region C_{FC} = 0.13
(2) BI14, Site-Specific C_{FC} = 0.51
(3) Piecewise CDF Match
Measured FC
Measured FC (Plastic, Not Considered)
FC Pins

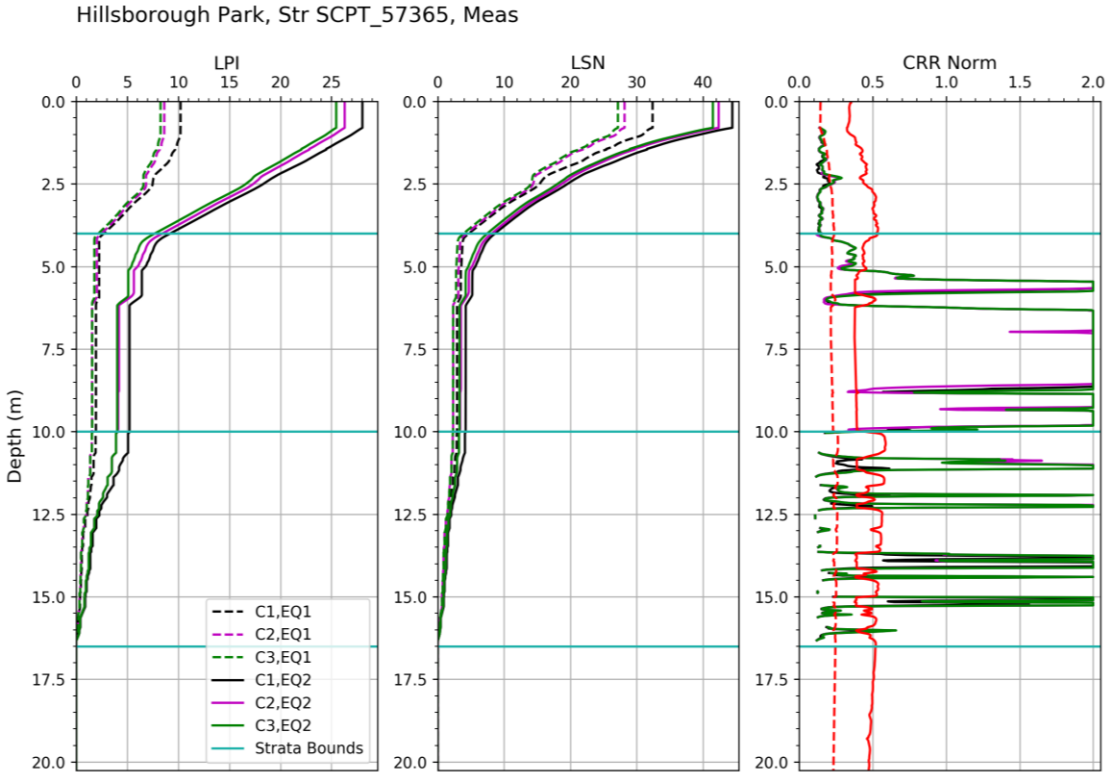
Hillsborough Park, Str SCPT_57365, Meas
LPI
LSN
CRR Norm
Depth (m)
C1,EQ1
C2,EQ1
C3,EQ1
C1,EQ2
C2,EQ2
C3,EQ2
Strata Bounds

Appendix B

Supplementary Material for Chapter 4

(System Response of an Interlayered Deposit with Spatially Distributed Ground Deformations in the Chi-Chi Earthquake)

Supplementary Figures

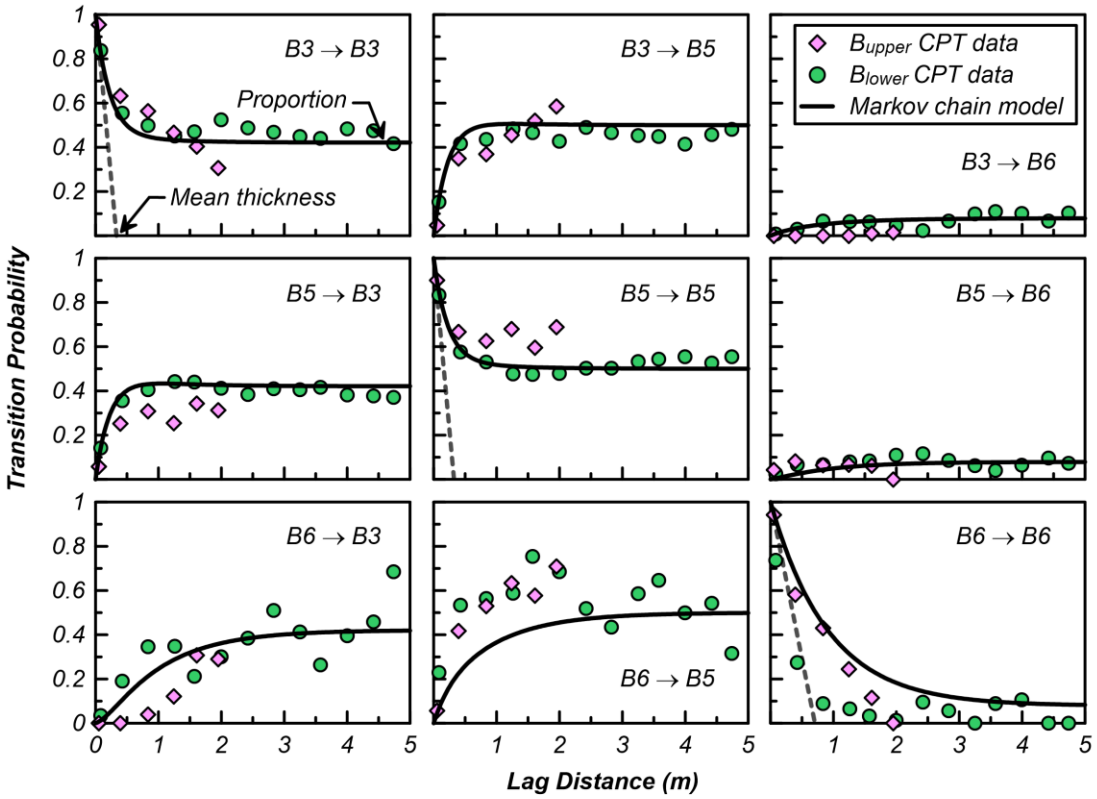

Figure B.1. Vertical upward (-z direction) transiograms depicting measured CPT data and Markov chain models used for T-PROGS simulations for Wufeng Site C stratum B. Note: each data point represents a 40 cm lag interval for the measured CPT data within the indicated portion of the stratum (i.e., B_{upper} and B_{lower}, above and below 5 m, respectively).

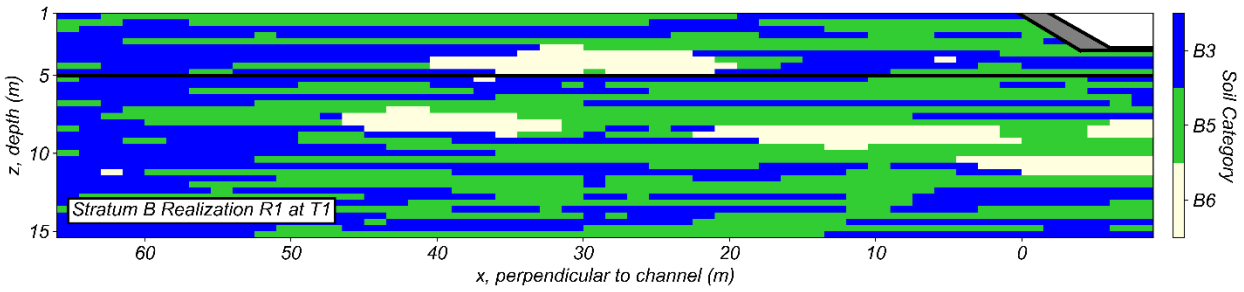

(a)

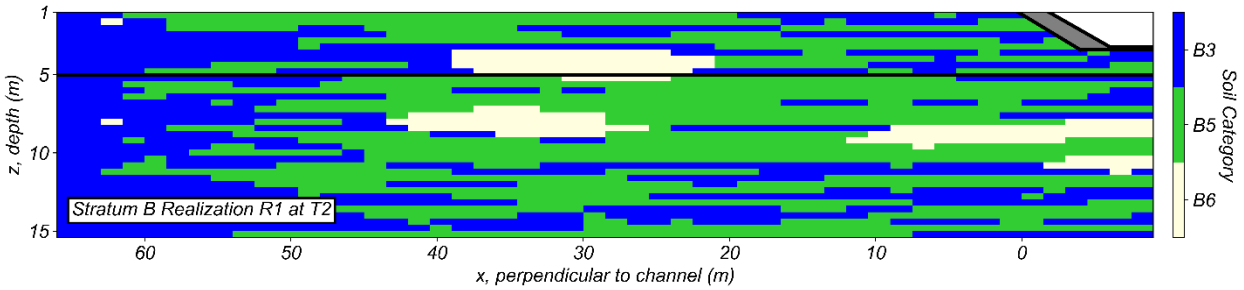

(b)

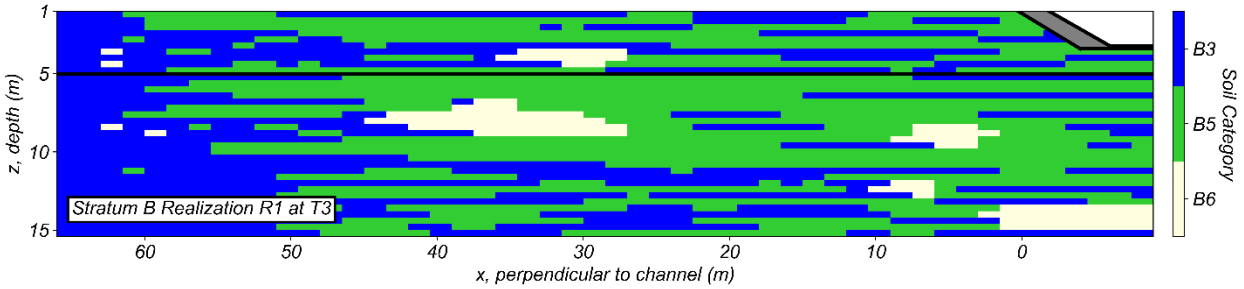

(c)

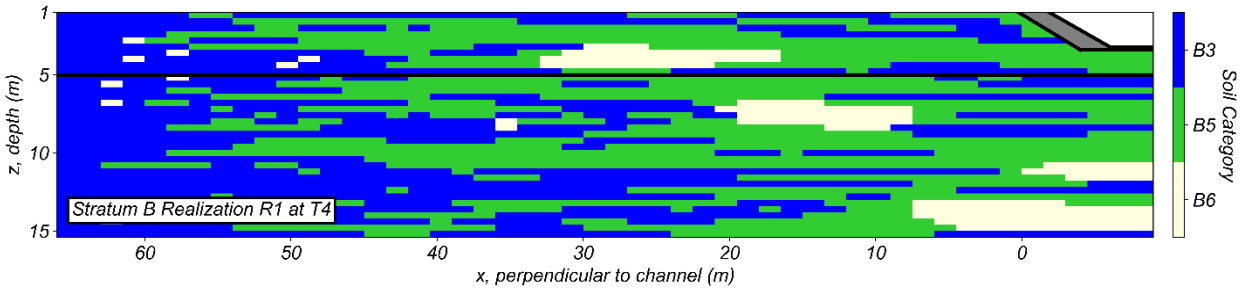

(d)

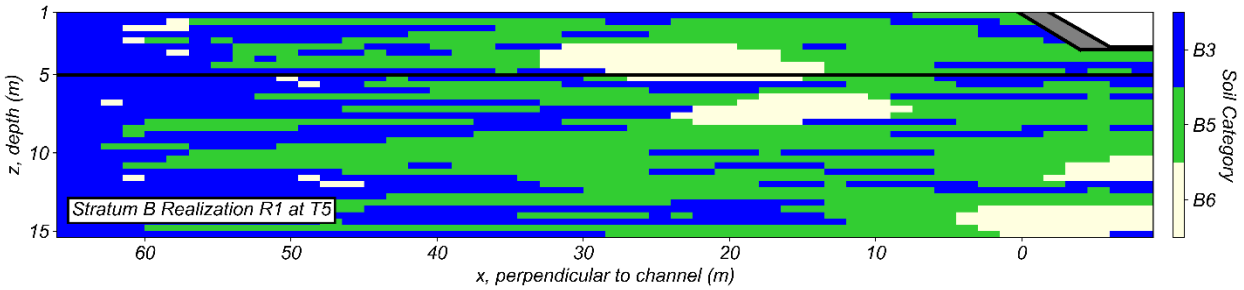

(e)

Figure B.2. Geostatistical realization R1 of stratum B from the baseline T-PROGS simulation for five transects located at (a) T1 (y =42.5 m), (b) T2 (y =32.5 m; baseline), (c) T3 (y =22.5 m), (d) T4 (y =12.5 m), and (e) T5 (y =2.5 m).

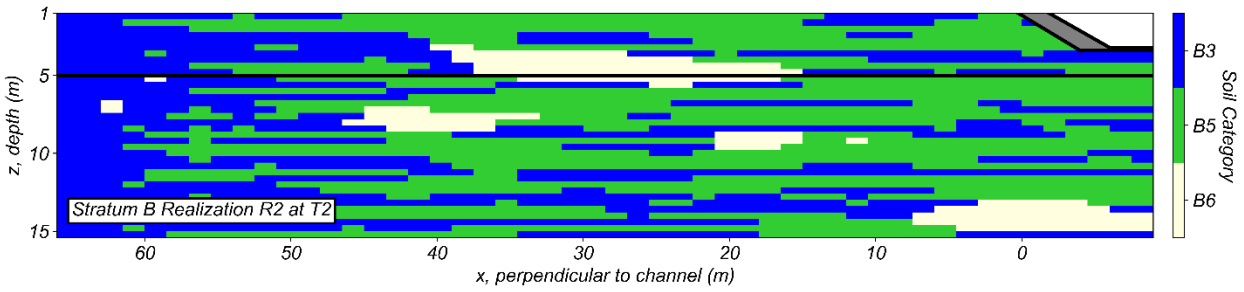

(a)

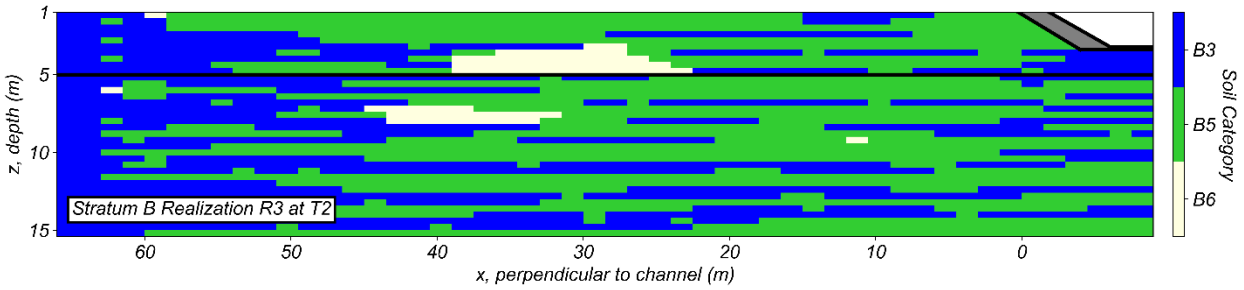

(b)

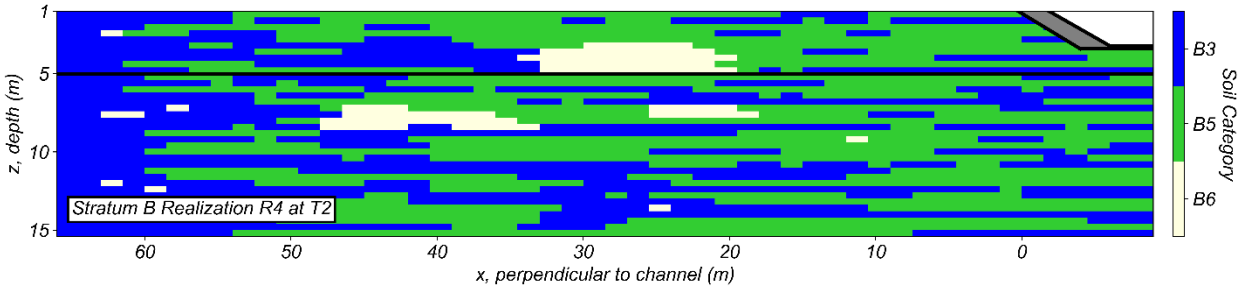

(c)

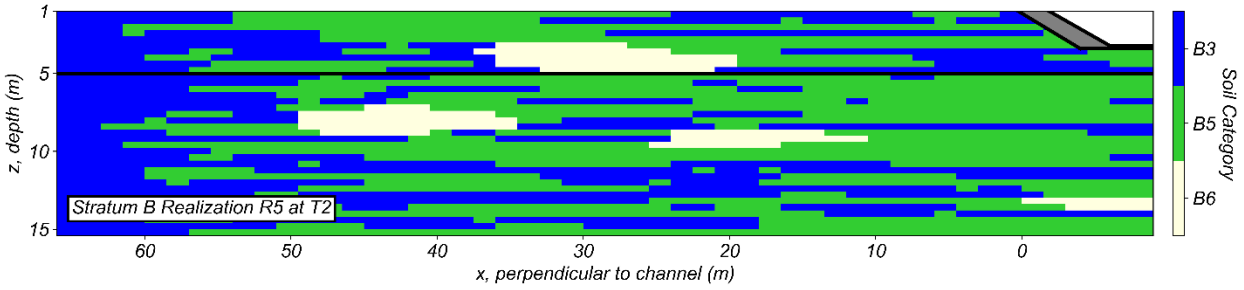

(d)

Figure B.3**.** Geostatistical realizations of stratum B from baseline T-PROGS simulations at transect T2 (y=32.5m): (a) R2, (b) R3, (c) R4, and (d) R5.

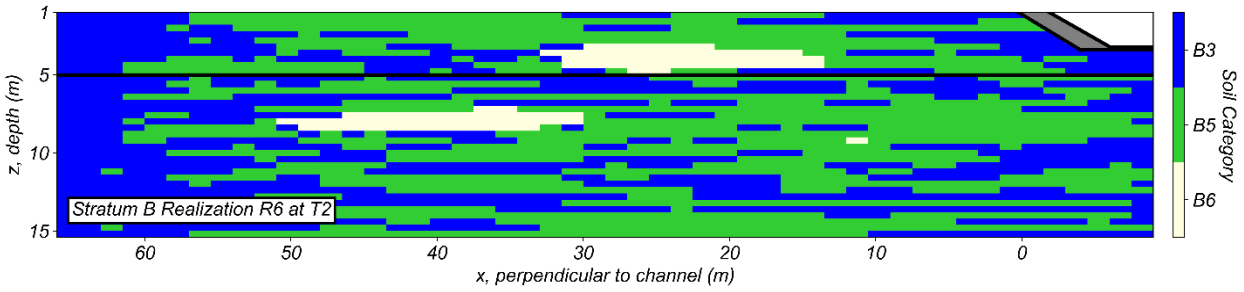

(a)

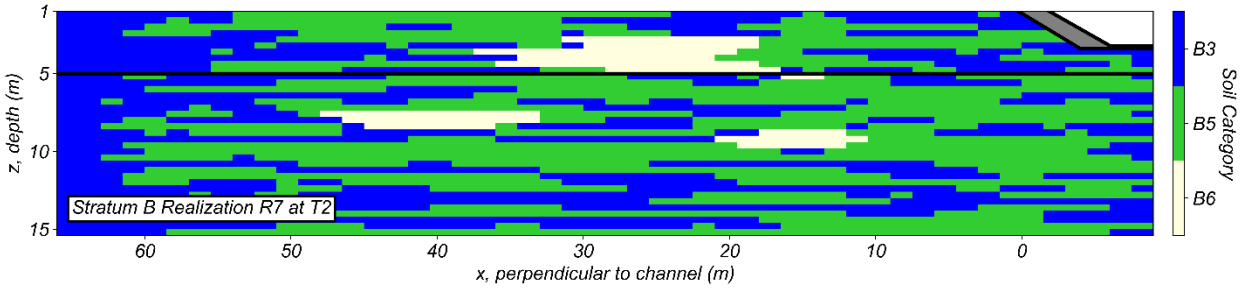

(b)

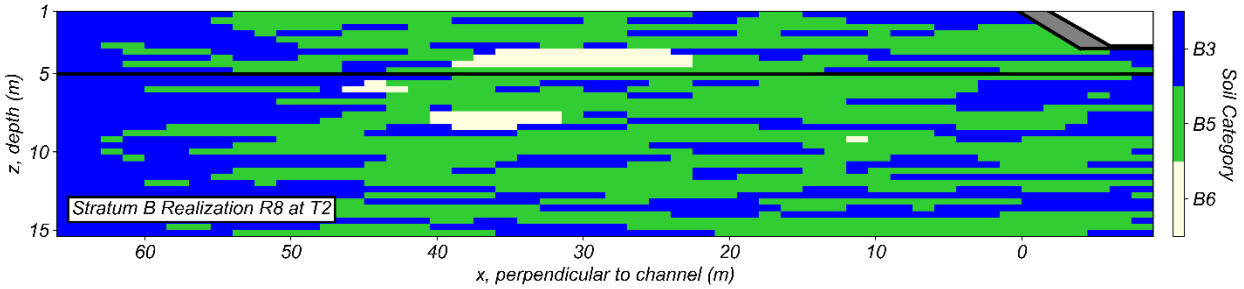

(c)

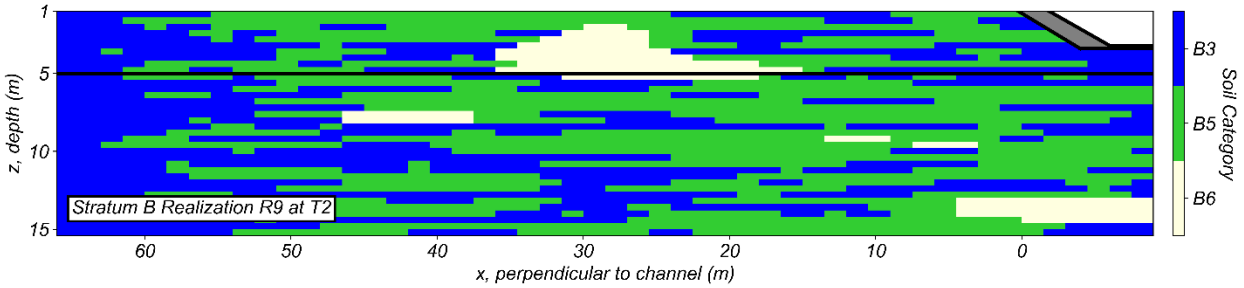

(d)

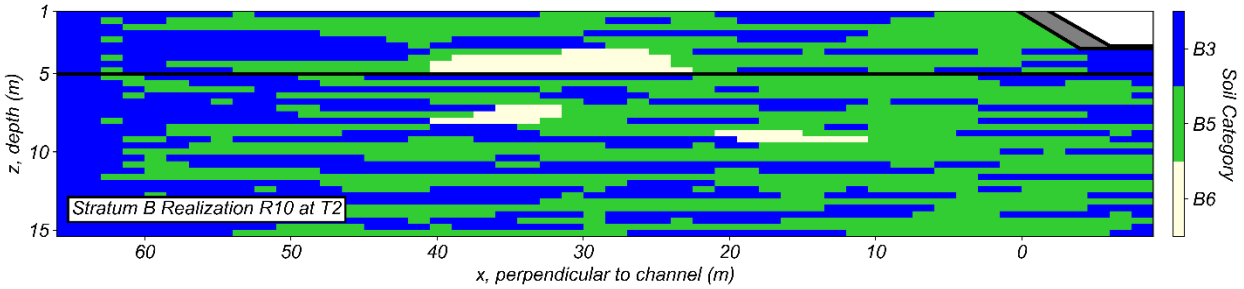

(e)

Figure B.4. Geostatistical realizations of stratum B from T-PROGS simulations with halved B3 and B5 mean lengths (i.e., 10 m) at transect T2 (y=32.5m): (a) R6, (b) R7, (c) R8, (d) R9, and (e) R10.

Appendix C

Supplementary Material for Chapter 6

(System Response of an Interlayered Deposit with a Localized Graben Deformation in the Northridge Earthquake)

Supplementary Tables

Table C.1: PM4Sand calibration lookup table for unit C1.

q_{c1Ncs}	D_R	G_o	$CRR_{M7.5,1atm}$ [a]	h_{po}	C_ε
60	0.346	566	0.122	2.10	50000000
65	0.376	586	0.126	1.78	1000000
70	0.404	605	0.131	1.57	200000
75	0.431	624	0.136	1.36	14000
80	0.457	641	0.141	1.20	1100
85	0.482	658	0.147	1.08	150
90	0.505	674	0.153	0.97	40
100	0.549	704	0.168	0.81	5
110	0.590	733	0.186	0.73	1.4
120	0.629	759	0.209	0.73	0.7
130	0.665	784	0.241	0.83	0.4
140	0.699	807	0.286	1.08	0.25
150	0.731	829	0.352	2.06	0.22
160	0.762	850	0.453	4.05	0.2
170	0.792	871	0.615	4.60	0.2
180	0.820	890	0.800	5.65	0.2
190	0.847	908	0.800	3.27	0.2
200	0.873	926	0.800	1.90	0.2
220	0.922	959	0.800	0.68	0.2
240	0.968	990	0.800	0.25	0.2
280	1.053	1047	0.800	0.04	0.2

Notes: Default values per Boulanger & Ziotopoulou (2017) are used for all unlisted secondary parameters.
[a] The vertical effective stress is assumed as 1 atm for all calibrations, as consistent with the typical expected conditions for unit C1.
[b] The CRR is bounded at a maximum value of 0.8.

Table C.2: PM4Silt calibration lookup table for zone B_{sat}.

$s_{u,peak,eq}/\sigma'_{vc}$	$s_{u,cs,eq}/\sigma'_{vc}$	h_{po}	$n^{b,wet}$
0.200	0.167	7	0.74
0.250	0.208	15	0.68
0.300	0.250	26	0.59
0.325	0.271	35	0.53
0.350	0.292	46	0.43
0.375	0.331	55	0.41
0.400	0.375	60	0.38
0.425	0.425	60	0.01
0.450	0.450	80	0.01
0.500	0.500	100	0.01
0.583	0.583	200	0.01
0.708	0.708	400	0.01
0.833	0.833	600	0.01
1.000	1.000	1000	0.01
1.200	1.200	1600	0.01

Notes: Calibrations were performed for a constant vertical effective stress of 0.85 atm. Constant values of $G_o = 592$ and $e_o = 0.77$ are assumed for all calibrations. Default values per Boulanger & Ziotopoulou (2018) are used for all other unlisted secondary parameters.

Supplementary Figures

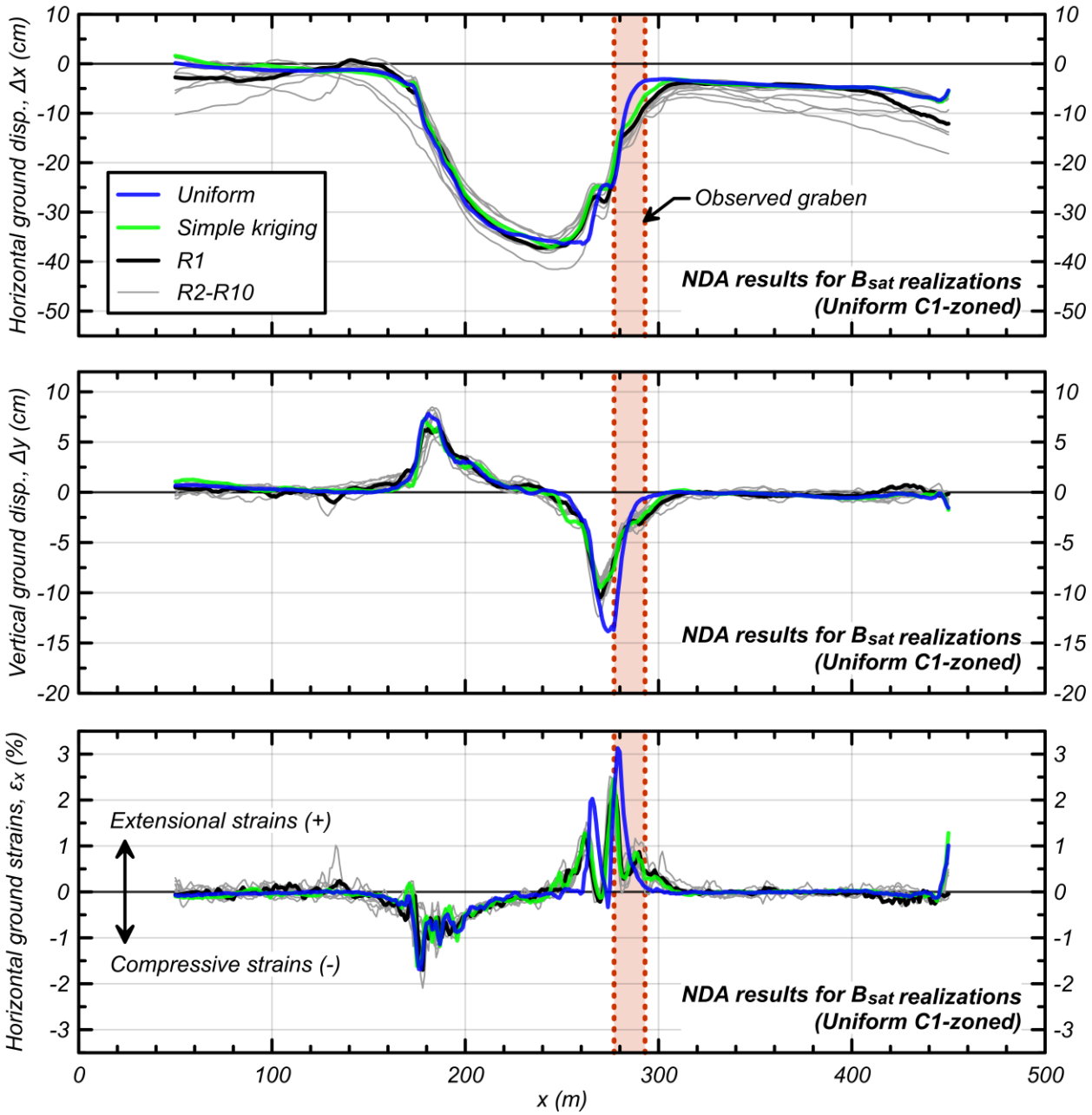

Figure C.1. Ground deformation results from NDAs for twenty stochastic realizations of B_{sat} (only), depicting the horizontal displacements; vertical displacements; and horizontal ground strains. Deformations for NDAs with kriged fields and the uniform baseline model are also shown. All results were obtained at 1 m increments along the model surface for x = 50-450 m.

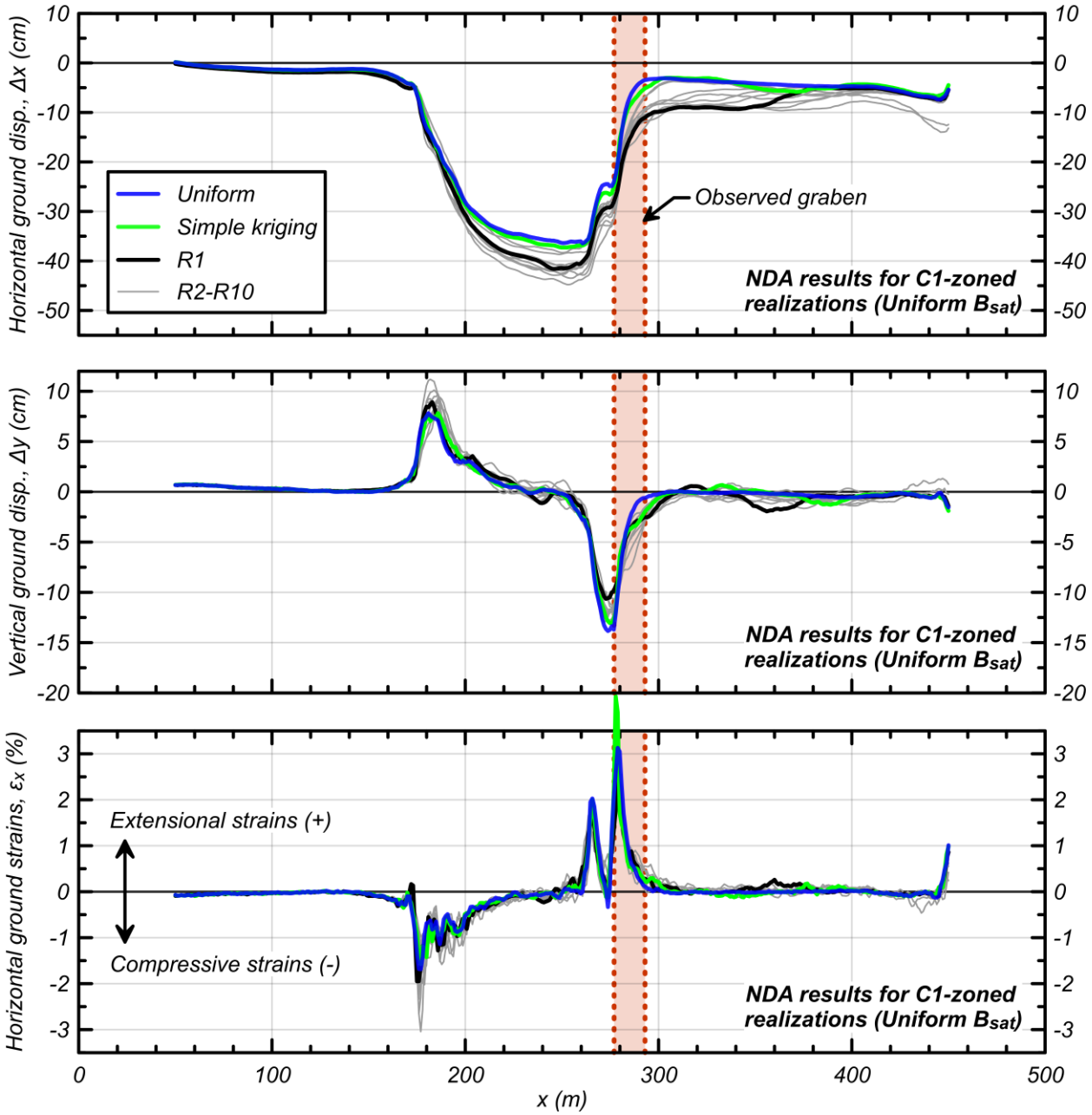

Figure C.2. Ground deformation results from NDAs for twenty stochastic realizations of C1-zoned (only), depicting the horizontal displacements; vertical displacements; and horizontal ground strains. Deformations for NDAs with kriged fields and the uniform baseline model are also shown. All results were obtained at 1 m increments along the model surface for x = 50-450 m.

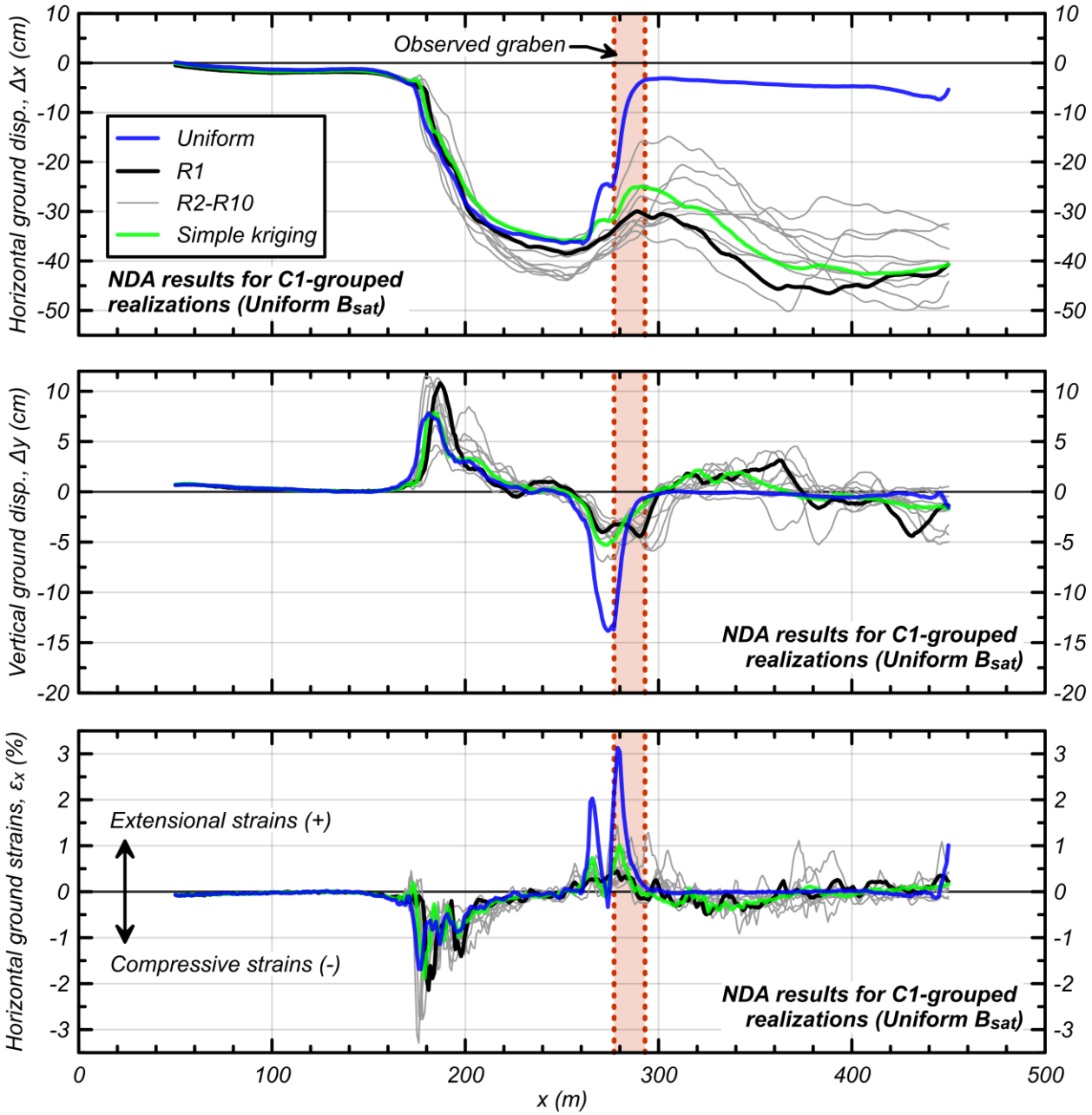

Figure C.3. Ground deformation results from NDAs for twenty stochastic realizations of C1-grouped (only), depicting the horizontal displacements; vertical displacements; and horizontal ground strains. Deformations for NDAs with kriged fields and the uniform baseline model are also shown. All results were obtained at 1 m increments along the model surface for x = 50-450 m.

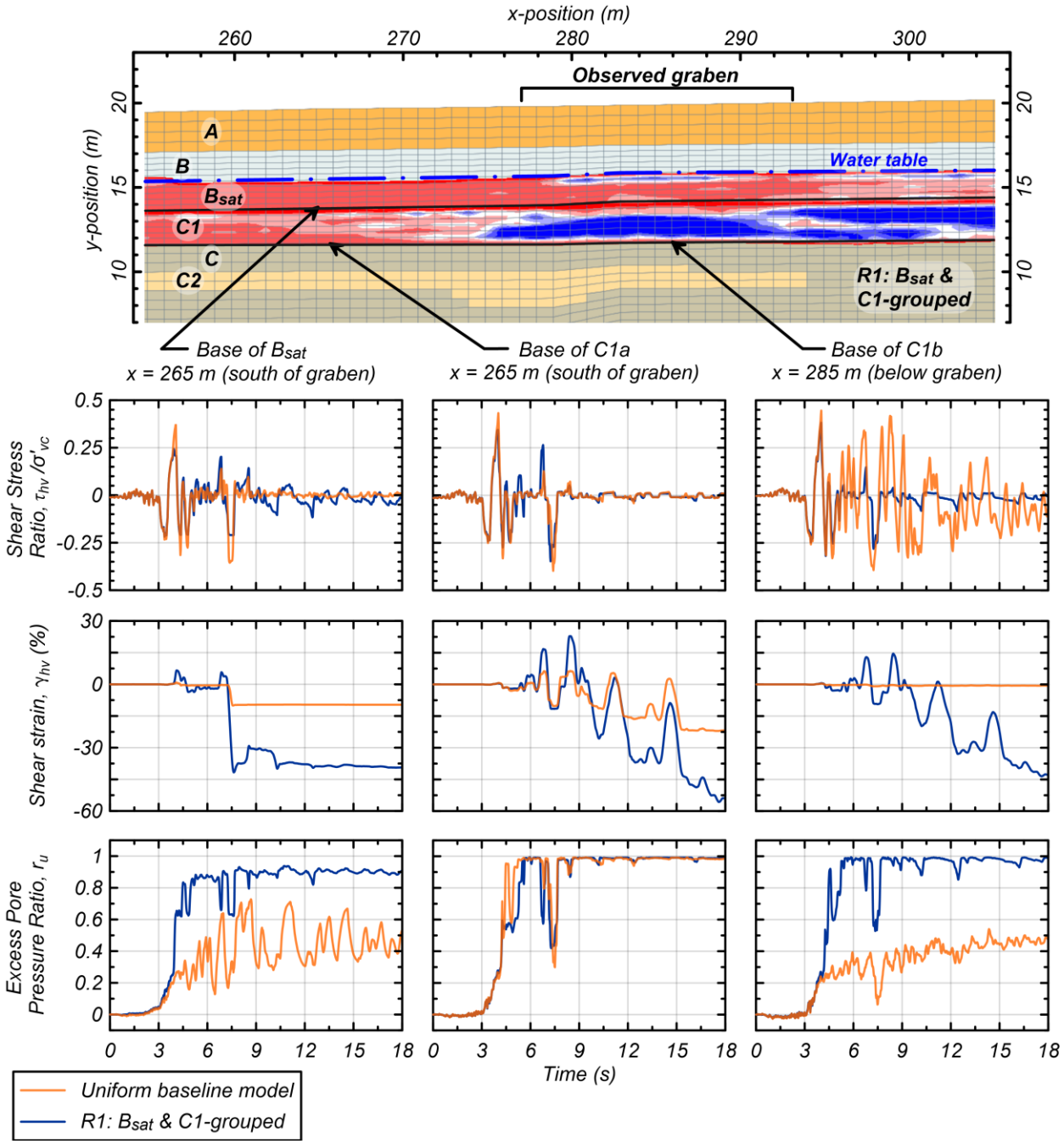

Figure C.4. Time histories of the shear stress ratio, shear strain, and excess pore pressure ratio for three monitored points from the uniform baseline and stochastic (R1: B_{sat} & C1-grouped) NDAs.

Appendix D

Stochastic NDA Workflow for Earthquake Ground Deformations

D.1. About

This appendix presents a workflow for performing Nonlinear Dynamic Analyses (NDAs) with stochastic fields for evaluating earthquake ground deformations at sites with interlayered and/or spatially variable subsurface soils. Site data from cone penetration tests (CPTs) are processed for determining representative soil properties and spatial correlations using Jupyter Notebooks in Python. Stochastic subsurface modeling using sequential Gaussian simulations (SGS) is performed using the open-source SGeMS program. A batch program is used to perform two-dimensional (2D) NDAs in the Fast Lagrangian Analysis of Continua (FLAC) finite difference program. The FLAC models use the PM4Sand and PM4Silt constitutive models, for evaluating the liquefaction and cyclic softening behavior of sand-like and clay-like soils.

This workflow is presented as an example that was used to evaluate the Wynne Avenue case history site, which experienced a localized graben deformation in the 1994 Northridge Earthquake (see Chapter 6). Some prior experience with Python and FLAC is expected, however, this workflow may be a good starting point for those interested in delving deeper into the use of these tools for evaluating earthquake ground deformations. This workflow may contain bugs, some inefficient lines of code, and other features that could be organized in a more optimal and user-friendly format. There are several other geostatistical methods for subsurface modeling and numerical software for NDA modeling available, as well as future releases of those programs that may eventually render portions of this workflow unusable. As this workflow gains greater use, the author hopes to maintain it with bug-fixes and new features. Please feel free to contact the author directly with questions, comments, requests, or collaborative ideas.

D.2. Required Programs

This workflow uses the following list of programs:

- **Microsoft Excel (2007 or later)** – This is used to facilitate the input for and readability of outputs from the Jupyter Notebook files.

- **Jupyter Notebook (with Python 3.9)** – The conda environment "cpt_geostat.yml" includes all necessary Python packages and is provided with the electronic distribution of this workflow for reproducibility. However, all the packages therein should already be available with common Python package distribution software (e.g., Anaconda), except for "geostatspy" (Pyrcz et al. 2021; https://pypi.org/project/geostatspy/).
- **GSLIB (Version 2.0)** – The variogram calculation uses a copy of the "gamv" executable, which can be downloaded from http://www.gslib.com/main_gd.html. Documentation is provided by Deutsch and Journel (1997).
- **SGeMS (v2.5b)** – The open-source version of this program is used for developing stochastic realizations. It can be downloaded from http://sgems.sourceforge.net/. The version used in this workflow was last updated in 2011, but works well for current purposes. Paid and updated versions of this software are maintained by AR2Tech, who were acquired by Seequent in 2021. Documentation is provided by Remy et al. (2009).
- **FLAC (Version 8.1)** – This finite difference program is used to perform the NDAs. It requires a license to use (Itasca 2019).
    - **PM4Sand (Version 3.1) –** This user-defined FLAC constitutive model can be downloaded and installed from https://pm4sand.engr.ucdavis.edu/. Documentation is provided by Boulanger and Ziotopoulou (2017).
    - **PM4Silt (Version 1) –** This user-defined FLAC constitutive model can be downloaded and installed from https://pm4silt.engr.ucdavis.edu/. Documentation is provided by Boulanger and Ziotopoulou (2018).

D.3. Workflow Stages and Details

This workflow is divided into four overarching analysis stages: (1) CPT processing and evaluation, (2) representative properties, (3) geostatistical modeling in SGeMS, and (4) NDA modeling in FLAC. The

general use and details for all input, calculation, and output files are described. This appendix includes printouts of the workflow scripts as used to specifically evaluate the Wynne Avenue case history site (i.e., Attachments D-1 to D-4). Stratum-specific workflows are only shown herein for the evaluation of the saturated sandy clay B_{sat} soil unit at Wynne Avenue. Refer to Chapter 6 for details regarding site-specific modeling choices for Wynne Avenue. The printouts attached to this appendix include Jupyter Notebooks, SGeMS parameter files, and FLAC FISH files. The input and output files are not provided herein, but can be accessed electronically.

D.3.1. CPT Processing and Evaluation

In this analysis stage, all CPTs applicable to the site of interest are processed and correlations are performed to estimate soil properties necessary for simplified evaluations of liquefaction (e.g., liquefaction vulnerability indices), subsurface geostatistical modeling, and NDA modeling. A unique attribute of this workflow is its ability to consider distinct soil properties for delineated strata or layers.

This analysis stage requires input from CPT data ASCII text files and one Excel workbook:

- **cpt_data** (folder with .txt files) – This folder should contain one text file for each CPT sounding considered. The CPT data should include at least 3 columns (space- or tab-delimited) for depth, tip resistance, and skin friction. The code is currently configured for units of m and atm. Inverse filtering or similar thin-layer corrections can be applied to the CPT data prior to preparation of the text files.
- **INPUT_LIQcalcs_[site].xlsx** – This Excel workbook should be composed of at least three sheets: (1) *Input_Strat*, (2) *Input_CPT*, and (3) *[cpt_id]_lab*.
    - The *Input_Strat* sheet assigns an integer-valued "strat_ID" and group name (string) to each unique stratum or layer delineated at the site. The division of strata is subject to modeler-interpretations, and should consider geological and lithological distinctions. Interlayers (e.g., a significant pocket of distinctive soils embedded in a larger stratum) can be

considered without need of assigning different labels for the same stratum. Thin and frequent interlayers of unique soil lithologies within strata can be assigned as alternate integer-values "facies" in the "CPT_Liq-Resist_BI14.ipynb" notebook. Each stratum should be assigned moist and saturated unit weights (kN/m^3), a cone bearing factor (N_{kt}) for clay-like soils, a soil behavior type index (I_C) liquefaction susceptibility threshold, the I_C to fines content (FC) correlation as either BI14 (Boulanger and Idriss 2014) or BBD22 (Bassal et al. 2022), and inputs of the FC correction factor (C_{FC}) for BI14 or the FC and I_C pins for BBD22.

- The *Input_CPT* sheet lists the ID of each considered CPT sounding with CPT-specific information, including the file path, spatial location relative to the expected analysis grid (x and y in m), top elevation (m), the depth of each boundary/contact between strata (m), the ordered sequence of strata occurrence by strat_ID, and water levels during the investigation and earthquake (m).
- The *[cpt_id]_lab* sheet includes laboratory data (often taken from boring samples) near a CPT sounding for evaluating the FC-I_C correlation. Additional sheets can be included for other CPT soundings with adjacent sample data. This sheet should at a minimum list the depth (m), FC (%), and Y/N flag for consideration in the correlation development (this can be input based on expected susceptibility as indicated by the Atterberg limit values).

These calculations are executed by running three Jupyter Notebooks and one Python function file. These are included in Attachment D-1:

- **LIQresist_fxns.py** – This python function file contains functions for calculating the vertical effective and total stresses, the I_C per Robertson (2009), the undrained shear strength ratio for clay-like soils (s_u/σ'_{vc}) for a given N_{kt}, and the cyclic resistance ratio (CRR) per Boulanger and Idriss (2014), as well as other accompanying parameters. This must be placed in the working directory to run the "CPT_Liq-Resist_BI14.ipynb" notebook.

- **CPT_Site-Specific-FC.ipynb** – This Jupyter notebook evaluates the FC-I_C correlation based on either the BI14 or BBD22 methods. It provides a C_{FC} per BI14 and produces an interactive plot for testing alternate FC and percentile pin assumptions for the BBD22 method. It also evaluates the FC uncertainty for the BBD22 method using bootstrapping.
- **CPT_Liq-Resist_BI14.ipynb** – This Jupyter notebook estimates the liquefaction resistance of sand-like soils for multiple (sitewide) CPTs, based on strata-specific inputs per the Boulanger & Idriss (2014; BI14) methodology. It also estimates the undrained shear strengths and sensitivity for clay-like soils. It can smooth the CPT data for results at median or averaged intervals.
- **CPT_LVIs.ipynb** – This Jupyter notebook estimates several CPT-based liquefaction vulnerability indices (LVIs).

The execution of the above files outputs two Excel workbooks:

- **OUTPUT_LIQresist_[site].xlsx** – This Excel workbook provides a sheet for each CPT sounding, listing the estimates of various output parameters with depth. This output workbook is used as input to subsequent calculations.
- **LVI_Summary_[site].xlsx** – This Excel workbook provides a sheet for each CPT sounding, listing estimates of the CRR, factor of safety against liquefaction triggering, and various LVIs with depth. A summary sheet is also provided, listing the cumulative LVI values at each sounding.

D.3.2. Representative Properties

This analysis stage evaluates representative properties for each stratum of interest, by calculating cumulative distribution functions (CDFs) with spatial declustering. It also includes calculations that assist with normalizing the data, and evaluating spatial correlations from variograms (as needed for subsequent geostatistical analyses). These analyses are intended to run within an individual analysis folder for each stratum of interest. The attached example files evaluate representative values for the peak undrained shear strength ratio under earthquake loading ($s_{u,peak,eq}/\sigma'_{vc}$) for the B_{sat} stratum.

This analysis stage requires input from two Excel workbooks. These inputs apply to calculations of all strata and should be placed outside the stratum-specific analysis folders:

- **INPUT_LIQcalcs_[site].xlsx** – This is the same Excel workbook used as input for the "CPT processing and evaluations" stage.
- **OUTPUT_LIQresist_[site].xlsx** – This is the same Excel workbook that was output from the "CPT processing and evaluations" stage. It is used as an input file for the current analyses.

These calculations are executed by running three Jupyter Notebooks for each stratum of interest. These are included in Attachment D-2. The "gamv.exe" executable file from GSLIB should also be included in the working directory:

- **Props_CDFs.ipynb** – This Jupyter notebook evaluates the empirical CDFs for data from each individual CPT sounding and all combined soundings, for a soil parameter of interest. The CDFs can provide representative percentile values for use in NDAs. The notebook also assigns a spatial weight to each CPT sounding via a cell-based declustering algorithm by Pyrcz and Deutsch (2003), using codes borrowed from the GeostatsPy Python package by Pyrcz et al. (2021).
- **Props_Normalize.ipynb** – This Jupyter notebook converts the data distribution of a soil parameter (as obtained from CPTs) to standard normal. This calculation should be performed on the residuals of detrended data, if spatial detrending is considered (note that detrending was not considered at Wynne Avenue). The "nscore" algorithm used in GSLIB (as converted to Python within GeostatsPy) is used herein, which allows for the use of decluster weighting.
- **Props_Variogram.ipynb** – This Jupyter notebook calculates and models a variogram from a CPT sample dataset, for a single stratum and parameter of interest. For simplicity, only one azimuth direction can be plotted and printed at any time. However, the azimuth can be updated with the interactive tool. The "gamv.exe" executable used in GSLIB (as wrapped from the original executable to Python by M. Pyrcz) is used herein.

- **gamv.exe** – This GSLIB executable file is needed for calculating variograms from 3D data and can be directly downloaded from http://www.gslib.com/main_gd.html.

The execution of the above files outputs one Excel workbook, five CSV file sets, and some GSLIB "gamv.exe" outputs:

- **CDF_[site]_[stratum]_[property]_[facies].xlsx** – This Excel workbook provides a sheet for each CPT sounding, listing all CPT depths, parameter values, and CDF values for the parameter of interest, sorted by increasing parameter values. It also provides an *Overall* sheet for all combined CPT data, including decluster-weighted data. Finally, it provides a *Percentiles* sheet that summarizes the parameter values from individual CPT soundings, combined soundings, and combined soundings with decluster-weighting at five percentile values (i.e., 16%, 33%, 50%, 67%, 84%).
- **Data_[site]_[stratum]_[property].csv** – This CSV file is produced from the CDF calculation and presents the coordinate location (x, y, and z in m), depth below top of CPT (m), parameter value, facies value, and decluster weights for all combined CPT data.
- **Data_[site]_[stratum]_[property]_norm.csv** – This CSV file is produced from the normalization calculation. It retains all values from the previous output file, but also presents normalized parameter values.
- **Data_[site]_[stratum]_[property]_transtable.csv** – This CSV file is produced from the normalization calculation. It provides a list of all parameter data values for the combined CPT data, with and without normalization, ordered by increasing values. It is later used to back-transform the stochastic fields.
- **variogram_data_[direction]_[stratum]_[property].csv –** This CSV file is produced from the variogram calculation. It provides the lag value, semivariogram value, and number of points considered for each value in the variogram calculation.

- **variogram_model_[direction]_[stratum]_[property].csv –** This CSV file is produced from the variogram model estimate. For discretized lag values, it provides the semivariogram, covariance, and correlogram model values.
- **gamv_out.dat** – This file converts the input soil data into a common GSLIB file format that can later be used with SGeMS. All other "gamv" outputs can be ignored.

D.3.3. Geostatistical Modeling

This analysis stage produces stochastic field realizations for each stratum and parameter of interest. The analysis grid is first built in FLAC and output for use in SGeMS. The SGeMS program is then used to develop the stochastic fields from sequential Gaussian simulations (SGS) conditioned on the normalized data. The results are then back-transformed to retain a distribution corresponding to the available data.

One advantage of SGeMS for the analyses herein is its capability of allowing the input of an irregular grid for developing the stochastic fields. This is highly beneficial for pairing with FLAC models with heterogeneous stratigraphic layers. The user-interface and 3D visualization capabilities of SGeMS are also found to be intuitive and simple to use relative to currently available open-source codes. However, the latest open-source version of SGeMS (v2.5b) is no longer maintained. This portion of the code may be updated at a future time for full integration with Python.

This analysis stage requires input from one CSV file, and one GSLIB-formatted file per stratum:

- **[stratum]_[property].gslib** – This is the same "gamv_out.dat" file produced from the variogram calculation in the "representative properties" stage. It presents the normalized data in the GSLIB file format. It can be directly input in SGeMS.
- **Data_[site]_[stratum]_[property]_transtable.csv** – This is the same Excel workbook that was output from the "representative properties" stage. It is used as an input file for the current analyses.

These calculations are executed by running one FLAC batch file for two user-generated FLAC FISH-language files, the SGeMS "SGSIM" calculation that calls one user-generated parameter file, and one Jupyter Notebook. These are included in Attachments D-3 and D-4:

- **1_mesh.fis** – This FISH file is used to build the FLAC mesh for a subsurface with a heterogeneous stratigraphy (it is used again in the "NDA modeling in FLAC" stage).
- **print_grid_[property].fis** – This FISH file is used to output the irregular mesh grid points, for subsequent stochastic field calculations.
- **run_mesh.dat** – This batch file should be called from FLAC in command-driven mode. It calls the two preceding FISH files.
- **SGSIM_[stratum]_params.txt** – This ASCII text file is a user-generated parameter file called by SGeMS to run the sequential Gaussian simulation (labeled as SGSIM by SGeMS). It requests the analysis inputs and outputs, including the variogram model and the previously input site data and point set.
- **BackTransform_fromSGEMS.ipynb** – This Jupyter notebook back-transforms the standard normal stochastic realizations to match the original data distributions. The "backtr" algorithm used in GSLIB (as converted to Python within GeostatsPy) is used herein, which allows for the use of a transformation table based on the original "nscore" calculation.

The execution of the above files outputs one ASCII text file, one GSLIB-formatted file, and two CSV files:

- **[stratum/property]_ptset.txt** – This text file presents the pointset values as output from the FLAC calculation. Four space-delimited columns are presented for the FLAC-defined "i" and "j" gridpoint values, and the centroid x and y locations (m) between gridpoints (center of each FLAC element).

- **[stratum/property]_ptset.gslib** – This is the preceding "_ptset.txt" file, which has manually been converted to the GSLIB file format. It was obtained by adding proper headers for interpretation by SGeMS. It is used as input for the SGeMS calculation.
- **SGS_[stratum]_[no. realizations]real.csv** – This CSV file is produced from SGeMS, and contains the spatial locations (x, y, and z in m) and standard normal parameter values for all stochastic realizations.
- **SGS_[stratum]_[no. realizations]real_backtr.csv** – This CSV file is produced from the back-transformation calculation. It presents the back-transformed stochastic realizations.

D.3.4. NDA Modeling in FLAC

This analysis stage runs NDA models in FLAC using the PM4Sand and PM4Silt constitutive models. It considers stochastic field realizations for every stratum. Several of the codes in this section are written specifically for the example at Wynne Avenue, but can be modified for other sites.

This analysis stage requires input from one set of CSV files, and two sets of ASCII text files:

- **SGSIM_[stratum].csv** – This is same CSV output file produced by the back-transformation as "[…]_backtr.csv," but with headers removed to allow readability in FLAC.
- **[stratum]_[model parameter].txt** – This text file contains a look-up table for all variable parameters within a stochastically-generated stratum.
- **[recording station]_[event]_[orientation]_vel_FLAC.txt** – This text file contains the velocity time history for all processed ground motions. It is expected that these motions have been modified for input at the FLAC base as outcropping motions.

These calculations are executed by running one FLAC batch file for six user-generated FLAC FISH-language files. These are included in Attachment D-4:

- **1_mesh.fis** – This FISH file is used to build the FLAC mesh for a subsurface with a heterogeneous stratigraphy.
- **2_initialize_MC.fis** – This FISH file establishes general and stratum-specific properties for the static model, assigns these properties to the mesh, and initializes pore water pressures and saturation.
- **3_static_MC.fis** – This FISH file solves for the phreatic water surface and general static equilibrium
- **4_static_PM4.fis** – This FISH file assigns the dynamic soil models (PM4Sand and PM4Silt) to both uniform and stochastic layers, solves for static equilibrium, and prepares model parameters for dynamic calculation.
- **5_dyn_hist.fis** – This FISH file establishes the step size for output time histories, assigns extra variables, sets points for tracking time histories, and prepares result tables.
- **6_dynflow.fis** – This FISH file reads in the time histories, sets parameters for dynamic analyses, runs analyses, and sets output results tables.
- **batch_[site]_SGS.dat** – This batch file should be called from FLAC in command-driven mode. It calls the six preceding FISH files, and reruns the model for up to ten sets of stochastic realizations.

The execution of the above files outputs several FLAC save files throughout the analysis that can be used for evaluating model results. The example analysis at Wynne Avenue produces text files that indicate the horizontal and vertical displacements along the ground surface.

D.4. Electronic Copies

Printouts are only provided in this appendix for the primary calculation files. The full workflow for this Wynne Avenue case study, including input and output files, are available in electronic form at the DesignSafe Data Depot at https://doi.org/10.17603/ds2-nne2-2s11 (Bassal 2022). Please cite the Bassal (2022) repository for any use of this workflow.

D.5. Data Availability

Some of the data used for the Wynne Avenue case study example were provided by third parties. The CPT data was obtained from the United States Geological Survey (USGS 2021) and the borings, field VSTs, and laboratory index test data was obtained from Bennett et al. (1998). Ground motions were obtained from the PEER NGA-West2 Ground Motion Database (Ancheta et al. 2013).

D.6. Acknowledgements

This work was made possible by the financial support of the National Science Foundation (award CMMI-1635398) and California Department of Water Resources (contract 4600009751) for different aspects of the work presented herein. This work greatly benefited from the guidance and assistance of Professor Ross W. Boulanger at the University of California, Davis. Portions of the FLAC codes have been retained from previous work within the research group of Ross W. Boulanger, with possible contributions from Nick Paull, Jack Montgomery, Katerina Ziotopoulou, Richie Armstrong, and others. Portions of the Jupyter Notebook codes are pulled from the GeostatsPy example notebooks by Michael Pyrcz at the University of Texas at Austin (https://github.com/GeostatsGuy). The author is grateful for the above support and availability of material from the above sources.

D.7. References

Ancheta, T. D., Darragh, R. B., Stewart, J. P., et al. (2013). “PEER NGA-West2 Database.” Pacific Earthquake Engineering Research Center. PEER Report No. 2013/03. University of California, Berkeley, CA.

Bassal, P. (2022). "Stochastic NDA Workflow for Ground Deformations at Wynne Avenue in the Northridge Earthquake", in Stochastic Nonlinear Dynamic Analyses for Earthquake Ground Deformations. DesignSafe-CI. https://doi.org/10.17603/ds2-nne2-2s11

Bassal, P. C., & Boulanger, R. W. (Submitted). “System Response of an Interlayered Deposit with a Localized Graben Deformation in the Northridge Earthquake.” Soil Dynamics and Earthquake Engineering, special issue for the 4th Int. Conf. on Performance-Based Design in Earthquake Geotechnical Engineering.

Bassal, P. C., Boulanger, R. W., & DeJong, J. T. (2022). “Site-Specific CPT-based Fines Content Correlations using Percentile Matching.” In proc., ASCE Geo-Congress 2022, Charlotte, NC.

Bennett, M. J., Ponti, D. J., Tinsley III, J. C., Holzer, T. L., & Conaway, C. H. (1998). “Subsurface geotechnical investigations near sites of ground deformations caused by the January 17, 1994, Northridge, California, earthquake.” Washington, DC: USGS.

Boulanger, R. W., & Idriss, I. M. (2014). “CPT and SPT based liquefaction triggering procedures.” Report No. UCD/CGM.-14/01.

Boulanger, R. W., & Ziotopoulou, K. (2017). “PM4Sand (Version 3.1): A sand plasticity model for earthquake engineering applications.” Report No. UCD/CGM-17/01, Center for Geotech. Modeling, Dept. of Civil and Environ. Eng., Univ. of Cal., Davis, CA, 113 pp.

Boulanger, R. W., & Ziotopoulou, K. (2018). “PM4Silt (Version 1): A silt plasticity model for earthquake engineering applications.” Report No. UCD/CGM-18/01, Center for Geotech. Modeling, Dept. of Civil and Environ. Eng., Univ. of Cal., Davis, CA, 108 pp.

Deutsch, C. V. & Journel, A. G. (1997). “GSLIB Geostatistical Software Library and User’s Guide.” Oxford University Press, New York, second edition.

Itasca (2019). "FLAC, Fast Lagrangian Analysis of Continua, User’s Guide, Version 8.1." Itasca Consulting Group, Inc., Minneapolis, MN.

Pyrcz, M. J., & Deutsch, C.V., (2003). “Declustering and Debiasing.” Geostatistical Association of Australasia, Newsletter 19, October.

Pyrcz, M.J., Jo. H., Kupenko, A., Liu, W., Gigliotti, A.E., Salomaki, T., & Santos, J., (2021). GeostatsPy Python Package, PyPI, Python Package Index, https://pypi.org/project/geostatspy/.

Remy, N., Boucher, A., & Wu, J. (2009). “Applied geostatistics with SGeMS : a user's guide.” Cambridge University Press.

Robertson, P. K. (2009). “Interpretation of cone penetration tests - a unified approach.” Can. Geotech. J. 46: 1337-1355. doi: 10.1 l39/T09-065.

United States Geological Survey (2021). “Table of CPT Data, Los Angeles County.” https://earthquake.usgs.gov/research/cpt/data/losangeles; [accessed 01 August 2021].

Attachment D-1

CPT Processing and Evaluation: Python Function Script and Jupyter Notebooks

```python
# -*- coding: utf-8 -*-
"""
Liquefaction Resistance Functions
Created on Sun Apr 19 17:58:25 2020 - Updated Aug 5, 2021

@author: PB

These liquefaction resistance functions, based on the Boulanger & Idriss 2014
triggering correlations, can be used for a simplified liquefaction triggering
calculation or for determining inputs for a Nonlinear Dynamic Analysis
using PM4Sand and PM4Silt.
"""

import numpy as np

def vstress(z,dz,zwater_inv,zwater_eq,UWm,UWsat,UWw,Patm):
    """
    Parameters
    ----------
    z : Array of float64
        Depth values from cpt (m).
    dz : Array of float64
        Increment of z (m) as measured from previous layer. Must be same length
        as z.
    zwater_inv : float64
        Water depth during investigation (m).
    zwater_eq : float64
        Water depth during earthquake (m).
    UWm : Array of float64
        Unit weight of soil above WT (kN/m3). Must be same length as z.
    UWsat : Array of float64
        Unit weight of saturated soil below WT (kN/m3). Must be same length as
        z.
    UWw : float64
        Unit weight of water (kN/m3).
    Patm : float64
        Atmospheric pressure (kPa).

    Returns
    -------
    sigv_inv : Array of float64
        Total vertical stress along profile, during investigation (kPa).
    pwp_inv : Array of float64
        Pore water pressure along profile, during investigation (kPa).
    sigveff_inv : Array of float64
        Total vertical effetive stress along profile, during investigation
        (kPa).
    sigv_eq : Array of float64
        Total vertical stress along profile, during earthquake (kPa).
    pwp_eq : Array of float64
        Pore water pressure along profile, during earthquake (kPa).
    sigveff_eq : Array of float64
        Total vertical effetive stress along profile, during earthquake (kPa).
    """

    #  Determine vertical stresses during investigation (atm)
    sigv_inv = np.zeros(len(z))
    if zwater_inv == 0:
        sigv_inv[0] = UWsat[0]*dz[0] # assume top dz is sat
    else:
        sigv_inv[0] = UWm[0]*dz[0] # assume top dz is unsat
    for i in range(1,len(z)):
```

```
60          if z[i] < zwater_inv:
61              sigv_inv[i] = sigv_inv[i-1] + UWm[i]*dz[i]
62          else:
63              sigv_inv[i] = sigv_inv[i-1] + UWsat[i]*dz[i]
64      sigv_inv = sigv_inv/Patm  # Vertical total stress array
65      pwp_inv  = UWw*np.maximum(np.zeros(np.shape(z)),z-zwater_inv)/Patm # Pore
        water pressure array
66      sigveff_inv = sigv_inv - pwp_inv  # Vertical effective stress array
67
68      #  Determine vertical stresses during earthquake (atm)
69      sigv_eq = np.zeros(len(z))
70      if zwater_eq == 0:
71          sigv_eq[0] = UWsat[0]*dz[0] # assume top dz is sat
72      else:
73          sigv_eq[0] = UWm[0]*dz[0] # assume top dz is unsat
74      for i in range(1,len(z)):
75          if z[i] < zwater_eq:
76              sigv_eq[i] = sigv_eq[i-1] + UWm[i]*dz[i]
77          else:
78              sigv_eq[i] = sigv_eq[i-1] + UWsat[i]*dz[i]
79      sigv_eq = sigv_eq/Patm  # Vertical total stress array
80      pwp_eq  = UWw*np.maximum(np.zeros(np.shape(z)),z-zwater_eq)/Patm # Pore
        water pressure array
81      sigveff_eq = sigv_eq - pwp_eq  # Vertical effective stress array
82      return sigv_inv,pwp_inv,sigveff_inv,sigv_eq,pwp_eq,sigveff_eq
83
84
85  def R19_Ic(z,qc,fs,zwater_eq,sigv_inv,sigveff_inv,Ic_cut):
86      """
87      Parameters
88      ----------
89      z : Array of float64
90          Depth values from cpt (m).
91      qc : Array of float64
92          Tip resistance as obtained from cpt (atm).
93      fs : Array of float64
94          Side friction as obtained from cpt (atm).
95      zwater_eq : float64
96          Water depth during earthquake (m).
97      sigv_inv : Array of float64
98          Total vertical stress along profile, during investigation (atm).
99      sigveff_inv : Array of float64
100         Total vertical effetive stress along profile, during investigation
            (atm).
101     Ic_cut : Array of float64
102         User-defined Ic cutoff for liquefaction at all depths. Must be same
            length as z.
103
104     Returns
105     -------
106     F : Array of float64
107         Normalized friction ratio (%).
108     n : Array of float64
109         Stress exponent.
110     C_n : Array of float64
111         Overburden correction factor (unitless).
112     Q : Array of float64
113         Normalized CPT penetration resistance (unitless).
114     Ic : Array of float64
115         Soil behavior type index for all depths.
116     flag : List
117         Flags all depths as 'unsaturated','not susceptible','susceptible'.
```

```
118         """
119
120         #  Robertson 2009 iterative correlations to determine Ic
121         F = 100*fs/(qc-sigv_inv)   # Friction ratio
122
123         Ic = np.ones(len(z))
124         for iter in range(20):
125             n = np.minimum(1,np.maximum(0.2*np.ones(np.shape(Ic)),0.381*Ic+0.05*
            sigveff_inv-0.15))
126             C_n = np.minimum(10*np.ones(np.shape(Ic)),(1/sigveff_inv)**n)
127             Q = np.abs(qc-sigv_inv)*C_n
128             Ic = np.sqrt((3.47-np.log10(Q))**2+(np.log10(F)+1.22)**2)
129
130         flag = ['  ']*len(z) # flag susceptibility based on WT and Ic_cut
131         for i in range(len(z)):
132             if z[i] < zwater_eq:
133                 flag[i] = "unsaturated"
134             elif Ic[i] > Ic_cut[i]:
135                 flag[i] = "not susceptible"
136             else:
137                 flag[i] = "susceptible"
138         return F,n,C_n,Q,Ic,flag
139
140     def SuRatio(z,qc,fs,sigv_eq,sigveff_eq,Ic_cut,Ic,Nkt):
141         """
142         Calculates Su Ratio from CPT data. Data is input along
143         the depth.
144
145         Parameters
146         ----------
147         z : Array of float64
148             Depth values from cpt (m).
149         qc : Array of float64
150             Tip resistance as obtained from cpt (atm).
151         fs : Array of float64
152             Sleeve friction as obtained from cpt (atm).
153         sigv_eq : Array of float64
154             Total vertical stress along profile, during earthquake (atm).
155         sigveff_eq : Array of float64
156             Total vertical effetive stress along profile, during earthquake (atm).
157         Ic_cut : Array of float64
158             User-defined Ic cutoff for liquefaction at all depths. Must be same
            length as z.
159         Ic : Array of float64
160             Soil behavior type index for all depths.
161         Nkt : Array of float64
162             Cone bearing factor (best estimate). Must be same length as z.
163
164         Returns
165         -------
166         SuRat : Array of float64
167             Su ratio (best estimate) for all soil above Ic cutoff.
168         Su : Array of float64
169             Su (best estimate) for all soil above Ic cutoff in atm.
170         St : Sensitivity for all soil above Ic cutoff (assumes fs = remolded)
171
172         """
173         #  Determine Su ratios
174         SuRat = np.ones(len(z))
175         Su = np.ones(len(z))
176         St = np.ones(len(z))
177         for i in range(len(z)):
```

```
            if Ic[i] > Ic_cut[i]:
                SuRat[i] = max(0,(qc[i]-sigv_eq[i])/(sigveff_eq[i]*Nkt[i]))
                Su[i] = max(0,(qc[i]-sigv_eq[i])/(Nkt[i]))
                St[i] = max(1,Su[i]/fs[i])
            else:
                SuRat[i] = float('nan')
                Su[i] = float('nan')
                St[i] = float('nan')
        return SuRat,Su,St


    def BI14_CRR(z,qc,sigveff_eq,Ic_cut,Ic,flag,FC_method,CFC,Icpin,FCpin):
        """
        Parameters
        ----------
        z : Array of float64
            Depth values from cpt (m).
        qc : Array of float64
            Tip resistance as obtained from cpt (atm).
        sigveff_eq : Array of float64
            Total vertical effetive stress along profile, during earthquake (atm).
        Ic_cut : Array of float64
            User-defined Ic cutoff for liquefaction at all depths. Must be same
            length as z.
        Ic : Array of float64
            Soil behavior type index for all depths.
        flag : List
            Flags all depths as 'unsaturated','not susceptible','susceptible'.
        FC_method : List
            Flags fines content correlation method all depths as BI14 or BBD22
        CFC : Array of float64
            Fines content correction factor per BI14 ()
        Icpin,FCpin : Arrays of float64
            Fines content factors per percentile match method of Bassal et al. 2022
            (3 x z arrays)

        Returns
        -------
        FC : Array of float64
            Fines content (%).
        qc1N : Array of float64
            qc normalized to one atmosphere.
        qc1Ncs : Array of float64
            qc normalized to one atmosphere and clean sand corrected.
        CRR_norm : Array of float64
            Normalized cyclic resistance ratio of sand (M=7.5, 1 atm).

        """

        EFC1 = np.ones(len(z)) # arrays necessary here due to strata breakdown
        EFC2 = np.ones(len(z))
        FC = np.ones(len(z))  # Loop to solve for FC Estimate
        for i in range(len(z)):
            if FC_method[i] == 'BI14':  # FC per BI14
                FC[i] = np.maximum(0,np.minimum((80*(Ic[i]+CFC[i])-137),100))
            else:   # FC per BBD22 (3-point percentile matching)
                EFC1[i] = abs((FCpin[i,1]-FCpin[i,0]))/max(.01,abs((Icpin[i,1]-Icpin
                [i,0])))
                EFC2[i] = abs((FCpin[i,1]-FCpin[i,2]))/max(.01,abs((Icpin[i,1]-Icpin
                [i,2])))
                if Ic[i] > Ic_cut[i]:
                    FC[i] = 100
```

```
            elif Ic[i] <= Icpin[i,1]:
                FC[i] = np.maximum(0,np.minimum(EFC1[i]*(Ic[i]- Icpin[i,1])+
                FCpin[i,1],100))
            else: FC[i] = np.maximum(0,np.minimum(EFC2[i]*(Ic[i]- Icpin[i,1])+
            FCpin[i,1],100))

    # qc1Ncs per BI14
    qc1Ncs = np.ones(len(z))*100
    for iter in range(10):
        #MSFmax = np.minimum(1.09+(qc1Ncs/180)**3,2.2*np.ones(np.shape(z)))
        #MSF = 1+(MSFmax-1)*(8.64*np.exp(-M/4)-1.325)
        #C_sig =
        1/(37.3-8.27*(np.minimum(qc1Ncs,211*np.ones(np.shape(z)))**0.264))
        #K_sig = np.minimum(1-C_sig*np.log(sigveff_eq),1.1*np.ones(np.shape(z)))
        m = 1.338-0.249*(np.maximum(21*np.ones(np.shape(z)),
                                    np.minimum(qc1Ncs,254*np.ones(np.shape(z
                                    )))))**0.264
        C_m = np.minimum((1/sigveff_eq)**m,1.7*np.ones(np.shape(z)))
        qc1N = qc*C_m
        dqc1N = (11.9+qc1N/14.6)*np.exp(1.63-9.7/(FC+2)-(15.7/(FC+2))**2)
        qc1Ncs = qc1N+dqc1N

    # Just in case, remove qc values that are better represented by Su
    for i in range(len(z)):
        if Ic[i] > Ic_cut[i]:
            qc1N[i] = float('nan')
            qc1Ncs[i] = float('nan')

    # Normalized CRR of sand (M=7.5, 1 atm) per BI14
    CRR_norm = np.ones(len(z))
    for i in range(len(z)):
        if flag[i] == "unsaturated" or flag[i] == "not susceptible":
            CRR_norm[i]= float('nan')
        else:
            CRR_norm[i] = min(np.exp(qc1Ncs[i]/113+(qc1Ncs[i]/1000)**2
                                    -(qc1Ncs[i]/140)**3+(qc1Ncs[i]/137)**4-2.8
                                    ),2.0)
    return FC,qc1N,qc1Ncs,CRR_norm
```

Site-Specific CPT-based Fines Content Correlations

The following notebook compares site-specific correlations with soil behavior type index (I_C) data from a single cone penetration test (CPT) and fines content (FC) measurements from nearby borehole samples. Two methods are explored: the **Boulanger & Idriss (2014)** method (**BI14**), and the **Bassal et al. (2022)** method (**BBD22**). The fines correction factor C_{FC} for the BI14 method is obtained by linear regression from the data input in this notebook. The **percentile match parameters** (FC and Ic at three percentiles) for the BBD22 method can be input a priori, or estimated and adjusted by way of an interactive plot. This notebook is part of a calculation series for numerical and geostatistical modeling for geotechnical earthquake engineering.

By Patrick C. Bassal (Ver 0: 01/02/2022)

References:

Bassal, P. C., Boulanger, R. W., and DeJong, J. T. (2022). "Site-Specific CPT-based Fines Content Correlations using Percentile Matching." In proc., Geo-Congress 2022, Charlotte, NC. Reston, VA: ASCE. https://doi.org/10.1061/9780784484043.053.

Boulanger, R. W., and Idriss, I. M. (2014). "CPT and SPT based liquefaction triggering procedures." Report No. UCD/CGM.-14/01.

Step 1: Input CPT and lab data from nearby borehole samples

Import all necessary libraries below. These libraries are standard packages that are typically included with the download of a Python distribution package (e.g., Anaconda).

In [2]:
```
import numpy as np                # for array calculations
import matplotlib.pyplot as plt   # for plotting
import pandas as pd               # for building dataframe tables
import seaborn as sns             # advanced statistical graphics
import random                     # randomization (for bootstrapping to determine uncertainty)

from ipywidgets import interactive               # widgets
from ipywidgets import VBox, HBox
from ipywidgets import widgets
from ipywidgets import Layout
from ipywidgets import Label
from IPython.display import display
```

Provide input values in this next box. Properly formatted CPT data text files (e.g., .txt as default) and lab data files (e.g., .xlsx as default) are necessary for this step to work properly. See example files with this distribution. The following two boxes read and display these inputs for double checking.

In [3]:
```
#  Input CPT data and lab files (most inputs should be adjusted herein)
site_name = 'Wynne' # site name used in title for results
cpt = 'CPT_5a' # name of CPT (if input file is xlsx, use input sheet name)
stratum = 'C1 and C2' # stratum name used in title for results
cpt_file = 'cpt_data/%s_IF.txt' %(cpt) # CPT file location
dflab = pd.read_excel("INPUT_LIQcalcs_Wynne.xlsx", sheet_name='%s_lab' %(cpt)) # Load lab summary sheet (with z, FC, Y/N flag)
sttop = 5.7 # top depth of stratum considered (m)
stbot = 11.9 # bottom depth of stratum considered (m)
zwater_inv = 4.3   # water depth during investigation (m)

# General inputs
Ic_cut = 2.6       # Set Ic cut-off for liquefaction susceptibility (all values above are capped for percentile method)
UWm = 18           # moist unit weight (kPa) - simplified estimate for whole profile
UWsat = 19         # saturated weight of water (kPa) - simplified estimate for whole profile
Patm = 101.3       # atmospheric pressure (kPa)
gammaw = 9.81      # unit weight of water (kPa)
Ic_int = 0.5       # Length of Ic interval (m) to avg at sample location (for plots)
slope_max = 300.0  # max slope (FC/Ic; inverse on FC-Ic plot) for piecewise correlation to prevent downturns (default at 300)

# Default BBD22 percentile match inputs (Do not need to run, if unknown); BI14 correction factor will be obtained from data
# Ppin = [1, 35, 97] # Selected percentile pins (must be array of 3 values in percent)
# FCpin = [7.8, 22.3, 55.7] # Selected fines content pins (must be array of 3 values)
```

In [4]:
```
# Read CPT data
z_cpt,qc,fs = np.loadtxt(cpt_file,skiprows=1,unpack=True) # unpack CPT data (z in m, qc/fs in atm; 1atm = 0.101325 MPa)
dfcpt = pd.DataFrame(np.column_stack((z_cpt,qc,fs)), columns = ['z_cpt','qc','fs'])

#  Impose limits on qc (tip resistance) and fs (skin friction) to avoid any negative values
qc  = np.maximum(0.01*np.ones(np.shape(qc)),qc)
fs  = np.maximum(0.001*np.ones(np.shape(fs)),fs)
zmax = max(z_cpt)
```

```
dz_cpt = (np.max(z_cpt)-np.min(z_cpt))/(len(z_cpt)-1) # assume constant dz at all depths

dfcpt.head(n=12)
#print(np.stack(([z_cpt[0:11]],[qc[0:11]],[fs[0:11]]))) # check that first few values of CPT data are reasonable
```

Out[4]:

	z_cpt	qc	fs
0	0.1	0.2721	0.08214
1	0.2	21.2060	0.43837
2	0.3	30.8997	1.01956
3	0.4	27.1453	1.31701
4	0.5	23.9093	1.00689
5	0.6	19.0827	0.70112
6	0.7	16.0184	0.51660
7	0.8	14.0606	0.47447
8	0.9	12.4070	0.27767
9	1.0	12.6392	0.18121
10	1.1	12.9228	0.28654
11	1.2	13.8294	0.16507

In [5]:

```
#  Load lab data as values (only z, FC, and Y/N flag for susceptibility needed)
z_lab = dflab.to_numpy()[:,0]
FC_lab = dflab.to_numpy()[:,1]
consider = dflab.to_numpy()[:,2]
# LL = dflab.to_numpy()[:,3]
# PL = dflab.to_numpy()[:,4]
# PI = dflab.to_numpy()[:,5]
# wc = dflab.to_numpy()[:,6]

dflab # print summary
```

Out[5]:

	z_lab	FC_lab	consider	LL	PL	PI	wc	Unnamed: 7
0	0.914411	43	Y	NaN	NaN	NaN	NaN	NaN
1	0.914411	43	Y	21.0	NaN	3.0	12.1	NaN
2	0.975372	41	Y	NaN	NaN	NaN	11.7	assigns
3	1.066813	44	Y	22.0	NaN	4.0	12.1	NaN
4	1.066813	41	Y	22.0	NaN	4.0	11.7	NaN
...	...	...	...	...	...	...	...	...
79	10.363326	10	Y	NaN	NaN	NaN	NaN	NaN
80	11.003414	61	N	NaN	NaN	NaN	NaN	NaN
81	11.247257	31	Y	NaN	NaN	NaN	NaN	NaN
82	13.716167	63	N	43.0	NaN	22.0	21.8	NaN
83	16.154596	39	Y	NaN	NaN	NaN	NaN	NaN

84 rows × 8 columns

Step 2: Calculate I_c along the CPT

Determine I_c based on CPT measurements of tip resistance and skin friction using the Robinson 2009 correlation. The presented plot can be used to assist in redefining stratum extents and percentile match properties.

In [6]:

```
# ================================================================
#  Determine vertical stresses  (during investigation, atm)
sigv_inv = np.zeros(len(z_cpt))
for i in range(len(z_cpt)):
    if z_cpt[i] < zwater_inv:
        sigv_inv[i] = UWm*z_cpt[i]
    else:
        sigv_inv[i] = zwater_inv*UWm+(z_cpt[i]-zwater_inv)*UWsat
sigv_inv = sigv_inv/Patm  # Vertical total stress array
pwp_inv  = gammaw*np.maximum(np.zeros(np.shape(z_cpt)),z_cpt-zwater_inv)/Patm # Pore water pressure array
sigveff_inv = sigv_inv - pwp_inv  # Vertical effective stress array
```

```
F = 100*fs/(qc-sigv_inv)   # Friction ratio

# ================================================================
#  Robertson 2009 iterative correlations to determine Ic
Ic = np.ones(len(z_cpt))
for iter in range(20):
    n = np.minimum(1,np.maximum(0.2*np.ones(np.shape(Ic)),0.381*Ic+0.05*sigveff_inv-0.15))
    C_n = np.minimum(10*np.ones(np.shape(Ic)),(1/sigveff_inv)**n)
    Q = np.abs(qc-sigv_inv)*C_n
    Ic = np.sqrt((3.47-np.log10(Q))**2+(np.log10(F)+1.22)**2)

dfcpt['Ic'] = Ic.tolist() # add Ic to dataframe

# ================================================================
# Plot qtN, Ic, and boundary lines for full profile
fig, axes = plt.subplots(1, 2, figsize=(8, 8))
ax = axes.ravel()  #similar to .flatten()

# Plot strata boundary lines
ax[0].plot([0,max(qc)],[sttop,sttop],'g')
ax[1].plot([0,max(qc)],[sttop,sttop],'g')
ax[0].plot([0,max(qc)],[stbot,stbot],'g')
ax[1].plot([0,max(qc)],[stbot,stbot],'g')

# Plot qtN (normalized tip resistance)
ax[0].grid()
ax[0].plot(qc,z_cpt,'k')

# Plot Ic
ax[1].grid()
ax[1].plot(Ic,z_cpt,'b',linewidth=1,label = 'Ic')

# Set axis extents
ax[0].axis([0, min(max(qc[z_cpt<=zmax]),400), min(z_cpt), zmax])
ax[1].axis([1, 4, min(z_cpt), zmax])

# Format axis Labels
ax[0].set_ylim(ax[0].get_ylim()[::-1])
ax[0].xaxis.tick_top()
ax[0].xaxis.set_label_position('top')
ax[0].set_xlabel('$q_{tN}  (atm)$', fontsize=14)
ax[0].set_ylabel('Depth (m)', fontsize=14)
ax[1].set_ylim(ax[1].get_ylim()[::-1])
ax[1].xaxis.tick_top()
ax[1].xaxis.set_label_position('top')
ax[1].set_xlabel('$I_c$', fontsize=14)

fig.tight_layout()
plt.show()
plt.clf()
```

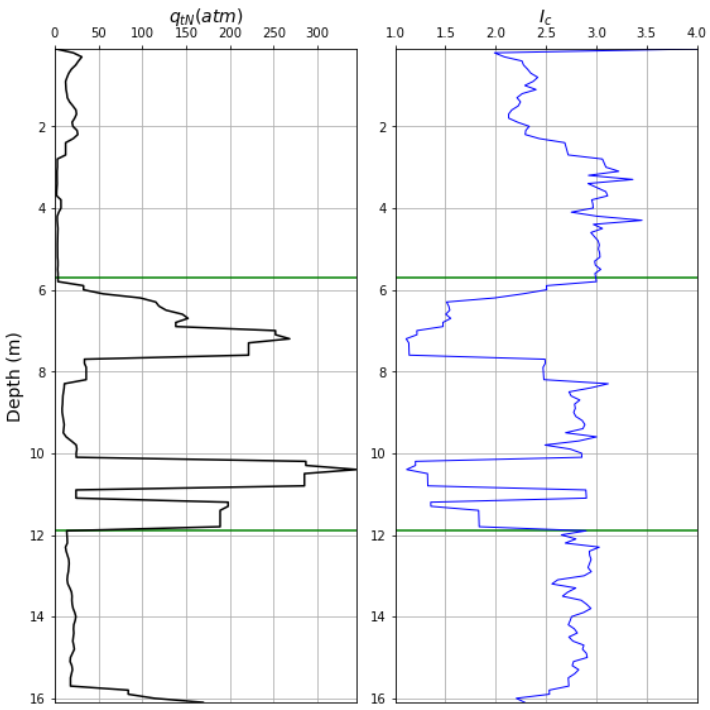


```
<Figure size 432x288 with 0 Axes>
```

Step 3: Prepare Data and Calculate CDFs

The next box calculates the cumulative distributions of the measured I_c data, with cropping performed to account for the depth of the strata of interest and an upper cap to limit values to sandy soils not influened by high plasticity.

In [7]:

```
# Crop and sort Ic, and cap to only values less than the Ic-cutoff (only low plasticity soils)
dfcpt_x = dfcpt[(z_cpt <= stbot) & (z_cpt > sttop)] # crop all cpt values to strata bounds
Ic_crop = Ic[(z_cpt <= stbot) & (z_cpt > sttop)] # Ic cropped values as list for later calcs
z_crop = z_cpt[(z_cpt <= stbot) & (z_cpt > sttop)] # store the z_cpt cropped values for later calcs
dfcpt_x = dfcpt_x[dfcpt_x.Ic <= Ic_cut] # remove layers not being considered
dfcpt_x = dfcpt_x.sort_values(by='Ic') # sort these CPT values
N_Ic = (np.arange(len(dfcpt_x['z_cpt']))+.5)/float(len(dfcpt_x['z_cpt'])) # discretize for CDF
dfcpt_x['N_Ic'] = N_Ic.tolist() # add N_Ic to dataframe
dfcpt_x.head()
```

Out[7]:

	z_cpt	qc	fs	Ic	N_Ic
71	7.2	268.2599	0.37497	1.109966	0.012821
103	10.4	344.5896	0.71436	1.114865	0.038462
72	7.3	221.3615	0.16552	1.136777	0.064103
73	7.4	221.3615	0.16552	1.138098	0.089744
74	7.5	221.3615	0.16552	1.139416	0.115385

Next, similarly crop and cap the FC lab data. Calculate the average measured I_c within a specified depth interval from the FC sample depth. An optional code sequence is included for adjusting the adjacent depth I_c to only consider values below the susceptibility cutoff.

In [8]:

```
# Prepare lab data
dflab_x = dflab[(z_lab <= stbot) & (z_lab > sttop)] # crop all lab values to strata bounds
dflab_x = dflab_x[dflab_x.consider != 'N'] # remove layers not being considered

# ================================================================
# Find median Ic for depths near FC (disregard all Ic values greater than Ic-cutoff)
Ic_nearFC = np.zeros(len(dflab_x['z_lab']))
for i in range(len(Ic_nearFC)):
    Ic_nearFC[i] = np.median(Ic[(z_cpt <= min((dflab_x.iloc[i]['z_lab']+Ic_int/2),stbot))
                                & (z_cpt >= max(sttop,(dflab_x.iloc[i]['z_lab']-Ic_int/2)))])
dflab_x['Ic_nearFC'] = Ic_nearFC.tolist() # add Ic_nearFC to dataframe

# OPTIONAL to adjust Ic_nearFC for only values below Ic cutoff:
```

```
# minIc = np.zeros(len(dflab_x['z_lab']))
# for i in range(len(Ic_nearFC)):
#     minIc[i] = (min(Ic[(z_cpt <= min((dflab_x.iloc[i]['z_lab']+Ic_int/2),stbot)) & (z_cpt >= max(sttop,(dflab_x.iloc[i]['z_lab
#     if (minIc[i]>2.6):
#         # if no Ic value in range is less than 2.6, do not consider and plot at median of all
#         Ic_nearFC[i] = np.median(Ic[(z_cpt <= min((dflab_x.iloc[i]['z_lab']+Ic_int/2),stbot))
#               & (z_cpt >= max(sttop,(dflab_x.iloc[i]['z_lab']-Ic_int/2)))])
#         dflab_x.at[dflab_x.index[i],'consider']='N'
#     else: # else take the median of Ic values less than 2.6
#         Ic_nearFC[i] = np.median(Ic[(z_cpt <= min((dflab_x.iloc[i]['z_lab']+Ic_int/2),stbot))
#                                     & (z_cpt >= max(sttop,(dflab_x.iloc[i]['z_lab']-Ic_int/2)))
#                                     & (Ic <= Ic_cut)])
# dflab_x = dflab_x[dflab_x.consider != 'N'] # now again, remove layers with Ic > cutoff
dflab_x
```

Out[8]:

	z_lab	FC_lab	consider	LL	PL	PI	wc	Unnamed: 7	Ic_nearFC
64	5.791270	42	Y	23.0	NaN	4.0	24.3	NaN	2.751382
65	5.791270	40	Y	22.0	NaN	4.0	23.0	NaN	2.751382
66	5.943672	30	Y	NaN	NaN	NaN	22.9	NaN	2.507853
67	5.943672	35	Y	20.0	NaN	1.0	23.1	NaN	2.507853
68	6.035113	33	Y	NaN	NaN	NaN	19.7	NaN	2.504712
69	6.096074	31	Y	NaN	NaN	NaN	18.3	NaN	2.269952
70	6.187515	23	Y	NaN	NaN	NaN	NaN	NaN	1.988941
71	6.644721	6	Y	NaN	NaN	NaN	NaN	NaN	1.533748
72	6.797123	23	Y	NaN	NaN	NaN	NaN	NaN	1.477298
73	6.949525	20	Y	NaN	NaN	NaN	NaN	NaN	1.475569
74	7.315289	16	Y	NaN	NaN	NaN	17.4	NaN	1.138098
75	7.437210	9	Y	NaN	NaN	NaN	NaN	NaN	1.138098
77	8.656425	17	Y	NaN	NaN	NaN	NaN	NaN	2.784266
79	10.363326	10	Y	NaN	NaN	NaN	NaN	NaN	1.203550
81	11.247257	31	Y	NaN	NaN	NaN	NaN	NaN	1.830948

Declustered sample weights based on the representative depth of each sample are prepared for consideration of both a weighted and non-weighted FC distribution.

In [9]:

```
# Determine depth weights for lab FC distribution by nearest-neighbor declustering
# this algorithm only weights non-susceptible (Ic > cutoff) thicknesses (assumes lateral similarity of boring-CPT pair for this)
dflab_x = dflab_x.sort_values(by='z_lab')
z_lab_declus = dflab_x['z_lab'].to_numpy() # obtain arrays for the params we are working with
FC_declus = dflab_x['FC_lab'].to_numpy()
h_declus = np.zeros(len(FC_declus)) # store susceptible thicknesses for each FC
w_declus = np.zeros(len(FC_declus)) # store decluster weight for each FC
for i in range(len(FC_declus)):
    if i == 0: # conditions for top and bottom samples
        ztop = sttop
        zbot = np.mean([z_lab_declus[i+1],z_lab_declus[i]])
    elif i == len(FC_declus)-1:
        ztop = np.mean([z_lab_declus[i-1],z_lab_declus[i]])
        zbot = stbot
    else:
        ztop = np.mean([z_lab_declus[i-1],z_lab_declus[i]])
        zbot = np.mean([z_lab_declus[i+1],z_lab_declus[i]])
    # count CPT Ic values within neighborhood of FC
    h_declus[i] = np.count_nonzero((Ic_crop[(z_crop>=ztop) & (z_crop<zbot) & (Ic_crop <= Ic_cut)]))*dz_cpt
w_declus = (h_declus/sum(h_declus)) # solve for weights that sum to 1
dflab_x['w_FC'] = w_declus.tolist() # add weights to dataframe

# CDF values of lab FC without weighting
dflab_x = dflab_x.sort_values(by='FC_lab') # sort the lab values
N_FC = (np.arange(len(dflab_x['z_lab']))+.5)/float(len(dflab_x['z_lab'])) # discretize for CDF (no weight)
dflab_x['N_FC'] = N_FC.tolist() # add N_FC to dataframe
dflab_x = dflab_x.reset_index(drop=True) # reset index values

# CDF values of lab FC with weighting
N_FC_w = np.zeros(len(w_declus)) # accumulating weights to calculate the weighted CDF
N_FC_w[0] = dflab_x['w_FC'][0]*0.5 # starting percentile; half the value to prevent CDF extending to ends
for i in range(1,len(dflab_x['w_FC'])):
    N_FC_w[i] = N_FC_w[i-1]+dflab_x['w_FC'][i]
dflab_x['N_FC_w'] = N_FC_w.tolist() # add to dataframe
dflab_x
```

Out[9]:

	z_lab	FC_lab	consider	LL	PL	PI	wc	Unnamed: 7	Ic_nearFC	w_FC	N_FC	N_FC_w
0	6.644721	6	Y	NaN	NaN	NaN	NaN	NaN	1.533748	0.076923	0.033333	0.038462
1	7.437210	9	Y	NaN	NaN	NaN	NaN	NaN	1.138098	0.179487	0.100000	0.217949
2	10.363326	10	Y	NaN	NaN	NaN	NaN	NaN	1.203550	0.205128	0.166667	0.423077
3	7.315289	16	Y	NaN	NaN	NaN	17.4	NaN	1.138098	0.051282	0.233333	0.474359
4	8.656425	17	Y	NaN	NaN	NaN	NaN	NaN	2.784266	0.051282	0.300000	0.525641
5	6.949525	20	Y	NaN	NaN	NaN	NaN	NaN	1.475569	0.076923	0.366667	0.602564
6	6.187515	23	Y	NaN	NaN	NaN	NaN	NaN	1.988941	0.076923	0.433333	0.679487
7	6.797123	23	Y	NaN	NaN	NaN	NaN	NaN	1.477298	0.025641	0.500000	0.705128
8	5.943672	30	Y	NaN	NaN	NaN	22.9	NaN	2.507853	0.025641	0.566667	0.730769
9	6.096074	31	Y	NaN	NaN	NaN	18.3	NaN	2.269952	0.025641	0.633333	0.756410
10	11.247257	31	Y	NaN	NaN	NaN	NaN	NaN	1.830948	0.179487	0.700000	0.935897
11	6.035113	33	Y	NaN	NaN	NaN	19.7	NaN	2.504712	0.025641	0.766667	0.961538
12	5.943672	35	Y	20.0	NaN	1.0	23.1	NaN	2.507853	0.000000	0.833333	0.961538
13	5.791270	40	Y	22.0	NaN	4.0	23.0	NaN	2.751382	0.000000	0.900000	0.961538
14	5.791270	42	Y	23.0	NaN	4.0	24.3	NaN	2.751382	0.000000	0.966667	0.961538

Step 4: Define correlation functions

Define correlation functions:

- The Boulanger and Idriss 2014 (BI14) correlation, with C_{FC} determined from a linear regression of available FC data
- The Bassal et al. 2022 (BBD22) percentile match for three selected percentiles of the fines content data

The functions are written as inverse functions (with FC dependent on I_c), as would be done for a forward analysis to estimate FC from CPT data.

The standard deviations of both FC and I_c are also calculated for BI14, representing the standard deviation of the measured lab points to the trendlines.

In [10]:

```
# Boulanger and Idriss (2014) correlation which allows for a CFC intercept calibration parameter (Inverse: Ic to FC)
def BI14_inv(Ic_eval,FC_lab,Ic_nearFC):
    # Ic_eval represents the full Ic vector within depth of interest
    N = len(FC_lab) # calculate number samples
    B = 1/80        # slope is set by BI14
    x = FC_lab
    y = Ic_nearFC
    sum_x = np.sum(x)
    sum_xsq = np.sum(x**2)
    sum_y = np.sum(y)
    sum_xy = np.sum(x*y)
    A = (sum_y-B*sum_x)/N # intercept is adjusted
    CFC = 137/80 - A     # CFC per BI14
    sigIc = ((np.float64(1)/(N-2))*np.sum((y-A-B*x)**2))**0.5 # Array calculation of sigy
    sigFC = ((np.float64(1)/(N-2))*np.sum((x-np.minimum(100,np.maximum(y/B-A/B,0)))**2))**0.5 # Array calculation of sigx
    FC_estimate = np.empty(len(Ic_eval))
    for i in range(len(Ic_eval)):
            FC_estimate[i] = max(0,min((80*(Ic_eval[i]+CFC)-137),100))
    return CFC, FC_estimate, sigIc, sigFC

# Boulanger and Idriss (2014) correlation which allows for a CFC input
def BI14_inv_CFC(Ic_eval,CFC,FC_lab,Ic_nearFC):              # Ic_eval represents the Ic vector where FC is evaluated
    FC_estimate = np.empty(len(Ic_eval))
    for i in range(len(Ic_eval)):
        FC_estimate[i] = max(0,min((80*(Ic_eval[i]+CFC)-137),100))
    A = 137/80 - CFC
    B = 1/80
    sigIc = ((np.float64(1)/(len(FC_lab)-2))*np.sum((Ic_nearFC-A-B*FC_lab)**2))**0.5 # Array calculation of sigy
    sigFC = ((np.float64(1)/(len(FC_lab)-2))*np.sum((FC_lab-np.minimum(100,np.maximum(Ic_nearFC/B-A/B,0)))**2))**0.5
    return FC_estimate, sigIc, sigFC

# Bassal et al. (2022) FC-Ic percentile matching method (for 3 pins)
def BBD22_inv(Ic_eval,Ic_suscept,Ic_cut,slope_max,Ppin,FCpin):
    # Ic_eval is used for FC prediction (full Ic vector within depth of interest)
    # Ic_suscept is used for CDF (cropped for depths of interest and capped to exclude highly plastic soils)
    Icpin = np.zeros(3)
    Icpin[0] = np.percentile(Ic_suscept, Ppin[0])
    Icpin[1] = np.percentile(Ic_suscept, Ppin[1])
    Icpin[2] = np.percentile(Ic_suscept, Ppin[2])
```

```
    EFC1 = np.minimum(abs((FCpin[1]-FCpin[0]))/max(.01,abs((Icpin[1]-Icpin[0]))),slope_max)
    EFC2 = np.minimum(abs((FCpin[1]-FCpin[2]))/max(.01,abs((Icpin[1]-Icpin[2]))),slope_max)
    FC_estimate = np.empty(len(Ic_eval))  # Loop to solve for FC Estimate
    for i in range(len(Ic_eval)):
        if Ic_eval[i] > Ic_cut:
            FC_estimate[i] = 100
        elif Ic_eval[i] <= Icpin[1]:
            FC_estimate[i] = np.maximum(0,np.minimum(EFC1*(Ic_eval[i]- Icpin[1])+FCpin[1],100))
        else: FC_estimate[i] = np.maximum(0,np.minimum(EFC2*(Ic_eval[i]- Icpin[1])+FCpin[1],100))
    return Icpin,FC_estimate
```

The next cell estimates C_{FC} for BI14 from the relevant lab data. If not already input at the start of this notebook, it will also determine default BBD22 input at percentile pin values of 16, 50 and 84%, set to match the cumulative distribution function (CDF) of the available FC data.

In [11]:
```
try: # check if Ppin was given; if not start here
   Ppin
except NameError:
    Ppin = [16, 50, 84]

try: # check if FCpin was given; if not guess based on CDF at Ppin
   FCpin
except NameError:
    #FCpin = [np.percentile(dflab_x['FC_lab'],Ppin[0]), np.percentile(dflab_x['FC_lab'],Ppin[1]),
    #         np.percentile(dflab_x['FC_lab'],Ppin[2])] # FCpin guess for no-weights
    FCpin = [np.interp(Ppin[0]/100,dflab_x['N_FC_w'],dflab_x['FC_lab']),
               np.interp(Ppin[1]/100,dflab_x['N_FC_w'],dflab_x['FC_lab']),
               np.interp(Ppin[2]/100,dflab_x['N_FC_w'],dflab_x['FC_lab'])] # FCpin guess for weighted CDF

# Find CFC and Icpin based on estimates
CFCest,FCest_BI14,sigIc,sigFC = BI14_inv(Ic_crop,dflab_x['FC_lab'],dflab_x['Ic_nearFC'])
Icpin,FCest_BBD2 = BBD22_inv(Ic_crop,dfcpt_x['Ic'],Ic_cut,slope_max,Ppin,FCpin)
FCest_BI14,sigIc,sigFC = BI14_inv_CFC(Ic_crop,CFCest,dflab_x['FC_lab'],dflab_x['Ic_nearFC'])
print("Default BI14 CFC from lab data = %.3f" %(CFCest))
print("Default BI22 FC pin =", [round(elem, 1) for elem in FCpin])
print("Default BI22 Percentile pin =",Ppin)
print("Default BI22 Ic pin =",[round(elem, 2) for elem in Icpin])
```

```
Default BI14 CFC from lab data = 0.027
Default BI22 FC pin = [8.0, 16.5, 31.0]
Default BI22 Percentile pin = [16, 50, 84]
Default BI22 Ic pin = [1.2, 1.51, 2.48]
```

Step 5: Plot figure comparing performance of all correlations

This step runs the correlation functions and displays an interactive group of plots for the stratum considered of:

- I_c vs FC correlations based on measurements
- FC with depth from the correlations
- FC cumulative distributions from the correlations and for the "declustered" FC of susceptible soils

In [12]:
```
# Prepare interactive widget prior to plotting (this code mimics Interactive Variogram Calculation by Dr. Michael Pyrcz)
title = widgets.Text(value='                    FC-Ic Percentile Match Correlation, Interactive Demo - By Patrick Bassal',layou
Per_1 = widgets.FloatSlider(min = 0, max = 100, value = Ppin[0], step = 1, description = 'Per-1',orientation='vertical',layout=L
Per_1.style.handle_color = 'gray'

Per_2 = widgets.FloatSlider(min = 0, max = 100, value = Ppin[1], step = 1, description = 'Per-2',orientation='vertical',layout=L
Per_2.style.handle_color = 'gray'

Per_3 = widgets.FloatSlider(min = 0, max = 100, value = Ppin[2], step = 1, description = 'Per-3',orientation='vertical',layout=L
Per_3.style.handle_color = 'gray'

FC_1 = widgets.FloatSlider(min = 0, max = 100, value = FCpin[0], step = 1, description = 'FC-1',orientation='vertical',layout=La
FC_1.style.handle_color = 'red'

FC_2 = widgets.FloatSlider(min = 0, max = 100, value = FCpin[1], step = 1, description = 'FC-2',orientation='vertical',layout=La
FC_2.style.handle_color = 'red'

FC_3 = widgets.FloatSlider(min = 0, max = 100, value = FCpin[2], step = 1, description = 'FC-3',orientation='vertical',layout=La
FC_3.style.handle_color = 'red'

CFC = widgets.FloatSlider(min = -.6, max = .6, value = CFCest, step = .01, description = '$C_{FC}$',orientation='vertical',layou
CFC.style.handle_color = 'magenta'

ui1 = widgets.HBox([Per_1,Per_2,Per_3,FC_1,FC_2,FC_3,CFC],) # basic widget formatting
ui = widgets.VBox([title,ui1],)

def myplot(Per_1,Per_2,Per_3,FC_1,FC_2,FC_3,CFC):
    FCpin = [FC_1,FC_2,FC_3]
    Ppin = [Per_1,Per_2,Per_3]
```

```
    FCest_BI14,sigIc,sigFC = BI14_inv_CFC(Ic_crop,CFC,dflab_x['FC_lab'],dflab_x['Ic_nearFC'])
    Icpin,FCest_BBD22 = BBD22_inv(Ic_crop,dfcpt_x['Ic'],Ic_cut,slope_max,Ppin,FCpin)

    # ================================================================
    # Make plots: ax1 - Ic vs FC
    #             ax2 - FC with depth from all correlations
    #             ax3 - CDF Plots

    fig = plt.figure(figsize=(6.5, 4.8),dpi=250)
    gs = fig.add_gridspec(4, 2,hspace=.5,wspace=.3, height_ratios=[1, 1,1.5,.65])
    ax1 = fig.add_subplot(gs[0:2, 0])
    ax3 = fig.add_subplot(gs[2:4, 0])
    ax2 = fig.add_subplot(gs[0:3, 1]) # ax2 spans two rows

    # Correlation 1 - BI14
    Ic_ax1 = np.linspace(1.0,4.0,100) # Ic for ax1 plot, BI14 correlation
    FC_ax1_BI14 = np.minimum(100,np.maximum(80*(Ic_ax1+CFC)-137,0)) # Ic for ax1 plot, BI14 correlation
    ax1.plot(FC_ax1_BI14,Ic_ax1,'m-',linewidth=1)

    FC_ax2_BI14 = np.minimum(100,np.maximum(80*(Ic_crop+CFC)-137,0))
    for i in range(len(FC_ax2_BI14)):
        if FC_ax2_BI14[i] >99.7:
            FC_ax2_BI14[i] = float('nan')
    ax2.plot(FC_ax2_BI14,z_crop,'m-',linewidth=1,label = 'BI14, $C_{FC}$=%.3f ($\sigma_{FC}$=%.2f)' %(CFC,sigFC))

    FCax3_BI14 = np.minimum(100,np.maximum(80*(dfcpt_x['Ic']+CFC)-137,0))
    ax3.plot(FCax3_BI14,dfcpt_x['N_Ic'],'m-',linewidth=1)

    # Correlation 2 - BBD22
    Icpin,FC_ax1_BBD22 = BBD22_inv(Ic_ax1,dfcpt_x['Ic'],Ic_cut,slope_max,Ppin,FCpin)
    ax1.plot(FC_ax1_BBD22,Ic_ax1,'g-',linewidth=1)

    Icpin,FC_ax2_BBD22 = BBD22_inv(Ic_crop,dfcpt_x['Ic'],Ic_cut,slope_max,Ppin,FCpin)
    for i in range(len(FC_ax2_BBD22)):
        if FC_ax2_BBD22[i] >99.7:
            FC_ax2_BBD22[i] = float('nan')
    ax2.plot(FC_ax2_BBD22,z_crop,'g-',linewidth=1,label="BBD22, 3-point Percentile Match")

    Icpin,FC_ax3_BBD22 = BBD22_inv(dfcpt_x['Ic'].to_numpy(),dfcpt_x['Ic'],Ic_cut,slope_max,Ppin,FCpin)
    ax3.plot(FC_ax3_BBD22,dfcpt_x['N_Ic'],'g-',linewidth=1)

    # Measured FC and Percentile Pins
    ax1.plot(dflab_x['FC_lab'],dflab_x['Ic_nearFC'],'bD',markersize=3)
    ax2.plot(dflab_x['FC_lab'],dflab_x['z_lab'],'bD',markersize=3,label="Measured FC")
    ax3.plot(dflab_x['FC_lab'],dflab_x['N_FC_w'],'bD--',markersize=3)
    ax1.plot([float(FCpin[0]),float(FCpin[1]),float(FCpin[2])],[float(Icpin[0]),float(Icpin[1]),float(Icpin[2])],
                    'ro',markersize=3)
    ax2.plot(-1,-1,'ro',markersize=3,label="FC Pins") # not plotted but used for legend
    ax3.plot([float(FCpin[0]),float(FCpin[1]),float(FCpin[2])],[float(Ppin[0]/100),float(Ppin[1]/100),float(Ppin[2]/100)],
                    'ro',markersize=3)

    # Set axis extents
    ax1.axis([0, 100, 1, 4])
    ax2.axis([0, 100, min(z_crop), max(z_crop)])
    ax3.axis([0, 100, 0, 1])

    # Format axis Labels
    ax1.set_ylabel('Soil Behavior Type Index, $I_c$', fontsize=7)
    ax2 = plt.gca()
    ax2.set_ylim(ax2.get_ylim()[::-1])
    ax2.xaxis.tick_top()
    ax2.xaxis.set_label_position('top')
    ax2.set_xlabel('Fines Content, FC (%)', fontsize=7)
    ax2.set_ylabel('Depth Below Ground Surface along CPT Trace (m)', fontsize=7)
    ax3.set_xlabel('Fines Content, FC (%)', fontsize=7)
    ax3.set_ylabel('Cumulative Distribution', fontsize=7)
    ax1.tick_params(labelsize=6.5)
    ax2.tick_params(labelsize=6.5)
    ax3.tick_params(labelsize=6.5)

    # Format Legend
    ax2.legend(bbox_to_anchor=(.42,-.25), loc="lower center", fontsize=7)

    # Grid and final touchups
    ax1.minorticks_on(); ax2.minorticks_on(); ax3.minorticks_on()
    ax1.grid(); ax2.grid(); ax3.grid()
    ax1.set_title('%s, %s, %s \n' %(site_name,cpt,stratum), fontsize=9, loc='left')
    plt.show()

# connect function to plot to the widgets
interactive_plot = widgets.interactive_output(myplot, {'Per_1':Per_1,'Per_2':Per_2,'Per_3':Per_3,'FC_1':FC_1,'FC_2':FC_2,'FC_3':
interactive_plot.clear_output(wait = True)               # reduce flickering by delaying plot updating
```

Interactive Display

This interactive display allows exploration of different inputs for the model parameters, to visualize their effect in real time. The parameters

- $Per-(1-3)$: Three percentile values selected tp pin the BBD22 correlation method.
- $FC-(1-3)$: Three fines content values selected to pin the BBD22 correlation method.
- C_{FC}: The fines content correction factor for the BI14 correlation method.

Default parameters for BBD22 can be preselected as inputs at the start of this notebook. If inputs are not given, The default C_{FC} is selected based on all considered (low plasticity) lab data.

NOTE: The sliders allow nonsensical values. For BBD22, please ensure that the red FC pins on the charts remain pinned to the green correlation line. They may deviate if the maximum slope is exceeded, or if the pin values (i.e., percentiles or FC) are not sequentially increasing.

In [13]:
```
display(ui, interactive_plot)                          # display the interactive plot
# plt.savefig('%s_Plot.png' %(site_name), dpi=250, format='png',pad_inches=0.1) # NOTE: save feature currently not working
    # save plots workaround is to copy codes for plotting above to a cell below with the selected parameter values
```

In [14]:
```
# Find CFC and Icpin based on estimates
FCpin_final = [FC_1.value, FC_2.value, FC_3.value]
Ppin_final = [Per_1.value, Per_2.value, Per_3.value]
CFC = CFCest # recommended to use the CFC calculated from data, not slider

CFC_final,FCest_BI14_final,sigIc_final,sigFC_final = BI14_inv(Ic_crop,dflab_x['FC_lab'],dflab_x['Ic_nearFC'])
Icpin_final,FCest_BBD22_final = BBD22_inv(Ic_crop,dfcpt_x['Ic'],Ic_cut,slope_max,Ppin_final,FCpin_final)
FCest_BI14,sigIc,sigFC = BI14_inv_CFC(Ic_crop,CFCest,dflab_x['FC_lab'],dflab_x['Ic_nearFC'])
print("Selected BI14 CFC from lab data = %.3f" %(CFC_final))
print("Selected BI22 FC pin =", [round(elem, 1) for elem in FCpin_final])
print("Selected BI22 Percentile pin =",Ppin_final)
print("Selected BI22 Ic pin =",[round(elem, 2) for elem in Icpin_final])
```

```
Selected BI14 CFC from lab data = 0.027
Selected BI22 FC pin = [8.0, 16.5, 31.0]
Selected BI22 Percentile pin = [16.0, 50.0, 84.0]
Selected BI22 Ic pin = [1.2, 1.51, 2.48]
```

Step 6: Estimate of FC uncertainty (σ_{FC}) for BBD22 distribution

This step uses a bootstrapping algorithm based on the number of susceptible samples from the weighted BBD22 FC CDF, to determine the standard deviation (uncertainty) of three percentile values (i.e., P16, P50, and P84). This method is best used with the default BBD22 distribution (set to match the declustered FC distribution at P16, P50, and P84). An average uncertainty is provided for use in probabilistic assessments.

In [15]:
```
# Estimate uncertainty for the BBD22 FC CDF for P16, P50 and P84 using bootstrapping at P16, P50, P84
# subroutine modified from "SubsurfaceDataAnalytics_bootstrap.ipynb" by Dr. Michael Pyrcz (https://github.com/GeostatsGuy/Python

# Find BBD22 CDF (can alternatively use FC sample CDF)
Icpin,FCcdf_BBD22 = BBD22_inv(dfcpt_x['Ic'].to_numpy(),dfcpt_x['Ic'],Ic_cut,slope_max,Ppin_final,FCpin_final)

N = np.count_nonzero(dflab_x['w_FC']>(0.5/len(dflab_x['w_FC']))) # number of samples considered (only samples with 0.5/N weight)
L = 20000                                  # set the number of realizations for uncertainty calculation
mean = np.zeros(L); stdev = np.zeros(L)    # declare arrays to hold the realizations of the statistics
P16 = np.zeros(L)
P50 = np.zeros(L); P84 = np.zeros(L)
for l in range(0, L):                      # loop over realizations
    samples = random.choices(FCcdf_BBD22, weights=None, cum_weights=None, k=N) # sampling with replacement
    # samples = random.choices(dflab_x['FC_lab'].to_numpy(), weights=dflab_x['w_FC'].to_numpy(), k=len(dflab_x)) # alt. FC sampl
    P16[l] = np.percentile(q = 16, a = samples)
    P50[l] = np.percentile(q = 50, a = samples)
    P84[l] = np.percentile(q = 84, a = samples)
    mean[l] = np.mean(samples)

plt.subplot(111)
plt.hist(P16, facecolor='red',bins=np.linspace(0,100,50),alpha=0.2,density=False,edgecolor='black',label='P16')
plt.hist(P50, facecolor='blue',bins=np.linspace(0,100,50),alpha=0.2,density=False,edgecolor='black',label = 'P50')
plt.hist(P84, facecolor='green',bins=np.linspace(0,100,50),alpha=0.2,density=False,edgecolor='black',label = 'P84')
plt.xlim([0,100]); plt.ylim([0,10000.0])
plt.xlabel('Fines Content (%)'); plt.ylabel('Frequency'); plt.title('Bootstrap Uncertainty in BBD22 CDF P16, P50 and P84')
plt.legend(loc='upper left')
plt.grid(True)
plt.subplots_adjust(left=0.0, bottom=0.0, right=2.0, top=1.2, wspace=0.2, hspace=0.2)
plt.show()

print('Summary Statistics for Uncertainty in Percentiles')
print('P16 mean and standard deviation: ',np.mean(P16),', ', np.std(P16))
```

```
print('P50 mean and standard deviation: ',np.mean(P50),', ', np.std(P50))
print('P84 mean and standard deviation: ',np.mean(P84),', ', np.std(P84))
print('Approximate total BBD22 uncertainty, σFC: ', np.round(np.mean([np.std(P16),np.std(P50),np.std(P84)]),2))
```

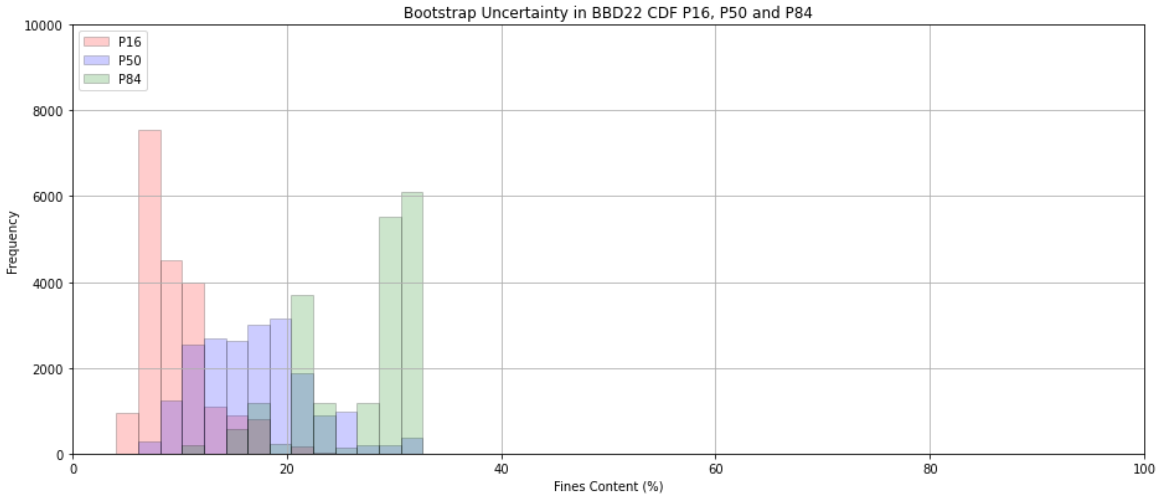


```
Summary Statistics for Uncertainty in Percentiles
P16 mean and standard deviation:  9.488396251469416 ,  3.2756825776789875
P50 mean and standard deviation:  16.931621287200954 ,  4.961076173092821
P84 mean and standard deviation:  26.596562786277598 ,  5.214245344656096
Approximate total BBD22 uncertainty, σFC:  4.48
```

In [ ]:

Interactive widget example results from ***CPT_Site-Specific-FC.ipynb:***

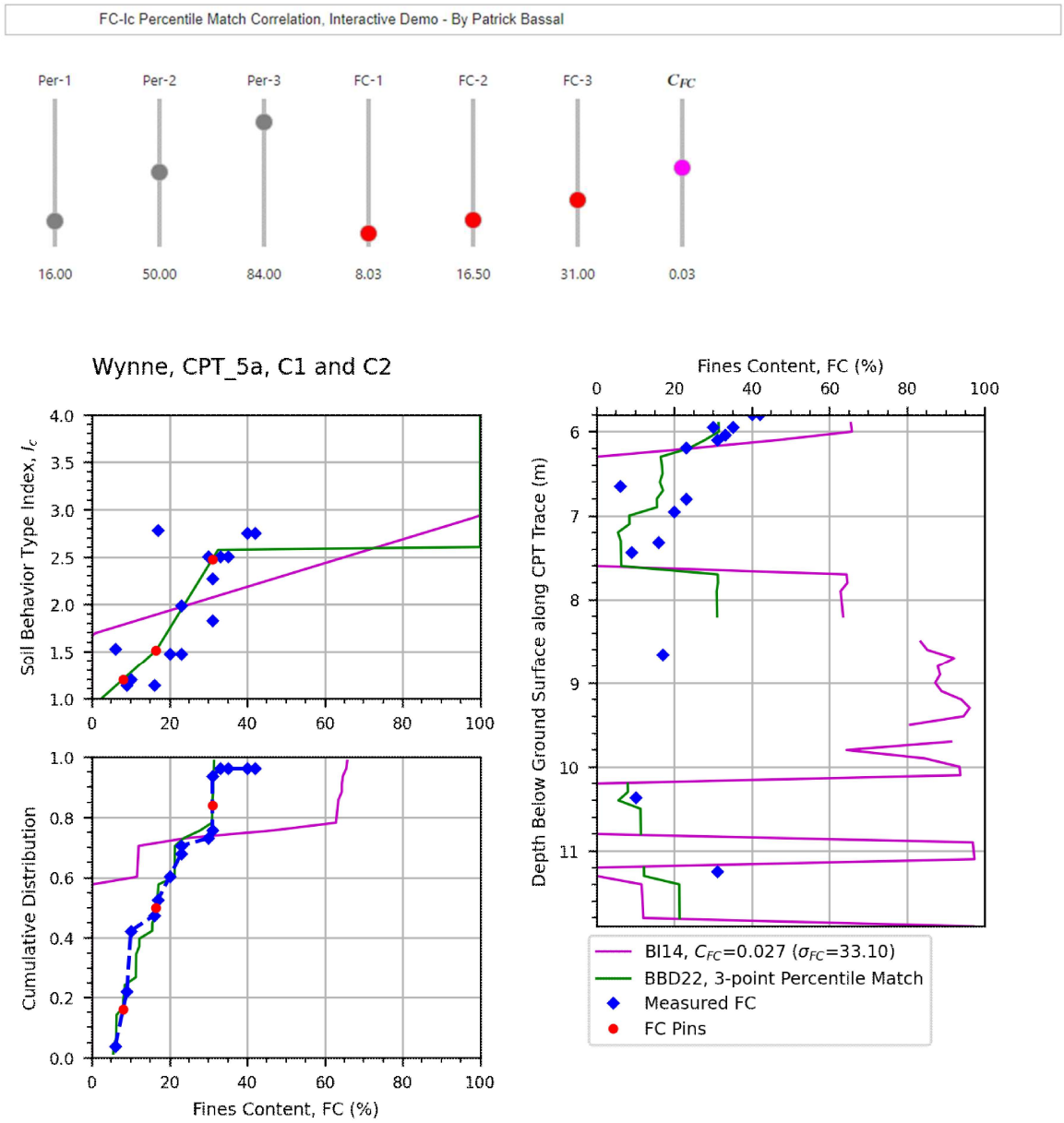

Sitewide CPT-based Liquefaction Resistance

The following notebook estimates the liquefaction resistance of sand-like soils for multiple (sitewide) CPTs, based on strata-specific inputs per the Boulanger & Idriss (2014; BI14) methodology, with the soil behaviour type index (I_c) from Robertson (2009). It also estimates the undrained shear strengths and sensitivity for clay-like soils. It outputs an excel (.xlsx) file with summary results for each CPT. The results can be used for various evaluations of earthquake-induced liquefaction triggering potential and ground deformations, by providing data parameters for (1) simplified methods (e.g., Liquefaction Vulnerability Indices), (2) advanced analyses (e.g, nonlinear dynamic analyses), and (3) geostatistical modeling of the subsurface (e.g., sequential Guassian simulation).

An excel input file formatted in accordance with the provided example is necessary to run this notebook, with (1) a summary sheet that calls out the site-wide CPT data files and delineates strata transitions, and (2) a summary sheet of strata-specific properties. Either the BI14 or Bassal et al. (2022) methods can be used for the fines content correction (a separate notebook in this series can provide the inputs for these FC correlation methods). The CPT data for tip resistance and skin friction is expected in units of atm.

By Patrick C. Bassal (Ver 0: 01/05/2022)

References:

Bassal, P. C., Boulanger, R. W., and DeJong, J. T. (2022). "Site-Specific CPT-based Fines Content Correlations using Percentile Matching." In proc., Geo-Congress 2022, Charlotte, NC. Reston, VA: ASCE. https://doi.org/10.1061/9780784484043.053.

Boulanger, R. W., and Idriss, I. M. (2014). "CPT and SPT based liquefaction triggering procedures." Report No. UCD/CGM.-14/01.

Robertson, P. K. (2009). "Performance based earthquake design using the CPT." Proc., IS Tokyo Conf., CRC Press/Balkema, Taylor & Francis Group, Tokyo.

Step 1: Import libraries

Import all necessary libraries below. Note that the "LIQresist_fxn.py" python file must be copied into the working directory.

In [12]:
```
import numpy as np                # for array calculations
import pandas as pd               # for building dataframe tables

from LIQresist_fxns import vstress,R19_Ic,SuRatio,BI14_CRR  # this python file must be saved in directory
```

Step 2: Input CPT data and strata properties

Provide input values in this next box. The (1) summary sheet of the site-wide CPTs and strata transitions considered, and (2) summary sheet of strata-specific properties, are necessary for this step to work properly. See example files with this distribution.

In [13]:
```
#  Input CPT data and lab files:
site_name = 'Wynne' # site name used in title for results
input_file = 'INPUT_LIQcalcs_%s.xlsx' %(site_name) # name of formatted excel input file (see example)
    # NOTE: Spreadsheet not updated for use of u2 reading (use pore pressure corrected qc directly for each cpt file)
output_file = 'OUTPUT_LIQresist_%s.xlsx' %(site_name) # Name of desired output file

# General inputs:
Patm = 101.3       # atmospheric pressure (kPa)
gammaw = 9.81      # unit weight of water (kPa)

dz_new = 0.3        # new discretization (m), takes median qc and fs over interval. Use 0 for original data spacing.
# Recommend keep interval consistent with geostatistic mesh, to retain variance reduction effects over discretization scale.

# Load relevant excel sheets:
dfcpt = pd.read_excel (input_file, sheet_name='Input_CPT') # Load CPT summary sheet
dfcpt.dropna(subset = ["cpt_id"], inplace=True) # remove nan rows
num_cpts = len(dfcpt.index) # number of CPTs considered
dfstrat = pd.read_excel (input_file, sheet_name='Input_Strat') # Load strata summary sheet (with percentile and FC estimates)
num_strat = len(dfstrat.index) # number of strata considered (may be diff than # sequences)

writer = pd.ExcelWriter(output_file, engine='xlsxwriter') # Prepare excel output
dfcpt
```

Out[13]:

	cpt_id	cpt_file	x	y	top_elev	strat_seq	bnd_1	bnd_2	bnd_3	bnd_4	bnd_5	bnd_6	bnd_7	bnd_8	zwater_inv	zwater_eq
0	CPT_1	./cpt_data/CPT_1_IF.txt	353	0	20.9	12346	2.6	4.7	6.0	8.7	NaN	NaN	NaN	NaN	4.7	4.7
1	CPT_2	./cpt_data/CPT_2_IF.txt	298	0	20.2	123467	2.5	4.4	5.8	8.2	14.7	NaN	NaN	NaN	4.4	4.4
2	CPT_3	./cpt_data/CPT_3_IF.txt	292	0	20.1	12346567	2.5	4.4	5.8	8.1	9.9	10.6	14.4	NaN	4.4	4.4

	cpt_id	cpt_file	x	y	top_elev	strat_seq	bnd_1	bnd_2	bnd_3	bnd_4	bnd_5	bnd_6	bnd_7	bnd_8	zwater_inv	zwater_eq
3	CPT_4	./cpt_data/CPT_4_IF.txt	283	0	20.0	12346567	2.4	4.3	5.8	8.1	9.5	10.6	14.6	NaN	4.3	4.3
4	CPT_5a	./cpt_data/CPT_5a_IF.txt	279	0	19.9	12346567	2.4	4.3	5.9	8.3	9.7	11.8	15.7	NaN	4.3	4.3
5	CPT_6	./cpt_data/CPT_6_IF.txt	265	0	19.7	12346	2.4	4.1	6.1	8.0	NaN	NaN	NaN	NaN	4.1	4.1
6	CPT_7a	./cpt_data/CPT_7a_IF.txt	235	0	19.1	12346567	2.2	3.8	5.9	7.8	9.4	10.1	15.5	NaN	3.8	3.8
7	CPT_8	./cpt_data/CPT_8_IF.txt	205	0	18.3	123467	1.7	4.0	4.8	6.8	15.0	NaN	NaN	NaN	4.0	4.0
8	CPT_9	./cpt_data/CPT_9_IF.txt	268	0	19.8	123465	2.4	4.1	6.4	8.0	9.5	NaN	NaN	NaN	4.1	4.1
9	CPT_10	./cpt_data/CPT_10_IF.txt	272	0	19.8	12346567	2.4	4.2	6.2	8.0	9.8	10.8	15.8	NaN	4.2	4.2
10	CPT_11	./cpt_data/CPT_11_IF.txt	276	0	19.9	12346567	2.5	4.2	6.0	8.3	9.8	11.8	15.7	NaN	4.2	4.2
11	CPT_12	./cpt_data/CPT_12_IF.txt	113	0	18.1	12367	2.5	4.0	6.7	14.7	NaN	NaN	NaN	NaN	4.0	4.0
12	CPT_13	./cpt_data/CPT_13_IF.txt	0	0	17.5	1236	2.9	4.3	7.1	NaN	NaN	NaN	NaN	NaN	4.3	4.3
13	CPT_14	./cpt_data/CPT_14_IF.txt	500	0	23.0	1246	3.7	6.8	9.6	NaN	NaN	NaN	NaN	NaN	6.6	6.6

Define a function below to categorize stratum into different facies based on Ic or another metric. Currently 2 Ic cutoff values are being used for the entire site. This categorization can be used for future indicator-based geostatistical analyses.

In [14]:
```
# Create function to categorize data into lithofacies based on Ic value (user can define alternate fxn for facies categories)
Ic_cuts = [2.05, 2.6] # divide into three categories for this example (facies will be 1, 2, or 3)
                      # Ic cutoff can alternatively be assigned on a per stratum basis during next step

def facies_Ic(Ic, Ic_cuts):
    facies = np.ones((len(Ic)))
    for f in range (len(Ic_cuts)):
        for i in range(len(Ic)):
            if Ic[i] > Ic_cuts[f]:
                facies[i] = f + 2
    return facies
```

Step 3: Run resistance calculations and output to Excel

This step loops through all CPTs and outputs the results to the excel file specified in Step 1.

In [15]:
```
for cpti in range(num_cpts):

    # ================================================================
    #  Load CPT file
    cpt_file = dfcpt.iloc[cpti]["cpt_file"]
    cpt_id = dfcpt.iloc[cpti]["cpt_id"]
    z_full,qc_full,fs_full = np.loadtxt(cpt_file,skiprows=1,unpack=True) # load cpt file

    #  Impose limits on qc (tip resistance) and fs (skin friction) to avoid any negative values
    qc_full  = np.maximum(0.01*np.ones(np.shape(qc_full)),qc_full)
    fs_full  = np.maximum(0.001*np.ones(np.shape(fs_full)),fs_full)

    if dz_new > 0: # Discretize CPTs if dz_new is given
        dz_full = (max(z_full)-min(z_full))/(len(z_full)-1) # dz value for CPT readings
        int_pts = int(dz_new/dz_full) # number points to average within depth interval
        z = np.empty(int((len(z_full)-1)/int_pts)+1) # prepare new z
        qc = np.empty(int((len(z_full)-1)/int_pts)+1) # prepare new qc
        fs = np.empty(int((len(z_full)-1)/int_pts)+1) # prepare new fs
        count = 0 # Loop over z values to calculate columns with average intervals
        for i in range(len(z)):
            z[i] = np.median(z_full[count:(count+int_pts)])
            qc[i] = np.median(qc_full[count:(count+int_pts)])
            fs[i] = np.median(fs_full[count:(count+int_pts)])
            count = count + int_pts
    else: z = z_full; qc = qc_full; fs = fs_full

    dz = np.zeros(len(z)) # create array for difference in z (current-past)
    dz[0]= z[0]
    for i in range(1,len(z)):
        dz[i] = z[i]-z[i-1]

    #  Input CPT summary data
    zwater_inv = dfcpt.iloc[cpti]["zwater_inv"]   # water depth during investigation (m)
    zwater_eq = dfcpt.iloc[cpti]["zwater_eq"]   # water depth during earthquake (m)

    # Read boundaries and strata-specific values
    strat_seq = int(dfcpt.iloc[cpti]["strat_seq"]) # integer string of strata sequence
    num_seq = len(str(strat_seq))
    bnd_1 = dfcpt.iloc[cpti]["bnd_1"] # boundary depth (m) 1
```

```
    bnd_2 = dfcpt.iloc[cpti]["bnd_2"] # boundary depth (m) 2
    bnd_3 = dfcpt.iloc[cpti]["bnd_3"] # boundary depth (m) 3
    bnd_4 = dfcpt.iloc[cpti]["bnd_4"] # boundary depth (m) 4
    bnd_5 = dfcpt.iloc[cpti]["bnd_5"] # boundary depth (m) 5
    bnd_6 = dfcpt.iloc[cpti]["bnd_6"] # boundary depth (m) 6
    bnd_7 = dfcpt.iloc[cpti]["bnd_7"] # boundary depth (m) 7
    bnd_8 = dfcpt.iloc[cpti]["bnd_8"] # boundary depth (m) 8

    # Create arrays and read stratum specific params necessary for calculation
    UWm = np.zeros(len(z))
    UWsat = np.zeros(len(z))
    Nkt = np.zeros(len(z))
    Ic_cut = np.zeros(len(z))
    FC_method = np.array(['            ']*len(z))   # choice of BI14 or BBD22 for FC correction
    CFC = np.zeros(len(z))   # use for BI14 method
    Icpin = np.zeros([len(z),3]) # use for BBD22 method
    FCpin = np.zeros([len(z),3]) # use for BBD22 method
    stratum = np.array(['           ']*len(z))   # stratum name
    stbnd = np.array((bnd_1,bnd_2,bnd_3,bnd_4,bnd_5,bnd_6,bnd_7,bnd_8)) # Array with bounding depths
    for st in range(num_seq): # Loop to calc different props for each strata
        strat_ID = str(strat_seq)[st] # Assign stratum name
        if st == 0: # Assign stratum depth range
            sttop = 0 # Top depth of stratum
        else:
            sttop = stbnd[st-1] # Top depth of stratum
        if st == num_seq-1:  # Bottom depth of stratum
            stbot = max(z)
        else:
            stbot = stbnd[st]
        # Assign arrays of strata-specific values along CPT depth
        # <= and >= combo done on purpose to capture full depth, even though it allows overlap
        UWm[(z <= stbot) & (z >= sttop)] = dfstrat.loc[dfstrat['strat_ID']==int(strat_ID)]["UWm"]
        UWsat[(z <= stbot) & (z >= sttop)] = dfstrat.loc[dfstrat['strat_ID']==int(strat_ID)]["UWsat"]
        Nkt[(z <= stbot) & (z >= sttop)] = dfstrat.loc[dfstrat['strat_ID']==int(strat_ID)]["Nkt"]
        Ic_cut[(z <= stbot) & (z >= sttop)] = dfstrat.loc[dfstrat['strat_ID']==int(strat_ID)]["Ic_cut"]
        FC_method[(z <= stbot) & (z >= sttop)] = dfstrat.loc[dfstrat['strat_ID']==int(strat_ID)]["FC_method"]
        CFC[(z <= stbot) & (z >= sttop)] = dfstrat.loc[dfstrat['strat_ID']==int(strat_ID)]["CFC"]
        Icpin[(z <= stbot) & (z >= sttop),0] = dfstrat.loc[dfstrat['strat_ID']==int(strat_ID)]["Ic1"]
        Icpin[(z <= stbot) & (z >= sttop),1] = dfstrat.loc[dfstrat['strat_ID']==int(strat_ID)]["Ic2"]
        Icpin[(z <= stbot) & (z >= sttop),2] = dfstrat.loc[dfstrat['strat_ID']==int(strat_ID)]["Ic3"]
        FCpin[(z <= stbot) & (z >= sttop),0] = dfstrat.loc[dfstrat['strat_ID']==int(strat_ID)]["FC1"]
        FCpin[(z <= stbot) & (z >= sttop),1] = dfstrat.loc[dfstrat['strat_ID']==int(strat_ID)]["FC2"]
        FCpin[(z <= stbot) & (z >= sttop),2] = dfstrat.loc[dfstrat['strat_ID']==int(strat_ID)]["FC3"]
        stratum[(z <= stbot) & (z >= sttop)] = dfstrat.loc[dfstrat['strat_ID']==int(strat_ID)]["stratum"]


    # ======================================================================
    #  Determine vertical stresses
    sigv_inv,pwp_inv,sigveff_inv,sigv_eq,pwp_eq,sigveff_eq = vstress(
        z,dz,zwater_inv,zwater_eq,UWm,UWsat,gammaw,Patm)

    # ======================================================================
    #  Robertson 2009 iterative correlations to determine Ic
    F,n,C_n,Q,Ic,flag = R19_Ic(
        z,qc,fs,zwater_eq,sigv_inv,sigveff_inv,Ic_cut)

    # ======================================================================
    #  Determine Su ratios
    SuRat,Su,St = SuRatio(
        z,qc,fs,sigv_eq,sigveff_eq,Ic_cut,Ic,Nkt)

    # ======================================================================
    #  CRR - Cyclic Resistance Ratio
    FC,qc1N,qc1Ncs,CRR_norm = BI14_CRR(
        z,qc,sigveff_eq,Ic_cut,Ic,flag,FC_method,CFC,Icpin,FCpin)

    # ======================================================================
    #  Facies Category
    facies = facies_Ic(Ic,Ic_cuts)

    # ======================================================================
    #  Print excel file with summary of liquefaction resistance variables with depth

    data_temp = np.transpose(np.vstack((z,sigv_eq,sigveff_eq,qc,fs,F,Q,Ic,FC,qc1N,qc1Ncs,CRR_norm,SuRat,Su,St,facies)))
    df_out = pd.DataFrame(data_temp)
    df_out.rename(columns={0:'z (m)',1:'sigv_eq',2:'sigveff_eq',3:'qc (atm)',
                           4:'fs (atm)',5:'F (%)',6:'Q',7:'Ic',8:'FC (%)',9:'qc1N',
                           10:'qc1Ncs', 11:'CRRnorm', 12:'SuRat', 13:'Su', 14:'St', 15:'facies'},
                  inplace=True)
    df_out['stratum'] = stratum.tolist()
    df_out.to_excel(writer, sheet_name='%s' %(cpt_id))
```

In [16]:

```
writer.save() # Save final excel output
```

In [ ]:

```

```

Sitewide CPT-based Liquefaction Vulnerability Indices

The following notebook estimates several CPT-based Liquefaction Vulnerability Indices (LVIs) as referenced below. It requires the output excel file of the liquefaction resistance notebook, as input. Results are provided in excel format along each input CPT trace and as cumulative index values.

By Patrick C. Bassal (Ver 0: 04/28/2022)

References:

Boulanger, R. W., and Idriss, I. M. (2014). CPT and SPT based liquefaction triggering procedures. Report No. UCD/CGM.-14/01.

Iwasaki, T., Tatsuoka, F., Tokida K., & Yasuda, S. (1978). "A practical method for assessing soil liquefaction potential based on case studies at various sites in Japan." In Proc., 2nd Int. Conf. on Microzonation. Washington, DC: National Science Foundation.

Maurer, B., Green, R., & Taylor, O. S. (2015). "Moving towards an improved index for assessing liquefaction hazard: Lessons from historical data." Soils Found. 55 (4): 778–787. https://doi.org/10.1016/j.sandf.2015.06.010.

Zhang, G., Robertson, P. K., & Brachman, R. W. I. (2002). "Estimating liquefaction-induced ground settlements from CPT for level ground." Can. Geotech. J. 39: 1168–1180. DOI: 10.1139/T02-047.

Zhang, G., Robertson, P. K., & Brachman, R. W. I. (2004). "Estimating liquefaction induced lateral displacements using the standard penetration test or cone penetration test." J. Geotech. & Geoenv. Eng., ASCE, 130(8), 861–871.

Step 1: Import libraries

Import all necessary libraries below.

In [1]:
```
import numpy as np                # for array calculations
import pandas as pd               # for building dataframe tables
import scipy as sp                # stats and math packages
from scipy import interpolate     # for 2D interpolation
```

Step 2: Input Liquefaction Resistance Data

In [2]:
```
#  Input CPT data and lab files:
site_name = 'Wynne' # site name used in title for results
resist_file = 'OUTPUT_LIQresist_%s.xlsx' %(site_name) # name of formatted excel file for liquefaction resistance (see example)

# General inputs:
a_max = 0.51       # Peak ground acceleration
M = 6.7            # Earthquake Magnitude
Patm = 101.3       # atmospheric pressure (kPa)
gammaw = 9.81      # unit weight of water (kPa)
LVI_max_z = 20     # use 999 for max(z) or set limit
LDslope = 1.75     # slope for LDI per Zhang et al. 04 (S/100; %)
H1 = 8             # Non-liquifiable crust thickness for LPIish (Maurer et al. 2015) (m)

# Prepare output:
summary_file = 'LVI_Summary_%s.xlsx' %(site_name)
writer = pd.ExcelWriter(summary_file, engine='xlsxwriter') # Prepare excel output
```

Step 3: Run LVIs for All CPTs

This step loops through all CPTs and outputs the results to the excel file specified in Step 1.

In [3]:
```
cpts = pd.ExcelFile(resist_file).sheet_names  # list of all CPT names at site (pulled from excel sheet names)
LVIsummary = np.zeros([len(cpts),7]) # prepare LVI summary output frame (7 var)
for cpti in range(len(cpts)):
    df = pd.read_excel(resist_file, sheet_name='%s' %(cpts[cpti])) # read cpt sheet
    z = df["z (m)"].values # read full cpt array
    LVI_max_z_cap = min(max(z),LVI_max_z)
    qc1Ncs = df["qc1Ncs"].values
    CRR_norm = df["CRRnorm"].values
    sigveff_eq = df["sigveff_eq"].values
    sigv_eq = df["sigv_eq"].values

    dz = np.zeros(len(z)) # create array for difference in z (current-past)
    dz[0]= z[0]
    for i in range(1,len(z)):
```

```
    dz[i] = z[i]-z[i-1]

# ================================================================
#  Normalizing Variables
MSFmax = np.minimum(1.09+(qc1Ncs/180)**3,2.2*np.ones(np.shape(z)))
MSF = 1+(MSFmax-1)*(8.64*np.exp(-M/4)-1.325)
C_sig = 1/(37.3-8.27*(np.minimum(qc1Ncs,211*np.ones(np.shape(z)))**0.264))
K_sig = np.minimum(1-C_sig*np.log(sigveff_eq),1.1*np.ones(np.shape(z)))

# ================================================================
#  CSR - Cyclic Stress Ratio
rd = np.minimum(np.ones(np.shape(z)),np.exp(-1.012-1.126*np.sin(z/11.73+5.133)+
                                            M*0.106+M*0.118*np.sin(z/11.28+5.142)))
CSR = 0.65*(np.maximum(np.ones(np.shape(z)),sigv_eq/sigveff_eq))*a_max*rd
CSR_norm = CSR/(MSF*K_sig)

# ================================================================
#  Triggering Factor of Safety
FSliq = np.ones(len(z))
for i in range(len(z)):
    if np.isnan(CRR_norm[i]) == 1:
        FSliq[i] = float('nan')
    else:
        FSliq[i] = min(CRR_norm[i]/CSR_norm[i],2) # cap at 2

# ================================================================
#  LVI Calculations

LVI_length = int(round(LVI_max_z_cap/np.mean(dz),0))
gamma_lim = np.maximum(np.zeros(np.shape(z)),
                       np.minimum(1.859*(2.163-0.478*(qc1Ncs)**0.264)**3,
                                  0.5*np.ones(np.shape(z))))
F_alpha = np.minimum(0.943*np.ones(np.shape(z)),
                     -11.74+8.34*(qc1Ncs)**0.264-1.371*(qc1Ncs)**0.528)
gamma_max = np.zeros(len(z))
for i in range(len(z)):
    if np.isnan(FSliq[i]) == 1:
        gamma_max[i] = float('nan')
    elif FSliq[i] < F_alpha[i]:
        gamma_max[i] = gamma_lim[i]
    else:
        gamma_max[i] = min(gamma_lim[i],0.035*(1-F_alpha[i])
                           *(2-FSliq[i])/(FSliq[i]-F_alpha[i]))

# LPI (Iwasaki et al. 1978)
LPI_calc = np.zeros(LVI_length)
LPI_cum = np.zeros(LVI_length)
for i in range(LVI_length):
    if np.isnan(FSliq[i]) == 1 or ((1-FSliq[i]) < 0) or ((10-0.5*z[i]) < 0):
        LPI_calc[i] = 0
    else:
        LPI_calc[i] = (1-FSliq[i])*(10-0.5*z[i])*dz[i]
LPI = sum(LPI_calc)
LPI_cum[LVI_length-1] = LPI_calc[LVI_length-1]
for i in range (LVI_length-2,-1,-1):
    LPI_cum[i] = LPI_calc[i] + LPI_cum[i+1]

# LPIish (Maurer et al. 2015)
LPIish_calc = np.zeros(LVI_length)
LPIish_cum = np.zeros(LVI_length)
for i in range(LVI_length):
    if np.isnan(FSliq[i]) == 1:
        LPIish_calc[i] = 0
    elif FSliq[i]<=1 and (H1*(np.exp(5/(25.56*(1-FSliq[i])))-1))<=3:
        LPIish_calc[i] = (1-FSliq[i])*(25.56/z[i])*dz[i]
    else:
        LPIish_calc[i] = 0
LPIish = sum(LPIish_calc)
LPIish_cum[LVI_length-1] = LPIish_calc[LVI_length-1]
for i in range (LVI_length-2,-1,-1):
    LPIish_cum[i] = LPIish_calc[i] + LPIish_cum[i+1]

# LDI (Zhang et al. 2004)
LDI_calc = np.zeros(LVI_length)
LDI_cum = np.zeros(LVI_length)
for i in range(LVI_length):
    if np.isnan(FSliq[i]) == 1:
        LDI_calc[i] = 0
    else:
        LDI_calc[i] = gamma_max[i]*dz[i]
LDI = sum(LDI_calc)
LDI_cum[LVI_length-1] = LDI_calc[LVI_length-1]
for i in range (LVI_length-2,-1,-1):
    LDI_cum[i] = LDI_calc[i] + LDI_cum[i+1]
```

```
#CLT
CLT_calc = np.zeros(LVI_length)
for i in range(LVI_length):
    if np.isnan(FSliq[i]) == 1:
        CLT_calc[i] = 0
    elif FSliq[i] < 1:
        CLT_calc[i] = dz[i]
    else:
        CLT_calc[i] = 0
CLT = sum(CLT_calc)

# Zhang et al. 2002 interpolation for vol strain
qc1Ncs_lookup = np.r_[0, 33:201, 5000]
FSliq_lookup = np.r_[0,0.5,0.6,0.7,0.8, 0.9, 1, 1.1, 1.2, 1.3, 2.]
epsv_lookup = np.zeros((11,len(qc1Ncs_lookup)))
for j in range(1,170):
      epsv_lookup[0,j] = 102*(qc1Ncs_lookup[j])**(-0.82) # FSliq=0
      epsv_lookup[1,j] = 102*(qc1Ncs_lookup[j])**(-0.82) #FSliq=0.5

for j in range(1,116):
      epsv_lookup[2,j] = 102*(qc1Ncs_lookup[j])**(-0.82) # FSliq=0.6

for j in range(116,170):
      epsv_lookup[2,j] = 2411*(qc1Ncs_lookup[j])**(-1.45) # FSliq=0.6

for j in range(1,80):
      epsv_lookup[3,j] = 102*(qc1Ncs_lookup[j])**(-0.82) # FSliq=0.7

for j in range(79,170):
      epsv_lookup[3,j] = 1701*(qc1Ncs_lookup[j])**(-1.42) # FSliq=0.7

for j in range(1,49):
      epsv_lookup[4,j] = 102*(qc1Ncs_lookup[j])**(-0.82) # FSliq=0.8

for j in range(49,170):
      epsv_lookup[4,j] = 1690*(qc1Ncs_lookup[j])**(-1.46) # FSliq=0.8

for j in range(1,29):
      epsv_lookup[5,j] = 102*(qc1Ncs_lookup[j])**(-0.82) # FSliq=0.9

for j in range(29,170):
      epsv_lookup[5,j] = 1430*(qc1Ncs_lookup[j])**(-1.48) # FSliq=0.9

for j in range(1,170):
      epsv_lookup[6,j] = 64*(qc1Ncs_lookup[j])**(-0.93) # FSliq=1.0
      epsv_lookup[7,j] = 11*(qc1Ncs_lookup[j])**(-0.65) # FSliq=1.1
      epsv_lookup[8,j] = 9.7*(qc1Ncs_lookup[j])**(-0.69) # FSliq=1.2
      epsv_lookup[9,j] = 7.6*(qc1Ncs_lookup[j])**(-0.71) # FSliq=1.3
      epsv_lookup[10,j] = 0 # FSliq=2

for i in range (0,11):
    epsv_lookup[i,0] = epsv_lookup[i,1]
    epsv_lookup[i,169] = epsv_lookup[i,168]

epsv = np.zeros(len(z))
ip = sp.interpolate.interp2d(qc1Ncs_lookup,FSliq_lookup,epsv_lookup)
for i in range(len(z)):
    if np.isnan(FSliq[i]) == 1:
        epsv[i] = 0
    else:
        epsv[i] = ip(qc1Ncs[i],FSliq[i])

# Sv1D
Sv1D_calc = np.zeros(LVI_length)
Sv1D_cum = np.zeros(LVI_length)
for i in range(LVI_length):
    Sv1D_calc[i] = epsv[i]/100*dz[i]
Sv1D = sum(Sv1D_calc)
Sv1D_cum[LVI_length-1] = Sv1D_calc[LVI_length-1]
for i in range (LVI_length-2,-1,-1):
    Sv1D_cum[i] = Sv1D_calc[i] + Sv1D_cum[i+1]

# LSN
LSN_calc = np.zeros(LVI_length)
LSN_cum = np.zeros(LVI_length)
for i in range(LVI_length):
    LSN_calc[i] = 10*epsv[i]*dz[i]/max(z[i],dz[i])
LSN = sum(LSN_calc)
LSN_cum[LVI_length-1] = LSN_calc[LVI_length-1]
for i in range (LVI_length-2,-1,-1):
    LSN_cum[i] = LSN_calc[i] + LSN_cum[i+1]

# LD (for slope per Zhang et al. 2004)
```

```
    ratio = LDslope+0.2
    LD = LDI*ratio

    LVIsummary[cpti,0] = round(LPI,2)
    LVIsummary[cpti,1] = round(LSN,2)
    LVIsummary[cpti,2] = round(Sv1D,4)
    LVIsummary[cpti,3] = CLT
    LVIsummary[cpti,4] = round(LDI,3)
    LVIsummary[cpti,5] = round(LD,3)
    LVIsummary[cpti,6] = round(LPIish,3)

    # ================================================================
    #  Print excel file with summary, liq resistance vs depth, LVIs vs depth
    data_temp = np.transpose(np.vstack((z[0:LVI_length],CSR_norm,FSliq,LPI_cum,LSN_cum,LDI_cum,Sv1D_cum,LPIish_cum)))
    df_lvi = pd.DataFrame(data_temp)
    df_lvi.rename(columns={0:'z (m)',1:"CSRnorm",2:"FS",3:"LPI",4:"LSN",5:"LDI",6:"Sv1D",7:"LPIish"},
                  inplace=True)
    df_lvi.to_excel(writer, sheet_name='%s' %(cpts[cpti]))
```

Print and display summary of all LVI values at ground surface

In [4]:

```
df_LVIsummary = pd.DataFrame(LVIsummary,index=cpts)
df_LVIsummary.index.names = ['cpts']
df_LVIsummary.rename(columns={0:'LPI',1:'LSN',2:'Sv1D',3:'CLT',4:'LDI',5:'LD-slope',6:"LPIish"},
                inplace=True)
df_LVIsummary.to_excel(writer, sheet_name='LVISummary')
df_LVIsummary
```

Out[4]:

cpts	LPI	LSN	Sv1D	CLT	LDI	LD-slope	LPIish
CPT_1	6.92	5.96	0.0495	2.05	0.702	1.370	2.149
CPT_2	4.76	5.52	0.0379	1.75	0.391	0.762	0.000
CPT_3	4.34	3.82	0.0353	1.60	0.418	0.815	1.408
CPT_4	5.96	5.27	0.0411	1.80	0.558	1.088	1.851
CPT_5a	5.01	4.91	0.0406	1.80	0.501	0.977	2.099
CPT_6	7.37	6.54	0.0454	1.80	0.672	1.310	3.403
CPT_7a	8.89	8.43	0.0557	2.40	0.745	1.453	2.764
CPT_8	8.09	7.97	0.0589	2.65	0.783	1.527	2.763
CPT_9	7.95	7.28	0.0487	2.10	0.641	1.250	1.911
CPT_10	4.34	3.62	0.0309	1.40	0.420	0.819	1.604
CPT_11	5.39	4.77	0.0419	1.80	0.507	0.989	1.781
CPT_12	1.96	1.61	0.0196	0.80	0.278	0.542	1.112
CPT_13	2.64	2.34	0.0235	1.20	0.228	0.445	0.460
CPT_14	6.06	5.40	0.0444	1.80	0.653	1.273	0.700

In [5]:

```
writer.save() # Save final excel output
```

In [ ]:

Attachment D-2

Representative Properties: Jupyter Notebooks

Cumulative Distributions and Declustering from Sitewide CPT Data

The following notebook outputs empirical cumulative distribution functions (CDFs or ECDFs) from sitewide CPT data for a specified stratum and input parameter. The ECDFs can be used to visualize the variability within and between individual CPTs, as well as to obtain representative percentiles for each stratum (e.g., for use in nonlinear dynamic analyses). A cell-based declustering algorithm is also used to evaluate the influence of spatially weighting the data. The summary CDF results (.xlsx) and a simple parameter file (.csv) are printed.

Two input excel (.xlsx) files are necessary for this code to run correctly (1) a parameter file with sheets for each CPT (labeled by CPT ID) and columns for "z (m)", "stratum", and parameter of interest (the output of the liquefaction resistance notebook can be used here), and (2) a summary sheet of all CPTs with columns for "cpt_id", "x", and "y" (the liquefaction input file can be used here).

By Patrick C. Bassal (Ver 0: 02/15/2022)

Step 1: Import libraries

Import all necessary libraries below. These libraries are standard packages that are typically included with the download of a Python distribution package (e.g., Anaconda).

In [1]:
```
import numpy as np                # for array calculations
import pandas as pd               # for building dataframe tables
import matplotlib.pyplot as plt   # plotting

# For declustering data
import geostatspy.GSLIB as GSLIB          # GSLIB utilities, visualization, and wrapper
import geostatspy.geostats as geostats    # GSLIB methods converted to Python
```

Step 2: Input processed CPT parameters

Provide input values in this next box. An excel file with all CPTs (one sheet per CPT), and parameters of interest (columns) for all depths (rows) is necessary for this step to work properly (e.g., OUTPUT*LIQresist*'site'.xlsx as obtained from the liquefaction resistance notebook). One column must indicate the stratum name, for stratum specific parameter distributions. See example files with this distribution.

In [2]:
```
#  Input CPT data and lab files (most inputs should be adjusted herein)
site_name = 'Wynne' # site name as used in input/output file names
stratum = 'Bsat' # stratum of interest (must match exact name in 'stratum' column from parameter excel file)
facies = 0  # pick facies (use 0 for ALL facies)
param = 'SuRat' # parameter of interest (must match exact column name from parameter excel file)
param_file = '../OUTPUT_LIQresist_%s.xlsx' %(site_name) # excel file w/ processed data (see example)
summary_file = '../INPUT_LIQcalcs_%s.xlsx' %(site_name) # excel file w/ summary data (cpt_id, x, y; see example)
per_array = [16,33,50,67,84] # array of percentiles for summary stats (avoid ends for small datasets)

output_cdf = 'CDF_%s_%s_%s_%i.xlsx' %(site_name,stratum,param,facies) # Output file name with CDFs
writer = pd.ExcelWriter(output_cdf, engine='xlsxwriter') # Prepare excel output

output_data = 'Data_%s_%s_%s.csv' %(site_name,stratum,param) # Output csv file name with data
```

This step just lists the CPTs that are relevant for the calculation and ensure they contain the stratum of interest. You can alternatively input this list manually. Note: the excel parameter file may need to be closed if an error is received.

In [3]:
```
all_cpts = pd.ExcelFile(param_file).sheet_names  # list of all CPTs at site (pulled from sheet names)
cpts = [] # start with empty list for CPTs with stratum of interest
for i in range(len(all_cpts)): # loop through all sheets and return cpts with stratum of interest
    df = pd.read_excel(param_file, sheet_name='%s' %(all_cpts[i]))
    if stratum in df['stratum'].values:
        cpts.append(all_cpts[i])
cpts
```

Out[3]:
```
['CPT_1',
 'CPT_2',
 'CPT_3',
 'CPT_4',
 'CPT_5a',
 'CPT_6',
 'CPT_7a',
 'CPT_8',
 'CPT_9',
 'CPT_10',
 'CPT_11',
 'CPT_12',
 'CPT_13']
```

Step 3: Determine CDFs for each CPT

The next box will loop through all CPTs and outputs the individual CDFs and percentiles to the excel file specified in Step 1.

In [4]:
```
sum_stats = np.zeros((len(cpts)+2,len(per_array))) # create array for calculating summary percentiles
for i in range(len(cpts)): # loop over relevant cpts
    df = pd.read_excel(param_file, sheet_name='%s' %(cpts[i])) # read cpt sheet
    z_full = df["z (m)"].values # full cpt depth array
    var_full = df["%s" %(param)].values # full cpt variable array

    if facies == 0:
        z = z_full[(df["stratum"].values == stratum)]  # slice depth array at stratum of interest
        var = var_full[df["stratum"].values == stratum] # slice variable array at stratum of interest
    else:
        z = z_full[(df["stratum"].values == stratum) &
                   (df["facies"].values == facies)]  # keep stratum/facies of interest
        var = var_full[(df["stratum"].values == stratum) &
                       (df["facies"].values == facies)] # keep stratum/facies of interest

    mat_tmp = np.transpose(np.vstack((z,var))) # combine depth with variable
    mat = mat_tmp[~np.isnan(mat_tmp).any(axis=1)] # remove all rows with NaN values
    mat_sort = mat[mat[:,1].argsort()] # sort by prop value
    mat_n = (np.arange(len(mat))+.5)/float(len(mat)) # discretized CDF value (0.5 to adjust tails)
    np.set_printoptions(suppress=True) # ensures non-scientific notation
    cdf_1cpt = np.column_stack((mat_sort,np.transpose(mat_n))) # combine columns for 1 cpt (z, var, CDF)

    # Output individual CPT CDFs to excel:
    df_out = pd.DataFrame(cdf_1cpt) # convert result to dataframe
    df_out.rename(columns={0:'z (m)',1:'%s' %(param),2:'CDF'}, inplace=True) # column names
    df_out.to_excel(writer, sheet_name='%s' %(cpts[i])) # write to excel file

    # Store percentile values for summary:
    for per in range(len(per_array)):
        # sum_stats[i,per] = np.percentile(cdf_1cpt[:,1],per_array[per]) # percentile function
        sum_stats[i,per] = np.interp(per_array[per]/100,cdf_1cpt[:,2],cdf_1cpt[:,1]) # prefered to match CDF

    # Combine all cpt data in one dataframe for plotting and printing:
    cpt_list = ['%s' %(cpts[i])]*len(cdf_1cpt) # list of cpt name
    df_temp = pd.DataFrame(np.column_stack((np.transpose(cpt_list),cdf_1cpt)), # build dataframe
                           columns=['CPT','z (m)','%s' %(param),'CDF_Individual'])
    if i > 0:   # append
        df_plot = df_plot.append(df_temp)
    else: df_plot = df_temp

df_plot['z (m)'] = df_plot['z (m)'].astype(float)  # convert numeric cols to float to avoid issues
df_plot['%s' %(param)] = df_plot['%s' %(param)].astype(float)
df_plot['CDF_Individual'] = df_plot['CDF_Individual'].astype(float)
df_plot
```

Out[4]:

	CPT	z (m)	SuRat	CDF_Individual
0	CPT_1	5.60	0.415376	0.100000
1	CPT_1	5.00	0.467284	0.300000
2	CPT_1	5.30	0.486820	0.500000
3	CPT_1	4.70	0.532739	0.700000
4	CPT_1	5.90	0.611898	0.900000
...	...	...	...	...
9	CPT_13	4.35	0.383066	0.678571
10	CPT_13	5.15	0.399858	0.750000
11	CPT_13	5.35	0.595566	0.821429
12	CPT_13	5.75	0.699699	0.892857
13	CPT_13	5.55	0.717954	0.964286

101 rows × 4 columns

Step 4: Determine combined CDF for all CPT data (without declustering)

This step prepares and outputs the combined CDF (no decluster weighting) and percentiles to the excel file specified in Step 1.

In [5]:
```
# Prepare combined CDF with no weighting
df_all = df_plot.drop(['CDF_Individual'],axis=1).sort_values(
```

```
    ['%s' %(param)]).reset_index(drop=True) #  remove previous CDFs & sort by prop value
df_all_n = pd.DataFrame({'CDF_NoWt': (np.arange(len(df_all))+.5)/float(len(df_all))})
    # discretized CDF value (0.5 to adjust tails)
df_all = df_all.join(df_all_n)  # combined, sorted array (cpt name, z, param, CDF)
df_all
```

Out[5]:

	CPT	z (m)	SuRat	CDF_NoWt
0	CPT_9	5.30	0.061054	0.004950
1	CPT_9	5.00	0.124353	0.014851
2	CPT_11	5.60	0.141362	0.024752
3	CPT_7a	5.60	0.159647	0.034653
4	CPT_9	4.70	0.171349	0.044554
...	...	...	...	...
96	CPT_12	4.95	0.853835	0.955446
97	CPT_12	5.55	0.874045	0.965347
98	CPT_12	5.35	0.897084	0.975248
99	CPT_4	4.35	0.911435	0.985149
100	CPT_12	5.15	0.934274	0.995050

101 rows × 4 columns

Next, we will plot the CDFs (no decluster weighting)

In [6]:

```
# Set general plot parameters
plt.rcParams.update(plt.rcParamsDefault)
plt.rcParams['font.family'] = 'arial';
plt.rcParams['font.style'] = 'italic';
plt.rcParams['font.size'] = 8;
plt.rcParams['figure.dpi'] = 300
plt.rcParams["figure.figsize"] = (7,3)
# plt.rcParams.update(plt.rcParamsDefault) # restore to default if needed

plt.gca().set_prop_cycle(plt.cycler(
    'color', plt.cm.viridis_r(np.linspace(0, 1, len(cpts))))) # set color cycle
ax1 = plt.subplot(111)

for i in range(len(cpts)): # loop over relevant cpts to plot individual CPT data
    ax1.plot((df_plot['%s' %(param)][df_plot["CPT"] == cpts[i]]),
             (df_plot["CDF_Individual"][df_plot["CPT"] == cpts[i]]),
             alpha=0.8, label = cpts[i])

# Plot combined CPT data
ax1.plot(df_all['%s' %(param)],
         df_all["CDF_NoWt"],
         'k-', linewidth=3, label = 'Overall (No Wt)')

ax1.legend(loc='lower right', ncol=2)
ax1.set_xlabel('%s' %(param)); ax1.set_ylabel('Cumulative Probability')

plt.grid(True)
plt.title('Sitewide Cumulative Distribution Functions, %s, Stratum %s' %(site_name, stratum))
#plt.subplots_adjust(left=0.0, bottom=0.0, right=1, top=1, wspace=0.2, hspace=0.2) # plot size
plt.show()
plt.clf(); plt.cla(); plt.close(); # clean plot after this
```

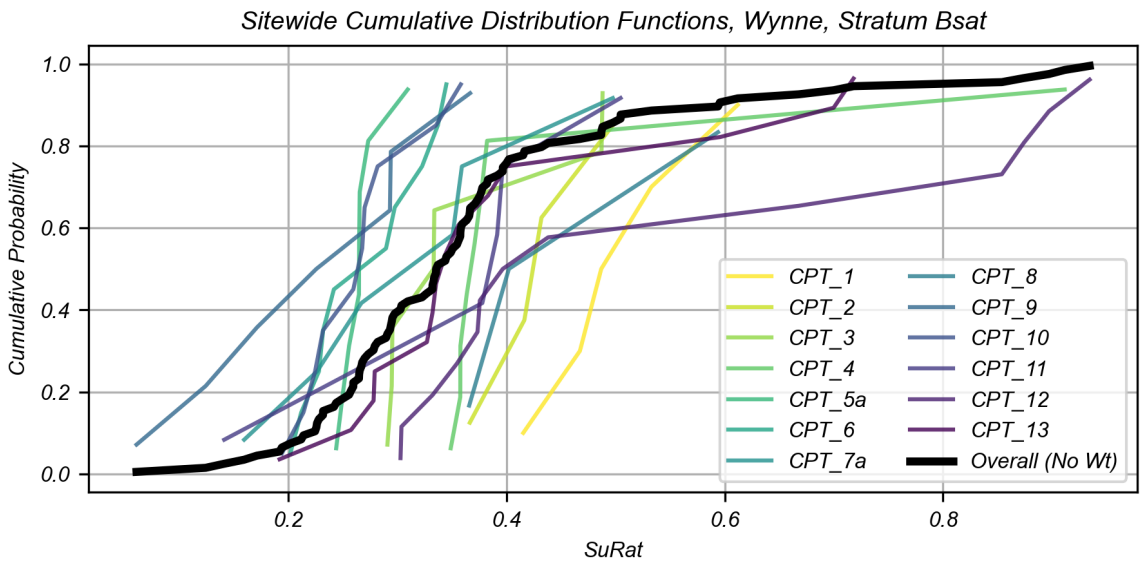

Step 5: Cell-based Spatial Declustering

Cell-based spatial declustering will be used to provide a weight to each CPT considered for the parameter in question. The weights acount for any spatial redundancy in the CPT locations (i.e., less weight will be given to concentrated clusters of CPT data, whereas more weight will be given to CPTs in sparesly sampled areas). This will be useful for determining representative statistics and distributions for site or region of interest. It is important to recognize that we may only be interested in a subset of the site (e.g. region or extent of failure mechanism), and the region can be adjusted in the box below.

The cell-based declustering algorithm used herein was reimplemented from the geostatistical GSLIB fortran code by Dr. Michael Pyrcz for geostats.py (https://github.com/GeostatsGuy/GeostatsPy). This workflow follows similar Jupyter notebook workflows by Dr. Pyrcz (https://github.com/GeostatsGuy/PythonNumericalDemos) with the added implemenation of the CDF results and visualizations. Please refer to the posted examples at those links for more details on this code and methodology.

In [7]:

```
# Cell-based declustering for all relevant CPTs
dfcpt = pd.read_excel (summary_file, sheet_name='Input_CPT') # Load CPT summary sheet (df with cpt_id, x, y)
dfcpt = dfcpt[dfcpt['cpt_id'].isin(cpts)] # remove rows not considered based on cpt_id column

# add median parameter values at relevant cpts:
v_med = np.zeros(len(cpts))
for i in range(len(cpts)): # loop over relevant cpts
    v_med[i] = np.median((df_all['%s' %(param)][df_all["CPT"] == cpts[i]]).astype(float))
dfcpt['v_med'] = v_med.tolist() # add median parameter to summary dataframe

# select range of data for declustering
# [IMPORTANT: be sure to consider over what region this data will be used]
xmin = min(dfcpt['x'])-1; xmax = max(dfcpt['x'])+1 # range of x values
ymin = min(dfcpt['y'])-1; ymax = max(dfcpt['y'])+1 # range of y values
vmin = min(v_med); vmax = max(v_med);

# Plot data to visualize
cmap = plt.cm.viridis_r  # color map
GSLIB.locmap(dfcpt,'x','y','v_med',xmin,xmax,ymin,ymax,vmin,vmax,
             'CPT Location Map of %s (%s, %s)' %(param,site_name,stratum),
             'X(m)','Y(m)','%s' %(param),cmap,'locmap_%s_%s_%s' %(site_name,stratum,param))
plt.clf(); plt.cla(); plt.close(); # clean plot after this
```

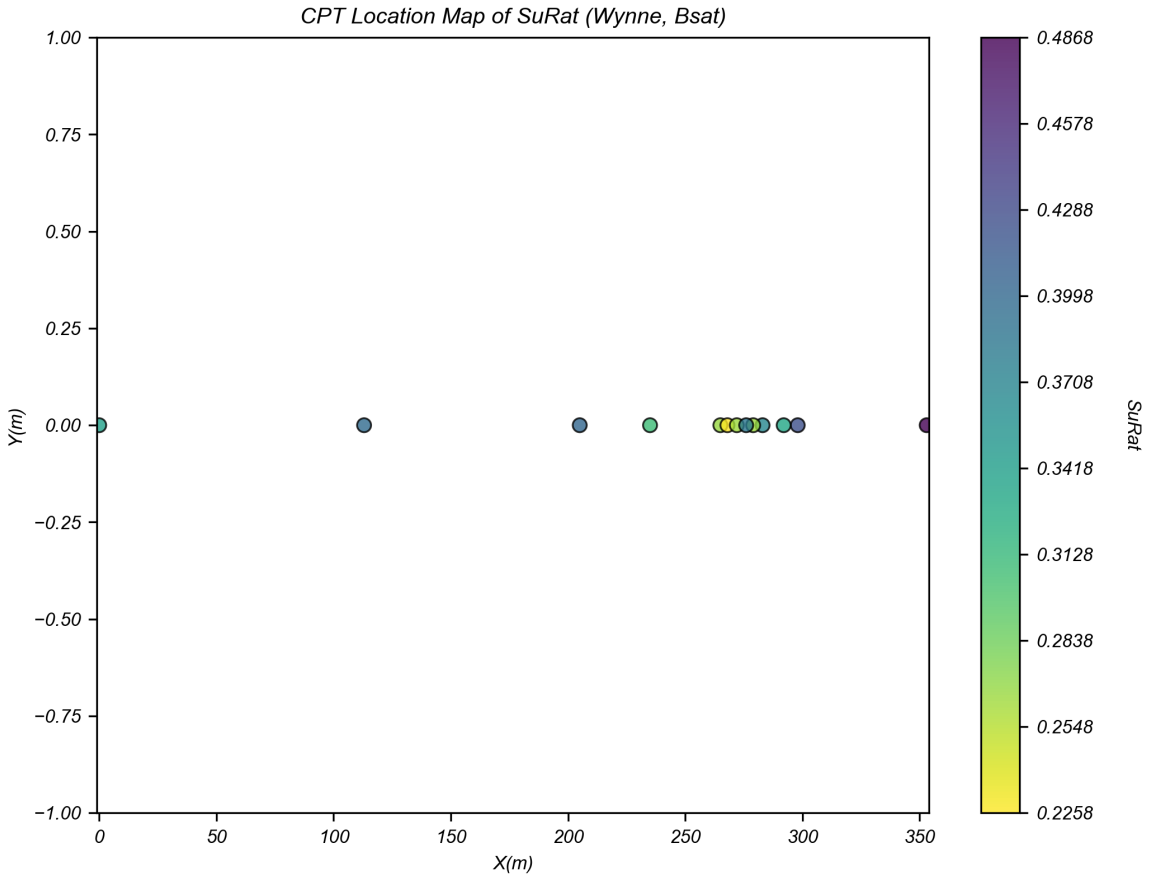

The following cell will run the declustering algorithm for the x, y, and variable values.

- **iminmax** - use 0 to maximize the decluster mean and 1 to minimize it, and can be re-adjusted after considering the peak orientation of the plot produced below (This is **IMPORTANT**).
- **noff** - is the number of cell mesh offsets for averaging the declustered mean
- **ncell** - is the number of cell sizes to consider between **cmin** and **cmax**

In [10]:

```
# Run declustering algorithm from geostats.py
# set iminmax to 1 for min or 0 for max, depending on cell size plot peak
wts, cell_sizes, dmeans = geostats.declus(
    dfcpt,'x','y','v_med',iminmax = 0,
    noff= 10,ncell=100,cmin=5,cmax=100) # Limit cmax depending on problem!!

# Plot parameter vs cell size to interpret impact of cell-based declustering
plt.subplot(111)
plt.scatter(cell_sizes,dmeans, s=30, alpha = 0.2, edgecolors = "black", facecolors = 'blue')
plt.xlabel('Cell Size (m)')
plt.ylabel('%s Mean' %(param))
plt.title('Parameter Mean vs. Cell Size')
plt.subplots_adjust(left=0.0, bottom=0.0, right=0.8, top=0.5, wspace=0.2, hspace=0.2)
plt.show()
plt.clf(); plt.cla(); plt.close(); # clean plot after this
```

```
There are 13 data with:
   mean of      0.34336803416753325
   min and max  0.2258472715562668 and 0.4868203782442037
   standard dev 0.0730248259713743
```

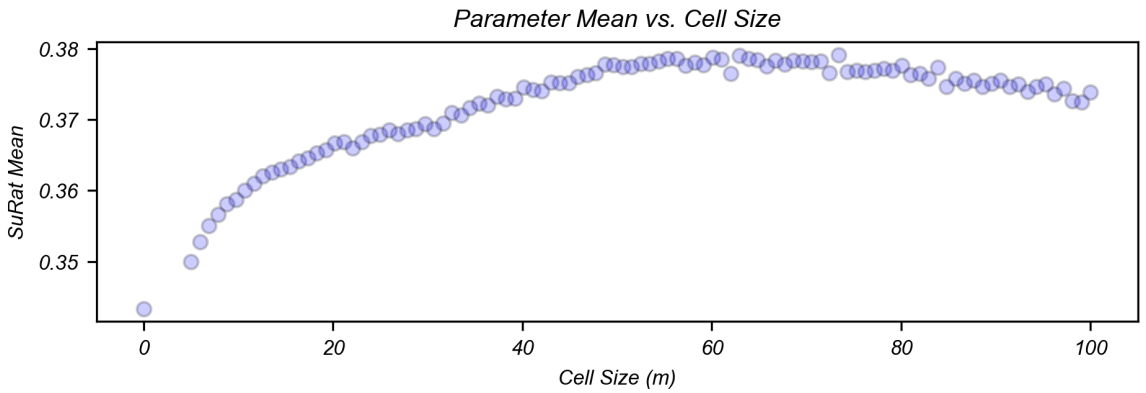

In [11]:

```
# Plot map of weights after declustering
dfcpt['Wts'] = wts  # add weights to the sample data DataFrame
GSLIB.locmap(dfcpt,'x','y','Wts',xmin,xmax,ymin,ymax,round(min(wts),1),round(max(wts),1),
             'CPT Location Map of Weights (%s, %s)' %(site_name,stratum),
             'X(m)','Y(m)','Weights',cmap,'locmap_weights_%s_%s' %(site_name,stratum))
plt.clf(); plt.cla(); plt.close(); # clean plot after this
```

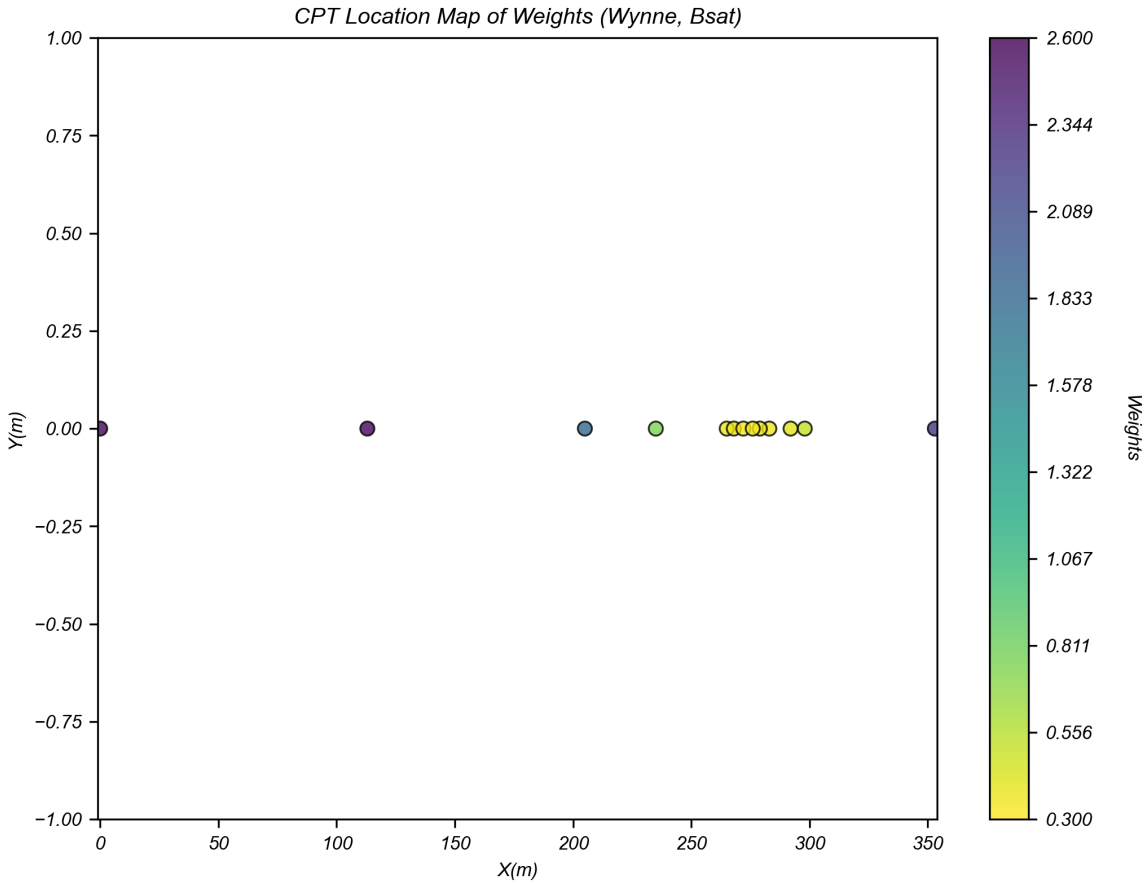

In [12]:

```
# CDF values of parameter with weighting
wts_all = np.zeros(len(df_all)) # accumulating weights to calculate the weighted CDF
CDF_w = np.zeros(len(df_all)) # accumulating weights to calculate the weighted CDF

# starting percentile (normalize by total weight):
for i in range(len(df_all)):
    wts_all[i] = wts[np.transpose(cpts)==df_all["CPT"][i]]

CDF_w[0] = wts_all[0]/sum(wts_all)*0.5
```

```
for i in range(1,len(df_all)):
    CDF_w[i] = CDF_w[i-1] + wts_all[i]/sum(wts_all)
df_all_Nwt = pd.DataFrame({'Wts': wts_all, 'CDF_Wt': CDF_w}).astype(float) # df of weighted CDF
df_all_wt = df_all.join(df_all_Nwt)  # join to dataframe of combined data

# Output combined CPT CDFs to excel:
df_all_wt.to_excel(writer, sheet_name='Overall') # write to excel file
df_all_wt
```

Out[12]:

	CPT	z (m)	SuRat	CDF_NoWt	Wts	CDF_Wt
0	CPT_9	5.30	0.061054	0.004950	0.365754	0.001624
1	CPT_9	5.00	0.124353	0.014851	0.365754	0.004873
2	CPT_11	5.60	0.141362	0.024752	0.344087	0.007928
3	CPT_7a	5.60	0.159647	0.034653	0.755754	0.014640
4	CPT_9	4.70	0.171349	0.044554	0.365754	0.017889
...	...	...	...	...	...	...
96	CPT_12	4.95	0.853835	0.955446	2.556667	0.927105
97	CPT_12	5.55	0.874045	0.965347	2.556667	0.949811
98	CPT_12	5.35	0.897084	0.975248	2.556667	0.972517
99	CPT_4	4.35	0.911435	0.985149	0.354921	0.975669
100	CPT_12	5.15	0.934274	0.995050	2.556667	0.998376

101 rows × 6 columns

In [13]:

```
# Plot combined CPT data
plt.gca().set_prop_cycle(plt.cycler(
    'color', plt.cm.viridis_r(np.linspace(0, 1, len(cpts))))) # set color cycle
ax1 = plt.subplot(111)
for i in range(len(cpts)): # loop over relevant cpts to plot individual CPT data
    ax1.plot((df_plot['%s' %(param)][df_plot["CPT"] == cpts[i]]),
             (df_plot["CDF_Individual"][df_plot["CPT"] == cpts[i]]),
             alpha=0.8, label = cpts[i])

# Plot combined CPT data
ax1.plot(df_all_wt['%s' %(param)],
         df_all_wt["CDF_NoWt"],
         'k-', linewidth=3, label = 'Overall (No Wt)')
ax1.plot(df_all_wt['%s' %(param)],
         df_all_wt["CDF_Wt"],
         c = 'darkred',linewidth=3, label = 'Overall (Wt)')

ax1.legend(loc='lower right', ncol=2)
ax1.set_xlabel('%s' %(param)); ax1.set_ylabel('Cumulative Probability')
plt.grid(True)
plt.title('Sitewide Cumulative Distribution Functions, %s, Stratum %s' %(site_name, stratum))
plt.show()
```

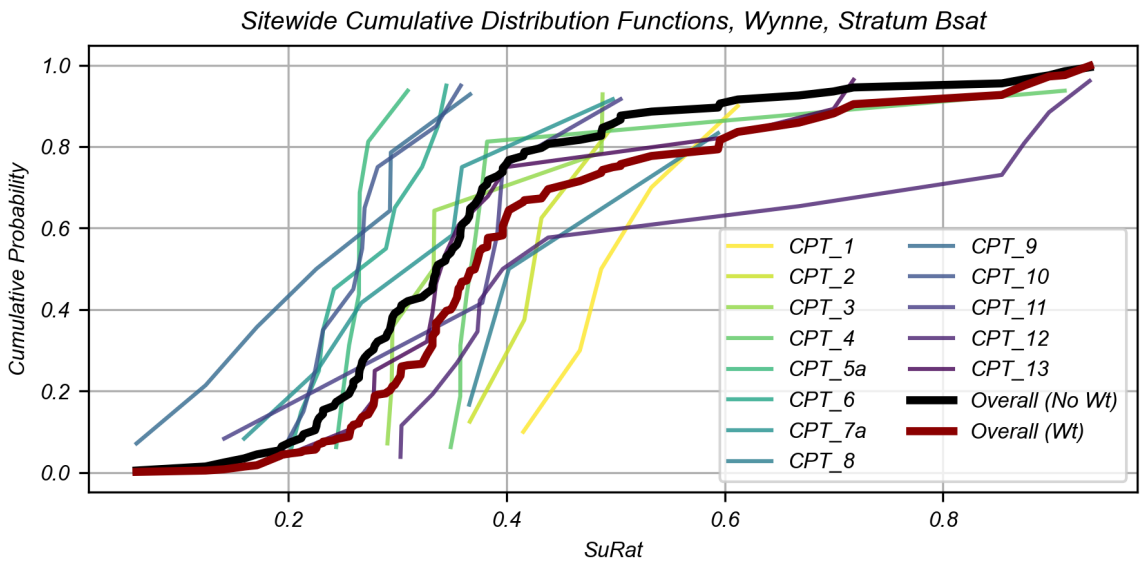

Step 6: Print Summary Statistics and '.xlsx' File for CDFs

In [14]:
```
# Output stats to excel
# Store combined percentile values for summary:
for per in range(len(per_array)):
    sum_stats[len(cpts),per] = np.interp(per_array[per]/100,df_all_wt['CDF_NoWt'],
                                         df_all_wt['%s' %(param)]) # unweighted combined CPTs
    sum_stats[len(cpts)+1,per] = np.interp(per_array[per]/100,df_all_wt['CDF_Wt'],
                                           df_all_wt['%s' %(param)]) # weighted combined CPTs

labels = np.hstack((cpts,"Combined_NoWt","Combined_Wt")) # create lab for summary stats
df_stat = pd.DataFrame(sum_stats) # convert to dataframe
df_stat.set_index(labels,inplace=True) # puts CPT name as index

for per in range(len(per_array)): # loop to label columns
    df_stat.rename(columns={per:'%s_%s' %(param,per_array[per])},
                           inplace=True)  # rename columns
df_stat.to_excel(writer, sheet_name='Percentiles') # save to excel
df_stat
```

Out[14]:

	SuRat_16	SuRat_33	SuRat_50	SuRat_67	SuRat_84
CPT_1	0.430949	0.470214	0.486820	0.525851	0.588150
CPT_2	0.373400	0.407382	0.424210	0.445100	0.494429
CPT_3	0.293356	0.295369	0.333216	0.362978	0.487427
CPT_4	0.355752	0.358588	0.367196	0.376112	0.498659
CPT_5a	0.248463	0.257057	0.264925	0.265456	0.281318
CPT_6	0.213575	0.231223	0.265745	0.302636	0.335686
CPT_7a	0.190365	0.245917	0.308854	0.355088	0.433816
CPT_8	0.365829	0.383649	0.402196	0.499913	0.593799
CPT_9	0.100299	0.162420	0.225847	0.293392	0.321635
CPT_10	0.215083	0.230466	0.263736	0.272417	0.330064
CPT_11	0.195773	0.316401	0.384678	0.394116	0.454871
CPT_12	0.320292	0.369504	0.396627	0.706855	0.883722
CPT_13	0.272848	0.327687	0.339735	0.379832	0.622641
Combined_NoWt	0.238506	0.288327	0.335493	0.373820	0.487388
Combined_Wt	0.277062	0.332240	0.370974	0.421321	0.621055

In [15]:
```
writer.save() # Save final excel output of CDF summary results
```

Step 7: Print Combined Data as '.csv'

This step re-outputs some of the combined data (ordered by depth) to a simple format that will be used later for conditioning the geostatistical calculations in this workflow sequence (e.g, variograms, indicator and random field simulations). Currently only one parameter is printed, but the code can be adjusted to call others as well.

In [16]:

```
# Write parameter file for geostatistics: x, y, z, facies, v, wt

for CPTi in range(len(cpts)): # loop over relevant cpts
    cpt_id = dfcpt.iloc[CPTi]["cpt_id"] # assign from summary table (dfcpt, called previously)
    x = dfcpt.iloc[CPTi]["x"]
    y = dfcpt.iloc[CPTi]["y"]
    top_elev = dfcpt.iloc[CPTi]["top_elev"]

    df = pd.read_excel(param_file, sheet_name='%s' %(cpts[CPTi])) # read cpt sheet
    z = df["z (m)"][df["stratum"].values == stratum] # cpt depth array for stratum
    var = df["%s" %(param)][df["stratum"].values == stratum] # cpt variable array for stratum
    facies = df["facies"][df["stratum"].values == stratum] # cpt facies array for stratum

    wts_print = np.zeros(len(z)) # read in weights
    for j in range(len(z)):
        wts_print[j] = wts[np.transpose(cpts)==cpt_id]

    # Prepare data set and append to file
    xfull = np.ones(len(z))*x
    yfull = np.ones(len(z))*y
    data = np.transpose(np.vstack((xfull,yfull,(top_elev-z),
                                   z,var,facies, wts_print))) # combine columns
    data = data[~np.isnan(data).any(axis=1), :]    # remove all rows with nan
    df_temp = pd.DataFrame(data, columns=['x','y','z','z_dep','%s' %(param),'facies','wt'])
        # creates temporary dataframes for appending
    if CPTi > 0:   # append
        df_print = df_print.append(df_temp)
    else:  df_print = df_temp
df_print.to_csv(output_data, index=False) # print to csv
df_print
```

Out[16]:

	x	y	z	z_dep	SuRat	facies	wt
0	353.0	0.0	16.20	4.70	0.532739	3.0	2.253333
1	353.0	0.0	15.90	5.00	0.467284	3.0	2.253333
2	353.0	0.0	15.60	5.30	0.486820	3.0	2.253333
3	353.0	0.0	15.30	5.60	0.415376	3.0	2.253333
4	353.0	0.0	15.00	5.90	0.611898	3.0	2.253333
...	...	...	...	...	...	...	...
9	0.0	0.0	11.35	6.15	0.278224	3.0	2.556667
10	0.0	0.0	11.15	6.35	0.343978	3.0	2.556667
11	0.0	0.0	10.95	6.55	0.279287	3.0	2.556667
12	0.0	0.0	10.75	6.75	0.335493	3.0	2.556667
13	0.0	0.0	10.55	6.95	0.332227	3.0	2.556667

101 rows × 7 columns

In [ ]:

Normalize CPT data

The following notebook converts the data distribution of a parameter obtained from a CPT for a given stratum to standard normal. The nscore program used in GSLIB (as converted to Python by Michael Pyrcz) is used herein, which allows for the use of decluster weighting.

A ".csv" file with columns of the data for the parameter of interest and weights is needed. The outputs from the Props_CDFs.ipynb notebook can be used. The residual data about a trend case be used in the case of detrended data.

By Patrick C. Bassal (Ver 0: 02/15/2022)

Step 1: Import libraries

Import all necessary libraries below. These libraries are standard packages that are typically included with the download of a Python distribution package (e.g., Anaconda).

In [1]:
```
import numpy as np                # for array calculations
import pandas as pd               # for building dataframe tables
import matplotlib.pyplot as plt   # plotting
from matplotlib import cm         # for colormap

# For nscore transform as implemented by Michael Pyrcz
import geostatspy.GSLIB as GSLIB          # GSLIB utilities, visualization, and wrapper
import geostatspy.geostats as geostats    # GSLIB methods converted to Python
```

Step 2: Input dataframe and pick facies/parameter

Provide input values in this next box. Only one facies and parameter will be considered in this workbook. The dataframe will be read from a .csv input file with columns for all dimensions, the parameter, and facies value. See example files with this distribution.

In [2]:
```
#  Input CPT data and lab files (most inputs should be adjusted herein)
facies = 0  # pick facies (use 0 for ALL facies)
param = 'SuRat' # parameter of interest (must match exact column name from .csv for stratum)
param_csv = 'Data_Wynne_Bsat_SuRat' # excel file with processed data (see example; remove .csv from name)

output_data = '%s_norm.csv' %(param_csv) # Output csv file name for normalized data
output_trans = '%s_transtable.csv' %(param_csv) # Output csv file name for trasnformation table
```

Cleanup the dataframe to only include the facies being considered.

In [3]:
```
df = pd.read_csv('%s.csv' %(param_csv))  # read the .csv file as a DataFrame
if facies != 0:                          # crop unused facies
    df = df[df.facies == facies]
df                                       # preview Dataframe
```

Out[3]:

	x	y	z	z_dep	SuRat	facies	wt
0	353.0	0.0	16.20	4.70	0.532739	3.0	2.253333
1	353.0	0.0	15.90	5.00	0.467284	3.0	2.253333
2	353.0	0.0	15.60	5.30	0.486820	3.0	2.253333
3	353.0	0.0	15.30	5.60	0.415376	3.0	2.253333
4	353.0	0.0	15.00	5.90	0.611898	3.0	2.253333
...	...	...	...	...	...	...	...
96	0.0	0.0	11.35	6.15	0.278224	3.0	2.556667
97	0.0	0.0	11.15	6.35	0.343978	3.0	2.556667
98	0.0	0.0	10.95	6.55	0.279287	3.0	2.556667
99	0.0	0.0	10.75	6.75	0.335493	3.0	2.556667
100	0.0	0.0	10.55	6.95	0.332227	3.0	2.556667

101 rows × 7 columns

Step 3: Normalize Data

The nscore transform from GSLIB (as implemented in Python by Michael Pyrcz) is used here. This will produce the transformed values, and a tranformation table between original and normal score values.

In [4]:
```
df["N_%s" %(param)], tvVar, tnsVar = geostats.nscore(df,"%s" %(param),"wt")
# nscore transform for variable (can include decluster weight)
df
```

Out[4]:

	x	y	z	z_dep	SuRat	facies	wt	N_SuRat
0	353.0	0.0	16.20	4.70	0.532739	3.0	2.253333	0.734974
1	353.0	0.0	15.90	5.00	0.467284	3.0	2.253333	0.545770
2	353.0	0.0	15.60	5.30	0.486820	3.0	2.253333	0.604969
3	353.0	0.0	15.30	5.60	0.415376	3.0	2.253333	0.400901
4	353.0	0.0	15.00	5.90	0.611898	3.0	2.253333	0.945889
...	...	...	...	...	...	...	...	...
96	0.0	0.0	11.35	6.15	0.278224	3.0	2.556667	-1.012267
97	0.0	0.0	11.15	6.35	0.343978	3.0	2.556667	-0.294809
98	0.0	0.0	10.95	6.55	0.279287	3.0	2.556667	-0.921435
99	0.0	0.0	10.75	6.75	0.335493	3.0	2.556667	-0.363502
100	0.0	0.0	10.55	6.95	0.332227	3.0	2.556667	-0.517331

101 rows × 8 columns

Plot and compare cumulative distributions of variable before and after normalization

In [5]:
```
vmin = min(df["%s" %(param)])/1.1
vmax = max(df["%s" %(param)])*1.1

plt.subplot(221)                                        # plot original histogram
plt.hist(df["%s" %(param)], weights=df["wt"], bins=np.linspace(vmin,vmax,10000),
         histtype="step",alpha=1,density=True,cumulative=True,edgecolor='red',label='Original')
plt.xlim([vmin,vmax]); plt.ylim([0,1.0])
plt.xlabel("%s" %(param)); plt.ylabel('Frequency'); plt.title("%s" %(param))
plt.legend(loc='upper left')
plt.grid(True)

plt.subplot(222)                                        # plot nscore transformed histogram
plt.hist(df["N_%s" %(param)], weights=df["wt"], facecolor='blue',bins=np.linspace(-3.0,3.0,10000),
         histtype="step",alpha=1,density=True,cumulative=True,edgecolor='blue',label = 'Trans')
plt.xlim([-3.0,3.0]); plt.ylim([0,1.0])
plt.xlabel("%s" %(param)); plt.ylabel('Frequency'); plt.title('Nscore %s' %(param))
plt.legend(loc='upper left')
plt.grid(True)

plt.subplot(223)                                        # plot original barchart
plt.hist(df["%s" %(param)], weights=df["wt"], facecolor='red',bins=np.linspace(vmin,vmax,20),
         histtype="stepfilled",alpha=.2,density=True,cumulative=False,edgecolor='red',label='Original')
plt.xlim([vmin,vmax])
plt.xlabel("%s" %(param)); plt.ylabel('Frequency'); plt.title("%s" %(param))
plt.legend(loc='upper right')
plt.grid(True)

plt.subplot(224)                                        # plot nscore transformed barchart
plt.hist(df["N_%s" %(param)], weights=df["wt"], facecolor='blue',bins=np.linspace(-3.0,3.0,20),
         histtype="stepfilled",alpha=.2,density=True,cumulative=False,edgecolor='blue',label = 'Trans')
plt.xlim([-3.0,3.0])
plt.xlabel("%s" %(param)); plt.ylabel('Frequency'); plt.title('Nscore %s' %(param))
plt.legend(loc='upper right')
plt.grid(True)

plt.subplots_adjust(left=0.0, bottom=0.0, right=2.0, top=2.2, wspace=0.2, hspace=0.3)
plt.show()
```

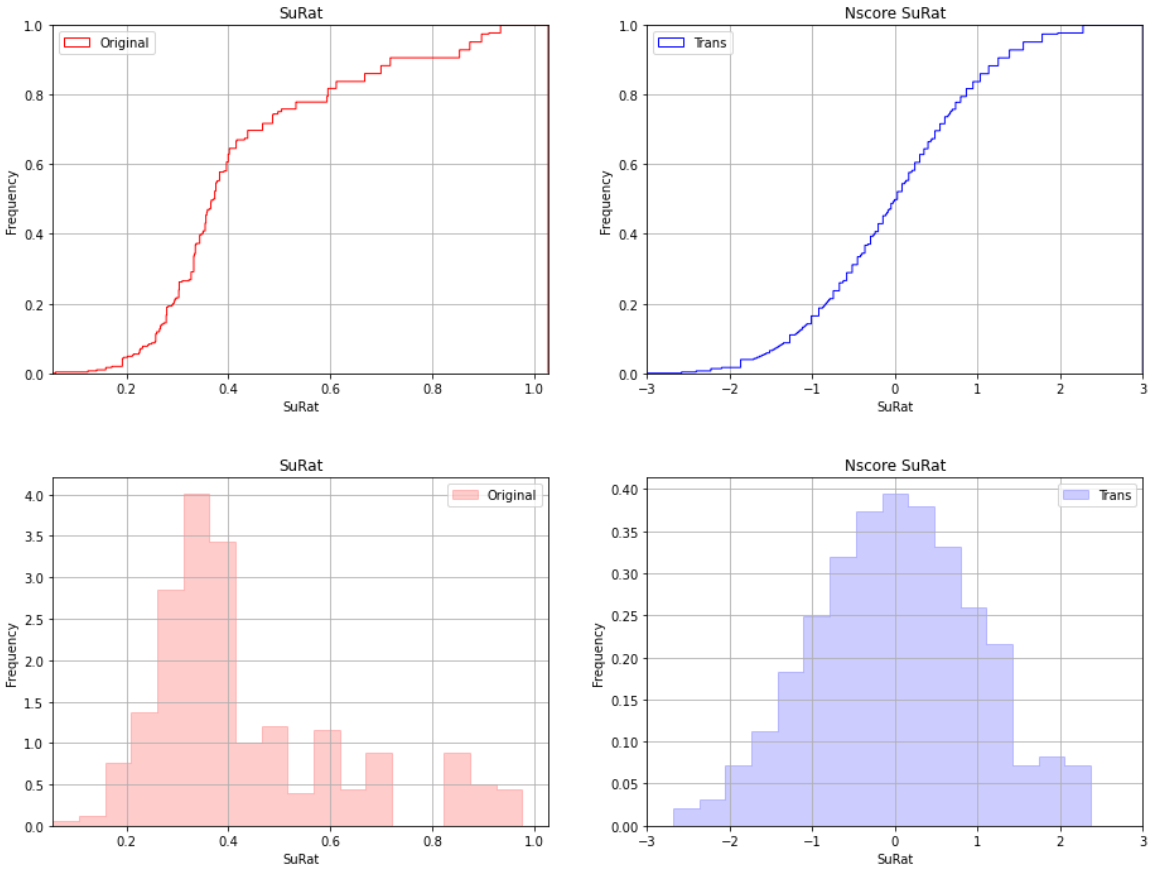

Print both the full dataframe and the transformation table at the data values to ".csv" file

In [6]:
```
df.to_csv(output_data, index=False) # print full dataframe

df_trans = pd.DataFrame(np.transpose(np.vstack((tvVar, tnsVar))),
                        columns=['%s' %(param),'N_%s' %(param)]) # print transform table
df_trans.to_csv(output_trans, index=False)
```

In [ ]:
```
```

Variogram Calculation and Modeling from CPT data

The following notebook calculates and models a variogram from a CPT sample dataset, for a single stratum and parameter of interest. For simplicity, only one azimuth direction can be plotted and printed at any time. However, the azimuth can be updated with the interactive tool. The gamv program used in GSLIB (as wrapped from the original executable to Python by Michael Pyrcz) is used herein.

At the current time, it seems the 3D gamv code has not been translated to python, and so a wrapper is most efficient here. **The gamv.exe executable must be included in your directory for this current code to run** (this can be downloaded from http://www.gslib.com/main_gd.html).

A ".csv" file with columns of the data for the parameter of interest is needed. The outputs from either the Props_CDFs.ipynb or Props_Normalize.ipynb notebooks can be used. The residual data about a trend will be used in the case of detrended data.

Reference: Deutsch, C.V. and Journel, A.G. (1997). "GSLIB Geostatistical Software Library and User's Guide." Oxford University Press, New York, second edition. 369 pages.

Important note: Much of this workflow has imitated the style of the freely available notebooks by Michael Pyrcz (https://github.com/GeostatsGuy), including some direct line copies of code. The source code for the geostatspy libraries used in this workflow can also be viewed at his Github page. Users interested in seeing the original application of these codes and following future updates should check out his available material. The purpose of this current workflow is to provide greater accessibility to these tools and a straightforward workflow for geotechnical modeling.

By Patrick C. Bassal (Ver 0: 02/16/2022)

Step 1: Import libraries

Import all necessary libraries below. These libraries are standard packages that are typically included with the download of a Python distribution package (e.g., Anaconda).

In [1]:
```
import numpy as np                # for array calculations
import pandas as pd               # for building dataframe tables
import matplotlib.pyplot as plt   # plotting
from matplotlib import cm         # for colormap

# For nscore transform as implemented by Michael Pyrcz
import geostatspy.GSLIB as GSLIB          # GSLIB utilities, visualization, and wrapper
import geostatspy.geostats as geostats    # GSLIB methods converted to Python

# Some libararies to assist with interactive plotting
import sys   # supress output to screen for interactive variogram modeling
import io
from ipywidgets import interactive # widgets and interactivity
from ipywidgets import widgets
from ipywidgets import Layout
from ipywidgets import Label
from ipywidgets import VBox, HBox
```

Step 2: Input dataframe and pick facies/parameter

Provide input values in this next box. Only one facies and parameter will be considered in this workbook. The dataframe will be read from a .csv input file with columns for all dimensions, the parameter, and facies value. See example files with this distribution.

In [2]:
```
#  Input CPT data and lab files (most inputs should be adjusted herein)
stratum = 'Bsat' # stratum of interest (for naming files)
facies = 0  # pick facies (use 0 for ALL facies)
param = 'N_SuRat' # parameter of interest (must match exact column name from .csv for stratum)
param_csv = 'Data_Wynne_Bsat_SuRat_norm' # excel file with processed data (see example; remove .csv from name)
```

Cleanup the dataframe to only include the facies being considered.

In [3]:
```
df = pd.read_csv('%s.csv' %(param_csv))  # read the .csv file as a DataFrame
if facies != 0:                          # crop unused facies
    df = df[df.facies == facies]
df                                       # preview Dataframe
```

Out[3]:

	x	y	z	z_dep	SuRat	facies	wt	N_SuRat
0	353.0	0.0	16.20	4.70	0.532739	3.0	2.253333	0.734974
1	353.0	0.0	15.90	5.00	0.467284	3.0	2.253333	0.545770

	x	y	z	z_dep	SuRat	facies	wt	N_SuRat
2	353.0	0.0	15.60	5.30	0.486820	3.0	2.253333	0.604969
3	353.0	0.0	15.30	5.60	0.415376	3.0	2.253333	0.400901
4	353.0	0.0	15.00	5.90	0.611898	3.0	2.253333	0.945889
...	...	...	...	...	...	...	...	...
96	0.0	0.0	11.35	6.15	0.278224	3.0	2.556667	-1.012267
97	0.0	0.0	11.15	6.35	0.343978	3.0	2.556667	-0.294809
98	0.0	0.0	10.95	6.55	0.279287	3.0	2.556667	-0.921435
99	0.0	0.0	10.75	6.75	0.335493	3.0	2.556667	-0.363502
100	0.0	0.0	10.55	6.95	0.332227	3.0	2.556667	-0.517331

101 rows × 8 columns

Step 3: Visualize Data

Plot the data in 3D. Some data processing can be considered here to set parameter extents. The z value can be updated here to instead consider depth, which may be better correlated to strength values than elevation (however, if this decision is made, then all future geostatistical modeling should be done in terms of depth and a coordinate transformation later applied).

In [4]:
```
xmin = min(df['x'].values)/1.05; xmax = max(df['x'].values)*1.05    # spatial extents in x, y, z (or z_dep)
ymin = min(df['y'].values)/1.05; ymax = max(df['y'].values)*1.05
zmin = min(df['z'].values)/1.05; zmax = max(df['z'].values)*1.05
# zmin = min(df['z_dep'].values)/1.05; zmax = max(df['z_dep'].values)*1.05 # use depth?
vmin = min(df["%s" %(param)].values);
vmax = max(df["%s" %(param)].values) # data trimming can be performed later
# feature = 'Porosity'; feature_units = 'percentage'         # name and units of the feature of interest
cmap = plt.cm.viridis                                      # set the color map
```

In [5]:
```
ax = plt.subplot(111, projection='3d')
p = ax.scatter(df['x'].values, df['y'].values, df['z'].values,
               c=df["%s" %(param)].values, cmap=cmap)  # use depth?
ax.set_xlabel('X (m)'); ax.set_ylabel('Y (m)'); ax.set_zlabel('Z (m)')
ax.set_xlim(xmin,xmax); ax.set_ylim(ymin,ymax); ax.set_zlim(zmin,zmax)
ax.set_title("3D Data Map")
cbar = plt.colorbar(p, orientation="vertical", ticks=np.linspace(vmin,vmax,10),fraction=0.02)
cbar.set_label("%s" %(param), rotation=270, labelpad=20)

plt.subplots_adjust(left=0.0, bottom=0.0, right=2.0, top=2.2, wspace=0.2, hspace=0.2) # plot formatting
plt.show()
```

```
C:\Users\PB\AppData\Local\Temp/ipykernel_24036/2575246008.py:5: UserWarning: Attempting to set identical bottom == top == 0.0 re
sults in singular transformations; automatically expanding.
  ax.set_xlim(xmin,xmax); ax.set_ylim(ymin,ymax); ax.set_zlim(zmin,zmax)
```

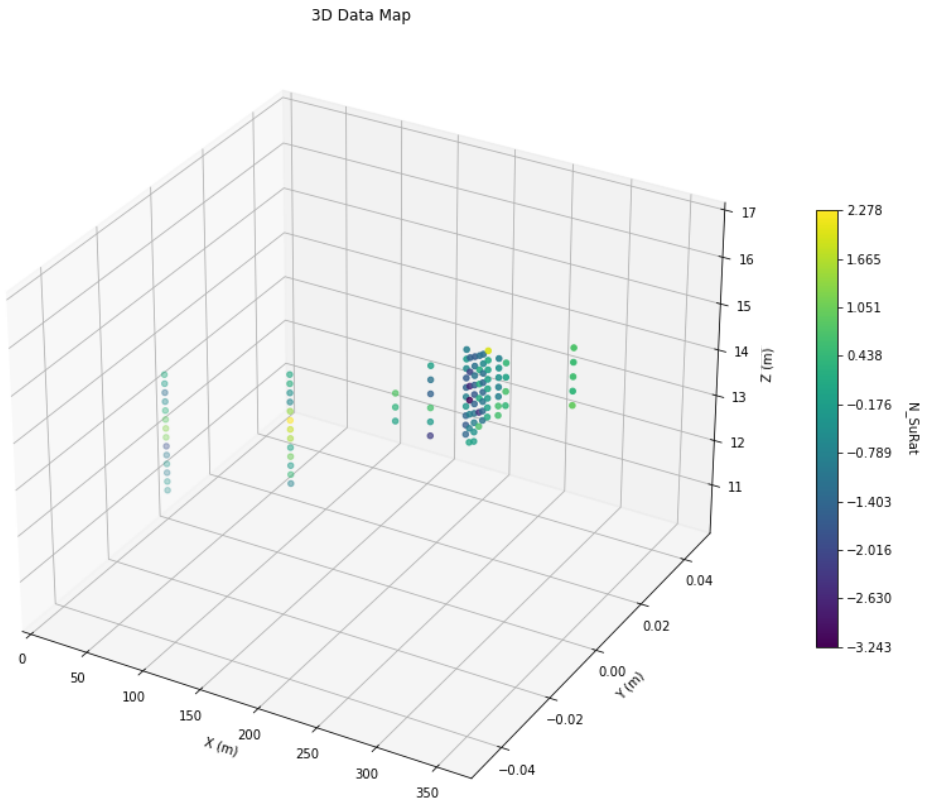

In [6]:
```
df.describe().transpose()                                    # summary table of DataFrame stats
```

Out[6]:

	count	mean	std	min	25%	50%	75%	max
x	101.0	216.762376	105.750002	0.000000	113.000000	268.000000	279.000000	353.000000
y	101.0	0.000000	0.000000	0.000000	0.000000	0.000000	0.000000	0.000000
z	101.0	14.080198	1.297480	10.550000	13.550000	14.400000	15.050000	16.200000
z_dep	101.0	5.206931	0.641951	4.100000	4.700000	5.150000	5.600000	6.950000
SuRat	101.0	0.367649	0.167881	0.061054	0.265529	0.335493	0.396627	0.934274
facies	101.0	3.000000	0.000000	3.000000	3.000000	3.000000	3.000000	3.000000
wt	101.0	1.114822	0.991401	0.344087	0.354921	0.404444	2.556667	2.556667
N_SuRat	101.0	-0.394402	1.021283	-3.243303	-1.141649	-0.363502	0.241281	2.278340

Step 4: Variogram Calculation

The vertical-direction experimental variogram data and variogram model are first evaluated. Next the two orthogonal horizontal directions are evaluated. The interactive plots allow exploring different data analysis and modeling assumptions.

Remember to keep the **gamv.exe** executable opf GSLIB in your working directory!

The vertical experimental variogram is calculated below. The GSLIB.gamv_3d function in the geostats.py library is used here (wrapper written for GSLIB code).

In [11]:
```
# interactive calculation of the experimental variogram (VERTICAL)
l = widgets.Text(value='Variogram Calculation Interactive Demo, Michael Pyrcz, UT Austin (Modified by Patrick Bassal)',
                 layout=Layout(width='950px', height='30px'))
lagdist = widgets.FloatSlider(min = 0.1, max = 5, value = 0.2, step = 0.05, description = 'lag distance',
                              orientation='vertical',layout=Layout(width='90px', height='200px'))
lagdist.style.handle_color = 'gray'

lag_tol = widgets.FloatSlider(min = 0.05, max = 50, value = 0.1, step = 0.05, description = 'lag tolerance',
                              orientation='vertical',layout=Layout(width='90px', height='200px'))
```

```
lag_tol.style.handle_color = 'gray'

nlag = widgets.IntSlider(min = 1, max = 100, value = 7, step = 1, description = 'number of lags',
                         orientation='vertical',layout=Layout(width='90px', height='200px'))
nlag.style.handle_color = 'gray'

azi = widgets.FloatSlider(min = 0, max = 360, value = 90, step = 5, description = 'azimuth',
                          orientation='vertical',layout=Layout(width='90px', height='200px'))
azi.style.handle_color = 'cyan'

atol = widgets.FloatSlider(min = 5, max = 90, value = 20, step = 5, description = 'azimuth tolerance',
                           orientation='vertical',layout=Layout(width='120px', height='200px'))
atol.style.handle_color = 'cyan'

bandwh = widgets.FloatSlider(min = 1, max = 10, value = 1, step = 1, description = 'horiz. bandwidth',
                             orientation='vertical',layout=Layout(width='100px', height='200px'))
bandwh.style.handle_color = 'cyan'

dip = widgets.FloatSlider(min = -90, max = -30, value = -90, step = 0.5, description = 'dip',
                          orientation='vertical',layout=Layout(width='90px', height='200px'))
dip.style.handle_color = 'lightgreen'

dtol = widgets.FloatSlider(min = 5, max = 90, value = 20, step = 5, description = 'dip tolerance',
                           orientation='vertical',layout=Layout(width='90px', height='200px'))
dtol.style.handle_color = 'lightgreen'

bandwd = widgets.FloatSlider(min = 1, max = 10, value = 1, step = 1, description = 'dip bandwidth',
                             orientation='vertical',layout=Layout(width='100px', height='200px'))
bandwd.style.handle_color = 'lightgreen'


ui1 = widgets.HBox([lagdist,lag_tol,nlag,azi,atol,bandwh,dip,dtol,bandwd]) # basic widget formatting
ui = widgets.VBox([l,ui1],)

def f_make(lagdist,lag_tol,nlag,azi,atol,bandwh,dip,dtol,bandwd): # function to take parameters, calc variogram and plot
#     text_trap = io.StringIO()
#     sys.stdout = text_trap
    global lagsv,gammasv,nppsv
    tmin = -9999.9; tmax = 9999.9 # trimming values (not allowed for the GSLIB wrapper for some reason)
    lagsv, gammasv, nppsv = GSLIB.gamv_3d(df,"x","y","z","%s" %(param),
                                          nlag,lagdist,lag_tol,azi,atol,bandwh,dip,dtol,bandwd,isill=int(0))

    plt.subplot(111)                                  # plot experimental variogram
    plt.scatter(lagsv,gammasv,color = 'black',alpha = 0.8)
    plt.plot([0,max(lagsv)+lagdist],[1.0,1.0],color = 'black')

    for i, txt in enumerate(nppsv):   # label points with number data pairs
        plt.annotate(txt, (lagsv[i], gammasv[i]))

    plt.xlabel(r'Lag Distance $\bf(h)$, (m)')
    plt.ylabel(r'$\gamma \bf(h)$')
    plt.title('Vertical ' + param + ' Variogram - Dip ' + str(dip))
    plt.xlim([0,max(lagsv)+lagdist]); plt.ylim([0,1.5])
    plt.grid(True)

    plt.subplots_adjust(left=0.0, bottom=0.0, right=1.5, top=1.0, wspace=0.3, hspace=0.3)
    plt.show()

    return

# connect the function to make the samples and plot to the widgets
interactive_plot = widgets.interactive_output(
    f_make,{'lagdist':lagdist,'lag_tol':lag_tol,'nlag':nlag,'azi':azi,'atol':atol,
                                                'bandwh':bandwh,"dip":dip,"dtol":dtol,'bandwd':bandwd})
interactive_plot.clear_output(wait = True)              # reduce flickering by delaying plot updating
```

The variogram calculation parameters are summarized below:

- **azimuth** - the azimuth of the lag vector (0 is due North, or +y direction; 90 is due East, or +x direction)
- **azimuth tolerance** - the maximum allowable departure from the azimuth
- **unit lag distance** - spacing of the lag distance bins
- **lag distance tolerance** - tolerance for each lag (half of desired bin size; > 0.5*lagdist will include pairs in more than one bin)
- **number of lags** - number of lags in the experimental variogram
- **horizontal bandwidth** - maximum departure from the lag vector (in azimuth plane)
- **dip** - the dip of lag vector (0 is horizontal, -90 is vertical or in the -z direction)

- **dip tolerance** - the maximum allowable departure from the dip
- **dip bandwidth** - maximum departure from the lag vector (in dip plane)

In [12]:
```
display(ui, interactive_plot)                          # display the interactive plot
```

The variogram model for the vertical direction is next estimated. Three variogram models are considered: spherical, exponential and gaussian. The geostats.py and GSLIB.py libraries are again used herein. No other variogram functions or nesting of functions is considered for simplicity.

In [13]:
```
# interactive calculation of variogram model (VERTICAL)
l = widgets.Text(value='Variogram Modeling, Michael Pyrcz, UT Austin (Modified by Patrick Bassal)',
                 layout=Layout(width='950px', height='30px'))
nug = widgets.FloatSlider(min = 0, max = 1.0, value = 0.0, step = 0.1, description = 'nug',
                          orientation='vertical',layout=Layout(width='60px', height='200px'))
nug.style.handle_color = 'gray'
it1 = widgets.Dropdown(options=['Spherical', 'Exponential', 'Gaussian'],value='Spherical',
                       description='Type1:',disabled=False,layout=Layout(width='200px', height='30px'))
c1 = widgets.FloatSlider(min=0.5, max = 1.5, value = 1.0, step = 0.05, description = 'c1',
                         orientation='vertical',layout=Layout(width='60px', height='200px'))
c1.style.handle_color = 'gray'
hmaj1 = widgets.FloatSlider(min=0.2, max = 20.0, value = 1.0, step = 0.2, description = 'hmaj1',
                            orientation='vertical',layout=Layout(width='60px', height='200px'))
hmaj1.style.handle_color = 'black'

ui1 = widgets.HBox([nug,it1,c1,hmaj1])  # basic widget formatting
ui = widgets.VBox([l,ui1],)

def convert_type(it):
    if it == 'Spherical':
        return 1
    elif it == 'Exponential':
        return 2
    else:
        return 3

n_lag = 500; xlag = 0.05;
def f_make(nug,it1,c1, hmaj1):   #fxn to take parameters, make sample & plot
    text_trap = io.StringIO()
    sys.stdout = text_trap

    it1 = convert_type(it1)

    vario = GSLIB.make_variogram(nug,1,it1,c1,0.0,hmaj1,hmaj1) # make model object (assume hmaj=hmin here)

    index_maj,h_maj,gam_maj,cov_maj,ro_maj = geostats.vmodel(n_lag,xlag,0.0,vario) # project model in major azimuth
    plt.subplot(111)      # plot experimental variogram
    plt.scatter(lagsv,gammasv,color = 'black', alpha = 0.8)
    plt.plot(h_maj,gam_maj,color = 'black')
    plt.xlabel(r'Lag Distance $\bf(h)$, (m)')
    plt.ylabel(r'$\gamma \bf(h)$')

    for i, txt in enumerate(nppsv):   # label points with number data pairs
        plt.annotate(txt, (lagsv[i], gammasv[i]))

    if atol.value < 90.0:
        plt.title('Vertical ' + param + ' Variogram - Dip ' + str(dip.value))
    plt.xlim([0,max(lagsv)]); plt.ylim([0,1.5])
    plt.grid(True)

    plt.subplots_adjust(left=0.0, bottom=0.0, right=2.2, top=1.5, wspace=0.3, hspace=0.3)
    plt.show()

# connect the function to make the samples and plot to the widgets
interactive_plot = widgets.interactive_output(f_make, {'nug':nug, 'it1':it1,'c1':c1, 'hmaj1':hmaj1})
interactive_plot.clear_output(wait = True)               # reduce flickering by delaying plot updating
```

Parameters considered for variogram model:

- **nug**: nugget effect
- **c1**: the sill (variance beyond range of spatial correlation; typ. assumed as 1 for normalized data)
- **hmaj1**: range in the major direction
- **hmin1**: range in the minor direction (not used for vertical variogram)

In [14]:
```
```

```
display(ui, interactive_plot)                          # display the interactive plot
```

In [15]:

```
# print variogram results
vario = GSLIB.make_variogram(nug.value,1,convert_type(it1.value),c1.value,0.0,hmaj1.value,hmaj1.value)
index_maj,h_maj,gam_maj,cov_maj,ro_maj = geostats.vmodel(n_lag,xlag,0.0,vario)
datav = list(zip(lagsv, gammasv, nppsv)) # combine columns (variogram data)
datavm = list(zip(index_maj,h_maj,gam_maj,cov_maj,ro_maj)) # combine columns (variogram model)

fname_datav = 'variogram_data_vert_%s_%s.csv' %(stratum,param) #filename for variogram calculation
df_print = pd.DataFrame(datav, columns=['lag','semivar','Npts']) # temp df for printing
df_print.to_csv(fname_datav, index=False) # print to csv

fname_datavm = 'variogram_model_vert_%s_%s.csv' %(stratum,param) #filename for variogram calculation
df_print = pd.DataFrame(datavm, columns=
                        ['index_maj','h_maj','gam_maj','cov_maj','ro_maj']) # temp df for printing
df_print.to_csv(fname_datavm, index=False) # print to csv
```

The following code and output sequences are for calculating and modeling the two orthogonal variograms (note that only one horizotnal variogram is applicable in 2D space). The same procedures are used as above, however, the default estimates and slider values are adjusted to depict the typically longer correlation lengths and sparser data in the horizontal directions. The two orthognal azimuth directions are depicted in the same plot for convenience.

In [16]:

```
# interactive calculation of the experimental variogram (HORIZONTAL)
l = widgets.Text(value='Variogram Calculation Interactive Demo, Michael Pyrcz, UT Austin (Modified by Patrick Bassal)',
                 layout=Layout(width='950px', height='30px'))
lagdist = widgets.FloatSlider(min = 1, max = 50, value = 10, step = 0.5, description = 'lag distance',
                              orientation='vertical',layout=Layout(width='90px', height='200px'))
lagdist.style.handle_color = 'gray'

lag_tol = widgets.FloatSlider(min = 0.5, max = 50, value = 5, step = 0.5, description = 'lag tolerance',
                              orientation='vertical',layout=Layout(width='90px', height='200px'))
lag_tol.style.handle_color = 'gray'

nlag = widgets.IntSlider(min = 1, max = 100, value = 10, step = 1, description = 'number of lags',
                         orientation='vertical',layout=Layout(width='90px', height='200px'))
nlag.style.handle_color = 'gray'

azi = widgets.FloatSlider(min = 0, max = 360, value = 90, step = 5, description = 'azimuth',
                          orientation='vertical',layout=Layout(width='90px', height='200px'))
azi.style.handle_color = 'cyan'

atol = widgets.FloatSlider(min = 5, max = 90, value = 20, step = 5, description = 'azimuth tolerance',
                           orientation='vertical',layout=Layout(width='120px', height='200px'))
atol.style.handle_color = 'cyan'

bandwh = widgets.FloatSlider(min = 5, max = 300, value = 5, step = 5, description = 'horiz. bandwidth',
                             orientation='vertical',layout=Layout(width='100px', height='200px'))
bandwh.style.handle_color = 'cyan'

dip = widgets.FloatSlider(min = -90, max = 0, value = 0, step = 0.5, description = 'dip',
                          orientation='vertical',layout=Layout(width='90px', height='200px'))
dip.style.handle_color = 'lightgreen'

dtol = widgets.FloatSlider(min = 0.5, max = 90, value = 1.0, step = 0.5, description = 'dip tolerance',
                           orientation='vertical',layout=Layout(width='90px', height='200px'))
dtol.style.handle_color = 'lightgreen'

bandwd = widgets.FloatSlider(min = 0.1, max = 4, value = 0.2, step = 0.1, description = 'dip bandwidth',
                             orientation='vertical',layout=Layout(width='100px', height='200px'))
bandwd.style.handle_color = 'lightgreen'


ui1 = widgets.HBox([lagdist,lag_tol,nlag,azi,atol,bandwh,dip,dtol,bandwd]) # basic widget formatting
ui = widgets.VBox([l,ui1],)

def f_make(lagdist,lag_tol,nlag,azi,atol,bandwh,dip,dtol,bandwd): # fxn to take params, calc variogram & plot
#    text_trap = io.StringIO()
#    sys.stdout = text_trap
    global lags,gammas,npps,lags2,gammas2,npps2
    tmin = -9999.9; tmax = 9999.9 # trimming values (not allowed for the GSLIB wrapper for some reason)
    lags, gammas, npps = GSLIB.gamv_3d(df,"x","y","z","%s" %(param),
                                       nlag,lagdist,lag_tol,azi,atol,bandwh,dip,dtol,bandwd,isill=int(0))
    lags2, gammas2, npps2 = GSLIB.gamv_3d(df,"x","y","z","%s" %(param),
                                          nlag,lagdist,lag_tol,azi+90,atol,bandwh,dip,dtol,bandwd,isill=int(0))

    plt.subplot(111)                                   # plot experimental variogram
    plt.scatter(lags,gammas,color = 'black',label = 'Major Azimuth ' +str(azi), alpha = 0.8)
    plt.scatter(lags2,gammas2,color = 'red',label = 'Minor Azimuth ' +str(azi+90.0), alpha = 0.8)
```

```
    plt.plot([0,max(lags)+lagdist],[1.0,1.0],color = 'black')

    for i, txt in enumerate(npps):   # label points with number data pairs
        plt.annotate(txt, (lags[i], gammas[i]))
    for i, txt in enumerate(npps2):   # label points with number data pairs
        plt.annotate(txt, (lags2[i], gammas2[i]))

    plt.xlabel(r'Lag Distance $\bf(h)$, (m)')
    plt.ylabel(r'$\gamma \bf(h)$')
    if atol < 90.0:
        plt.title('Directional ' + param + ' Variogram - Azi. ' + str(azi) + ', Azi. Tol.' + str(atol))
    else:
        plt.title('Omni Directional ' + param + ' Variogram ')
    plt.xlim([0,max(lags)+lagdist]); plt.ylim([0,max(max(gammas),max(gammas2))])
    plt.legend(loc="lower right")
    plt.grid(True)

    plt.subplots_adjust(left=0.0, bottom=0.0, right=1.5, top=1.0, wspace=0.3, hspace=0.3)
    plt.show()

    return

# connect the function to make the samples and plot to the widgets
interactive_plot = widgets.interactive_output(
    f_make, {'lagdist':lagdist,'lag_tol':lag_tol,'nlag':nlag,'azi':azi,'atol':atol,
             'bandwh':bandwh,"dip":dip,"dtol":dtol,'bandwd':bandwd})
interactive_plot.clear_output(wait = True)               # reduce flickering by delaying plot updating
```

In [17]:

```
display(ui, interactive_plot)                           # display the interactive plot
```

In [18]:

```
# interactive calculation of variogram model (HORIZONTAL)
l = widgets.Text(value='Variogram Modeling, Michael Pyrcz, UT Austin (Modified by Patrick Bassal)',
                 layout=Layout(width='950px', height='30px'))
nug = widgets.FloatSlider(min = 0, max = 1.0, value = 0.0, step = 0.1, description = 'nug',
                          orientation='vertical',layout=Layout(width='60px', height='200px'))
nug.style.handle_color = 'gray'
it1 = widgets.Dropdown(options=['Spherical', 'Exponential', 'Gaussian'],value='Spherical',
                       description='Type1:',disabled=False,layout=Layout(width='200px', height='30px'))
c1 = widgets.FloatSlider(min=0.5, max = 1.5, value = 1.0, step = 0.05, description = 'c1',
                         orientation='vertical',layout=Layout(width='60px', height='200px'))
c1.style.handle_color = 'gray'
hmaj1 = widgets.FloatSlider(min=2.0, max = 500.0, value = 10.0, step = 2.0, description = 'hmaj1',
                            orientation='vertical',layout=Layout(width='60px', height='200px'))
hmaj1.style.handle_color = 'black'
hmin1 = widgets.FloatSlider(min = 2.0, max = 500.0, value = 10.0, step = 2.0, description = 'hmin1',
                            orientation='vertical',layout=Layout(width='60px', height='200px'))
hmin1.style.handle_color = 'red'

ui1 = widgets.HBox([nug,it1,c1,hmaj1,hmin1])  # basic widget formatting
ui = widgets.VBox([l,ui1],)

def convert_type(it):
    if it == 'Spherical':
        return 1
    elif it == 'Exponential':
        return 2
    else:
        return 3

n_lag = 1000; xlag = 1;
def f_make(nug,it1,c1, hmaj1, hmin1):  #function to take parameters, make sample and plot
    text_trap = io.StringIO()
    sys.stdout = text_trap

    it1 = convert_type(it1)

    vario = GSLIB.make_variogram(nug,1,it1,c1,0.0,hmaj1,hmin1) # make model object
    index_maj,h_maj,gam_maj,cov_maj,ro_maj = geostats.vmodel(n_lag,xlag,0.0,vario) # project model in major azimuth
    index_min,h_min,gam_min,cov_min,ro_min = geostats.vmodel(n_lag,xlag,90.0,vario)

    plt.subplot(111)                                    # plot experimental variogram
    plt.scatter(lags,gammas,color = 'black',label = 'Major Azimuth ' +str(azi.value), alpha = 0.8)
    plt.plot(h_maj,gam_maj,color = 'black')
    plt.scatter(lags2,gammas2,color = 'red',label = 'Minor Azimuth ' +str(azi.value+90.0), alpha = 0.8)
    plt.plot(h_min,gam_min,color = 'red')
    plt.xlabel(r'Lag Distance $\bf(h)$, (m)')
    plt.ylabel(r'$\gamma \bf(h)$')

    for i, txt in enumerate(npps):   # label points with number data pairs
```

```
        plt.annotate(txt, (lags[i], gammas[i]))
    for i, txt in enumerate(npps2):   # label points with number data pairs
        plt.annotate(txt, (lags2[i], gammas2[i]))

    if atol.value < 90.0:
        plt.title('Directional '+ param +' Variogram - Azi. '+str(azi.value) +', Azi. Tol.'+str(atol.value))
    else:
        plt.title('Omni Directional ' + param + ' Variogram ')
    plt.xlim([0,max(lags)]); plt.ylim([0,1.5])
    plt.legend(loc="lower right")
    plt.grid(True)

    plt.subplots_adjust(left=0.0, bottom=0.0, right=2.2, top=1.5, wspace=0.3, hspace=0.3)
    plt.show()

# connect the function to make the samples and plot to the widgets
interactive_plot = widgets.interactive_output(
    f_make, {'nug':nug, 'it1':it1,'c1':c1, 'hmaj1':hmaj1, 'hmin1':hmin1})
interactive_plot.clear_output(wait = True)   # reduce flickering by delaying plot updating
```

In [19]:

```
display(ui, interactive_plot)                          # display the interactive plot
```

In [20]:

```
# print variogram results (currently for one direction)
vario = GSLIB.make_variogram(nug.value,1,convert_type(it1.value),c1.value,0.0,hmaj1.value,hmaj1.value)
index_maj,h_maj,gam_maj,cov_maj,ro_maj = geostats.vmodel(n_lag,xlag,0.0,vario)
datav = list(zip(lags, gammas, npps)) # combine columns (variogram data)
datavm = list(zip(index_maj,h_maj,gam_maj,cov_maj,ro_maj)) # combine columns (variogram model)

fname_datav = 'variogram_data_x_%s_%s.csv' %(stratum,param) #filename for variogram calculation
df_print = pd.DataFrame(datav, columns=['lag','semivar','Npts']) # temp df for printing
df_print.to_csv(fname_datav, index=False) # print to csv

fname_datavm = 'variogram_model_x_%s_%s.csv' %(stratum,param) #filename for variogram calculation
df_print = pd.DataFrame(datavm, columns=
                        ['index_maj','h_maj','gam_maj','cov_maj','ro_maj']) # temp df for printing
df_print.to_csv(fname_datavm, index=False) # print to csv
```

In [ ]:

Interactive widget example for vertical variogram calculation from ***Props_Variogram.ipynb:***

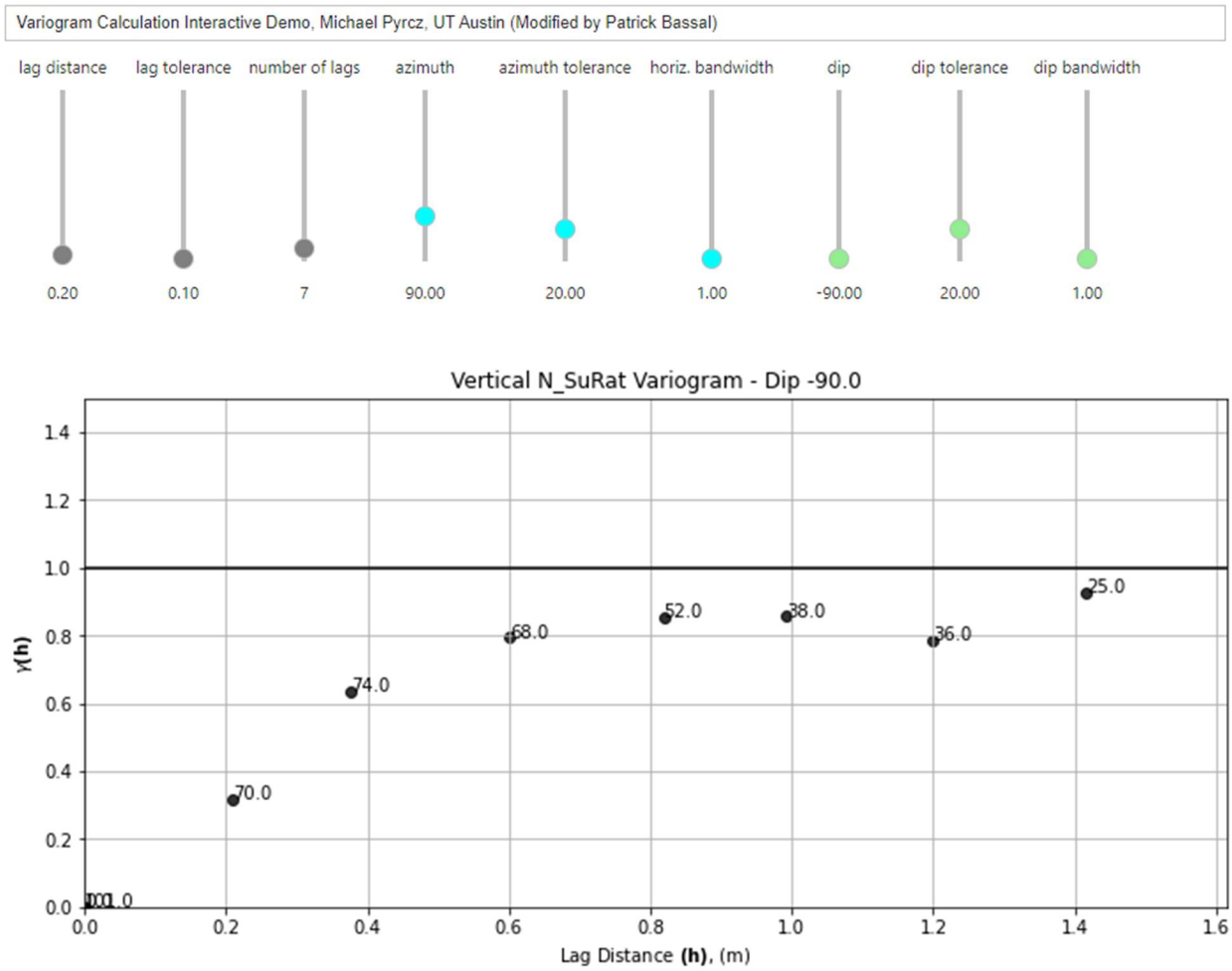

Interactive widget example for vertical variogram model from ***Props_Variogram.ipynb:***

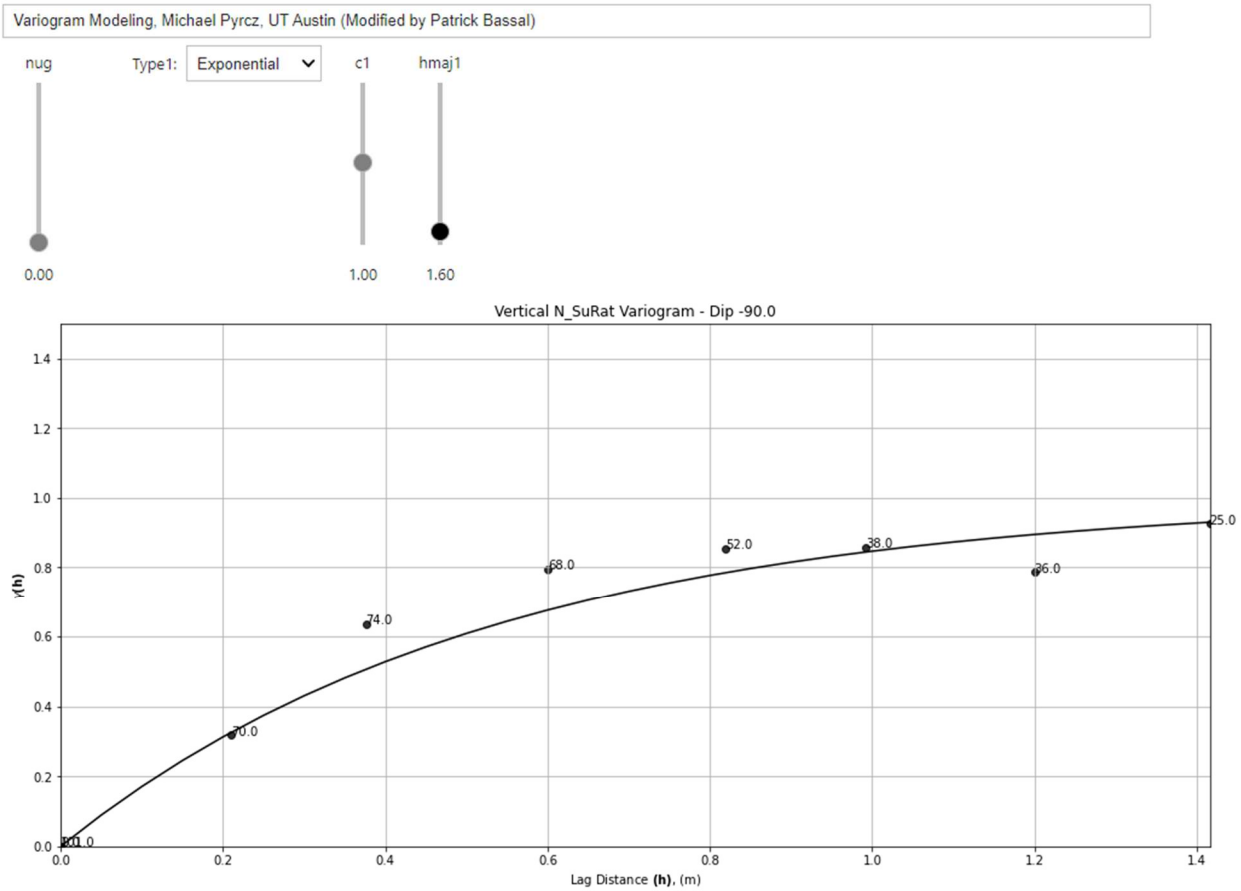

Attachment D-3

Geostatistical Modeling: FLAC FISH files, SGeMS parameter file, and Jupyter Notebook

```
;-------------------------------------------------------------------------------
; About: Stochastic NDA Workflow - (1) Mesh generation
; By: Patrick Bassal, Oct 2021
; Project: Wynne Ave
;-------------------------------------------------------------------------------
; Notes:
; - This calculation generates a FLAC mesh, assigns material groups to zones,
; and sets static boundary conditions.
; - All values here-in are site-dependent and subject to modeler interpretations
;-------------------------------------------------------------------------------

; Set-up model for flow/dynamics, assign 70 extra variables:
config gwflow cppudm dynamic ats extra 70


;-------------------------------------------------------------------------------
; Generate the mesh (method for layered free-field sites)
; - Step 1: Generate overall grid based on row/column zone count
; - Step 2: Divide mesh into regions for modeling stratigraphic heterogeneity.
; First apportion # rows (j ranges) for major strata that are roughly
; horizontally planar, then apportion # cols (i ranges) based on elevation
; changes of interest. The mesh is then generated for each group based on
available
; data.
;-------------------------------------------------------------------------------

; Assing number of zones per row/column:
def $mesh ; (Note: All calculations are performed in FISH langauge functions)
    $jrow = 40; max rows (0.25m - 0.8m zone heights)
    $icol = 500; max columns (1m zone widths)
    $jrowP1 = int($jrow + 1) ; max row gridpts
    $icolP1 = int($icol + 1) ; max col gridpts
end
$mesh

grid $icol,$jrow ; generate the overall grid
model mohr i=1,$icol j=1,$jrow ; sub-section with larger elements

; Generate grnd surface, B, C1, C, and D bounds for horizontal CPT intervals
; (will generate C2 and saturated boundary separately)
; CPTs: WYN 13 - 8
gen 0,0  0,3.3  205,3.3  205,0  rat=1,1   i=1,206  j=1,7 ; base to top of D
gen same 0,9.2  205,11.6  same   rat=1,1  i=1,206  j=7,21 ; top of D to top of C
gen same 0,10.9 205,13.3 same   rat=1,1   i=1,206  j=21,27 ; top of C to top of
C1
gen same 0,14.6 205,16.6 same   rat=1,1   i=1,206  j=27,37 ; top of C1 to top
of B
gen same 0,17.5 205,18.6 same   rat=1,1   i=1,206  j=37,$jrowP1 ; top of B to
ground

; CPTs: WYN 8 - 6
gen 205,0  205,3.3  265,4.1  265,0  rat=1,1   i=206,266  j=1,7
gen same 205,11.6 265,11.8 same     rat=1,1   i=206,266  j=7,21
gen same 205,13.3 265,13.8 same     rat=1,1   i=206,266  j=21,27
gen same 205,16.6 265,17.3 same     rat=1,1   i=206,266  j=27,37
gen same 205,18.6 265,19.74 same     rat=1,1   i=206,266  j=37,$jrowP1

; CPTs: WYN 6 - 5
gen 265,0  265,4.1  279,4.2  279,0  rat=1,1   i=266,280  j=1,7
gen same 265,11.8 279,11.8 same     rat=1,1   i=266,280  j=7,21
gen same 265,13.8 279,14.1 same     rat=1,1   i=266,280  j=21,27
gen same 265,17.3 279,17.5 same     rat=1,1   i=266,280  j=27,37
gen same 265,19.74 279,19.9 same     rat=1,1   i=266,280  j=37,$jrowP1
```

```
60
61  ; CPTs: WYN 5 - 4 (this small interval used to create declivity at base)
62  gen 279,0  279,4.2  283,5.4  283,0  rat=1,1 i=280,284  j=1,7
63  gen same 279,11.8 283,11.9 same     rat=1,1 i=280,284  j=7,21
64  gen same 279,14.1 283,14.3 same     rat=1,1 i=280,284  j=21,27
65  gen same 279,17.5 283,17.6 same     rat=1,1 i=280,284  j=27,37
66  gen same 279,19.9 283,19.96 same     rat=1,1 i=280,284  j=37,$jrowP1
67
68  ; CPTs: WYN 4 - 14
69  gen 283,0  283,5.4   $icol,5.9   $icol,0  rat=1,1 i=284,$icolP1  j=1,7
70  gen same   283,11.9  $icol,13.7  same     rat=1,1 i=284,$icolP1  j=7,21
71  gen same   283,14.3  $icol,16.4  same     rat=1,1 i=284,$icolP1  j=21,27
72  gen same   283,17.6  $icol,19.3  same     rat=1,1 i=284,$icolP1  j=27,37
73  gen same   283,19.96  $icol,23.0  same     rat=1,1 i=284,$icolP1  j=37,$jrowP1
74
75
76  ;-------------------------------------------------------------------------
77  ; Assign strata/material groups to all mesh zones
78  ;-------------------------------------------------------------------------
79
80  ; Mark boundaries of major strata/material groups to assign regions:
81  mark j=37 ; bottom of A
82  mark j=7 ; bottom of C
83  mark j=21 ; bottom of C1
84  mark i=181 j=21,27 ; mark extent of C1
85  mark j=27 ; bottom of B
86
87  ; Assign and label material groups by region:
88  group 'A'         region 499,39
89  group 'Bunsat'    region 499,35 ; unsat portion of B (assign Bsat later)
90  group 'C1'        region 499,25
91  group 'C'         region 2,25
92  group 'C'         region 499,15
93  group 'D'         region 499,2
94
95  ; Assign and label material groups by individual zones (for smaller details
96  ; including interlayered lenses or pockets of distinct soils):
97  group 'C'         i=181,182 j=21,25
98  group 'C'         i=183,184 j=21,24
99  group 'C'         i=185,186 j=21,23
100 group 'C'         i=187,188 j=21,22
101 group 'C'         i=189,190 j=21
102
103 group 'C2'         i=230,245 j=17
104 group 'C2'         i=246,273 j=16,17
105 group 'C2'         i=274 j=15,17
106 group 'C2'         i=275,281 j=14,17
107 group 'C2'         i=282,287 j=15,17
108 group 'C2'         i=287,294 j=15,16
109
110 ; assign Bsat (saturated clay) based on water table estimates from site data:
111 def $satclay
112     loop $j (27,36) ; loop rows
113         loop $i (1,113) ; loop columns (WYN 13 - 12)
114             if model ($i, $j) # 1
115                 if y($i,$j) < ($i-0)*(14.1-13.2)/(113-0)+13.2
116                     z_group($i,$j) = 'Bsat'
117                 endif
118             endif
119         endloop
120         loop $i (114,205) ; loop columns (WYN 12 - 8)
121             if model ($i, $j) # 1
122                 if y($i,$j) < ($i-113)*(14.3-14.1)/(205-113)+14.1
```

```
                    z_group($i,$j) = 'Bsat'
                endif
            endif
        endloop
        loop $i (206,235) ; loop columns (WYN 8 - 7)
            if model ($i, $j) # 1
                if y($i,$j) < ($i-205)*(15.3-14.3)/(235-205)+14.3
                    z_group($i,$j) = 'Bsat'
                endif
            endif
        endloop
        loop $i (236,353) ; loop columns (WYN 7 - 1)
            if model ($i, $j) # 1
                if y($i,$j) < ($i-236)*(16.2-15.3)/(353-236)+15.3
                    z_group($i,$j) = 'Bsat'
                endif
            endif
        endloop
        loop $i (354,$icol) ; loop columns (WYN 7 - 1)
            if model ($i, $j) # 1
                if y($i,$j) < ($i-353)*(16.4-16.2)/($icol-353)+16.2
                    z_group($i,$j) = 'Bsat'
                endif
            endif
        endloop
    endloop
end
$satclay

unmark ; remove marks after materials assigned


;--------------------------------------------------------------------------
; Assign initial static boundary conditions
;--------------------------------------------------------------------------

fix x y j=1
fix x   i=1
fix x   i=$icolP1
```

```
;-------------------------------------------------
; About: Stochastic NDA Workflow - Print grid
; By: Patrick Bassal, Oct 2021
; Project: Wynne Ave
; Stratum/Group: Bsat
;-------------------------------------------------
; Print grid coordinates for material group within FLAC mesh

def $ptgrid_array ; creates array grid or zone data
    array $ptgrid(2246,4) ; 1- grid i, 2- grid j, 3- xcorr, 4- ycorr;
    iteratively assign based on number grids
    ;(WARNING: Must assign array size manually as $icol*$jrow)
    $cnt = 1
    loop $i (1,$icol) ; range of x data of interest
        loop $j (1,$jrow) ;
            if z_group($i,$j) = 'Bsat' ; call out group of interest
                $ptgrid($cnt,1)=$i
                $ptgrid($cnt,2)=$j
                $ptgrid($cnt,3)=(x($i,$j)+x($i+1,$j)+x($i,$j+1)+x($i+1,$j+1))/4.
                0 ; x-center of zone
                $ptgrid($cnt,4)=(y($i,$j)+y($i+1,$j)+y($i,$j+1)+y($i+1,$j+1))/4.
                0 ; y-center of zone
                $cnt = $cnt + 1
            endif
        endloop
    endloop
end
$ptgrid_array

def $ptgrid_print
    array $griddata(1,1)
    $file = 'ptgrid_data_Bsat.txt'; filename
    status = open($file,1,1)
    $griddata(1,1) = 'gridi, gridj, xcen, ycen'
    status = write($griddata,1)
    loop $m (1,2246); iteratively assign array size
        $griddata(1,1) = string($ptgrid($m,1))
        loop $n (2,4)
            $griddata(1,1) = $griddata(1,1) +' '+ string($ptgrid($m,$n))
        endloop
        status = write($griddata,1)
    endloop
    status = close
end
$ptgrid_print


```

```
;------------------------------------------------------------------------------
; About: Batch program to call and print FLAC mesh
; By: Patrick Bassal, Oct 2021
; Project: Wynne Ave
;------------------------------------------------------------------------------

call 1_mesh.fis
call print_grid_Bsat.fis
```

```
<parameters>  <algorithm name="sgsim" />
  <Grid_Name value="Bsat_ptset" region=""  />
  <Property_Name  value="SGSIM_Bsat" />
  <Nb_Realizations  value="10" />
  <Seed  value="14071790" />
  <Kriging_Type  value="Simple Kriging (SK)"  />
  <Assign_Hard_Data  value="0"  />
  <Hard_Data  grid="Bsat_NSuRat_30cm" region="" property="Variable"  />
  <Max_Conditioning_Data  value="100" />
  <Search_Ellipsoid  value="500 500 500
0 0 0" />
  <AdvancedSearch  use_advanced_search="0"></AdvancedSearch>
  <Use_Target_Histogram  value="0"  />
  <Variogram  nugget="0" structures_count="1"  >
  <structure_1  contribution="1"  type="Exponential"   >
    <ranges max="80"  medium="1.6"  min="0"   />
    <angles x="269.5"  y="0"  z="0"   />
  </structure_1>
</Variogram>
</parameters>
```

Back Transform SGeMS Realization

The following notebook converts a "normalized" simulation result to the original distribution. The backtr program used in GSLIB (as converted to Python by Michael Pyrcz) is used herein, since it allows for the use of a transformation table based on the original nscore calculation using declustering weights.

A ".csv" file with columns of the simulation results (as obtained from SGeMs) is used herein. The transformation lookup table as obtained from the nscore program is also needed.

By Patrick C. Bassal (Ver 0: 02/19/2022)

Step 1: Import libraries

Import all necessary libraries below. These libraries are standard packages that are typically included with the download of a Python distribution package (e.g., Anaconda).

In [1]:
```
import numpy as np                # for array calculations
import pandas as pd               # for building dataframe tables
import matplotlib.pyplot as plt   # plotting
from matplotlib import cm         # for colormap

# For nscore transform as implemented by Michael Pyrcz
import geostatspy.GSLIB as GSLIB          # GSLIB utilities, visualization, and wrapper
import geostatspy.geostats as geostats    # GSLIB methods converted to Python
```

Step 2: Input simulation results and transformation table

The simulation dataframe will be read from a .csv input file with columns for all simulations. See example files with this distribution.

In [2]:
```
#  Input CPT data and lab files (most inputs should be adjusted herein)
param = 'SuRat' # parameter of interest (must match exact column name from .csv for transform table)
sim_csv = 'SGS_Bsat_20real' # excel file with simulation results (see example; remove .csv)
trans_csv = 'Data_Wynne_Bsat_SuRat_transtable' # excel file w/ trans table (see example; remove .csv)
start_col = 3 # index of first column to transform
stop_col = 22 # index of last column to transform

output_sim = '%s_backtr.csv' %(sim_csv) # Output csv file name for normalized data
```

We'll first display the simulation results as a dataframe

In [3]:
```
df = pd.read_csv('%s.csv' %(sim_csv))  # read the .csv file as a DataFrame
df                                     # preview Dataframe
```

Out[3]:

	X	Y	Z	SGSIM_Bsat_0__real0	SGSIM_Bsat_0__real1	SGSIM_Bsat_0__real10	SGSIM_Bsat_0__real11	SGSIM_Bsat_0__real12	SGSIM_Bsat_0_
0	0.5	11.091000	0	-0.479724	-0.392269	-0.269972	-1.292700	-0.258998	0.
1	0.5	11.461000	0	-1.858570	-0.814039	-1.613870	-1.416120	-0.974764	-1.
2	0.5	11.831000	0	1.329670	1.159120	0.751815	0.186300	0.755019	0.
3	0.5	12.201000	0	1.288390	0.530578	1.279490	1.527590	1.159190	0.
4	0.5	12.570000	0	-1.232490	-1.038790	-0.278388	-0.199313	-0.938004	-0.
...	...	...	...	...	...	...	...	...	
2241	495.5	16.502001	0	0.912748	-2.599390	1.295040	-1.899100	-0.574411	-0.
2242	496.5	16.511000	0	1.063660	-2.660780	1.172070	-1.955890	-0.582222	-0.
2243	497.5	16.521000	0	1.217720	-2.542900	1.287110	-1.822840	-0.432289	-0.
2244	498.5	16.531000	0	1.376590	-2.626710	1.076670	-1.555170	-0.334581	-0.
2245	499.5	16.540001	0	1.852720	-2.900830	0.689784	-1.234960	-0.582565	0.

2246 rows × 23 columns

Next, we'll display the transformation table as a dataframe and select extrapolation values for the tails of distribution. Note that GSLIB recommends a histogram smoothing option for transform distributions fom sparse data. This has not been implemented for the current workflow.

In [4]:
```
df_trans = pd.read_csv('%s.csv' %(trans_csv))  # read the .csv file as a DataFrame
tvVar = df_trans["%s" %(param)].values         # read table values into columns
tnsVar = df_trans["N_%s" %(param)].values
df_trans                                       # preview Dataframe
```

Out[4]:

	SuRat	N_SuRat
0	0.061054	-2.943204
1	0.124353	-2.584747
2	0.141362	-2.407793
3	0.159647	-2.228950
4	0.171349	-2.099446
...	...	...
96	0.853835	1.387634
97	0.874045	1.555462
98	0.897084	1.784002
99	0.911435	1.972393
100	0.934274	2.278340

101 rows × 2 columns

In [5]:
```
# select minimum and maximum values for tail extrapolation
# (this is not a cutoff, and values must go beyond the ends of original data in transform table)
vmin = max(0,min(tvVar)-0.5*np.std(tvVar))
vmax = max(tvVar)+0.5*np.std(tvVar)
print(vmin,vmax)
```

```
0 1.017798265918982
```

Step 3: Back Transform the Normalized Simulations to Original Distribution

The "backtr" back transform from GSLIB (as implemented in Python by Michael Pyrcz) is used here. This uses the tranformation table between original and normal score values. The extrapolation type can then be assumed (a second-order power law is assumed currently for both the upper and lower tails).

In [6]:
```
dfnew = df.copy()    # prepare a new dataframe for back transformed values
for i in range(start_col,stop_col+1):   # loop through all realizations and perform backtransform
    dfnew.iloc[:,i] = geostats.backtr(df,df.columns[i],tvVar,tnsVar,vmin,vmax,2,2,2,2)
dfnew
```

Out[6]:

	X	Y	Z	SGSIM_Bsat_0__real0	SGSIM_Bsat_0__real1	SGSIM_Bsat_0__real10	SGSIM_Bsat_0__real11	SGSIM_Bsat_0__real12	SGSIM_Bsat_0_
0	0.5	11.091000	0	0.332237	0.335423	0.344651	0.257102	0.345863	0.
1	0.5	11.461000	0	0.192238	0.294815	0.214008	0.239909	0.278663	0.
2	0.5	11.831000	0	0.795873	0.703381	0.549568	0.387877	0.552769	0.
3	0.5	12.201000	0	0.754594	0.460048	0.745694	0.870689	0.703392	0.
4	0.5	12.570000	0	0.258780	0.275911	0.344423	0.354711	0.279093	0.
...	...	...	...	...	...	...	...	...	
2241	495.5	16.502001	0	0.605189	0.122946	0.761244	0.189339	0.327781	0.
2242	496.5	16.511000	0	0.677255	0.117045	0.705418	0.184239	0.327173	0.
2243	497.5	16.521000	0	0.712600	0.128375	0.753314	0.192705	0.332808	0.
2244	498.5	16.531000	0	0.842792	0.120320	0.681308	0.225900	0.336867	0.
2245	499.5	16.540001	0	0.902319	0.093972	0.504567	0.258705	0.327146	0.

2246 rows × 23 columns

Plot and compare cumulative distributions of simulations before and after backtransform

In [7]:
```
sim_i = 3 # simulation column number for plotting

plt.subplot(221)                                    # plot nscore simulation histogram
```

```
plt.hist(df[df.columns[sim_i]], bins=np.linspace(-3.0,3.0,10000),histtype="step",
         alpha=1,density=True,cumulative=True,edgecolor='red',label='Original')
plt.xlim([-3.0,3.0]); plt.ylim([0,1.0])
plt.xlabel("%s" %(param)); plt.ylabel('Frequency'); plt.title('Normal Sim %s' %(param))
plt.legend(loc='upper left')
plt.grid(True)

plt.subplot(222)                                    # plot back transformed histogram
plt.hist(dfnew[dfnew.columns[sim_i]], facecolor='blue',bins=np.linspace(vmin,vmax,10000),histtype="step",
         alpha=1,density=True,cumulative=True,edgecolor='blue',label = 'Trans')
plt.xlim([vmin,vmax]); plt.ylim([0,1.0])
plt.xlabel("%s" %(param)); plt.ylabel('Frequency'); plt.title("Backtransformed Sim %s" %(param))
plt.legend(loc='upper left')
plt.grid(True)

plt.subplot(223)                                    # plot original barchart
plt.hist(df[df.columns[sim_i]], facecolor='red',bins=np.linspace(-3.0,3.0,20),histtype="stepfilled",
         alpha=.2,density=True,cumulative=False,edgecolor='red',label='Original')
plt.xlim([-3.0,3.0])
plt.xlabel("%s" %(param)); plt.ylabel('Frequency'); plt.title("Normal Sim %s" %(param))
plt.legend(loc='upper right')
plt.grid(True)

plt.subplot(224)                                    # plot nscore transformed barchart
plt.hist(dfnew[dfnew.columns[sim_i]], facecolor='blue',bins=np.linspace(vmin,vmax,20),histtype="stepfilled",
         alpha=.2,density=True,cumulative=False,edgecolor='blue',label = 'Trans')
plt.xlim([vmin,vmax])
plt.xlabel("%s" %(param)); plt.ylabel('Frequency'); plt.title('Backtransformed Sim %s' %(param))
plt.legend(loc='upper right')
plt.grid(True)

plt.subplots_adjust(left=0.0, bottom=0.0, right=2.0, top=2.2, wspace=0.2, hspace=0.3)
plt.show()
```

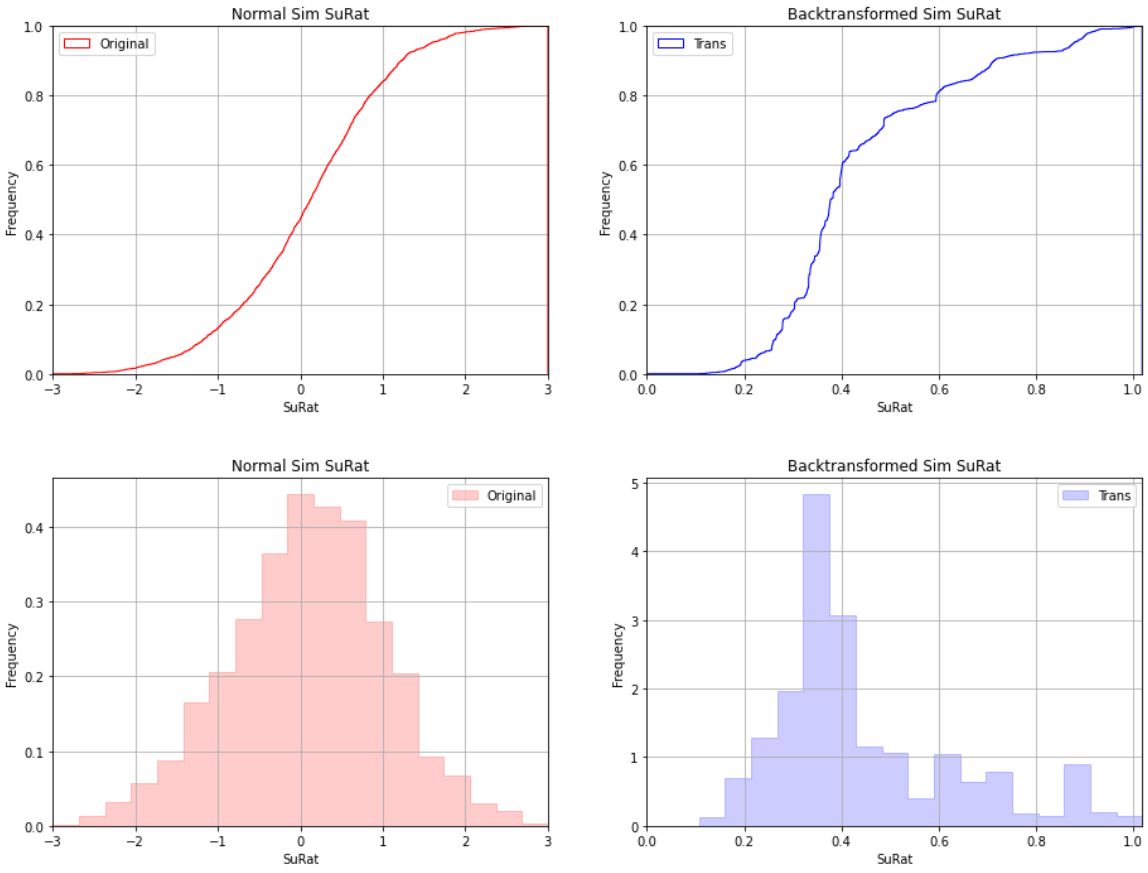

Print the full backtransform dataframe to a ".csv" file

In [8]:
```
dfnew.to_csv(output_sim, index=False) # print full dataframe
```

Attachment D-4

NDA Modeling in FLAC: FLAC FISH files

```
;-------------------------------------------------------------------------
; About: Stochastic NDA Workflow - (1) Mesh generation
; By: Patrick Bassal, Oct 2021
; Project: Wynne Ave
;-------------------------------------------------------------------------
; Notes:
; - This calculation generates a FLAC mesh, assigns material groups to zones,
; and sets static boundary conditions.
; - All values here-in are site-dependent and subject to modeler interpretations
;-------------------------------------------------------------------------

; Set-up model for flow/dynamics, assign 70 extra variables:
config gwflow cppudm dynamic ats extra 70


;-------------------------------------------------------------------------
; Generate the mesh (method for layered free-field sites)
; - Step 1: Generate overall grid based on row/column zone count
; - Step 2: Divide mesh into regions for modeling stratigraphic heterogeneity.
; First apportion # rows (j ranges) for major strata that are roughly
; horizontally planar, then apportion # cols (i ranges) based on elevation
; changes of interest. The mesh is then generated for each group based on
available
; data.
;-------------------------------------------------------------------------

; Assing number of zones per row/column:
def $mesh ; (Note: All calculations are performed in FISH langauge functions)
    $jrow = 40; max rows (0.25m - 0.8m zone heights)
    $icol = 500; max columns (1m zone widths)
    $jrowP1 = int($jrow + 1) ; max row gridpts
    $icolP1 = int($icol + 1) ; max col gridpts
end
$mesh

grid $icol,$jrow ; generate the overall grid
model mohr i=1,$icol j=1,$jrow ; sub-section with larger elements

; Generate grnd surface, B, C1, C, and D bounds for horizontal CPT intervals
; (will generate C2 and saturated boundary separately)
; CPTs: WYN 13 - 8
gen 0,0  0,3.3  205,3.3  205,0  rat=1,1   i=1,206  j=1,7 ; base to top of D
gen same 0,9.2  205,11.6  same   rat=1,1  i=1,206  j=7,21 ; top of D to top of C
gen same 0,10.9 205,13.3 same   rat=1,1   i=1,206  j=21,27 ; top of C to top of
C1
gen same 0,14.6 205,16.6 same   rat=1,1   i=1,206  j=27,37 ; top of C1 to top
of B
gen same 0,17.5 205,18.6 same   rat=1,1   i=1,206  j=37,$jrowP1 ; top of B to
ground

; CPTs: WYN 8 - 6
gen 205,0  205,3.3  265,4.1  265,0  rat=1,1   i=206,266  j=1,7
gen same 205,11.6 265,11.8 same     rat=1,1   i=206,266  j=7,21
gen same 205,13.3 265,13.8 same     rat=1,1   i=206,266  j=21,27
gen same 205,16.6 265,17.3 same     rat=1,1   i=206,266  j=27,37
gen same 205,18.6 265,19.74 same     rat=1,1   i=206,266  j=37,$jrowP1

; CPTs: WYN 6 - 5
gen 265,0  265,4.1  279,4.2  279,0  rat=1,1   i=266,280  j=1,7
gen same 265,11.8 279,11.8 same     rat=1,1   i=266,280  j=7,21
gen same 265,13.8 279,14.1 same     rat=1,1   i=266,280  j=21,27
gen same 265,17.3 279,17.5 same     rat=1,1   i=266,280  j=27,37
gen same 265,19.74 279,19.9 same     rat=1,1   i=266,280  j=37,$jrowP1
```

```
60
61  ; CPTs: WYN 5 - 4 (this small interval used to create declivity at base)
62  gen 279,0  279,4.2  283,5.4  283,0  rat=1,1 i=280,284  j=1,7
63  gen same 279,11.8 283,11.9 same     rat=1,1 i=280,284  j=7,21
64  gen same 279,14.1 283,14.3 same     rat=1,1 i=280,284  j=21,27
65  gen same 279,17.5 283,17.6 same     rat=1,1 i=280,284  j=27,37
66  gen same 279,19.9 283,19.96 same     rat=1,1 i=280,284  j=37,$jrowP1
67
68  ; CPTs: WYN 4 - 14
69  gen 283,0  283,5.4   $icol,5.9   $icol,0  rat=1,1 i=284,$icolP1  j=1,7
70  gen same   283,11.9  $icol,13.7  same     rat=1,1 i=284,$icolP1  j=7,21
71  gen same   283,14.3  $icol,16.4  same     rat=1,1 i=284,$icolP1  j=21,27
72  gen same   283,17.6  $icol,19.3  same     rat=1,1 i=284,$icolP1  j=27,37
73  gen same   283,19.96  $icol,23.0  same     rat=1,1 i=284,$icolP1  j=37,$jrowP1
74
75
76  ;-------------------------------------------------------------------------
77  ; Assign strata/material groups to all mesh zones
78  ;-------------------------------------------------------------------------
79
80  ; Mark boundaries of major strata/material groups to assign regions:
81  mark j=37 ; bottom of A
82  mark j=7 ; bottom of C
83  mark j=21 ; bottom of C1
84  mark i=181 j=21,27 ; mark extent of C1
85  mark j=27 ; bottom of B
86
87  ; Assign and label material groups by region:
88  group 'A'         region 499,39
89  group 'Bunsat'    region 499,35 ; unsat portion of B (assign Bsat later)
90  group 'C1'        region 499,25
91  group 'C'         region 2,25
92  group 'C'         region 499,15
93  group 'D'         region 499,2
94
95  ; Assign and label material groups by individual zones (for smaller details
96  ; including interlayered lenses or pockets of distinct soils):
97  group 'C'         i=181,182 j=21,25
98  group 'C'         i=183,184 j=21,24
99  group 'C'         i=185,186 j=21,23
100 group 'C'         i=187,188 j=21,22
101 group 'C'         i=189,190 j=21
102
103 group 'C2'         i=230,245 j=17
104 group 'C2'         i=246,273 j=16,17
105 group 'C2'         i=274 j=15,17
106 group 'C2'         i=275,281 j=14,17
107 group 'C2'         i=282,287 j=15,17
108 group 'C2'         i=287,294 j=15,16
109
110 ; assign Bsat (saturated clay) based on water table estimates from site data:
111 def $satclay
112     loop $j (27,36) ; loop rows
113         loop $i (1,113) ; loop columns (WYN 13 - 12)
114             if model ($i, $j) # 1
115                 if y($i,$j) < ($i-0)*(14.1-13.2)/(113-0)+13.2
116                     z_group($i,$j) = 'Bsat'
117                 endif
118             endif
119         endloop
120         loop $i (114,205) ; loop columns (WYN 12 - 8)
121             if model ($i, $j) # 1
122                 if y($i,$j) < ($i-113)*(14.3-14.1)/(205-113)+14.1
```

```
                    z_group($i,$j) = 'Bsat'
                endif
            endif
        endloop
        loop $i (206,235) ; loop columns (WYN 8 - 7)
            if model ($i, $j) # 1
                if y($i,$j) < ($i-205)*(15.3-14.3)/(235-205)+14.3
                    z_group($i,$j) = 'Bsat'
                endif
            endif
        endloop
        loop $i (236,353) ; loop columns (WYN 7 - 1)
            if model ($i, $j) # 1
                if y($i,$j) < ($i-236)*(16.2-15.3)/(353-236)+15.3
                    z_group($i,$j) = 'Bsat'
                endif
            endif
        endloop
        loop $i (354,$icol) ; loop columns (WYN 7 - 1)
            if model ($i, $j) # 1
                if y($i,$j) < ($i-353)*(16.4-16.2)/($icol-353)+16.2
                    z_group($i,$j) = 'Bsat'
                endif
            endif
        endloop
    endloop
end
$satclay

unmark ; remove marks after materials assigned


;-------------------------------------------------------------------------
; Assign initial static boundary conditions
;-------------------------------------------------------------------------

fix x y j=1
fix x   i=1
fix x   i=$icolP1
```

```
;-------------------------------------------------------------------------------
; About: Stochastic NDA Workflow - (2) Mesh initialization
; By: Patrick Bassal, Oct 2021
; Project: Wynne Ave
;-------------------------------------------------------------------------------
; Notes:
; - This calculation establishes general and stratum-specific properties for
; the static model, assigns these properties to the mesh, and initializes pore
; water pressures and saturation.
; - All values here-in are site-dependent and subject to modeler interpretations
;-------------------------------------------------------------------------------

;-------------------------------------------------------------------------------
; Define general properties
;-------------------------------------------------------------------------------

def $General_Props
    $grav=9.80665 ; gravity (m/s^2)
    $Pa=101.3e3 ; atmospheric pressure (Pa)
    $rho_w  = 1000.0 ; Water density (kg/m^3)
    $UW_w= $rho_w*$grav ; unit weight of water
    $kw=2e9 ; bulk modulus of water in Pa (pure water is 2e9)
    $sat_ex = 1.0 ; assume sat level is ~1 m higher than gw due to capillarity
end
$General_Props


;-------------------------------------------------------------------------------
; Define initial soil properties (to establish static stresses)
; - The shear wave velocity and unit weight were developed from site data and
; correlations
; - The mohr-coulomb(MC) model is used for all soils initially (before dynamics)
;-------------------------------------------------------------------------------

def $Static_Props

    ;General (all soils)
    $Ko = 0.5            ; Assumed condition for (horizontal stress/vertical
    stress)
    $pois = $Ko/(1+$Ko)  ; Approximation based on Ko
    $Gs = 2.67           ; Specific Gravity (assumed)
    $K_G_ratio = (2.0/3.0)*(1+$pois)/(1-2*$pois)
    $Init_phi= 32 ; initial friction angle (deg; assumed for stress
    intialization)
    $Init_coh= $Pa/10.0 ; Initial cohesion (Pa; assumed for stress
    intialization)
    $Init_coh_hi= $Pa ; Initial cohesion (Pa; assumed for stress intialization)

    ;Stratum A
    $Init_Vs_A = 120 ; initial shear wave velocity (m/s)
    $rho_sat_kNm3_A = 19 ; sat unit weight (kN/m3)
    $rho_sat_A = ($rho_sat_kNm3_A/$grav)*1000. ; sat unit weight (kg/m3)
    $por_A=($rho_sat_A-$Gs*$rho_w)/($rho_w-$Gs*$rho_w) ;
    $rho_A = $Gs*$rho_w*(1-$por_A) ; dry density (kg/m^3)
    $Init_G_A=$rho_sat_A*($Init_Vs_A^2) ; initial shear modulus (Pa)
    $Init_K_A=$Init_G_A*$K_G_ratio ; bulk modulus (Pa)

    ;Stratum Btop (Bunsat)
    $Init_Vs_Btop = 127 ; initial shear wave velocity (m/s)
    $rho_sat_kNm3_Btop = 19 ; sat unit weight (kN/m3)
    $rho_sat_Btop = ($rho_sat_kNm3_Btop/$grav)*1000. ; sat unit weight (kg/m3)
    $por_Btop=($rho_sat_Btop-$Gs*$rho_w)/($rho_w-$Gs*$rho_w) ;
    $rho_Btop = $Gs*$rho_w*(1-$por_Btop) ; dry density (kg/m^3)
```

```
61        $Init_G_Btop=$rho_sat_Btop*($Init_Vs_Btop^2) ; initial shear modulus (Pa)
62        $Init_K_Btop=$Init_G_Btop*$K_G_ratio ; bulk modulus (Pa)
63
64        ;Stratum Bbot (Bsat)
65        $Init_Vs_Bbot = 142 ; initial shear wave velocity (m/s)
66        $rho_sat_kNm3_Bbot = 19 ; sat unit weight (kN/m3)
67        $rho_sat_Bbot = ($rho_sat_kNm3_Bbot/$grav)*1000. ; sat unit weight (kg/m3)
68        $por_Bbot=($rho_sat_Bbot-$Gs*$rho_w)/($rho_w-$Gs*$rho_w) ;
69        $rho_Bbot = $Gs*$rho_w*(1-$por_Bbot) ; dry density (kg/m^3)
70        $Init_G_Bbot=$rho_sat_Bbot*($Init_Vs_Bbot^2) ; initial shear modulus (Pa)
71        $Init_K_Bbot=$Init_G_Bbot*$K_G_ratio ; bulk modulus (Pa)
72
73        ;C1 sands
74        $Init_Vs_C1 = 176 ; initial shear wave velocity (m/s)
75        $rho_sat_kNm3_C1 = 19 ; sat unit weight (kN/m3)
76        $rho_sat_C1 = ($rho_sat_kNm3_C1/$grav)*1000. ; sat unit weight (kg/m3)
77        $por_C1=($rho_sat_C1-$Gs*$rho_w)/($rho_w-$Gs*$rho_w) ;
78        $rho_C1 = $Gs*$rho_w*(1-$por_C1) ; dry density (kg/m^3)
79        $Init_G_C1=$rho_sat_C1*($Init_Vs_C1^2) ; initial shear modulus (Pa)
80        $Init_K_C1=$Init_G_C1*$K_G_ratio ; bulk modulus (Pa)
81
82        ;C2 sands
83        $Init_Vs_C2 = 197 ; initial shear wave velocity (m/s)
84        $rho_sat_kNm3_C2 = 19 ; sat unit weight (kN/m3)
85        $rho_sat_C2 = ($rho_sat_kNm3_C2/$grav)*1000. ; sat unit weight (kg/m3)
86        $por_C2=($rho_sat_C2-$Gs*$rho_w)/($rho_w-$Gs*$rho_w) ;
87        $rho_C2 = $Gs*$rho_w*(1-$por_C2) ; dry density (kg/m^3)
88        $Init_G_C2=$rho_sat_C2*($Init_Vs_C2^2) ; initial shear modulus (Pa)
89        $Init_K_C2=$Init_G_C2*$K_G_ratio ; bulk modulus (Pa)
90
91        ;Stratum C clays
92        $Init_Vs_C = 180 ; initial shear wave velocity (m/s)
93        $rho_sat_kNm3_C = 19 ; sat unit weight (kN/m3)
94        $rho_sat_C = ($rho_sat_kNm3_C/$grav)*1000. ; sat unit weight (kg/m3)
95        $por_C=($rho_sat_C-$Gs*$rho_w)/($rho_w-$Gs*$rho_w) ;
96        $rho_C = $Gs*$rho_w*(1-$por_C) ; dry density (kg/m^3)
97        $Init_G_C=$rho_sat_C*($Init_Vs_C^2) ; initial shear modulus (Pa)
98        $Init_K_C=$Init_G_C*$K_G_ratio ; bulk modulus (Pa)
99
100       ;Base Material (Stratum D)
101       $Init_Vs_D = 320 ; initial shear wave velocity (m/s)
102       $rho_sat_kNm3_D = 20 ; sat unit weight (kN/m3)
103       $rho_sat_D = ($rho_sat_kNm3_D/$grav)*1000. ; sat unit weight (kg/m3)
104       $por_D=($rho_sat_D-$Gs*$rho_w)/($rho_w-$Gs*$rho_w) ;
105       $rho_D = $Gs*$rho_w*(1-$por_D) ; dry density (kg/m^3)
106       $Init_G_D=$rho_sat_D*($Init_Vs_D^2)*0.7
107       ; shear modulus (assume dyn redux factor = 0.7) (Pa)
108       $Init_K_D=$Init_G_D*$K_G_ratio ; bulk modulus (Pa)
109
110       ; Permeability (m^2/(Pa*sec))
111       ; FLAC uses permeability k = Kh / gammawater
112       ;    k m^2/(Pa*sec) = Kh (m/s) / 9807 (Pa/m) = Kh(m/s)*1.02e-04
113       $permv_A    = 1.0e-6 * 1.02e-4   ; vert. permeability k22 (m^2/(Pa*sec))
114       $permv_B    = 1.0e-8 * 1.02e-4
115       $permv_C1   = 1.0e-6 * 1.02e-4
116       $permv_C2   = 3.0e-7 * 1.02e-4
117       $permh_A    = 2*$permv_A   ; horiz. permeability k11 (m^2/(Pa*sec))
118       $permh_B    = 10*$permv_B
119       $permh_C1   = 2*$permv_C1
120       $permh_C2   = 2*$permv_C2
121   end
122   $Static_Props
123
```

```
124
125 ;-------------------------------------------------------------------------------
126 ; Assign initial soil properties (to establish static stresses)
127 ;-------------------------------------------------------------------------------
128
129 def $Assign_Static_Props
130     ; Assign A
131     command
132         model mohr group 'A'
133         prop den=$rho_A por=$por_A &
134             coh=$Init_coh fric=$Init_phi &
135             bulk=$Init_K_A shear=$Init_G_A &
136             k11=$permh_A k22=$permv_A &
137         group 'A'
138     endcommand
139
140     ; Assign Bunsat
141     command
142         model mohr group 'Bunsat'
143         prop den=$rho_Btop por=$por_Btop &
144             coh=$Init_coh fric=$Init_phi &
145             bulk=$Init_K_Btop shear=$Init_G_Btop &
146             k11=$permh_B k22=$permv_B &
147         group 'Bunsat'
148     endcommand
149
150     ; Assign Bsat
151     command
152         model mohr group 'Bsat'
153         prop den=$rho_Bbot por=$por_Bbot &
154             coh=$Init_coh fric=$Init_phi &
155             bulk=$Init_K_Bbot shear=$Init_G_Bbot &
156             k11=$permh_B k22=$permv_B &
157         group 'Bsat'
158     endcommand
159
160     ; Assign C1
161     command
162         model mohr group 'C1'
163         prop den=$rho_C1 por=$por_C1 &
164             coh=$Init_coh fric=$Init_phi &
165             bulk=$Init_K_C1 shear=$Init_G_C1 &
166             k11=$permh_C1 k22=$permv_C1 &
167         group 'C1'
168     endcommand
169
170     ; Assign C2
171     command
172         model mohr group 'C2'
173         prop den=$rho_C2 por=$por_C2 &
174             coh=$Init_coh fric=$Init_phi &
175             bulk=$Init_K_C2 shear=$Init_G_C2 &
176             k11=$permh_C2 k22=$permv_C2 &
177         group 'C2'
178     endcommand
179
180     ; Assign C
181     command
182         model mohr group 'C'
183         prop den=$rho_C por=$por_C &
184             coh=$Init_coh fric=$Init_phi &
185             bulk=$Init_K_C shear=$Init_G_C &
186             k11=$permh_B k22=$permv_B & ; assume same as B
```

```
        group 'C'
    endcommand

    ; Assign D
    command
        model mohr group 'D'
        prop den=$rho_D por=$por_D &
            coh=$Init_coh fric=$Init_phi &
            bulk=$Init_K_D shear=$Init_G_D &
            k11=$permh_C2 k22=$permv_C2 &
        group 'D'
    endcommand
end
$Assign_Static_Props

set grav $grav ; set gravity


;------------------------------------------------------------------------------
; Intialize pore water pressures and saturation
; - Separate calcs for each set of zones with variable water table
; - Calculation loops trough all gridpts and averages values for zone estimate
;------------------------------------------------------------------------------

def $initialize_pp_new
    $gw_dep1 = 13.2
    $gw_dep2 = 14.1
    $i1 = 0
    $i2 = 113
    loop $j (1,jgp); loop gridpts
        loop $i (int($i1+1),$i2)
            $sat_est=($i-$i1)*($gw_dep2-$gw_dep1)/($i2-$i1)+$gw_dep1+$sat_ex
            $gw_est=($i-$i1)*($gw_dep2-$gw_dep1)/($i2-$i1)+$gw_dep1
            if y($i,$j) > $sat_est
                sat($i,$j) = 0.0
            else
                sat($i,$j) = 1.0
                gpp($i,$j) = ($gw_est-y($i,$j))*$rho_w*$grav
            endif
        endloop
    endloop
    loop $j (1,$jrow) ; loop zones
        loop $i (int($i1+1),int($i2-1))
            $sat_est=($i-$i1)*($gw_dep2-$gw_dep1)/($i2-$i1)+$gw_dep1+$sat_ex
            if y($i,$j) < $sat_est
                pp($i,$j)=(gpp($i,$j)+gpp($i,$j+1))/2
            endif
        endloop
    endloop

    $gw_dep1 = 14.1
    $gw_dep2 = 14.3
    $i1 = 113
    $i2 = 205
    loop $j (1,jgp); loop gridpts
        loop $i (int($i1+1),$i2)
            $sat_est=($i-$i1)*($gw_dep2-$gw_dep1)/($i2-$i1)+$gw_dep1+$sat_ex
            $gw_est=($i-$i1)*($gw_dep2-$gw_dep1)/($i2-$i1)+$gw_dep1
            if y($i,$j) > $sat_est
                sat($i,$j) = 0.0
            else
                sat($i,$j) = 1.0
                gpp($i,$j) = ($gw_est-y($i,$j))*$rho_w*$grav
```

```
            endif
        endloop
    endloop
    loop $j (1,$jrow) ; loop zones
        loop $i (int($i1+1),int($i2-1))
            $sat_est=($i-$i1)*($gw_dep2-$gw_dep1)/($i2-$i1)+$gw_dep1+$sat_ex
            if y($i,$j) < $sat_est
                pp($i,$j)=(gpp($i,$j)+gpp($i,$j+1))/2
            endif
        endloop
    endloop

    $gw_dep1 = 14.3
    $gw_dep2 = 15.3
    $i1 = 205
    $i2 = 235
    loop $j (1,jgp); loop gridpts
        loop $i (int($i1+1),$i2)
            $sat_est=($i-$i1)*($gw_dep2-$gw_dep1)/($i2-$i1)+$gw_dep1+$sat_ex
            $gw_est=($i-$i1)*($gw_dep2-$gw_dep1)/($i2-$i1)+$gw_dep1
            if y($i,$j) > $sat_est
                sat($i,$j) = 0.0
            else
                sat($i,$j) = 1.0
                gpp($i,$j) = ($gw_est-y($i,$j))*$rho_w*$grav
            endif
        endloop
    endloop
    loop $j (1,$jrow) ; loop zones
        loop $i (int($i1+1),int($i2-1))
            $sat_est=($i-$i1)*($gw_dep2-$gw_dep1)/($i2-$i1)+$gw_dep1+$sat_ex
            if y($i,$j) < $sat_est
                pp($i,$j)=(gpp($i,$j)+gpp($i,$j+1))/2
            endif
        endloop
    endloop

    $gw_dep1 = 15.3
    $gw_dep2 = 16.2
    $i1 = 235
    $i2 = 353
    loop $j (1,jgp); loop gridpts
        loop $i (int($i1+1),$i2)
            $sat_est=($i-$i1)*($gw_dep2-$gw_dep1)/($i2-$i1)+$gw_dep1+$sat_ex
            $gw_est=($i-$i1)*($gw_dep2-$gw_dep1)/($i2-$i1)+$gw_dep1
            if y($i,$j) > $sat_est
                sat($i,$j) = 0.0
            else
                sat($i,$j) = 1.0
                gpp($i,$j) = ($gw_est-y($i,$j))*$rho_w*$grav
            endif
        endloop
    endloop
    loop $j (1,$jrow) ; loop zones
        loop $i (int($i1+1),int($i2-1))
            $sat_est=($i-$i1)*($gw_dep2-$gw_dep1)/($i2-$i1)+$gw_dep1+$sat_ex
            if y($i,$j) < $sat_est
                pp($i,$j)=(gpp($i,$j)+gpp($i,$j+1))/2
            endif
        endloop
    endloop

    $gw_dep1 = 16.2
```

```
313         $gw_dep2 = 16.4
314         $i1 = 353
315         $i2 = $icolP1
316         loop $j (1,jgp); loop gridpts
317             loop $i (int($i1+1),$i2)
318                 $sat_est=($i-$i1)*($gw_dep2-$gw_dep1)/($i2-$i1)+$gw_dep1+$sat_ex
319                 $gw_est=($i-$i1)*($gw_dep2-$gw_dep1)/($i2-$i1)+$gw_dep1
320                 if y($i,$j) > $sat_est
321                     sat($i,$j) = 0.0
322                 else
323                     sat($i,$j) = 1.0
324                     gpp($i,$j) = ($gw_est-y($i,$j))*$rho_w*$grav
325                 endif
326             endloop
327         endloop
328         loop $j (1,$jrow) ; loop zones
329             loop $i (int($i1+1),int($i2-1))
330                 $sat_est=($i-$i1)*($gw_dep2-$gw_dep1)/($i2-$i1)+$gw_dep1+$sat_ex
331                 if y($i,$j) < $sat_est
332                     pp($i,$j)=(gpp($i,$j)+gpp($i,$j+1))/2
333                 endif
334             endloop
335         endloop
336     end
337     $initialize_pp_new
338
339     ; Assign water w/ low bulk mod. for fast solve & allow 9.81kPa or 1m capillary
        rise:
340     ; Make sure kw greater than Eq 1.70 in FLAC 8.1 Fluid-Mech Manual
341     water den=$rho_w bulk=1e4 tension= 9810
342
343     ; Assign boundary conditions for pore pressures and saturation:
344     fix sat pp i=1 ; left edge (fix both for applied pp; permeable bounds for now)
345     fix sat pp i=$icolP1 ; right edge
346     fix sat pp j=$jrowP1 ; top points
347
348
```

```
;--------------------------------------------------------------------------------
; About: Stochastic NDA Workflow - (3) Initial static solve
; By: Patrick Bassal, Oct 2021
; Project: Wynne Ave
;--------------------------------------------------------------------------------
; Notes:
; - This calculation solves for the phreatic water surface and general static
; equilibrium
; - All values here-in are site-dependent and subject to modeler interpretations
;--------------------------------------------------------------------------------

his 999 unbalance ; set to track model convergence

;--------------------------------------------------------------------------------
; Solve for the phreatic water surface
;--------------------------------------------------------------------------------

; Assign water w/ low bulk mod. for fast solve & allow 9.81kPa or 1m capillary
rise:
; Make sure kw greater than Eq 1.70 in FLAC 8.1 Fluid-Mech Manual
set flow on mech off dyn off
water den=$rho_w bulk=1e4 tension= 9810
step 100000 ; can inc. to ensure steady state phraetic, depends on perm of soils

;ALTERNATIVE: "funsat" to set phraetic surface (gives transient evolution of
surface)
; does not speed up flow calculation from my experience
;;set flow on mech off dyn off
;;water den=$rho_w bulk=$kw tension= 9810
;;set funsat on
;;step 60000
;;set funsat off

def $unsat_dens ; fix unsat density above phraetic surface
    loop $i (1,izones)
        loop $j (1,jzones)
            $ip1 = $i+1
            if model($i,$j) # 1 ;(only for non-null zones)
                if sat($i,$j)<0.5
                    if sat($i+1,$j)<0.5
                        ; unsat unit weight (kg/m^3) as (18/19)*rho_sat:
                        $rho_unsat=0.947*(density($i,$j)+porosity($i,$j)*$rho_w)

                        command
                            prop den=$rho_unsat i=$i j=$j
                        endcommand
                    endif
                endif
            endif
        endloop
    endloop
end
$unsat_dens


;--------------------------------------------------------------------------------
; Solve for static equilibirum
;--------------------------------------------------------------------------------

; Function to keep Ko from falling outside reasonable ranges
def $Ko_limits
    $Ko_min  = 0.45
    $Ko_max  = 3.0
```

```
    loop $i (1,izones)
        loop $j (1,jzones)
            if model($i,$j) # 1
                $sxx = sxx($i,$j) + pp($i,$j)
                $syy = syy($i,$j) + pp($i,$j)
                $Ko_this = $sxx / min($syy,-$Pa/100)
                if $Ko_this < $Ko_min
                    sxx($i,$j) = $Ko_min * $syy - pp($i,$j)
                endif
                if $Ko_this > $Ko_max
                    sxx($i,$j) = $Ko_max * $syy - pp($i,$j)
                endif
            endif
        end_loop
    end_loop
end

set dyn off flow off mech on
water den=$rho_w bulk=1.0e4 tension= 9810 ; repeated as before

solve sratio 0.01

$Ko_limits
solve sratio 0.01

$Ko_limits
solve sratio 0.01

$Ko_limits
solve sratio 0.001

$Ko_limits
solve sratio 0.001

; solve coupled
set mech on flow on
$Ko_limits
solve sratio 0.001

;-------------------------------------------------------------------------
;  Establish some extra variables for static conditions
;-------------------------------------------------------------------------

def $exi ; initial values for initial stress and ru calculations
    loop $ievs (1,izones) ; loop through all non-null zones
        loop $jevs (1,jzones)
            if model ($ievs, $jevs) # 1
                ex_1($ievs,$jevs)=(-sxx($ievs,$jevs)-pp($ievs,$jevs))/(-syy($
                ievs,$jevs)-pp($ievs,$jevs)) ; initial ko (static EP
                coefficient)
                ex_3($ievs,$jevs)=sxy($ievs,$jevs)/(-syy($ievs,$jevs)-pp($ievs,$
                jevs))                       ; initial alpha(=Tstatic/svc')
                ex_5($ievs,$jevs)=-syy($ievs,$jevs)-pp($ievs,$jevs)
                                                    ; initial yy effective
                stress
                ex_7($ievs,$jevs)=pp($ievs,$jevs)
                                                                        ;
                initial pore water pressure
            endif
        endloop
    endloop
end
$exi
```

```
;-------------------------------------------------------------------------
; About: Stochastic NDA Workflow - (4) Dynamic soil models and static solve
; By: Patrick Bassal, Oct 2021
; Project: Wynne Ave
;-------------------------------------------------------------------------
; Notes:
; - This calculation assigns the dynamic soil models (PM4Sand and PM4Silt) to
; both uniform and stochastic layers, solves for static equilibrium, and
prepares
; model parameters for dynamic calculation.
; - All values here-in are site-dependent and subject to modeler
interpretations.
;-------------------------------------------------------------------------
;
;  Set constitutive models for each soil group (during shaking)
model dll pm4sand group 'A'
model dll pm4silt group 'Bunsat'
model dll pm4silt group 'Bsat'
model dll pm4sand group 'C1'
model dll pm4sand group 'C2'
model dll pm4silt group 'C'
model elastic group 'D'

;-------------------------------------------------------------------------
; Assign calibrated model params for all uniform soil groups
;-------------------------------------------------------------------------
;   PM4Sand Layers
prop  P_atm = $Pa  &
    D_r=0.496  G_o=705.0  h_po=0.60 &
    c_e=3.5  group = A

prop  P_atm = $Pa  &
    D_r=0.665  G_o=784.0  h_po=0.84 &
    c_e=0.5  group = C2

;   PM4Silt Layers
prop  P_atm = $Pa   &
    Su_Rat =0.54  G_o=597.0  h_po=120.0 &
    e_o = 0.83  n_bwet=0.0 &
    group = Bunsat

prop  P_atm = $Pa   &
    Su_Rat =0.83  G_o=646.0  h_po=120.0 &
    h_o=0.9  e_o = 0.83 &
    group = C

;   Elastic Layers (Shear-compatible reduced value is assumed for base unit D)
prop  P_atm = $Pa  &
    bulk_mod=$Init_K_D    shear_mod=$Init_G_D  group = D


;-------------------------------------------------------------------------
; Assign calibrated model params for all stochastic soil groups
; - Note that two soil groups are stochastically modeled herein: Bsat & C1
;-------------------------------------------------------------------------

;   Read calibrated lookup tables for stochastic soil groups
table 10 read C1_hpo.txt
table 11 read C1_ce.txt
table 15 read Bsat_hpo.txt
table 16 read Bsat_nbw.txt
table 17 read Bsat_su_cs.txt

```

```
;  Input qc1Ncs stochastic field for C1
def $field_C1
    $real_num = $nreal; realization number
    $simfile= 'SGSIM_C1.csv' ; backtransformed sim output with HEADER REMOVED
    (.csv)!
    array $fieldC1(1890); length of field array (num zones, must manually input)
    status = open($simfile, 0, 1)
    status = read($fieldC1,1890)
    status = close

    $cnt = 1
    loop $i (1,$icol) ; loop rows
        loop $j (1,$jrow) ; loop columns
            if z_group($i,$j) = 'C1' ;'C1a' or 'C1b'
                ex_2($i,$j) = parse($fieldC1($cnt),$real_num+3)
                    ; select col of real. (after 3 coord. cols)
                ex_2($i,$j) = max(min(ex_2($i,$j),280),60)
                    ; limit to avoid extrap beyond lookup table
                $qc1ncs = ex_2($i,$j)
                $Dr = 0.478*$qc1ncs^0.264-1.063   ; [Idriss & Boulanger,
                2008]
                $Vs1cs  =(62.6*$qc1ncs^0.231)    ; Andrus et al. (2004) (m/sec)
                $kcs=1+(25)*(0.009-0.0109*($Vs1cs/100)+0.0038*($Vs1cs/100)^2)
                    ; FC>35 correction, lowered to model iteration
                $Vs1=$Vs1cs/$kcs
                $Ko = 0.5 ; Lateral earth pressure coefficient at rest
                $Go=((19/9.81)*1000*($Vs1^2/$Pa))/((1.0+2*$Ko)/3.0)^0.5
                    ; UCD/CGM-12/01 Report Equations 78 & 79,
                    UWsat=19
                $hpo = table(10,$qc1ncs) ; lookup h_po
                $ce = table(11,$qc1ncs)
                    ; lookup c_e (post-liq strain per Tasiopoulou et al. 2019)

                $permv=(1.0e-9)*exp(0.069*min(max($qc1ncs,100),200)) *1.02e-4
                    ; perm fxn from Robertson 2010 (adjusted for data and
                    limits)
                $permh=$permv*2

                command
                    ;model dll pm4sand i=$i j=$j
                    prop P_atm = $Pa  i=$i j=$j
                    prop D_r   = $Dr  i=$i j=$j
                    prop G_o   = $Go  i=$i j=$j
                    prop h_po  = $hpo i=$i j=$j
                    prop c_e   = $ce  i=$i j=$j
                    prop k11   = $permh  i=$i j=$j
                    prop k22   = $permv  i=$i j=$j
                end_command
                $cnt = $cnt + 1
            endif
        endloop
    endloop
end
$field_C1

;  Input SuRat,peak stochastic field for Bsat
def $field_Bsat
    $real_num = $nreal; realization number
    $simfile= 'SGSIM_Bsat.csv' ; backtransformed sim output with HEADER REMOVED
    (.csv)!
    array $fieldBsat(2246); length of field array (num zones, must manually
    input)
    status = open($simfile, 0, 1)
```

```
119         status = read($fieldBsat,2246)
120         status = close
121
122         $cnt = 1
123         loop $i (1,$icol) ; loop rows
124             loop $j (1,$jrow) ; loop columns
125                 if z_group($i,$j) = 'Bsat'
126                     ex_4($i,$j) = parse($fieldBsat($cnt),$real_num+3)
127                         ; select col of real. (after 3 coord. cols)
128                     ex_4($i,$j) = max(min(ex_4($i,$j),1.2),0.25)
129                         ; limit to avoid extrap (and keep realistic)
130                     $SuRat_pk = ex_4($i,$j)
131                     ex_6($i,$j) = table(17,$SuRat_pk)
132                         ; lookup critical state SuRat from peak (assign to var for
                            plotting)
133                     $SuRat    = ex_6($i,$j) ;
134                     $hpo = table(15,$SuRat_pk) ; lookup hpo
135                     $nbwet = table(16,$SuRat_pk)
136                         ; lookup nbwet (reproduces SuRatpk for monotonic at low
                            values <0.5)
137
138                     command
139                         ;model dll pm4silt i=$i j=$j
140                         prop  P_atm = $Pa    i=$i j=$j
141                         prop Su_Rat = $SuRat i=$i j=$j
142                         prop G_o    = 592.0  i=$i j=$j  ; assume constant (no
                            correlation w/ SuRat)
143                         prop h_po   = $hpo   i=$i j=$j
144                         prop n_bwet = $nbwet i=$i j=$j
145                         prop e_o    = 0.77   i=$i j=$j; assume constant (no
                            correlation w/ SuRat)
146                     end_command
147                     $cnt = $cnt + 1
148                 endif
149             endloop
150         endloop
151     end
152     $field_Bsat
153
154
155     ;-------------------------------------------------------------------------
156     ; Establish static equilibrium again (if phraetic surface depends on material,
        flow can be on)
157     ;-------------------------------------------------------------------------
158
159     water den=$rho_w bulk=1.0e4 tension= 9810 ; Assign low bulk mod for rapid
        convergence
160
161     set dyn off flow off mech on
162     solve sratio 0.01
163
164     set flow on
165
166     $Ko_limits
167     solve sratio 0.01
168
169     $Ko_limits
170     solve sratio 0.01
171
172     $Ko_limits
173     solve sratio 0.001
174     ;
175
```

```
free pp i=1  ; free pp at left boundary (impenetrable)
free pp i=$icolP1 ; free pp at right boundary (impenetrable)
step 1

; Set elastic columns only if using absorbing(free-field) side boundary
conditions
def $outer_elastic
    $num_elas = int(5) ; number of elastic columns
    $izonetr = int(izones-$num_elas+1) ; top right column start
    ;setting outer columns to elastic to maintain confinement
    loop $jj (7,jzones) ; loop the layers (above D)
        loop $ii (1,$num_elas)
            $dummy = z_prop($ii,$jj,'shearG')
            $GElas = $dummy*0.7 ; shear modulus (Pa)
            $KElas = $GElas*(2.0/3.0)*(1+$pois)/(1-2*$pois) ; bulk modulus (Pa)
            command
                model elastic i=$ii j=$jj
                prop bulk=$KElas shear=$GElas i=$ii j=$jj
            endcommand
        endloop
        loop $ii ($izonetr,izones)
            $dummy = z_prop($ii,$jj,'shearG')
            $GElas = $dummy*0.7 ; shear modulus (Pa)
            $KElas = $GElas*(2.0/3.0)*(1+$pois)/(1-2*$pois) ; bulk modulus (Pa)
            command
                model elastic i=$ii j=$jj
                prop bulk=$KElas shear=$GElas i=$ii j=$jj
            endcommand
        endloop
    endloop
end
;$outer_elastic

water density $rho_w bulk $kw tension= 9810; Assign actual estimated water props
solve ; solve static equilibrium again


;-------------------------------------------------------------------------
; Prepare dynamic modeling parameters
;-------------------------------------------------------------------------

set dynamic on
set dy_damp=rayl 0.005 1.0; central freq of 1 Hz assumed for Rayleigh damping
solve dytime 0.01 ; Solve a little to check model

;   Zero time, displacements, and velocities, prior to executing dynamics
set dytime = 0.0 ; reset dynamic time
set gwtime= 0.0 ; reset groundwater time
initial xdisp 0 ydisp 0 ; reset displacements
initial xvel  0 yvel  0 ; reset velocity
prop First_Call = 0.0 ; zero out past stress history (PM4Sand/PM4Silt)
;-------------------------------------------------------
;
$exi ; recalc initial extra props final time (later used for parameter
development)
```

```
;-------------------------------------------------------------------------
; About: Stochastic NDA Workflow - (5) Dynamic time histories
; By: Patrick Bassal, Oct 2021
; Project: Wynne Ave
;-------------------------------------------------------------------------
; Notes:
; - This calculation establishes the step size for output time histories, assigns
; extra variables, sets points for tracking time histories, and prepares result tables.
; - All values here-in are site-dependent and subject to modeler interpretations.
;-------------------------------------------------------------------------

;-------------------------------------------------------------------------
; Establish the step size for output time histories
;-------------------------------------------------------------------------

def $find_step
    $tstepguess = 0.02  ;desired timestep between hist recordings!
    $n = int($tstepguess/min(gwtdel,dytdel)) ; taken as minimum of gw and dy time
    $tstep = $n*min(gwtdel,dytdel) ; actual timestep between hist recordings based on integer n
end
$find_step


;-------------------------------------------------------------------------
; Prepare some new extra variables for results of interest
;-------------------------------------------------------------------------

def $set_evs
    array ai(4) ; set up strain array (allows calc of extensional strain)
    $stepcount = $stepcount + 1 ; only calculate when recording $n apart
    if $stepcount > $n
        $stepcount = 0
        loop $ievs (1,izones)
            loop $jevs (1,jzones)
                if model ($ievs, $jevs) # 1
                    ex_13($ievs, $jevs)=max(abs(ssi($ievs,$jevs)),ex_13($ievs,$jevs))           ; maximum shear strain
                    ex_15($ievs, $jevs)=(-sxx($ievs,$jevs)-pp($ievs,$jevs))/(-syy($ievs,$jevs)-pp($ievs,$jevs)) ; ko
                    ex_25($ievs, $jevs)=sxy($ievs,$jevs)/(-syy($ievs,$jevs)-pp($ievs,$jevs))    ; alpha
                    ex_28($ievs, $jevs)= ydisp($ievs,$jevs)-ydisp($ievs,1)
                                        ; ydisp relative to base
                    ex_30($ievs, $jevs)= xdisp($ievs,$jevs)-xdisp($ievs,1)
                                        ; xdisp relative to base
                    ex_31($ievs, $jevs)=pp($ievs, $jevs)-ex_7($ievs, $jevs)
                                        ; pore pressure change (ex7 is pp after PM4 is set)
                    ex_32($ievs, $jevs)=max(ex_31($ievs,$jevs),ex_32($ievs,$jevs))              ; max excess pore pressure
                    ex_33($ievs, $jevs)=1.0-(-esyy($ievs, $jevs)/ex_5($ievs, $jevs))            ; ru=1-sv'/svc'
                    ex_35($ievs, $jevs)=max(ex_33($ievs,$jevs),ex_35($ievs,$jevs))              ; maximum ru=1-sv'/svc'
                    ex_45($ievs, $jevs)=sxy($ievs,$jevs)/ex_5($ievs, $jevs)
                                        ; CSR (tau/svc')
                    ex_47($ievs, $jevs)=max(ex_45($ievs,$jevs),ex_47($ievs,$jevs))              ; max CSR (tau/svc')
```

```
47                      ex_49($ievs, $jevs)=max(abs(xacc($ievs,$jevs)),ex_49($ievs,$
                        jevs))          ; abs max xacc
48                      ex_51($ievs, $jevs)=max(abs(yacc($ievs,$jevs)),ex_49($ievs,$
                        jevs))          ; abs max
                        yacc
49                      dum = fsi($ievs, $jevs,ai)
                                                                        ; set up
                        strain array
50                      ex_52($ievs, $jevs)= ai(4)
                                                                        ; xy
                        strain
51                      ex_53($ievs, $jevs)= ai(1)
                                                                        ; xx
                        strain (extensional)
52                      ex_54($ievs, $jevs)= max(ex_53($ievs, $jevs),ex_54($ievs, $
                        jevs))          ; max xx strain (tension)
53                      ex_55($ievs, $jevs)= min(ex_53($ievs, $jevs),ex_55($ievs, $
                        jevs))          ; min xx strain
                        (compression)
54                      ex_60($ievs, $jevs)= abs(xacc($ievs,$jevs))*$tstep+ex_60($
                        ievs, $jevs)      ; Cumulative absolute velocity (CAV)
55                      ex_61($ievs, $jevs)= 0.1602*(xacc($ievs,$jevs)^2)+ex_61($
                        ievs, $jevs)       ; Arias Intensity
56                  endif
57              endloop
58          endloop
59      endif
60  end
61
62
63  ;-------------------------------------------------------------------------
64  ; Specify some preset locations for data output
65  ;-------------------------------------------------------------------------
66
67  def $data_locate
68     $j_Atop_zn = $jrow
69     $j_Atop_gp = $j_Atop_zn + 1
70     $j_Bunsat_zn = int(33)
71     $j_Bunsat_gp = $j_Bunsat_zn + 1
72     $j_Bsat_zn = int(27)
73     $j_Bsat_gp = $j_Bsat_zn + 1
74     $j_C1_zn = int(21)
75     $j_C1_gp = $j_C1_zn + 1
76     $j_C2_zn = int(16)
77     $j_C2_gp = $j_C2_zn + 1
78     $j_Cbot_zn = int(7)
79     $j_Cbot_gp = $j_Cbot_zn + 1
80     $i_lt1_zn = int(112)
81     $i_lt1_gp = int($i_lt1_zn+1)
82     $i_lt2_zn = int(204)
83     $i_lt2_gp = int($i_lt2_zn+1)
84     $i_lt3_zn = int(265)
85     $i_lt3_gp = int($i_lt3_zn+1)
86     $i_rt1_zn = int(285)
87     $i_rt1_gp = int($i_rt1_zn+1)
88     $i_rt2_zn = int(294)
89     $i_rt2_gp = int($i_rt2_zn+1)
90     $i_rt3_zn = int(352)
91     $i_rt3_gp = int($i_rt3_zn+1)
92  end
93  $data_locate
94
95
```

```
;-------------------------------------------------------------------------------
; Manually assign locations for histories of interest
; - Many history points can be specified (do not seem to slow code)
;-------------------------------------------------------------------------------

def $store_hist ; binned by property
    command
        ; xacc
        his 50 xacc  i=$i_lt1_gp   j=$j_Atop_gp
        his 51 xacc  i=$i_lt1_gp   j=$j_Bunsat_gp
        his 52 xacc  i=$i_lt1_gp   j=$j_Bsat_gp
        his 53 xacc  i=$i_lt1_gp   j=$j_C1_gp
        his 54 xacc  i=$i_lt1_gp   j=$j_C2_gp
        his 55 xacc  i=$i_lt1_gp   j=$j_Cbot_gp
        his 56 xacc  i=$i_lt2_gp   j=$j_Atop_gp
        his 57 xacc  i=$i_lt2_gp   j=$j_Bunsat_gp
        his 58 xacc  i=$i_lt2_gp   j=$j_Bsat_gp
        his 59 xacc  i=$i_lt2_gp   j=$j_C1_gp
        his 60 xacc  i=$i_lt2_gp   j=$j_C2_gp
        his 61 xacc  i=$i_lt2_gp   j=$j_Cbot_gp
        his 62 xacc  i=$i_lt3_gp   j=$j_Atop_gp
        his 63 xacc  i=$i_lt3_gp   j=$j_Bunsat_gp
        his 64 xacc  i=$i_lt3_gp   j=$j_Bsat_gp
        his 65 xacc  i=$i_lt3_gp   j=$j_C1_gp
        his 66 xacc  i=$i_lt3_gp   j=$j_C2_gp
        his 67 xacc  i=$i_lt3_gp   j=$j_Cbot_gp
        his 68 xacc  i=$i_rt1_gp   j=$j_Atop_gp
        his 69 xacc  i=$i_rt1_gp   j=$j_Bunsat_gp
        his 70 xacc  i=$i_rt1_gp   j=$j_Bsat_gp
        his 71 xacc  i=$i_rt1_gp   j=$j_C1_gp
        his 72 xacc  i=$i_rt1_gp   j=$j_C2_gp
        his 73 xacc  i=$i_rt1_gp   j=$j_Cbot_gp
        his 74 xacc  i=$i_rt2_gp   j=$j_Atop_gp
        his 75 xacc  i=$i_rt2_gp   j=$j_Bunsat_gp
        his 76 xacc  i=$i_rt2_gp   j=$j_Bsat_gp
        his 77 xacc  i=$i_rt2_gp   j=$j_C1_gp
        his 78 xacc  i=$i_rt2_gp   j=$j_C2_gp
        his 79 xacc  i=$i_rt2_gp   j=$j_Cbot_gp
        his 80 xacc  i=$i_rt3_gp   j=$j_Atop_gp
        his 81 xacc  i=$i_rt3_gp   j=$j_Bunsat_gp
        his 82 xacc  i=$i_rt3_gp   j=$j_Bsat_gp
        his 83 xacc  i=$i_rt3_gp   j=$j_C1_gp
        his 84 xacc  i=$i_rt3_gp   j=$j_C2_gp
        his 85 xacc  i=$i_rt3_gp   j=$j_Cbot_gp
        his 86 xacc  i=$i_rt1_gp   j=1
        his 87 xacc  i=$i_lt3_gp   j=24 ; add to middle of C1
        his 88 xacc  i=$i_rt1_gp   j=24 ; add to middle of C1


        ; xdisp
        his 100 ex_30  i=$i_lt1_gp   j=$j_Atop_gp
        his 101 ex_30  i=$i_lt1_gp   j=$j_Bunsat_gp
        his 102 ex_30  i=$i_lt1_gp   j=$j_Bsat_gp
        his 103 ex_30  i=$i_lt1_gp   j=$j_C1_gp
        his 104 ex_30  i=$i_lt1_gp   j=$j_C2_gp
        his 105 ex_30  i=$i_lt1_gp   j=$j_Cbot_gp
        his 106 ex_30  i=$i_lt2_gp   j=$j_Atop_gp
        his 107 ex_30  i=$i_lt2_gp   j=$j_Bunsat_gp
        his 108 ex_30  i=$i_lt2_gp   j=$j_Bsat_gp
        his 109 ex_30  i=$i_lt2_gp   j=$j_C1_gp
        his 110 ex_30  i=$i_lt2_gp   j=$j_C2_gp
        his 111 ex_30  i=$i_lt2_gp   j=$j_Cbot_gp
```

```
158           his 112 ex_30  i=$i_lt3_gp   j=$j_Atop_gp
159           his 113 ex_30  i=$i_lt3_gp   j=$j_Bunsat_gp
160           his 114 ex_30  i=$i_lt3_gp   j=$j_Bsat_gp
161           his 115 ex_30  i=$i_lt3_gp   j=$j_C1_gp
162           his 116 ex_30  i=$i_lt3_gp   j=$j_C2_gp
163           his 117 ex_30  i=$i_lt3_gp   j=$j_Cbot_gp
164           his 118 ex_30  i=$i_rt1_gp   j=$j_Atop_gp
165           his 119 ex_30  i=$i_rt1_gp   j=$j_Bunsat_gp
166           his 120 ex_30  i=$i_rt1_gp   j=$j_Bsat_gp
167           his 121 ex_30  i=$i_rt1_gp   j=$j_C1_gp
168           his 122 ex_30  i=$i_rt1_gp   j=$j_C2_gp
169           his 123 ex_30  i=$i_rt1_gp   j=$j_Cbot_gp
170           his 124 ex_30  i=$i_rt2_gp   j=$j_Atop_gp
171           his 125 ex_30  i=$i_rt2_gp   j=$j_Bunsat_gp
172           his 126 ex_30  i=$i_rt2_gp   j=$j_Bsat_gp
173           his 127 ex_30  i=$i_rt2_gp   j=$j_C1_gp
174           his 128 ex_30  i=$i_rt2_gp   j=$j_C2_gp
175           his 129 ex_30  i=$i_rt2_gp   j=$j_Cbot_gp
176           his 130 ex_30  i=$i_rt3_gp   j=$j_Atop_gp
177           his 131 ex_30  i=$i_rt3_gp   j=$j_Bunsat_gp
178           his 132 ex_30  i=$i_rt3_gp   j=$j_Bsat_gp
179           his 133 ex_30  i=$i_rt3_gp   j=$j_C1_gp
180           his 134 ex_30  i=$i_rt3_gp   j=$j_C2_gp
181           his 135 ex_30  i=$i_rt3_gp   j=$j_Cbot_gp
182           his 136 ex_30  i=$i_rt1_gp   j=1
183
184
185           ; yacc
186           his 150 yacc  i=$i_lt1_gp   j=$j_Atop_gp
187           his 151 yacc  i=$i_lt1_gp   j=$j_Bunsat_gp
188           his 152 yacc  i=$i_lt1_gp   j=$j_Bsat_gp
189           his 153 yacc  i=$i_lt1_gp   j=$j_C1_gp
190           his 154 yacc  i=$i_lt1_gp   j=$j_C2_gp
191           his 155 yacc  i=$i_lt1_gp   j=$j_Cbot_gp
192           his 156 yacc  i=$i_lt2_gp   j=$j_Atop_gp
193           his 157 yacc  i=$i_lt2_gp   j=$j_Bunsat_gp
194           his 158 yacc  i=$i_lt2_gp   j=$j_Bsat_gp
195           his 159 yacc  i=$i_lt2_gp   j=$j_C1_gp
196           his 160 yacc  i=$i_lt2_gp   j=$j_C2_gp
197           his 161 yacc  i=$i_lt2_gp   j=$j_Cbot_gp
198           his 162 yacc  i=$i_lt3_gp   j=$j_Atop_gp
199           his 163 yacc  i=$i_lt3_gp   j=$j_Bunsat_gp
200           his 164 yacc  i=$i_lt3_gp   j=$j_Bsat_gp
201           his 165 yacc  i=$i_lt3_gp   j=$j_C1_gp
202           his 166 yacc  i=$i_lt3_gp   j=$j_C2_gp
203           his 167 yacc  i=$i_lt3_gp   j=$j_Cbot_gp
204           his 168 yacc  i=$i_rt1_gp   j=$j_Atop_gp
205           his 169 yacc  i=$i_rt1_gp   j=$j_Bunsat_gp
206           his 170 yacc  i=$i_rt1_gp   j=$j_Bsat_gp
207           his 171 yacc  i=$i_rt1_gp   j=$j_C1_gp
208           his 172 yacc  i=$i_rt1_gp   j=$j_C2_gp
209           his 173 yacc  i=$i_rt1_gp   j=$j_Cbot_gp
210           his 174 yacc  i=$i_rt2_gp   j=$j_Atop_gp
211           his 175 yacc  i=$i_rt2_gp   j=$j_Bunsat_gp
212           his 176 yacc  i=$i_rt2_gp   j=$j_Bsat_gp
213           his 177 yacc  i=$i_rt2_gp   j=$j_C1_gp
214           his 178 yacc  i=$i_rt2_gp   j=$j_C2_gp
215           his 179 yacc  i=$i_rt2_gp   j=$j_Cbot_gp
216           his 180 yacc  i=$i_rt3_gp   j=$j_Atop_gp
217           his 181 yacc  i=$i_rt3_gp   j=$j_Bunsat_gp
218           his 182 yacc  i=$i_rt3_gp   j=$j_Bsat_gp
219           his 183 yacc  i=$i_rt3_gp   j=$j_C1_gp
220           his 184 yacc  i=$i_rt3_gp   j=$j_C2_gp
```

```
his 185 yacc  i=$i_rt3_gp   j=$j_Cbot_gp
his 186 yacc  i=$i_rt1_gp   j=1


; ydisp
his 200 ex_28  i=$i_lt1_gp   j=$j_Atop_gp
his 201 ex_28  i=$i_lt1_gp   j=$j_Bunsat_gp
his 202 ex_28  i=$i_lt1_gp   j=$j_Bsat_gp
his 203 ex_28  i=$i_lt1_gp   j=$j_C1_gp
his 204 ex_28  i=$i_lt1_gp   j=$j_C2_gp
his 205 ex_28  i=$i_lt1_gp   j=$j_Cbot_gp
his 206 ex_28  i=$i_lt2_gp   j=$j_Atop_gp
his 207 ex_28  i=$i_lt2_gp   j=$j_Bunsat_gp
his 208 ex_28  i=$i_lt2_gp   j=$j_Bsat_gp
his 209 ex_28  i=$i_lt2_gp   j=$j_C1_gp
his 210 ex_28  i=$i_lt2_gp   j=$j_C2_gp
his 211 ex_28  i=$i_lt2_gp   j=$j_Cbot_gp
his 212 ex_28  i=$i_lt3_gp   j=$j_Atop_gp
his 213 ex_28  i=$i_lt3_gp   j=$j_Bunsat_gp
his 214 ex_28  i=$i_lt3_gp   j=$j_Bsat_gp
his 215 ex_28  i=$i_lt3_gp   j=$j_C1_gp
his 216 ex_28  i=$i_lt3_gp   j=$j_C2_gp
his 217 ex_28  i=$i_lt3_gp   j=$j_Cbot_gp
his 218 ex_28  i=$i_rt1_gp   j=$j_Atop_gp
his 219 ex_28  i=$i_rt1_gp   j=$j_Bunsat_gp
his 220 ex_28  i=$i_rt1_gp   j=$j_Bsat_gp
his 221 ex_28  i=$i_rt1_gp   j=$j_C1_gp
his 222 ex_28  i=$i_rt1_gp   j=$j_C2_gp
his 223 ex_28  i=$i_rt1_gp   j=$j_Cbot_gp
his 224 ex_28  i=$i_rt2_gp   j=$j_Atop_gp
his 225 ex_28  i=$i_rt2_gp   j=$j_Bunsat_gp
his 226 ex_28  i=$i_rt2_gp   j=$j_Bsat_gp
his 227 ex_28  i=$i_rt2_gp   j=$j_C1_gp
his 228 ex_28  i=$i_rt2_gp   j=$j_C2_gp
his 229 ex_28  i=$i_rt2_gp   j=$j_Cbot_gp
his 230 ex_28  i=$i_rt3_gp   j=$j_Atop_gp
his 231 ex_28  i=$i_rt3_gp   j=$j_Bunsat_gp
his 232 ex_28  i=$i_rt3_gp   j=$j_Bsat_gp
his 233 ex_28  i=$i_rt3_gp   j=$j_C1_gp
his 234 ex_28  i=$i_rt3_gp   j=$j_C2_gp
his 235 ex_28  i=$i_rt3_gp   j=$j_Cbot_gp
his 236 ex_28  i=$i_rt1_gp   j=1


; Shear strain increments (zone)
his 250 ex_52  i=$i_lt1_zn   j=$j_Atop_zn
his 251 ex_52  i=$i_lt1_zn   j=$j_Bunsat_zn
his 252 ex_52  i=$i_lt1_zn   j=$j_Bsat_zn
his 253 ex_52  i=$i_lt1_zn   j=$j_C1_zn
his 254 ex_52  i=$i_lt1_zn   j=$j_C2_zn
his 255 ex_52  i=$i_lt1_zn   j=$j_Cbot_zn
his 256 ex_52  i=$i_lt2_zn   j=$j_Atop_zn
his 257 ex_52  i=$i_lt2_zn   j=$j_Bunsat_zn
his 258 ex_52  i=$i_lt2_zn   j=$j_Bsat_zn
his 259 ex_52  i=$i_lt2_zn   j=$j_C1_zn
his 260 ex_52  i=$i_lt2_zn   j=$j_C2_zn
his 261 ex_52  i=$i_lt2_zn   j=$j_Cbot_zn
his 262 ex_52  i=$i_lt3_zn   j=$j_Atop_zn
his 263 ex_52  i=$i_lt3_zn   j=$j_Bunsat_zn
his 264 ex_52  i=$i_lt3_zn   j=$j_Bsat_zn
his 265 ex_52  i=$i_lt3_zn   j=$j_C1_zn
his 266 ex_52  i=$i_lt3_zn   j=$j_C2_zn
his 267 ex_52  i=$i_lt3_zn   j=$j_Cbot_zn
```

```
284           his 268 ex_52  i=$i_rt1_zn   j=$j_Atop_zn
285           his 269 ex_52  i=$i_rt1_zn   j=$j_Bunsat_zn
286           his 270 ex_52  i=$i_rt1_zn   j=$j_Bsat_zn
287           his 271 ex_52  i=$i_rt1_zn   j=$j_C1_zn
288           his 272 ex_52  i=$i_rt1_zn   j=$j_C2_zn
289           his 273 ex_52  i=$i_rt1_zn   j=$j_Cbot_zn
290           his 274 ex_52  i=$i_rt2_zn   j=$j_Atop_zn
291           his 275 ex_52  i=$i_rt2_zn   j=$j_Bunsat_zn
292           his 276 ex_52  i=$i_rt2_zn   j=$j_Bsat_zn
293           his 277 ex_52  i=$i_rt2_zn   j=$j_C1_zn
294           his 278 ex_52  i=$i_rt2_zn   j=$j_C2_zn
295           his 279 ex_52  i=$i_rt2_zn   j=$j_Cbot_zn
296           his 280 ex_52  i=$i_rt3_zn   j=$j_Atop_zn
297           his 281 ex_52  i=$i_rt3_zn   j=$j_Bunsat_zn
298           his 282 ex_52  i=$i_rt3_zn   j=$j_Bsat_zn
299           his 283 ex_52  i=$i_rt3_zn   j=$j_C1_zn
300           his 284 ex_52  i=$i_rt3_zn   j=$j_C2_zn
301           his 285 ex_52  i=$i_rt3_zn   j=$j_Cbot_zn
302           his 286 ex_52  i=$i_rt1_zn   j=1
303
304
305           ; volumetric strain increments (zone)
306           his 300 vsi  i=$i_lt1_zn   j=$j_Atop_zn
307           his 301 vsi  i=$i_lt1_zn   j=$j_Bunsat_zn
308           his 302 vsi  i=$i_lt1_zn   j=$j_Bsat_zn
309           his 303 vsi  i=$i_lt1_zn   j=$j_C1_zn
310           his 304 vsi  i=$i_lt1_zn   j=$j_C2_zn
311           his 305 vsi  i=$i_lt1_zn   j=$j_Cbot_zn
312           his 306 vsi  i=$i_lt2_zn   j=$j_Atop_zn
313           his 307 vsi  i=$i_lt2_zn   j=$j_Bunsat_zn
314           his 308 vsi  i=$i_lt2_zn   j=$j_Bsat_zn
315           his 309 vsi  i=$i_lt2_zn   j=$j_C1_zn
316           his 310 vsi  i=$i_lt2_zn   j=$j_C2_zn
317           his 311 vsi  i=$i_lt2_zn   j=$j_Cbot_zn
318           his 312 vsi  i=$i_lt3_zn   j=$j_Atop_zn
319           his 313 vsi  i=$i_lt3_zn   j=$j_Bunsat_zn
320           his 314 vsi  i=$i_lt3_zn   j=$j_Bsat_zn
321           his 315 vsi  i=$i_lt3_zn   j=$j_C1_zn
322           his 316 vsi  i=$i_lt3_zn   j=$j_C2_zn
323           his 317 vsi  i=$i_lt3_zn   j=$j_Cbot_zn
324           his 318 vsi  i=$i_rt1_zn   j=$j_Atop_zn
325           his 319 vsi  i=$i_rt1_zn   j=$j_Bunsat_zn
326           his 320 vsi  i=$i_rt1_zn   j=$j_Bsat_zn
327           his 321 vsi  i=$i_rt1_zn   j=$j_C1_zn
328           his 322 vsi  i=$i_rt1_zn   j=$j_C2_zn
329           his 323 vsi  i=$i_rt1_zn   j=$j_Cbot_zn
330           his 324 vsi  i=$i_rt2_zn   j=$j_Atop_zn
331           his 325 vsi  i=$i_rt2_zn   j=$j_Bunsat_zn
332           his 326 vsi  i=$i_rt2_zn   j=$j_Bsat_zn
333           his 327 vsi  i=$i_rt2_zn   j=$j_C1_zn
334           his 328 vsi  i=$i_rt2_zn   j=$j_C2_zn
335           his 329 vsi  i=$i_rt2_zn   j=$j_Cbot_zn
336           his 330 vsi  i=$i_rt3_zn   j=$j_Atop_zn
337           his 331 vsi  i=$i_rt3_zn   j=$j_Bunsat_zn
338           his 332 vsi  i=$i_rt3_zn   j=$j_Bsat_zn
339           his 333 vsi  i=$i_rt3_zn   j=$j_C1_zn
340           his 334 vsi  i=$i_rt3_zn   j=$j_C2_zn
341           his 335 vsi  i=$i_rt3_zn   j=$j_Cbot_zn
342           his 336 vsi  i=$i_rt1_zn   j=1
343
344           ; xxstrain (zone)
345           his 350 ex_53  i=$i_lt1_zn   j=$j_Atop_zn
346           his 351 ex_53  i=$i_lt1_zn   j=$j_Bunsat_zn
```

```
347           his 352 ex_53  i=$i_lt1_zn   j=$j_Bsat_zn
348           his 353 ex_53  i=$i_lt1_zn   j=$j_C1_zn
349           his 354 ex_53  i=$i_lt1_zn   j=$j_C2_zn
350           his 355 ex_53  i=$i_lt1_zn   j=$j_Cbot_zn
351           his 356 ex_53  i=$i_lt2_zn   j=$j_Atop_zn
352           his 357 ex_53  i=$i_lt2_zn   j=$j_Bunsat_zn
353           his 358 ex_53  i=$i_lt2_zn   j=$j_Bsat_zn
354           his 359 ex_53  i=$i_lt2_zn   j=$j_C1_zn
355           his 360 ex_53  i=$i_lt2_zn   j=$j_C2_zn
356           his 361 ex_53  i=$i_lt2_zn   j=$j_Cbot_zn
357           his 362 ex_53  i=$i_lt3_zn   j=$j_Atop_zn
358           his 363 ex_53  i=$i_lt3_zn   j=$j_Bunsat_zn
359           his 364 ex_53  i=$i_lt3_zn   j=$j_Bsat_zn
360           his 365 ex_53  i=$i_lt3_zn   j=$j_C1_zn
361           his 366 ex_53  i=$i_lt3_zn   j=$j_C2_zn
362           his 367 ex_53  i=$i_lt3_zn   j=$j_Cbot_zn
363           his 368 ex_53  i=$i_rt1_zn   j=$j_Atop_zn
364           his 369 ex_53  i=$i_rt1_zn   j=$j_Bunsat_zn
365           his 370 ex_53  i=$i_rt1_zn   j=$j_Bsat_zn
366           his 371 ex_53  i=$i_rt1_zn   j=$j_C1_zn
367           his 372 ex_53  i=$i_rt1_zn   j=$j_C2_zn
368           his 373 ex_53  i=$i_rt1_zn   j=$j_Cbot_zn
369           his 374 ex_53  i=$i_rt2_zn   j=$j_Atop_zn
370           his 375 ex_53  i=$i_rt2_zn   j=$j_Bunsat_zn
371           his 376 ex_53  i=$i_rt2_zn   j=$j_Bsat_zn
372           his 377 ex_53  i=$i_rt2_zn   j=$j_C1_zn
373           his 378 ex_53  i=$i_rt2_zn   j=$j_C2_zn
374           his 379 ex_53  i=$i_rt2_zn   j=$j_Cbot_zn
375           his 380 ex_53  i=$i_rt3_zn   j=$j_Atop_zn
376           his 381 ex_53  i=$i_rt3_zn   j=$j_Bunsat_zn
377           his 382 ex_53  i=$i_rt3_zn   j=$j_Bsat_zn
378           his 383 ex_53  i=$i_rt3_zn   j=$j_C1_zn
379           his 384 ex_53  i=$i_rt3_zn   j=$j_C2_zn
380           his 385 ex_53  i=$i_rt3_zn   j=$j_Cbot_zn
381           his 386 ex_53  i=$i_rt1_zn   j=1
382
383           ; Shear stress increments (zone)
384           his 450 sxy  i=$i_lt1_zn   j=$j_Atop_zn
385           his 451 sxy  i=$i_lt1_zn   j=$j_Bunsat_zn
386           his 452 sxy  i=$i_lt1_zn   j=$j_Bsat_zn
387           his 453 sxy  i=$i_lt1_zn   j=$j_C1_zn
388           his 454 sxy  i=$i_lt1_zn   j=$j_C2_zn
389           his 455 sxy  i=$i_lt1_zn   j=$j_Cbot_zn
390           his 456 sxy  i=$i_lt2_zn   j=$j_Atop_zn
391           his 457 sxy  i=$i_lt2_zn   j=$j_Bunsat_zn
392           his 458 sxy  i=$i_lt2_zn   j=$j_Bsat_zn
393           his 459 sxy  i=$i_lt2_zn   j=$j_C1_zn
394           his 460 sxy  i=$i_lt2_zn   j=$j_C2_zn
395           his 461 sxy  i=$i_lt2_zn   j=$j_Cbot_zn
396           his 462 sxy  i=$i_lt3_zn   j=$j_Atop_zn
397           his 463 sxy  i=$i_lt3_zn   j=$j_Bunsat_zn
398           his 464 sxy  i=$i_lt3_zn   j=$j_Bsat_zn
399           his 465 sxy  i=$i_lt3_zn   j=$j_C1_zn
400           his 466 sxy  i=$i_lt3_zn   j=$j_C2_zn
401           his 467 sxy  i=$i_lt3_zn   j=$j_Cbot_zn
402           his 468 sxy  i=$i_rt1_zn   j=$j_Atop_zn
403           his 469 sxy  i=$i_rt1_zn   j=$j_Bunsat_zn
404           his 470 sxy  i=$i_rt1_zn   j=$j_Bsat_zn
405           his 471 sxy  i=$i_rt1_zn   j=$j_C1_zn
406           his 472 sxy  i=$i_rt1_zn   j=$j_C2_zn
407           his 473 sxy  i=$i_rt1_zn   j=$j_Cbot_zn
408           his 474 sxy  i=$i_rt2_zn   j=$j_Atop_zn
409           his 475 sxy  i=$i_rt2_zn   j=$j_Bunsat_zn
```

```
410           his 476 sxy  i=$i_rt2_zn   j=$j_Bsat_zn
411           his 477 sxy  i=$i_rt2_zn   j=$j_C1_zn
412           his 478 sxy  i=$i_rt2_zn   j=$j_C2_zn
413           his 479 sxy  i=$i_rt2_zn   j=$j_Cbot_zn
414           his 480 sxy  i=$i_rt3_zn   j=$j_Atop_zn
415           his 481 sxy  i=$i_rt3_zn   j=$j_Bunsat_zn
416           his 482 sxy  i=$i_rt3_zn   j=$j_Bsat_zn
417           his 483 sxy  i=$i_rt3_zn   j=$j_C1_zn
418           his 484 sxy  i=$i_rt3_zn   j=$j_C2_zn
419           his 485 sxy  i=$i_rt3_zn   j=$j_Cbot_zn
420           his 486 sxy  i=$i_rt1_zn   j=1
421
422           ; pore pressure increments (zone)
423           his 500 pp  i=$i_lt1_zn   j=$j_Atop_zn
424           his 501 pp  i=$i_lt1_zn   j=$j_Bunsat_zn
425           his 502 pp  i=$i_lt1_zn   j=$j_Bsat_zn
426           his 503 pp  i=$i_lt1_zn   j=$j_C1_zn
427           his 504 pp  i=$i_lt1_zn   j=$j_C2_zn
428           his 505 pp  i=$i_lt1_zn   j=$j_Cbot_zn
429           his 506 pp  i=$i_lt2_zn   j=$j_Atop_zn
430           his 507 pp  i=$i_lt2_zn   j=$j_Bunsat_zn
431           his 508 pp  i=$i_lt2_zn   j=$j_Bsat_zn
432           his 509 pp  i=$i_lt2_zn   j=$j_C1_zn
433           his 510 pp  i=$i_lt2_zn   j=$j_C2_zn
434           his 511 pp  i=$i_lt2_zn   j=$j_Cbot_zn
435           his 512 pp  i=$i_lt3_zn   j=$j_Atop_zn
436           his 513 pp  i=$i_lt3_zn   j=$j_Bunsat_zn
437           his 514 pp  i=$i_lt3_zn   j=$j_Bsat_zn
438           his 515 pp  i=$i_lt3_zn   j=$j_C1_zn
439           his 516 pp  i=$i_lt3_zn   j=$j_C2_zn
440           his 517 pp  i=$i_lt3_zn   j=$j_Cbot_zn
441           his 518 pp  i=$i_rt1_zn   j=$j_Atop_zn
442           his 519 pp  i=$i_rt1_zn   j=$j_Bunsat_zn
443           his 520 pp  i=$i_rt1_zn   j=$j_Bsat_zn
444           his 521 pp  i=$i_rt1_zn   j=$j_C1_zn
445           his 522 pp  i=$i_rt1_zn   j=$j_C2_zn
446           his 523 pp  i=$i_rt1_zn   j=$j_Cbot_zn
447           his 524 pp  i=$i_rt2_zn   j=$j_Atop_zn
448           his 525 pp  i=$i_rt2_zn   j=$j_Bunsat_zn
449           his 526 pp  i=$i_rt2_zn   j=$j_Bsat_zn
450           his 527 pp  i=$i_rt2_zn   j=$j_C1_zn
451           his 528 pp  i=$i_rt2_zn   j=$j_C2_zn
452           his 529 pp  i=$i_rt2_zn   j=$j_Cbot_zn
453           his 530 pp  i=$i_rt3_zn   j=$j_Atop_zn
454           his 531 pp  i=$i_rt3_zn   j=$j_Bunsat_zn
455           his 532 pp  i=$i_rt3_zn   j=$j_Bsat_zn
456           his 533 pp  i=$i_rt3_zn   j=$j_C1_zn
457           his 534 pp  i=$i_rt3_zn   j=$j_C2_zn
458           his 535 pp  i=$i_rt3_zn   j=$j_Cbot_zn
459           his 536 pp  i=$i_rt1_zn   j=1
460
461           ; Ru (zone)
462           his 550 ex_33  i=$i_lt1_zn   j=$j_Atop_zn
463           his 551 ex_33  i=$i_lt1_zn   j=$j_Bunsat_zn
464           his 552 ex_33  i=$i_lt1_zn   j=$j_Bsat_zn
465           his 553 ex_33  i=$i_lt1_zn   j=$j_C1_zn
466           his 554 ex_33  i=$i_lt1_zn   j=$j_C2_zn
467           his 555 ex_33  i=$i_lt1_zn   j=$j_Cbot_zn
468           his 556 ex_33  i=$i_lt2_zn   j=$j_Atop_zn
469           his 557 ex_33  i=$i_lt2_zn   j=$j_Bunsat_zn
470           his 558 ex_33  i=$i_lt2_zn   j=$j_Bsat_zn
471           his 559 ex_33  i=$i_lt2_zn   j=$j_C1_zn
472           his 560 ex_33  i=$i_lt2_zn   j=$j_C2_zn
```

```
473           his 561 ex_33  i=$i_lt2_zn   j=$j_Cbot_zn
474           his 562 ex_33  i=$i_lt3_zn   j=$j_Atop_zn
475           his 563 ex_33  i=$i_lt3_zn   j=$j_Bunsat_zn
476           his 564 ex_33  i=$i_lt3_zn   j=$j_Bsat_zn
477           his 565 ex_33  i=$i_lt3_zn   j=$j_C1_zn
478           his 566 ex_33  i=$i_lt3_zn   j=$j_C2_zn
479           his 567 ex_33  i=$i_lt3_zn   j=$j_Cbot_zn
480           his 568 ex_33  i=$i_rt1_zn   j=$j_Atop_zn
481           his 569 ex_33  i=$i_rt1_zn   j=$j_Bunsat_zn
482           his 570 ex_33  i=$i_rt1_zn   j=$j_Bsat_zn
483           his 571 ex_33  i=$i_rt1_zn   j=$j_C1_zn
484           his 572 ex_33  i=$i_rt1_zn   j=$j_C2_zn
485           his 573 ex_33  i=$i_rt1_zn   j=$j_Cbot_zn
486           his 574 ex_33  i=$i_rt2_zn   j=$j_Atop_zn
487           his 575 ex_33  i=$i_rt2_zn   j=$j_Bunsat_zn
488           his 576 ex_33  i=$i_rt2_zn   j=$j_Bsat_zn
489           his 577 ex_33  i=$i_rt2_zn   j=$j_C1_zn
490           his 578 ex_33  i=$i_rt2_zn   j=$j_C2_zn
491           his 579 ex_33  i=$i_rt2_zn   j=$j_Cbot_zn
492           his 580 ex_33  i=$i_rt3_zn   j=$j_Atop_zn
493           his 581 ex_33  i=$i_rt3_zn   j=$j_Bunsat_zn
494           his 582 ex_33  i=$i_rt3_zn   j=$j_Bsat_zn
495           his 583 ex_33  i=$i_rt3_zn   j=$j_C1_zn
496           his 584 ex_33  i=$i_rt3_zn   j=$j_C2_zn
497           his 585 ex_33  i=$i_rt3_zn   j=$j_Cbot_zn
498           his 586 ex_33  i=$i_rt1_zn   j=1
499
500           ; CSR (tau/svc')
501           his 600 ex_45  i=$i_lt1_zn   j=$j_Atop_zn
502           his 601 ex_45  i=$i_lt1_zn   j=$j_Bunsat_zn
503           his 602 ex_45  i=$i_lt1_zn   j=$j_Bsat_zn
504           his 603 ex_45  i=$i_lt1_zn   j=$j_C1_zn
505           his 604 ex_45  i=$i_lt1_zn   j=$j_C2_zn
506           his 605 ex_45  i=$i_lt1_zn   j=$j_Cbot_zn
507           his 606 ex_45  i=$i_lt2_zn   j=$j_Atop_zn
508           his 607 ex_45  i=$i_lt2_zn   j=$j_Bunsat_zn
509           his 608 ex_45  i=$i_lt2_zn   j=$j_Bsat_zn
510           his 609 ex_45  i=$i_lt2_zn   j=$j_C1_zn
511           his 610 ex_45  i=$i_lt2_zn   j=$j_C2_zn
512           his 611 ex_45  i=$i_lt2_zn   j=$j_Cbot_zn
513           his 612 ex_45  i=$i_lt3_zn   j=$j_Atop_zn
514           his 613 ex_45  i=$i_lt3_zn   j=$j_Bunsat_zn
515           his 614 ex_45  i=$i_lt3_zn   j=$j_Bsat_zn
516           his 615 ex_45  i=$i_lt3_zn   j=$j_C1_zn
517           his 616 ex_45  i=$i_lt3_zn   j=$j_C2_zn
518           his 617 ex_45  i=$i_lt3_zn   j=$j_Cbot_zn
519           his 618 ex_45  i=$i_rt1_zn   j=$j_Atop_zn
520           his 619 ex_45  i=$i_rt1_zn   j=$j_Bunsat_zn
521           his 620 ex_45  i=$i_rt1_zn   j=$j_Bsat_zn
522           his 621 ex_45  i=$i_rt1_zn   j=$j_C1_zn
523           his 622 ex_45  i=$i_rt1_zn   j=$j_C2_zn
524           his 623 ex_45  i=$i_rt1_zn   j=$j_Cbot_zn
525           his 624 ex_45  i=$i_rt2_zn   j=$j_Atop_zn
526           his 625 ex_45  i=$i_rt2_zn   j=$j_Bunsat_zn
527           his 626 ex_45  i=$i_rt2_zn   j=$j_Bsat_zn
528           his 627 ex_45  i=$i_rt2_zn   j=$j_C1_zn
529           his 628 ex_45  i=$i_rt2_zn   j=$j_C2_zn
530           his 629 ex_45  i=$i_rt2_zn   j=$j_Cbot_zn
531           his 630 ex_45  i=$i_rt3_zn   j=$j_Atop_zn
532           his 631 ex_45  i=$i_rt3_zn   j=$j_Bunsat_zn
533           his 632 ex_45  i=$i_rt3_zn   j=$j_Bsat_zn
534           his 633 ex_45  i=$i_rt3_zn   j=$j_C1_zn
535           his 634 ex_45  i=$i_rt3_zn   j=$j_C2_zn
```

```
536           his 635 ex_45  i=$i_rt3_zn   j=$j_Cbot_zn
537           his 636 ex_45  i=$i_rt1_zn   j=1
538
539       endcommand
540   end
541
542
543   ;-------------------------------------------------------------------------
544   ; Prepare histories for dynamic loading
545   ;-------------------------------------------------------------------------
546
547   hist 1 dytime ; setting time history (in actual seconds)
548   hist nstep = $n ; set up recording times
549
550   ; set calculations to begin at first calculation step
551   set fishcall 0 $set_evs
552
553
554   ;-------------------------------------------------------------------------
555   ; Calculate table of displacements and extensional strains along ground surface
556   ; - Other calcs can be performed here depending on parameters of interests
557   ;-------------------------------------------------------------------------
558
559   def $disp_table
560       $rownum = int(501) ; number table rows (need later for printing table)
561       float $grnd_disp ; prepare array as float
562       array $grnd_disp(4,501) ; array of x-value, rel x-disp, rel y-disp, exx
563       $steps = $steps + 1 ; only calculate when recording $n apart
564       if $steps > $n; as before
565           $steps = 0
566           loop $i (1,501) ; loop through all surface zones
567               $grnd_disp(1,$i) = x($i,$jrowP1) ; x-value
568               $grnd_disp(2,$i) = xdisp($i,$jrowP1)-xdisp($i,1) ; rel x-disp
569               $grnd_disp(3,$i) = ydisp($i,$jrowP1)-ydisp($i,1) ; rel y-disp
570               $grnd_disp(4,$i) = ex_53($i,$jrow)*100 ; x-tens
571           endloop
572       endif
573   end
574   $disp_table
575   set fishcall 15 $disp_table ; this calls calculation step for table values
576
577
578   $store_hist ; activate histories
```

```
;-------------------------------------------------------------------------
; About: Stochastic NDA Workflow - (6) Dynamic analysis
; By: Patrick Bassal, Oct 2021
; Project: Wynne Ave
;-------------------------------------------------------------------------
; Notes:
; - This calculation reads in the time histories, sets parameters for dynamic
; analyses, runs analyses, and sets output results tables.
; - All values here-in are site-dependent and subject to modeler
interpretations.
;-------------------------------------------------------------------------

;-------------------------------------------------------------------------
; Read velocities from input motions
; - Must be single column with header
;-------------------------------------------------------------------------

hist read 901 USC003_NR_S_vel_FLAC.txt
hist read 902 USC003_NR_Vert_vel_FLAC.txt


;-------------------------------------------------------------------------
; Prepare modeling parameters and input ground motion
;-------------------------------------------------------------------------

;set corr_ffrot on ; prevent rotation if all boundaries are quiet (not used for
Wynne)
water density $rho_w bulk $kw tension= 1.0e5; 100 kPa limit capillary rise
during shaking
                    ; Some elements go to 0 sat, but this is better than large
                    neg pp zone
set dyn on mech on flow on ; coupled flow
set large ; large strains

def $EQinput ; input motion from shear stress wave [dens*Vs*particlevel(time
series)]
    $dens= density(1,1) + $rho_w*porosity(1,1) ; total density at base
    $Vs= sqrt(shear_mod(1,1)/$dens) ; s-wave velocity at base
    $Vp=1600 ; p-wave velocity for vertical motion (assume saturated at input
    location)
    $units= 1.0 ; conversion factor based on input units
    $shakedir= 1.0 ; -1.0 for positive direction, +1.0 to flip (want North for
    Wynne)
    $ampscale= 1.00 ; additional scaling term
    $EQConst= $dens*$Vs*$units*$shakedir*$ampscale ; full (2A) outcrop mtn as
    input wave
    $EQConstVert= $dens*$Vp*$units*$shakedir*$ampscale ; similar for vertical
    motion
    command
        ; Attach side boundaries (uses periodic boundary condition):
        free x y i=1 j=2,$jrowP1 ; free then attach mesh sides (except base
        grid pts)
        free x y i=$icolP1 j=2,$jrowP1
        attach  aside from 1,2  to 1,$jrowP1 &
                bside from $icolP1,2 to $icolP1,$jrowP1
        fix y j=1   ; fixing model base (helps prevent displacements)

        ; ALTERNATIVE: Next line for free-field side boundaries (not used for
        Wynne)
        ;apply ffield           ; undoes all prior fixed conditions

        apply ss $EQConst hist 901 i=1,$icolP1 j=1 ; shear stress time history
        apply ns $EQConstVert hist 902 i=1,$icolP1 j=1 ; normal stress time
```

```
        history
        apply squiet nquiet i=1,$icolP1 j=1 ; compliant/viscous base (normal
        and shear)

    endcommand
end
$EQinput


;------------------------------------------------------------------------------
; Export results to output file
; - function below outputs displacements and lateral strain along top of model
; - this reads and writes $grnd_disp array from previous FLAC modeling code (5).
;------------------------------------------------------------------------------

def $disp_export
    array $data(1,1)
    status = open($dispfile,1,1)
    $data(1,1) = 'x(m),relxdisp(m),relydisp(m),exx(%)'
    status = write($data,1)
    loop $num (1,$rownum)
        $data(1,1)=string($grnd_disp(1,$num))+'  '+string($grnd_disp(2,$num))
        $data(1,1)=$data(1,1)+'  '+string($grnd_disp(3,$num))+'  '+string($
        grnd_disp(4,$num))
        status = write($data,1)
    endloop
    status = close
end


;------------------------------------------------------------------------------
; Run dynamic model!
; - Loop is performed to output save files and results
;------------------------------------------------------------------------------

def $solveEQ ; loop and save increments during shaking
    $time = 0
    loop $nt (1,3) ; loop for 3 saves every 6s (for 18s motion)
        $time = $time + 6.0 ; set time steps for saving results
        $intdt = int($time) ; ensures integer value
        $fname = '.\R' + string($nreal) + '\$Save_' + string($intdt) + '.sav'
        ; assign folder and name for save file (.sav)
        $dispfile = '.\R' + string($nreal) + '\disp_'+string($intdt)+'.txt'
        ; assign folder and name for results table file (.txt)
        command
            solve dytime $time ; solve to next time step
            $disp_export ; fish code to write table
            save @$fname ; save during shaking
        endcommand
    endloop
end
$solveEQ
```

```
;-------------------------------------------------------------------------
; About: Batch program to run FLAC with alternate geostatistical realizations
; By: Patrick Bassal, Oct 2021
; Project: Wynne Ave
;-------------------------------------------------------------------------
; Notes:
; - Below code is repeated for each realization
;   - Nested loops of FISH or Restore within a FISH function not allowed
; - Input tables cannot exceed 200 characters in length
;   - This limits batch run with current file structure to < ~15 realizations
;-------------------------------------------------------------------------

; Run first 3 FISH files that are common for each realization:
call 1_mesh.fis
call 2_initialize_MC.fis
call 3_static_MC.fis

; Repeat below code for each realization:
restore 3_static_MC.sav
def $sim
    $nreal = int(1)
end
$sim

call 4_static_PM4.fis
save .\R1\4_static_PM4.sav
call 5_dyn_hist.fis
call 6_dynflow.fis
new
;-----------------------------------

restore 3_static_MC.sav
def $sim
    $nreal = int(2)
end
$sim

call 4_static_PM4.fis
save .\R2\4_static_PM4.sav
call 5_dyn_hist.fis
call 6_dynflow.fis
new
;-----------------------------------

restore 3_static_MC.sav
def $sim
    $nreal = int(3)
end
$sim

call 4_static_PM4.fis
save .\R3\4_static_PM4.sav
call 5_dyn_hist.fis
call 6_dynflow.fis
new
;-----------------------------------

restore 3_static_MC.sav
def $sim
    $nreal = int(4)
end
$sim

```

```
call 4_static_PM4.fis
save .\R4\4_static_PM4.sav
call 5_dyn_hist.fis
call 6_dynflow.fis
new
;-----------------------------------

restore 3_static_MC.sav
def $sim
    $nreal = int(5)
end
$sim

call 4_static_PM4.fis
save .\R5\4_static_PM4.sav
call 5_dyn_hist.fis
call 6_dynflow.fis
new
;-----------------------------------

restore 3_static_MC.sav
def $sim
    $nreal = int(6)
end
$sim

call 4_static_PM4.fis
save .\R6\4_static_PM4.sav
call 5_dyn_hist.fis
call 6_dynflow.fis
new
;-----------------------------------

restore 3_static_MC.sav
def $sim
    $nreal = int(7)
end
$sim

call 4_static_PM4.fis
save .\R7\4_static_PM4.sav
call 5_dyn_hist.fis
call 6_dynflow.fis
new
;-----------------------------------

restore 3_static_MC.sav
def $sim
    $nreal = int(8)
end
$sim

call 4_static_PM4.fis
save .\R8\4_static_PM4.sav
call 5_dyn_hist.fis
call 6_dynflow.fis
new
;-----------------------------------

restore 3_static_MC.sav
def $sim
    $nreal = int(9)
end
```

```
$sim

call 4_static_PM4.fis
save .\R9\4_static_PM4.sav
call 5_dyn_hist.fis
call 6_dynflow.fis
new
;-----------------------------------

restore 3_static_MC.sav
def $sim
    $nreal = int(10)
end
$sim

call 4_static_PM4.fis
save .\R10\4_static_PM4.sav
call 5_dyn_hist.fis
call 6_dynflow.fis
new
;-----------------------------------
```